# JOURNAL OF THEORETICAL AND APPLIED MECHANICS

The journal content is indexed in Similarity Check, the Crossref initiative to prevent plagiarism.

✶ ✶ ✶ ✶ ✶

✶ ✶ ✶ ✶ ✶

# FAULTS DETECTION IN GAS TURBINE ROTOR USING VIBRATION ANALYSIS UNDER VARYING CONDITIONS

Benrabeh Djaidir, Ahmed Hafaifa, Abdallah Kouzou

*Applied Automation and Industrial Diagnostics Laboratory, Faculty of Science and Technology, University of Djelfa, Algeria*
*e-mail: b.djaidir@univ.djelfa.dz; hafaifa.ahmed.dz@ieee.org; kouzouabdellah@ieee.org*

Monitoring of rotating machines is a very important task in most industrial sectors, which requires a chosen number of performance indicators during the exploitation of such kind of equipments. Indeed, for understanding the undesirable phenomena complexity of the industrial systems under operation, a reliable and an accurate mathematical modeling is required to ensure the diagnosis and the control of these phenomena. This work proposes development of a fault monitoring system of a gas turbine type GE MS 3002 based on vibration analysis technique using spectral analysis tools. The obtained results prove the effectiveness of the presented monitoring tool approach which is applied on the gas turbine, for avoiding the operation under vibration mode and for generating optimal performance during the exploitation of the gas turbine.

*Keywords:* default bearings, dynamic behavior, faults detection, gas turbine, monitoring system

## 1. Introduction

Vibration analysis of rotating machines in industrial plants is widely used to ensure premature faults diagnosis before these machines may break down. Gas turbines are the most important pivotal rotating machines belonging to the family of internal combustion engines that are used intensively in oil and gas industrial plants. Indeed, it is used to achieve the main function of generating mechanical energy in form of shaft rotation from kinetic energy of gases produced in the combustion chamber (Djaidir *et al.*, 2015, 2016; Djeddi *et al.*, 2015, 2016; Eshati *et al.*, 2013; Jurado and Carpio, 2006; Kim *et al.*, 2011). However, these machines are subject to some phenomena inducing important vibrations that can be very critical to their mechanical state.

The work presented in this paper proposes a supervision approach based on vibration analysis, to ensure a permanent fault diagnosis of the studied gas turbine, where the main aim is to prevent failures that may cause malfunctions and to fulfill an optimal operation availability of such a machine. Indeed, there are several methods that have been used for characterization and modeling of the gas turbine parameters. However, these methods are less exploitable for the control of such systems due to its complexity. The proposed approach in this work is based on the analysis of the magnitude and the harmonics spectrum of signals resulting from measured vibrations on the gas turbine under different failures that may affect this kind of machine during its normal operation.

Gas turbines are widely used in many industrial applications such as oil industry where they are mainly used for wells re-injection and gas transportation along the pipelines. These machines are subject to various instability factors that are influencing directly their operating performances. Therefore, in order to improve the performances of these systems, many researches previously built mathematical models that represent the real time operation state more accurately and instantaneously. Madhavan *et al.* (2014) developed a vibration model based on

damage detection of rotor blades in a gas turbine engine. They showed that the developed model can be used to carry out the analysis of mechanical components failures detection of the system under study. Liu *et al.* (2015) studied the influence of large scale wind turbine blade vibration based on the influence of the aerodynamic effects. Usman *et al.* (2015) presented the impact of operating conditions and exhaust gas recirculation on the performance of rotors dynamics of a gas turbine system. However, the current development of new technologies has allowed researchers and industrial practices to improve the performance of gas turbines and to contribute effectively to developing new methods and algorithms for controlling of such systems. In this context, many industrial monitoring systems are being developed by several researchers to ensure fault detection, as well as for the diagnosis of defects (Ali *et al.*, 2015; Djaidir *et al.*, 2015, 2016; Djeddi *et al.*, 2015, 2016; Günyaz, 2013; Krzyzynski *et al.*, 2000; Liu *et al.*, 2015; Sanaye and Tahani, 2010; Simani and Patton, 2008).

The present paper deals with the modeling of gas turbine defects based on vibration analysis using mathematical techniques, where a number of assumptions representing different operating parameters of the studied gas turbines have been taken into account. In this paper, the analysis of dynamic behavior of rotor vibration of the gas turbine type GE MS 3002 is proposed. This gas turbine rotates at high speed up to 7100 tr/min and it is supported by bearings that may be subject to faults during normal operation, which may contribute directly to the deterioration of the gas turbine in a rapid manner.

The obtained in this paper results show clearly the effectiveness of the presented modeling of the defects in a gas turbine. The presented approach allows one to build a diagnostic strategy based on the vibration behavior analysis. On the other side, the experimental procedure for tracking the anomalies in the gas turbine is presented. It is based on the use of the obtained vibration signal spectrum and the associated analysis.

## 2. Dynamic vibration behavior in gas turbine

Gas turbines are heavily utilized in industry, where they are used mainly for producing and ensuring important mechanical energy (Ford *et al.*, 2013; Guasch, 2013; Lee *et al.*, 2013; Rahmoune *et al.*, 2015). They are used for driving of fixed appliances where important output power is required such as in electrical power generator, in powerful compressors, in powerful pumps, etc. Therefore, the analysis of dynamic behavior of the gas turbine is attracting much attention from the researcher and industrialists. It is based on the study of vibration behavior of the main element of the gas turbine which is the high pressure rotor (HP) (Madhavan *et al.*, 2014; Rahmoune *et al.*, 2015).

The vibration signal is presented by the following expression

$$x(t) = A\sin(wt + \phi) \tag{2.1}$$

where $w$ is the frequency of vibration, $\phi$ is the phase and $A$ the amplitude of vibration in micrometers [$\mu$m].

The vibration speed $\nu(t)$ and the vibration acceleration $a(t)$ are obtained by differentialing vibration expression (2.1) as follows

$$\nu(t) = \frac{dx(t)}{dt} = Aw\cos(wt + \phi) \qquad a(t) = \frac{d\nu(t)}{dt} = -Aw^2\sin(wt + \phi) \tag{2.2}$$

Practically, all units are based on millimeters and seconds.

Based on equations (2.1) and (2.2), the following expressions can be deduced

$$|x| = \frac{|\nu|}{w} = \frac{|a|}{w^2} \qquad |\nu| = |x|w = \frac{|a|}{w} \qquad |a| = |\nu|w = |x|w^2 \tag{2.3}$$

where $x$ is the displacement, $\nu$ is the vibration speed, $a$ is the vibration acceleration and $w$ is the frequency of vibration.

Equation (2.3) highlights the importance of the choice of physical variables for data measurement and monitoring of the gas turbine. Compared to the model based on speed measurement, the displacement measurements are used to reduce the high and the medium frequency vibration effects, which can amplify the low frequency vibration components. In this case, radial vibrations in the gas turbine are studied in the simple case of a circular cross-section of the rotor in the transverse position.

The dominant torsional displacement is the rotation of the cross sections given by the angular displacement $\alpha$. The simplified displacement is used as follows

$$\begin{aligned}
&u_1(x_1, x_2, x_3, t) \approx 0 \qquad u_2(x_1, x_2, x_3, t) \approx -x_3\alpha(x_1, t) \\
&u_3(x_1, x_2, x_3, t) \approx x_2\alpha(x_1, t)
\end{aligned} \tag{2.4}$$

For the deformation calculations, the Hamilton functional is used

$$\varepsilon_{11} = \varepsilon_{22} = \varepsilon_{33} = \varepsilon_{23} \qquad \varepsilon_{12} = -\frac{1}{2}x_3\frac{\partial\alpha}{\partial x_1} \qquad \varepsilon_{13} = \frac{1}{2}x_2\frac{\partial\alpha}{\partial x_1} \tag{2.5}$$

The Hamilton functional construction is given by the following equation

$$H(\alpha) = \int\limits_{t_0}^{t_1}\int\limits_{0}^{l}\left[\frac{1}{2}\rho I_1\left(\frac{\partial\alpha}{\partial t}\right)^2 - \frac{1}{2}GI_1\left(\frac{\partial\alpha}{\partial x_2}\right)^2 + M_1\alpha\right] dx_1\, dt$$

$$I_1 = \int\limits_{S}(x_2^2 + x_3^2)\, dx_2\, dx_3 \tag{2.6}$$

The rotor motion is given by

$$\rho I_1\frac{\partial^2\alpha}{\partial^2 t^2} - \frac{\partial}{\partial x_1}\left(GI_1\frac{\partial\alpha}{\partial x_1}\right) = M_1 \qquad \forall x_1 \in [0, l], \quad \forall t \in \Re \tag{2.7}$$

where $G = E/[2(1 + \nu)]$ is the shear modulus of the rotor in the limitat conditions $x_1 = 0$ and $x_1 = l$

$$\begin{aligned}
&\alpha(0, t) = 0 \qquad GI_1\frac{\partial\alpha}{\partial x_1}(0, t) = 0 \\
&\alpha(l, t) = 0 \qquad GI_1\frac{\partial\alpha}{\partial x_1}(l, t) = 0
\end{aligned} \tag{2.8}$$

The conditions in the initial state are given by $\alpha = 0$ and the condition $GI_1 = \partial\alpha/\partial x_1 = 0$ when no torsion at the free end is provided. The stress on the rotor surface is determined by using the following equation

$$\begin{bmatrix} \sigma_{11} \\ \sigma_{22} \\ \sigma_{33} \\ \sigma_{23} \\ \sigma_{13} \\ \sigma_{12} \end{bmatrix} = \begin{bmatrix} E & \nu E & \nu E & 0 & 0 & 0 \\ \nu E & E & \nu E & 0 & 0 & 0 \\ \nu E & \nu E & E & 0 & 0 & 0 \\ 0 & 0 & \frac{E}{2(1+\nu)} & 0 & 0 & 0 \\ 0 & 0 & 0 & \frac{E}{2(1+\nu)} & 0 & 0 \\ 0 & 0 & 0 & 0 & 0 & \frac{E}{2(1+\nu)} \end{bmatrix} \begin{bmatrix} 0 \\ 0 \\ 0 \\ -x_3\alpha_{x_1} \\ -x_2\alpha_{x_1} \\ 0 \end{bmatrix} \tag{2.9}$$

In practice, gas turbines systems are complex and are generally non-stationary. Consequently, their non-linear behavior makes the modeling step of the vibrations very difficult. Hence, implementation of a reliable predictive tool is required to ensure the control and the diagnosis of

such systems. For this purpose, vibration analysis techniques are used, tested and validated in this paper.

The vibration analysis used is based on the real vibration data collected on the studied gas turbine at different phases of operation. For the present application, the points of measurements are shown in Fig. 1, where a moving accelerometer is used for these measurements for both levels. Indeed, there are three sensors that are used with accelerometers on different positions (horizontal, vertical and axial) at each level, as shown in Fig. 1.
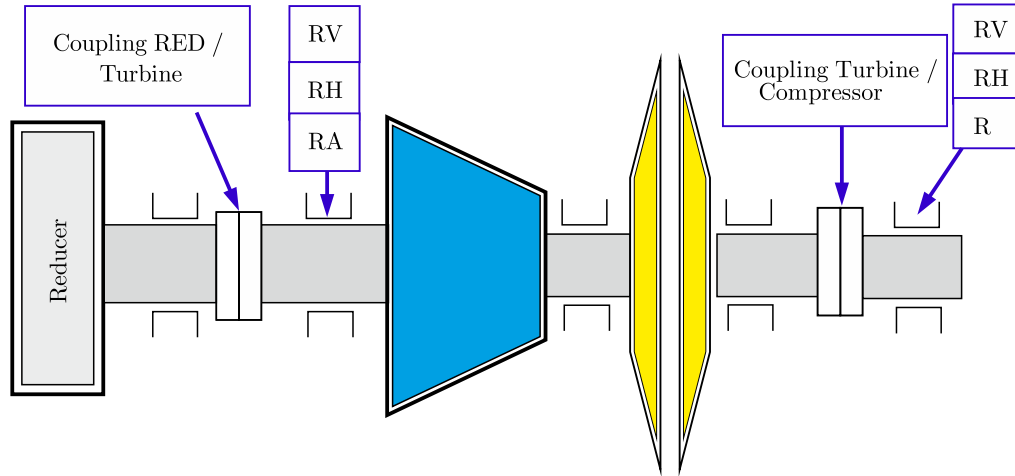


Fig. 1. Experimental installation of the gas turbine system

The recorded vibrations of the studied gas turbine can be quantified by three fundamental quantities. The displacement, the speed and the acceleration. The model considered comprises two entrances, the room temperature and the fuel mass flow rate which is expressed as follows

$$\dot{m}_c = \sqrt{\Delta P}\frac{1}{2}\rho\mu^2 = \frac{\sqrt{\Delta P}}{k} \ \Rightarrow \ \dot{m}_c = \frac{1}{k}\sqrt{\Delta P} \tag{2.10}$$

The air mass flow $\dot{m}_a$ is given by

$$\begin{aligned}\dot{m}_a &= k'(P_2 - P_1)\\\dot{m}_a &= k'(PCD - P_{atm})\end{aligned} \tag{2.11}$$

It is necessary to control the combustion of the gas turbine by regulating the ratio of the efficiency $F$ given by

$$F = \frac{T_3 - T_2}{\eta_b CV + T_3} \tag{2.12}$$

The sensors are installed on the gas turbine to provide dynamic behavior measurements of the high pressure (HP) turbine shaft speed, the low pressure (BP) turbine shaft speed and the temperature of the blades.

## 3. Gas turbine parameters modelling and analysis

All the rotating machines used in different industries applications are subject to more or less vibrations. These vibrations are due basically to poor distribution of mobile masses, especially in the rotor, which is essentially caused by imperfect machining during their fabrication or a lack of homogeneity of the metal constituting the rotor. Indeed, the origin of vibrations observed in a gas turbine can be caused by different phenomena such as (Galindo *et al.*, 2013; Günyaz, 2013; Krzyzynski *et al.*, 2000):

- Unbalance of the rotor,
- Rapid braking of the shaft,
- A mechanical failure; such as a broken blade,
- Permanent deformation of the rotor.

The rotating part of the gas turbine consists of two shafts on which several wheels holding the blades are mounted, where the line connection between the bodies of the two shafts is ensured by bearings. Therefore, vibration behavior of such machines extremely depends on these components. It is obvious that each such rotating machine is exposed to dynamic excitations extremely diverse and specific to its mode of operation. At the same time, the fixed and moving parts are vibrating structures, depending on their modal characteristics and their vibration damping capacities. Each part of the system (fixed or mobile) generates dynamic vibration constraints that cause fatigue of the rotating machine parts. It is impossible for a rotating machine which is designed, even with more and more advanced materials, not to vibrate. However, the manufacturers of such machines try to improve the quality of materials and design to built rotating machines that can support more severe vibration constraints.

The research work presented in this paper allows modeling and analysis of dynamic vibration based on the spectral analysis by considering various defects that may occur in this type of machines.

### 3.1. Spectral analysis

The Fourier Transform (FT) can convert a periodical signal into a series sum (which may be infinite) of sine and cosine functions. Suppose a real signal $x(t)$ is defined with a finite energy. The Fourier Transform of the signal $x(t)$ is defined by the following equation

$$FT_f\{x(t)\} = X(f) = \langle x(t), e^{2\pi i f t} \rangle = \int\limits_{-\infty}^{+\infty} x(t)e^{-2\pi i f t} \, dt \tag{3.1}$$

A discrete signal $x(k)$ of length $N$ presenting the number of values during a fixed interval, can be presented as follows

$$X(m) = \sum_{k=0}^{N-1} x(k)e^{-\frac{2\pi i m k}{N}} \tag{3.2}$$

On the other side, the spectrum of an aperiodic signal is given by its FT

$$X(\omega) = FT[x(t)] \tag{3.3}$$

where $FT[x(t)]$ is spectrum of $x(t)$.

The spectral energy density (SED) in the case of a discrete signal is defined through the discrete Fourier transform as follows

$$P_x(m) = |x(m)|^2 \qquad S_x(m) = |X(m)| \tag{3.4}$$

It can be shown that the energy of the signal, which is defined as the integral energy transferred at each instant $x(t)$, which can also be expressed as the integral of energy contributions carried by each frequency given by

$$E = \int\limits_{-\infty}^{+\infty} |x(t)|^2 \, dt = \int\limits_{-\infty}^{+\infty} |x(\omega)|^2 \frac{d\omega}{2\pi} = \int\limits_{-\infty}^{+\infty} |x(f)|^2 \, df \tag{3.5}$$

The energy spectrum of the signal is replaced by the square module of the FT of the square module of $c_n$ by the spectrum of energy $|x(\omega)|^2 = |x(f)|^2$ of $x(t)$ with $\lim_{T\to\infty} T c_n = \left| \int_{-\infty}^{+\infty} x(t) e^{-i\omega t} \, dt \right|$.

In this paper, the estimation method of the spectral density is proposed for the vibration faults detection and isolation in gas turbine. This method presents a good spectral analysis tool from the point of view of calculation and allows obtaining good results for a large class of signals in the studied gas turbine.

### 3.2. Vibration analysis

As mentioned previously, the gas turbines are subject to unstable phenomena, because the shaft cannot be perfectly balanced. The presence of residual unbalance on the shaft line is counted by adding point masses. The addition of a large unbalance to the shaft is explained by the loss of a blade on one of the disks. The imbalance is characterized by its kinetic energy when the mass $m_b$ is located at the point $B$ in the plane of the disk at a distance $d$ from its geometric centre $C$, Fig. 2.
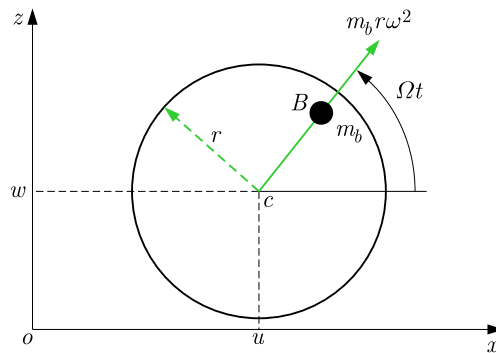


Fig. 2. Centrifugal forces due to unbalance

The coordinates of the unbalance in the fixed coordinate system are given by

$$x(t) = u_B + d\cos\Omega t \quad \Rightarrow \quad \frac{x(t)}{dt} = u_b - d\Omega\sin\Omega t$$
$$z(t) = w_B + d\sin\Omega t \quad \Rightarrow \quad \frac{z(t)}{dt} = w_b + d\Omega\cos\Omega t \tag{3.6}$$

Its kinetic energy is given by

$$T_{Bal} = \frac{1}{2}m_b[(\dot{u}_B^2 + \dot{w}_B^2) + \Omega^2 d^2 + 2\Omega d\dot{u}_B\sin\Omega t - 2\Omega d\dot{w}_B\cos\Omega t] \tag{3.7}$$

The term $\Omega^2 d^2/2$ is constant and will not intervene in the equations. The mass of the imbalance is negligible in comparison to the rotor mass; the expression of the kinetic energy can be approximated by

$$T_{Bal} \approx m_b d\Omega(\dot{u}_B\sin\Omega t - \dot{w}_B\cos\Omega t) \tag{3.8}$$

By introducing the generalized coordinates, it can be rewritten as follows

$$T_{Bal} \approx m_b d\Omega(\dot{A}_u\dot{Y}_B^3 + \dot{B}_u Y_B^2 + \dot{C}_u Y_B^2 + \dot{D}_u)\sin\Omega t - (\dot{A}_w\dot{Y}_B^3 + \dot{B}_w Y_B^2 + \dot{C}_w Y_B^2 + \dot{D}_w)\cos\Omega t \tag{3.9}$$

The unbalance generates strong vibrations at the operational rotation speed of the turbine. They appear when the gravity axis of the rotor (equilibrium mass axis) does not correspond to its axis

of rotation. This unbalance is caused by an inhomogeneous distribution of mass around the axis of rotation. In the case of turbocharger stationary motion, where the bearing part is used to guide the rotating shaft and the radial load is small and comprised primarily of the unbalance, which may be reduced if necessary. On the other side, the ball bearing damage causes several major factors; such as surface material fatigue as a result of constraints that produce flaking and cracking. Furthermore, the superficial fatigue can be aggravated by some effects such as insufficient lubrication, surface conditions, shock. Also for the elements in contact, the wear can aggravate the unstable phenomena during the operation of the machine.

For a ball bearing, Fig. 3, it comprises $n_b$ number of balls, and rotates at the frequency $f_r$ (shaft rotation frequency). The presence of a vibration defect creates shocks between the rotating elements of the channel whose frequencies are defined by the expressions in equations (3.9) and (3.14).



With D: ball center diameter, d: the ball diameter: $\varphi$ contact angle between the ball and the raceway
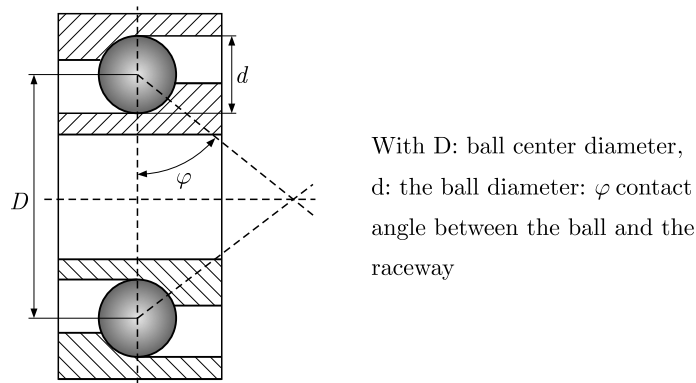
Fig. 3. Geometric characteristics of the bearing

The frequencies relative to the defects on each rotating elements are functions of the passage frequency of the rotating element in the outer ring. It is given by the following equation

$$f_{be} = \frac{f_r n_b}{2}\Big(1 - \frac{d}{D}\cos\phi\Big) \tag{3.10}$$

The passage frequency of the rotating element in the defected inner ring, is given by the following equation

$$f_{bi} = \frac{f_r n_b}{2}\Big(1 + \frac{d}{D}\cos\phi\Big) \tag{3.11}$$

The defects frequency on the ball are given by

$$f_B = \frac{f_r n_b}{2}\Big[1 - \Big(\frac{d}{D}\cos\phi\Big)^2\Big] \tag{3.12}$$

The passage frequency of the defected ball in the outer ring or in the inner ring is presented as follows

$$f_c = \frac{f_r}{2}\Big[1 - \Big(\frac{d}{D}\cos\phi\Big)\Big] \tag{3.13}$$

Taking into account the modulation of the signal by the frequency $f_c$, the above equations are modified, so the defects in the inner ring become

$$f_{bi} = \frac{f_r n_b}{2}\Big(1 + \frac{d}{D}\cos\phi\Big) \pm f_c \tag{3.14}$$

And the defects on the ball are expressed as

$$f_B = \frac{f_r n_b}{2}\Big[1 - \Big(\frac{d}{D}\cos\phi\Big)^2\Big] \pm f_c \qquad (3.15)$$

This signal modulation leads to functional modeling imperfections of the examined gas turbine. In the following Section, the proposed approach based on spectral analysis at a low range frequency will be applied to a practical case which is considered in a real machine in the presence of an unbalance anomaly.

## 4. Industrial investigations

In this study of the vibration behavior based on the analysis of measured signals on a gas turbine installed in the gas center of TIMZHERT, at Hassi R-Mel, south of Algeria, has been examined. Figure 4 shows the studied gas turbine with the specifications given in Table 1. This machine undergoes vibration effects observed during its operation. The measurements were carried out on this turbine via a mobile accelerometer for ensuring diagnosis of various vibration phenomena occuring at bearing No. 1 of the studied gas turbine. While guaranteeing the maintenance policy, vibrations are measured, processed and used for diagnosis to assess mechanical conditions of the examined turbine.
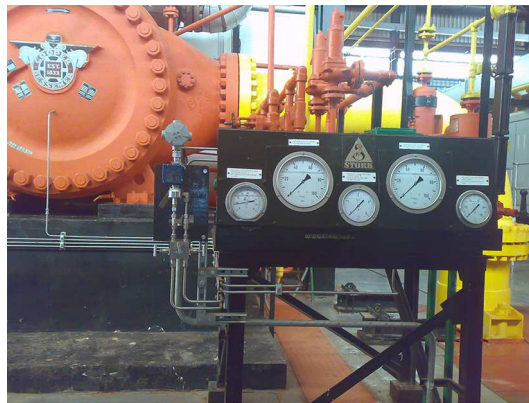


Fig. 4. Studied GE 3002 gas turbine

**Table 1.** Specifications of the examined turbine

| Parameter | Value or symbol |
|---|---|
| Designer: General Electric | GE |
| Type | MS 3002 |
| Serial No. | 226293 |
| HP speed axial compressor | 7100 tr/min |
| No. floor wheel (s) HP | 01 |
| No. axial compressor stage | 15 |
| BP speed | 6500 tr/min |
| No. BP wheel | 01 |
| Turbine power 80% | 9400 CV |
| Fuel consumption rate (100%H 27°C) | 3.84 m³/h |
| Pressure of exhaust gas | 1009.3 bars |
| global peas | 63000 k |

### 4.1. Applications results

In this Section, the obtained experimental results using the measurements performed on the studied gas turbine are presented. The results were performed on each bearing (bearing 1 and 4) in the vertical direction and with a rotation speed of the shaft $\omega = 7100 \, \text{tr/min}$. The characteristic frequencies of the bearing defects are listed in Table 2. The values given in Table were drawn on the basis of dimensions of the bearing and on the basis of rotation frequency of the shaft, using the frequency $f_r = V \, (\text{tr/min})/60 \, \text{s} = 7100/60 = 118.33 \, \text{Hz}$ (where $V$ is the shaft rotation speed and $n_b = 15$ is the number of beads).

**Table 2.** Characteristic frequencies of bearing defects

| $f_r$ [Hz] | $f_{be}$ [Hz] | $f_{bi}$ [Hz] |
|------------|---------------|---------------|
| 118.33     | 748           | 1029          |

According to the obtained results of measurements, it is found that the measured values on the turbine at bearing 1 indicate the presence of vibrations in the vertical direction over a range of frequencies (0-10000 Hz). In order to diagnose this vibration failure, a spectral analysis has been carried out. The obtained experimental results using the experimental conditions show the amplitude of the signal versus the frequency, see Figs. 5 and 5b. It is important to clarify that the bearing life depends on the load acting on the shaft, on the rotational speed and on the point of application of the force.
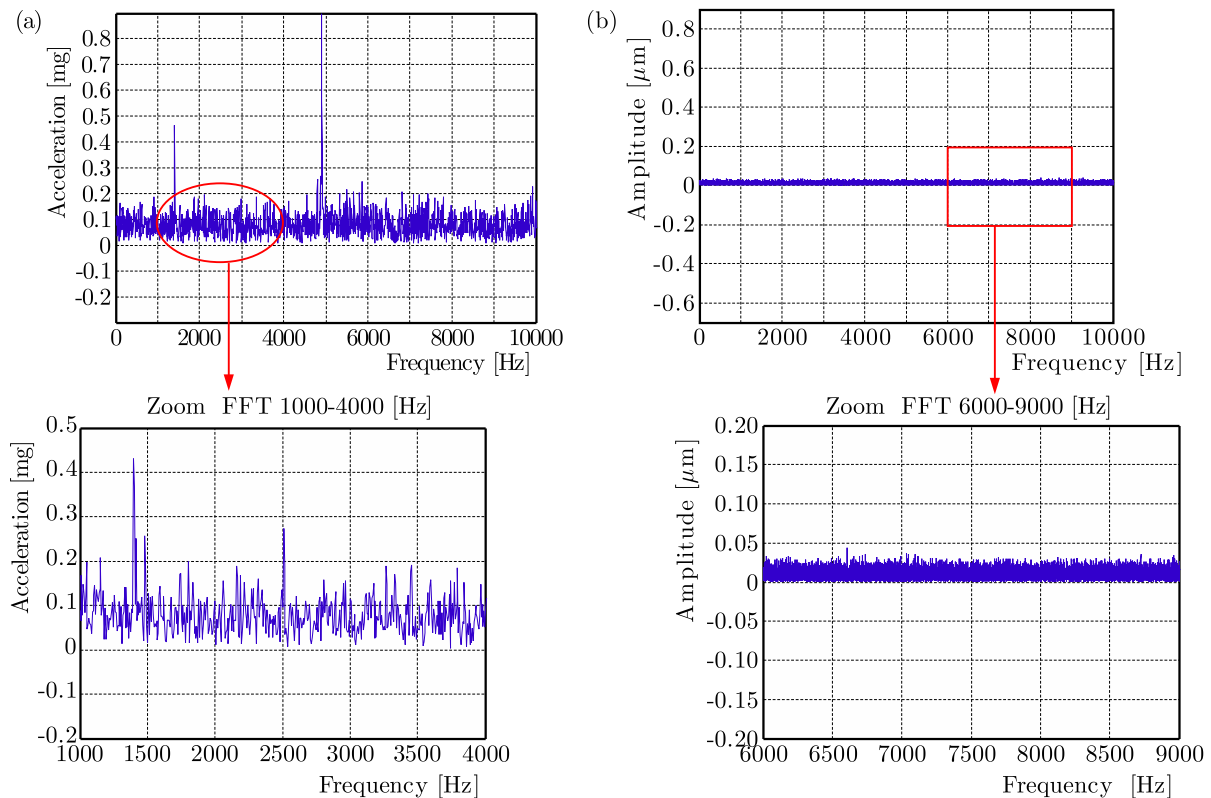


Fig. 5. Vibration signal: (a) of a defected bearing, (b) of a bearing with a fault located in the inner ring

The gas turbine is operated by a set of commands that support the machine during starting and accelerating till the loading phase. This automatic control helps to maintain the system to be stable. The measurements of variables such as pressure, velocity and acceleration are performed using an instrumentation device, as shown in Fig. 6.
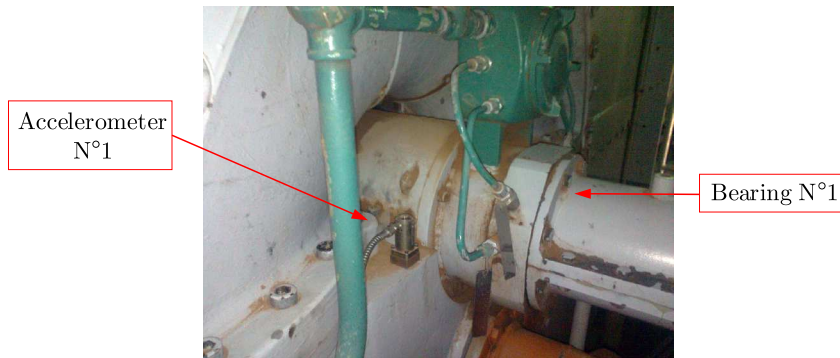
Fig. 6. Position of installed sensors in the studied gas turbine

Analysis of various elements of the studied gas turbine was carried out on this installation, starting from the study of rotation speed and its frequency, which must define the parameters useful for the proposed monitoring system. This is based on the knowledge of variations of the expected unstable phenomena, given by characteristic frequencies of possible defects such as unbalance, the alignment and the attachment. Also, the resulting vibrations due to forces developed or transmitted by the bearings caused by the unbalance have been analyzed. To analyze these phenomena, Movilog 2 with FFT mono channel and the accelerometer with speed of 100 mV/g type (HS-AM004) are used, see Figs. 7a and 7b.
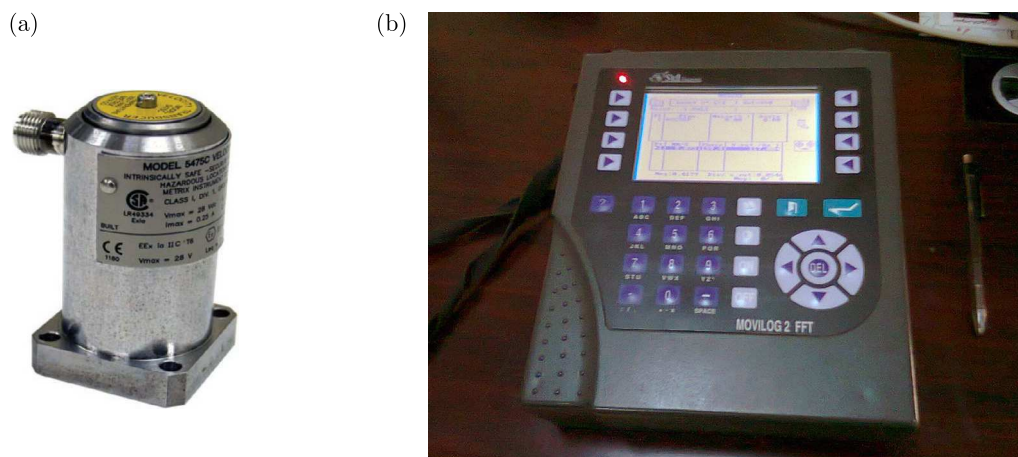


Fig. 7. (a) Used accelerometer; (b) Movilog 2 with FFT mono channel

This is done with the input of balancing data for the selected rotation speed ($V = 118$ rpm), rotor mass ($M = 3400$ kg) and rotor radius ($R = 75$ mm). At the rotational speed of 7100 rpm, where $f_r = 118.33$ Hz in the frequency range of 0-10000 Hz, the large amplitude peaks are observed, where $f_r$ is the rotation frequency of the shaft as shown in Fig. 8. This figure is the continuous display of the spectral density of the measured vibration signal within frequency regions corresponding to proper modes of the inner ring.

The appearance of such components as the shaft of the turbine (HP rotor) runs with the defected bearing is explained by the presence of oscillations in the torque load. These fluctuations have the feature to occur at the same characteristic frequency of the defect. In the present diagnostic method, the appearance of these components is used as a reference for diagnosing the presence of the anomalies in the studied gas turbine.

The levels shown in Tables 3 present the overall levels from the accelerometers within the frequency ranges (1000 Hz - 10000 Hz).
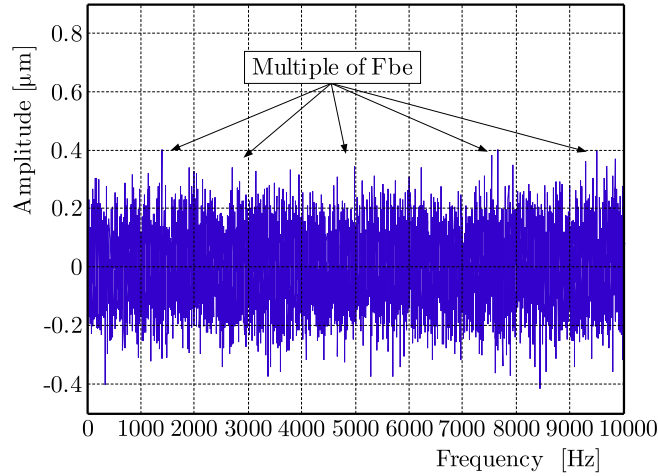
Fig. 8. Vibration signal of the bearing with a fault located in the outer ring

**Table 3.** Overall levels from accelerometers of the studied gas turbine

| SC1 | | Kurtosis | Crete factor | Acc. [mg] 10000 Hz | Speed [mm/s] 1000 Hz Pic |
|---|---|---|---|---|---|
| HP | RV | 3.0 | 4.6 | 208.8 | 2.9 |
| | | 6.9 | 7.0 | 89.8 | 1.3 |
| | | 2.9 | 4.5 | 61.8 | 2.6 |
| | RH | 3.0 | 5.0 | 32.0 | 0.2 |
| | | 7.0 | 7.0 | 13.3 | 0.1 |
| | | 2.9 | 5.2 | 7.0 | 0.2 |
| | AX | 2.7 | 4.5 | 160.6 | 0.7 |
| | | 6.3 | 7.1 | 69.9 | 0.2 |
| | | 2.6 | 4.4 | 45.6 | 0.7 |
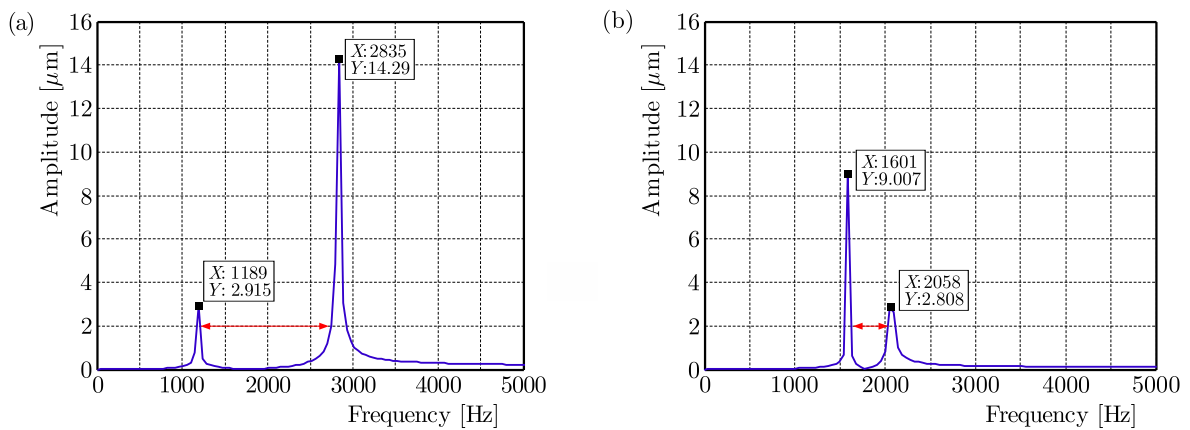


Fig. 9. Amplitude of the unbalance response: (a) test 1, (b) test 2

For unbalance defects, the operator can compensate for this misalignment by adding or removing known masses at specific locations on the rotor. These imbalance defects are mainly due to the manufacturing errors. They can explained by the presence of poor homogeneity of the materials used in the rotor structure. In order to verify the capacity of the system to balancing strong unbalances, additional balancing tests were carried out. Figures 9a,b and 10a,b show results of tests with two balancing speeds, the main goal is to reduce the overall vibration levels at all speeds and to kept the amplitude of vibration to be stable.

(a)



(b)
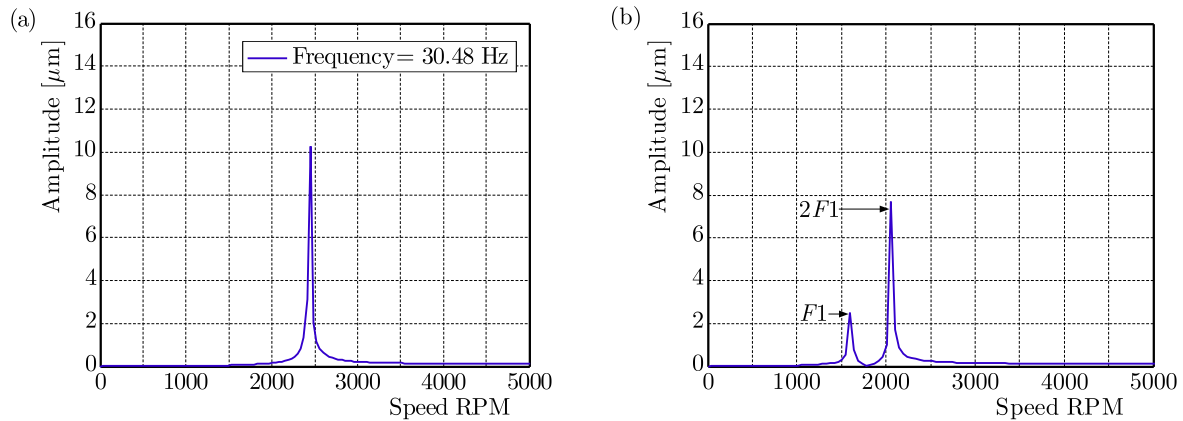


Fig. 10. Amplitude of the unbalance response: (a) test 3, (b) test 4

A misalignment is occurred when the peak amplitude is captured, generally up to 2 or 3 times the rotation frequency. The vibration measurements are in function of choice of the measurement points. In the studied case, the bearings are chosen as the points of measurement and data collecting on the examined gas turbine. Figures 11a and 11b successively present the evolution of the spectral structure (time signal) when a fault alignment is occurred.

(a)



(b)
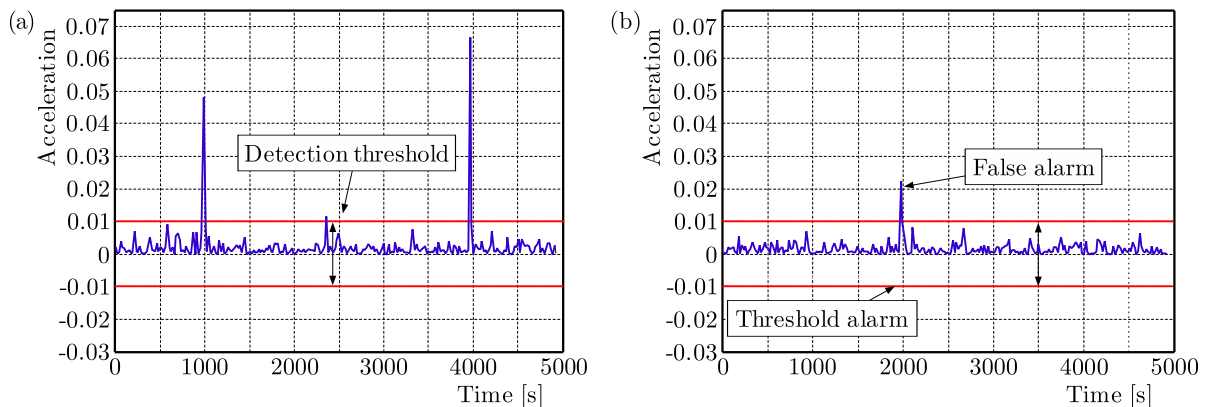


Fig. 11. (a) Time measurement signal of the acceleration in the presence of alignment defects;
(b) temporal signal without defects

At a speed of 7100 rpm, for a frequency range of 0-5000 Hz, a peak is observed (the shaft rotation frequency) which characterizes the misalignment fault. In Fig. 11b, the fault is directional, which is the case of the detected and identified misalignment on the gas turbine rotor. The results obtained were used to analyze the signature of an axial vibration fault. Unlike unbalanced, this defect is often seen in the axial direction.

## 5. Conclusion

The understanding of the dynamic vibration behavior in gas turbines allows identification and localization of the source of the vibration anomaly as well as quantification of the defect. In this paper, the rotor dynamics is studied to ensure the improvement of security and performance of the studied system. The developed model allows one to analyze the dynamic behavior of a HP turbine rotor type MS 3002 rotating at a high speed and supported by bearings having defects that are presenting instabilities areas varying with the rotation frequency and creating furthermore new critical frequencies. On the other side, it is shown that some important effects

can occur. Firstly, the wear of components regarding the rotor elements or mass distribution which can generate new critical speeds. Secondly, the defect in the inner ring of a bearing can generate the passing frequency which varies with the speed of rotation. Thirdly, the alignment effect manifests itself as a large amplitude component of the rotation frequency of the rotor in the radial direction, sometimes in the axial direction in the case of a rotor cantilever.

# References

1. ALI U., FONT PALMA C., HUGHES K.J., INGHAM D.B., MA L., POURKASHANIAN M., 2015, Impact of the operating conditions and position of exhaust gas recirculation on the performance of a micro gas turbine, *Computer Aided Chemical Engineering*, **37**, 2417-2422

2. ASHOUR O., KHALIDI A., FADLUN E., GIANNINI N., PIERI M., CECCHERINI A., 2012, On-line monitoring of gas turbines to improve their availability, reliability, and performance using both process and vibration data, *Proceeding of the 3rd Gas Processing Symposium*, 334-343

3. DJAIDIR B., HAFAIFA A., KOUZOU A., 2015, Monitoring gas turbines using speedtronic Mark VI Control Systems, *Pipeline and Gas Journal*, **242**, 10, 48-86

4. DJAIDIR B., HAFAIFA A., KOUZOU A., 2016, Vibration detection in gas turbine rotor using artificial neural network, *International Conference on Acoustics and Vibration ATAVI'16*, March 21-23, 2016, Hammamet-Tunisia

5. DJEDDI A.Z., HAFAIFA A., KOUZOU A., ABUDURA S., 2016, Exploration of reliability algorithms using modified Weibull distribution: Application on gas turbine, *International Journal of System Assurance Engineering and Management*, DOI 10.1007/s13198-016-0480-9, First online: 12 May 2016, 1-10

6. DJEDDI A.Z., HAFAIFA A., SALAM A., 2015, Gas turbine reliability model based on tangent hyperbolic reliability function, *Journal of Theoretical and Applied Mechanics*, **53**, 3, 723-730

7. ESHATI S., ABU A., LASKARIDIS P., KHAN F., 2013, Influence of water-air ratio on the heat transfer and creep life of a high pressure gas turbine blade, *Applied Thermal Engineering*, **60**, 1-2, 335-347

8. FORD C.L., CARROTTE J.F., WALKER A.D., 2013, The application of porous media to simulate the upstream effects of gas turbine injector swirl vanes, *Computers and Fluids*, **77**, 143-151

9. GALINDO J., FAJARDO P., NAVARRO R., GARCA-CUEVAS L.M., 2013, Characterization of a radial turbocharger turbine in pulsating flow by means of CFD and its application to engine modeling, *Applied Energy*, **103**, 116-127

10. GUASCH A., QUEVEDO J., MILNE R., 2000, Fault diagnosis for gas turbines based on the control system, *Engineering Applications of Artificial Intelligence*, **13**, 4, 477-484

11. GUEMANA M., HAFAIFA A., RAHMOUNE M.B., 2015, Reliability study of gas turbines for improving their availability by ensuring optimal exploitation, *OIL GAS European Magazine*, **2**, 88-91

12. GÜNYAZ A., 2013, A modeling and control approach to advanced nuclear power plants with gas turbines, *Energy Conversion and Management*, **76**, 899-909

13. HADROUG N., HAFAIFA A., KOUZOU A., CHAIBET A., 2016, Faults detection in gas turbine using hybrid adaptive network based fuzzy inference systems to controlling there dynamic behavior, *Diagnostyka – The Journal of Polish Society of Technical Diagnostics (PSTD)*, **17**, 4, 3-17

14. JAGADURI R.T., RADMAN G., 2007, Modeling and control of distributed generation systems including PEM fuel cell and gas turbine, *Electric Power Systems Research*, **77**, 1, 83-92

15. JURADO F., CARPIO J., 2006, Improving distribution system stability by predictive control of gas turbines, *Energy Conversion and Management*, **47**, 18/19, 2961-2973

16. KIM K.H., KO H.-J., PEREZ-BLANCO H., 2011, Analytical modeling of wet compression of gas turbine systems, *Applied Thermal Engineering*, **31**, 5, 834-840

17. Krzyzynski T., Popp K., Sextro W., 2000, On some irregularities in dynamic response of cyclic periodic structures, *Chaos, Solitons and Fractals*, **11**, 1597-1609

18. Lee M.C., Chung J.H., Park W.S., Park S., Yonn Y., 2013, The combustion tuning methodology of an industrial gas turbine using a sensitivity analysis, *Applied Thermal Engineering*, **50**, 1, 714-721

19. Liu X., Lu C., Liang S., Godbole A., Chen Y., 2015, Influence of the vibration of large-scale wind turbine blade on the aerodynamic load, *Energy Procedia*, **75**, 873-879

20. Madhavan S., Rajeev J., Sujatha C., Sekha A.S., 2014, Vibration based damage detection of rotor blades in a gas turbine engine, *Engineering Failure Analysis*, **46**, 26-39

21. Nikpey H., Assadi M., Breuhaus P., Mørkved P.T., 2014, Experimental evaluation and ANN modeling of a recuperative micro gas turbine burning mixtures of natural gas and biogas, *Applied Energy*, **117**, 30-41

22. Rahmoune M.B., Hafaifa A., Guemana M., 2015, Neural network monitoring system used for the frequency vibration prediction in gas turbine, *The 3rd International Conference on Control, Engineering and Information Technology CEIT'2015*, 25-27 May 2015 Tlemcen, Algeria

23. Sanaye S., Tahani M., 2010, Analysis of gas turbine operating parameters with inlet fogging and wet compression processes, *Applied Thermal Engineering*, **30**, 2/3, 234-244

24. Sextro W., Popp K., Krzyzynski T., 2001, Localization in nonlinear mistuned systems with cyclic symmetry, *Nonlinear Dynamics*, **25**, 207-220

25. Simani S., Patton R.J., 2008, Fault diagnosis of an industrial gas turbine prototype using a system identification approach, *Control Engineering Practice*, **16**, 7, 769-786

# PARAMETER ESTIMATION OF A DISCRETE MODEL OF A REINFORCED CONCRETE SLAB

Małgorzata Abramowicz, Stefan Berczyński, Tomasz Wróblewski

*West Pomeranian University of Technology, Szczecin, Poland*

*e-mail: mabramowicz@zut.edu.pl*

This paper presents parameter estimation of a mathematical model regarding natural vibrations of a reinforced concrete slab. Parameter estimation is based on experiments conducted on a real reinforced concrete slab. Estimated parameters include: substitute longitudinal modulus of elasticity of the reinforced concrete slab, which takes into account longitudinal reinforcement, effective thickness of the reinforced concrete slab and coefficient of damping. Using appropriate criteria during, the process of parameter estimation of the reinforcement concrete slab models has a great impact on obtaining precise results. The estimation criteria are selected in order to achieve consistency of natural vibration frequencies along with the Frequency Response Function measured during experiments with those calculated with the mathematical model. The model and all the calculations have been made using MATLAB programming environment.

*Keywords:* rigid finite element (RFE) model, reinforced concrete slab, estimation criteria, modal parameters, vibrations

## 1. Introduction

Steel-concrete composite beams are the main focus of our previous papers (Berczyński and Gutowski, 2006; Wróblewski *et al.*, 2013). A composite beam is a connection of two or more structural elements made of materials with various properties. An example of such a structure is a steel-concrete composite beam which consists of a steel I-beam and a concrete slab which rests on it. The present paper focuses on the reinforced concrete slab element.

The main topic of the paper is the modelling of vibration of a concrete slab. A 3D RFE (Rigid Finite Element Method) model is presented. Originally developed algorithms of parameter estimation of the reinforced concrete slab model are presented. The estimations were based on experimental results, including beam natural vibration frequencies and FRF (Frequency Response Function) determined empirically (Berczyński and Gutowski, 2006).

As there is no commercially available rigid finite element-based software, an original computer program has been developed in MATLAB environment. The created program can be used to solve the problem of free vibration and to control parameters which can be introduced to describe selected structural elements.

The estimation process is performed in two parallel stages. In the first stage experimental tests are conducted. In the second stage, the computational model of the concrete slab is defined. Solving the eigenproblem gives natural frequencies and FRF runs. Then, using optimisation methods for frequency criteria and FRF runs consistency, parameters of the concrete slab model are chosen to obtain models whose dynamic properties are close to those observed during the experiment.

## 2. Experimental research of vibrations of a reinforced concrete slab

The experimental stand consisted of two steel bearers at the beam axle spacing of 2 m. The bearers were braced with angle sections. During dynamic tests the beam was suspended on frames with four steel wire ropes 3 mm in diameter and, in this way, a free beam scheme was implemented. Bearer deformability and its effect of obtained results were considered to be negligible in the scheme. Rope deformability was selected so that frequency vibration typical for solid body in motion was beyond the range of the investigated slab free vibration. A diagram of the test stand as well as the suspended beam are presented in Fig. 1.
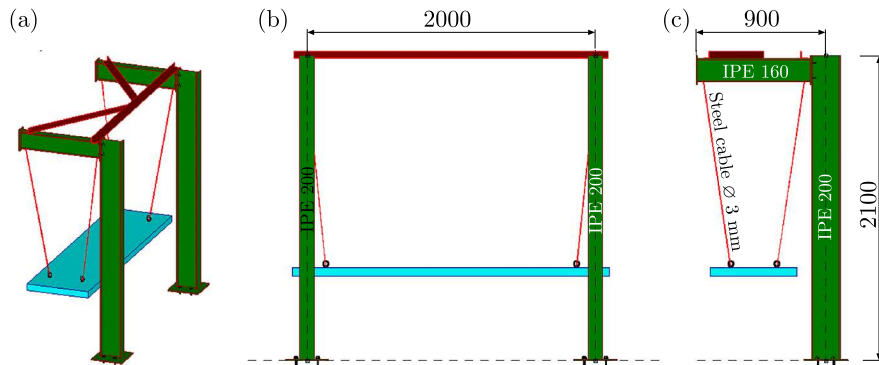


Fig. 1. Test stand: (a) overview, (b) view from the side, (c) head-on view

The aim of the conducted tests was to determine fundamental dynamic characteristics. An impulse excitation was used. Vibration acceleration was a measured value which was considered as the response of the system (Ewins, 2000; Wilde, 2008). Acceleration was measured using triaxial piezoelectric sensors. The sensors were attached with wax to circular steel washers, 25 mm in diameter, placed on the reinforced concrete slab. The washers were fixed with a modified epoxy resin.

The impulse excitation was performed using a modal hammer KISLER 9726A20000 (500 g). LMS SCADAS III analyser connected to the work station fitted with a computer aided system. *Test.Lab* package manufactured by LMS was used to record signals. Impact Testing module of the *Test.Lab* package was used for impulse tests. During each cycle of measurements, acceleration in nine measurement points was recorded. Ten excitation cycles were performed in a predefined spot of the beam. Signal averaging was conducted automatically according to the algorithm implemented in Impact Testing module.

The obtained characteristics of frequency response functions were determined as the ratio of vibration acceleration to the force. The frequency response functions were used to determine the so-called modal model using Modal Analysis module of the *Test.Lab* system (He and Fu, 2001). A stability analysis method using *PolyMAX* algorithms was used for parameter estimation of the modal model. This method is based on the frequency response functions.

## 3. The analysed reinforced concrete slab

The reinforced concrete slab (dimensions: 60 mm thick, 600 mm wide and 2200 mm long) was made of C25/30 concrete. The concrete mix was purchased from a local concrete producer. It was made of cement-based class 42.5 with addition of a BV plasticiser. The ratio was $W/C$ of 0.64 with the consistency of S3. The maximum size of aggregate was reduced to 8 mm owing to a relatively small size of the investigated elements.

Ribbed steel bars, 6 mm in diameter made from A-I steel, were used as concrete reinforcement. The longitudinal reinforcement was placed every 75 mm while transverse reinforcement every 150 mm. A reinforcing fabric from top and bottom was used.

The impulse excitation was applied to the slab at three points (see Fig. 2a): $2 - Z$ – vertical impact at the slab axis performed with the modal hammer, $1 - Z$ – vertical impact at the edge of slab performed with the modal hammer, $2 + Z$ – horizontal impact at the face of slab performed with the modal hammer.

Excitations points in Fig. 2 a are designated with the symbol ●. Various excitation points aimed at producing different vibration forms of the slab are presented in Table 1.

**Table 1.** Excitation points and directions

| Symbol | Excitation | | Excited vibration forms |
|---|---|---|---|
| | Point | Direction | |
| $1 - Z$ | 1 | $Z$ | flexural and torsional |
| $2 - Z$ | 2 | $Z$ | flexural |
| $2 + X$ | 2 | $X$ | axial |

Measurement points were defined at the upper area of the slab, spaced in three rows (9 points in each row) which gave a total of 27 measurement points (see Fig. 2b).
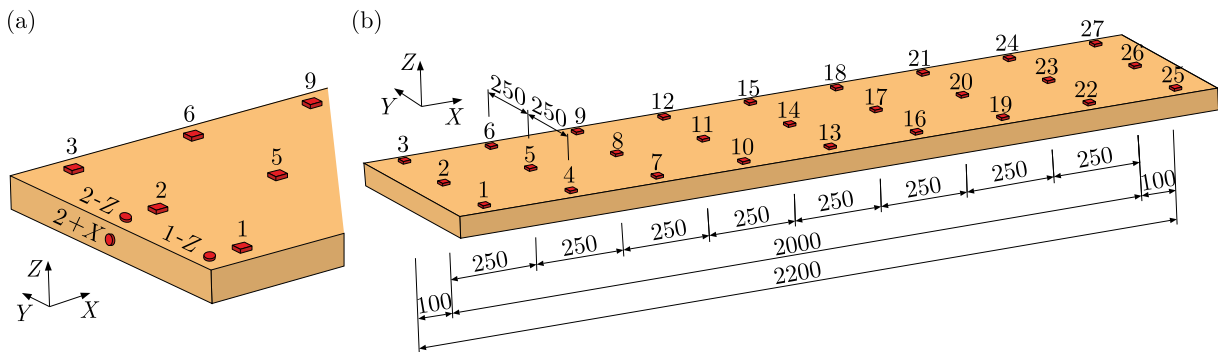


Fig. 2. Investigated slab: (a) excitation points, (b) measurement point grid

In Fig. 3, some mode shapes of the concrete slab obtained during the dynamic research are presented.

Dynamic characteristics of the frequency response functions were obtained and used to identify the coefficient of damping and other parameters. Peak amplitude values of FRF runs were determined. The peak amplitude values were corresponding to the next resonance vibrations of the reinforced concrete slab. Two types of vibrations were analysed: flexural vibrations (impulse excitation $2 - Z$) and torsional vibrations (impulse excitation $1 - Z$). For flexural and torsional vibrations, the peak amplitude values were determined for five resonances.

The authors developed their own software in MATLAB, which automatically defines the peak amplitude of FRF runs corresponding to the resonance vibration of the reinforced concrete slab. The software enabled determination of the values in tabular and graphical forms. For the analysis of FRF runs, eight representative measurement points were selected. For flexual vibration (impulse excitation $2 - Z$) points 2, 5, 23 and 26 were selected, which were located on the axis of the reinforced concrete slab (see Fig. 2b). For torsional vibration (impulse excitation $1 - Z$) points 1, 3, 25 and 27 were selected, which were located on the corners of the reinforced concrete slab (see Fig. 2b). Peak amplitudes of the run of FRF corresponding resonances are summarised in Table 2.
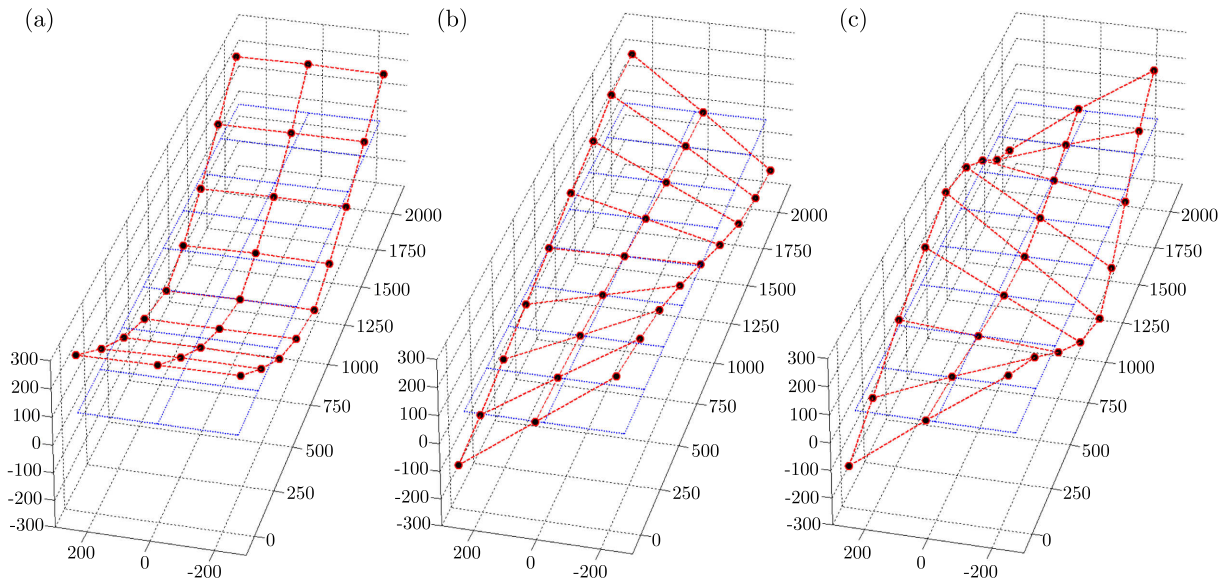
Fig. 3. Flexural and torsional experimental mode shapes for the reinforced concrete slab, excitation $1 - Z$: (a) $1_{flex} = 50.04\,\text{Hz}$, (b) $1_{tors} = 113.34\,\text{Hz}$, (c) $2_{tors} = 232.75\,\text{Hz}$

**Table 2.** Amplitude of frequency response functions for the reinforced concrete slab determined during measurement, impulse excitation $1 - Z$, direction $Z$

| Points | 1 | | 3 | | 25 | | 27 | |
|---|---|---|---|---|---|---|---|---|
| FRF | FRF [m·s$^{-2}$/N] | $f_i^{exp}$ [Hz] | FRF [m·s$^{-2}$/N] | $f_i^{exp}$ [Hz] | FRF [m·s$^{-2}$/N] | $f_i^{exp}$ [Hz] | FRF [m·s$^{-2}$/N] | $f_i^{exp}$ [Hz] |
| $1_{tors}$ | 1.915 | 113 | 2.000 | 113 | 1.968 | 113 | 1.966 | 113 |
| $2_{tors}$ | 3.117 | 233 | 3.162 | 233 | 3.152 | 233 | 3.165 | 233 |
| $3_{tors}$ | 2.63 | 368 | 2.599 | 368 | 2.676 | 367 | 2.598 | 367 |
| $4_{tors}$ | 2.077 | 526 | 2.051 | 526 | 2.022 | 526 | 1.992 | 526 |
| $5_{tors}$ | 2.632 | 708 | 0.51 | 707 | 2.321 | 708 | 0.553 | 709 |

In Fig. 4, frequency response functions with marked peak amplitude values (from torsional vibrations) for point 27 for direction $Z$, impulsive excitation $1 - Z$ are presented.
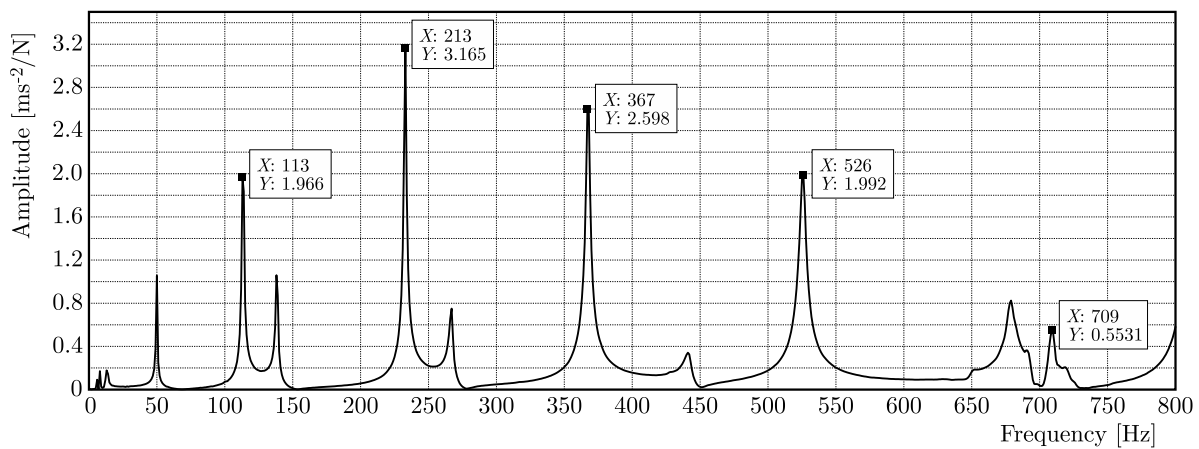


Fig. 4. Amplitude of the frequency response functions for the reinforced concrete slab, excitation $1 - Z$, point 27, direction $Z$

### 4. The spatial computational model of the reinforced concrete slab

A discrete computational model of the slab has been developed in the convention of the Rigid Finite Element Method. The method consists in dividing a real system into rigid finite elements which are represented by spring-damping elements (SDEs). While rigid finite elements (RFEs) are characterised by masses and mass moments of inertia, spring-damping elements are defined by stiffness and damping coefficients. The RFE method was developed by Kruszewski *et al.* (1999) and Wittbrodt *et al.* (2006).

Modelling of continuous elements in the finite element method starts from primary segmentation. For a slab, the segmentation must be conducted in two directions, i.e. in the longitudinal direction along $\Delta L$ and in transverse direction along $\Delta B$. The model is divided into segments of equal or comparable length. The primary segmentation of the present study is shown in Fig. 5a. Then, at the center of gravity of each element, an SDE is placed which focuses spring and damping properties of that element. Each SDE is broken down into four smaller SDEs, so that it is possible to connect the corners of four adjacent finite elements – this is secondary segmentation. In every set of four SDEs, two of them are parallel to the main axis $X$ and the other two are parallel to the main axis $Y$. In the classic approach (Kruszewski *et al.*, 1999) spring properties of respective elements are reflected by SDEs spaced as shown in Fig. 5b.
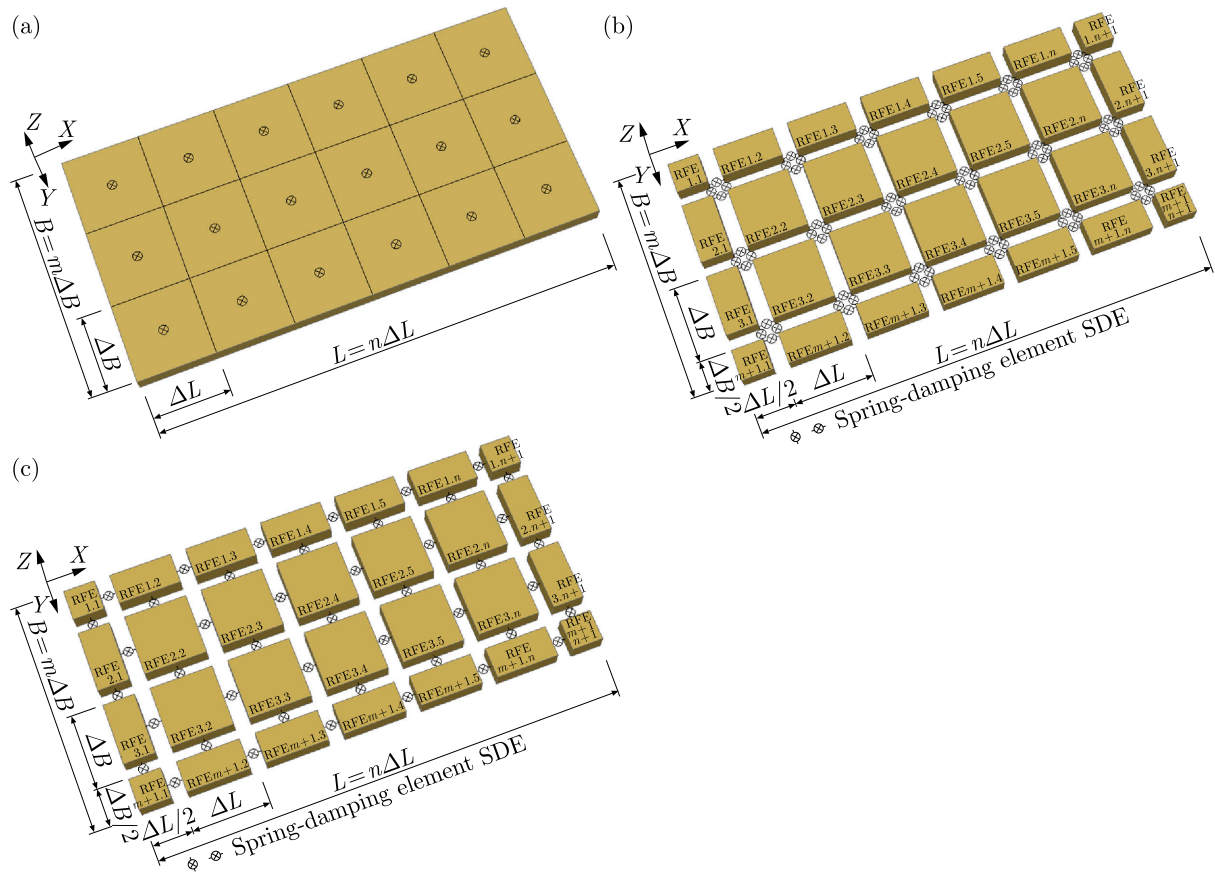


Fig. 5. 3D finite element method: (a) primary segmentation, (b) secondary segmentation – classic positioning of SDEs, (c) secondary segmentation – modified positioning of SDEs

In the classic approach, the elements have 5 degrees of freedom. By placing an SDE at the corners, it is possible to neglect rotation in the axes perpendicular to the area of a primary element. The proposed model attempts to define the slab with 6 degrees of freedom (three translational and three rotational displacements). In order to limit element rotation in the axis

perpendicular to the area of the primary element, SDEs must be moved from the corners to the centers of finite elements as shown in Fig. 5c. A similar approach was used in (Adamiec-Wójcik and Wojciech, 2012).

Each rigid finite element has its own independent coordinate system $X_{RFE}^{(i)}, Y_{RFE}^{(i)}, Z_{RFE}^{(i)}$ which is selected so that it overlaps the principal central axes of inertia of a given RFE. Given this assumption, mass and moments of inertia are the only parameters necessary to describe any RFE. These quantities can be given in form of a diagonal mass matrix

$$\mathbf{M}^{(i)} = \text{diag}\left[m^{(i)}, m^{(i)}, m^{(i)}, J_X^{(i)}, J_Y^{(i)}, J_Z^{(i)}\right] \tag{4.1}$$

The first three terms of the matrix are equal to the mass of the RFE, while the other three are RFE mass moments of inertia relative to the axes $X_{RFE}^{(i)}$, $Y_{RFE}^{(i)}$, $Z_{RFE}^{(i)}$. The values of the diagonal element of the mass matrix $\mathbf{M}^{(i)}$ for modelling of RFEs inside the slab are determined in the following way

$$m^{(i)} = h_c \Delta L \Delta B \rho_c \tag{4.2}$$

where $h_c$ is thickness of the reinforced concrete slab, $\rho_c$ – mass density of RFE material

$$J_X^{(i)} = \frac{m^{(i)}}{12}(\Delta L^2 + h_c^2) \qquad J_Y^{(i)} = \frac{m^{(i)}}{12}(\Delta B^2 + h_c^2)$$
$$J_Z^{(i)} = \frac{m^{(i)}}{12}(\Delta L^2 + \Delta B^2) \tag{4.3}$$

Every SDE of $k$ number has its own independent coordinate system with the main axes $X_{SDE}^{(k)}$, $Y_{SDE}^{(k)}$, $Z_{SDE}^{(k)}$. The main axes of the SDE have such property that forces acting on the SDE in a direction compatible with these axes result in its translational deformations which occur only in the direction along which these forces are applied. The main parameters which describe an SDE of $k$ number are coefficients defining its spring and damping properties. The spring properties are described by means of two matrices: a matrix of translational stiffness coefficients $\mathbf{K}_T^{(k)}$ and a matrix of rotational stiffness coefficients $\mathbf{K}_R^{(k)}$. Both matrices are diagonal and they are $3 \times 3$ in size

$$\mathbf{K}_T^{(k)} = \text{diag}\left[k_{T,X}^{(k)}, k_{T,Y}^{(k)}, k_{T,Z}^{(k)}\right] \qquad \mathbf{K}_R^{(k)} = \text{diag}\left[k_{R,X}^{(k)}, k_{R,Y}^{(k)}, k_{R,Z}^{(k)}\right] \tag{4.4}$$

The values of translational and rotational stiffness coefficients are determined according to the following rules:

— for SDEs parallel to the main axis $X$

$$k_{T,X-X}^{(k)} = \frac{E_c h_{c,eff} \Delta B}{\Delta L} \qquad k_{T,Y-X}^{(k)} = \frac{G_c h_{c,eff} \Delta B}{\Delta L \chi}$$
$$k_{T,Z-X}^{(k)} = \frac{G_c h_{c,eff} \Delta B}{\Delta L \chi} \qquad k_{R,X-X}^{(k)} = \frac{G_c h_{c,eff}^3 \Delta B}{6 \Delta L}$$
$$k_{R,Y-X}^{(k)} = \frac{E_c h_{c,eff}^3 \Delta B}{12(1-\nu_c^2)\Delta L} \qquad k_{T,Z-X}^{(k)} = \frac{E_c h_{c,eff} \Delta B^3}{12 \Delta L} \tag{4.5}$$

— for SDEs parallel to the main axis $Y$

$$k_{T,X-Y}^{(k)} = \frac{G_c h_{c,eff} \Delta L}{\Delta B \chi} \qquad k_{T,Y-Y}^{(k)} = \frac{E_c h_{c,eff} \Delta L}{\Delta B}$$
$$k_{T,Z-Y}^{(k)} = \frac{G_c h_{c,eff} \Delta L}{\Delta B \chi} \qquad k_{R,X-Y}^{(k)} = \frac{E_c h_{c,eff}^3 \Delta L}{12(1-\nu_c^2)\Delta B}$$
$$k_{R,Y-Y}^{(k)} = \frac{G_c h_{c,eff}^3 \Delta L}{6 \Delta B} \qquad k_{T,Z-Y}^{(k)} = \frac{E_c h_{c,eff} \Delta L^3}{12 \Delta B} \tag{4.6}$$

where $E_c$ is the substitute dynamic longitudinal modulus of elasticity of the reinforced concrete slab (which takes into account the effect of reinforcement used), $G_c$ – substitute dynamic transverse modulus of elasticity of the reinforced concrete slab (which takes into account the effect of reinforcement used), $h_{c,eff}$ – effective thickness of the reinforced concrete slab, $\nu_c$ – Poisson's ratio of concrete, $\chi$ – coefficient of cross-section shape (Timoshenko shear coefficient), which takes into account the nonuniform tangential stress pattern. The method of calculating the coefficient was described by Berczyński and Wróblewski (2010). The Timoshenko shear coefficient of cross-section of a rectangle shape is 1.2.

Dumping properties are described by means of two matrices of damping coefficients: $\mathbf{C}_T^{(k)}$ and $\mathbf{C}_R^{(k)}$. Both matrices are diagonal and they are $3 \times 3$ in size. The relation between equivalent stiffness $k_{i,j}^{(k)}$ and damping coefficients $c_{i,j}^{(k)}$ can be given by

$$c_{i,j}^{(k)} = \frac{\eta}{\omega} k_{i,j}^{(k)} \qquad i = T, R \qquad j = X, Y, Z \tag{4.7}$$

where $\eta$ is the loss ratio, $\omega$ – vibration frequency.

Results obtained with the modified RFE method model were compared with the analytical solution, the TM (Theoretical Model), and with the FEM model with flexible and deformable rigid bodies implemented in the Finite Element Method. The FEM model was developed in Abaqus environment and it was used for calculations. The slab was modelled with $50 \times 50$ second-order cubic elements with reduced integration for second-order functions (C3D20R). The solution was developed and reported by Liew *et al.* (1993), Leissa (1973). Leiss (1973) provided a solution for thin slabs, whereas Liew *et al.* (1993) found a solution of eigenmodes for medium-thick rectangular slabs. The authors presented their findings for various boundary conditions (21 cases) for different side length/width ratios ($a/b$) and different slab thickness/width ratios ($h/b$). Their approach was based on the energy function defined using the Mindlin theory of plates with the Rayleigh-Ritz minimisation procedure, providing a solution to the eigenvalue problem (Szcześniak, 2000). According to the theory of plates of medium thickness, it is typically assumed that a plate has thickness greater or equal $1/10$ of the smaller of the remaining two dimensions. The reinforced concrete slab used in our tests had the thickness to width ratio of $60/600$, i.e. $1/10$ precisely. Therefore, the theory of medium-thick plates could be applied for the modelling of both the former and the latter. The results were compared for a free-ends slab (the same scheme was used in empirical investigations). Liew *et al.* (1993) conducted analytical calculations for a slab with various length/width ratios for comparison purposes. Here, a 1500 mm long, 600 mm wide and 60 mm thick slab was used in the tests. Therefore, the length to width ratio of 2.5 and the thickness to width ratio of 0.1 was obtained. The Poisson ratio $\mu_c$ was 0.3, Young's modulus $E_c$ was $3.0 \cdot 10^{10}$ N/m$^2$ and the mass density $\rho_c$ was 2400 kg/m$^3$. In an earlier work (Liew *et al.*, 1993), the results were presented in a dimensionless form
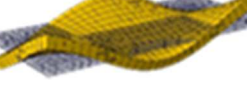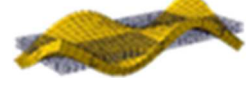
$$\lambda = \frac{\omega B^2}{\pi^2} \sqrt{\frac{\rho_c h_c}{D}} \tag{4.8}$$

where $\omega$ is the angular frequency, $B$ – length of the shorter side of the slab width, $D$ – bending flexural stiffness of the slab.

$$D = \frac{E_c h_c^3}{12(1 - \nu_c^2)} \tag{4.9}$$

The results are presented in Table 3. The calculations for the RFE model were conducted for the initial mesh of $30 \times 12$ elements, the slab dimensions were the same as those given above. Table 3 presents a comparison of solutions for the three models: the theoretical model (TM) based on the precise solution, the Rigid Finite Element (RFE) model and the Finite Element Method (FEM) model.

**Table 3.** A comparison of dimensionless vibration frequencies of the slab for the TM, RFE and FEM models

| i | Vibration forms of the slab | Reinforced concrete slab 60 mm×600 mm×1500 mm | | | | |
|---|---|---|---|---|---|---|
| | | TM | RFE | | FEM | |
| | | $\lambda_{i\_TM}$ | $\lambda_{i\_RFE}$ | $\Delta_{i\_TM}$ | $\lambda_{i\_FEM}$ | $\Delta_{i\_TM}$ |
| 1 | | 0.3455 | 0.3605 | 4.3% | 0.3457 | 0% |
| 2 | | 0.5137 | 0.5144 | 0.1% | 0.5154 | 0% |
| 3 | | 0.9486 | 0.9826 | 3.6% | 0.9502 | 0% |
| 4 | | 1.0952 | 1.0939 | −0.1% | 1.0994 | 0% |
| 5 | | 1.8109 | 1.8080 | −0.2% | 1.8199 | 0% |
| 6 | | 1.8220 | 1.8952 | 4.0% | 1.8282 | 0% |
| 7 | | 2.1919 | 2.1860 | −0.3% | 2.1981 | 0% |
| 8 | | 2.3566 | 2.3884 | 1.4% | 2.3654 | 0% |
| 9 | | 2.7173 | 2.7164 | 0% | 2.7332 | 0.6% |

The terms $\Delta_{i\_RFE}$ and $\Delta_{i\_FEM}$ defined by (4.10) are used to show the percentage differences for dimensionless values of slab frequency vibrations obtained for the TM, RFEM and FEM models.

$$\Delta_{i\_RFE} = \frac{\lambda_{i\_RFE} - \lambda_{i\_TM}}{\lambda_{i\_TM}} \qquad \Delta_{i\_FEM} = \frac{\lambda_{i\_FEM} - \lambda_{i\_TM}}{\lambda_{i\_TM}} \tag{4.10}$$

The first column shows the obtained vibration forms of the slab for the dimensionless values of the slab frequencies.

A very good convergence of the results was obtained for the RFE and TM models. The largest difference was 4.3%. The largest discrepancy between the FEM and TM models was observed for higher eigenmodes (0.6% for 9th eigenmode). However, the results obtained for the torsional (2, 4, 5 and 9) and flexural vibrations (1, 3 and 6), which are significant for parameter estimation of composite beams, were quite convergent for both the former and the latter.

During the analysis of various values of the parameter $\Delta$ for various mesh densities in the $X$ axis, a constant mesh density of 12 was used for the $Y$ axis. In the second case, with various mesh densities in the $Y$ axis, a constant mesh density of 30 was used for the $X$ axis. It was

examined that for other constants for $X$ and $Y$ axes the same results were obtained. It was found that with an increase in mesh density, the eigenmode frequencies were asymptotically approaching the solution for the sufficient mesh density which provided a good convergence with the analytical solution. Nevertheless, the problem of mesh density selection was also affected by the fact that larger densities significantly increased calculation time.

## 5. Parameter estimation – algorithm I

The estimated parameters included the substitute longitudinal modulus of elasticity of the reinforced concrete slab $E_c$ which took into account longitudinal reinforcement and effective thickness of the reinforced concrete slab $h_{c,eff}$. Other parameters used for the identification of the computational model were taken from the literature or from the design of the analysed slab.

The differential equation of free vibration obtained from the general differential equation of motion, while neglecting outside interaction acting on the slab and damping effects, can be presented as

$$\mathbf{M\ddot{q} + Kq = 0} \tag{5.1}$$

where $\mathbf{q}$ is the vector of generalised coordinates.

Methods of solving equation (5.1) to determine free vibration frequencies and corresponding vibration modes are described in detail in literature (Wilde, 2008).

The quantities $S_{flex}$ and $S_{tors}$ (5.2) are sums of squares of the relative deviations of the first n numerical frequencies of flexural and torsional vibrations with their analogous frequencies determined during the experiment

$$S_{flex} = \sum_{i=1}^{n} \left( \frac{f_{i\_flex}^{num} - f_{i\_flex}^{exp}}{f_{i\_flex}^{exp}} \right)^2 \qquad S_{tors} = \sum_{i=1}^{n} \left( \frac{f_{i\_tors}^{num} - f_{i\_tors}^{exp}}{f_{i\_tors}^{exp}} \right)^2 \tag{5.2}$$

where $n$ is the number of selected frequencies, $f_{i\_flex}^{exp/num}$ – experimental/numerical frequencies of flexural vibrations, $f_{i\_tors}^{exp/num}$ – experimental/numerical frequencies of torsional vibrations.

The quantity $S$ is a sum of flexural and torsional vibrations in the process of estimation in which an appropriate weight function $w_{flex}$ was attributed to flexural and wtors to torsional frequencies

$$S = w_{flex}S_{flex} + w_{tors}S_{tors} \tag{5.3}$$

An additional criterion imposed was the condition of compatibility of the experimental and mathematical fundamental frequency of longitudinal vibrations:

$$f_{1\_long}^{exp} = f_{1\_long}^{num} \tag{5.4}$$

The algorithm assumes a limit (5.4) that has the greatest impact on the identified slab modulus of elasticity $E_c$.

In order to determine model parameters that allow the best mapping of frequencies with those obtained experimentally, the paramter $S$ index was minimised. To solve the problem, an optimisation procedure implemented in *Optimization Toolbox* package, which is a part of MATLAB, was used.

For adopted criterion (5.3), the following numerical experiments was performed. In the 1st stage of parameter estimation criterion (5.3) was minimised assuming $w_{flex} = 1.0$ and $w_{tors} = 0.0$. This means comparison of only flexural frequencies of natural vibration during the estimation

process. The estimation resulted in a good compatibility of frequencies of natural vibration observed in the experiments and in numerical calculations (see Table 4 – Analysis I). Differences in compatibility for flexure frequencies for the reinforced concrete slab were under 1.4% and for torsional frequencies under 3.1%. The iteration algorithm was tested for convergence by introducing various starting points to determine parameters of the the model. Each time, after the iteration was complete, the values of estimated variables were similar.

**Table 4.** Comparison of natural vibration frequencies measured during dynamic tests with numerical results algorithm I of the estimation, Analysis I-III

| Analysis | I | | | II | | | III | | |
|---|---|---|---|---|---|---|---|---|---|
| FRF | $f_i^{exp}$ [Hz] | $f_i^{num}$ [Hz] | $\Delta$ [%] | $f_i^{exp}$ [Hz] | $f_i^{num}$ [Hz] | $\Delta$ [%] | $f_i^{exp}$ [Hz] | $f_i^{num}$ [Hz] | $\Delta$ [%] |
| $1_{tors}$ | 113.34 | 110.2 | −2.8 | 113.34 | 113.4 | 0.1 | 113.34 | 111.33 | −1.8 |
| $2_{tors}$ | 232.75 | 227.4 | −2.3 | 232.75 | 233.97 | 0.5 | 232.75 | 229.7 | 1.3 |
| $3_{tors}$ | 367.33 | 358.33 | −2.5 | 367.33 | 368.61 | 0.3 | 367.33 | 361.94 | −1.5 |
| $4_{tors}$ | 525.61 | 509.55 | −3.1 | 525.61 | 524.03 | −0.3 | 525.61 | 514.64 | −2.1 |
| $5_{tors}$ | 707.99 | 686.87 | −3.0 | 707.99 | 706.18 | −0.3 | 707.99 | 693.65 | −2.0 |
| $1_{flex}$ | 50.00 | 50.64 | 1.3 | 50.00 | 52.13 | 4.3 | 50.00 | 51.16 | 2.3 |
| $2_{flex}$ | 138.34 | 138.94 | 0.4 | 138.34 | 143.00 | 3.4 | 138.34 | 140.36 | 1.5 |
| $3_{flex}$ | 266.76 | 270.53 | 1.4 | 266.76 | 278.36 | 4.3 | 266.76 | 273.28 | 2.4 |
| $4_{flex}$ | 441.54 | 443.22 | 0.4 | 441.54 | 455.9 | 3.3 | 441.54 | 447.67 | 1.4 |
| $5_{flex}$ | 649.34 | 654.85 | 0.8 | 649.34 | 673.31 | 3.7 | 649.34 | 661.34 | 1.8 |
| $1_{long}$ | 933.12 | 933.12 | 0.0 | 933.12 | 933.12 | 0.0 | 933.12 | 933.12 | 0.0 |
| $E_c$ [N/m²] | 4.248E+10 | | | 4.127E+10 | | | 4.205E+10 | | |
| $h_{c,ff}$ [m] | 0.057 | | | 0.059 | | | 0.058 | | |
| $S_{tors}$ | 3.718E-03 | | | 5.500E-05 | | | 1.548E-03 | | |
| $w_{tors}$ | 0.0 | | | 1.0 | | | 1.0 | | |
| $S_{flex}$ | 4.711E-04 | | | 7.262E-03 | | | 1.890E-03 | | |
| $w_{flex}$ | 1.0 | | | 0.0 | | | 1.0 | | |
| $S$ | 4.711E-04 | | | 5.500E-05 | | | 3.438E-03 | | |

The following Section presents results of the 2nd stage of estimation for weight functions $w_{flex} = 0.0$ and $w_{tors} = 1.0$. This means comparison of only torsional frequencies of natural vibration during the estimation process. The estimation results are presented in Table 4 – Analysis II. Differences in compatibility for torsional frequencies for the reinforced concrete slab were under 0.5% and for flexural frequencies under 4.3%.

The following part of the paper presents results of the 3rd stage of estimation for weight functions $w_{flex} = 1.0$ and $w_{tors} = 1.0$. This means comparison of flexual and torsional frequencies of natural vibration during the estimation process. The estimation results are presented in Table 4 – Analysis III. Differences in compatibility for torsional frequencies for the reinforced concrete slab were under 2.1% and for flexural frequencies under 2.4%.

## 6.  Parameter estimation for the model – algorithm II

While working on the finite element method model of the slab, an assumption was made that the substitute dynamic longitudinal modulus of elasticity of the reinforced concrete slab $E_c$, effective thickness of the reinforced concrete slab $h_{c,eff}$, and the loss ratio of concrete $\eta_c$ would be determined based on identification. The value of the loss ratio is dependent on frequency, temperature and other factors.

The loss ratio of concrete varies in the range $(2\text{-}6)\cdot 10^{-4}$ according to (Silva, 2000). High diversity of concrete types results in a very different range of concrete damping values. Damping depends on concrete density, amount of cement slurry, load history, intensity of stress, etc.

Parameter estimation was conducted by fitting the frequency response functions calculated with the finite element method model to the characteristics obtained in experimental research. A system of differential equations defining the oscillating motion with damping can be given by

$$\mathbf{M}\ddot{\mathbf{q}}(t) + \mathbf{C}\dot{\mathbf{q}}(t) + \mathbf{K}\mathbf{q}(t) = \mathbf{f}(t) \tag{6.1}$$

where $\mathbf{q}$ is the vector of generalised displacement, $\mathbf{M}$, $\mathbf{C}$, $\mathbf{K}$ – inertia, dumping and stiffness matrices, $\mathbf{f}$ – vector of generalised forces. The vectors $\mathbf{q}$ and the system response $\mathbf{f}$ are functions of time $t$. The above system of differential equations can be solved, depending on the form of the excitation signal, using either Fourier or Laplace integral transform (Marchelek, 1991). By using the Laplace transform, it is possible to move from time domain over to the domain of the complex frequency $s$. Given zero initial conditions, while performing the Laplace transform, the system of equations (6.1) takes the following form

$$(\mathbf{M}s^2 + \mathbf{C}s + \mathbf{K})\mathbf{q}(s) = \mathbf{f}(s) \tag{6.2}$$

A consequence of using the Laplace transform is algebraisation of the system of equations (6.1). While solving a system of linear algebraic equations, we assume that the matrix $(\mathbf{M}s^2 + \mathbf{C}s + \mathbf{K})$ is not singular, i.e. that there is a matrix inverse to it. As a result, Equation (6.2) takes the form

$$\mathbf{q}(s) = (\mathbf{M}s^2 + \mathbf{C}s + \mathbf{K})^{-1}\mathbf{f}(s) \tag{6.3}$$

To find a solution in the frequency form, if the excitation applied to the system is periodic (solution for a steady state), the Fourier transform can be used. A solution is found directly in the Laplace solution by substituting it to Equation (6.3) $s = \mathrm{j}\omega$, where $\mathrm{j} = \sqrt{-1}$

$$\mathbf{q}(\mathrm{j}\omega) = (\mathbf{K} - \omega^2\mathbf{M} + \mathrm{j}\omega\mathbf{C})^{-1}\mathbf{f}(\mathrm{j}\omega) \tag{6.4}$$

where

$$\mathbf{A}(\mathrm{j}\omega) = \mathbf{K} - \omega^2\mathbf{M} + \mathrm{j}\omega\mathbf{C} \tag{6.5}$$

is referred to as the dynamic stiffness matrix, while

$$\mathbf{W}(\mathrm{j}\omega) = \mathbf{A}^{-1}(\mathrm{j}\omega) = (\mathbf{K} - \omega^2\mathbf{M} + \mathrm{j}\omega\mathbf{C})^{-1} \tag{6.6}$$

is the dynamic flexibility matrix.

Dynamic flexibility is a characteristic obtained on the premise that the system input is a force and its output is a displacement. During experimental research, acceleration was measured. A characteristic found given the condition that the system input is the force and its output is the displacement is called inertance $\mathbf{G}(\mathrm{j}\omega)$. Both dynamic flexibility and inertance are frequency characteristics defined for steady motion and they are therefore closely interrelated (Uhl, 1997).

$$|\mathbf{G}(\mathrm{j}\omega)| = \omega^2|\mathbf{W}(\mathrm{j}\omega)| \tag{6.7}$$

To find the inertance of a system based on a finite element model, it is necessary to know the stiffness matrix $\mathbf{K}$, inertia matrix $\mathbf{M}$ and damping matrix $\mathbf{C}$. The methods were described in-depth elsewhere in the literature (Kruszewski *et al.*, 1999; Wróblewski *et al.*, 2013).

Our identification criterion was minimization of the coefficient JFRF (6.7) which is a double sum for $m$-th measurement points, a sum of relative quadratic deviation of the first $n$-th measurement points for a given FRF amplitude to the same amplitude determined in experimental

research. While determining loss ratios, an attempt was made to fit the calculated amplitudes with those determined experimentally

$$J_{FRF} = \sum_{i=1}^{m} \sum_{i=1}^{n} \left( \frac{FRF_{i,amp}^{num} - FRF_{i,amp}^{exp}}{FRF_{i,amp}^{exp}} \right)^2 \qquad (6.8)$$

The above algorithm allowed one to select an analysed point and, as a result, it was possible to choose vibration forms (flexural and torsional vibration) and vibration modes $(1, 2, \ldots, n)$. Both flexural and torsional vibration forms were taken into account in the estimation procedure. An optimization procedure implemented in Optimization Toolbox package, which is a part of MATLAB, was used.

The results of analysis are presented in Table 5. First analysis was conducted for torsional vibration for point 1 (vibration modes from 2 to 4) and for flexural vibration for point 2 (vibration modes from 2 to 4). In the identification, 5 points from each amplitude of every FRF were taken into consideration.

**Table 5.** Results of estimated parameters during optimisation – algorithm II of the estimation, Analysis I-III

| Analysis | I | II | III |
|---|---|---|---|
| $E_c$ [n/m$^2$] | 4.230E+10 | 4.300E+10 | 4.224E+10 |
| $h_{c,eff}$ [m] | 0.0570 | 0.0577 | 0.0570 |
| $\eta_c$ [−] | 0.0090 | 0.0112 | 0.0091 |
| $J$ | 9.4703 | 4.7114 | 3.7924 |

Second analysis was conducted for torsional vibration for point 1 (vibration modes from 2 to 4) and for flexural vibration for point 2 (vibration mode 3). In the identification, 5 points from each amplitude of every FRF were taken into consideration. Third analysis was performed for torsional vibration for point 1 (vibration mode 2) and for flexural vibration for point 2 (vibration modes from 2 to 4). In the identification, 5 points from each amplitude of every FRF were taken into consideration.
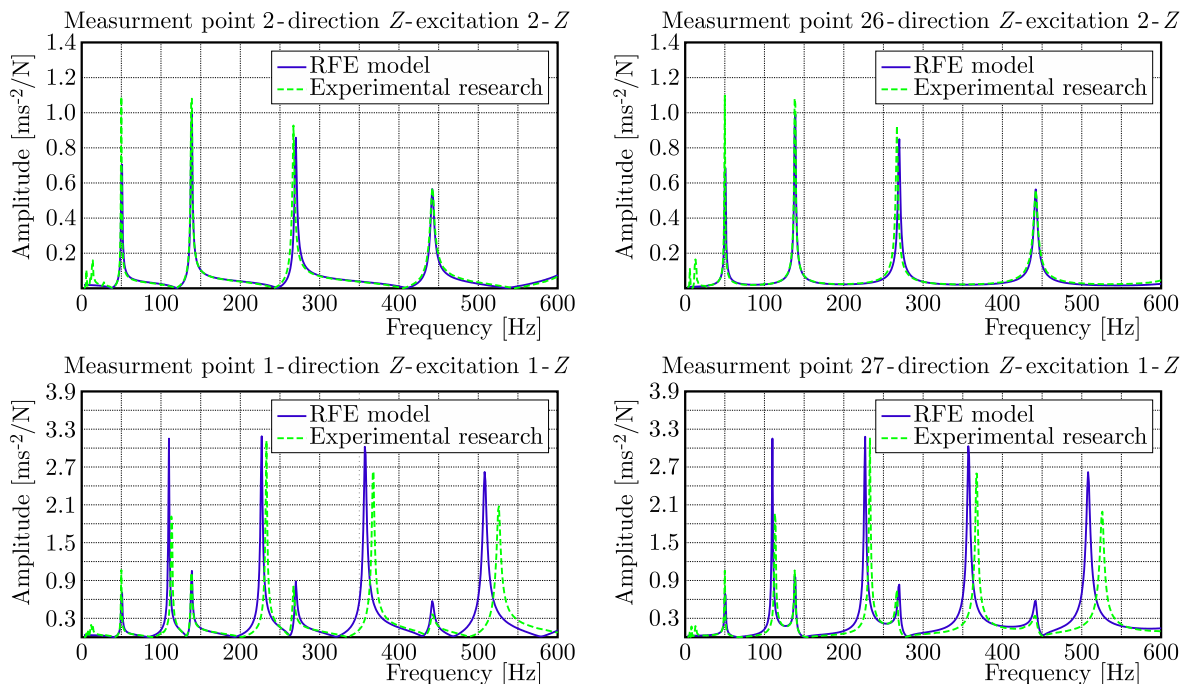


Fig. 6. A comparison of the frequency response functions for the reinforced concrete slab – Analysis III

A comparison of FRFs determined using the above estimated parameters with those determined experimentally is presented in Fig. 6. As the consistency of the FRFs was high, it was fair to state that the identified parameters were determined correctly.

## 7. Conclusions

The numerical tests show a very good convergence of the algorithms developed for estimating the parameters of a mathematical model of the reinforced concrete slab. They enable creation of a model representing the actual reinforced concrete slab and allowed one to determine dynamic characteristics very similar to those measured during the experiments.

Following the identification, it can be observed that the identified parameters for algorithms I and II are very similar. Both algorithms provide convergent results of identification, which indicates the appropriateness of the model and algorithms.

A very good fit of FRFs calculated using the model with those obtained in the experimental research is achieved. The originally developed spatial finite element model allows one to take into account both flexural and torsional vibration forms. The goal was to achieve consistency of frequencies and FRFs observed during tests with those calculated using the analytical model.

This well-developed 3D model of the reinforced concrete slab has allowed the authors to develop a model of a steel-concrete composite beam which has been the focus of their research attempts.

## References

1. ADAMIEC-WÓJCIK I., WOJCIECH S., 2012, Rigid finite element method in modelling of vibrations of electrostatic precipitators (in Polish), *Modelowanie Inżynierskie*, **43**, 7-14

2. BERCZYŃSKI S., GUTOWSKI P., 2006, Identification of the dynamic models of machine tool supporting systems. Part I: An algorithm of the method, *Journal of Vibration and Control*, **12**, 279-295

3. BERCZYŃSKI S., WRÓBLEWSKI T., 2005, Vibration of steel-concrete composite beams using the Timoshenko beam model, *Journal of Vibration and Control*, **11**, 829-848

4. BERCZYŃSKI S., WRÓBLEWSKI T., 2010, Experimental verification of natural vibration models of steel-concrete composite beams, *Journal of Vibration and Control*, **16**, 2057-2081

5. EWINS D.J., 2000, *Modal Testing: Theory, Practice, and Application*, Hertfordshire, Research Studies Press

6. HE J., FU Z.F., 2001, *Modal Analysis*, Butterworth-Heinemann

7. KRUSZEWSKI J., SAWIAK S., WITTBRODT E., 1999, *The Rigid Finite Element Method in Structural Dynamics* (in Polish), WNT, Warszawa

8. LEISSA A.W., 1973, The free vibration of rectangular plates, *Journal of Sound and Vibration*, **31**, 3, 257-293

9. LIEW K. M., XIANG Y., KITIPORNCHAI S., 1993, Transverse vibration of thick rectangular plates. I – Comprehensive sets of boundary conditions, *Computer and Structures*, **49**, 1, 1-29

10. MARCHELEK K., 1991, *Dynamics of Machine Tools* (in Polish), WNT, Warszawa

11. SILVA C.W.D, 2000, *Vibration. Fundamentals and Practice*, CRC Press, Boca Raton, FL.

12. SZCZEŚNIAK W., 2000, *Selected Aspects of the Dynamics of Plates* (in Polish), Oficyna Wydawnicza Politechniki Warszawskiej, Warszawa

13. UHL T., 1997, *Computer-Aided Identification of Models of Mechanical Structures* (in Polish), WNT, Warszawa

14. WILDE K., 2008, *Modal Diagnostics of Civil Engineering Structures*, Gdańsk University of Technology

15. WITTBRODT E., ADAMIEC-WÓJCIK I., WOJCIECH S., 2006, *Dynamics of Flexible Multibody Systems. Rigid Finite Element Method*, Springer-Verlag, Berlin, Heidelberg, New York

16. WRÓBLEWSKI T., BERCZYŃSKI S., ABRAMOWICZ M., 2013, Estimation of the parameters of the discrete model of a steelconcrete composite beam, *Archives of Civil and Mechanical Engineering*, **13**, 209-219

# SOME ASPECTS OF THE EXPERIMENTAL ASSESSMENT OF DYNAMIC BEHAVIOR OF THE RAILWAY TRACK

Vladimir Solonenko, Narzankul Mahmetova, Janat Musayev, Mikhail Kvashnin

*Kazakh Academy of Transport and Communications Named after M. Tynyshpayev, Department of Transport Engineering and Technologies, Almaty, Kazakhstan*

*e-mail: v.solonenko@mail.ru; mussaev75@yandex.kz; mussaev1975@mail.ru; kvashnin_mj55@mail.ru*

Azamat Alpeisov, Algazy Zhauyt

*Kazakh National Technical University Named after K.I. Satpayev, Department of Applied Mechanics and Basics of Machine Design, Almaty, Kazakhstan*

*e-mail: ssitm@mail.ru; ali84jauit@mail.ru*

The paper suggests application of an experimental method for the assessment of the dynamic effect of a locomotive underframe on the railway track. The assessment is to be based on spectral analysis of the response of structural elements of the railway track undergoing a shock pulse. Application of digital measuring systems for monitoring of motion of the train is also proposed.

*Keywords:* railway track, dynamic effect, integrated monitoring, spectral analysis, railway track elements

## 1. Introductions

A railway track is a subsystem of the railway transport infrastructure, including track super structure, roadbed; drainage, anti-deformation, protective and strengthening structures of the roadbed located in the right-of-way, as well as other engineering structures (Kaewunruen and Remennikov, 2007). The state of the track depends on the continuity and safety of the rolling stock movement as well as the effective use of technical facilities of the railways (Knothe and Grassie, 1993; Liang and Zhu, 2001). Under conditions of constant exposure to natural and anthropogenic factors, the track takes heavy loads from the passing trains. In this case, all the track elements in terms of reliability, durability and stability must ensure a safe and smooth movement of trains with the greatest loads from sets of wheels of the rolling stock on rails and with maximum movement speeds, and have sufficient reserves (Smutny, 2004). During operation of the railway structures, it is necessary to consider their ability to maintain the initial parameters after exposure to natural and man-induced impacts. The nature of these effects is determined by the impact of various factors, including the level of vibrations occurring during rolling stock motion. Vibration actions have a significant impact on the railway track state (Wu and Thompson, 2004). The causes of their occurrence are as follows:

- Moving loads (quasi-static excitation), i.e. deflection of the track and supporting system along with movement of the train. On a fixed point on the rail-track, the fluctuating loads cause the occurrence of flexural waves both in the rails and in the surrounding soil. The mechanism of this excitation is not yet known in details (including the influence of boundary conditions, dissimilarity of the track and ground on wave propagation) (Abdelkrim *et al.*, 2003). If a high-speed train is moving along the track laid on a soft ground, the speed of its movement can exceed the speed of propagation of the surface (Rayleigh) wave in the ground. This creates high level vibrations just like flight of a supersonic aircraft is

accompanied by sonic boom. Above all, such vibration has an effect not only on the state of the track as a whole, but on its components individually (Alves Costa *et al.*, 2010). To solve this problem, the ballast layer of the rail-track is placed on a compacted soil or concrete slabs with pile foundation, which reaches more dense soil layers (Berggren *et al.*, 2010). If the rail-track is laid in a tunnel, its lining and arch invert provides a rigid base reducing the vibration level propagating in the surrounding soil.

- Roughness of the surface of wheels and rails. Random roughness in the area of the rail contact with the wheel causes excitation of the entire rolling stock-rail-track system (Bodare, 2009). Such roughness occurs primarily in the manufacturing process, so during inspection, it is necessary to control and test the state of the track and wheels. However, it cannot prevent the occurrence of roughness in the process of operation.

- Parametric excitation. If the rail support has a discrete structure of cross-sleepers, the elastic supports above the concrete basis (as opposed to the rails embedded in concrete) and the wheel while running on the rail "feel" the change in the support stiffness. Variable elastic forces create vibrations of the wheel and rail at a frequency that depends on the speed of the rolling stock and spatial discreteness of the support. Other discreteness (and excitation frequencies corresponding to it) is characterized by the distance between the wheelsets and bogies (Choi, 2013a,b). If the excitation frequencies coincide with the natural frequencies of the railway track, the vibrations of the track and surrounding soil can be quite considerable. The frequency of the impact $f_k$ [Hz], corresponding to the $n$-th characteristic distance $l_v$ [m] (see Fig. 1) is determined via the rolling stock speed $V$ [m/s], according to the formula.
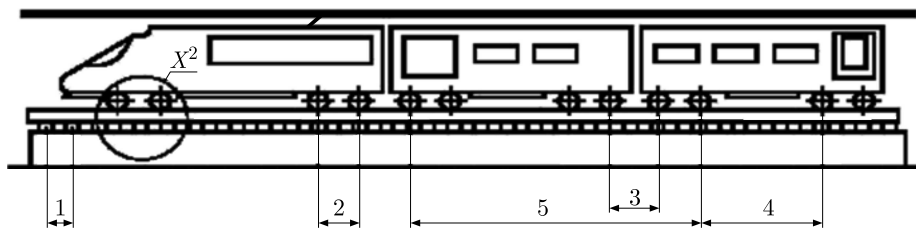


Fig. 1. Characteristic parameters of the vibration source; 1 – distance between supporting elements of the track, 2 – distance between wheelsets of the bogie carriage, 3 – distance between the adjacent bogie carriages of the adjacent railcars, 4 – distance between bogie carriages of one railcar, 5 – distance between railcars

- Wheel (rail) defects. In addition to the roughness on the surface of wheels and rails, there can be also observed rough defects occurring during rail-track operation. The major defects are associated with the presence of wheel flats and corrugations of the rails. Moreover, the wheels are subjected to such defects as out-of-roundness, out-of-balance and eccentricity (Choi *et al.*, 2011a,b). In the course of time, the defects accumulate, especially if the track is not provided with a timely and proper technical care and maintenance.

- Discontinuities in the running surface of rails (in track switches, rail joints, etc.) causing the occurrence of bumps. If length of the joint or welded rails is equal to the distance between the carriage bogies, the vibration level may be increased significantly.

- Suspension of the rolling stock.

- Random or periodic changes in hardness of the rail running surface due to defects in workmanship or (more likely) resulting from the ageing process of the rail-track.

- Loads in the transverse direction, particularly during motion of the rolling stock along a curved track of small radius, or when passing turnouts.

- Changing the mode of motion. Acceleration or deceleration of the rolling stock is accompanied by the occurrence of variable forces and oscillations.
- External factors. For example, temperature and humidity of the rail head influence its wear and tear and, consequently, result in vibration occurrence (Kaewunruen and Remennikov, 2006a,b, 2007a,b).

The vibration level due to the above reasons depends on the input impedances (resistance of the medium to spread mechanical vibrations) of the rail head and wheel rim in the area of their contact. The value of the input impedance of the rail head is determined by the track superstructure, its basis as well as characteristics of the surrounding soil (Li *et al.*, 2009; Li and Berggren, 2010).

## 2. Materials and methods

The wheel output impedance essentially depends on the unsprung mass of the locomotive underframe. However, total mass of the locomotive underframe together with the load is also very important for the rigid suspension (due to structural features of the damper and its behavior at high frequencies).

Given the above, to increase the level of safety of railway operation, it is necessary to apply progressive methods of diagnostics and monitoring aimed at the assessment of the vibration level occurring during operation and of the current status of all elements of the railway track. The need and urgency of implementing innovative systems and means of diagnostics and monitoring of the railway facility are reflected in Programs for the development of railway system until 2020 in the Republic of Kazakhstan.

Based on the study of dynamic processes occurring in strategic facilities (Clark, 2004), in particular in the railway track superstructure, it is suggested to carry out a comprehensive monitoring of the railway track system.

The monitoring system allows establishing a permanent instrumental control over the railway track state for a long period. In addition, it is possible to carry out an objective assessment of the impact of structural features of the track elements (rails, fasteners, cross-sleepers, etc.) on the level of vibrations occurring during notion of the rolling stock and take the best optimum decisions in the design of new and improvement of the existing track systems (Hall, 2002). The monitoring system includes standards (requirements for the arrangement and maintenance of the track superstructure by taking into account the operating conditions), controlled parameters, means of monitoring and measurement modes, assessment of the maximum permissible thresholds and tolerances.

The monitoring system has been developed using a mobile vibration-measuring equipment. The system consists of vibration sensors MV-25D-B which convert mechanical vibrations into electric signal. Transformation of an analog signal into a digital form is carried out within the electronic unit of the analog-to-digital converter (ADC manufactured by "L-CARD" Co., model E-14-440). Collection of digital data from ADC and common measurements control is implemented by means of a special software for PC. A general view to the mobile vibration-measuring system is shown in Fig. 2. All the measurement tools included in the mobile vibration-measuring facility are certified and calibrated. The operation of the system is powered by a rechargeable battery (Hamet, 1999).

The following may be referred to the main advantages of the mobile vibration-measuring system:

(i) the modular principle of the system configuration with universal power supply;

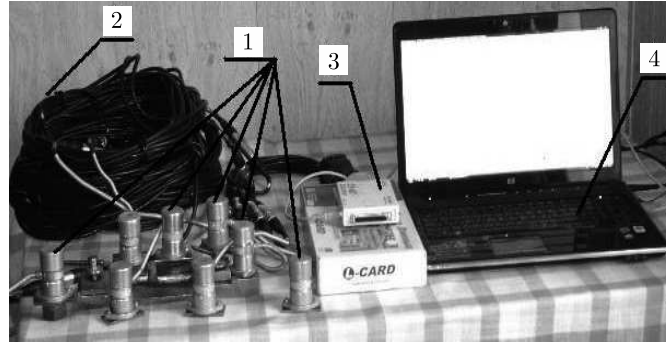(ii) application of vibration sensors with high sensitivity in a wide range of frequencies and impact amplitudes;

Fig. 2. General view of the mobile vibration-measuring system; 1 – vibration sensors, 2 – patch cable, 3 – multichannel ADC, 4 – laptop

(iii) application of multichannel ADC providing transfer of digitized data with high pin-point accuracy to the parallel port of a personal computer;

(iv) data acquisition in a digital format with possibility of software processing of the acquired information, its storage and systematization for the purpose of correlation detection;

(v) high reliability and working capacity in a wide range of climatic conditions;

(vi) insignificant dimensions and mass of all components.

Processing of the signals registered by vibration sensors is carried out by means of a special software installed on a laptop. Direct recording of a signal is carried out by means of application of the software LGraph2. This software provides possibility for setting the signals recording parameters and signals visualization in real time. Functionally, LGraph2 software represents a digital oscilloscope. Then the results of measurements are stored on the hard disk drive of the computer in "txt" format. As a result of primary data translation in the text format, they represent a dependence of electrical voltage generated by the sensor on time. The vibration sensors are calibrated before determination of the transformation coefficients.

There is a relationship for $U_n$ depending on time $t_n$, $n = 0, \ldots, N-1$, where $N$ is the number of counts, $T = t_{N-1}$ is the time length of signal realization. The actual vibration speed is calculated per voltage values

$$v_n = \frac{U_n}{K_n} \tag{2.1}$$

where $K_n$ is the sensor transformation coefficient.

The vibration sensors are preliminarily calibrated on vibration table ESE 201 to determine the transformation coefficients. The transition from the time to frequency domain is carried out using the direct Fourier transformation

$$V_k = \sum_{n=0}^{N-1} v_n \exp\left(\frac{-2\pi \mathrm{i} k_n}{N}\right) \tag{2.2}$$

In order to obtain the amplitude-time dependence of the vibrational displacement (oscillograms), it is necessary to integrate the function $v_n$ (Fig. 3). For this, let us use the property of the direct Fourier transformation (DFT)

$$\widehat{F}' = 2\pi \mathrm{i} f \widehat{F} \tag{2.3}$$

where $\widehat{F}$ is DFT of the function $F$ with respect to $V_k$ (Fig. 4). Then, by the inverse of Fourier transformation (IFT), we obtain (Fig. 5)

$$S_k = \frac{V_k}{2\pi \mathrm{i} f_k + \pi V_0 \Delta f} \tag{2.4}$$
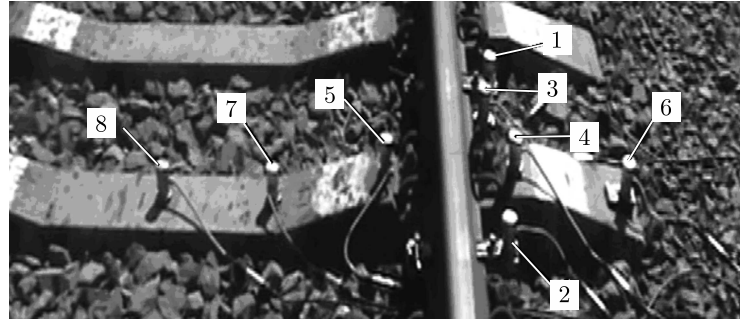
Fig. 3. Amplitude-time dependence of vibrational speed obtained on the rail base during passage of locomotive VL80
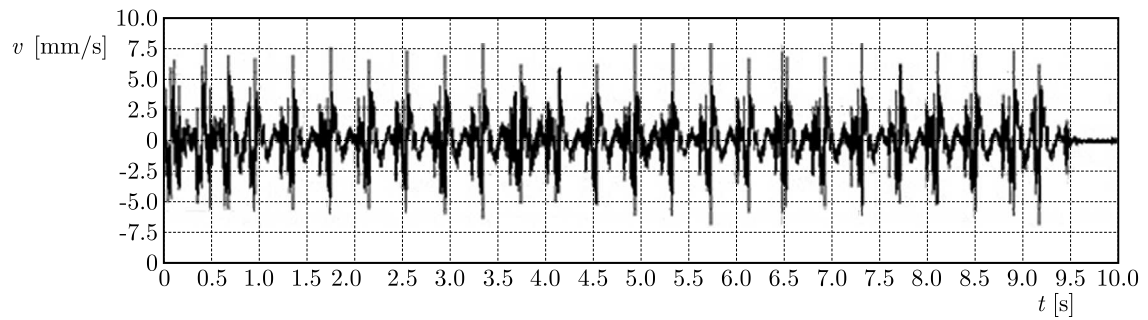


Fig. 4. Spectrum of vibrational speed obtained on the rail base during passage of locomotive VL80
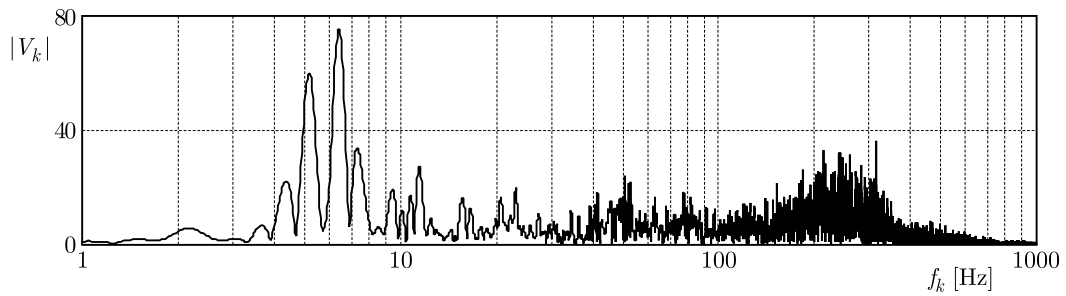


Fig. 5. Spectrum of displacement obtained on the rail base during passage of locomotive VL80
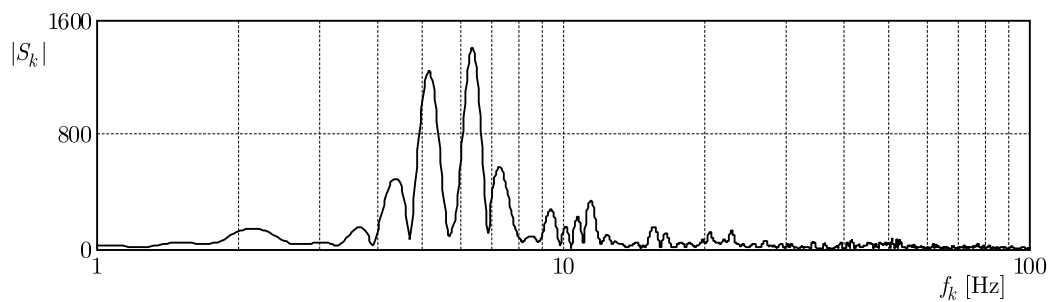


Fig. 6. Amplitude-time dependence of the vibrational displacement obtained on the rail base during passage of locomotive VL80

where $\Delta f = 1/T$ (signal sampling by frequency), $f_k = \Delta f_k$. Figure 6 shows the oscillogram spectrum obtained on the rail base during passage of locomotive VL80.

Let us make IFT to return to the time domain

$$S_n = \frac{1}{N} \sum_{k=0}^{N-1} S_k \exp\left(\frac{2\pi i k_n}{N}\right) \qquad (2.5)$$
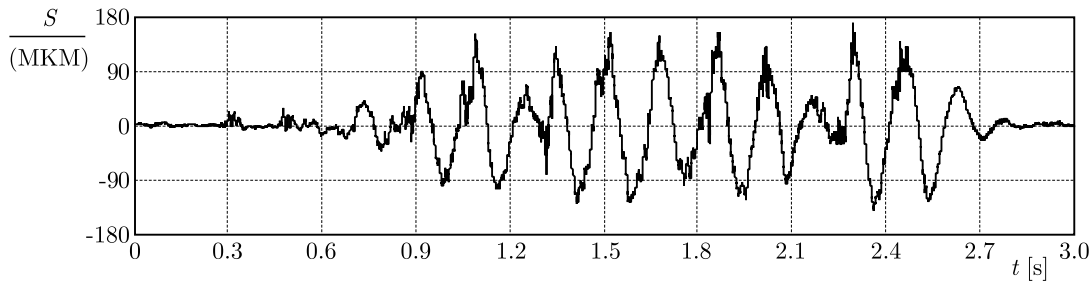
Fig. 7. Spectrum of vibrational acceleration obtained on the rail base during passage of locomotive VL80

Hence, we obtain the amplitude-time dependence of the vibrational displacement on time (Fig. 7). For obtaining of amplitude-time dependence of vibrational accelerations (accelerograms), it is necessary to differentiate $v_n$ and consider elimniation of distortion of the sensor transformation coefficient in the frequency domain over $1000\,\mathrm{Hz}$. For differentiation, let us again make use of DFT property represented by expression (2.3), and use Butterworth filter for the elimination of distortion in the low frequencies domain

$$A_k = V_k H_k (2\pi \mathrm{i} f_k) \tag{2.6}$$

where $H_k$ is Butterworth filter

$$H_k = \frac{1}{\sqrt{1 + \left(\frac{f_k}{f_B}\right)^{2p}}} \frac{1}{\sqrt{1 + \left(\frac{f_H}{f_{k+1}}\right)^{2p}}} \tag{2.7}$$

where $(f_H, f_B)$ is the range of frequencies passing through the filter; $p$ is the filter order. Butterworth filter characteristics are given in Fig. 8.
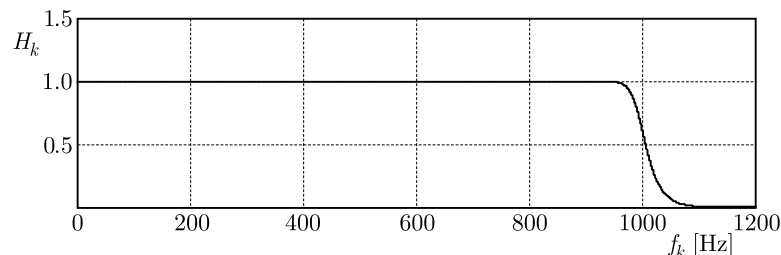


Fig. 8. Butterworth filter characteristics in the low frequency domain at $f_H = 0.1\,\mathrm{Hz}$, $f_B = 1000\,\mathrm{Hz}$, $p = 50$

For the obtained amplitude $A_k$ (Fig. 7) let us make IFT. As a result, Eq. (2.7), we obtain the amplitude-time dependence of vibrational accelerations filtered in the low frequency domain in the following form

$$a_n = \frac{1}{N} \sum_{k=0}^{N-1} A_k \exp\left(\frac{2\pi \mathrm{i} k_n}{N}\right) \tag{2.8}$$

For the assessment of data acquired during diagnostics and monitoring, the author of this paper has developed a package of application software for data processing and visualization based on Mathsoft Engineering & Education Inc. "MATHCAD" products.

The procedure is developed for diagnostics of the track superstructure and then given are the results of its testing and adaptation to track sections with intermediate rail fastenings FOSSLOH, ZHBR-65SHD, ZHBR-65, KZF-07.

The diagnostic technique is based on spectrum analysis of the track superstructure elements to the impact force. Excitation of free vibrations is carried out by a mechanical shock to the rail using a hammer. The use of rubber in the impact device is explained by impermissibility of the rail running surface damage (Kumaran *et al.*, 2003).

The modulus of spectrum density of the response to the impact force is determined by

$$|N(f)| = |S(f)|\,|M(f)| \tag{2.9}$$

where $|S(f)|$ is the modulus of spectrum of the impact force impulse $F(t)$, $|M(f)|$ is the modulus of the amplitude-frequency characteristic of the track superstructure element under investigation.

During selection of the optimal parameter of the impact system, the following function is taken as the impact force impulse according to Hertz theory

$$F(t) = \begin{cases} S_0 \sin \frac{\pi t}{\tau}; & \text{at} \quad 0 \leqslant t \leqslant \tau \\ 0 & \text{at} \quad t > \tau \end{cases} \tag{2.10}$$

The modulus of spectrum density has the following form

$$|S(f)| = \frac{2S_0\tau}{\pi} \frac{\cos(\pi f\tau)}{1 - (2\pi f\tau)^2} \tag{2.11}$$

where $S_0$ is the initial amplitude of vibrations of the track superstructure under the impact force (2.10), $\tau$ is the impulse length of collision of the impact system with the object, which in the first approximation is determined according to Hertz impact theory, i.e.:

$$\tau = \frac{4.531}{\sqrt[5]{V_0}} \left( \frac{M\left(\frac{1-\mu_1^2}{E_1} + \frac{1-\mu_2^2}{E_2}\right)}{\pi\sqrt{R}} \right)^{\frac{2}{5}} \tag{2.12}$$

where $E_1$, $E_2$ and $\mu_1$, $\mu_2$ are Young's moduli and Poisson's ratios of the hammer and rail steel material, respectively, $R$ is radius of the contact surface of the impact system, $V_0$ is linear velocity of the hammer, $M$ is reduced mass of the colliding bodies equal to

$$M = \frac{m_1 m_2}{m_1 + m_2} \tag{2.13}$$

where $m_1$ and $m_2$ are masses of the hammer and railway track structure, respectively.

In addition to the optimal choice of value $\tau$, the external energy delivered to the monitored object must be sufficient for excitation of normal bending vibrations in the track superstructure on the fundamental mode. The initial amplitude of these vibrations $S_0$ must be such as to give possibility to carry out qualitative spectrum analysis of recordable responses of the impact force ($S_0 > 10\zeta$) at a prescribed sensitivity of the receiving vibratory sensor $\zeta$. The initial amplitude of vibrations is determined by the formula

$$S_0 = \frac{F}{2\pi m f_0} \tag{2.14}$$

where $F$ is the initial force impulse, $f_0$ is the frequency of the first bending mode of the railway track, $m = m_1 + m_2$.

The sensors layout depends on the priority task of research and may vary during diagnostics in very wide ranges. Figure 9 gives an example of the sensors positioning during diagnostics of the track superstructure.
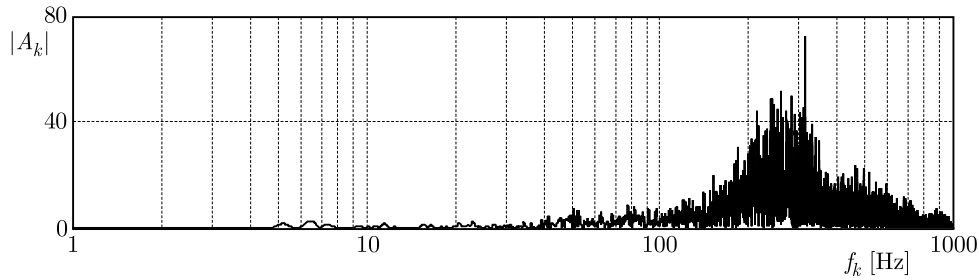
Fig. 9. General view of the sensors positioning during diagnostic of the track superstructure; 1, 2 on the rail base, 3 on resilient clamp, 4 on cross-sleeper outside the rail, 5 on cross-sleeper inside the rail, 6 at cross-sleeper end, 7, 8 in center of the cross-sleeper

The following parameters are measured and analyzed during execution of diagnostics:

(i) frequencies corresponding to the modes of bending vibrations of the track superstructure $f_i$ (determined by spectra of responses obtained on different elements of the railway track);

(ii) logarithmic decrement to be determined on the basis of connection between the logarithmic decrement and width of the spectrum line

$$d_i = \pi \frac{\Delta f_i}{f_i} \tag{2.15}$$

where $d_i$, $\Delta f_i$, $f_i$ is the logarithmic decrement, width of the spectrum line, frequency of vibration modes of interest;

(iii) dynamic response factor $\beta_i$ is determined on the basis of the formula

$$\beta_i = \frac{1}{\sqrt{\left(1 - \frac{f_v^2}{f_i^2}\right)^2 + \left(\frac{d_i}{\pi} \frac{f_v}{f_i}\right)^2}} \tag{2.16}$$

where $f_v$ is the impact frequency;

(iv) $Q$ factor of the track superstructure on the vibration modes of interest is determined by the formula

$$Q_i = \frac{\pi}{d_i} \tag{2.17}$$

(v) speed of the rolling stock at which resonance phenomena occur, and which are determined based on the dependence of the impact frequency $f_v$ on the rolling stock speed $v$ and the parameters of vibration excitation $l_v$

$$f_v = \frac{V}{l_v} \tag{2.18}$$

## 3. Experimental results and discussion

In the paper, the topical issues of an experimental method for the assessment of dynamic impact of the locomotive body on the track is studied. The proposed method is based on spectral analysis of the railway track structural element responses to the impact impulse and monitoring of train motion with the use of digital measuring equipment.

To increase the level of safety of railway operation, the authors elaborated progressive methods of diagnostics and monitoring and introduced special engineering and technical measures

to examine the impact of vibrations occurring during motion of the train on the current state of all railway track elements.

Figure 7 presents a structural diagram of data visualization of the railway track monitoring and the processing program.

The monitoring of trains movement along the studied track structure has been conducted for 6-15 days (depending on the loading level). It included the following ((Liang and Zhu, 2001):

- recording of dynamic processes in the railway track elements at different characters of the rolling load;
- determination of contact conditions between the track superstructure elements (rail-rail fastening, rail fastening-cross sleeper, cross sleeper-ballast section) using the vibroacoustic method (Fig. 10);
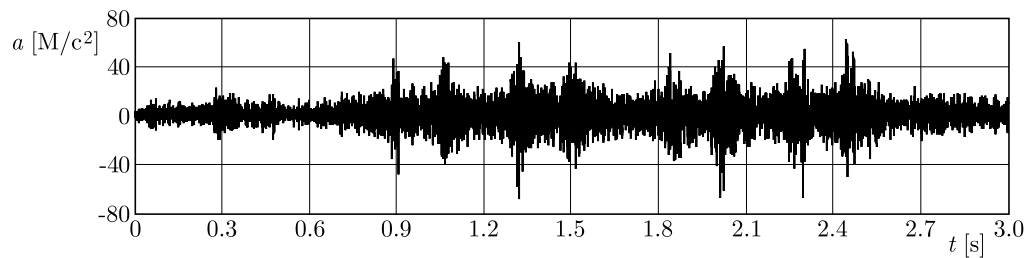


Fig. 10. Amplitude-time dependence of vibrational acceleration obtained on the rail base during during passage of locomotive VL80

- determination of normal (resonance) frequencies and damping properties of elements of the railway track (Fig. 11);
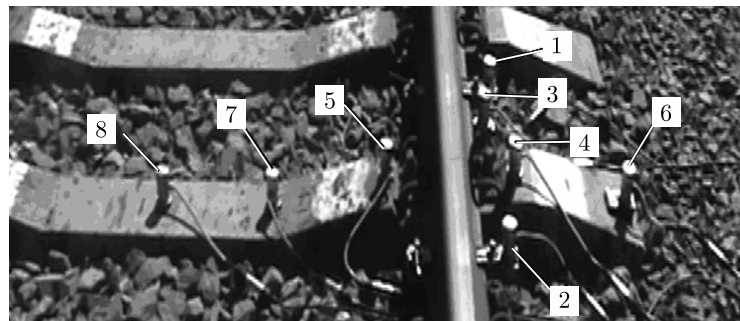


Fig. 11. Diagrams of the spectral density of vibration acceleration of free vibrations of the reinforced concrete cross-sleeper center: curve 1 – good contact of the cross-sleeper with the crushed stone underlayer, 2 – poor contact of the cross-sleeper with the crushed stone underlayer, 3 – the absence of contact of the cross-sleeper with the crushed stone underlayer

- forecasting of the rolling stock speed at which resonance phenomena occurred (Fig. 12);
- determination of impact conditions of the locomotive underframe on the track (Figs. 13 and 14).

## 4.  Conclusions

Conducting a complex monitoring of the railway track allows one to carry out an objective assessment of the condition of track elements (different types of rail fastenings Table 1, various ballast fineness) on the level of vibrations occurring during motion of the rolling stock. It enables
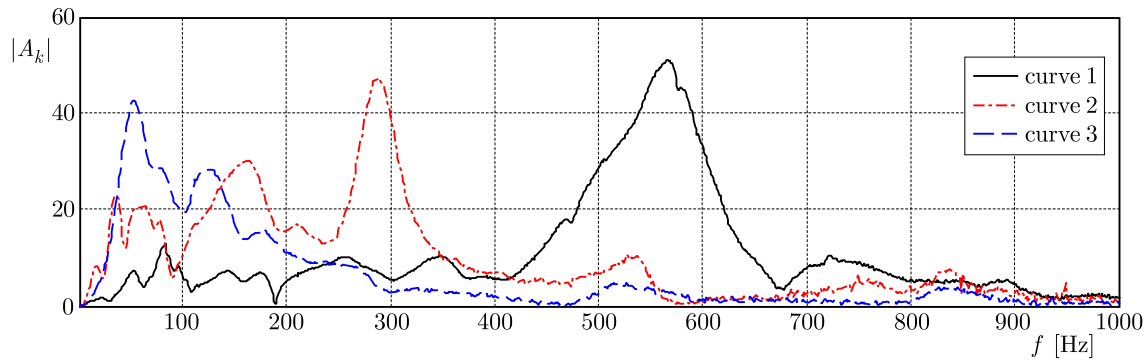
Fig. 12. Diagrams of the spectral density of vibration acceleration of free vibrations for different designs of the track superstructure: curve 1 – fastening of FOSSLOH type, 2 – fastening of KZF-07 type, 3 – fastening of ZHBR-65SHD type
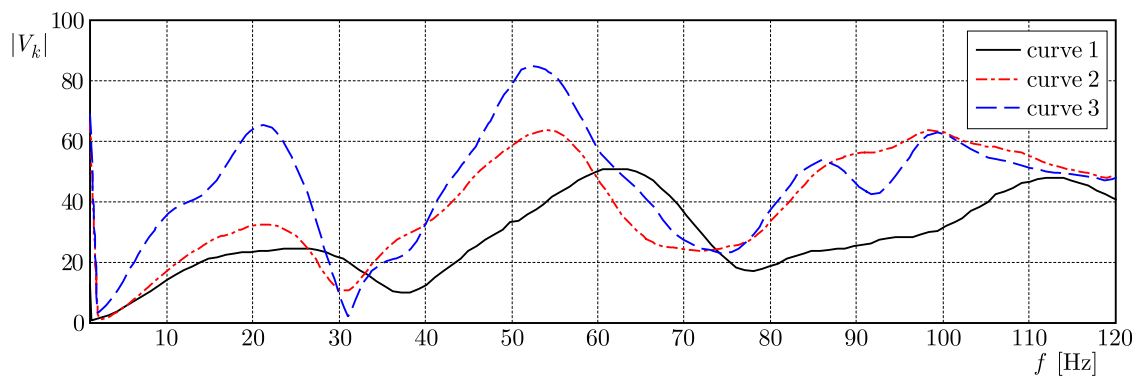


Fig. 13. Dependence of the dynamic response factor on speed of motion of the rolling stock for different solutions of the track superstructure: curve 1 – fastening of FOSSLOH type, 2 – fastening of KZF-07 type, 3 – fastening of ZHBR-65SHD type
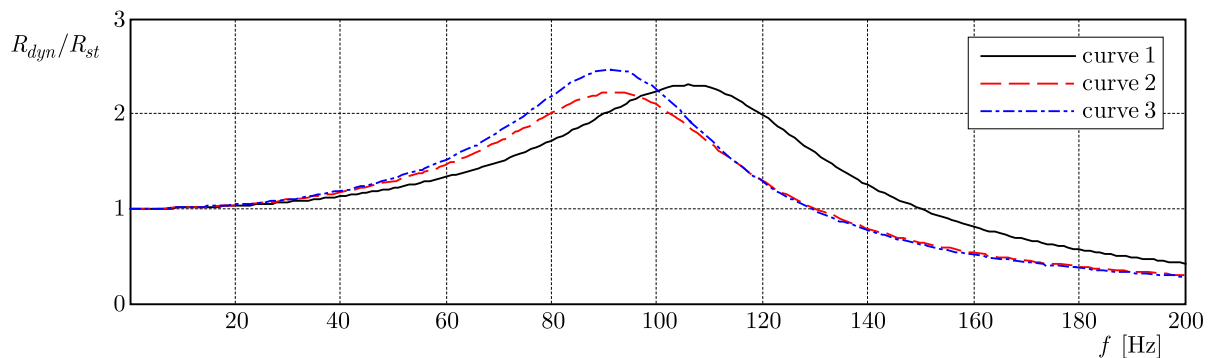


Fig. 14. Correlation of the rail base dynamic to the static force ratioo on electric with velocity of locomotive VL-80

making the most optimum decisions for the design of new tracks and renovation of the existing facilities. In addition, regular monitoring allows increasing the level of safety of the railway track and its operational lifetime as well as reducing the costs of current maintenance. The further direction of research should provide the development of complex systems for monitoring of railway tracks with the use of vibration-measuring equipment for the most objective assessment of their state.

**Table 1.** Results of track superstructure diagnostics with various types of intermediate rail fastenings

| Type of fastening | $f_1$ [Hz] | $f_2$ [Hz] | $d_1$ | $d_2$ | $Q_1$ | $Q_2$ | $V_2$ [km/h] |
|---|---|---|---|---|---|---|---|
| FOSSLOH | 22 | 62 | 3.6 | 1.4 | 1.06 | 2.3 | 106 |
| KZF-07 | 21 | 54 | 2.84 | 1.45 | 1.24 | 2.23 | 92 |
| ZHBR-65SHD | 20 | 53 | 2.9 | 1.3 | 1.22 | 2.47 | 91 |
| ZHBR-65 | 14 | 33 | 3.3 | 1.52 | 1.18 | 2.13 | 56 |

## References

1. ABDELKRIM M., BONNET G., BUHAN P., 2003, A computational procedure for predicting the long term residual settlement of a platform induced by repeated traffic loading, *Computers and Geotechnics*, **30**, 463-476

2. ALVES COSTA P., CALÇADA R., CARDOSO A.S., BODARE A., 2010, Influence of soil non-linearity on the dynamic response of high-speed railway track, *Soil Dynamics and Earthquake Engineering*, **30**, 4, 221-235

3. BERGGREN E.G., KAYNIA A.M., DEHLBOM B., 2010, Identification of substructure properties of railway tracks by dynamic stiffness measurements and simulations, *Journal of Sound and Vibration*, **329**, 3999-4016

4. BODARE A., 2009, Evaluation of track stiffness with a vibrator for prediction of train-induced displacement on railway embankments, *Soil Dynamics and Earthquake Engineering*, **29**, 8, 1187--1197

5. CHOI J.Y., 2013a, Influence of track support stiffness of ballasted track on dynamic wheel-rail forces, *Journal of Transportation Engineering*, **139**, 709-718

6. CHOI J.Y., 2013b, Prediction of displacement induced by tilting trains running on ballasted tracks through measurement of track impact factors, *Engineering Failure Analysis*, **31**, 360-374

7. CHOI J.Y., LEE D.W., PARK Y.G., 2011a, A study on the evaluation of track support stiffness on the various track type in urban transit, *Journal of the Korean Society for Railway*, **14**, 3, 262-270

8. CHOI J.Y., PARK Y.G., LEE S.M., 2011b, The evaluation of track impact factor on the various track type in urban transit, *Journal of the Korean Society for Railway*, **14**, 3, 248-255

9. CLARK R., 2004, Rail flaw detection: overview and needs for future developments, *NDT&E International*, **37**, 2, 111-118

10. HALL L., 2002, Simulations and analyses of train-induced ground vibrations in nite element models, *Soil Dynamics and Earthquake Engineering*, **23**, 403-413

11. HAMET J.F., 1999, Railway noise: use of the Timoshenko model in rail vibration studies, *Acustica*, **85**, 1-12

12. KAEWUNRUEN S., REMENNIKOV A., 2006a, Non-destructive testing (NDT): a tool for dynamic health monitoring of railway track structures, *Materials Australia*, **39**, 6, 14-16

13. KAEWUNRUEN S., REMENNIKOV A., 2006b, Sensitivity analysis of free vibration characteristics of an in-situ railway concrete sleeper to variations of rail pad parameters, *Journal of Sound and Vibration*, **298**, 1/2, 453-461

14. KAEWUNRUEN S., REMENNIKOV A., 2007a, Effect of improper ballast tamping packing on dynamic behaviors of on-track railway concrete sleeper, *International Journal of Structural Stability and Dynamics*, **7**, 1, 167-177

15. KAEWUNRUEN S., REMENNIKOV A.M., 2007b, Field trials for dynamic characteristics of railway track and its components using impact excitation technique, *NDT&E International*, **40**, 7, 510-519

16. KNOTHE K., GRASSIE S.L., 1993, Modelling of railway track and vehicle/track interaction at high frequencies, *Vehicle System Dynamics*, **22**, 3/4, 209-262

17. Kumaran G., Menon D., Krishman Nair K., 2003, Dynamic studies of rail track sleepers in a track structure system, *Journal of Sound and Vibration*, **268**, 485-501

18. Li M.X.D., Berggren E.G., 2010, A study of the effect of global track stiffness and its variations on track performance: simulation and measurement, *Journal of Rail and Rapid Transit*, **224**, 375-382

19. Li M.X.D., Berggren E.G., Berg M., 2009, Assessment of vertical track geometry quality based on simulations of dynamic track-vehicle interaction, *Journal of Rail and Rapid Transit*, **223**, 131-139

20. Liang B., Zhu D., 2001, Dynamic analysis of the vehicle-subgrade model of a vertical coupled system, *Journal of Sound and Vibration*, **245**, 79-92

21. Okada K., Ghataora G.S., 2002, Use of cyclic penetration test to estimate the stiffness of railway subgrade, *NDT&E International*, **35**, 65-74

22. Smutny J., 2004, Measurement and analysis of dynamic and acoustic parameters of rail fastening, *NDT&E International*, **37**, 119-129

23. Wu T.X., Thompson D.J., 2004, The effects of track nonlinearity on wheel/rail impact, *Journal of Rail and Rapid Transit*, **218**, 1, 1-15

# STRENGTH OF A METAL SEVEN-LAYER RECTANGULAR PLATE WITH TRAPEZOIDAL CORRUGATED CORES

Ewa Magnucka-Blandzi, Zbigniew Walczak, Leszek Wittenbeck

*Institute of Mathematics, Poznan University of Technology, Poznań, Poland*

*e-mail: ewa.magnucka-blandzi@put.poznan.pl, zbigniew.walczak@put.poznan.pl, leszek.wittenbeck@put.poznan.pl*

Marcin Rodak

*Institute of Applied Mechanics, Poznan University of Technology, Poznań, Poland*

*e-mail: marcin.rodak@put.poznan.pl*

The subject of analytical and numerical investigations in this paper is a metal seven-layer rectangular plate with a trapezoidal corrugated main core and two trapezoidal corrugated cores of faces. The hypothesis of deformation of the normal to the middle surface of the plate after bending and field of displacements is formulated. The plate is simply supported on all its edges and subjected to a uniform pressure. Equations of equilibrium are derived based on the theorem of minimum total potential energy and are solved with the use of the Galerkin method. The influence of the trapezoidal corrugation pitch of the cores on the deflection and the equivalent stress is analysed.

*Keywords:* rectangular layered plate, corrugated cores, hypothesis of deformation, deflection, stresses

## 1. Introduction

The basic theoretical models of sandwich structures were formulated in the mid of the 20th century. Two decades later, Plantema (1966) and Allen (1969) elaborated first monographs devoted to bending, buckling and design problems of sandwich beams, plates and shells. Noor *et al.* (1996), Vinson (2001), Carrera (2003), Carrera and Brischetto (2009) presented a review of the problems related to computational models, applications and analysis of sandwich structures. Kazemahvazi and Zenkert (2009) developed an analytical model for the compressive and shear response of monolithic and hierarchical corrugated composite cores. Ji *et al.* (2010) described design procedures and the construction process of a glass fiber reinforced polymer corrugated-core sandwich bridge superstructure. Seong *et al.* (2010) introduced bi-directionally corrugated cores in order to reduce anisotropic behaviour of sandwich plates with open channel cores under the bending load. Magnucka-Blandzi (2011) described and solved analytically the problem of a simply supported rectangular sandwich plate under compression in plane. Poirier *et al.* (2013) proposed a methodology for designing lightweight laser-welded steel sandwich panels with superior structural performance. Jha *et al.* (2013) presented static analysis of orthotropic functionally graded elastic, rectangular and simply supported plates under transverse loads. Zhang *et al.* (2013) investigated compressive strengths and the dynamic response of corrugated sandwich plates with unfilled and foam filled sinusoidal plate cores. Magnucka-Blandzi and Magnucki (2014) determined analytically transverse shear moduli of corrugated cores in four different shapes. The influence of the corrugation shape on the shear modulus was studied. Lewinski *et al.* (2015) studied transverse shear moduli of two thin-walled trapezoidal corrugated cores of seven-layer sandwich plates. Magnucka-Blandzi *et al.* (2015) presented a mathematical modelling of the transverse shearing effect for sandwich beams with sinusoidal corrugated cores.

The buckling and bending problems were solved. Magnucki *et al.* (2016) formulated two analytical models of a seven-layer steel beam with a transverse sinusoidal corrugated main core and two sandwich facings with steel foam cores, and solved the problem of bending and buckling. Cheon and Kim (2015) suggested an equivalent plate model to analyze the mechanical behaviour of corrugated-core sandwich panels under tensile and bending loads. Mantari and Granados (2015) presented a static analysis of functionally graded plates. In the paper, a simply supported square sandwich plate was subjected to a bi-sinusoidal load. Vaidya *et al.* (2015) investigated the response of sandwich steel beams with corrugated cores to quasi-static loading by employing experimental and computational approaches. A parametric study was also carried out on large-scale structural size beams of a few meters in length.

The subject of this study is a metal seven-layer rectangular plate with a trapezoidal corrugated main core and two trapezoidal corrugated cores of facings. The plate is simply supported and loaded with a uniformly distributed pressure.

## 2. Mathematical modelling of a seven-layer plate

### 2.1. Displacements and strains

A seven-layer rectangular plate with the trapezoidal corrugated main core, two inner flat sheets, two trapezoidal corrugated cores of the facings and two outer flat sheets is shown in Fig. 1. The plate is simply supported on all its edges and subjected to a uniform pressure $p_0$.
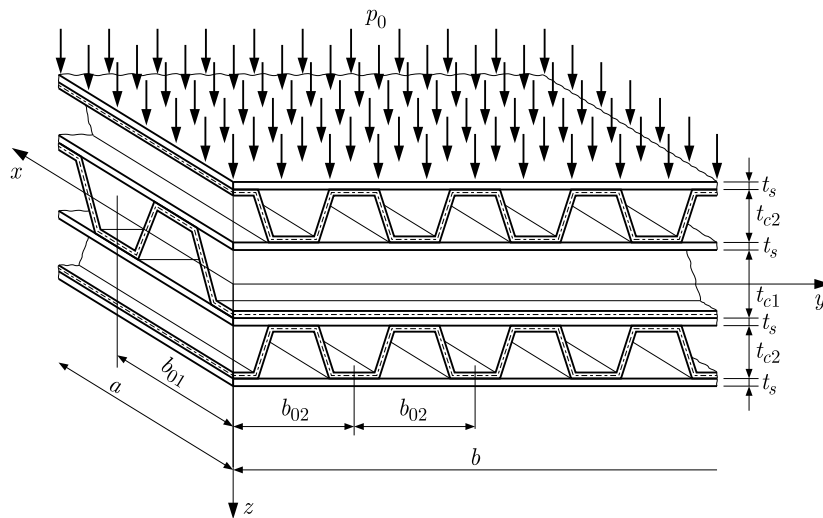


Fig. 1. Scheme of the seven-layer rectangular plate

The direction of the core facings corrugations is orthogonal to the one of the main core corrugation. Trapezoidal corrugations of the main core and facings cores are shown in Fig. 2.
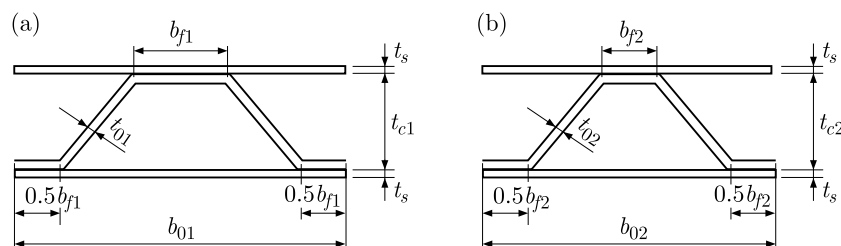


Fig. 2. Scheme of the corrugations of the (a) main core and (b) faces cores

Taking into account the layered structures of the plate, it is easy to notice that the straight line normal to the middle plane of the plate before bending does not remain straight and normal after bending. The hypothesis is assumed that the straight line – normal after bending – takes a shape of a broken line (Fig. 3). The problem of the hypothesis for multi-layer structures was described, e.g. by Carrera (2003) and Magnucki *et al.* (2016).
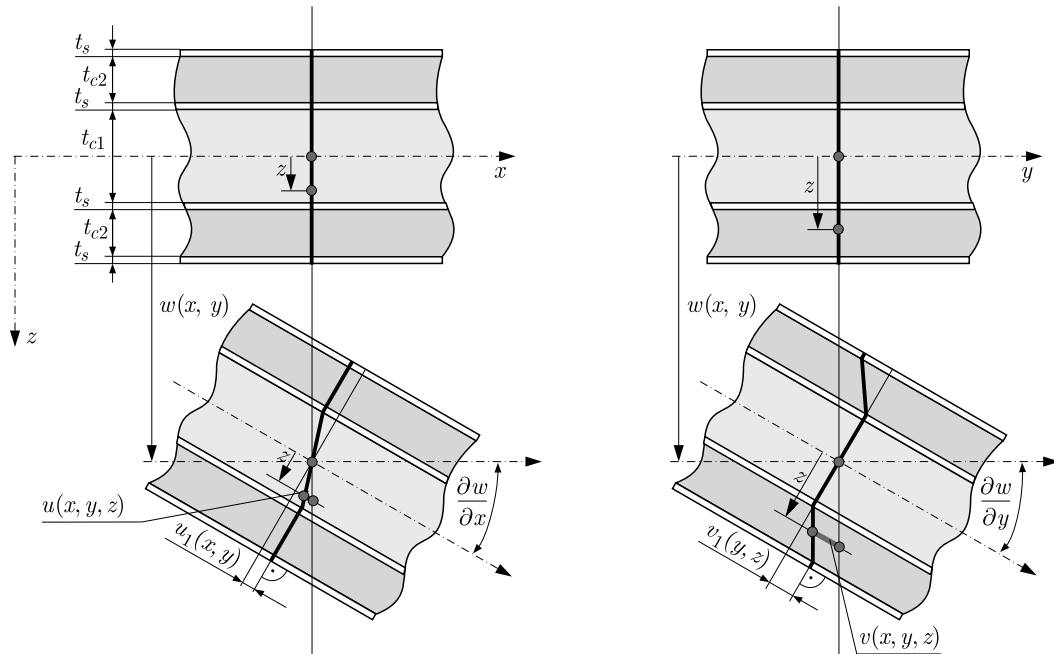


Fig. 3. Deformation of the normal to the middle plane of the plate

The displacements with consideration of the hypothesis are as follows:
1) outer flat sheets
- the upper sheet for $-(0.5 + 2x_1 + x_2) \leqslant \zeta \leqslant -(0.5 + x_1 + x_2)$

$$u(x, y, z) = -t_{c1}\Big[\zeta\frac{\partial w}{\partial x} + \psi(x, y)\Big] \qquad v(x, y, z) = -t_{c1}\Big[\zeta\frac{\partial w}{\partial y} + x_2\phi(x, y)\Big] \qquad (2.1)$$

- the lower sheet for $0.5 + x_1 + x_2 \leqslant \zeta \leqslant 0.5 + 2x_1 + x_2$

$$u(x, y, z) = -t_{c1}\Big[\zeta\frac{\partial w}{\partial x} - \psi(x, y)\Big] \qquad v(x, y, z) = -t_{c1}\Big[\zeta\frac{\partial w}{\partial y} - x_2\phi(x, y)\Big] \qquad (2.2)$$

2) trapezoidal corrugated cores of the facings
- the upper core for $-(0.5 + x_1 + x_2) \leqslant \zeta \leqslant -(0.5 + x_1)$

$$
\begin{aligned}
u(x, y, z) &= -t_{c1}\Big[\zeta\frac{\partial w}{\partial x} + \psi(x, y)\Big] \\
v(x, y, z) &= -t_{c1}\Big\{\zeta\frac{\partial w}{\partial y} - \Big[\zeta + \Big(\frac{1}{2} + x_1\Big)\Big]\phi(x, y)\Big\}
\end{aligned}
\qquad (2.3)
$$

- the lower core for $0.5 + x_1 \leqslant \zeta \leqslant 0.5 + x_1 + x_2$

$$
\begin{aligned}
u(x, y, z) &= -t_{c1}\Big[\zeta\frac{\partial w}{\partial x} - \psi(x, y)\Big] \\
v(x, y, z) &= -t_{c1}\Big\{\zeta\frac{\partial w}{\partial y} - \Big[\zeta - \Big(\frac{1}{2} + x_1\Big)\Big]\phi(x, y)\Big\}
\end{aligned}
\qquad (2.4)
$$

3) inner flat sheets
  - the upper sheet for $-(0.5 + x_1) \leqslant \zeta \leqslant -0.5$

$$u(x, y, z) = -t_{c1}\Big[\zeta\frac{\partial w}{\partial x} + \psi(x, y)\Big] \qquad v(x, y, z) = -t_{c1}\zeta\frac{\partial w}{\partial y} \qquad (2.5)$$

  - the lower sheet for $0.5 \leqslant \zeta \leqslant 0.5 + x_1$

$$u(x, y, z) = -t_{c1}\Big[\zeta\frac{\partial w}{\partial x} - \psi(x, y)\Big] \qquad v(x, y, z) = -t_{c1}\zeta\frac{\partial w}{\partial y} \qquad (2.6)$$

4) main corrugated core for $-0.5 \leqslant \zeta \leqslant 0.5$

$$u(x, y, z) = -t_{c1}\zeta\Big[\frac{\partial w}{\partial x} - 2\psi(x, y)\Big] \qquad v(x, y, z) = -t_{c1}\zeta\frac{\partial w}{\partial y} \qquad (2.7)$$

where $x_1 = t_s/t_{c1}$, $x_2 = t_{c2}/t_{c1}$ are dimensionless parameters, $\xi = z/t_{c1}$ – dimensionless coordinate, $t_{c1}$, $t_{c2}$, $t_s$ – thicknesses of the main core, facing cores and flat sheets (Fig. 2), $\psi(x, y) = u_1(x, y)/t_{c1}$, $\phi(x, y) = v_1(x, y)/t_{c2}$ – dimensionless functions of displacements, $u_1(x, y)$, $v_1(x, y)$ – displacements in the $x$ and $y$ directions, respectively, $w(x, y)$ – deflection (Fig. 3) – deflections of each layer are equal and referenced to the middle plate layer, so $w(x, y, z) \equiv w(x, y)$ and $\varepsilon_z \equiv 0$.

Thus, the linear relations for strains are as follows:

1) outer flat sheets (upper/lower)

$$\varepsilon_x^{(u/l)} = \frac{\partial u}{\partial x} = -t_{c1}\Big(\zeta\frac{\partial^2 w}{\partial x^2} \pm \frac{\partial \psi}{\partial x}\Big) \qquad \varepsilon_y^{(u/l)} = \frac{\partial v}{\partial y} = -t_{c1}\Big(\zeta\frac{\partial^2 w}{\partial y^2} \pm x_2\frac{\partial \phi}{\partial y}\Big)$$

$$\gamma_{xz} = \gamma_{yz} = 0 \qquad \gamma_{xy}^{(u/l)} = \frac{\partial u}{\partial y} + \frac{\partial v}{\partial x} = -t_{c1}\Big(2\zeta\frac{\partial^2 w}{\partial x \partial y} \pm \frac{\partial \psi}{\partial y} \pm x_2\frac{\partial \phi}{\partial x}\Big)$$

$$(2.8)$$

2) trapezoidal corrugated cores of the facings (upper/lower)

$$\varepsilon_x^{(u/l)} = -t_{c1}\Big(\zeta\frac{\partial^2 w}{\partial x^2} \pm \frac{\partial \psi}{\partial x}\Big) \qquad \varepsilon_y^{(u/l)} = -t_{c1}\Big\{\zeta\frac{\partial^2 w}{\partial y^2} - \Big[\zeta \pm \Big(\frac{1}{2} + x_1\Big)\Big]\frac{\partial \phi}{\partial y}\Big\}$$

$$\gamma_{xz} = 0 \qquad \gamma_{yz} = \phi(x, y)$$

$$\gamma_{xy}^{(u/l)} = -t_{c1}\Big\{2\zeta\frac{\partial^2 w}{\partial x \partial y} \pm \frac{\partial \psi}{\partial y} - \Big[\zeta \pm \Big(\frac{1}{2} + x_1\Big)\Big]\frac{\partial \phi}{\partial x}\Big\}$$

$$(2.9)$$

3) inner flat sheets (upper/lower)

$$\varepsilon_x^{(u/l)} = -t_{c1}\Big(\zeta\frac{\partial^2 w}{\partial x^2} \pm \frac{\partial \psi}{\partial x}\Big) \qquad \varepsilon_y^{(u/l)} = -t_{c1}\zeta\frac{\partial^2 w}{\partial y^2}$$

$$\gamma_{xz} = \gamma_{yz} = 0 \qquad \gamma_{xy}^{(u/l)} = -t_{c1}\Big(2\zeta\frac{\partial^2 w}{\partial x \partial y} \pm \frac{\partial \psi}{\partial y}\Big)$$

$$(2.10)$$

The sign "+" refers to the upper facing ($u$), and the sign "−" refers to the lower facing ($l$).

4) main corrugated core

$$\varepsilon_x = -t_{c1}\zeta\Big[\frac{\partial^2 w}{\partial x^2} - 2\frac{\partial \psi}{\partial x}\Big] \qquad \varepsilon_y = -t_{c1}\zeta\frac{\partial^2 w}{\partial y^2}$$

$$\gamma_{xz} = 2\psi(x, y) \qquad \gamma_{yz} = 0 \qquad \gamma_{xy} = -2t_{c1}\zeta\Big(\frac{\partial^2 w}{\partial x \partial y} - \frac{\partial \psi}{\partial y}\Big)$$

$$(2.11)$$

Strains (2.8)-(2.11) make a basis for formulation of the elastic strain energy of the seven-layer plate.

### 2.2. Total potential energy of the plate

The elastic strain energy of the plate is a sum of the energy of the individual layers

$$U_\varepsilon^{(plate)} = U_\varepsilon^{(s-o)} + U_\varepsilon^{(c-2)} + U_\varepsilon^{(s-i)} + U_\varepsilon^{(c-1)} \tag{2.12}$$

Consecutive components of the sum are as follows:
1) energy of the outer flat sheets

$$U_\varepsilon^{(s-o)} = \frac{t_{c1}}{2} \int_0^a \int_0^b \left\{ \int_{-(\frac{1}{2}+2x_1+x_2)}^{-(\frac{1}{2}+x_1+x_2)} [\Phi_{\sigma,\varepsilon}^{(u,s-o)}]\, d\zeta + \int_{\frac{1}{2}+x_1+x_2}^{\frac{1}{2}+2x_1+x_2} [\Phi_{\sigma,\varepsilon}^{(l,s-o)}]\, d\zeta \right\}\, dx\, dy \tag{2.13}$$

where

$$\Phi_{\sigma,\varepsilon}^{(u/l,s-o)} = \sigma_x^{(u/l)}\varepsilon_x^{(u/l)} + \sigma_x^{(u/l)}\varepsilon_x^{(u/l)} + \tau_{xy}^{(u/l)}\gamma_{xy}^{(u/l)} \tag{2.14}$$

stresses (Hooke's law)

$$\sigma_x^{(u/l)} = \frac{E}{1-\nu^2}(\varepsilon_x^{(u/l)} + \nu\varepsilon_y^{(u/l)}) \qquad \tau_{xy}^{(u/l)} = \frac{E}{2(1+\nu)}\gamma_{xy}^{(u/l)} \tag{2.15}$$

and strains – expressions (2.8).

Integration of expression (2.13) with respect to the coordinate $\zeta$ provides

$$U_\varepsilon^{(s-o)} = \frac{Et_{c1}^3}{1-\nu^2} \int_0^a \int_0^b \left( C_2^{(s-o)} f_{22}^{(s-o)} - c_1^{(s-o)} f_{12}^{(s-o)} + x_1 f_{11}^{(s-o)} \right)\, dx\, dy \tag{2.16}$$

where

$$c_2^{(s-o)} = \frac{1}{12}[28x_1^2 + 18x_1(1+2x_2) + 3(1+2x_2)^2]x_1 \qquad c_1^{(s-o)} = (1+3x_1+2x_2)x_1$$

$$f_{22}^{(s-o)} = \left(\frac{\partial^2 w}{\partial x^2}\right)^2 + 2\nu\frac{\partial^2 w}{\partial x^2}\frac{\partial^2 w}{\partial y^2} + \left(\frac{\partial^2 w}{\partial y^2}\right)^2 + 2(1-\nu)\left(\frac{\partial^2 w}{\partial x\partial y}\right)^2$$

$$f_{12}^{(s-o)} = \left(\frac{\partial^2 w}{\partial x^2} + \nu\frac{\partial^2 w}{\partial y^2}\right)\frac{\partial\psi}{\partial x} + x_2\left(\nu\frac{\partial^2 w}{\partial x^2} + \frac{\partial^2 w}{\partial y^2}\right)\frac{\partial\phi}{\partial y} + (1-\nu)\left(\frac{\partial\psi}{\partial y} + x_2\frac{\partial\phi}{\partial x}\right)\frac{\partial^2 w}{\partial x\partial y}$$

$$f_{11}^{(s-o)} = \left(\frac{\partial\psi}{\partial x}\right)^2 + \frac{1-\nu}{2}\left(\frac{\partial\psi}{\partial y}\right)^2 + x_2\left[2\nu\frac{\partial\psi}{\partial x}\frac{\partial\phi}{\partial y} + (1-\nu)\frac{\partial\phi}{\partial x}\frac{\partial\psi}{\partial y}\right]$$

$$+ x_2^2\left[\frac{1-\nu}{2}\left(\frac{\partial\phi}{\partial x}\right)^2 + \left(\frac{\partial\phi}{\partial y}\right)^2\right]$$

2) energy of the corrugated cores of the facings

$$U_\varepsilon^{(c-2)} = \frac{1}{2} \int_0^a \int_0^b \left\{ \frac{1}{b_{02}} \int_{A_{Tr}} [\Phi_{\sigma,\varepsilon}^{(u,c-2)}]\, dA_{Tr}^{(c-2)} + \frac{1}{b_{02}} \int_{A_{Tr}} [\Phi_{\sigma,\varepsilon}^{(l,c-2)}]\, dA_{Tr}^{(c-2)} \right\}\, dx\, dy \tag{2.17}$$

where

$$\Phi_{\sigma,\varepsilon}^{(u/l,c-2)} = \sigma_x^{(u/l)}\varepsilon_x^{(u/l)} + \sigma_y^{(u/l)}\varepsilon_y^{(u/l)} + \tau_{xy}^{(u/l)}\gamma_{xy}^{(u/l)} + \tau_{yz}^{(u/l)}\gamma_{yz}^{(u/l)} \tag{2.18}$$

stresses

$$\sigma_x^{(u/l)} = E\varepsilon_x^{(u/l)} \qquad \sigma_y^{(u/l)} = E_y^{(c-2)}\varepsilon_y^{(u/l)} \qquad \tau_{xy}^{(u/l)} = G_{xy}^{(c-2)}\gamma_{xy}^{(u/l)}$$

$$\tau_{yz}^{(u/l)} = G_{yz}^{(c-2)}\gamma_{yz}^{(u/l)} \tag{2.19}$$

and strains – expressions (2.9).

The area of one pitch of the trapezoidal corrugated cross section (Fig. 2)

$$A_{Tr}^{(c-2)} = 2t_{c2}^2 x_{02}(x_{f2}x_{b2} + \widetilde{s}_{a2}) \tag{2.20}$$

where $x_{02} = t_{02}/t_{c2}$, $x_{f2} = b_{f2}/b_{02}$, $x_{b2} = b_{02}/t_{c2}$ are dimensionless parameters, $\widetilde{s}_{a2}$ – dimensionless length of one pitch – trapezoid

$$\widetilde{s}_{a2} = \sqrt{(1 - x_{02})^2 + x_{b2}^2\Big(\frac{1}{2} - x_{f2}\Big)^2}$$

Integration of expression (2.17) provides

$$U_\varepsilon^{(c-2)} = Et_{c1}^3 \int_0^a \int_0^b \Big[ f_{22}^{(c-2)} + \widetilde{E}_y^{(c-2)} f_{12}^{(c-2)} + \widetilde{G}_{xy}^{(c-2)} f_{11}^{(c-2)} + \widetilde{G}_{yz}^{(c-2)} f_{10}^{(c-2)} \Big]\ dx\,dy \tag{2.21}$$

where

$$f_{22}^{(c-2)} = c_{2x}^{(c-2)}\Big(\frac{\partial^2 w}{\partial x^2}\Big)^2 - 2c_{1x}^{(c-2)}\frac{\partial^2 w}{\partial x^2}\frac{\partial \psi}{\partial x} + c_{0x}^{(c-2)}\Big(\frac{\partial \psi}{\partial x}\Big)^2$$

$$\widetilde{E}_y^{(c-2)} = \frac{x_{b2}x_{02}^3}{2(3x_{f2}x_{b2} + \widetilde{s}_{a2})(1 - x_{02})^2} \qquad f_{10}^{(c-2)} = x_2\frac{\phi^2(x,y)}{t_{c1}^2}$$

$$f_{12}^{(c-2)} = C_{2y}^{(c-2)}\Big(\frac{\partial^2 w}{\partial y^2}\Big)^2 - C_{1y}^{(c-2)}\frac{\partial^2 w}{\partial y^2}\frac{\partial \phi}{\partial y} + C_{0y}^{(c-2)}\Big(\frac{\partial \phi}{\partial y}\Big)^2$$

$$f_{11}^{(c-2)} = 4C_{2y}^{(c-2)}\Big(\frac{\partial^2 w}{\partial x \partial y}\Big)^2 + C_{0y}^{(c-2)}\Big(\frac{\partial \phi}{\partial x}\Big)^2 - \Big(2C_{1y}^{(c-2)}\frac{\partial \phi}{\partial x} + c_{1xy}^{(c-2)}\frac{\partial \psi}{\partial y}\Big)\frac{\partial^2 w}{\partial x \partial y}$$

$$\qquad + x_2\Big(x_2\frac{\partial \phi}{\partial x} + \frac{\partial \psi}{\partial y}\Big)\frac{\partial \psi}{\partial y}$$

$$C_{2x}^{(c-2)} = \frac{1}{2}x_2 x_{02}\Big[x_2^2(1 - x_{02})^2\Big(x_{f2} + \frac{\widetilde{s}_{a2}}{3x_{b2}}\Big) + (1 + 2x_1 + x_2)\Big(x_{f2} + \frac{\widetilde{s}_{a2}}{x_{b2}}\Big)\Big]$$

$$G_{xy}^{(c-2)} = \frac{x_{02}}{2(1 + \nu)} \qquad C_{1x}^{(c-2)} = x_2 x_{02}(1 + 2x_1 + x_2)\Big(x_{f2} + \frac{\widetilde{s}_{a2}}{x_{b2}}\Big)$$

$$C_{0x}^{(c-2)} = 2x_2 x_{02}\Big(x_{f2} + \frac{\widetilde{s}_{a2}}{x_{b2}}\Big) \qquad C_{1y}^{(c-2)} = \frac{1}{2}x_2^2\Big(1 + 2x_1 + \frac{4}{3}x_2\Big)$$

$$C_{0y}^{(c-2)} = \frac{1}{3}x_2^3 \qquad C_{2y}^{(c-2)} = x_2\Big[x_1^2 + x_1(1 + x_2) + \frac{1}{4}\Big(1 + 2x_2 + \frac{4}{3}x_2^2\Big)\Big]$$

$$C_{1xy}^{(c-2)} = 2x_2(1 + 2x_1 + x_2) \qquad \widetilde{G}_{yz}^{(c-2)} = \frac{2}{(1 - \nu^2)x_{b2}f_v}\Big(\frac{x_{02}}{\widetilde{s}_{a2}}\Big)^3$$

details in Lewinski *et al.* (2015)
3) energy of the inner flat sheets

$$U_\varepsilon^{(s-i)} = \frac{t_{c1}}{2} \int_0^a \int_0^b \left\{ \int_{-(\frac{1}{2}+x_1)}^{-\frac{1}{2}} [\Phi_{\sigma,\varepsilon}^{(u,s-i)}]\ d\zeta + \int_{\frac{1}{2}}^{\frac{1}{2}+x_1} [\Phi_{\sigma,\varepsilon}^{(l,s-i)}]\ d\zeta \right\}\ dx\,dy \tag{2.22}$$

where

$$\Phi_{\sigma,\varepsilon}^{(u/l,s-i)} = \sigma_x^{(u/l)}\varepsilon_x^{(u/l)} + \sigma_x^{(u/l)}\varepsilon_x^{(u/l)} + \tau_{xy}^{(u/l)}\gamma_{xy}^{(u/l)} \tag{2.23}$$

stresses (Hooke's law)

$$\sigma_x^{(u/l)} = \frac{E}{1 - \nu^2}\Big(\varepsilon_x^{(u/l)} + \nu\varepsilon_y^{(u/l)}\Big) \qquad \tau_{xy}^{(u/l)} = \frac{E}{2(1 + \nu)}\gamma_{xy}^{(u/l)} \tag{2.24}$$

and strains – expressions (2.10).

Integration of expression (2.22) with respect to the coordinate $\zeta$ provides

$$U_{\varepsilon}^{(s-i)} = \frac{Et_{c1}^3}{1-\nu^2} \int_0^a \int_0^b \left( C_2^{(s-i)} f_{22}^{(s-i)} - C_1^{(s-i)} f_{12}^{(s-i)} + x_1 f_{11}^{(s-i)} \right) dx\, dy \qquad (2.25)$$

where

$$C_2^{(s-i)} = \frac{1}{4}\left(1 + 2x_1 + \frac{4}{3}x_1^2\right)x_1 \qquad C_1^{(s-i)} = (1+x_1)x_1 \qquad f_{22}^{(s-i)} = f_{22}^{(s-o)}$$

$$f_{12}^{(s-i)} = \left(\frac{\partial^2 w}{\partial x^2} + \nu\frac{\partial^2 w}{\partial y^2}\right)\frac{\partial \psi}{\partial x} + (1-\nu)\frac{\partial^2 w}{\partial x \partial y}\frac{\partial \psi}{\partial y} \qquad f_{11}^{(s-i)} = \left(\frac{\partial \psi}{\partial x}\right)^2 + \frac{1-\nu}{2}\left(\frac{\partial \psi}{\partial y}\right)^2$$

4) energy of the main corrugated core

$$U_{\varepsilon}^{(c-1)} = \frac{1}{2b_{01}} \int_0^a \int_0^b \left\{ \int_{A_{Tr}} [\Phi_{\sigma,\varepsilon}^{(c-1)}]\, dA_{Tr}^{(c-1)} \right\} dx\, dy \qquad (2.26)$$

where

$$\Phi_{\sigma,\varepsilon}^{(c-1)} = \sigma_x \varepsilon_x + \sigma_y \varepsilon_y + \tau_{xy}\gamma_{xy} + \tau_{xz}\gamma_{xz} \qquad (2.27)$$

stresses

$$\sigma_x = E_x^{(c-1)}\varepsilon_x \qquad \sigma_y = E\varepsilon_y \qquad \tau_{xy} = G_{xy}^{(c-1)}\gamma_{xy} \qquad \tau_{xz} = G_{xz}^{(c-1)}\gamma_{xz} \qquad (2.28)$$

and strains – expressions (2.11).

The area of one pitch of the trapezoidal corrugated cross section (Fig. 2)

$$A_{Tr}^{(c-1)} = 2t_{c1}^2 x_{01}(x_{f1}x_{b1} + \widetilde{s}_{a1}) \qquad (2.29)$$

where $x_{01} = t_{01}/t_{c1}$, $x_{f1} = b_{f1}/b_{01}$, $x_{b1} = b_{01}/t_{c1}$ are dimensionless parameters, $\widetilde{s}_{a1}$ – dimensionless length of one pitch – trapezoid

$$\widetilde{s}_{a1} = \sqrt{(1-x_{01})^2 + x_{b1}^2\left(\frac{1}{2} - x_{f1}\right)^2}$$

Integration of expression (2.30) provides

$$U_{\varepsilon}^{(c-1)} = Et_{c1}^3 \int_0^a \int_0^b \left(\frac{1}{24}\widetilde{E}_x^{(c-1)}f_{22}^{(c-1)} + \frac{1}{24}\widetilde{E}_y^{(c-1)}f_{12}^{(c-1)} + \frac{1}{6}\widetilde{G}_{xy}^{(c-1)}f_{11}^{(c-1)} + 2G_{xz}^{(c-1)}f_{10}^{(c-1)}\right) dx\, dy$$

$$(2.30)$$

where

$$f_{22}^{(c-1)} = \left(\frac{\partial^2 w}{\partial x^2}\right)^2 - 4\frac{\partial^2 w}{\partial x^2}\frac{\partial \psi}{\partial x} + 4\left(\frac{\partial \psi}{\partial x}\right)^2 \qquad f_{12}^{(c-1)} = \left(\frac{\partial^2 w}{\partial y^2}\right)^2$$

$$f_{10}^{(c-1)} = \frac{\psi^2(x,y)}{t_{c1}^2} \qquad f_{11}^{(c-1)} = \left(\frac{\partial^2 w}{\partial x \partial y}\right)^2 - 2\frac{\partial^2 w}{\partial x \partial y}\frac{\partial \psi}{\partial y} + \left(\frac{\partial \psi}{\partial y}\right)^2$$

$$\widetilde{E}_x^{(c-1)} = \frac{x_{b1}x_{01}^3}{2(x_{f1}x_{b1} + \widetilde{s}_{a1})} \qquad \widetilde{G}_{xy}^{(c-1)} = \frac{x_{01}}{2(1+\nu)}$$

$$\widetilde{E}_y^{(c-1)} = 2\frac{x_{01}}{x_{b1}}(1-x_{01})^2(3x_{f1}x_{b1} + \widetilde{s}_{a1}) \qquad \widetilde{G}_{xz}^{(c-1)} = \frac{1-x_{01}}{4(1-\nu^2)x_{b1}f_u}\left(\frac{x_{01}}{\widetilde{s}_{a1}}\right)^3$$

detail in Lewinski *et al.* (2015).

The work of the load, a uniformly distributed pressure $p_0$, is in the following form

$$W = \int\limits_0^a \int\limits_0^b p_0 w(x,y) \, dx \, dy \tag{2.31}$$

The total potential energy is a sum of elastic strain energy (2.12) and work (2.31).

## 3. Equations of equilibrium and its solution

The principle of minimum total potential energy

$$\delta(U_\varepsilon^{(plate)} - W) = 0 \tag{3.1}$$

where $U_\varepsilon^{(plate)}$ is the elastic strain energy of the plate (2.12) and $W$ is the work of the load (2.35).

The system of the equations of equilibrium – three partial differential equations derived based on principle (3.1) is in the following form

$$\Re_w^{(s-o-i)} + \Re_w^{(c-2)} + \Re_w^{(c-1)} = \frac{p_0}{E t_{c1}^3} \tag{3.2}$$

where

$$\Re_w^{(s-o-i)} = \frac{1}{1-\nu^2}\left\{2(C_2^{(s-o)} + C_2^{(s-i)})\nabla^4 w - C_1^{(s-o)}\left[\frac{\partial}{\partial x}(\nabla^2 \psi) + x_2 \frac{\partial}{\partial y}(\nabla^2 \phi)\right]\right.$$

$$\left. - C_1^{(s-i)}\frac{\partial}{\partial x}(\nabla^2 \psi)\right\}$$

$$\Re_w^{(c-2)} = 2\Re_{w,w}^{(c-2)} - \Re_{w,\psi}^{(c-2)} - \Re_{w,\phi}^{(c-2)}$$

$$\Re_{w,w}^{(c-2)} = C_{2x}^{(c-2)}\frac{\partial^4 w}{\partial x^4} + C_{2y}^{(c-2)}\left(4\widetilde{G}_{xy}^{(c-2)}\frac{\partial^4 w}{\partial x^2 \partial y^2} + \widetilde{E}_y^{(c-2)}\frac{\partial^4 w}{\partial y^4}\right)$$

$$\Re_{w,\psi}^{(c-2)} = \frac{\partial}{\partial x}\left(2C_{1x}^{(c-2)}\frac{\partial^2 \psi}{\partial x^2} + C_{1xy}^{(c-2)}\widetilde{G}_{xy}^{(c-2)}\frac{\partial^2 \psi}{\partial y^2}\right)$$

$$\Re_{w,\phi}^{(c-2)} = C_{1y}^{(c-2)}\frac{\partial}{\partial x}\left(2\widetilde{G}_{xy}^{(c-2)}\frac{\partial^2 \phi}{\partial x^2} + \widetilde{E}_y^{(c-2)}\frac{\partial^2 \phi}{\partial y^2}\right)$$

$$\Re_w^{(c-1)} = \frac{1}{12}\Re_{w,w}^{(c-1)} - \frac{1}{6}\Re_{w,\psi}^{(c-1)} \qquad \Re_{w,w}^{(c-1)} = \widetilde{E}_x^{(c-1)}\frac{\partial^4 w}{\partial x^4} + 4\widetilde{G}_{xy}^{(c-1)}\frac{\partial^4 w}{\partial x^2 \partial y^2} + \widetilde{E}_y^{(c-1)}\frac{\partial^4 w}{\partial y^4}$$

$$\Re_{w,\psi}^{(c-1)} = \frac{\partial}{\partial x}\left(\widetilde{E}_x^{(c-1)}\frac{\partial^2 \psi}{\partial x^2} + 2\widetilde{G}_{xy}^{(c-1)}\frac{\partial^2 \psi}{\partial y^2}\right) \qquad \nabla^4 w = \frac{\partial^4 w}{\partial x^4} + 2\frac{\partial^4 w}{\partial x^2 \partial y^2} + \frac{\partial^4 w}{\partial y^4}$$

and

$$\Re_\psi^{(s-o-i)} + \Re_\psi^{(c-2)} + \Re_\psi^{(c-1)} = 0 \tag{3.3}$$

where

$$\Re_\psi^{(s-o-i)} = \frac{1}{1-\nu^2}\left\{(C_1^{(s-o)} + C_1^{(s-i)})\frac{\partial}{\partial x}(\nabla^2 w) - 2x_1\left[2\frac{\partial^2 \psi}{\partial x^2} + (1-\nu)\frac{\partial^2 \psi}{\partial y^2}\right]\right.$$

$$\left. - x_1 x_2(1+\nu)\frac{\partial^2 \phi}{\partial x \partial y}\right\}$$

$$\Re_\psi^{(c-2)} = \frac{\partial}{\partial x}\left(2C_{1x}^{(c-2)}\frac{\partial^2 w}{\partial x^2} + C_{1xy}^{(c-2)}\widetilde{G}_{xy}^{(c-2)}\frac{\partial^2 w}{\partial y^2}\right) - 2\left(C_{0x}^{(c-2)}\frac{\partial^2 \psi}{\partial x^2} + x_2\widetilde{G}_{xy}^{(c-2)}\frac{\partial^2 \psi}{\partial y^2}\right)$$

$$- x_2^2 \widetilde{G}_{xy}^{(c-2)}\frac{\partial^2 \phi}{\partial x \partial y}$$

$$\Re_\psi^{(c-1)} = \frac{1}{6}\frac{\partial}{\partial x}\left(\widetilde{E}_x^{(c-1)}\frac{\partial^2 w}{\partial x^2} + 2\widetilde{G}_{xy}^{(c-1)}\frac{\partial^2 w}{\partial y^2}\right) - \frac{1}{3}\left(\widetilde{E}_x^{(c-1)}\frac{\partial^2 \psi}{\partial x^2} + \widetilde{G}_{xy}^{(c-1)}\frac{\partial^2 \psi}{\partial y^2}\right) - 4\widetilde{G}_{xz}^{(c-1)}\frac{\psi(x,y)}{t_{c1}^2}$$

and

$$\Re_\phi^{(s-o-i)} + \Re_\phi^{(c-2)} = 0 \tag{3.4}$$

where

$$\Re_\phi^{(s-o-i)} = \frac{1}{1-\nu^2}\Big\{ x_2 C_1^{(s-o)}\frac{\partial}{\partial y}(\nabla^2 w) - x_1 x_2^2\Big[(1-\nu)\frac{\partial^2\phi}{\partial x^2} + 2\frac{\partial^2\phi}{\partial y^2}\Big] - x_1 x_2(1+\nu)\frac{\partial^2\psi}{\partial x\partial y}\Big\}$$

$$\Re_\phi^{(c-2)} = \Re_{\phi,w}^{(c-2)} - x_2^2 \widetilde{G}_{xy}^{(c-2)}\frac{\partial^2\psi}{\partial x\partial y} - \Re_{\phi,\phi}^{(c-2)}$$

$$\Re_{\phi,w}^{(c-2)} = C_{1y}^{(c-2)}\frac{\partial}{\partial y}\Big( 2\widetilde{G}_{xy}^{(c-2)}\frac{\partial^2 w}{\partial x^2} + \widetilde{E}_y^{(c-2)}\frac{\partial^2 w}{\partial y^2}\Big)$$

$$\Re_{\phi,\phi}^{(c-2)} = 2C_{0y}^{(c-2)}\Big( \widetilde{G}_{xy}^{(c-2)}\frac{\partial^2\phi}{\partial x^2} + \widetilde{E}_y^{(c-2)}\frac{\partial^2\phi}{\partial y^2}\Big) - 2x_2\widetilde{G}_{yz}^{(c-2)}\frac{\phi(x,y)}{t_{c1}^2}$$

$$\nabla^2 w = \frac{\partial^2 w}{\partial x^2} + \frac{\partial^2 w}{\partial y^2}$$

Three equations of equilibrium (3.2), (3.3) and (3.4) with three unknown functions $w(x,y)$, $\psi(x,y)$ and $\phi(x,y)$ are approximately solved assuming three unknown functions in the forms

$$w(x,y) = w_a \sin\frac{\pi x}{a}\sin\frac{\pi y}{b} \qquad \psi(x,y) = \psi_a \cos\frac{\pi x}{a}\sin\frac{\pi y}{b}$$
$$\phi(x,y) = \phi_a \sin\frac{\pi x}{a}\cos\frac{\pi y}{b} \tag{3.5}$$

where $w_a$, $\psi_a$, $\phi_a$ are parameters of the functions, $a$, $b$ – sizes of the plate (Fig. 1).

Substituting these functions into equations (3.2), (3.3) and (3.4) and using the Galerkin method, three algebraic equations are obtained

$$\alpha_{11}w_a - \alpha_{12}\frac{b}{\pi}\psi_a - \alpha_{13}\frac{a}{\pi}\phi_a = \frac{16}{\pi^3}\frac{a^2 b^2}{t_{c1}^3}\frac{p_0}{e} \qquad \alpha_{21}\frac{\pi}{a}w_a - \alpha_{22}\psi_a - \alpha_{23}\phi_a = 0$$
$$\alpha_{31}\frac{\pi}{b}w_a - \alpha_{32}\psi_a - \alpha_{33}\phi_a = 0 \tag{3.6}$$

where the dimensionless elements

$$\alpha_{11} = \alpha_{11}^{(1)} + \alpha_{11}^{(2)} + \alpha_{11}^{(3)} \qquad \alpha_{11}^{(1)} = \frac{2}{1-\nu^2}(C_2^{(s-o)} + C_2^{(s-i)})\Big(\frac{b}{a} + \frac{a}{b}\Big)^2$$

$$\alpha_{23} = x_2\Big(\frac{x_1}{1-\nu} + x_2\widetilde{G}_{xy}^{(c-2)}\Big) \qquad \alpha_{11}^{(3)} = \frac{1}{12}\Big[\widetilde{E}_x^{(c-1)}\Big(\frac{b}{a}\Big)^2 + 4\widetilde{G}_{xy}^{(c-1)} + \widetilde{E}_y^{(c-1)}\Big(\frac{a}{b}\Big)^2\Big]$$

$$\alpha_{11}^{(2)} = 2\Big[C_{2x}^{(c-2)}\Big(\frac{b}{a}\Big)^2 + C_{2y}^{(c-2)}\Big(4\widetilde{G}_{xy}^{(c-2)} + \widetilde{E}_y^{(c-2)}\Big(\frac{a}{b}\Big)^2\Big)\Big]$$

$$\alpha_{12} = \frac{1}{1-\nu^2}(C_1^{(s-o)} + C_1^{(s-i)})\Big(\frac{b}{a} + \frac{a}{b}\Big) + 2C_{1x}^{(c-2)}\frac{b}{a} + C_{1xy}^{(c-2)}\widetilde{G}_{xy}^{(c-2)}\frac{a}{b}$$
$$+ \frac{1}{6}\Big(\widetilde{E}_x^{(c-1)}\frac{b}{a} + 2\widetilde{G}_{xy}^{(c-1)}\frac{a}{b}\Big)$$

$$\alpha_{13} = \frac{x_2}{1-\nu^2}C_1^{(s-o)}\Big(\frac{b}{a} + \frac{a}{b}\Big) + C_{1y}^{(c-2)}\Big(2\widetilde{G}_{xy}^{(c-2)}\frac{b}{a} + \widetilde{E}_y^{(c-2)}\frac{a}{b}\Big)$$

$$\alpha_{21} = \alpha_{12} \qquad \alpha_{31} = \alpha_{13} \qquad \alpha_{32} = \alpha_{23}$$

$$\alpha_{22} = \frac{2x_1}{1-\nu^2}\Big[2\frac{b}{a} + (1-\nu)\frac{a}{b}\Big] + 2\Big(C_{0x}^{(c-2)}\frac{b}{a} + x_2\widetilde{G}_{xy}^{(c-2)}\frac{a}{b}\Big) + \frac{1}{3}\Big(\widetilde{E}_x^{(c-1)}\frac{b}{a} + \widetilde{G}_{xy}^{(c-1)}\frac{a}{b}\Big)$$
$$+ \frac{4}{\pi^2}\widetilde{G}_{xz}^{(c-1)}\frac{ab}{t_{c1}^2}$$

$$\alpha_{33} = \frac{x_1 x_2^2}{1-\nu^2}\Big[(1-\nu)\frac{b}{a} + 2\frac{a}{b}\Big] + 2C_{0y}^{(c-2)}\Big(\widetilde{G}_{xy}^{(c-2)}\frac{b}{a} + \widetilde{E}_y^{(c-2)}\frac{a}{b}\Big) + \frac{2x_2}{\pi^2}\widetilde{G}_{yz}^{(c-2)}\frac{ab}{t_{c1}^2}$$

Solving equations (3.6) one obtains

$$w_a = \frac{16}{\pi^6 \alpha_w} \frac{a^2 b^2}{t_{c1}^3} \frac{p_0}{E} \qquad \psi_a = \frac{16}{\pi^5} \frac{\alpha_\psi}{\alpha_w} \frac{a^2 b}{t_{c1}^3} \frac{p_0}{E} \qquad \phi_a = \frac{16}{\pi^5} \frac{\alpha_\phi}{\alpha_w} \frac{a^2 b}{t_{c1}^3} \frac{p_0}{E} \qquad (3.7)$$

where

$$\alpha_w = \alpha_{11} - (\alpha_\psi \alpha_{12} + \alpha_\phi \alpha_{13}) \qquad \alpha_\psi = \frac{b\alpha_{21}\alpha_{33} - a\alpha_{31}\alpha_{23}}{a(\alpha_{22}\alpha_{33} - \alpha_{23}^2)}$$

$$\alpha_\phi = \frac{a\alpha_{31}\alpha_{22} - b\alpha_{21}\alpha_{32}}{b(\alpha_{22}\alpha_{33} - \alpha_{23}^2)}$$

The stresses on the outer sheets and in the middle of the plate, for $\zeta_o = \mp(0.5 + 2x_1 + x_2)$ and $x = a/2$, $y = b/2$ are

$$\sigma_x = \frac{1}{1-\nu^2}\Big[\Big(\frac{b}{a} + \nu\frac{a}{b}\Big)\zeta_o \pm (\alpha_\psi + \nu x_2 \alpha_\phi)\Big]\frac{16}{\pi^4 \alpha_w} \frac{ab}{t_{c1}^2}p_0$$
$$\sigma_y = \frac{1}{1-\nu^2}\Big[\Big(\frac{a}{b} + \nu\frac{b}{a}\Big)\zeta_o \pm (\nu\alpha_\psi + x_2 \alpha_\phi)\Big]\frac{16}{\pi^4 \alpha_w} \frac{ab}{t_{c1}^2}p_0 \qquad (3.8)$$

and the equivalent stress (Huber-Mises-Hencky)

$$\sigma_{eq} = \sqrt{f_{\sigma x}^2 - f_{\sigma x}f_{\sigma y} + f_{\sigma y}^2} \frac{16}{\pi^4(1-\nu^2)\alpha_w} \frac{ab}{t_{c1}^2}p_0 \qquad (3.9)$$

where

$$f_{\sigma x} = \Big(\frac{b}{a} + \nu\frac{a}{b}\Big)\zeta_o \pm (\alpha_\psi + \nu x_2 \alpha_\phi) \qquad f_{\sigma y} = \Big(\frac{a}{b} + \nu\frac{b}{a}\Big)\zeta_o \pm (\nu\alpha_\psi + x_2 \alpha_\phi)$$

## 4. Finite element model of the seven-layer plate

A family of simply supported rectangular plates of dimensions $2024\,\text{mm} \times 2000\,\text{mm}$ subjected to a uniform load of 0.01 MPa has been considered. The linear static analysis was carried out using the finite element software ABAQUS. A quarter of the rectangular plate was modeled. The linear S4R shell elements were placed at the mid-surface of the plate layers (Fig. 4).
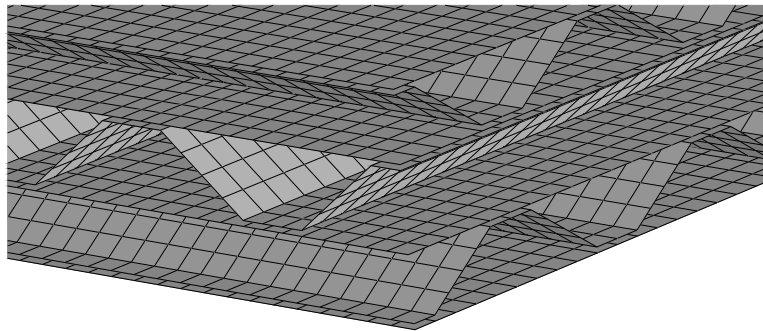


Fig. 4. The meshing scheme of a simply supported plate

The mesh density study was carried out to refine the global mesh size to 4 mm. The mesh convergence plot for the maximum deflection in the middle of the top face sheet is presented in Fig. 5.
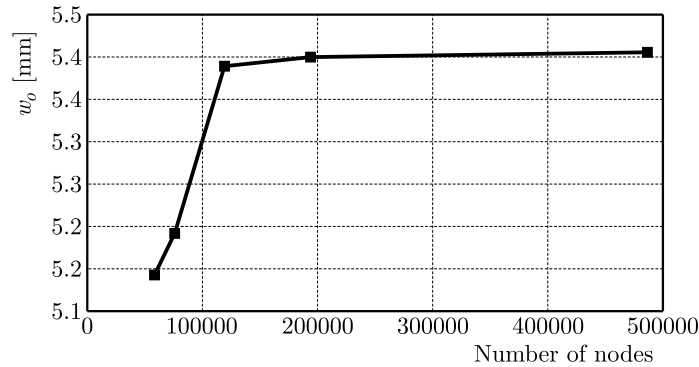
Fig. 5. The mesh convergence plot

Perfect bonding between the cores and the flat sheets was assumed. The interaction between flanges of the cores and the flat sheets was provided with the use of the tie constraint. The flanges of the cores were slave surfaces and the flat sheets were master surfaces.

The boundary conditions were imposed only to edges of the flat sheets (master surfaces) – each edge was simply supported. The implementation of the symmetry and the simply supported boundary conditions on a quarter of the plate is schematically shown in Fig. 6.
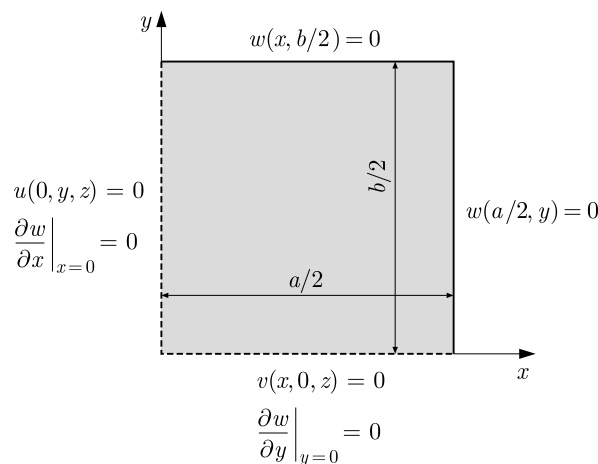


Fig. 6. The scheme of boundary conditions

## 5. Results of numerical calculations of deflection and stresses of the plate

The aim of these calculations was to verify the results obtained through the linear finite element analysis with those obtained through an analytical method. The maximum deflection and the equivalent stress of the family of seven-layer rectangular plates, using both analytical and finite element methods, was evaluated. The results of the parametric studies for changes of $b_{02}$ and $b_{01}$ are collected in Case 1 and Case 2, respectively.

**Case 1.** The study for constant area of the trapezoidal corrugation of the facing core $A_{Total}^{(c-2)} = nA_{Tr}^{(c-2)}$, where $n$ is the number of the corrugations and $A_{Tr}^{(c-2)}$ (2.20) is the area of one pitch of the trapezoidal corrugated cross section. The numerical calculations are carried out for the rectangular plate with the following sizes: $a = 2024$ mm, $b = 2000$ mm, $t_s = 0.8$ mm, $t_{c1} = 11.2$ mm, $t_{01} = 0.8$ mm, $b_{01} = 46$ mm, $b_{f1} = 10$ mm, $t_{c2} = 9.2$ mm, $b_{f2} = 8$ mm, $A_{Total}^{(c-2)} = 1811.83$ mm$^2$, $p_0 = 0.01$ MPa, and material constants

$E = 2 \cdot 10^5$ MPa, $\nu = 0.3$. The results of the calculations are presented in Table 1. The values in the ABAQUS columns in Table 1 enclosed in parentheses are percentage differences with respect to the analytical ones (the absolute value of the relative deviation).

**Table 1.** The deflection and the equivalent stresses of the plate for the first case $A_{Total}^{(c-2)} = $ const

| $n$ | $b_{02}$ [mm] | $t_{02}$ [mm] | $w_a$ | | $\sigma_{eq}$ | |
|---|---|---|---|---|---|---|
| | | | Analytical [mm] | ABAQUS [mm] | Analytical [MPa] | ABAQUS [MPa] |
| 50 | 40.0 | 0.8 | 5.30 | 5.41 (2.1%) | 59.4 | 60.01 (1.0%) |
| 60 | 33.333 | 0.751 | 5.33 | 5.43 (1.9%) | 59.7 | 60.86 (1.9%) |
| 70 | 28.571 | 0.6968 | 5.38 | 5.48 (1.8%) | 60.1 | 62.40 (3.8%) |
| 80 | 25.0 | 0.6409 | 5.43 | 5.53 (1.7%) | 60.5 | 63.44 (4.7%) |
| 90 | 22.222 | 0.5867 | 5.51 | 5.61 (1.8%) | 60.9 | 64.94 (6.4%) |
| 100 | 20.0 | 0.5363 | 5.61 | 5.72 (1.9%) | 61.2 | 66.29 (8.0%) |

**Case 2.** The study for constant area of the trapezoidal corrugation of the main core $A_{Total}^{(c-1)} = m A_{Tr}^{(c-1)}$, where $m$ is the number of the corrugations and $A_{Tr}^{(c-1)}$ (2.29) is the area of one pitch of the trapezoidal corrugated cross section. The numerical calculations are carried out for the rectangular plate with the following sizes: $a = 2024$ mm, $b = 2000$ mm, $t_s = 0.8$ mm, $t_{c1} = 11.2$ mm, $b_{f1} = 10$ mm, $t_{c2} = 9.2$ mm, $t_{02} = 0.8$ mm, $b_{02} = 40$ mm, $b_{f2} = 8$ mm, $A_{Total}^{(c-1)} = 1876.03$ mm$^2$, $p_0 = 0.01$ MPa, $E = 2 \cdot 10^5$ MPa, $\nu = 0.3$. The results of the calculations are presented in Table 2. The values in the ABAQUS columns in Table 2 enclosed in parentheses are percentage differences with respect to the analytical ones (the absolute value of the relative deviation).

**Table 2.** The deflection and the equivalent stresses of the plate for the second case $A_{Total}^{(c-1)} = $ const

| $n$ | $b_{01}$ [mm] | $t_{01}$ [mm] | $w_a$ | | $\sigma_{eq}$ | |
|---|---|---|---|---|---|---|
| | | | Analytical [mm] | ABAQUS [mm] | Analytical [MPa] | ABAQUS [MPa] |
| 44 | 46.0 | 0.8 | 5.30 | 5.41 (2.1%) | 59.34 | 60.01 (1.1%) |
| 54 | 37.481 | 0.7349 | 5.33 | 5.43 (1.8%) | 59.44 | 60.07 (1.1%) |
| 64 | 31.625 | 0.6652 | 5.41 | 5.49 (1.5%) | 59.73 | 60.47 (1.2%) |
| 74 | 27.351 | 0.5973 | 5.65 | 5.65 (0.0%) | 60.55 | 61.33 (1.3%) |
| 84 | 24.095 | 0.5245 | 6.48 | 5.98 (8.0%) | 63.90 | 63.00 (1.4%) |

## 6. Conclusions

As a conclusion, it can be said that the results obtained through the analytical and the numerical method are consistent with each other. It proves that the broken-line hypotheses assumed for deformation of the cross-section in $x$ and $y$ directions are sufficient for evaluating the plate deflection and equivalent stresses. It can also be seen that decreasing of the parameter $b_{01}$ has much more influence on the increase of the maximum deflection of the plate. This effect is due to a significant change in the shear rigidity of the plate.

# References

1. ALLEN H.G., 1969, *Analysis and Design of Structural Sandwich Panels*, Pergamon Press, Oxford, London, Edinburgh, New York, Toronto, Sydney, Paris, Braunschweig

2. CARRERA E., 2003, Historical review of Zig-Zag theories for multi-layered plates and shells, *Applied Mechanics Reviews*, **56**, 3, 287-308

3. CARRERA E., BRISCHETTO S., 2009, A survey with numerical assessment of classical and refined theories for the analysis of sandwich plates, *Applied Mechanics Reviews*, **62**, 1-010803, 1-17

4. CHEON Y.J., KIM H.G., 2015, An equivalent plate model for corrugated-core sandwich panels, *Journal of Mechanical Science and Technology*, **29**, 3, 1217-1223

5. JHA D.K., KANT T., SINGH R.K., 2013, Stress analysis of transversely loaded functionally graded plates with a higher order shear and normal deformation theory, *ASCE Journal of Engineering Mechanics*, **139**, 12, 1663-1680

6. JI H.S., SONG W., MA Z.J., 2010, Design, test and field application of a GFRP corrugated-core sandwich bridge, *Engineering Structures*, **32**, 2814-2824

7. KAZEMAHVAZI S., ZENKERT D., 2009, Corrugated all-composite sandwich structures. Part 1: Modeling, *Composite Science and Technology*, **69**, 7, 913-919

8. LEWINSKI J., MAGNUCKA-BLANDZI E., SZYC W., 2015, Determination of shear modulus of elasticity for thin-walled trapezoidal corrugated cores of seven-layer sandwich plates, *Engineering Transactions*, **63**, 4, 421-438

9. MAGNUCKA-BLANDZI E., 2011, Mathematical modelling of a rectangular sandwich plate with a metal foam core, *Journal of Theoretical and Applied Mechanics*, **49**, 2, 439-455

10. MAGNUCKA-BLANDZI E., MAGNUCKI K., 2014, Transverse shear modulus of elasticity for thin-walled corrugated cores of sandwich beams. Theoretical study, *Journal of Theoretical and Applied Mechanics*, **52**, 4, 971-980

11. MAGNUCKA-BLANDZI E., MAGNUCKI K., WITTENBECK L., 2015, Mathematical modelling of shearing effect for sandwich beams with sinusoidal corrugated cores, *Applied Mathematical Modelling*, **39**, 9, 2796-2808

12. MAGNUCKI K., MAGNUCKA-BLANDZI E., WITTENBECK L., 2016, Elastic bending and buckling of a steel composite beam with corrugated main core and sandwich faces – Theoretical study, *Applied Mathematical Modelling*, **40**, 2, 1276-1286

13. MANTARI J.L., GRANADOS E.V., 2015, A refined FSDT for the static analysis of functionally graded sandwich plates, *Thin-Walled Structures*, **90**, 150-158

14. NOOR A.K., BURTON W.S., BERT C.W., 1996, Computational models for sandwich panels and shells, *Applied Mechanics Reviews*, **49**, 3, 155-199

15. PLANTEMA F.J., 1966, *Sandwich construction – the bending and buckling of sandwich beams, plates, and shells*, John Wiley & Sons, New York, London, Sydney

16. POIRIER J.D., VEL S.S., CACCESE V., 2013, Multi-objective optimization of laser-welded steel sandwich panels for static loads using a genetic algorithm, *Engineering Structures*, **49**, 508-524

17. SEONG D.Y., JUNG C.G., YANG D.Y., MOON K.J., AHN D.G., 2010, Quasi-isotropic bending responses of metallic sandwich plates with bi-directionally corrugated cores, *Materials and Design*, **31**, 6, 2804-2812

18. VAIDYA S., ZHANG L., MADDALA D., HEGERT R., WRIGHT J.T., SHUKLA A., KIM J.H., 2015, Quasi-static response of sandwich steel beams with corrugated cores, *Engineering Structures*, **97**, 80-89

19. Vinson J.R., 2001, Sandwich structures, *Applied Mechanics Reviews*, **54**, 3, 201-214

20. Zhang J., Qin Q., Wang T.J., 2013, Compressive strengths and dynamic response of corrugated metal sandwich plates with unfilled and foam-filled sinusoidal plate cores, *Acta Mechanica*, **224**, 4, 759-775

# AN AUTOMATED CAD/CAE INTEGRATION SYSTEM FOR THE PARAMETRIC DESIGN OF AIRCRAFT WING STRUCTURES

Abdelkader Benaouali, Stanisław Kachel

*Military University of Technology (MUT), Warsaw, Poland*

*e-mail: abdelkader.benaouali@wat.edu.pl*

In order to take advantage of the sophisticated features offered by CAD and CAE packages for modeling and analysis during the design process, it is essential to build a bridge assuring a coherent link between these tools. Furthermore, this integration procedure must be automated so as to get rid of the repetitive costing effort. In this paper, a new automated procedure for the CAD/CAE integration, implemented for the parametric design and structural analysis of aircraft wing structures is presented. This procedure is based on the automation capacity available in modern computer aided tools via build-in basic programming languages as well as the capacity of the model data exchange. The geometric and numerical models can be controlled to generate a large variety of possible design cases through parameters introduced beforehand.

*Keywords:* CAD/CAE integration, design automation, aircraft wing, parametric design

## 1. Introduction

Due to the existing competition, manufacturing companies strive to decrease the product life cycle in order to produce more in a relatively reduced time (Asiedu and Gu, 1998). Consequently, a need has been raised for evolution in design tools, namely, Computer Aided Design (CAD) and Computer Aided Engineering (CAE) software (Sapuan *et al.*, 2006). One of the requirements is to shorten the time spent in the design process, especially when identical tasks exist while modeling different products or when the design process consists of repeated activities that can be programmed in a simple loop.

The progress in CAD and CAE technologies served as a major part in the improvement of the design process quality. The product development cycle changed from $design \Rightarrow build \Rightarrow test \Rightarrow fix$ to $design \Rightarrow analyze \Rightarrow test \Rightarrow build$ (Rowe, 2006). In the traditional approach, physical prototypes had to be built in order to be evaluated, and the design was based on the designers' experience and judgment. Nowadays, numerical analysis is used in the upstream phase simultaneously with the geometric design. The validation of a new design is performed using virtual prototyping, which involves modeling, engineering analysis and multidisciplinary optimization. CAD and CAE tools have become a quintessential part of the design process and have been widely applied in structure design (Dietrich *et al.*, 1999; Edke and Chang, 2006).

Generally, the limited capabilities of modeling features in CAE tools and those of structural analysis, if they are available, in CAD tools lead designers to use two or more independent software packages for modeling and analysis (Gujarathi and Ma, 2011). Moreover, looking for more efficient and lighter structures by a structural optimization process creates a need for sharing the geometric model and analysis information in an iterative environment.

Furthermore, to solve optimization problems, the model has to be updated after each iteration by changing the design parameters. If this task is to be performed manually, the designer has to perform a complicated and time consuming job, particularly in the case where the model is

governed by a large number of parameters (Roy *et al.*, 2008). Therefore, it is requisite not only to integrate CAD and CAE tools but also to automate the integration procedure in order to avoid designer's intervention at each iteration.

The integration between CAD and CAE tools can be easily performed due to the data exchange translators available in most popular CAD and CAE tools. In order to make the integration procedure automatic, the software used must offer the ability to automate tasks and access to features via a built-in programming language as well as the possibility to run in the batch mode.

In the recent years, a number of works has used the integration between CAD and CAE tools as a design solution. Su and Qin (2003) used IGES data files to integrate Pro/ENGINEER and ANSYS for a worm gearing design. Edke and Chang (2006) performed shape optimization of heavy load carrying components by integrating Solidworks, Pro/ENGINEER and ANSYS via IGES. Other works (Park and Dang, 2010; Wang *et al.*, 2014; Peng *et al.*, 2014) focused on developing an automated framework for CAD/CAE integration.

In this paper, a new procedure for the design process of aircraft wing structures is presented. The originality of the presented work lies in the full automation of the design process, the complexity in the case considered of the wing structure as well as the applicability to different types of wings via parametric modeling. The design process involves both geometric modeling and structural analysis by integrating two commercial CAD and CAE tools. The control of the geometric and numerical models can be done using design parameters, introduced manually in order to explore and compare different design cases. The approach is supported by a graphical user interface GUI in order to ease parameter data input and result access.

## 2.   Need for CAD/CAE integration

As mentioned before, the design is no longer a pure geometric modeling task due to the considerable progression of the numerical simulation becoming the key area in product design. Nowadays, the design process involves both Computer Aided Design (CAD) and Computer Aided engineering (CAE). In addition, the evolution in the design process requires geometric modeling and mechanical analysis to be driven in parallel. The model has to be submitted into analysis in order to be verified and, therefore, modified on the basis of the results obtained. Although most of the commercial CAE tools support modeling, available CAD functions do not fulfill all desired requirements. The aim to reach a better design in an iterative environment calls for a strong connection between CAD and CAE tools, which bring us to what is called "simulation driven design" (Fig. 1). This interconnection accelerates the loop design-analysis-redesign and thus reduces costs and improves product quality.
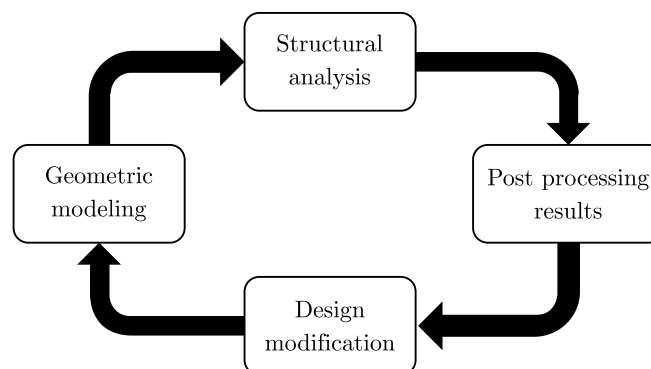


Fig. 1. Simulation driven design (CAD/CAE integration process)

The "Post processing results" step is an evaluation of the model based on the design objective taking into account the analysis results. Consequently, the modifications to be done are spotted in the "design modification" step then submitted to action when the next loop starts.

In order to ease the design modification, engineers tend to use the parametric modeling, that is to include parameters to drive the geometry in CAD models through parametric and variational approaches (Fig. 2). Thus, new designs can be generated simply by changing parameter values, which facilitates the definition of the design space.
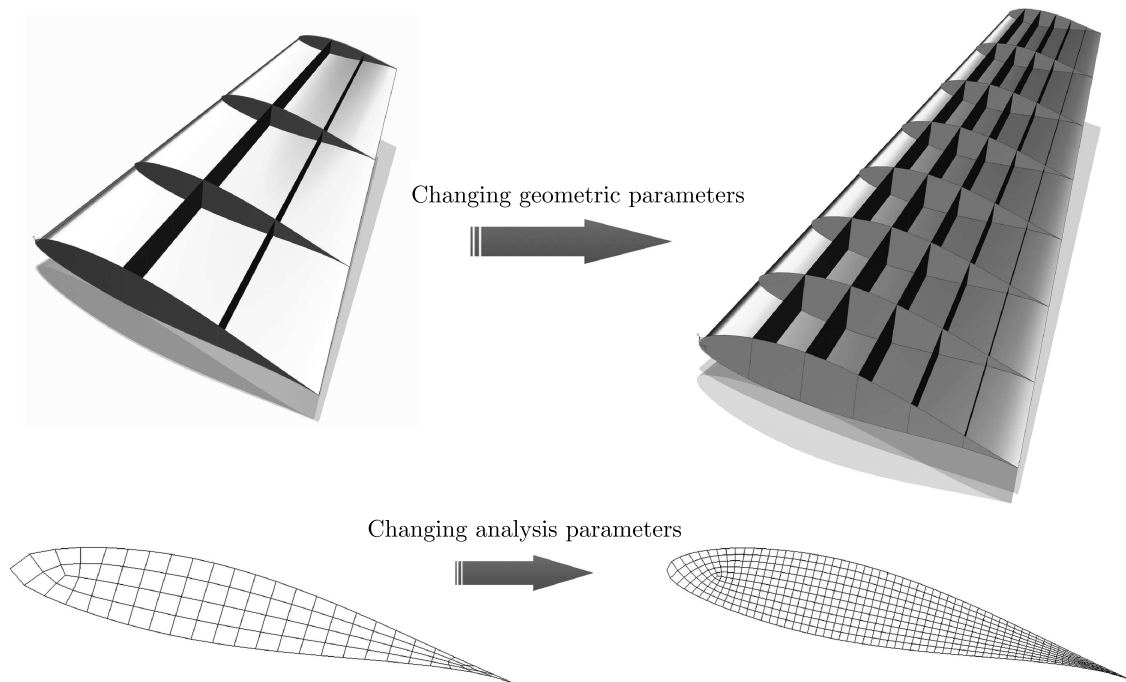


Fig. 2. Parametric modeling methodology on an aircraft wing

For the sake of ensuring the interconnection between CAD and CAE tools, data exchange translators have been developed and improved to transform data from one CAD system to another CAD file format. The CAD data translation can be done by the built-in export function supported in most of the commercial CAD. The common Data translation formats are: STEP, IGES, STL, parasolid. The geometric data can be easily provided to the CAE software via the built-in import function. Thus, the integration between CAD/CAE systems has been guaranteed. It remains to automate this export/import task so that the designer evades monotonous effort.

## 3. Design process automation

In order to modify the model, the designer must redo all tasks, namely, model the new geometry based on the new parameter values, export the model from CAD software and import it into CAE software, prepare the FEM model, submit into analysis and finally explore results. Therefore, the best way to reduce human unnecessary effort and time consumption is to precede by automation.

In other words, automation is the ability provided by the software to access modeling or analysis functionalities via a built-in programming language. The model in request can be generated after executing the program in-which several functions are called sequentially to exert different tasks. Accordingly, repeated tasks can be simply programmed in a loop and the model can be simply updated by modifying the variable values in the program. By adopting this methodology, companies can significantly reduce design time, perform more design iterations in

a relatively reduced time with a lower cost and, therefore, increase the overall quality of their design processes.

This automatic mechanism can be performed by CAD software based on the Application Programming Interfaces (APIs) and programming modules, such as the Pro/Toolkit of Pro/Engineer, CAA of CATIA, OpenAPI and OPEN GRIP of Unigraphics. In addition, most of the CAE packages are equipped with a parametric design language (PDL), e.g. Adaptive Programming Design Language (APDL) of Ansys, Patran Command Language (PCL) of Patran *et al.*. These PDLs are usually structured scripting languages by which the designers can import the geometric model, assign materials, prepare the FE mesh, apply loads and boundary conditions and submit the model to analysis. Moreover, the required analysis results can be extracted from the output file which can be post processed by programming as well. This is known as the automated finite element modeling technique AFEM (Nawijn *et al.*, 2006) and was used in many works to generate reliable FE models of complicated structures (Rocca and van Tooren, 2009; Sohaib, 2011).

The CAD and CAE software used in the integration system must allow the execution in the batch mode, that is without a graphic user interface (GUI). Consequently, it is possible to execute the CAD or CAE program from a windows command prompt which runs the corresponding software in an invisible mode. This will significantly decrease the required time for modeling and analysis compared to the graphic mode.

In addition to the two CAD and CAE tools, there is a need for an implementing software to complete the integration system. This software is responsible for controlling the integration process, it ensures the parameter value automatic modification in the programs, the execution of the programs in the software batch mode to invoke the modeling/analysis processes and the extraction of analysis results from the output of the CAE component.

The implementing software writes parameter values introduced by the designer to the modeling program. The CAD component, run in the batch mode, executes the program to generate the geometric model automatically and exports it to a common data format file. Again, the implementing software writes parameter values to the analysis program and runs the CAE component which imports the CAD model, identifies the analysis tasks, carries out the simulation process and provides the analysis results. Finally, the implementing software accesses result files and extracts the values required.

## 4. Implementation of the integration system

The selection of the software forming integration system depends on the designer choice and the available tools. In the present work, SIEMENS NX, MSC.PATRAN/NASTRAN and MATLAB have been chosen as CAD, CAE and implementing software, respectively. The flowchart of the integration system is depicted in Fig. 3.

### 4.1. CAD component

SIEMENS NX (formerly Unigraphics NX) is a leading parametric modeling CAD software. It offers various tools of automation: Knowledge Fusion, GRIP programming, Macros, NX Open, Journals, User Defined Objects etc.

Over the available automation tools, GRIP is used in our integration procedure. GRIP (Graphics Interactive Programming) is a convenient, flexible and powerful interactive graphic programming language. GRIP is used to create FORTRAN-like programs to operate the Unigraphics system. GRIP programming method can be used to automate most of the operations under the UG for developers. Commands are available to create geometric functions and modify existing geometry.
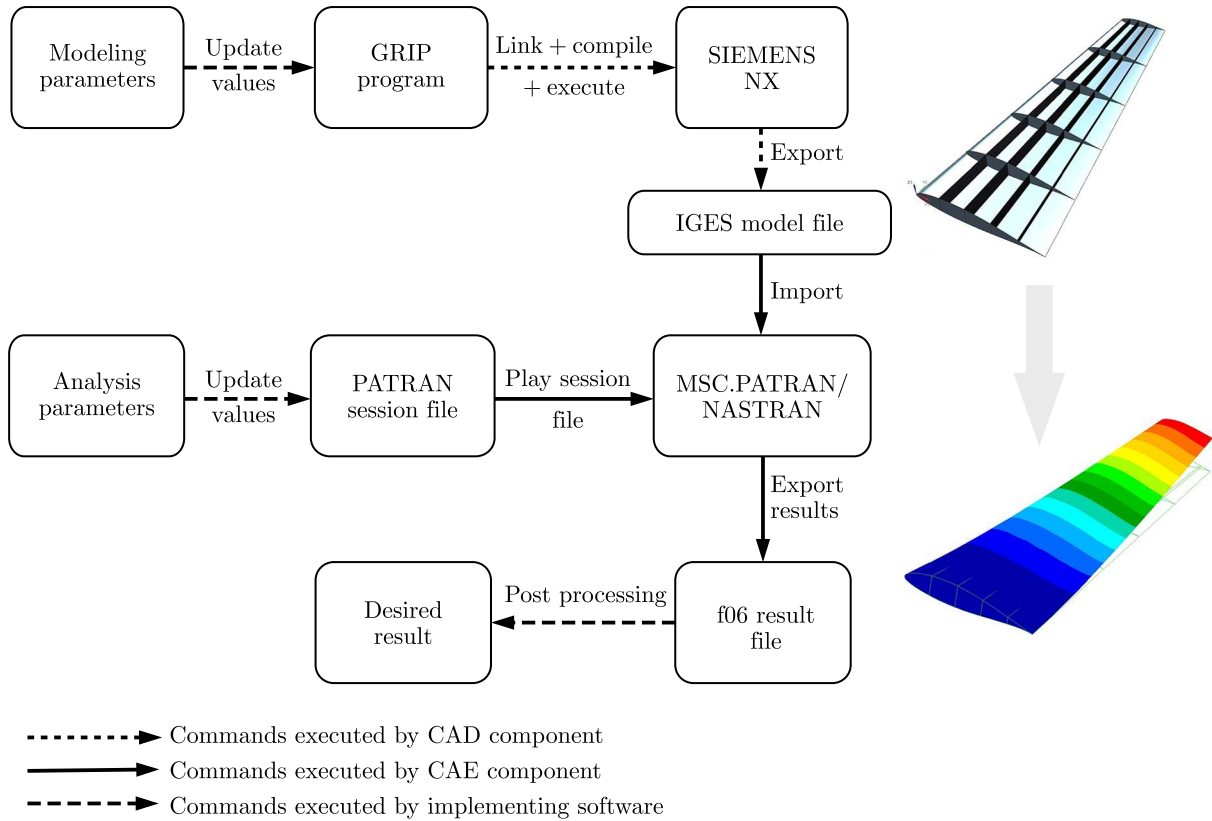
Fig. 3. Flowchart of the CAD/CAE integration system

The GRIP program is written to a text file with a (.grs) format. It has to be compiled then linked before it can be executed by the SIEMENS NX software. Thanks to the batch mode running ability, compilation, linkage and execution can be done by a WINDOWS command that operates on a batch file. This command can be executed from the implementing software MATLAB. Being the case, the designer avoid the action of opening GRADE (GRIP Advanced Development Environment) to compile and link the .grs file then SIEMENX NX software to execute the .grx file.

The GRIP program starts by creating a new active part which is necessary to execute the modeling process and ends by exporting the model to a geometry exchange format file, in our case IGES format. Unfortunately, there is no GRIP function to export the model in a format other than .prt. The solution is to use another tool for automation which is journaling, by writing a VB journal to export the model in IGES format and call it from the GRIP program.

## 4.2. CAE component

MSC/PATRAN is a pre/post-processing software for Finite Element Analysis (FEA), providing solid modeling, meshing, analysis setup and post-processing for multiple solvers including MSC NASTRAN, ABAQUS, LS-DYNA, ANSYS, etc. It uses a simple step-by-step approach that helps to create, analyze and interpret a mathematically realistic model of the structure.

The programming language which can be used in conjunction with MSC/PATRAN is called Patran command language (PCL). PCL is a high level block structured language. It has many features similar to traditional programming languages. The PCL program is in the form of a text file called the session file (.ses) formed by a succession of PCL functions.

The session file starts with importing the geometric model, then creating materials and properties, then it prepares the FE mesh, applies loads and boundary conditions and finally

submits the analysis job to MSC.NASTRAN (The FEA solver chosen). When the job is done, the result file (*.f06* Format) is generated.

## 5. Case study of an aircraft wing structure

One of the most critical components and complicated structures of an aircraft is the wing. It is a framework made up of spars and ribs and covered with a skin. The particular design of a wing depends on many factors, such as the size, weight, speed, rate of climb, and use of the aircraft. The parametric modeling of an aircraft wing is based on parameters which concern the shape, dimension and configuration of the wing. From the large number of wing parameters, the following can be listed (Kachel, 2013): airfoil specification, root chord length, wing span, taper ratio (ratio between the tip chord and the root chord), sweep angle, dihedral angle, twist angle, incidence or setting angle, number of spars (and their configuration), number of ribs (and their configuration).

### 5.1. Parametric geometry model generation

The aircraft wing shape is mainly described by the geometric profile called "airfoil". The airfoil profile can be defined from the coordinates of the upper and lower curves. These coordinates are provided in text files that can be read by the GRIP program as the first step (Fig. 4). If the coordinates are given in percentages, they must be multiplied by the root chord length as follows

$$x = \frac{x\%}{100}c \qquad y = \frac{y\%}{100}c \tag{5.1}$$

where $c$ is the value of the chord length.
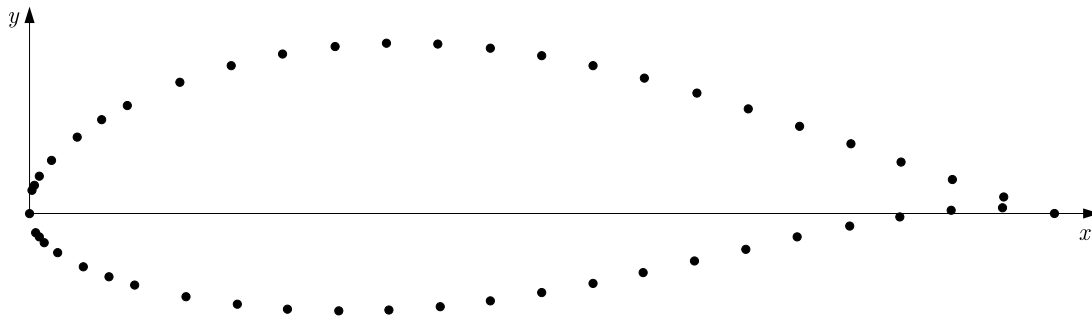


Fig. 4. Points defining of the aerodynamic profile

The developed aircraft wing modelling program uses the B-spline functions which make it possible to apply the parametric approach to the modelling process of virtual structures.

The B-spline curve has the zero value in all parametrisation subintervals, except for $m + 1$. Such curves can be defined recurrently in the following manner

$$N_{i,0}(x) = \begin{cases} 1 & x_i \leqslant x \leqslant x_{i+1} \\ 0 & \text{for other } x \end{cases} \tag{5.2}$$

the $m$ degree B-spline in the interval is defined as

$$N_{i,m}(x) = \frac{x - x_i}{x_{i+m} - x_i} N_{i,m-1}(x) + \frac{x_{i+m+1} - x}{x_{i+m+1} - x_{i+1}} N_{i+1,m-1}(x) \tag{5.3}$$

When taking into consideration equations (5.2) and (5.3), we can find a clear form of the B-spline curve of any degree, which is directly used in algorithms designed for determining curves in CAD systems. When applying the presented approach, we can easily describe the shape of the aerodynamic profile used to construct the aircraft wing.

The tip airfoil profile is created by applying multiple transformation on the root profile:

- Translation by the wing span
- Scale by the taper ratio
- Multiple rotations by sweep, twist and dihedral angles.

These transformations are programmed in the developed GRIP program as follows:

```
...
CSYS0=&WCS
MAT1=MATRIX/TRANSL,0,span,0
upper_curve(n)=TRANSF/MAT1,upper_curve(1)
CS(n)=TRANSF/MAT1,CSYS0
&WCS=CS(n)
MAT2=MATRIX/SCALE,taper_ratio
upper_curve(n)=TRANSF/MAT2,upper_curve(n),MOVE
MAT3=MATRIX/ZXROT,twist_angle
upper_curve(n)=TRANSF/MAT3,upper_curve(n),MOVE
...
```

Next, the wing skin, spar and rib surfaces are generated from the tip and root profiles. The creation of the spars and ribs is programmed in loops, where the increment represents the rib/spar position. For example, the loop for creating rib surfaces from curves can be written as follows:

```
...
DO/rb1:,i,2,n-1
rib(i)=BSURF/CURVE,upper_curve(i),lower_curve(i)
rb1:
...
```

The following flowchart (Fig. 5) illustrates the structure of the GRIP program and shows the steps to follow in order to achieve the desired wing model.

In order to construct a correct FEM model without free edges, it is necessary to associate the mesh nodes on the surface edges. Thus, the skin, rib and spar surfaces must be split into small parts: we define the part of a rib between two neighbor spars, or the leading edge and the first spar, or the last spar and the trailing edge as a rib part. Also, the part of a spar between two neighbor ribs as the spar part and the skin part between two neighbor ribs and two neighbor spars as a skin part (Fig. 6)

The next step is to export the model as IGES file. As mentioned before, this is done by calling a VB journal that executes this task. To perform different tasks by programming, surface part labels are used as function inputs. Although, when the wing model is imported in MSC.PATRAN as a single IGES file, the surface parts are labeled as a whole and, therefore, labels can not be distinguished in order to operate on a specific group of parts. The solution is to export/import the model as three separate IGES files: "skin.igs", "ribs.igs" and "spars.igs".

## 5.2. Automated FE model generation

For the CAE component, the first task programmed in the PATRAN session file is to import the model IGES files one by one to identify the surface labels. For example, after importing the first file "skin.igs", the number of surfaces imported can be determined, and thus it is known
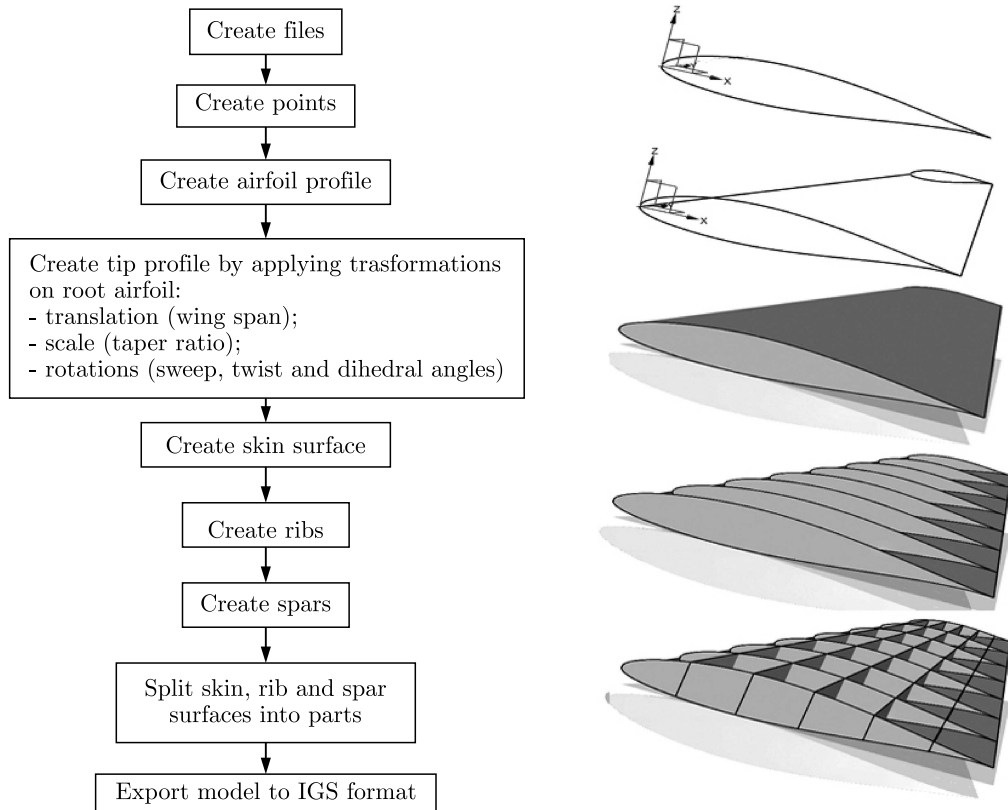
Fig. 5. GRIP program flowchart
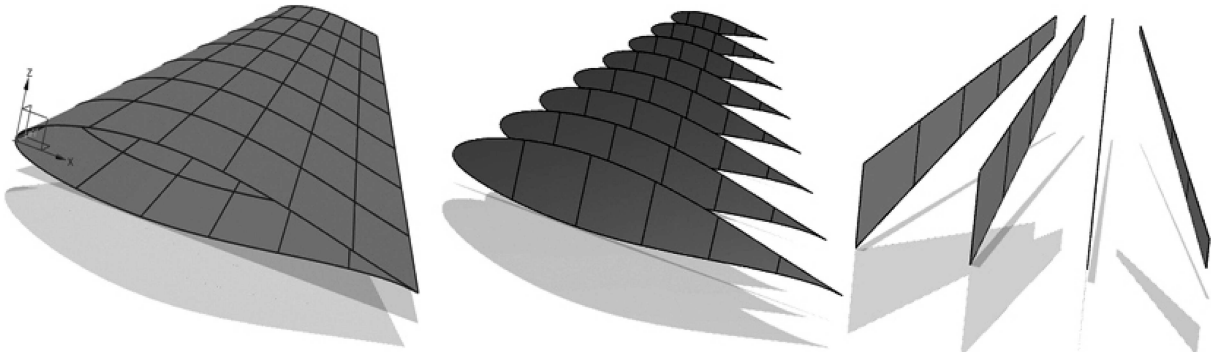


Fig. 6. Skin, spar and rib surfaces split into small parts

that the skin part labels are from 1 to the the determined number, and so on. To illustrate more, a portion from the session file, showing PCL code used to perform this, is presented below:

```
...
INTEGER entities_imported(9)       $$ number of patran entities imported by
type
INTEGER N_skin_parts    $$ total number of skin parts
INTEGER N_spar_parts    $$ total number of spar parts
INTEGER N_rib_parts     $$ total number of rib parts
ugi_import_iges_v5("C:\skin.igs", 0,"default_group",...,entities_imported)
N_skin_parts=entities_imported(3)   $$ "3" for entity type: surface
ugi_import_iges_v5("C:\spars.igs", 0,"default_group",...,entities_imported)
N_spar_parts=entities_imported(3)
```

```
ugi_import_iges_v5("C:\ribs.igs", 0,"default_group",...,entities_imported)
N_rib_parts=entities_imported(3)
```

In addition to the total number of spar parts and ribs parts, it is necessary to determine the number of ribs and spars in the model, noted $R$ and $S$, respectively. This can be performed using these equations

$$R = \frac{N\_skin\_parts}{2} - N\_spar\_parts + 1$$
$$S = N\_rib\_parts - \frac{N\_skin\_parts}{2} - 1$$

(5.4)

Next, materials and properties are created based on analysis parameters (materials and thicknesses), and the surfaces are meshed after specifying a mesh seed to control element sizes and to ensure node association (equivalence verification). The PCL program developed is written in such a way that the aircraft wing geometric model can be modified and the mesh will be updated accordingly (Fig. 7). Finally, loads and constraints are applied and the analysis job is submitted to MSC.NASTRAN software.



| Number of ribs = 8 | Number of ribs = 4 | Number of ribs = 6 |
| Number of spars = 4 | Number of spars = 2 | Number of spars = 3 |
| Taper ratio = 0.7 | Taper ratio = 0.4 | Taper ratio = 0.2 |

Fig. 7. Mesh update using the automated finite element modeling

After MSC.NASTRAN software finishes the analysis, output files are created. The MATLAB script reads the result files and looks for the specific result values, which can be displacements, stresses, natural frequencies, etc.

As analysis parameters, many choices are available, such as material specifications, thicknesses, load intensity (for static analysis), etc. For our simple case study, the aircraft wing is supposed to be clamped at its root. Both solution types "Linear static" and "Normal modes" can be supported by the presented integration procedure. For the static analysis, the wing is supposed to be subjected to a uniform pressure on its skin surface. Results desired can be either displacements or stresses of the wing structure due to the applied pressure for the static analysis, and natural frequencies for the normal mode analysis (Fig. 8).

### 5.3. Results and discussion

In order to simplify the use of the integration system, a MATLAB graphical user interface is implemented (Fig. 9). This GUI eases parameter value input and result access. The user can simply introduce the desired parameter values for modeling as well as for analysis, choose the analysis type and run the integration procedure. The script programs (GRIP program and PCL program) are then created according to parameter input values, and the software packages

Fig. 8. Plots of the static and dynamic analysis results: (a) displacement result plot, (b) stress result plot, (c) normal modes

(SIEMENS NX and PATRAN/NASTRAN) are executed in the invisible mode to carry on the desired task. When the analysis is completed, the results as well as preview graphics are shown in the same interface. Accordingly, there is no interaction of the user with the design software tools, and the overall time of the modeling and calculation is only about 45 seconds. Thus, exploring the behavior of a new design case (different geometric/analysis parameter value) is no longer a time/effort consuming task due the automation capacity of the approach.



Fig. 9. A graphical user interface for the integration procedure

One other original quality of the developped framework is that it offers the ability to investigate the behavior of the structure with respect to changes of a chosen parameter. This is done by running the procedure in a simple loop, where the parameter value changes at each iteration. Therefore, the structure response can be related to its parameters, through approximate mathematical expressions using interpolation techniques, which allows the use of conventional optimization algorithms. The automated integration procedure is, consequently, indispensable for conducting an optimization task. The parameters, for modeling as well as for analysis, can play the role of design variables, and the objective function can be set as one of the result cases (minimize the maximum stress, maximize the lowest frequency value, etc).

In the present work, the procedure is used to emphasize the dependency of the wing structure maximal stress and first natural frequency on some of its parameters. One of the requirements for the structural design is to limit the maximal stress over the structure under critical load

cases. In order to predict the resistance of the wing structure under some specific load intensity, the maximum von Mises stress over the structure is calculated for different values of the wing parameters. This allows one to verify if the von Mises stress reaches the critical value, known as the yield strength, for the design cases described by the parameter values. Similarly, to prevent the structure from free vibrations and resonance damage, natural frequency dependency on the wing parameters must be determined. Figure 10 shows the effect of variation of the wing chord and the spar thickness on the maximum von Mises stress over the structure as well as the change in the first frequency value in function of the wing span and the taper ratio.



Fig. 10. Dependency of the wing behavior on its parameters: (a) von Mises stress in function of the chord length, (b) von Mises stress in function of the spar thickness, (c) first frequency in function of the wing span, (d) first frequency in function of the taper ratio

The presented figures show that some relations (e.g. Figs. 10b-10d) between the structure behavior and design parameter can be modeled by simple mathematical functions (linear, polynomial,...) and hence reduce the huge computational cost that the optimization may require. Some other relations (e.g. Fig. 10a) which present a discontinuity point out the usability of conventional optimization algorithms only after the fitting operation. Therefore, the presented approach proves its indispensability as a preparatory step for the optimization problem. Moreover, including geometric parameters (wing taper ratio, sweep back angle,...) as optimization design variables is not possible using the optimization module in CAE software. Thanks to the present methodology, the optimization can examine a large design space where both geometric and analysis parameters of the wing structure can be mapped for optimal values.

## 6.    Conclusions

The CAD/CAE integration technique has become more and more popular in design process early stages as a tool for time and cost reduction. The idea behind this work is to develop a seamless automated integration procedure intended to ease design modification, explore a large design space in a relatively reduced time and to prepare for optimization activities. The developed procedure is based on popular commercial parametric CAD-CAE tools, SEMENS NX with its programming language GRIP and MSC.PATRAN/NASTRAN with its automation module PCL, and MATLAB as the implementing software. An aircraft wing structure has been the case to which the procedure was applied. The complexity of the considered case lies mainly in the encountered difficulties of programming the analysis tasks so as to be compatible with the changes of the geometry layout (change of the number of spars/ribs). In addition, acting on the imported entities (mainly surfaces) requires knowledge of their specific labels which are assigned automatically by MSC.PATRAN software, which complicates the programming task.

It has been shown that the presented approach is requisite for probing the design space and examine the structure behavior over it. Having the structure response in fucntion of its parameters constructs a primary base to conduct an optimization problem without the need for excessive computational time. Thus the presented work serves as a solid ground for the implementation of a generic aircraft wing optimization framework.

## References

1. ASIEDU Y., GU P., 1998, Product life cycle cost analysis: state of the art review, *International Journal of Production Research*, **36**, 4, 883-908

2. DIETRICH M., KĘDZIOR K., SKALSKI K., 1999, Design and manufacturing of the human bone endoprotheses using computer-aided systems, *Journal of Theoretical and Applied Mechanics*, **37**, 3, 481-503

3. EDKE M.S., CHANG K.H., 2006, Shape optimization of heavy load carrying components for structural performance and manufacturing cost, *Structural and Multidisciplinary Optimization*, **31**, 5, 344-354

4. GUJARATHI G.P., MA Y.-S., 2011, Parametric CAD/CAE integration using a common data model, *Journal of Manufacturing Systems*, **30**, 3, 118-132

5. KACHEL S., 2013, Optimization of wing parameters to achieve minimum weight at defined aerodynamic loads, *Journal of Theoretical and Applied Mechanics*, **51**, 1, 159-170

6. NAWIJN M., VAN TOOREN M.J.L., BERENDS J.P.T.J., ARENDSEN P., 2006, Automated finite element analysis in a knowledge based engineering environment, *44th AIAA Aerospace Science Meeting and Exhibit*, 9-12

7. PARK H.-S., DANG X.-P., 2010, Structural optimization based on CAD-CAE integration and metamodeling techniques, *Computer-Aided Design*, **42**, 10, 889-902

8. PENG L., LIU L., LONG T., YANG W., 2014, An efficient truss structure optimization framework based on CAD/CAE integration and sequential radial basis function metamodel, *Structural and Multidisciplinary Optimization*, **50**, 2, 329-346

9. ROCCA G.L., VAN TOOREN M.J.L., 2009, Knowledge-based engineering approach to support aircraft multidisciplinary design and optimization, *Journal of Aircraft*, **46**, 6, 1875-1885

10. ROWE J., 2006, *Virtual Reality*, Cadalyst

11. ROY R., HINDUJA S., TETI R., 2008, Recent advances in engineering design optimisation: Challenges and future trends, *CIRP Annals-Manufacturing Technology*, **57**, 2, 697-715

12. Sapuan S.M., Osman M.R., Nukman Y., 2006, State of the art of the concurrent engineering technique in the automotive industry, *Journal of Engineering Design*, **17**, 2, 143-157

13. Sohaib M., 2011, *Parameterized Automated Generic Model for Aircraft Wing Structural Design and Mesh Generation for Finite Element Analysis*, Master Thesis, Linköping University, Linköping, Sweden

14. Su D., Qin D., 2003, Integration of numerical analysis, virtual simulation and finite element analysis for the optimum design of worm gearing, *Journal of Materials Processing Technology*, **138**, 1, 429-435

15. Wang D., Hu F., Ma Z., Wu Z., Zhang W., 2014, A CAD/CAE integrated framework for structural design optimization using sequential approximation optimization, *Advances in Engineering Software*, **76**, 56-68

# ANALYSIS OF SELECTED DYNAMIC FEATURES OF
# A TWO-WHEELED TRANSMISSION SYSTEM

Piotr Krawiec

*Poznań University of Technology, Chair of Basics of Machine Design, Poznań, Poland*

*e-mail: piotr.krawiec@put.poznan.pl*

The paper presents results of analysis of selected dynamic features of an uneven-running two-
-wheeled strand transmission. The characteristic features of such type of transmissions is the
ability of obtaining variable kinematic and dynamic features by the application of wheels
with a noncircular envelope. Particularly, high interest of application of uneven-running
transmissions was done in the previous century. At that time, a concept of application
of such transmissions for process and machine control was invented. The applications in
textile and engineering industry are widely known. A mathematical model of the multiplying
transmission is presented. Few versions of dynamic features of the transmission for different
loads and solid moments of inertia are examined. The presented results can be very helpful
for designers of classical and uneven-running strand transmissions.

*Keywords;* transmission, variable gear ratio, mathematical model

## 1. Introduction

The analysis of dynamic features of a strand transmission with variable gear ratio is a complex
and a nontypical process. This complexity results from the specific character of such a trans-
mission, which is determined by the shape of the toothed wheel. It is found that there is a lack
of scientific literature concerning empirical research of strand transmissions with noncircular
toothed wheels.

The author of the work (Grzelak, 2007) presented the equation of motion of a strand trans-
mission with elliptical wheels. He also estimated the influence of initial orientation and the
geometry of rotating elements on the characteristics of velocity and acceleration, which are cau-
sed by an impulse of moment that is acting on the driving wheel. This problem was solved
with the application of Matlab software. The author showed that the elliptical transmission
with identical wheels can work as a transmission with a constant or periodically variable gear
ratio. However, during the analysis of kinematics and dynamics, he did not take into account
the following condition: length of the wrap of the transmission for any angle of rotation of the
wheel must be a constant value and must be equal to length of the standard belt.

The subject of the work by Buśkiewicz (2000) was analysis of torque transfer in the trans-
mission with one elliptical wheel and one circular wheel, which was eccentric fixed. The constant
length of wrap was not kept in that transmission. The relationships between torques on driving
and driven wheels were formulated for the analysed transmission.

The study by Kelm (2006) was about the determination of differences between lengths of
driving and driven strands of the uneven-running two-wheeled transmission. The author presen-
ted the application of a pulley with a slight out-of-round in the drive of the timing gear of a
combustion engine. He showed the advantages of such a solution in comparison with a classical
strand transmission with circular wheels.

In the available literature, there is a lack of discussion about strand vibrations in uneven-
running transmissions. The studies concerning classical strand transmissions are only known

(Kido *et al.*, 1994; Krasiński and Stachoń, 1997, 2004; Martins and Robson, 2013). These studies do not exhaust the topic with reference to theory of vibrations (Bajkowski, 1989; Kurnik, 1985). However, one can find many publications about the load capacity of transmissions with different types of belts (Bulushi *et al.*, 2015; Chen *et al.*, 1998; Jang *et al.*, 2014; Johannesson and Distner, 2002; Korolev, 1990).

The main purpose of the application of an uneven-running transmission is not transfer of power, but the obtaining of variable kinematic features. Therefore, forces resulting from continuous accelerating or decelerating of masses of noncircular belt pulleys have the essential influence on the load capacity of the transmission (without external resistant torque). The goal of the research is the determination of the influence of:

- mass moments of inertia of toothed wheels,
- values of coefficients of viscous damping,
- angular velocities of the driving shaft,
- resistant torques $M_{OP}$,
- load torques $M_S$

on the selected dynamic features of the uneven-running transmission.

Multiplying and reduction gear are taken into account in the research.

## 2. The mathematical model of an uneven-running transmission

Multiplying gear are taken into account in the presented research of transmissions.

Lagrange's equations of the 2nd type are basic equations for the determination of the equation of motion for the uneven-running transmission. The classical form of the equation is as follows

$$\frac{d}{dt}\left(\frac{\partial E_K}{\partial \dot{u}_i}\right) - \frac{\partial E_K}{\partial u_i} + \frac{\partial E_P}{\partial u_i} + \frac{\partial R_R}{\partial \dot{u}_i} = F_i \qquad i = 1, 2, \ldots, n \tag{2.1}$$

where $E_K$, $E_P$, $E_R$ are kinetic, potential and dissipation energy of the system, respectively, $\dot{u}$, $u$ – velocities and generalized coordinates, $F_i$ – generalized excitation.
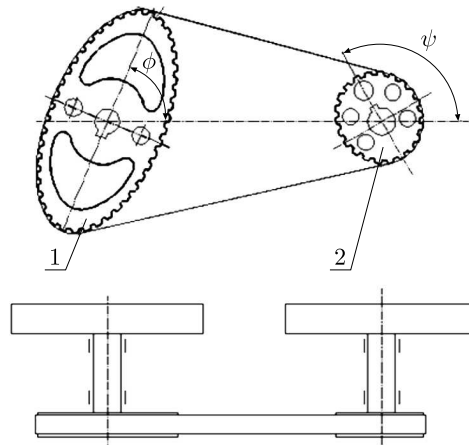


Fig. 1. A diagram of the strand transmission with noncircular cogbelt pulleys

In the analysed transmission

$$E_K = \frac{1}{2}J_1\dot{\varphi}^2 + \frac{1}{2}J_2\dot{\psi}^2 \qquad\qquad E_R = \frac{1}{2}C_1\dot{\varphi}^2 + \frac{1}{2}C_2\dot{\psi}^2$$

and $E_P = 0$ – assumption: the strand is inextensible.

After determining components of the energy and substituting these components to equation (2.1), the following form of the equation of motion for the strand transmission – multiplying gear (Fig. 1) has been obtained

$$J_1\ddot{\varphi} + J_2\ddot{\varphi}\frac{\partial\psi}{\partial\varphi} + J_2\dot{\psi}\frac{d}{dt}\frac{\partial\psi}{\partial\varphi} + C_1\dot{\varphi} + C_2\dot{\psi}\frac{\partial\psi}{\partial\varphi} = M_S - M_{OP}\frac{\partial\psi}{\partial\varphi} \tag{2.2}$$

where $J_1$, $J_2$ are reduced mass moments of inertia for the driving and driven wheels and shafts, respectively, $\varphi$ – angle of rotation of the driving wheel, $\psi$ – angle of rotation of the driven wheel, $C_1$, $C_2$ – coefficients of viscous damping in the bearings of driving and driven shafts, $M_S$ – load torque of the driving wheel, $M_{OP}$ – resistance torque.

It is assumed that the transmission will be loaded with a constant resistance torque which is defined as

$$M_{OP} = M_{OP\,max}(1 - e^{-\alpha\dot{\varphi}}) \tag{2.3}$$

In order to solve equation (2.2), one should determine the relationship $\psi = f(\varphi)$, which describes the change of the angle of rotation of the driven wheel in function of the angle of rotation of the driving wheel. The mean square trigonometric polynomial of the 6th degree is used for description of this relationship

$$\psi = a\varphi + b\sin(2\varphi) + c\sin(2\varphi) + d\cos(4\varphi) + e\sin(4\varphi) + f\cos(6\varphi) + \ldots + g(6\varphi)$$

The time derivative of the angle of rotation of the driven wheel (velocity) is determined as

$$\begin{aligned}
\dot{\psi} = \frac{d\psi}{dt} &= a\dot{\varphi} - 2b\sin(2\varphi)\dot{\varphi} + 2c\cos(2\varphi)\dot{\varphi} - 4d\sin(4\varphi)\dot{\varphi} \\
&+ \ldots + 4e\cos(4\varphi)\dot{\varphi} - 6f\sin(6\varphi)\dot{\varphi} - 6g\cos(6\varphi)\dot{\varphi} = \dot{\varphi}\frac{\partial\psi}{\partial\varphi}
\end{aligned} \tag{2.4}$$

that is

$$\dot{\psi} = \dot{\varphi}\frac{d\psi}{dt}$$

The second time derivative of the angle of rotation of the driven wheel is determined as follows (acceleration)

$$\begin{aligned}
\ddot{\psi} = \frac{d\dot{\psi}}{dt} &= a\ddot{\varphi} - 2b2\cos(2\varphi)\dot{\varphi}^2 - 2b\sin(2\varphi)\ddot{\varphi} - 2\cdot 2c\sin(2\varphi)\dot{\varphi}^2 \\
&+ \ldots + 2c\cos(2\varphi)\ddot{\varphi} - 4\cdot 4d\cos(4\varphi)\dot{\varphi}^2 - 4d\sin(4\varphi)\ddot{\varphi} - 4\cdot 4d\cos(4\varphi)\dot{\varphi}^2 \\
&- \ldots - 4e\cos(4\varphi)\ddot{\varphi} - 6\cdot 6f\cos(6\varphi)\dot{\varphi}^2 - 6f\sin(6\varphi)\ddot{\varphi} - 6\cdot 6g\sin(6\varphi)\dot{\varphi}^2 + 6g\cos(6\varphi)\ddot{\varphi}
\end{aligned}$$

For simplification of the record, the following denotation is taken into consideration: $d\psi/d\varphi = C_M$, where the index $M$ denotes the multiplying gear

$$\frac{d\psi}{d\varphi} = a - 2b\sin(2\varphi) + 2c\cos(2\varphi) - 4d\sin(4\varphi) + 4e\cos(4\varphi) - 6f\sin(6\varphi) - \ldots - 6g\cos(6\varphi) = C_M \tag{2.5}$$

while

$$\begin{aligned}
\frac{d^2\dot{\psi}}{d\dot{\varphi}^2} = \frac{d}{d\varphi}\left(\frac{d\psi}{d\varphi}\right) &= -4b\cos(2\varphi) - 4c\sin(2\varphi) - 16d\cos(4\varphi) - 16e\sin(4\varphi) \\
&- \ldots - 36f\cos(6\varphi) - 36g\sin(6\varphi) = -B_M
\end{aligned}$$

The following relationship is determined as the last one

$$
\frac{d}{dt}\left(\frac{d\dot\psi}{d\dot\varphi}\right) = -4b\cos(2\varphi)\dot\varphi - 4c\sin(2\varphi)\dot\varphi - 16d\cos(4\varphi)\dot\varphi - 16e\sin(4\varphi)\dot\varphi
$$
$$
- \ldots - 36f\cos(6\varphi)\varphi - 36g\sin(6\varphi)\dot\varphi
$$
(2.6)

For simplification of the record, the following denotation is taken into consideration:

$$
B_M\dot\varphi = 4b\cos(2\varphi)\dot\varphi + 4c\sin(2\varphi)\dot\varphi + 16d\cos(4\varphi)\dot\varphi + 16e\sin(4\varphi)\dot\varphi
$$
$$
+ \ldots + 36f\cos(6\varphi)\dot\varphi + 36g\sin(6\varphi)\dot\varphi
$$

On the basis of relationships (2.4)-(2.7) and proper substitutions, the following form of equation (2.2) is obtained for the multiplying gear

$$
J_1\ddot\varphi + J_2\ddot\varphi\left(\frac{\partial\psi}{\partial\varphi}\right)^2 - C_M^2 - J_2\dot\varphi^2 C_M B_M\dot\varphi + C_1\dot\varphi + C_2\dot\varphi(C_M)^2 = M_S - M_{OP}C_M
$$
(2.7)

and finally

$$
\ddot\varphi = \frac{(M_S + 2B_M C_M J_2)\dot\varphi^2 - (C_1 + C_2 C_M^2)\dot\varphi}{J_1 + J_2 C_M^2}
$$
(2.8)

## 3. Results of numerical calculations

A few variants of the dynamics of the two-wheeled uneven-running transmission for different values of load and mass moments of inertia are analysed below. In order to improve calculations, computer program Uneven-running strand transmission – Dynamics, NPC-D has been designed. This program has been written in Visual Basic. The constant step of integration with the value of 0.001 s has been assumed in calculations. The task has been solved with the use of the Runge--Kutta method of the 4th order.

At first, the multiplying gear with constant values of the kinematic excitation ($\omega_1 = 40$ rad/s) and with the following data: $J_1 = 0.06$ kg·m$^2$, $J_2 = 0.01$ kg·m$^2$, $C_1 = 0$ N·m·s, $C_2 = 0$ N·m·s, $M_S = 0$ N·m, $M_{OP} = 0$ N·m (Figs. 2 and 3) has been analysed. In order to simplify description of the axis in graphs, the following denotations are taken into consideration: $\omega$ – angular velocity, $a$ – acceleration.



Fig. 2. Velocity of wheel 1 and 2 in function of time ($\omega_1 = 40$ rad/s)

Next figures (Figs. 4 and 5) present characteristics of velocity and acceleration of the gear wheels of the multiplying gear with the following values: $\omega_1 = 1$ rad/s, $J_1 = 0.06$ kg·m$^2$, $J_2 = 0.01$ kg·m$^2$, $C_1 = 0.002$ N·m·s, $C_2 = 0.01$ N·m·s, $M_S = 0.1$ N·m, $M_{OP} = 0$ N·m.

Fig. 3. Acceleration of wheel 1 and 2 in function of time ($\omega_1 = 40\,\mathrm{rad/s}$)



Fig. 4. Velocity of wheel 1 and 2 in function of time ($\omega_1 = 1\,\mathrm{rad/s}$)



Fig. 5. Acceleration of wheel 1 and 2 in function of time ($\omega_1 = 1\,\mathrm{rad/s}$)

Figures 6 and 7 illustrate characteristics of the change in velocity and acceleration of the gear wheels of the multiplying gear for the following data: $J_1 = 0.3\,\mathrm{kg \cdot m^2}$, $J_2 = 0.3\,\mathrm{kg \cdot m^2}$, $C_1 = 0.02\,\mathrm{N \cdot m \cdot s}$, $C_2 = 0.02\,\mathrm{N \cdot m \cdot s}$, $M_{OP} = 4\,\mathrm{N \cdot m}$, $M_S = 9\,\mathrm{N \cdot m}$.

Fig. 6. Velocity of wheel 1 and 2 in function of time ($\omega_1 = 20\,\mathrm{rad/s}$)



Fig. 7. Acceleration of wheel 1 and 2 in function of time ($\omega_1 = 20\,\mathrm{rad/s}$)

## 4.    Summary

On the basis of the determined characteristics of the mathematical model of the transmission, one can draw the following conclusions and observations:

- Considerable accelerations of the driven wheels occur for low values of mass moments of inertia and for relatively high values of velocities.

- Constant gear ratio and constant accelerations can be obtained when the dimensions (mass) of the gear wheels are great.

- The transmission can not work with a too high rotational speed.

- In the case of multiplying gear with the following values of mass moments of inertia: $J_1 = 0.06\,\mathrm{kg{\cdot}m^2}$ and $J_2 = 0.01\,\mathrm{kg{\cdot}m^2}$, without the external load and on the assumption that frictional resistance is neglected; one can observe (during kinematic excitation) that the velocity of the driving wheel is characterized by considerable variability for a quasi--constant velocity of the driven wheel. In the range of velocity from $10\,\mathrm{rad/s}$ to $40\,\mathrm{rad/s}$, the acceleration of the driven wheel is 15 times higher than the acceleration of the driving wheel.

- For the multiplying gear with the considered conditions: viscosity friction, small torque $M_S$ and no resistance torque; the characteristics of rotational speed and acceleration are similar but their amplitudes are different, and the acceleration of wheel 1 is higher than the acceleration of wheel 2.

- The resistance torque which is placed in the description of the analysed transmission, does not cause any changes to the characteristics of velocity and acceleration. However, in this case, the acceleration of the driven wheel is higher than the acceleration of the driving wheel.

- Equal and relatively small values of mass moments of inertia for both wheels and the following assumptions: no frictional resistance and no loads; lead to higher amplitudes of velocity and acceleration in comparison with transmissions with different mass moments of inertia.

## References

1. Bajkowski J., 1989, *Theorie des vibrations*, Oran, Office des Publications Universitaires

2. Bulushi A., Rameshkumar G.R., Lokesha M., 2015, Fault diagnosis in belts using time and frequency based signal processing techniques, *International Journal of Multidisciplinary Sciences and Engineering*, **6**, 11, 12-20

3. Buśkiewicz J., 2000, Non-uniform torque transmitted by a non-circular belt gear, *Machine Dynamics Problems*, **24**, 3, 11-18

4. Chen T.F., Lee D.W., Sung C.K., 1998, An experimental study on transmission efficiency of a rubber V-belt CVT, *Mechanisms and Machine Theory*, **33**, 4, 351-363

5. Grzelak M., 2007, Impulse characteristics of strand transmission with elliptical rotors (in Polish), *XXIII Sympozjon Podstaw Konstrukcji Maszyn*, Rzeszów-Przemyśl, 225-233

6. Jang J.J.I., Kwon O.E., Chai M.J., Kim H.S., 2014, Power transmission dynamics in micro and macro slip regions for a metal v-belt continuously variable transmission under external vibrations, *International Journal of Automotive Technology*, **15**, 7, 1119-1128

7. Johannesson T., Distner M., 2002, Dynamic loading of synchronous belts, *Journal of Mechanical Design*, **124**, 3, 79-85

8. Kelm P., 2006, *Dynamiksimulation von Zahnriemengetrieben mit ungleichformiger Übersetzung*, Dresden, Tagung Zahnriemengetriebe TU, 56-64

9. Kido R., Kussano T., Fujii T., 1994, A new approach for analyzing load distribution of toothed belts at steady states using FEM, *SAE Society of Automotive Engineers Technical Paper Series 940690*, 1234-1243

10. Korolev N., 1990, Zugkraftverlauf und Belastungsverteilung in Zahnriemenantrieben, *Konstruktion*, **42**, 47-253

11. Krasiński M., Stachoń S., 1997, Analysis of dynamics of strand transmissions with vee-belts and cogbelts (in Polish), *XVIII Sympozjon Podstaw Konstrukcji Maszyn*, Kielce Ameliówka, 177-182

12. Krasiński M., Stachoń S., 2004, Investigations of dynamics of strand transmission with cogbelts (in Polish), *Czasopismo Techniczne*, **13**, 63-73

13. Kurnik W., 1985, *Theory of Vibrations – Casebook* (in Polish), Wydawnictwo Politechniki Warszawskiej, Warszawa

14. Martins D.R., Robson P., 2013, Nonlinear model of belt-tensioner system with experimental validation, *11th International Conference on Vibration Problems*, Lisbon, 1-10

# DETERMINATION OF CRACK INITIATION AND PROPAGATION IN TWO DISC SHAPED SPECIMENS USING THE IMPROVED MAXIMUM TANGENTIAL STRESS CRITERION

MOSLEH EFTEKHARI

*Department of Mining Engineering, Science and Research Branch, Islamic Azad University, Tehran, Iran*
*e-mail: eftekhari_mosleh@yahoo.com; mosleh.eftekhari@mi.iut.ac.ir*

ALIREZA BAGHBANAN, EHSAN MOHTARAMI

*Department of Mining Engineering; Isfahan University of Technology (IUT), Isfahan, Iran*

HAMID HASHEMOLHOSSEINI

*Department of Civil Engineering; Isfahan University of Technology (IUT), Isfahan, Iran*

The crack initiation angle and propagation path for two different disc shaped test specimens (i.e., SCB and CBD specimen) are investigated experimentally and theoretically. The Maximum Tangential Stress (MTS) criterion does not calculate the crack initiation angle in SCB and CBD specimens correctly. Moreover, at the angles after occurrence of pure mode II, where the stress intensity factor of mode I becomes negative, this criterion is not applicable. Therefore, in this research work, Improved MTS (IMTS) criterion which has been implemented in the extended finite element method and is applicable under tensile and compressive loading conditions to examine the crack propagation path in the aforementioned disc shaped specimens. Furthermore, an experimental study on a cracked Brazilian disc specimen has been conducted at different angles. Results of IMTS criterion in these specimens show that the crack propagation path and the crack initiation angle can be predicted theoretically by using IMTS criterion.

*Keywords:* Extended Finite Element Method (XFEM), maximum tangential stress (MTS) criterion, improved maximum tangential stress (IMTS) criterion, crack propagation, stress intensity factor

## 1. Introduction

Investigation of the fracture grow path is an important task to optimize size of rock pieces or control stability of cracked rock structures in many applications of rock engineering such as rock cuttings, excavations and rock stability analysis. In rock structures, most of failures occur under a mixed mode in practice (combination of the opening and shearing mode), and thus fracture path of cracked structures may grow in curved paths and not necessarily along the direction of the initial crack (Aliha *et al.*, 2010). Therefore, investigating the crack initiation angle and the crack propagation path under the mixed loading mode are favorite subjects for researchers in the field of rock mechanics. There are a large number of theoretical models (Erdogan and Sih, 1963; Hussain *et al.*, 1974; Nuismer, 1975; Palaniswamy and Knauss, 1972; Sih, 1974; Theocaris and Andrianopoulos, 1982) and experimental techniques (Grassl and Rempling, 2007; Isaksson and Ståhle, 2002; Lin *et al.*, 2009; Song *et al.*, 2004; Xeidakis *et al.*, 1997) for investigating the mixed mode of crack growth in rock materials. Theoretical failure criteria such as the Maximum Tangential Stress (MTS) criterion (Erdogan and Sih, 1963), the minimum strain energy density criterion (Sih, 1974), and the maximum energy release rate criterion (Hussain *et al.*, 1974) have been frequently used by researchers working on rock and geo-material fields in order to estimate

the direction of the mixed mode in the crack growth process. These failure models are usually developed based on stress, strain, and energy conditions in front of the crack tip, and the stress intensity factor is often used to estimate the crack growth direction.

Various numerical methods such as the boundary element method, finite difference method, meshless method and finite element method (FEM) are adopted to problem-solving in fracture mechanics. The common purpose of these methods has always been to achieve a precise, straightforward and a developed practical solution containing advantages of previous methods and upcoming their restrictions and shortcomings. This process of development of numerical methods led to the appearance of a novel method in 1999, called the extended finite element method (XFEM) which is based on the finite element method. This method takes advantage of all features of the finite element method in solving different problems, and it has resolved its shortcomings in predicting of crack initiation and propagation. In this method, the crack is defined as mesh independent, hence, the crack is able to grow anywhere through the finite element mesh. Extensive studies using this method which have been conducted in a short time after its appearance indicate that this method has a great capability in modeling problems associated with fracture mechanics (Budyn *et al.*, 2004; Campilho *et al.*, 2011; Fan and Jing, 2013; Huynh and Belytschko, 2009; Mergheim *et al.*, 2005; Singh *et al.*, 2012). Thus this method has been chosen as the numerical solution tool in our research work.

The Maximum Tangential Stress criterion in which the crack is propagated from the crack tip along the direction of maximum tangential stress has been used more extensively in the XFEM for the modeling of crack growth. The direction of crack propagation when the MTS criterion is assigned in numerical modeling depends on the calculated value of stress intensity factors as follows

$$\theta_c = 2\tan^{-1}\frac{1}{4}\left(\frac{K_{\mathrm{I}}}{K_{\mathrm{II}}} \pm \sqrt{\left(\frac{K_{\mathrm{I}}}{K_{II}}\right)^2 + 8}\right) \tag{1.1}$$

where $\theta_c$ is the crack initiation angle and $K_{\mathrm{I}}$ and $K_{\mathrm{II}}$ are stress intensity factors in modes I and II, respectively. When the crack is placed in a compressive stress field, the value of the stress intensity factor of mode I becomes negative and this criterion is no longer able to estimate the direction of crack propagation. While, rocks unlike most engineering materials often experience compressive loading and therefore most rock failures are also occurred under such conditions. Therefore, attempts have been made to study the initiation and propagation of cracks under compressive loading conditions in the literature. Lack of efficiency of the MTS criterion under compressive conditions has been addressed by other researchers (Al-Shayea, 2005; Aliha *et al.*, 2010; Bobet, 1997; Shen and Stephansson, 1994; Wu and Wong, 2012). Bobet (1997) compared results of crack initiation angle by MTS criterion with results obtained from uniaxial compressive tests and stated that this criterion did not offer a suitable estimation of the crack initiation angle. He also represented a stress-based criterion in order to estimate crack initiation angle on the boundary element method. Shen and Stephansson (1994) also developed the F criterion or the modified G criterion for the same purpose. Wu and Wong (2012) examined crack propagation under compressive loading using the Mohr-Coulomb criterion using the numerical manifold method.

Recently, the MTS criterion has been improved and implemented in XFEM in order to be utilized in different loading conditions from tensile to compressive loading (Eftekhari *et al.*, 2016). This criterion is called the Improved MTS (IMTS) criterion and it has been evaluated in some examples and then used in a cracked specimen under uniaxial compression. Results from the IMTS criterion are perfectly matched with the experimental and numerical modeling results reported in the literature (Eftekhari *et al.*, 2016).

Different laboratory specimens and experimental methods have been proposed and used to determine rock fracture toughness so far. However, a review of previous studies indicates that the

most commonly used specimens for conducting fracture tests and studying crack growth in rocks and geo-materials are disc shaped specimens such as Cracked Brazilian Disc (CBD) (Atkinson *et al.*, 1982; Awaji and Sato, 1978; Eftekhari *et al.*, 2015a), Hollow Centre Cracked Disc (HCCD) (Choi *et al.*, 1988; Eftekhari *et al.*, 2015c; Shiryaev and Kotkis, 1983), Flattened Brazilian Disc (Wang and Xing, 1999; Wang *et al.*, 2004), Modified Ring (Thiercelin, 1989; Thiercelin and Roegiers, 1986), Semi-Circular Bend (SCB) specimen (Chong *et al.*, 1987; Eftekhari *et al.*, 2015b; Kuruppu and Chong, 2012).

Two frequently employed disc type specimens are the cracked Brazilian disc subjected to diametral compression and the semicircular bend specimen subjected to three-point bend loading. Simple geometry, straight forward preparation and easy loading and also capability to perform different mode combinations are the main advantages of these specimens. Hence, these test specimens have been used frequently to investigate mixed mode crack growth of rock materials (Al-Shayea, 2005; Ayatollahi and Aliha, 2008; Chen *et al.*, 1998; Eftekhari *et al.*, 2015a; Eftekhari *et al.*, 2015b; Liu *et al.*, 2007). Recently, International Society for Rock Mechanics (ISRM) has suggested the SCB specimen to be the new standard specimen in the determination of the fracture toughness of pure mode I (Kuruppu *et al.*, 2015).

Figure 1 shows the geometry and loading condition of the CBD and SCB specimens used for mixed mode I/II fracture tests. In the CBD specimen, the angle $\beta$ is defined as an angle between the direction of centre crack with length $2a$ and the applied loading direction. The SCB specimen is a semicircular disc of radius $R$ which has an angled edge crack with respect to the applied load $P$. For both specimens, pure modes I and II and the mixed mode can be provided by changing the crack angle $\beta$. Obviously, $\beta = 0°$ is associated with the case of pure mode I condition. By increasing the loading angle from zero, mode II is introduced.



Fig. 1. Geometry and loading conditions of CBD and SCB specimens subjected to mixed mode I/II loading: (a) CBD specimen, (b) SCB specimen

Experimental results with CBD and SCB specimens have showed that the approximated crack initiation angle by the MTS criterion is different with the measured values by laboratory experiments (Aliha *et al.*, 2010). Aliha *et al.* (2010) introduced a criterion called Generalized MTS (GMTS) in order to estimate the crack propagation direction more accurately.

Theoretically, when $K_\mathrm{I}$ value is equal to zero, pure mode II occurs. In the SCB and CBD specimens, $K_\mathrm{I}$ value decreases by increasing the initial crack angle, and after the angle of occurrence of pure mode II, its value becomes negative (Eftekhari *et al.*, 2015a; Eftekhari *et al.*, 2015b). Results of investigations of crack initiation and propagation in the CBD specimen shows that the angle of appearance pure mode II happens at lower than $30°$ (Eftekhari *et al.*, 2015a),

thus, at the angles beyond this value, the stress intensity factor of mode I becomes negative and the MTS and GMTS criteria which are based on the stress intensity factor are no longer applicable. However, experimental results by this specimen have showed that at the crack angles higher than this value, fracture and crack propagation path occurs similar to the mixed mode (Al-Shayea, 2005; Ghazvinian *et al.*, 2013; Haeri *et al.*, 2014). This phenomenon was observed and reported in Eftekhari *et al.* (2015c), when they showed that the fracturing mode in macro and micro scales are different. The comparison result indicates that the fracture in micro-scale, unlike the macro-scale, includes a combination of different modes of fracturing (Eftekhari *et al.*, 2015c). Therefore, as also stated by Sharafisafa and Nazem (2014), it seems that crack propagation under compressive conditions is more controlled by tensile stresses around the crack tip.

In this research work, a numerical sensitivity analysis about crack propagation in SCB and CBD specimens with different initial crack angles when the IMTS criterion is assigned, has been conducted. The results have been also compared with laboratory tests and the reported results in the literature.

## 2. Extended Finite Element Method (XFEM) and Improved MTS (IMTS) criterion

Extended Finite Element Method (XFEM) was initially introduced by Belytschko and Black (1999). They presented a method based on the finite element method for modeling of crack propagation which does not need the re-meshing process. In this method, discontinuous enriched functions are added to the finite element approximation for crack demonstration and the crack grows arbitrarily within the finite element mesh. The most important and effective step toward improvement of the extended finite element method was taken by (Moës *et al.*, 1999) and (Dolbow, 1999). The existence of a crack in the extended finite element method leads to two different enrichments in the problem; crack interior and crack tip enrichment. The crack interior is enriched by a modified discontinuous Heaviside function (Eq. (2.1)), and the crack tip is enriched using functions presented in Eq. (2.2)

$$H(x) = \begin{cases} +1 & \text{for} \quad x > 0 \\ -1 & \text{for} \quad x < 0 \end{cases} \tag{2.1}$$

and

$$\{F_j(r, theta)\}_{j=1,2,3,4} = \left\{ \sqrt{r}\sin\frac{\theta}{2}, \sqrt{r}\cos\frac{\theta}{2}, \sqrt{r}\sin\frac{\theta}{2}\sin\theta, \sqrt{r}\cos\frac{\theta}{2}\sin\theta \right\} \tag{2.2}$$

Among these functions, only the first function ($\sqrt{r}\sin(\theta/2)$) is discontinuous, which is indicative of the function discontinuity along two faces of the crack. The extended finite element approximation for the displacement field is defined as follows

$$u^h(x) = \sum_{i \in I} N_i(x)u_i + \sum_{j \in J} N_j(x)H_j(x)a_j + \sum_{k \in K} N_k(x) \sum_{l=1}^{4} F_l(x)b_k^l \tag{2.3}$$

where $N(x)$ are shape functions, $u_i$ are nodal displacements (standard degrees of freedom), $a_j$ are vectors of additional degrees of nodal freedom associated with the Heaviside function, and $b_k^l$ are vectors of additional degrees of nodal freedom associated with the elastic asymptotic crack-tip functions. In equation (2.3), $I$ is the set of all nodes in the mesh, $J$ is the set of enriched nodes with discontinuous enrichment and $K$ is the set of nodes enriched with asymptotic enrichment.

All nodes of the element intersected by the crack are enriched by the step function, and also the nodes of element containing a crack tip are enriched by the near-tip displacement field. Equations and matrixes in the extended finite element method proceed similar to the conventional finite element method. The displacement field approximation space in form of the extended finite element (Eq. (2.3)) is replaced in equilibrium equations. From this enriched approximation, the standard discrete equation $\mathbf{Kd} = \mathbf{f}$ is obtained, where $\mathbf{d}$ is the vector of unknowns or degrees of freedom (for both common finite element degrees and additional degrees of freedom associated with enrichment), $\mathbf{f}$ is the external vector of forces and $\mathbf{K}$ is the stiffness matrix. The vectors and matrices are generally obtained by assemblage in each element.

A numerical code called MEX-FEM has been developed based on XFEM formulation with C++ programming language and employed into simulation of fracture propagation in some specimens of rock such as the cracked Brazilian disc (Eftekhari *et al.*, 2014, 2015a) and the semi-circular bend specimen (Eftekhari *et al.*, 2015b). In order to determine the direction of crack propagation, the Improved MTS criterion which was previously introduced and verified by the authors and reported in Eftekhari *et al.* (2016), is employed. A tension crack is propagated from the tip of a pre-existing crack in the direction of the maximum tangential tensile stress as also previously employed by Bobet for the modeling of crack propagation by the Boundary Element Method (Bobet and Einstein, 1998) and formulated as follows

$$\frac{\partial \sigma_\theta}{\partial \theta} = 0 \qquad \frac{\partial^2 \sigma_\theta}{\partial \theta^2} < 0 \qquad\qquad (2.4)$$

The direction of crack propagation with the IMTS criterion is similar to the MTS criterion, while the initiation angle is determined regarding the values of stress near the crack tip and it is completely independent of the value of the SIF. In this case, the SIF value does not compute by the interaction integral procedure. In order to find the direction of maximum tangential stress, the stress state near the crack tip is processed in two steps. Firstly, the values of stresses in the numerical integration points near the crack tip are transformed from the Cartesian system to the polar coordinate system in order to calculate the value of tangential stress. Since the numerical integration points are irregularly located near the crack tip, in the second step, the values of tangential stress in the proposed points with regular intervals in different angles are calculated by an interpolating process. In this way, the direction of maximum tangential stress is identified (Eftekhari *et al.*, 2016).

## 3. Simulation of SCB specimen using IMTS criterion

Observation of crack initiation angle on the SCB specimen in laboratory shows higher values compared to the numerical simulation values by the MTS criterion (Aliha *et al.*, 2010). Aliha *et al.* (2010) introduced a criterion called GMTS in order to estimate the crack propagation direction which, in this criterion, tangential stress is defined as the following expansion series and it estimates the crack initiation angle more accurate than the MTS criterion. This criterion includes a quantity called $T$ stress in addition to stress intensity factors. This stress is a non-singular and constant stress, and other values of the series are represented by $O(\sqrt{r})$ and are negligible.

$$\sigma_{\theta\theta} = \frac{1}{\sqrt{2\pi r}} \cos\frac{\theta}{2} \Big( K_{\mathrm{I}} \cos^2\frac{\theta}{2} - \frac{3}{2} K_{\mathrm{II}} \sin\theta \Big) + T \sin^2\theta + O(\sqrt{r}) \qquad\qquad (3.1)$$

The experimental results and those calculated by the GMTS criterion in the SCB specimen with the span ratio $(S/R)$ and crack length ratio $(a/R)$ of 0.43 and 0.3, respectively, are well matched (Aliha *et al.*, 2010). Thus, to examine this result with the IMTS criterion, simulations

with the span ratio ($S/R$) of 0.43 and crack length ratio ($a/R$) of 0.3 and the initial crack angles of 0, 15, 30, 45 and 60 are conducted. The results of crack initiation angle in the SCB specimen with the IMTS criterion and also experimental results and GMTS criterion as well as values calculated by the MTS criterion is demonstrated in Fig. 2.
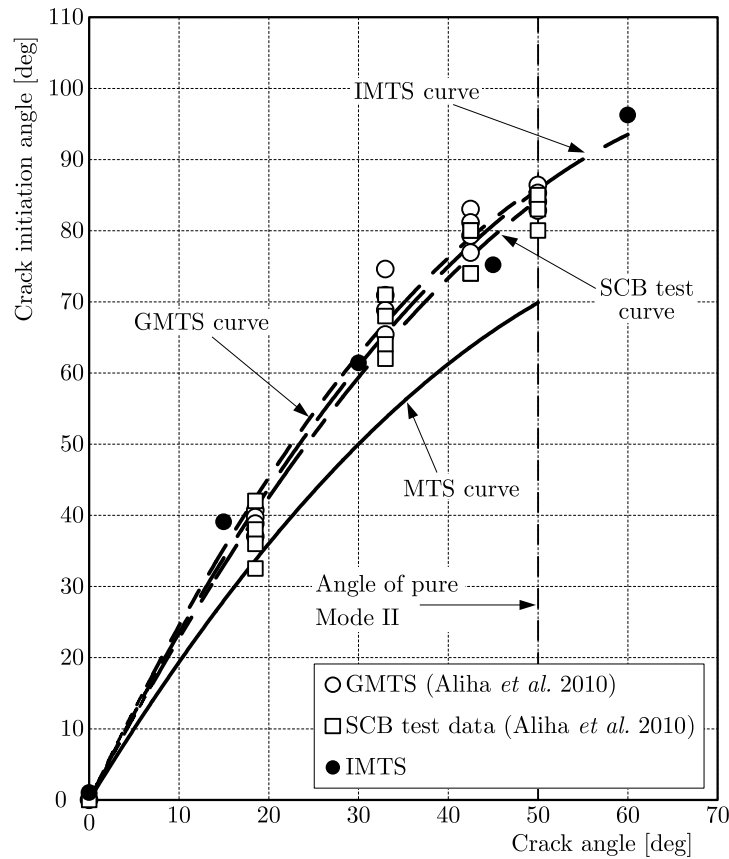


Fig. 2. Crack initiation angle in SCB specimen in laboratory and also simulation results using IMTS, GMTS and MTS criteria

It can be seen that the simulation results by the IMTS and GMTS criteria are well fitted with laboratory experimental results. In such a geometry of the SCB specimen, pure mode II occurs at angle of 50°. Obviously, for the crack angle beyond this value, the stress intensity factor of mode I becomes negative. Since GMTS and also MTS criteria are based on the values of stress intensity factors, investigation of the crack propagation direction at angles higher than 50° are not possible in this specimen. Meanwhile, the crack initiation angle at the initial crack angle of 60° is calculated using the IMTS criterion.

## 4. Simulation of CBD specimen using IMTS criterion

In contrary to the reported results about crack propagation in the SCB specimen, laboratory experimental results in the CBD specimen showed a lower approximation compared to the simulation results by the MTS criterion (Aliha *et al.*, 2010). Although the GMTS criterion gives an acceptable estimation of the value of crack initiation angle, as mentioned earlier, the MTS and GMTS criteria are applicable up to the initial crack angle in which pure mode II occurs. On the other hand, the angle of pure mode II in the CBD specimen happens when the initial crack angle is smaller than 30°. While the reported experimental results in the literature show

that the crack is propagated even at an angle larger than 30° (up to 60°), just like in the mixed mode (Al-Shayea, 2005; Ghazvinian *et al.*, 2013; Haeri *et al.*, 2014).

Due to the inaccessibility of results of the effect of the crack initiation angle on crack propagation path in the CBD specimen, in this research work, laboratory experiments are conducted with the initial crack angles of 0°, 15°, 30°, 45° and 60°. A dental plaster with tensile and uniaxial compressive strength of 3.8 and 30.15 MPa, respectively, and density of 1.81 kg/cm³ is used to prepare the CBD specimens. After weighting the plaster and mixing it with ocher powder (red color), 30 cc per 100 grams of the plaster according to the manufacturer's recommendation is added. Its initial holding time is about 15 minutes and within 7 days the maximum strength is achieved (Babanouri *et al.*, 2011).

Although the CBD specimen has been widely used in the modeling and laboratory experiments of rock fracture mechanics, it has not been proposed as a standard specimen by ISRM. Thus, there is no a specific and unique standard for this test. In this research work, an attempt has been made to use conditions and terms considered by other researchers in their experiments (Aliha *et al.*, 2010; Ghazvinian *et al.*, 2013; Haeri *et al.*, 2014), in preparing and conducting test specimens. The experimental and numerical investigations performed by Aliha *et al.* (2010) on the CBD specimens with different dimensions but with the same crack length ratios show that dimensions of the specimen does not affect the results. While the crack length ratio plays the crucial role in the final results. Thus, the same proposed crack length ratio used in the literature is employed in the current study. Diameter and thickness of the disc are 60 mm and 25 mm, respectively, and the crack length is 18 mm with the crack length ratio of 0.3.

According to the ISRM standard for the SCB specimen (Kuruppu *et al.*, 2015), crack thickness on the specimen should be smaller than 1.5 mm. In this research work, in order to create a crack in the specimen, a plastic film with thickness of 1 mm is used. The artificial crack is also kept in the middle part of the specimen.
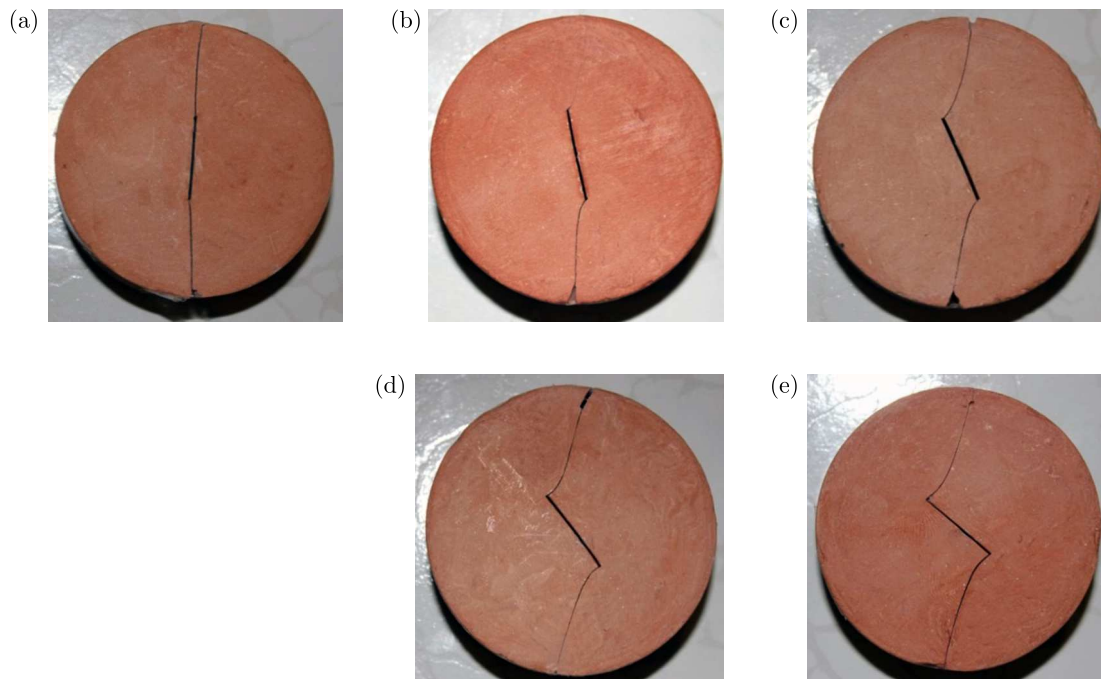


Fig. 3. Patterns of crack propagation in CBD specimen in laboratory with crack angles of (a) 0°, (b) 15° (c) 30°, (d) 45°, (e) 60°

All prepared specimens, according to the aforementioned angles experience a constant compressive loading conditions. All tests are also conducted according to the ISRM standard method

for the CCNBD specimen with rigid and parallel loading plates (Fowell, 1995). Furthermore, the loading rate was kept at 0.5 MPa/s as considered in the previous studies with the CBD specimen (Ghazvinian *et al.*, 2013; Haeri *et al.*, 2014). The patterns of crack propagation in the CBD specimen with different crack angles in laboratory are shown in Fig. 3.

The results show that in the case of the initial crack angle of 0°, the crack is propagated from its tip toward its initial direction. While at other angles, the crack is deviated from its direction and propagates toward loading points. Also it can be seen that the crack initiation angle is completely different from the results of the MTS criterion, which was presented earlier. The results of the crack initiation angle with the direction of the initial crack angle in the laboratory and also IMTS, MTS and GMTS criteria are shown in Fig. 4.
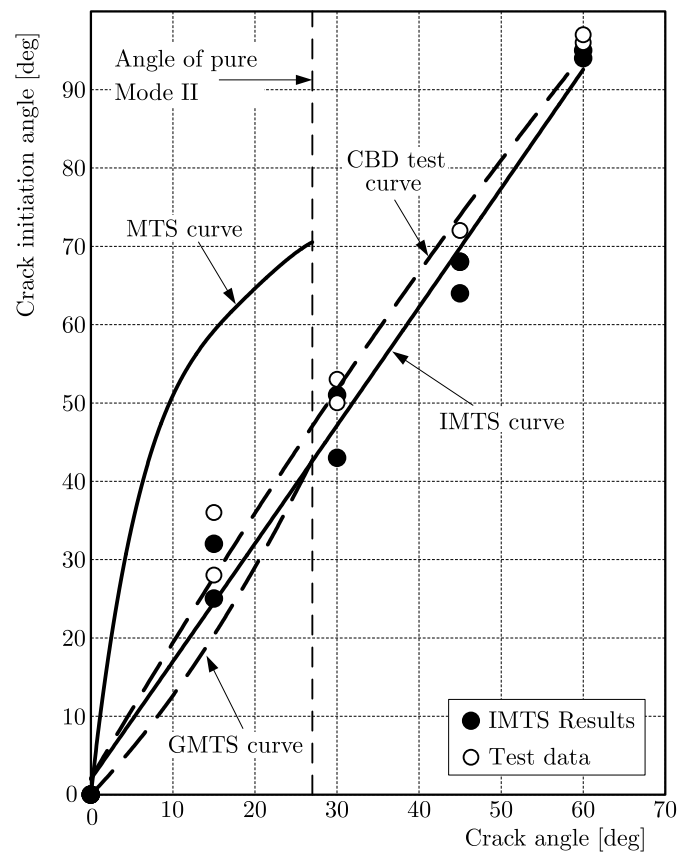


Fig. 4. Crack initiation angle in CBD specimen in laboratory and IMTS, GMTS and MTS criteria

It can be seen that the predicted values by the IMTS criterion are well matched with the laboratory experimental results and also GMTS simulation results, and completely differ from the calculated values by the MTS criterion. The GMTS and MTS criteria are applicable up to the angle of occurrence of pure mode II while in the IMTS criterion, prediction is also possible at angles beyond the predicted angle of pure mode II. The results of the crack propagation path in the specimens with different angles using the IMTS criterion are shown in Fig. 5.

The results of the crack propagation path by the IMTS criterion show that just like in the experimental specimens, the crack grows along its initial direction at the initial crack angle of zero, while at other angles, it deviates from its direction and propagates toward the loading points. By increasing the initial crack angle, the crack initiation angle is increased. In order to perform a more precise comparison, the results of the crack propagation path in the experimental specimens and also numerical simulations are shown in Fig. 6. The crack propagation path in the experimental specimen and numerical simulation is displayed by bold and dash lines, respectively.
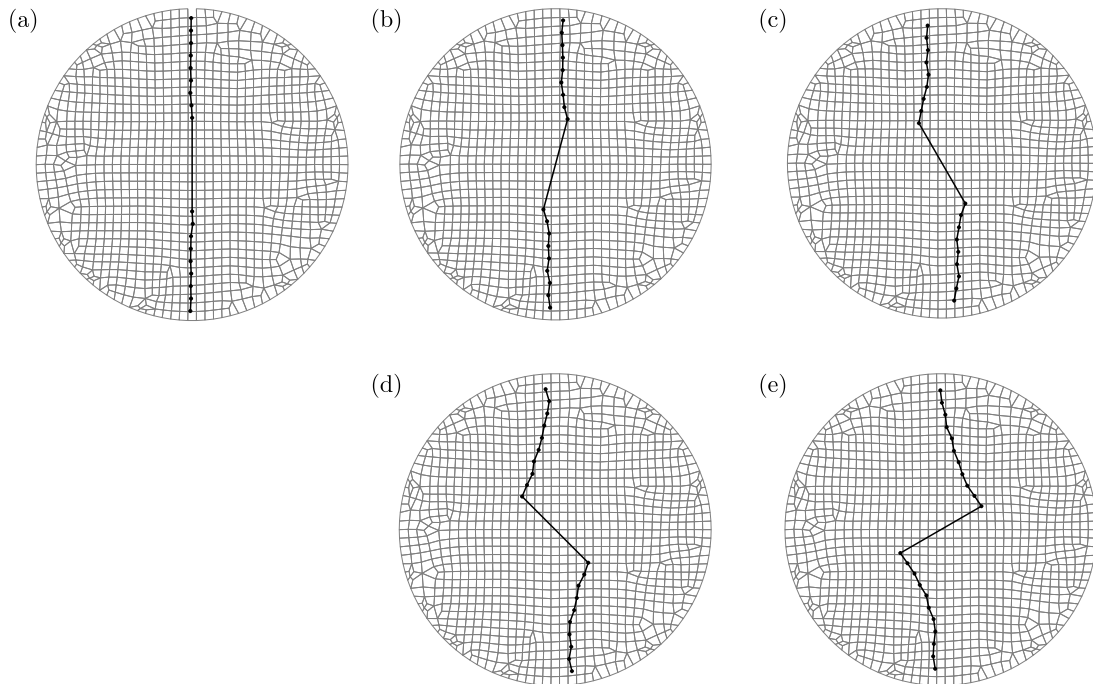
Fig. 5. Patterns of crack propagation in CBD specimen using IMTS criterion with crack angles of (a) 0°, (b) 15° (c) 30°, (d) 45°, (e) 60°
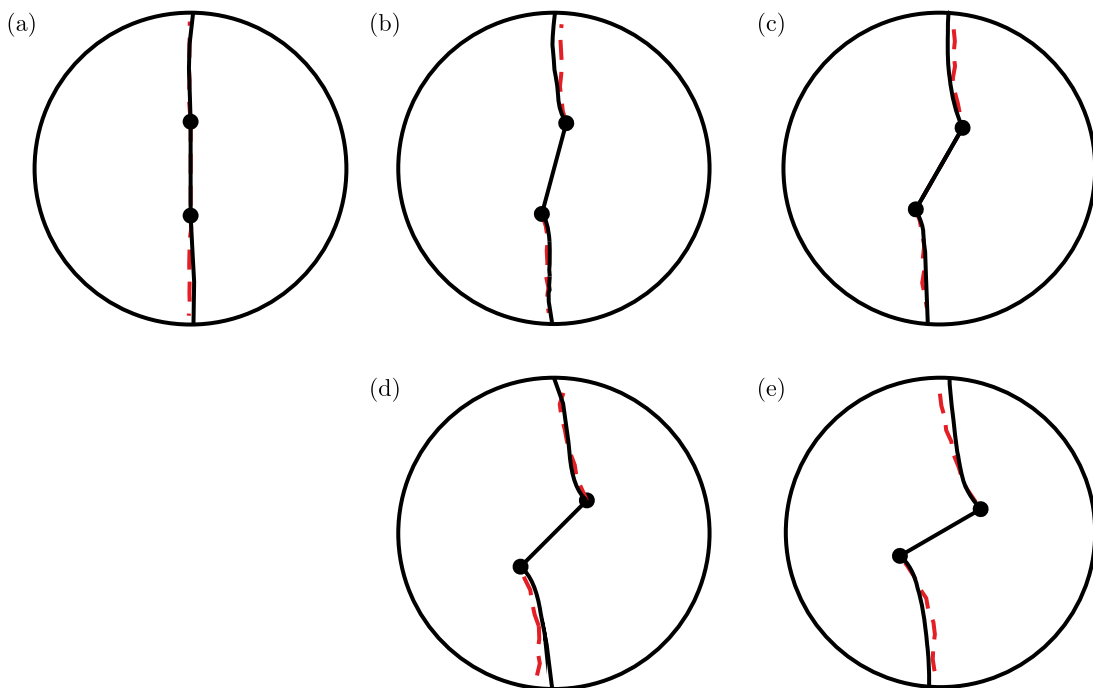


Fig. 6. Comparison of the results of the crack propagation path in experimental specimens with IMTS criterion in CBD specimen with the initial crack angle of (a) 0°, (b) 15° (c) 30°, (d) 45°, (e) 60°

According to the figure, it can be seen that there is a good agreement between the results of the crack propagation path using the IMTS criterion and the experimental results.

The results of application of the IMTS criterion in XFEM to predict the crack propagation path in different specimens show that this criterion can precisely calculate the crack propagation direction in a cracked specimen under tension or compression.

## 5. Conclusion

Maximum Tangential Stress (MTS) criterion does not calculate the crack initiation angle in SCB and CBD specimens correctly. Moreover, at the initial crack angles beyond the occurrence of pure mode II, where the stress intensity factor of mode I becomes negative, this criterion is not applicable. Therefore, in this research work, the IMTS criterion which has been implemented in the extended finite element method and is applicable under tensile and compressive loading conditions has been utilized to examine the crack propagation path in SCB and CBD specimens. Also, in order to evaluate the Improved MTS criterion in determination of the crack propagation path at angles beyond the occurrence of pure mode II, a laboratory experimental study on the CBD specimen has been conducted.

When the IMTS criterion is employed in simulation of the crack propagation path in the SCB specimen, the results are well matched with modeling results by the GMTS criterion and also laboratory experimental test results. In the IMTS criterion, the crack initiation angle at the initial crack angle of 60° could be calculated, whereas due to the negative stress intensity factor of mode I at this angle, the MTS and GMTS criteria are not applicable.

The estimation of crack propagation in the CBD specimen using the IMTS criterion shows a good agreement with the experimental results. Also it is observed that unlike MTS and GMTS criteria, the IMTS criterion is applicable in this specimen at initial crack angles beyond the occurrence of pure mode II. The results demonstrate that using the MTS criterion in simulating crack propagation in both SCB and CBD specimens introduces an unknown degree of uncertainty into the results. The MTS criterion underestimates the crack initiation angle in the SCB specimen and overestimates it in the CBD specimen compared with the laboratory experimental and also simulation results by the IMTS criterion. The results of the IMTS criterion show that it is well matched with the experimental results and can be used in different specimens under different tensile and compressive loading conditions.

## References

1. AL-SHAYEA N.A., 2005, Crack propagation trajectories for rocks under mixed mode I-II fracture, *Engineering Geology*, **81**, 84-97

2. ALIHA M., AYATOLLAHI M., SMITH D., PAVIER M., 2010, Geometry and size effects on fracture trajectory in a limestone rock under mixed mode loading, *Engineering Fracture Mechanics*, **77**, 2200-2212

3. ATKINSON C., SMELSER R., SANCHEZ J., 1982, Combined mode fracture via the cracked Brazilian disk test, *International Journal of Fracture*, **18**, 279-291

4. AWAJI H., SATO S., 1978, Combined mode fracture toughness measurement by the disk test, *Journal of Engineering Materials and Technology*, **100**, 175-182

5. AYATOLLAHI M., ALIHA M., 2008, On the use of Brazilian disc specimen for calculating mixed mode I-II fracture toughness of rock materials, *Engineering Fracture Mechanics*, **75**, 4631-4641

6. BABANOURI N., NASAB S.K., BAGHBANAN A., MOHAMADI H.R., 2011, Over-consolidation effect on shear behavior of rock joints, *International Journal of Rock Mechanics and Mining Sciences*, **48**, 1283-1291

7. BELYTSCHKO T., BLACK T., 1999, Elastic crack growth in finite elements with minimal remeshing, *International Journal for Numerical Methods in Engineering*, **45**, 601-620

8. BOBET A., 1997, *Fracture Coalescence in Rock Materials: Experimental Observations and Numerical Predictions*, Massachusetts Institute of Technology

9. BOBET A., EINSTEIN H.H., 1998, Numerical modeling of fracture coalescence in a model rock material, *International Journal of Fracture*, **92**, 221-252

10. Budyn E., Zi G., Moës N., Belytschko T., 2004, A method for multiple crack growth in brittle materials without remeshing, *International Journal for Numerical Methods in Engineering*, **61**, 1741-1770

11. Campilho R., Banea M., Chaves F., Da Silva L., 2011, Extended Finite Element Method for fracture characterization of adhesive joints in pure mode I, *Computational Materials Science*, **50**, 1543-1549

12. Chen C.-S., Pan E., Amadei B., 1998, Fracture mechanics analysis of cracked discs of anisotropic rock using the boundary element method, *International Journal of Rock Mechanics and Mining Sciences*, **35**, 195-218

13. Choi S., Haberfield C., Johnston I., 1988, Determining the tensile strength of soft rock, *Geotechnical Engineering*, **19**

14. Chong K.P., Kuruppu M.D., Kuszmaul J.S., 1987, Fracture toughness determination of layered materials, *Engineering Fracture Mechanics*, **28**, 43-54

15. Dolbow J.E., 1999, *An Extended Finite Element Method with Discontinuous Enrichment for Applied Mechanics*, Northwestern University

16. Eftekhari M., Baghbanan A., Hashemolhosseini H., 2014, Determining stress intensity factor for Cracked Brazilian Disc using extended Finite Element Method, *International Journal of Engineering Science*, **3**, 890-893

17. Eftekhari M., Baghbanan A., Hashemolhosseini H., 2015a, Extended finite element simulation of crack propagation in Cracked Brazilian Disc, *Journal of Mining and Environment*, **6**, 95-102

18. Eftekhari, M., Baghbanan, A., Hashemolhosseini, H., 2015b, Fracture propagation in a cracked semicircular bend specimen under mixed mode loading using extended finite element method, *Arabian Journal of Geosciences*, **8**, 9635-9646

19. Eftekhari M., Baghbanan A., Hashemolhosseini H., 2016, Crack propagation in rock specimen under compressive loading using extended finite element method, *Arabian Journal of Geosciences*, **9**, 1-10

20. Eftekhari M., Baghbanan A., Hashemolhosseini H., Amrollahi H., 2015c, Mechanism of fracture in macro-and micro-scales in hollow centre cracked disc specimen, *Journal of Central South University of Technology*, **22**, 4426-4433

21. Erdogan F., Sih G., 1963, On the crack extension in plates under plane loading and transverse shear, *Journal of Basic Engineering*, **85**, 519

22. Fan C., Jing X.Q., 2013, Numerical study of crack propagation path in three-point bending beam using Extended Finite Element Method, *Applied Mechanics and Materials*, **353-356**, 3615-3618

23. Fowell R., 1995, Suggested method for determining mode I fracture toughness using cracked chevron notched Brazilian disc (CCNBD) specimens, *International Journal of Rock Mechanics and Mining Sciences and Geomechanics Abstracts*, 57-64

24. Ghazvinian A., Nejati H.R., Sarfarazi V., Hadei M.R., 2013, Mixed mode crack propagation in low brittle rock-like materials, *Arabian Journal of Geosciences*, **6**, 4435-4444

25. Grassl P., Rempling R., 2007, Influence of volumetric-deviatoric coupling on crack prediction in concrete fracture tests, *Engineering Fracture Mechanics*, **74**, 1683-1693

26. Haeri H., Shahriar K., Marji M.F., Moarefvand P., 2014, Cracks coalescence mechanism and cracks propagation paths in rock-like specimens containing pre-existing random cracks under compression, *Journal of Central South University of Technology*, **21**, 2404-2414

27. Hussain M., Pu S., Underwood J., 1974, Strain energy release rate for a crack under combined mode I and mode II, *Fracture Analysis*, **1**, 560

28. Huynh D., Belytschko T., 2009, The extended finite element method for fracture in composite materials, *International Journal for Numerical Methods in Engineering*, **77**, 214-239

29. Isaksson P., Ståhle P., 2002, Mode II crack paths under compression in brittle solids – a theory and experimental comparison, *International Journal of Solids and Structures*, **39**, 2281-2297

30. Kuruppu M., Obara Y., Ayatollahi M., Chong K., Funatsu T., 2015, ISRM-suggested method for determining the mode I static fracture toughness using semi-circular bend specimen, *The ISRM Suggested Methods for Rock Characterization, Testing and Monitoring*, 2007-2014, Springer, 107-114

31. Kuruppu M.D., Chong K.P., 2012, Fracture toughness testing of brittle materials using semi-circular bend (SCB) specimen, *Engineering Fracture Mechanics*, **91**, 133-150

32. Lin Q., Fakhimi A., Haggerty M., Labuz J., 2009, Initiation of tensile and mixed-mode fracture in sandstone, *International Journal of Rock Mechanics and Mining Sciences*, **46**, 489-497

33. Liu H., Kou S., Lindqvist P.-A., Tang C., 2007, Numerical modelling of the heterogeneous rock fracture process using various test techniques, *Rock Mechanics and Rock Engineering*, **40**, 107-144

34. Mergheim J., Kuhl E., Steinmann P., 2005, A finite element method for the computational modelling of cohesive cracks, *International Journal for Numerical Methods in Engineering*, **63**, 276-289

35. Moës N., Dolbow J., Belytschko T., 1999, A finite element method for crack growth without remeshing, *International Journal for Numerical Methods in Engineering*, **46**, 131-150

36. Nuismer R., 1975, An energy release rate criterion for mixed mode fracture, *International Journal of Fracture*, **11**, 245-250

37. Palaniswamy K., Knauss W., 1972, Propagation of a crack under general, in-plane tension, *International Journal of Fracture*, **8**, 114-117

38. Sharafisafa M., Nazem M., 2014, Application of the distinct element method and the extended finite element method in modelling cracks and coalescence in brittle materials, *Computational Materials Science*, **91**, 102-121

39. Shen B., Stephansson O., 1994, Modification of the G-criterion for crack propagation subjected to compression, *Engineering Fracture Mechanics*, **47**, 177-189

40. Shiryaev A., Kotkis A., 1983. Methods for determining fracture toughness of brittle porous materials, *Industrial Laboratory*, **48**, 917-918

41. Sih G.C., 1974, Strain-energy-density factor applied to mixed mode crack problems, *International Journal of Fracture*, **10**, 305-321

42. Singh I., Mishra B., Bhattacharya S., Patil R., 2012, The numerical simulation of fatigue crack growth using extended finite element method, *International Journal of Fatigue*, **36**, 109-119

43. Song L., Huang S., Yang S., 2004, Experimental investigation on criterion of three-dimensional mixed-mode fracture for concrete, *Cement and Concrete Research*, **34**, 913-916

44. Theocaris P., Andrianopoulos N., 1982, A modified strain-energy density criterion applied to crack propagation, *Journal of Applied Mechanics*, **49**, 81-86

45. Thiercelin M., 1989, Fracture toughness and hydraulic fracturing, *International Journal of Rock Mechanics and Mining Sciences and Geomechanics Abstracts*, 177-183

46. Thiercelin, M., Roegiers, J., 1986, Fracture toughness determination with the modified ring test, *International Symposium on Engineering in Complex rock Formations*, Beijing, China, 1-8

47. Wang Q., Jia X., Kou S., Zhang Z., Lindqvist P.-A., 2004, The flattened Brazilian disc specimen used for testing elastic modulus, tensile strength and fracture toughness of brittle rocks: analytical and numerical results, *International Journal of Rock Mechanics and Mining Sciences*, **41**, 245-253

48. Wang Q.-Z., Xing L., 1999, Determination of fracture toughness K IC by using the flattened Brazilian disk specimen for rocks, *Engineering Fracture Mechanics*, **64**, 193-201

49. Wu Z., Wong L.N.Y., 2012, Frictional crack initiation and propagation analysis using the numerical manifold method, *Computers and Geotechnics*, **39**, 38-53

50. Xeidakis G., Samaras I., Zacharopoulos D., Papakaliatakis G., 1997, Trajectories of unstably growing cracks in mixed mode I-II loading of marble beams, *Rock Mechanics and Rock Engineering*, **30**, 19-33

# CRACK IDENTIFICATION IN PLATES USING 1-D DISCRETE WAVELET TRANSFORM

Anna Knitter-Piątkowska, Michał Guminiak

*Poznan University of Technology, Poznań, Poland*

*e-mail: anna.knitter-piatkowska@put.poznan.pl; michal.guminiak@put.poznan.pl*

George Hloupis

*Technological Educational Institute of Athens, Athens, Greece*

*e-mail: hloupis@teiath.gr*

In the present work, the defect detection while using Discrete Wavelet Transform in rectangular plate structures is investigated. The plate bending is described by using the Boundary Element Method with boundary integral equations formulated in a modified simplified approach. The boundary elements of a constant type in a non-singular approach are implemented. Defects are introduced by additional edges forming slots or holes in relation to the basic plate domain. Estimation of the defect position is performed while using wavelet coefficients of curvature and deformation signals as well as a newly proposed moving variance estimator.

*Keywords:* damage detection, crack, plates, wavelet transform, Boundary Element Method

## 1. Introduction

Damage generally can be defined as a change in the material which impairs functioning of the structural element at a given moment or in the future. As a result, it may lead to destruction of the element or, in the worst case, even of the whole structure. Defects usually have the form of delaminations, cracks, local material damage due to corrosion or fatigue; they may also take the form of voids or undesired inclusions. The issue of early detection, locating and quantifying structural damage is one of the most important engineering problems because it is closely linked to safety and durability of the object.

For years, many researchers have developed different methods of identifying defects with a focus on non-destructive testing (NDT). The essence of NDT is to locate failure in the structural element without changing its properties and functionality. Further analysis and subsequent stages of identification include: classification and severity assessment of damage, determination of its position, forecasting of probability of an element or the whole structure destruction and estimating the remaining potential lifetime of the structure.

Starting from the simplest NDT technique, namely visual inspection, one can mention methods basing on information from e.g. acoustic emission (Rogers, 2005), X-rays (Shinoba *et al.*, 2004), eddy current (Gros, 1995), ultrasonography (Zhang *et al.*, 2004), magnetic field (Lee *et al.*, 2004) or soft computing methods such as artificial neural networks (Waszczyszyn and Ziemiański, 2001) and evolutionary algorithms (Burczyński *et al.*, 2004). The traditional approach, based on the analysis of natural frequencies (Dems and Mróz, 2001) and modal shapes of structure vibrations (Ostachowicz and Kaczmarczyk, 2001), is still used and further developed. However, the global static or dynamic structural response is rather insensitive to localized damage.

A promising tool in structural identification is Wavelet Transform (WT) which can surprisingly well extract the desired detailed information from numerous data representing the global response of a defective structure. The application of WT for identification of cracks in structures

received a great attention over the last decade. Douka *et al.* (2003), Quek *et al.* (2001), Gentile and Messina (2003), Garstecki *et al.* (2004) as well as Kim and Melhem (2004) used the WT for crack detection in beams. The effectiveness of the discrete wavelet transform (DWT) combined with the inverse analysis for damage identification in beams was discussed in Knitter-Piatkowska and Garbowski (2013). In plate structures, a 2D WT used by Loutridis *et al.* (2005) and Rucka and Wilde (2004); Douka *et al.* (2004) used 1D WT to analytically determined mode shapes along several perpendicular lines while Chang and Chen (2004) used spatial wavelet analysis to estimate the crack size. Damage detection while using 1D and 2D DWT of a temperature field recorded on the surface of a plate structure was discussed in Ziopaja *et al.* (2011). More complex structures such as frames were analysed by Ovanesova and Suarez (2004) and trusses by Knitter-Piątkowska *et al.* (2014). The previous studies clearly demonstrate that the use of WT in search for structural damage is a promising and developing field of investigation.

Our intention in the present work is to examine performance of DWT as a method for crack identification in plates. The attention is focused on defects propagated from the external edge of a plate, which contributes new elements to the established knowledge. The position of the crack is determined as the absolute maximum of a moving variance estimator which uses the wavelet transformed response signals as the input. The feasibility of the proposed method is demonstrated by means of numerical examples. The effect of added noise on the performance of the method is investigated via noise immunity tests. The contribution of the current study is based on a simple fact which provides accurate results (even with high portions of added noise) and its implementation could be computationally efficient.

## 2. The discrete wavelet transform – theoretical foundations

In the current study, the WT will be implemented in which, for the representation of a signal $f(t)$, a linear combination of wavelet functions is applied. The theory of the WT has been presented in many publications, e.g. Meyer (1992) and Daubechies (1992). The foundations of the wavelet transformation will be mentioned below. As a matter of fact, the continuous wavelet transform of the signal $f(t)$ in the time and frequency domain can be defined as

$$Wf(a,b) = \int_{-\infty}^{\infty} f(t)\overline{\psi}_{a,b}(t)\, dt \tag{2.1}$$

where the overbar denotes the complex conjugate of the function under it. The function $\psi(t)$ is called the wavelet (mother) function, it belongs to the $L^2(\mathcal{R})$ field and must satisfy the condition of admissibility (Mallat, 1989) which leads to the inequality

$$\int_{0}^{\infty} \frac{|\Psi(\omega)|^2}{\omega}\, d\omega < \infty \tag{2.2}$$

where $\Psi(\omega)$ is the Fourier transform of $\psi(t)$, and it is defined as

$$\Psi(\omega) = \int_{-\infty}^{\infty} \psi(t)\mathrm{e}^{-\mathrm{i}\omega t}\, dt \tag{2.3}$$

In this case it becomes oscillatory because its average value is equal to zero. The character of mother function may be real or complex-valued. In the considered cases, real-valued family of wavelets is applied. The set of wavelets is obtained by scaling and translating of the function $\psi$, which leads to the relation

$$\psi_{a,b} = \frac{1}{\sqrt{|a|}}\psi\left(\frac{t-b}{a}\right) \tag{2.4}$$

where $t$ denotes time or a space coordinate, $a$ is the scale parameter and $b$ the translation parameter. The parameters $a$ and $b$ take real values ($a, b \in \mathcal{R}$) and additionally $a \neq 0$. The element $\sqrt{|a|}$ is the scale factor which ensures constant wavelet energy regardless of the scale. It means that $\|\psi_{a,b}\| = \|\psi\| = 1$.

In the present numerical approach, the leading role will be taken by DWT. DWT requires neither integration nor explicit knowledge of the scaling and wavelet function. The family of discrete wavelet functions can be obtained on the assumption that $a = 1/2^j$, $b = k/2^j$ and substitution of them into Eq. (2.4). It leads to the following relation

$$\psi_{j,k}(t) = 2^{\frac{j}{2}}\psi(2^j t - k) \tag{2.5}$$

in which $k$ and $j$ are scale and translation parameters, respectively. The meaning of these parameters can be clearly illustrated for the simplest Haar wavelet (Fig. 1).
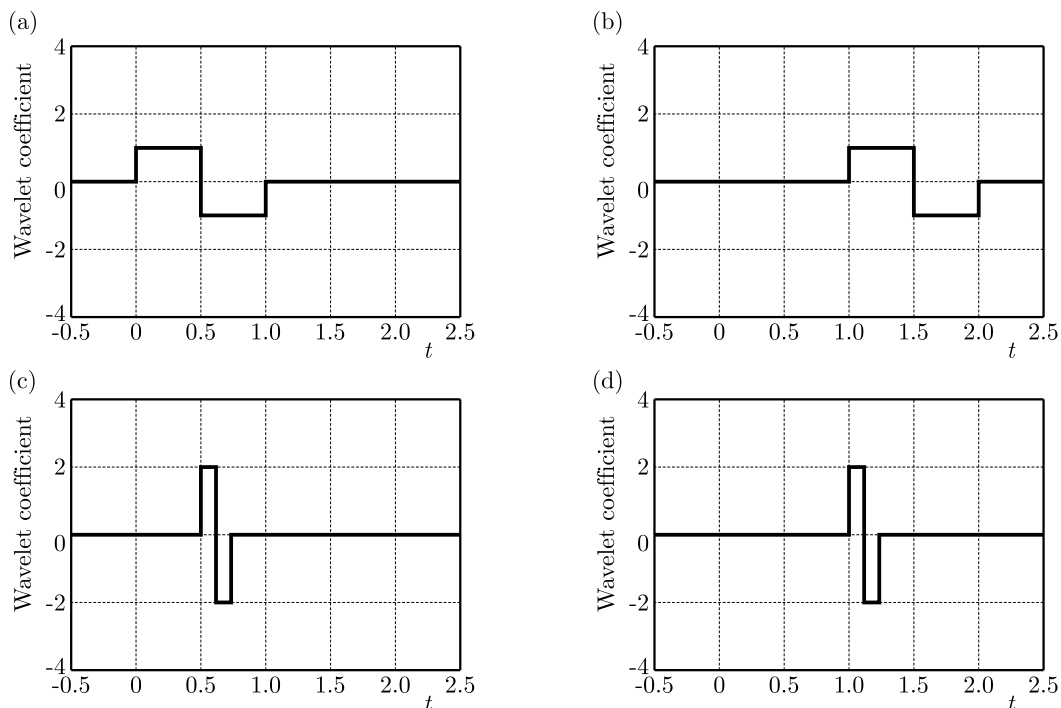


Fig. 1. Haar wavelet family: (a) mother wavelet $j = 0$, $k = 0$, (b) wavelet with parameters $j = 0$, $k = 1$, (c) $j = 2$, $k = 2$, (d) $j = 2$, $k = 4$

The main requirement (which is the one of contributions of the current study) is the use of a WT implementation algorithm that is computationally efficient in terms of required memory and processing power. The classical implementation of DWT consists of a pair of finite impulse response filters (FIR) (high-pass and low-pass) which are applied to the signal in parallel. The pyramid algorithm by Mallat (1989) computes the 1D convolution based WT at different levels of resolution. The produced coefficients are the result of a recursive convolution between the signal and corresponding filter for preselected values of $j$ and $k$. This convolution-based DWT requires a large number of arithmetic computations and memory allocations leading to quite demanding computing scheme. Towards to the direction of the computational efficient algorithmic approach, a light-weight implementation for performing the WT can be adopted. This is the Lifting Scheme (Daubechies and Sweldens, 1998; Sweldens, 1996) which requires fewer computations (half of those needed for the convolution based DWT). In general, it consists of three steps: split, lift and scale. The basic idea is to initially compute a trivial wavelet by splitting the analyzed signal into odd and even subsequences and then modifying these subsequences by consecutive predict and update steps.

For the selection of an appropriate wavelet, we adopt general recommendations by Ovaneso-va and Suarez (2004) for the selection of wavelets that can perform a Fast Wavelet Transform (FWT) and satisfy symmetry and exact reconstruction. The candidate wavelets are the bior-thogonal and the Haar. Fortunately, both wavelet families are supported by the Lifting Scheme. The last criterion that leads us to the choice of biorthogonal (bior.) wavelet (Cohen *et al.*, 1992) in the current study, is that the Haar is an irregular wavelet (while the biorthogonal is not) (Meyer, 1992). This property has been proved significant for crack detection (Ovanesova and Suarez, 2004).

The biorthogonal wavelets relax the assumption of a single orthogonal basis (such as the Haar) and belong to the family of wavelets that are derived from bases that are semi-orthogonal, biorthogonal or non-orthogonal. Instead, they have primary and dual scaling ($\varphi, \widetilde{\varphi}$) and wavelet ($\psi, \widetilde{\psi}$) functions – a characteristic that provides more flexibility to the construction of wavelet base.

The scaling and wavelet are related as

$$\int \widetilde{\psi}_{j,k}(x)\psi_{j'k'}(x) \, dx = 0 \tag{2.6}$$

as soon as $j \neq j'$ or $k \neq k'$ and even

$$\int \widetilde{\varphi}_{0,k}(x)\varphi_{0k'}(x) \, dx = 0 \tag{2.7}$$

as soon as $k \neq k'$.

One wavelet ($\widetilde{\psi}$) used for analysis of the signal $s$ produces coefficients $c_{j,k}$ as below

$$\widetilde{c}_{j,k} = \int s(x)\widetilde{\psi}_{j,k}(x) \, dx \tag{2.8}$$

while the other wavelet ($\psi$) is used for synthesis of the signal $s$ from wavelet coefficients as follows

$$s = \sum_{j,k} \widetilde{c}_{j,k}\psi_{j,k} \tag{2.9}$$

Naming the biorthogonal wavelets follows the convention biorNr.Nd, where Nr is the number of the order of the wavelet or scaling functions used for signal synthesis, while Nd is the order of functions used for signal analysis. In our study, we adopt the bior2.2 wavelet which is presented in Fig. 2.

## 3.  Problem formulation and numerical analysis

The aim of this work is to detect location of a defect provided that the defect (damage) exists in the considered plate structure. Numerical investigation is based on signal analysis of the structural static response. The plate material is assumed as linear-elastic. The plate bending is described and solved by the Boundary Element Method. The boundary integral equations are derived from a non-singular approach. Rectangular plates simply-supported along the edges are considered. The analysis of the structural response is conducted with the use of signal processing tool, namely the wavelet transformation in its discrete form. Defects in plates are modeled as slots near the plate boundary and introduced as a set of free edges. An example of the plate with a defected edge is illustrated in Fig. 3. The plate is loaded by a single concentrated $P$ force moving along the indicated line, for example 1), 2) or 3). The force $P$ can have a static or dynamic character. At the selected $D$ point measured are: deflection $w$, angle of rotation in
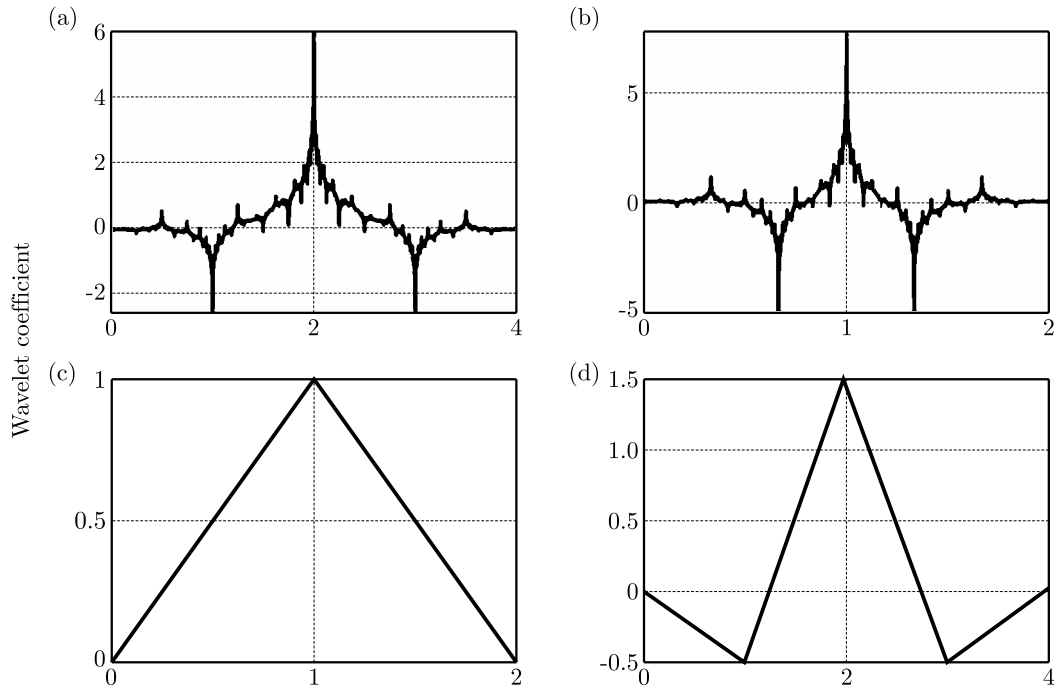
Fig. 2. Biorthogonal 2.2 wavelet: (a) analysis scaling function, (b) analysis wavelet function,
(c) synthesis scaling function, (d) synthesis wavelet function
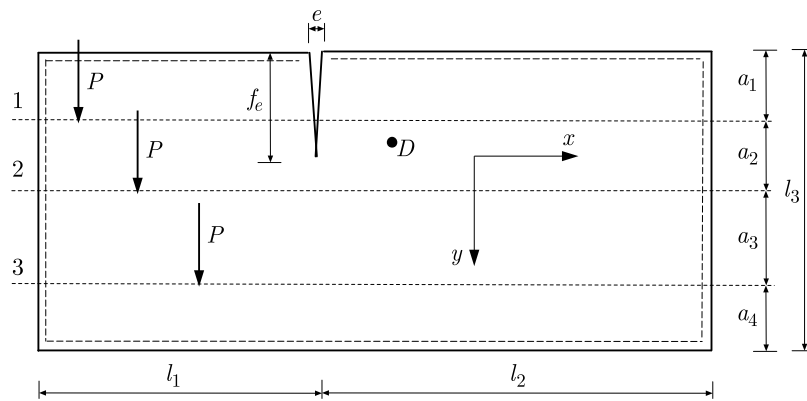


Fig. 3. Defective plate structure

arbitrary direction $\varphi$, curvatures $\kappa$ or internal forces such as bending and twisting moments or transverse forces as the response of the structure.

The measured response parameters have a character of the influence lines in its discrete form. The signal of the structural response defined in this way is processed while using DWT whose basis is described in Section 2.

The plate bending is described as the Boundary Element Method in a simplified modified approach where there is no need to introduce concentrated forces at the plate corners and equivalent shear forces at the plate continuous edges. This approach was widely described for static, dynamic and stability analysis in Guminiak (2007, 2014) and Guminiak and Sygulski (2007). The boundary integral equations are derived from Betti's theorem. For static analysis of a plate subjected by an external distributed load $q$ and concentrated force $P$, the governing equations have the form

$$c(\mathbf{x})w(\mathbf{x}) + \int\limits_{\Gamma} \left[ T_n^*(\mathbf{y},\mathbf{x})w(\mathbf{y}) - M_{ns}^*(\mathbf{y},\mathbf{x})\frac{dw(\mathbf{y})}{ds} - M_n^*(\mathbf{y},\mathbf{x})\varphi_n(\mathbf{y}) \right] d\Gamma(\mathbf{y})$$

$$= \int\limits_{\Gamma} [\widetilde{T}_n(\mathbf{y})w^*(\mathbf{y},\mathbf{x}) - M_n(\mathbf{y})\varphi_n^*(\mathbf{y},\mathbf{x})] \, d\Gamma(\mathbf{y}) + \int\limits_{\Omega} q(\mathbf{y})w^*(\mathbf{y},\mathbf{x}) \, d\Omega(\mathbf{y}) + P(\mathrm{i})w^*(\mathrm{i},x)$$

$$c(\mathbf{x})\varphi_n(\mathbf{x}) + \int\limits_{\Gamma} \left[ \overline{T}n^*(\mathbf{y},\mathbf{x})w(\mathbf{y}) - \overline{M}_{ns}^*(\mathbf{y},\mathbf{x})\frac{dw(\mathbf{y})}{ds} - \overline{M}_n^*(\mathbf{y},\mathbf{x})\varphi_n(\mathbf{y}) \right] d\Gamma(\mathbf{y})$$

$$= \int\limits_{\Gamma} [\widetilde{T}_n(\mathbf{y})\overline{w}^*(\mathbf{y},\mathbf{x}) - M_n(\mathbf{y})\overline{\varphi}_n^*(\mathbf{y},\mathbf{x})] \, d\Gamma(\mathbf{y}) + \int\limits_{\Omega} q(\mathbf{y})\overline{w}^*(\mathbf{y},\mathbf{x}) \, d\Omega(\mathbf{y}) + P(\mathrm{i})\overline{w}^*(\mathrm{i},x)$$

(3.1)

where the fundamental solution of the biharmonic equation

$$\nabla^4 w^*(\mathbf{y},\mathbf{x}) = \frac{1}{D}\delta(\mathbf{y},\mathbf{x}) \tag{3.2}$$

is given as Green's function

$$w^*(\mathbf{y},\mathbf{x}) = \frac{1}{8\pi D}r^2 \ln r \tag{3.3}$$

for a thin isotropic plate, $r = |\mathbf{y} - \mathbf{x}|$, $\delta$ is the Dirac delta, $x$ is the source point and $y$ – field point, $D = Eh^3/[12(1-\nu^2)]$ is the plate stiffness, $h$ – plate thickness, $E$ and $\nu$ are the Young's modulus and Poisson's ratio. The coefficient $c(\mathbf{x})$ is taken as $c(\mathbf{x}) = 1$ when $\mathbf{x}$ is located inside the plate domain; $c(\mathbf{x}) = 0.5$ when $\mathbf{x}$ is located on the smooth boundary and $c(\mathbf{x}) = 0$ when $\mathbf{x}$ is located outside the plate domain. The second boundary integral equation (2.9) can be obtained by replacing the unit concentrated force $P^* = 1$ and the unit concentrated moment $M_n^* = 1$. Such a replacement is equivalent to differentiation of the first boundary integral equation $(3.1)_1$ with respect to the coordinate $n$ at a point $\mathbf{x}$ belonging to the plate domain and letting this point approach the boundary and taking $n$ coincide with the normal to it. The expression $\widetilde{T}_n(\mathbf{y})$ denotes the shear force for clamped and for simply-supported edges, $\widetilde{T}_n(\mathbf{y}) = V_n(\mathbf{y})$ (an equivalent shear force) on the boundary far from the corner in the case of a simply supported edge or $\widetilde{T}_n(\mathbf{y}) = R_n(\mathbf{y})$ (distributed reaction force) on a small fragment of the boundary close to the corner. As the concentrated force at the corner is used only to satisfy the differential biharmonic equation of the thin plate, one can assume that it could be distributed along a plate edge segment close to the corner (Guminiak and Sygulski, 2007). The relation between $\varphi_s(\mathbf{y})$ and the deflection is specified by a simple relation $\varphi_s(\mathbf{y}) = dw(\mathbf{y})/ds$, hence the angle of rotation in the tangent direction $\varphi_s(\mathbf{y})$ can be evaluated using a finite difference scheme of the deflection with two or more adjacent nodal values. In the present analysis, the employed finite difference scheme includes the deflections of two adjacent nodes.

## 4. Procedure for crack identification

### 4.1. Wavelet selection

The fundamental question that arises before the application of wavelet analysis in any kind of time series is about the selection of the most appropriate wavelet. In our case, a preliminary selection has been made in accordance to the available selections in the Matlab Toolbox (Misiti *et al.*, 2000) since this is the software in which the proposed method is implemented. Following the recommendations from Section 2, we have explored several biorthogonal wavelets before we concluded that the biorthogonal 2.2 wavelet performed better.

### 4.2. Proposed methodology

The inspired idea behind the use of wavelets for crack identification lies in the fact that the existence of cracks introduces discontinuities in the structural response (Ovanesova and Suarez, 2004; Mallat, 1989; Meyer, 1992). It is not rare that these discontinuities cannot be visually observed from response signals (i.e. amplitudes of displacement), but they can be easily identified when these signals are projected onto the wavelet domain, especially from the detail coefficients. Thus, our novel approach focuses on the identification and enhancement of the information that we can derive from wavelet detail coefficients and can be directly correlated with crack location. The original procedure for crack identification can be summarized as below:

- Calculate (or measure in the case of real experiments) the signal that can be directly associated to the structural response. In the current study, we use curvatures $\kappa_x$, $\kappa_y$ and vertical displacement signals $w$.
- Compute the low level (up to scale 4) detail coefficients. This low level selection was successfully applied in previous studies as well (Ovanesova and Suarez, 2004).
- The crack location can be estimated as the local maximum (LM) of the absolute value in the detail coefficient.

In the case in which the aforementioned estimation is not clear (i.e. for noisy signals or when detail coefficients present more than one nearby LM) apply an appropriate estimator to isolate the LMM. In the current study, a moving variance estimator (MVE) is used as below

$$\text{MVE} = \frac{1}{n-1} \sum_{i=1}^{n} (x_i - \overline{x}_i)^2 \tag{4.1}$$

where $n$ is number of samples in the moving window. Small values of $n$ provide a more rapid detection of sharp changes (increased sensitivity) but may lead to false estimations due to outliers (decreased selectivity). On the contrary, higher values of $n$ are not prone to sharp peaks or outliers but they introduce significant delays between the real and the detected peak. In our case, $n = 3$ is selected as the best compromise between sensitivity and selectivity. This value corresponds to a moving window with length around 5% of the total number of measurements (which are $N = 64$).

The LM from detail coefficients are projected as the maximum of the moving variance estimator.

## 5. Numerical results

The aim of this work is to detect localization of a defect provided that the damage (crack) exists in the considered plate structure. Numerical investigation is conducted basing on signal analysis of the structural static response. A rectangular plate structure, simply-supported on the boundary is considered. The Boundary Element Method is applied to solve a thin plate bending problem. Each plate edge is divided into 30 boundary elements of the constant type. The collocation point is located slightly outside the plate edge, which is estimated by parameter $\varepsilon = \delta/d$, where $\delta$ is the real distance of the collocation point from the plate edge, and $d$ is the element length (Guminiak, 2014). For each example, $\varepsilon = 0.001$ is assumed. The diagonal boundary terms in the characteristic matrix are calculated analytically, and the rest of them using 12-point Gauss quadrature. The plates properties are: $E = 205.0\,\text{GPa}$, $\nu = 0.3$, $h = 0.02\,\text{m}$. All plates are loaded statically. A static concentrated external load $P = 1000\,\text{N}$ is replaced by an equivalent constant distributed loading $q$ acting over the square surface of dimensions $0.05\,\text{m} \times 0.05\,\text{m}$. Plate defects are introduced by the additional boundaries (free edges) forming

a hole in relation to the basic plate domain. The static concentrated load is applied at selected points along the direction parallel to one plate dimension. As the structural response, deflections and curvatures are taken into account. Curvatures $\kappa_x$, $\kappa_y$ can be identified using displacements given in three points: left, central and right, where the left and right points are located in direct vicinity of the central point. The curvature $\kappa_{xy}$ can be found while using displacements of four points located in direct vicinity of the central point. Subsequently, the curvatures can be calculated using classic difference operators. The measurement point is located near the damaged area of the considered plate. The minimum number of measurements is equal to 32 (Knitter--Piątkowska *et al.*, 2014). In the considered examples, a number of 64 measurements has been applied.

### 5.1.   Plate with middle crack

The plate loaded by a static concentrated $P$ force is considered and presented in Fig. 4. The coordinates of the measurement point $A$ are: $x_A = 2.15\,\text{m}$ and $y_A = 0.25\,\text{m}$. The introduced plate defect is described by the parameter $e = 0.005\,\text{m}$.
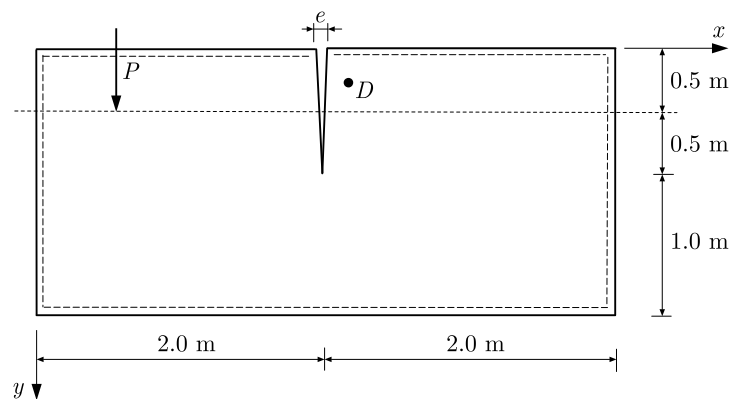


Fig. 4. The considered plate structure with a middle crack

The response signals that are used for the crack identification are: curvature $\kappa_x$, curvature $\kappa_y$ and displacement $w$, which are presented in Fig. 5, respectively.

For each above signal, a DWT using bior.2.2 wavelet has been performed. The obtained results are shown in Fig. 6 for detail 1 coefficients. The detail coefficients from the remaining scales of each transform are not presented since the significant information can be derived from coefficients of scale 1 only. At each figure, location of the crack is depicted as a vertical dotted line. A common pattern is unfolded for all three signals: the LMM clearly indicates the crack position. More specificly, for signal $\kappa_x$, the crack position is identified from the maximum of detail 1 coefficient while for $\kappa_y$ and displacement signals, the crack position is identified from the minimum. The importance of the previous observation is based on the fact that a simple threshold detector (applied to detail 1 coefficients) is used, and as a result, we can identify location of the crack with a significant accuracy.

A criticism to the previous findings can be raised if we assume that one of the response signals $\kappa_y$ (and probably other signals that are contaminated by noise), presents nearby LMM (in form of subordinate peaks) that may affect the accuracy of threshold detection that we propose earlier. For this reason, we applied MVE to detail 1 coefficients in order to enhance information of the crack location and thus to enhance the accuracy of the proposed threshold detector. Figure 7 shows the results where the crack location is presented with a very clear peak of MVE. This event eliminates any uncertainty about the crack identification procedure and provides a clear answer to the question "if there is a crack and where it is located".
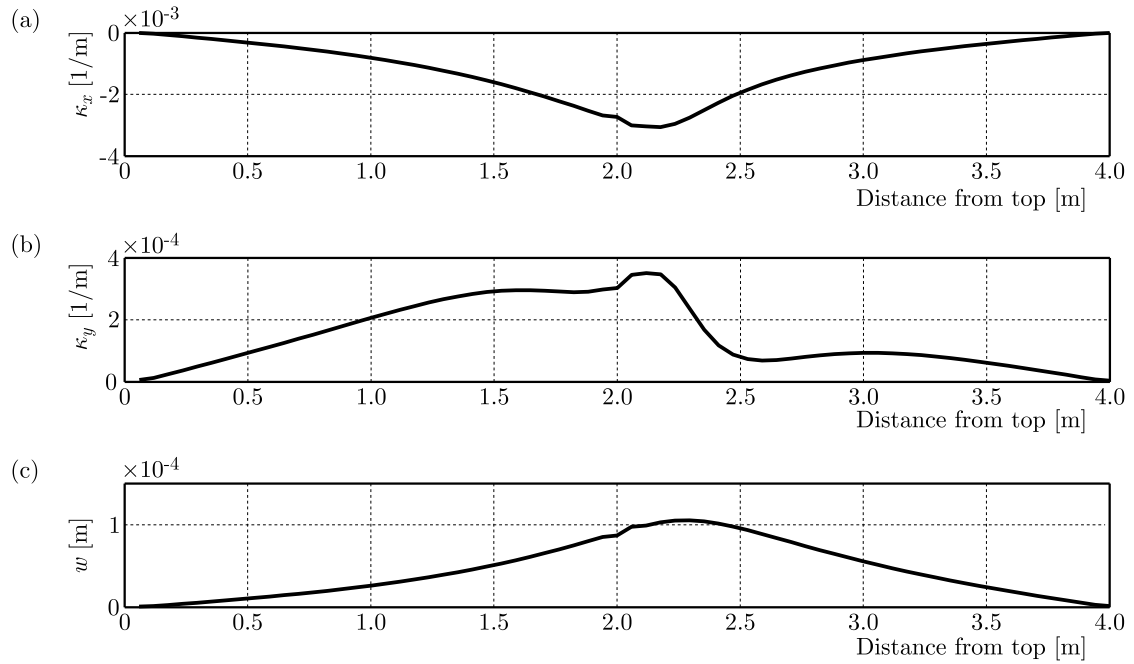
Fig. 5. Response signals for the plate with a middle crack: (a) curvature $\kappa_x$, (b) curvature $\kappa_y$ and (c) displacement $w$; number of measurements $N = 64$



Fig. 6. Detail coefficients at scale 1 of (a) curvature $\kappa_x$, (b) curvature $\kappa_y$ and (c) displacement signals $w$ of the plate with a middle crack; vertical dotted line indicates the actual location of the crack

## 5.2. Plate with a corner crack

The plate loaded by a static concentrated $P$ force is considered and presented in Fig. 8. The coordinates of the measurement point $D$ are: $x_A = 3.75\,\mathrm{m}$ and $y_A = 0.35\,\mathrm{m}$. The introduced plate defect is described by parameters: $e_1 = e_2 = e_3 = 0.005\,\mathrm{m}$.

The same procedure as in Section 5.1 is applied to the plate with a corner crack. Figure 9 shows the response signals where the corresponding results from DWT are shown in Fig. 10.

Fig. 7. MVE estimations for detail 1 coefficients of (a) curvature $\kappa_x$, (b) curvature $\kappa_y$ and (c) displacement signals $w$ of the plate with a middle crack; vertical dotted line indicates the actual location of the crack
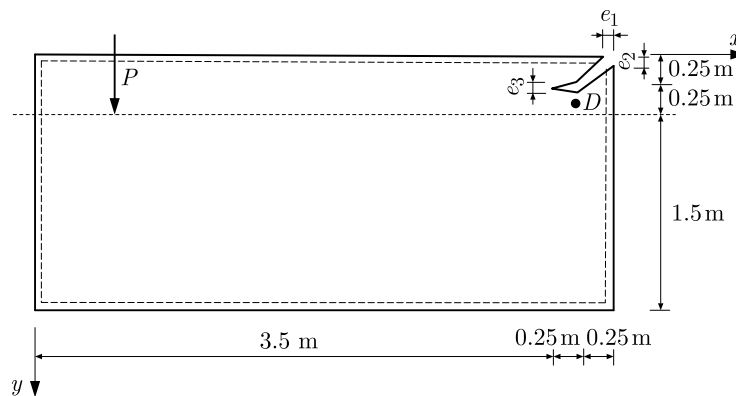


Fig. 8. Considered plate structure with a corner crack

The used wavelet is the bior.2.2, and the detail coefficients at scale 4 are taken into account. The vertical dotted line indicates the beginning of the corner crack. The results are clearer than in the case of the plate with the middle crack: the LMM can be easily detected as there are no subordinate peaks in the detail coefficients. The LMM again successfully points out the location of the crack. Thus, the use of MVE in this case is not presented since it will not add significant information to the crack identification procedure.

An important note, common for both cases, is regarding the detail coefficients amplitudes. As we can observe, the amplitude of detail coefficients is 50 times smaller than the amplitude or the corresponding response signal. This, in turn, means that the details coefficients are prone to add with white noise. The level of noise influence is further examined in the next Section.

### 5.3. Noise immunity test

Due to unavailability of experimental data, the proposed method has been tested for its noise immunity by adding to the response signals independent realizations of artificial White Gaussian
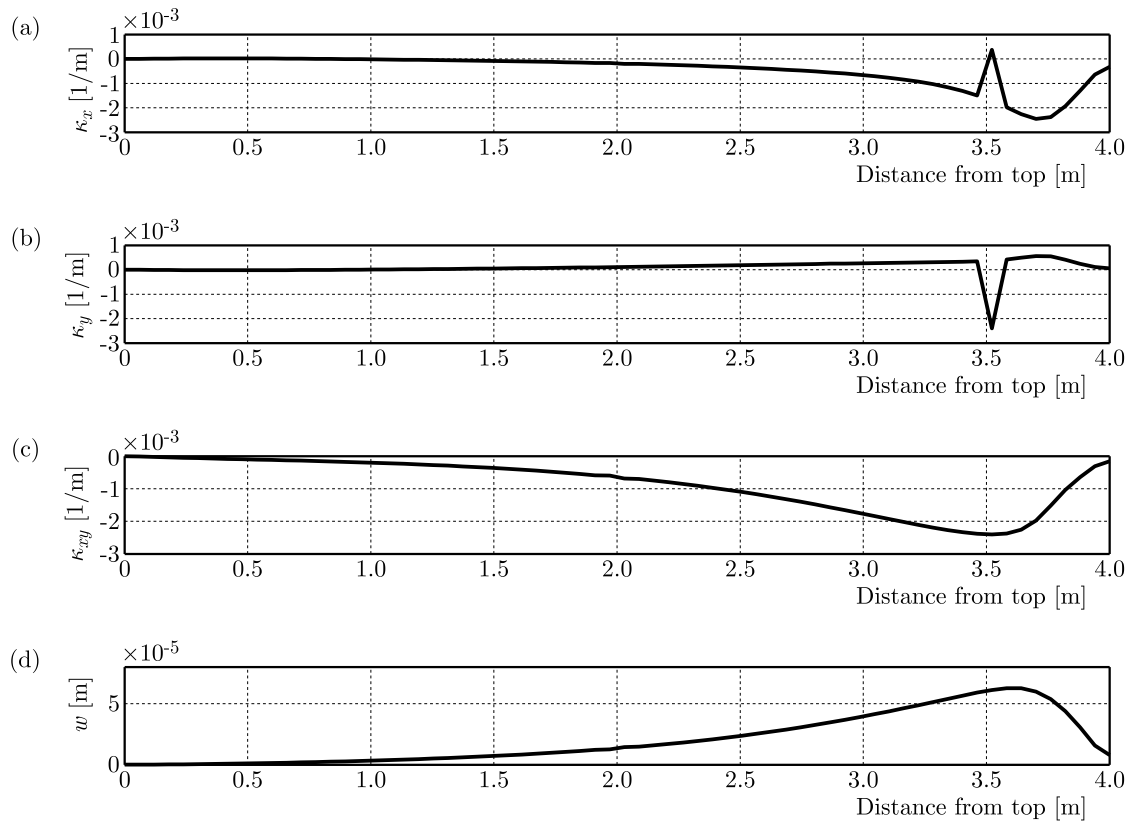
Fig. 9. Response signals for the plate with a corner crack (a) curvature $\kappa_x$, (b) curvature $\kappa_y$, (c) curvature $\kappa_{xy}$, and displacement $w$
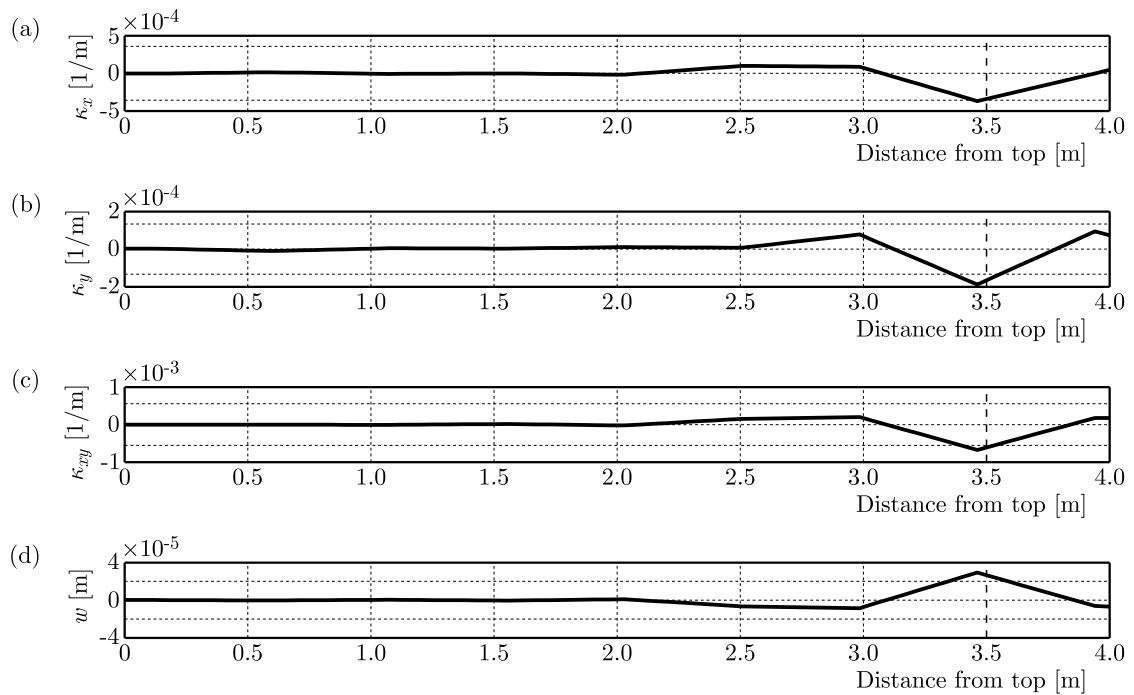


Fig. 10. Detail coefficients at scale 4 of: (a) curvature $\kappa_x$, (b) curvature $\kappa_y$, (c) curvature $\kappa_{xy}$ and (d) displacement $w$ signals of plate with corner crack; vertical dotted line indicates the actual location of crack

Noise (WGN). To ensure a large scale assessment, a range of 81 Signal-to-Noise (SNR) cases are considered (for each plate) in order to represent several measurement conditions. The range of the examined signals begins from 100 db (almost noiseless) up to 20 db (quite noisy signal) in 1 db decrements. Figure 11 presents the latter case (SNR = 20 db) for signals from the plate with a middle crack, whereas in Fig. 12, the corresponding MVE results are presented.
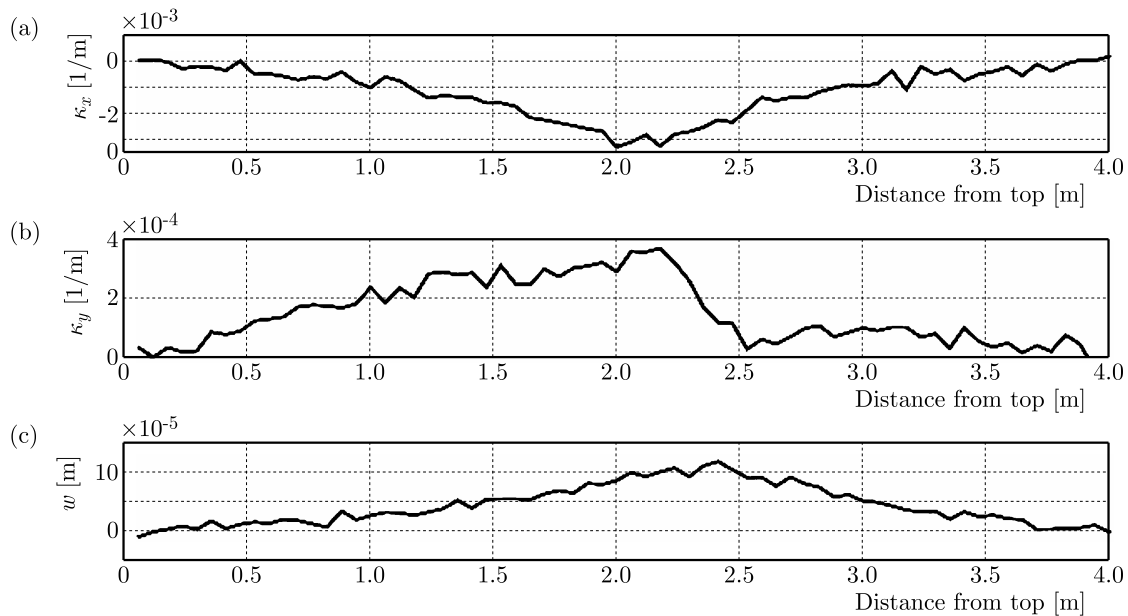


Fig. 11. The noisy case (SNR = 20 db) of response signals for the plate with a middle crack:
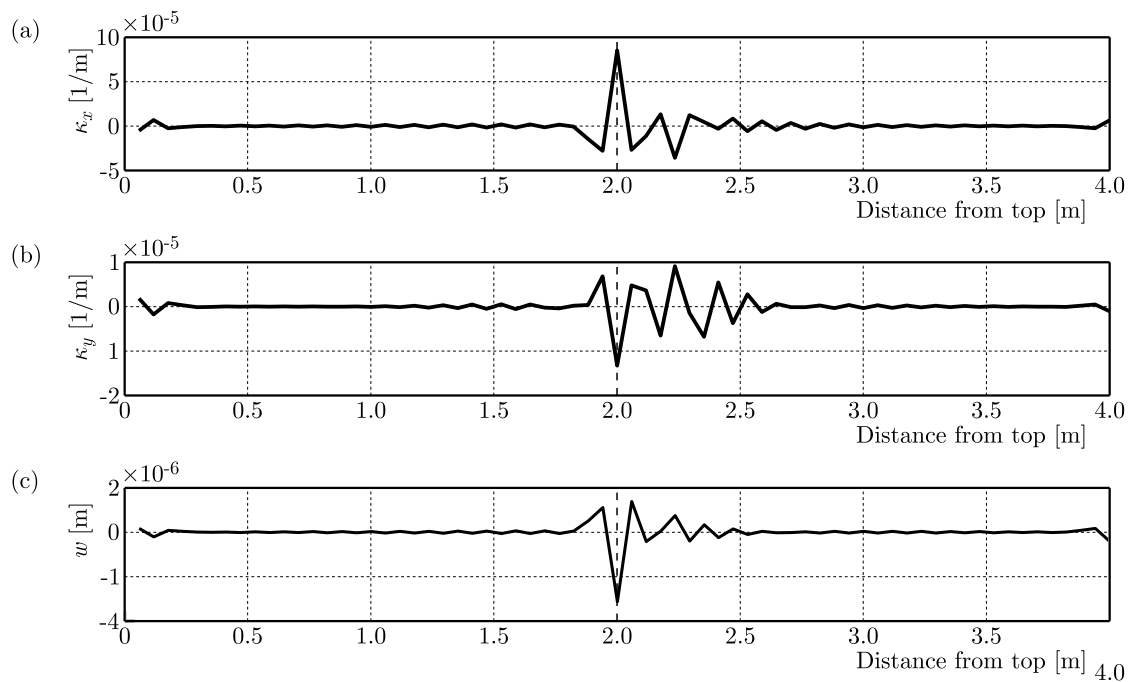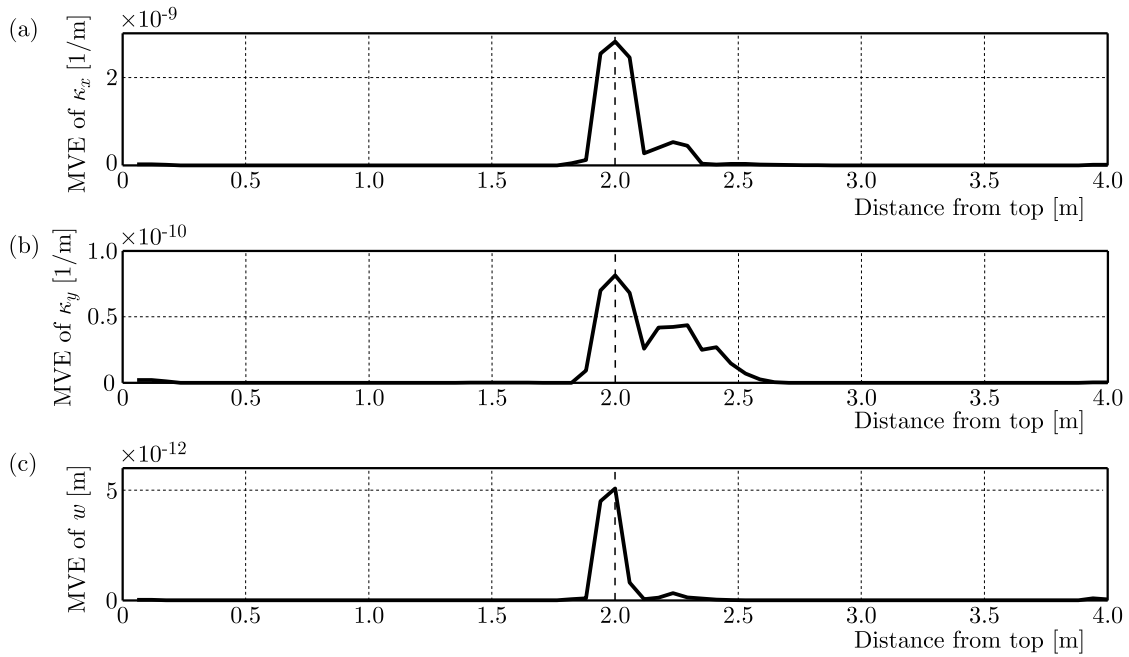(a) curvature $\kappa_x$, (b) curvature $\kappa_y$ and (c) displacement $w$
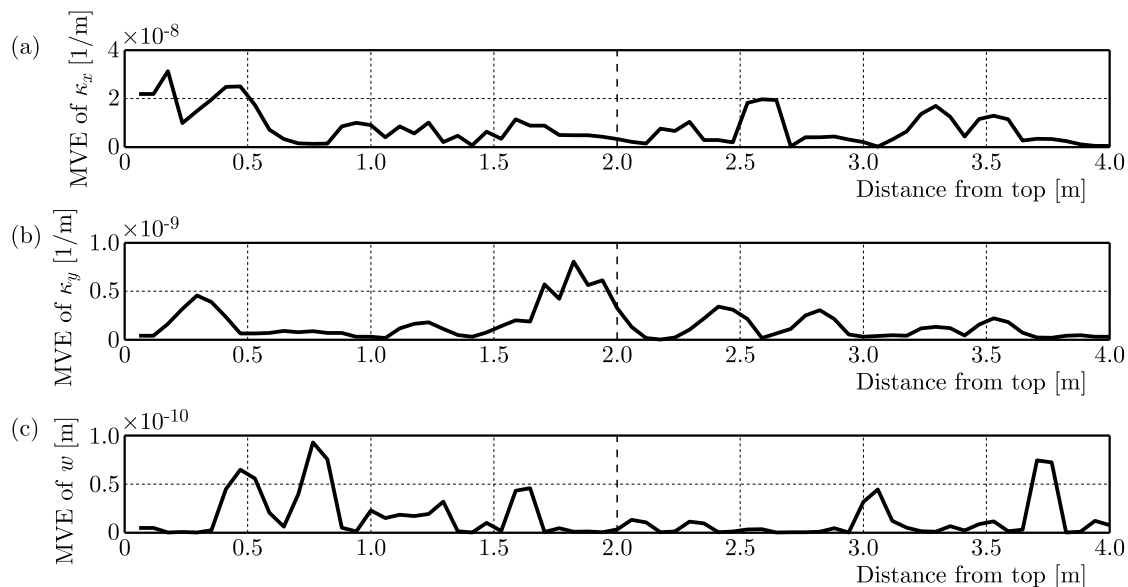


Fig. 12. MVE estimations for detail 1 coefficients of (a) curvature $\kappa_x$, (b) curvature $\kappa_y$ and
(c) displacement signals $w$ with SNR = 20 db of the plate with a middle crack; vertical dotted line
indicates the actual location of the crack

From Fig. 12, it is obvious that MVE fails to detect the crack location for every noisy signal. This situation is observed in the plate with the corner crack as well. Such observations have led us to the examination of the minimum $\mathrm{SNR}_{min}$ where the proposed method can successfully estimate the crack location. For example, with signals having SNR = 45 db, it is still possible to

identify the location as presented in Fig. 13. The results from the aforementioned noise tests are shown in Fig. 14. The results from Fig. 14 indicate that there is no common $\mathrm{SNR}_{min}$, but it is noticeable that for $\mathrm{SNR} \geqslant 40$ db the proposed method can estimate the crack location accurately. In addition, the results from noise tests for the plate with the corner crack reveal that the performance of MVE estimations for $\kappa_x$ and $\kappa_y$ signals is quite remarkable. This observation must be expected since (as shown in Fig. 9) these two specific signals present intrinsic discontinuity at the crack location (thus the DWT can easily detect it). The results from the curvature $\kappa_{xy}$ and displacement $w$ signals are less prominent but their $\mathrm{SNR}_{min}$ remains below 40 db. The detailed results of the performance of MVE on each signal can be found in Table 1.
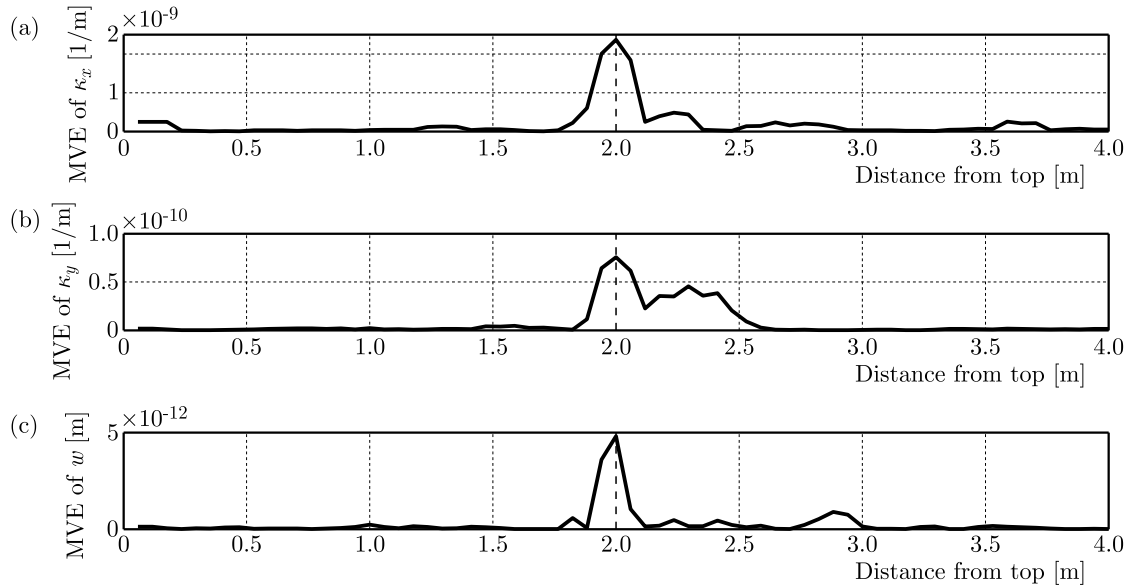


Fig. 13. MVE estimations for detail 1 coefficients of (a) curvature $\kappa_x$, (b) curvature $\kappa_y$ and (c) displacement signals $w$ with $\mathrm{SNR} = 45$ db of the plate with a middle crack; vertical dotted line indicates the actual location of the crack
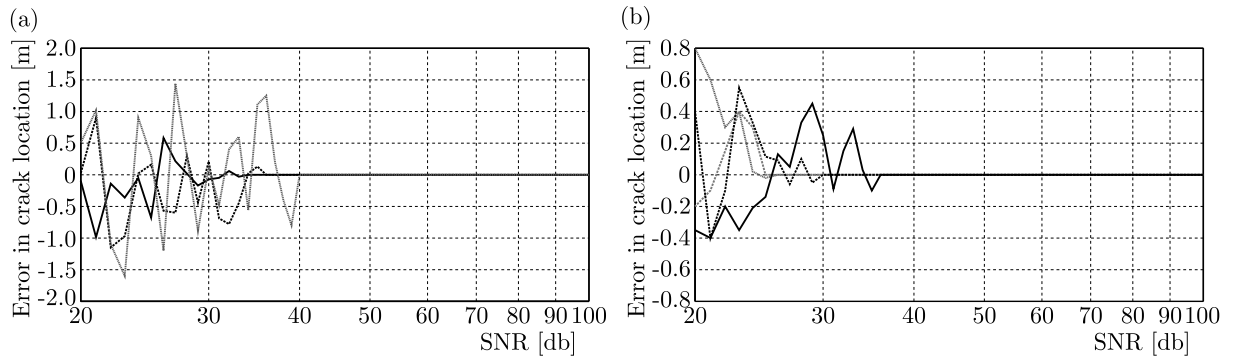


Fig. 14. MVE errors in crack location estimation for response signals with the middle crack (a) and the corner crack (b). The SNR is ranging from 20 db to 100 db (in 1 db steps): curvature $\kappa_x$ (black solid line), curvature $\kappa_y$ (black dashed line), displacement $w$ (grey dotted line) and curvature $\kappa_{xy}$ (grey dashed line)

Stacking the previous results together, it is clear that the crack location identification will be influenced (at least in one case) by noise if the corresponding response signals have $\mathrm{SNR} < 40$ db. This is the conservative point of view since there are response signals (the $\kappa_x$ and $\kappa_y$) that can perform nearly perfect (i.e. exact identification of crack location) with $\mathrm{SNR}_{min}$ reduced down to 36 db. The previous observations dictate that the proposed method is quite robust to additive

**Table 1.** Noise immunity test results

| response signal | Plate with middle crack | | | Plate with corner crack | | | |
|---|---|---|---|---|---|---|---|
| | $\kappa_x$ | $\kappa_y$ | $w$ | $\kappa_x$ | $\kappa_y$ | $\kappa_{xy}$ | $w$ |
| SNR$_{min}$ [db] | 34 | 36 | 40 | 25 | 26 | 30 | 36 |

noise, and for this reason, further study with experimental data must take place in order to validate the above conclusions.

## 6. Conclusions

The implementation of DWT for identification of signal discontinuity in the analysis of plate structures is presented in the given paper. Bending of a thin plate (static analysis) is described by boundary integral equations and solved using the BEM. Despite the fact, the studied problem is two-dimensional from the point of view of deformation description. Application of one-dimensional discrete DWT leads to satisfying results in defect detection. The proposed approach allows discovering small disturbances in the response signal of a defective structure and does not require a reference to the signal from an undamaged structure (additional errors avoided). The considered examples proved that DWT of the structural response signal expressed in deflections or curvatures established at a selected domain point, quite correctly identifies the presence and position of the defect. The data are gathered in one measurement point in equal time intervals. The detection of defect position can easily be implemented by using a simple threshold detector applied to the corresponding DWT detail coefficients. In the case where a small uncertainty exists, the making use of an additional detector (called Moving Variance Estimator – MVE) is proposed. The purpose of MvE is to enhance the information that may remain "hidden" (due to non-distinguishable peak) or "blurred" (due to subsequent peaks) near defect position, and this is the original element in the paper. The results indicate that the MVE performs quite satisfactory on deriving accurately the position of the defect, especially for deformation response signals.

Since the current study is a numerical one, it is expected that there will be a contamination of response signals by noise in real experiments. For this reason, additional research regarding the performance of the proposed method over noisy signals has been carried out. More specificly, we add independent realizations of artificial White Gaussian Noise to response signals generating a dataset with SNR from 20db to 100db (in 1db increments). We have noticed that even with the presence of noise there is a minimum SNR over which it is possible to reveal accurately the position of the defect using MVE. This minimum SNR has been estimated for both plates and for every response signal.

The importance and novelty of the current study does not lie only in the application of DWT for crack identification but goes a step further to the implementation of a real time system for crack location. In a such way, a prototype system will be highly benefited from the use of DWT since it is computationally efficient regarding signal processing resources. Moreover, by using the lifting approach implementation algorithm (Daubechies and Sewldens, 1998) we will be able to adapt two main advantages of the lifting approach against the widely used polyphase algorithm: doubling computation speed (Sweldens, 1996) and in-place computation of coefficients (without allocating extra memory) (Meyer, 1992). The above properties may be mission-critical in real-world installations where small memory buffers and very low-power microprocessors perform necessary calculations in wireless sensor network implementation.

## References

1. Burczyński T., Kuś W., Długosz A., Orantek P., 2004, Optimization and defect identification using distributed evolutionary algorithms, *Engeinnering Applications of Artificial Intelligence*, **17**, 337-344

2. Chang C., Chen L., 2004, Damage detection of a rectangular plate by spatial wavelet based approach, *Applied Acoustic*, **65**, 819-832

3. Cohen A., Daubechies J., Feauveau J., 1992, Biorthogonal bases of compactly supported wavelets, *Communications on Pure and Applied Mathematics*, **45**, 485-560

4. Daubechies I., 1992, *Ten Lectures on Wavelets*, Philadelphia: Society for Industrial and Applied Mathematics

5. Daubechies I., Sweldens, W., 1998, Factoring wavelet transforms into liftin steps, *Journal of Fourier Analysis and Applications*, **4**, 3

6. Dems K., Mróz, Z., 2001, Identification of damage in beam and plate structures using parameter-dependent frequency changes, *Engineering Computations*, **18**, 1/2, 96-120

7. Douka E., Loutridis S., Trochidis A., 2003, Crack identification in beams using wavelet analysis, *International Journal of Solid and Structures*, **40**, 3557-3569

8. Douka E., Loutridis S., Trochidis A., 2004, Crack identification in plates using wavelet analysis, *Journal of Sound and Vibration*, **270**, 279-295

9. Garstecki A., Knitter-Piatkowska A., Pozorski Z., Ziopaja K., 2004, Damage detection using parameter dependent dynamic experiments and wavelet transformation, *Journal of Engineering and Management*, **10**, 3, 191-197

10. Gentile A., Messina A., 2003, On the continuous wavelet transforms applied to discrete vibrational data for detecting open cracks in damaged beams, *International Journal of Solid and Structures*, **40**, 295-315

11. Gros X., 1995, An eddy current approach to the detection of damage caused by low-energy impacts on carbon fiber reinforced materials, *Meterials and Design*, **16**, 3, 167-173

12. Guminiak M., 2007, Static analysis of thin plates by the boundary Element Method in a non-singular approach, *Foundations of Civil and Environmental Engineering*, **9**, 75-93

13. Guminiak M., 2014, An alternative approach of initial instability analysis of Kirchhoff plates by the Boundary Element Method, *Engineering Trasnactions*, **62**, 1, 33-59

14. Guminiak M., Sygulski R., 2007, Vibrations of plates immersed in compressible fluid by the BEM, *9th International Conference on Modern Building Materials, Structures and Techniques*, P.V.M.J. Skibniewski (Edit.), Vilnius, Vilnius Gediminas Technical University Press "Technika", **1453**, 925-930

15. Jensen A., la Cour-Harbo A., 2001, *Ripplies in Mathematics*, Berlin, Springer

16. Kim H., Melhem H., 2004, Damage detection in structures by wavelet analysis, *Engineering Structures*, **26**, 347-362

17. Knitter-Piatkowska A., Garbowski, T., 2013, Damage detection through wavelet transform and inverse analysis, *VI International Conference on Adaptive Modelling and Simulation (ADMOS 2013)*, J. Moitinho de Almeida, P. Diez, C. Tiago, and N. Pares (Edit.), Barcelona, 389-400

18. Knitter-Piątkowska A., Guminiak M., Przychodzki M., 2014, *Damage Detection in Truss Structure Being the Part of Historic Railway Viaduct Wavelet Transformation*, T. Łodygowski, J. Rakowski and P. Litewka (Edit.), CRC Press/Balkema, Taylor and Francis Group

19. Lee J., Seo D.-W., Shoji T., 2004, Numerical consideration of magnetic camera for quantitative nondestructive evaluation, *Key Engineering Materials*, **270-273**, 630-635

20. Liew K., Wanq Q., 1998, Application of wavelet theory for crack identification in structures, *Journal of Engineering Mechanics*, **124**, 2, 152-157

21. LOUTRIDIS S., DOUKA E., HADJILEONTIADIS L., TROCHIDIS A., 2005, A two-dimensional wavelet transform for detection of cracks in plates, *Engineering Structures*, **27**, 1327-1338

22. MALLAT S., 1989, A theory for multiresolution signal decomposition: the wavelet representation, *IEEE Transactions on Pattern Analysis and Machine Intelligence*, **11**, 7, 674-693

23. MEYER Y., 1992, *Wavelets and Operators. Cambridge Studies in Advanced Mathematics*, Cambridge, UK, Cambridge University Press

24. MISITI M., MISITI Y., OPPENHEIM G., POGGI J.M., 2000, *Wavelet Toolbox – User's Guide*, Natick, MA, The MathWorks

25. OSTACHOWICZ W., KACZMARCZYK S., 2001, Vibrations of composite plates with SMA fibres in a gas stream with defects of the type of delamination, *Composite Structures*, **54**, 305-311

26. OVANESOVA A., SUAREZ L., 2004, Applications of wavelet transforms to damage detection in frame structures, *Engineering Structures*, **26**, 39-49

27. QUEK S., WANQ Q., ZHANG L., ANG K., 2001, Sensitivity analysis of crack detection in beams by wavelet technique, *International Journal of Mechanical Science*, **43**, 2899-2910

28. ROGERS L., 2005, Crack detection using acoustic emission methods – fundamentals and applications, *Key Engineering Materials*, **293-294**, 33-48

29. RUCKA M., WILDE K., 2004, Numerical simulation of damage detection in rectangular plate by two-dimensional wavelet transform, *Proceedings of International Workshop on Simulations in Urban Engineering*, Gdańsk, Poland, 205-208

30. SHINOBA K., MOROTOMI R., MUKAI K., YOSHIARA T., SHIRAI M., MIYAMOTO H., 2004, Application of digital radiography to aerospace-craft, *Key Engineering Materials*, **270-273**, 1361-1365

31. SWELDENS W., 1996, The lifting scheme: A custom-design construction of biorthogonal wavelets, *Applied and Computational Harmonic Analysis*, **3**, 2, 186-200

32. WANG Q., DENG X., 1999, Damage detection with spatial wavelets, *International Journal of Solids and Structures*, **36**, 3443-3448

33. WASZCZYSZYN Z., ZIEMIAŃSKI L., 2001, Neural networks in mechanics of structures and materials – new results and prospects of applications, *Computers and Structures*, **79**, 2261-2276

34. ZHANG G., HU H., TA D., 2004, Ultrasonic detection of the metallurgical defects in the steel and its evaluation by neural networks based on the wavelet transform noise suppression, *Key Engineering Materials*, **270-273**, 160-167

35. ZIOPAJA K., POZORSKI Z., GARSTECKI A., 2011, Damage detection using thermal experiments and wavelet transformation, *Inverse Problems in Science and Engineering*, **19**, 1, 127-153

# FATIGUE LIFE PREDICTION OF ALUMINIUM PROFILES FOR MECHANICAL ENGINEERING

Tomasz Tomaszewski, Janusz Sempruch

*University of Technology and Life Sciences in Bydgoszcz, Faculty of Mechanical Engineering, Bydgoszcz, Poland*

*e-mail: tomaszewski@utp.edu.pl*

The study presents a method to determine the $\sigma_a - N$ curve (high cycle fatigue) for profiles made of AW-6063 T6 aluminium alloy. Experimental material data for a mini specimen taken directly from the tested item and selected empirical correlations allowing for a size effect have been used. A model yielding the lowest relative error of estimating the fatigue life is presented.

*Keywords:* aluminium profile, high-cycles fatigue, mini specimen, size effect

## 1. Introduction

Modular frame systems made of aluminium profiles are an important innovation of the last fifteen years in the science of structures. They are applied in many industries, including mechanical engineering. Selecting a suitable profile size due to its strength and durability requires knowledge on fatigue, material and profile properties.

The $\sigma_a - N$ curve can be determined for a limited fatigue life using an analytical method based on commonly accepted quantities defining the curve (slope coefficient of the $\sigma_a - N$ curve in the range of high cycles ($m$)

$$\log \sigma_a = \frac{1}{m} \log N = b \tag{1.1}$$

and knee point for a specific group of materials ($\sigma_{AK}$, $\tau_{AK}$) – Fig. 1) or using experimental tests (Kocańda *et al.*, 1997). Comparison of fatigue characteristics of some selected materials are presented in the paper by Kurek *et al.* (2014).
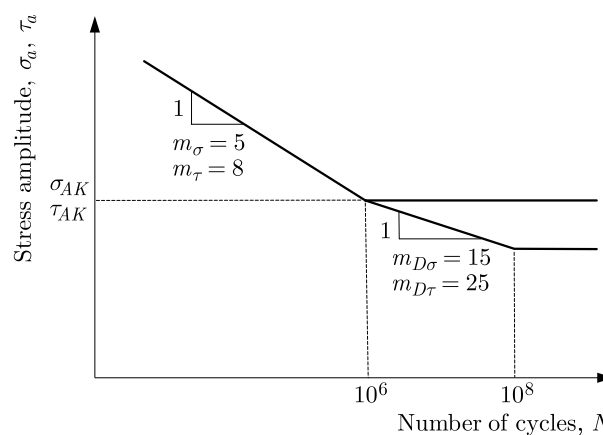


Fig. 1. Specific $\sigma_a - N$ curve estimated from FITNET procedure (FITNET, 2006)

Examplary records of the analytical approach to estimate the fatigue life are available in one of the FITNET procedures (path 2*b*). The approach includes analytical determination of the $\sigma_a - N$ curve at constant amplitude loads. The knee point is taken for $N_o = 10^6$ cycles and stress determined from the equation (FITNET, 2006):

— for normal stress

$$\sigma_W = f_{W,\sigma} R_m \tag{1.2}$$

— for shear stress

$$\tau_W = f_{W,\tau} R_m \tag{1.3}$$

where $f_{W,\sigma}$, $f_{W,\tau}$ are coefficients determined by the material and stress type, $R_m$ is tensile strength.

Stress values $\sigma_{AK}$, $\tau_{AK}$ (see Fig. 1) are calculated based on the product of stresses $\sigma_W$, $\tau_W$ and the correction factor allowing for the effect of selected factors on fatigue life (size, notch, roughness and average stress). The fatigue $\sigma_a - N$ curve is estimated from the fatigue life range allowing for the slope coefficient $m$ in accordance with Fig. 1.

For the analytical method, the results of the fatigue life estimation may be burdened by a high error resulting from natural high scatter of input values available in the literature. Figure 2 shows a histogram of the coefficient $m$ distribution compared to the gamma distribution for smooth steel specimens. Distribution width correlates to quality of the analytical test of the approximation, rendering the method inaccurate.
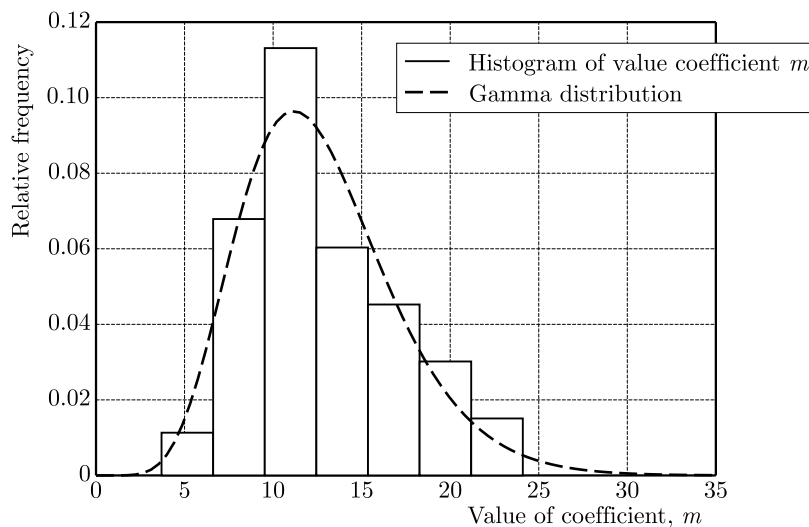


Fig. 2. Example of the distribution of the coefficient $m$ for a construction steel and smooth specimen – normal stress (Strzelecki and Sempruch, 2014)

The experimental approach is characterized by a significantly greater accuracy and is discussed in this work for aluminium profiles.

Aluminium profiles are manufactured in the extrusion process. Material properties change as a result of extrusion. The implementation of experimental methods for aluminium profiles often does not allow one to take full dimensional standard specimens. In the case of profiles, identification of prefabricated element properties requires non-standard specimens with reduced dimensions (referred to as mini specimens) due to limited dimensions of the tested item.

Figure 3 shows examplary applications of profiles and specimens taken directly from the profile. The purpose of the study is to discuss the method to determine strength and fatigue properties of profiles to further determine fatigue life and fatigue limit.
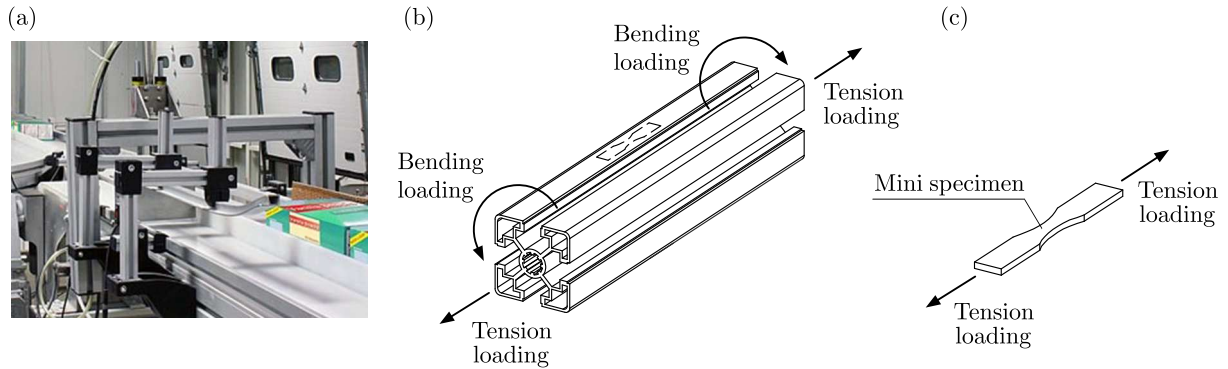
Fig. 3. Aluminium profiles: (a) application, (b) prevailing operational loads, (c) specimen for material tests

## 2. Test methods for aluminium mini specimens

### 2.1. Test stand

General strength and fatigue tests discussed in this study were performed on a standard servo-hydraulic testing machine (Instron 8874) – Fig. 4a. The machine features a dynamometer operating at $\pm 25$ kN force and 100 N·m torque. Monotonic tests were carried out using Instron 2620 Series dynamic strain gauge extensometer (12.5 mm gauge length with a travel of $\pm 5$ mm).

As a part of verification of the test method for mini specimens, the tests were performed on a testing machine of the author's own design – Fig. 4b (Tomaszewski and Sempruch, 2014a).
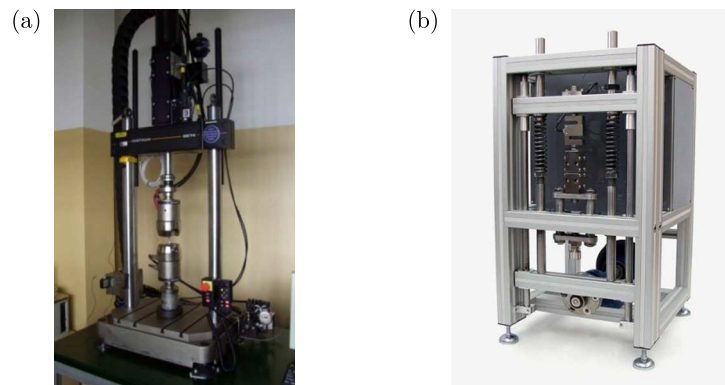


Fig. 4. Test stand used in the study: (a) Instron 8874, (b) own design

### 2.2. Applied loads

The fatigue properties were determined at a high-cycle fatigue regime. The tests were performed at controlled stress. The $\sigma_a - N$ curve was plotted based on 6 load levels for a total of 15 specimens. Test conditions conformed to standard requirements (PN-74/H-04327). A macro crack was used as a fatigue test end criterion. The tests were carried out at 5 Hz load change frequency, resulting from the technical capabilities of the servo-hydraulic testing machine used. The upper load level was limited by the experimental yield point ($R_{0.2} = 226$ MPa).

The tested specimen featured low resistance to buckling, thus the load cycle was changed at a constant tensile component (stress ratio $> 0$).

### 2.3. Fatigue test specimen

Flat specimens with variable width of the measured section were used throughout the tests (Fig. 5). The specimen size was determined by its ability to be taken from the specific profile

(Fig. 6). The value $t$ was determined by the profile wall thickness. Mini specimens were prepared by machining (milling). No additional working was used, e.g. grinding, polishing.
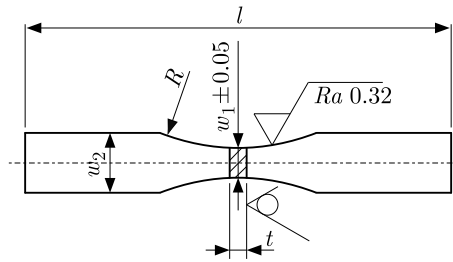


Fig. 5. Specimen used in high-cycle fatigue tests: $t = 1.58 \pm 0.03$, $w_1 = 3.5$, $w_2 = 7$, $l = 50$, $R = 25$

## 3. Example tests

### 3.1. Material and material identification

Experimental tests were performed on AW-6063 T6 aluminium alloy specimens. The tested material was taken directly from the profiles manufactured in the extrusion process. The fatigue properties were affected by a surface finish of the prefabricated element, thus the material was taken from anodized profile (most common profile surface treatment). Figure 6 shows the profile geometry.
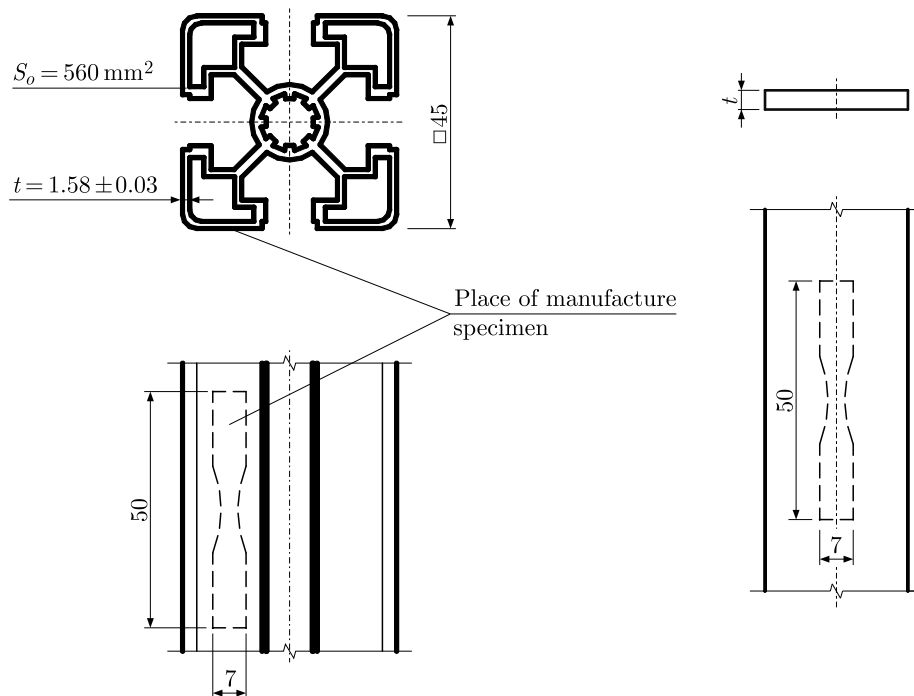


Fig. 6. Size of specimen taken form: (a) profile, (b) flat bar

Mechanical properties were determined in monotonic load conditions as per (PN-EN ISO 6892-1:2010). See Table 1 for results. The results show a low standard deviation. Table 2 shows selected material properties in accordance with the manufacturer's specification. Figure 7 shows static characteristics ($\varepsilon - \sigma$ curve).

**Table 1.** Mechanical properties of AW-6063 T6 aluminium alloy (anodized) – mini specimen ($S_o = 5.5\,\text{mm}^2$)

| No. | $R_m$ [MPa] | $R_{0.2}$ [MPa] | $R_u$ [MPa] | $E$ [MPa] | $A$ [%] | $Z$ [%] |
|-----|-------------|-----------------|-------------|-----------|---------|---------|
| 1 | 250 | 226 | 281 | 69 319 | 16.8 | 29.6 |
| 2 | 249 | 225 | 271 | 67 532 | 11.2 | 22.1 |
| 3 | 250 | 226 | 270 | 69 632 | 12.8 | 23.1 |
| 4 | 251 | 227 | 293 | 67 664 | 12 | 32.4 |
| 5 | 250 | 225 | 275 | 69 181 | 12.8 | 24.4 |
| Average value | 250 | 226 | 278 | 68 665 | 13.1 | 26.3 |
| Standard deviation | 0.7 | 0.8 | 9.4 | 989 | 2.2 | 4.4 |

**Table 2.** Mechanical properties of AW-6063 T6 aluminium alloy (anodized) – manufacturer's data

| $R_m$ [MPa] | $R_{0.2}$ [MPa] | $E$ [MPa] | $A$ [%] |
|-------------|-----------------|-----------|---------|
| 245 | 195 | 70 000 | 10 |
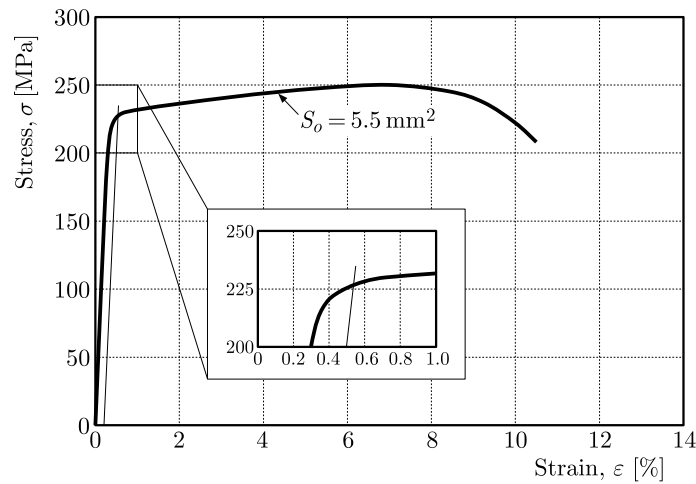


Fig. 7. Stress-strain diagram of a specimen taken from the anodized profile made of AW-6063 T6 aluminium alloy

### 3.2. Test results

Experimental tests aimed to determine the coefficient $m$. Fatigue life was determined at selected stress amplitude levels based on the tests of the mechanical property. Table 3 shows the test results.

The data are approximated to a linear equation corresponding to 50% likelihood of specimen failure. Figure 8 shows the diagram in a bi-logarithmic system. Experimental points and solid line corresponding to linear regression are shown compared to the confidence interval (grey area). The regression line shows a high coefficient of determination $R^2$. The coefficient $m$ for the analysed aluminium alloy taken from the profile is 7.35.

The effect of the cross-section must be taken into account to consider the curve as universal and reliable for the group of profiles. It is thus necessary to determine the correlation between the positions of each curve plotted for the specimens with different cross-sections. The studies presented in (Tomaszewski *et al.*, 2014) show that within the high-cycle fatigue range, the $\sigma_a - N$ curves plotted for the mini specimen ($S_o = 3.5\,\text{mm}^2$) and the standard specimen ($S_o = 28\,\text{mm}^2$) made of AW-6063 T6 aluminium alloy (from flat sections) are parallel (Table 4). This is indicated by a similar slope coefficient of the regression line ($m \approx \text{const}$) and statistical parallelism tests.

**Table 3.** Test results for fatigue life (PN-74/H-04327) for mini specimen ($S_o = 5.5\,\text{mm}^2$) made of AW-6063 T6 aluminium alloy taken from the profile

| Stress, $R = 0.1$ | | Fatigue life, |
|---|---|---|
| $\sigma_a$ [MPa] | $\sigma_{max}$ [MPa] | $N$ [cycles] |
| 97.9 | 220 | 36 855 |
| | | 38 946 |
| | | 48 011 |
| 89 | 200 | 88 337 |
| | | 94 717 |
| | | 107 079 |
| 80.1 | 180 | 146 563 |
| | | 166 113 |
| | | 180 036 |
| 75.7 | 170 | 305 253 |
| | | 365 625 |
| | | 429 974 |
| 66.8 | 150 | 604 432 |
| 62.3 | 140 | 932 905 |
| | | 1 182 165 |



$$\log \sigma_a = -0.136 \log N + 2.619$$
$$R^2 = 0.97$$

Mini specimen: $S_o = 5.5\,\text{mm}^2$
Stress cycle asymmetry: $R = 0.1$
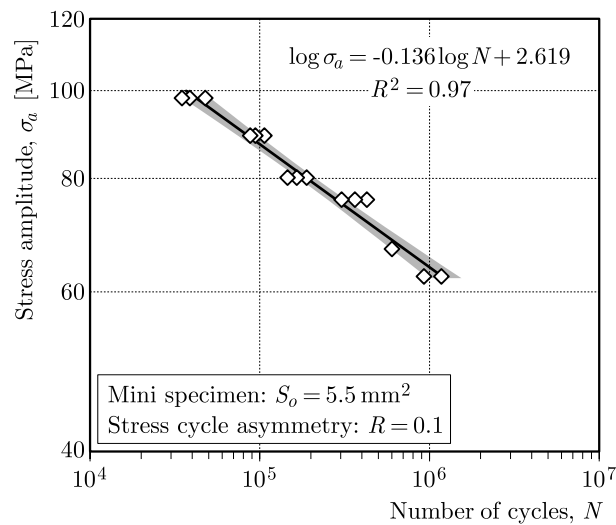
Fig. 8. Graphical representation of the $\sigma_a - N$ curve in the high-cycle fatigue regime for AW-6063 T6 aluminium alloy

**Table 4.** Comparison of the linear regression coefficients of the $\sigma_a - N$ curve for AW-6063 T6 aluminium alloy (from flat section)

| Cross-sectional area | Regression line, $R = 0.1$ | | Coefficient of determination |
|---|---|---|---|
| $S_o$ [mm$^2$] | $1/m$ | $b$ | $R^2$ |
| 28 | $-0.078$ | 2.319 | 0.97 |
| 3.5 | $-0.078$ | 2.374 | 0.93 |

The flat bars were shaped in the same conditions as the profiles. The size effect for aluminium alloy is not affected by the stress amplitude (load). With a known coefficient $m$ and the size effect for the specific group of structural materials, the fatigue properties can be determined for the entire family of the profiles.

## 4. Size effect

The size effect defines the relationship between the fatigue properties of the material or structural element and its size. The material strength decreases with an increase in size of the tested item subject to monotonic or fatigue loads (Carpinteri *et al.*, 2009). The reduction in strength is affected by factors related to a random distribution of defects in the material, shape and type of load and the effect of technological processes during production.

The size effect is commonly defined as a ratio of strength properties of a specimen with specific cross section and the standard specimen

$$K_Z = \frac{\sigma_{(-1)}}{\sigma_{(-1)n}} \qquad K_{HC} = \frac{\sigma}{\sigma_n} \qquad K_S = \frac{R_m}{R_{mn}} \tag{4.1}$$

where $\sigma_{(-1)}/\sigma/R_m$ is the fatigue limit/fatigue strength/tensile strength of the specimen with any cross-section, $\sigma_{(-1)n}/\sigma_n/R_{mn}$ is the fatigue limit/fatigue strength/tensile strength of the normative specimen (cross-section 20-80 mm$^2$) while maintaining the same material. Figure 9 shows schematic relation between the cross-sectional area and the coefficient $K$.
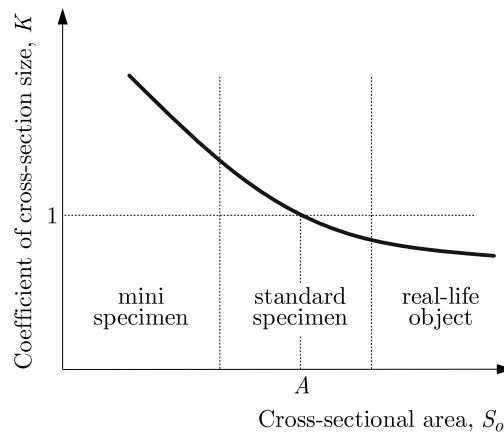


Fig. 9. Schematic relation between the cross-sectional area and the coefficient of cross-section size

Aluminium alloys show changes in fatigue properties depending on the cross-section of the tested specimen. The changes were verified based on the experimental tests of the coefficient $K$ (Eq. (4.1), Table 5) for AW-6063 T6 aluminium alloy taken from flat bars (Tomaszewski and Sempruch, 2015).

**Table 5.** Comparison of the coefficients $K_S$ and $K_{HC}$ (Tomaszewski and Sempruch, 2015)

| Cross-sectional area, $S_o$ [mm$^2$] | $K_S$ | $K_{HC}$ |
|---|---|---|
| 3.5 | 1.150 | 1.131 |
| 28* | 1 | 1 |

* equivalent point $A$ in Fig. 9

Notwithstanding the origin of the size effect, the fatigue life is estimated from empirical correlations between the coefficient $K$ value and a specific specimen dimension (e.g. diameter $d$).

Table 6 shows selected size effect correlations allowing for the range of application and the author of the given proposal. Due to the analysis of tests for specimens with rectangular cross-section, the correlations are examined for the cross-sectional area $S_o$.

**Table 6.** Quantitative correlation between cross-section coefficients $K_Z$, author's study based on (Shigley *et al.*, 2004)

| $K_Z$ | Range [mm] | Author |
|---|---|---|
| $\dfrac{0.947}{1 - 0.406/d}$ | $3.2 \leqslant d \leqslant 48$ | Moore |
| $0.931\Big(1 + \dfrac{0.014}{0.1 + (d/25.4)^2}\Big)$ | $d \leqslant 50$ | Heywood |
| $1$ | $d \leqslant 8$ | Shigley and Mitschke |
| $1.189d^{-0.097}$ | $8 \leqslant d \leqslant 250$ | |
| $0.6$ | $d \geqslant 250$ | |
| $1 - \dfrac{d - 7.62}{381}$ | $50 \leqslant d \leqslant 230$ | Roark |

## 5. Verification example

The purpose of the analysis is to estimate the $\sigma_a - N$ curve in a high-cycle fatigue regime for a selected profile based on experimental data obtained for a mini specimen. The correction coefficient of cross-section $K$ is used to shift the curve in parallel to the side of the lower fatigue life. The shift direction corresponds to a general trend known for metals, where fatigue properties decrease with an increase in the cross-sectional area.

Initial empirical size effect correlations are implemented for the fatigue limit. Since in the range of elastic deformation of the material the initiation and propagation of the fatigue crack are similar, the values presented in Table 5 can be used in the high-cycle fatigue regime.

Based on many experimental studies as well as on the author's own study (Tomaszewski and Sempruch, 2015), a change in fatigue properties manifest itself as an increase in specimens smaller than the standard specimens. The coefficient $K$ is higher than 1 in this range of specimen sizes (Table 5). Implemented empirical correlations will be analysed irrespective of the scope shown in Table 6.
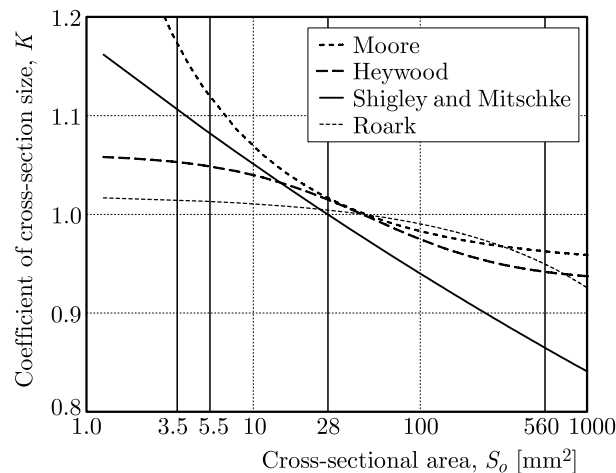


Fig. 10. Graphical comparison of the correlations of the cross-section coefficient based on Table 6

Figure 10 shows a graphical approach regarding the analytical correlations to determine $K$ coefficient: The curves are intersected by vertical lines corresponding to selected cross-sectional areas: $3.5\,\mathrm{mm}^2$, $5.5\,\mathrm{mm}^2$ (mini specimen), $28\,\mathrm{mm}^2$ (standard specimen), $560\,\mathrm{mm}^2$ (profile).

The analysed correlations do not allow for the material constants that are difficult to determine, and thus are easy to apply within the scope of basic engineering calculations. Allowing for the scatter of experimental results, the material data can be found in the model based on the weakest link theory (Weibull, 1949), fractal approach (Carpinteri *et al.*, 2009) or energy law (Bažant, 1984). Verification of correct implementation is described in (Tomaszewski *et al.*, 2014).

Quantitative assessment of the degree of conformity of empirical and analytical data (based on the correlations in Table 5) is performed for the following cross-sectional areas: 3.5 and $28\,\mathrm{mm}^2$. It results from the availability of experimental data and material properties similar to the target aluminium alloy the profile is made of. Table 7 shows the coefficient $K_{HC}$ determined based on analytical correlations and experimental data. The relative error estimated from the following equation is used in the quantitative analysis

$$\delta = \frac{\sigma_{ex} - \sigma_{cal}}{\sigma_{ex}} \cdot 100 \tag{5.1}$$

where $\sigma_{ex}$ is the experimental fatigue limit for a specific fatigue life, $\sigma_{cal}$ is the analytical fatigue limit for a specific fatigue life.

**Table 7.** Comparison of cross-section coefficient values determined based on analysed empirical correlations and experimental tests

| Cross-sectional area, $S_o$ [mm$^2$] | $K_{HC}$ | | | | |
|---|---|---|---|---|---|
| | Moore | Heywood | Shigley and Mitschke | Roark | Experimental tests (Tomaszewski and Sempruch, 2015) |
| 3.5 | 1.173 | 1.053 | 1.106 | 1.014 | 1.131 |
| 28 | 1.016 | 1.015 | 0.999 | 1.004 | 1 |

Table 8 shows the error $\delta$ determined based on equation (4.2). Application of the Roark equation does not give significant differences in the results, therefore this model will not be analyzed. Moore, Shigley and Mitschke equations have been used due to discrepancies in the obtained coefficient $K_{HC}$. Results from the Moore equation estimate higher $K_{HC}$ values corresponding to a higher fatigue life by positioning the $\sigma_a - N$ curve on the unsafe side in relation to the experimental data. The situation is reversed for the Shigley and Mitschke equations, and thus the values are lower.

**Table 8.** Relative errors for the analysed empirical correlations

| Cross-sectional area, $S_o$ [mm$^2$] | Relative error [%] | | |
|---|---|---|---|
| | Moore | Heywood | Shigley and Mitschke |
| 3.5 | −3.7 | 6.9 | 2.2 |
| 28 | −1.6 | −1.5 | 0.0 |

Table 9 shows the coefficient $K_{HC}$ calculated for the cross-sectional area of the mini specimen ($S_o = 5.5\,\mathrm{mm}^2$) and analysed profile ($S_o = 560\,\mathrm{mm}^2$). The $\sigma_a - N$ curve for the mini specimen has been shifted in parallel by the value of the calculated coefficient $K_{HC}$. Table 10 shows coefficients of linear regression for the straight lines.

The Moore equation overestimates the values, whereas Shigley and Mitschke equations underestimate the values, thus it seems that the most correct values for the cross-sectional area of $560\,\mathrm{mm}^2$ are between those curves (Fig. 11).

**Table 9.** Cross-section coefficient values determined based on the analysed empirical correlations

| Cross-sectional area, $S_o$ [mm$^2$] | $K_{HC}$ | | |
|---|---|---|---|
| | Moore | Heywood | Shigley and Mitschke |
| 5.5 | 1.119 | 1.049 | 1.082 |
| 560 | 0.962 | 0.942 | 0.865 |

**Table 10.** Comparison of linear regression coefficients of the $\sigma_a - N$ curves for AW-6063 T6 aluminium alloy

| Cross-sectional area, $S_o$ [mm$^2$] | Results | Regression line, $R = 0.1$ | |
|---|---|---|---|
| | | $1/m$ | $b$ |
| 5.5 | Experiment | $-0.136$ | 2.619 |
| 560 | analytically – Moore | $-0.136$ | 2.556 |
| | analytically – Heywood | $-0.136$ | 2.575 |
| | analytically – Shigley and Mitschke | $-0.136$ | 2.534 |
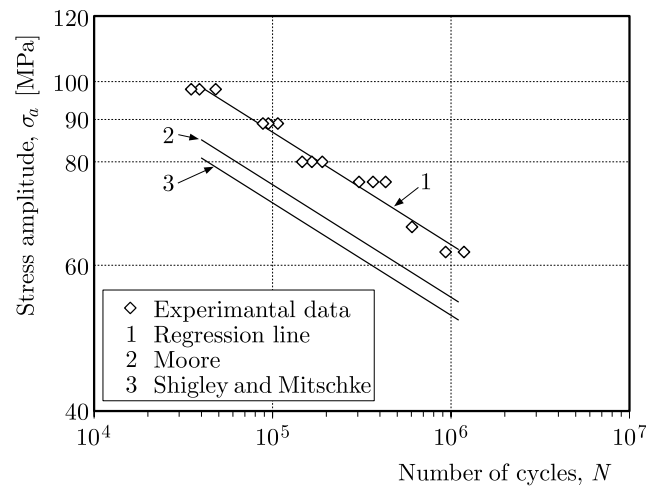


Fig. 11. Fatigue $\sigma_a - N$ curves plotted for the experimental data and analytical models of the size effect

A change in fatigue properties of the material or a structural element is most often analysed in the context of its fatigue life. For stress amplitudes $\sigma_a$ corresponding to 90 MPa and 60 MPa, the fatigue life is determined based on the regression equation (Moore, Shigley and Mitschke model). The results have been compared with the experimental data (Table 11).

## 6.  Summary

The article presents test methods to obtain material data for an aluminium profile and estimate the $\sigma_a - N$ curve for the actual cross-sectional area of the tested item (higher than the tested specimen). Thus, selected empirical correlations of the size effect are used in the study.

Due to the inability to obtain experimental data for the profile, the discussed correlations have been verified directly using the experimental test results for the mini specimen ($S_o = 3.5$ mm$^2$) and the standard specimen ($S_o = 28$ mm$^2$). The specimens in theory are made of the same material as the profile – AW-6063 T6 aluminium alloy. The calculated analytical $\sigma_a - N$ curves using Moore, Shigley and Mitschke equation for 28 mm$^2$ cross-section yield the lowest relative error at $-3.7$-2.0%.

**Table 11.** Differences in the fatigue life at two stress amplitude levels (90 MPa, 60 MPa) for the mini specimen ($S_o = 5.5\,\text{mm}^2$) and profile ($S_o = 560\,\text{mm}^2$) determined based on selected empirical correlations of the size effect

| Stress amplitude, $\sigma_a$ [MPa] | Fatigue life, $N$ | | |
|---|---|---|---|
| | Experiment $S_o = 5.5\,\text{mm}^2$ | Moore $S_o = 560\,\text{mm}^2$ | Shigley and Mitschke $S_o = 560\,\text{mm}^2$ |
| 90 | 77 254 | 26 407 | 18 195 |
| 60 | 1 523 040 | 520 609 | 358 715 |

Theoretical fatigue life determined using analytical method for the profile is three times (as per Moore equation) or four times (as per Shigley and Mitschke equation) lower than for the specimen taken directly from the profile. This approach is advantageous in terms of engineering calculations, since the fatigue values obtained will be on the safe side in relation to the actual values.

## References

1. BAŽANT Z.P., 1984, Size effect in blunt fracture concrete, rock, metal, *Journal of Engineering Mechanics ASCE*, **110**, 518-535

2. CARPINTERI A., SPAGNOLI A., VANTADORI S., 2009, Size effect in S-N curves: A fractal approach to finite-life fatigue strength, *International Journal of Fatigue*, **31**, 927-933

3. KOCAŃDA S., SZALA J., 1997, *Bases of Fatigue Calculation* (in Polish), PWN, Warszawa

4. KUREK M., ŁAGODA T., KATZY D., 2014, Comparison of fatigue characteristics of some selected materials, *Materials Testing (Materialprufung)*, **56**, 2, 92-95

5. FITNET FFS Procedure, 2006, European Fitness-for-Service, MK7

6. PN-74/H-04327 The study of metal fatigue. The test of axial tension – compression at constant cycle of external loads (in Polish)

7. PN-EN ISO 6892-1:2010 Metals – Tensile testing – Part 1: Test method at room temperature (in Polish)

8. SHIGLEY J.E., MISCHKE C.R., BROWN JR. T.H., 2004, *Standard Handbook of Machine Design*, 3rd Ed., McGraw-Hill

9. STRZELECKI P., SEMPRUCH J., 2014, Hybrid method for determining fatigue characteristic in high-cycle life, *20th International Conference Engineering Mechanics*

10. TOMASZEWSKI T., SEMPRUCH J., 2014, Verification of the fatigue test method applied with the use of mini specimen, *Key Engineering Materials*, **598**, 243-248

11. TOMASZEWSKI T., SEMPRUCH J., PIĄTKOWSKI T., 2014, Verification of selected models of size effect based on high-cycle fatigue testing on mini specimens made of EN AW-6063 aluminum alloy, *Journal of Theoretical and Applied Mechanics*, **52**, 4, 883-894

12. TOMASZEWSKI T., SEMPRUCH J., 2015, Analysis of size effect in high-cycle fatigue for EN AW-6063, *Solid State Phenomena*, **224**, 75-80

13. WEIBULL W., 1949, A statistical representation of fatigue failures in solids, *Transaction of the Royal Institute of Technology*, **27**

# INTELLIGENT HYBRID FUZZY LOGIC SYSTEM FOR DAMAGE DETECTION OF BEAM-LIKE STRUCTURAL ELEMENTS

Sasmita Sahu, Priyadarshi Biplab Kumar, Dayal R. Parhi

*Department of Mechanical Engineering, Robotics Lab., NIT Rourkela, India*

*e-mail: gudusasmita@gmail.com; p.biplabkumar@gmail.com; dayalparhi@yahoo.com*

Fuzzy logic has been used in different research fields for more than three decades. It has become a robust method to solve complex and intricate problems which are otherwise difficult to solve by traditional methods. But it still requires some human experience and knowledge. In the present study, an attempt is made to design a hybrid optimization technique for automatic formation of the fuzzy knowledge based rules using an evolutionary algorithm. This hybridization technique has been applied in the field of damage detection and location of cracks in cracked structural elements. In this paper, a robust fault diagnostic tool based on a differential evolution algorithm and fuzzy logic has been proposed. Theoretical and Finite Element analyzes are done to model the crack and to find the effect of the presence of cracks on changes of vibrational characteristic (natural frequencies) of a fixed-fixed beam. The inputs to DEA-FL system are the first three relative natural frequencies, and the outputs from the system are the relative crack depth and relative crack location. For the validation of the results obtained from the proposed method and to check the robustness of the controller, experimental analysis is performed. To find average error rates, the bootstrap method has been adopted.

*Keywords:* fuzzy logic, differential evolution algorithm, crack, natural frequency

## 1. Introduction

Zadeh (1965) introduced Fuzzy Logic (FL). He introduced a concept of the partial set membership rather than a classical set membership or non-membership. Fuzzy Logic was then presented as a way of processing data and not presented as a control method. Fuzzy Logic is a mathematical logic that attempts to solve problems by assigning values to an imprecise range of data to reach the most accurate result. FL is an approach to compute "degrees of truth" rather than fully "true" or "false" (1 or 0) of the classical logic. Due to its rule over the traditional method, it has been widely used in various fields. Some of researchers (Ganguli, 2001; Jiao *et al.*, 2015) also used this logic system in structural health monitoring, navigation of robots (Parhi, 2005), etc. Fuzzy Logic System (FLS) consists of fuzzy sets, membership functions and rule tables. The main aim of any FLS is first to define the membership functions. The MFs are defined by the parameters based on the author's experience. Some of the researchers have used genetic algorithms to fuzzy logic together, but in this case the results from the genetic algorithm layer is trained again in the fuzzy logic layer for refinement (Dash and Parhi, 2014), some have used hybridized membership functions to be applied in the fuzzy inference system (Thatoi *et al.*, 2014).

The Differential Evolution Algorithm (DEA) was proposed by Storn and Price (1997). The algorithm became popular due to its capacity of producing effective results with simplicity. This is a population oriented evolutionary algorithm (Tang, 2012). It has the capacity of memorising individual's optimal value by sharing the internal information. The operators involved are mutation, crossover and selection (Qin and Suganthan, 2005). Most of the time, it is considered as a greedy Genetic Algorithm while ensuring quality. DE has been successfully applied in diverse

fields such as mechanical engineering, communication, and pattern recognition (Dewhirst *et al.*, 2010).

Due to the competition to produce better and better results by using Artificial Intelligence (AI) techniques, different researchers have tried to hybridize different AI techniques or improved the performance of the AI techniques by using different enhanced operations. Some of the researchers have tuned parameters of DEA using a memtic algorithm (Neri, 2008), hybridized PSO with DEA (Thangaraj *et al.*, 2010), some have used FLS for diversity control of population of DEA (Amali and Baskar, 2013), and some others have used multi objective evolutionary algorithms for the enhancement of performance of FLC (Xue *et al.*, 2005). But less work has been proposed to integrate FLS and DEA using simple steps to be used in the field of vibration analysis of cracked structures for crack location.

Cracks, faults or damages are a serious threat to the current and future performance of a system. This may occur due to over stressing during operation in extreme environmental conditions or due to any accidental scenarios. The present crack may grow during working and may lead to failure if the crack grows beyond the critical limit. So it is needed to investigate the fault occurrence in structures at the earliest possible stage. Damage detection methods employing vibration characteristics of a component of a structure have emerged as a reliable method for predicting structural health (Khiem and Tran, 2013; Daneshmehr *et al.*, 2013). Damage assessment attempts to determine whether structural damage has occurred try to find the location and extent of the damage (Pawar and Sawant, 2014). The methods using vibration analysis offer some advantages over conventional methods. The frequency measurement method is easier to use in in real-time as it only requires a small number of sensors, and the measurement is straightforward. Furthermore, to make the analysis of nonlinearity in the vibration based fault detection methods, different researchers use the finite element analysis (Sinha *et al.*, 2002; Caddemi and Morassi, 2013). Nowaday, numbers of software packages are available in the market that makes the analysis easier (Musmar *et al.*, 2014; Parandaman and Jayaraman, 2014). This work aims at advancing damage detection methods by proposing this method of crack detection. The results suggest the evidence of presence of a crack. A 2-D finite element model has been developed to study modal properties and identify the presence of a crack in the structural element.

In the process of damage identification and detection, traditional mathematical techniques are rather insufficient due to difficulty in the modelling of highly nonlinear components. New methods of the modelling based on AI techniques have shown promising results for the modelling of nonlinearities. So the inverse problem of damage detection of any material of any section can be solved using computational intelligent techniques. In the effort to find a convenient solution to a problem using AI systems, several difficulties are faced by the designer. It is not an easy task to solve problems while running an algorithm. This clearly paves the way to find better AI systems in a hit and trial method. Due to the lack of a common framework, it remains often difficult to compare various AI systems conceptually and evaluate their performance comparatively. So the results are purely based on the problem definition and the designer when applied to different approaches.

In this paper, a hairline transverse crack is modeled using Finite Element Analysis (FEA). Then the first three natural frequencies are extracted and converted into relative values from FEA. The relative values of the natural frequencies (rfnf, rsnf, rtnf) are found out by comparing the natural frequencies of the uncracked and cracked beam. Relative values of the crack depth and crack location (rcd, rcl) are also found using a similar method. This work considers only the natural frequencies because they are less prone to error while calculating. The relative first natural frequency (rfnf), second (rsnf) and relative third natural frequency (rtnf) are treated as the input variables in the proposed method. The outputs from the system are the relative values

of crack depth (rcd) and crack location (rcl) which, in turn, contain the information of damage severity.

## 2. Cracked beam modelling

A mathematical model must be chosen to obtain results by numerical simulation. Most of the studies are made assuming the crack to be open and remain open during vibration. For theoretical and finite element analysis, it is assumed that there is no displacement and rotation of the beam at the clamped end and the crack is a non-propagating crack. Most of the studies are made assuming the crack to be open and remain open during vibration to make the mathematical modeling simple. A fixed-fixed beam with a transverse hairline crack has been modeled in the present work. Due to the presence of the crack, an additional flexibility is introduced which can be defined in a matrix form. In this work, a $2 \times 2$ matrix is considered. The dimension of the matrix depends on the degrees of freedom. The transverse surface crack has depth $a$, width $B$ and height $W$. Here, the fixed-fixed beam is subjected to the axial force $P_1$ and the bending moment $P_2$ as shown in Fig. 1.
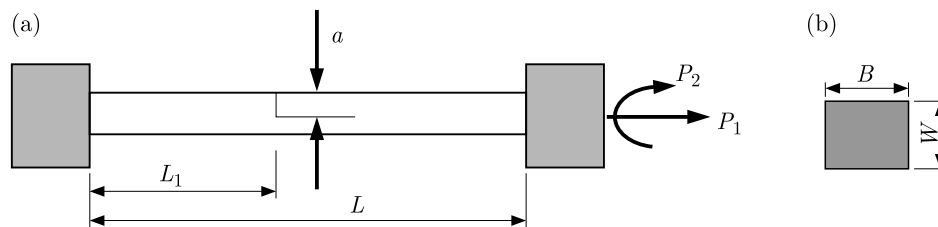


Fig. 1. (a) Cracked fixed-fixed beam, (b) cross sectional view of the cracked fixed-fixed beam

Tada *et al.* (1973) proposed the strain energy release rate at the fractured section as

$$J = \frac{1}{E'}(K_{11} + K_{12})^2 \tag{2.1}$$

where

$$frac1{E'} = \begin{cases} \dfrac{1 - \gamma^2}{E} & \text{for plain strain condition} \\ \dfrac{1}{E} & \text{for plain stress condition} \end{cases} \tag{2.2}$$

(1) where $K_{11}$, $K_{12}$ are the stress intensity factors of mode I (opening of the crack) for the load $P_1$ and $P_2$, respectively.

Taking $U_t$ as the strain energy due to the crack and applying Castigliano's theorem, the additional displacement along the force $P_i$ can be calculated

$$u_i = \frac{\partial U_t}{\partial P_i} \tag{2.3}$$

By definition, the flexibility influence coefficient $C_{ij}$ which forms the elements of the flexibility matrix can be written as

$$C_{ij} = \frac{\partial u_i}{\partial P_j} = \frac{\partial^2}{\partial P_i \partial P_j} \int_0^a J(a)\, da \tag{2.4}$$

After finding out all the four coefficients of the flexibility matrix, the local stiffness matrix can be obtained by taking the inversion of the compliance matrix, i.e.

$$\mathbf{K} = \begin{bmatrix} K_{11} & K_{12} \\ K_{21} & K_{22} \end{bmatrix} = \begin{bmatrix} C_{11} & C_{12} \\ C_{21} & C_{22} \end{bmatrix}^{-1} \tag{2.5}$$

From the governing equations of the free vibration mode of the cracked beam, the normal function for the system can be defined as

$$\begin{aligned} \overline{U}_1(\overline{x}) &= A_1 \cos(\overline{K}_u \overline{x}) + A_2 \sin(\overline{K}_u \overline{x}) & \overline{U}_2(\overline{x}) &= A_3 \cos(\overline{K}_u \overline{x}) + A_4 \sin(\overline{K}_u \overline{x}) \\ \overline{Y}_1(\overline{x}) &= A_5 \cosh(\overline{K}_y \overline{x}) + A_6 \sinh(\overline{K}_y \overline{x}) + A_7 \cos(\overline{K}_y \overline{x}) + A_8 \sin(\overline{K}_y \overline{x}) \\ \overline{Y}_2(\overline{x}) &= A_9 \cosh(\overline{K}_y \overline{x}) + A_{10} \sinh(\overline{K}_y \overline{x}) + A_{11} \cos(\overline{K}_y \overline{x}) + A_{12} \sin(\overline{K}_y \overline{x}) \end{aligned} \tag{2.6}$$

where

$$\begin{aligned} \overline{x} &= \frac{x}{L} & \overline{u} &= \frac{u}{L} & \overline{y} &= \frac{y}{L} & \beta &= \frac{L_1}{L} \\ \overline{K}_u &= \frac{\omega L}{C_u} & C_u &= \sqrt{\frac{E}{\rho}} & \overline{K}_u &= L\sqrt{\frac{\omega}{C_y}} & C_y &= \sqrt{\frac{EI}{\mu}} & \mu &= A\rho \end{aligned} \tag{2.7}$$

Here $U_1(x,t)$ and $U_2(x,t)$ are normal functions of longitudinal vibration for the sections before and after the crack and $Y_1(x,t)$, $Y_2(x,t)$ are normal functions of bending vibration for the same sections.

Analyzing the normal functions of the longitudinal and bending vibration condition, the characteristic equation (the determinant) of the system can be written as

$$|Q| = 0 \tag{2.8}$$

This determinant $|Q|$ is a function of the natural circular frequency $\omega$, the relative location of the crack $\beta$ and the local stiffness matrix $\mathbf{K}$ which, in turn, is a function of the relative crack depth $a/W$.

## 3. Finite element modelling of the cracked beam

For vibration analysis of the uncracked and cracked cantilever beam, ALGOR V 19.3 SP 2 Finite Element Program is used. First, the beam element with a different single crack is plotted using CATIA V5R15 software, and then they are treated in ALGOR environment. The uncracked and cracked beam model is then analyzed in ALGOR environment. First of all, mesh generation is performed. The mesh size is around 1.4529 mm and approximately 33369 elements are created. Then the parameters such as the element type (brick and isotropic), material name (aluminium alloy) are defined in the ALGOR environment. After that boundary conditions are given by constraining all degrees of freedom of the nodes located on the left end of the beam. The model unit is then changed to SI standards. Then, in the analysis window, a particular analysis type is selected (natural frequency, i.e. modal analysis). Then the analysis is performed and the first three modes of natural frequencies at different crack locations and crack depths of the fixed-fixed beam are recorded. Figure 2 shows the modes of vibration of the cracked beam after finite element analysis.

## 4. Definition of Fuzzy Logic System parameters while applied to Fault Detection

Fuzzy logic is a logic based system in which the fuzzy logic is used to represent different forms of knowledge to model interactions and relationships among system variables. Fuzzy logic systems are a very important tool for the modeling of complex systems. The shortcomings of fuzzy logic
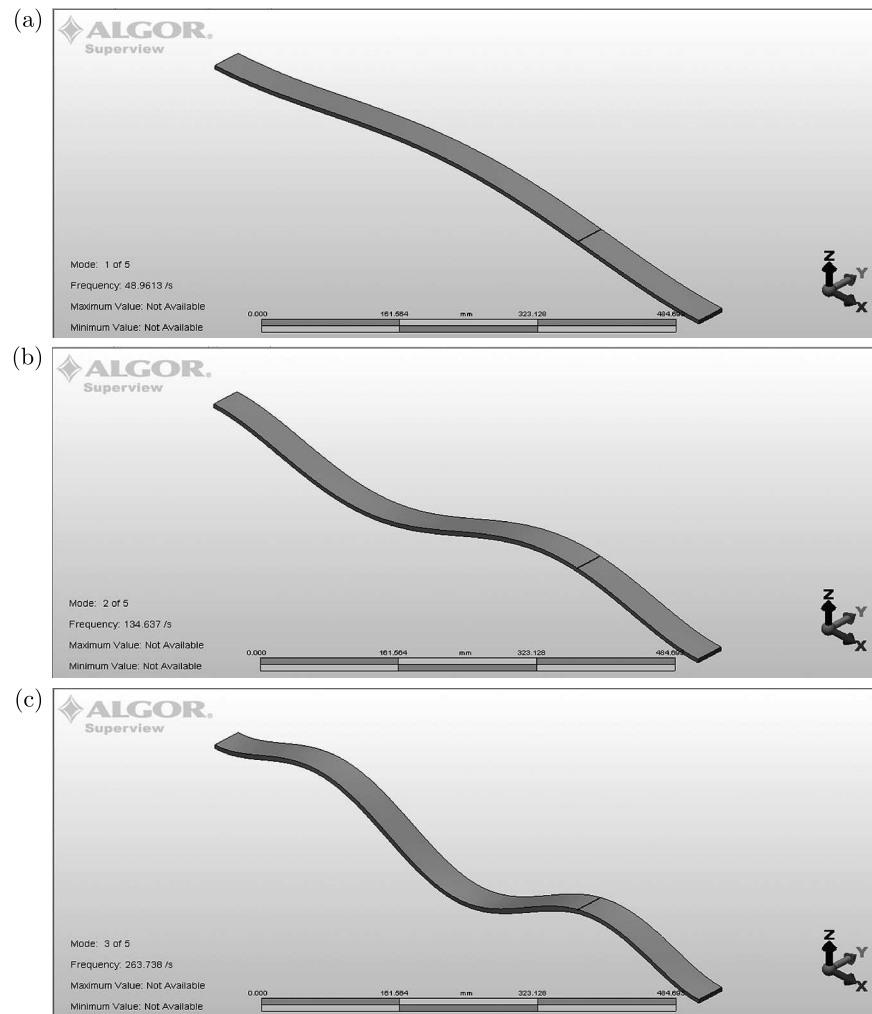
Fig. 2. First three modes of vibration of the cracked fixed-fixed beam

are systematic design and learning capacity. The main challenge of a fuzzy inference system is to design fuzzy rules according to the problem definition.

Another main issue is to design the membership function parameters (variable definition) involved with the rule. From the literature available, it can be observed that many methods have been formulated to tune the MF parameters using different evolutionary algorithms. But less of the work is done to optimize both fuzzy membership functions and fuzzy rules. So in the present work, an effort is made to optimize both the fuzzy membership function and the fuzzy rules.

The proposed fuzzy system is based on the Mamdani fuzzy model (Fig. 3). Fuzzy linguistic variables are defined before assigning different membership functions and definition of their ranges. These linguistic variables play a major role during formation of the rule table. These are linguistic objects or words rather than numbers.

The different linguistic variables used for input and output variables are given as below:

Input 1: (rfnf): low (L), medium (M), high (H)

Input 2: (rsnf): low (L), medium (M), high (H)

Input 3: (rtnf): low (L), medium (M), high (H)

Output 1: (rcd): small (S), medium (M), large (L)

Output 2: (rcl): small (S), medium (M), big (B)
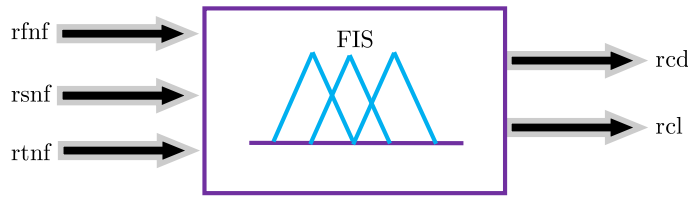
Fig. 3. Fuzzy controller with its input and output variables

The rule base section of the fuzzy inference system works on the application and implementation of the fuzzy rules. The fuzzy rules are usually of the form of "if-then" statements. The if – antecedent part and then – part is known as the consequent part. The two fuzzy parts are connected with the connectors like AND, OR, NOT, etc.

A typical rule in a Mamdani fuzzy system in the current problem is defined as below:

$$\text{If} \quad x_1 \text{ is LF}, \ x_2 \text{ is MF}, \ x_3 \text{ is LF} \quad \text{then} \quad y_1 \text{ is SD}, \ y_2 \text{ is ML} \tag{4.1}$$

Based on the fuzzy subset, the fuzzy rules are defined in a general form as follows

$$\text{If} \ (\text{fnf is fnf}_i \text{ and snf is snf}_j \text{ and tnf is tnf}_k) \quad \text{then} \quad (\text{cd is cd}_{ijk} \text{ and cl is cl}_{ijk}) \tag{4.2}$$

where $ij, k = 1, 2, 3$, because of "rfnf", "rsnf", "rtnf" have 3 membership functions each.

From above expression (4.2), two sets of rules can be written

$$
\begin{aligned}
&\text{If} \ (\text{rfnf is rfnf}_i \text{ and rsnf is rsnf}_j \text{ and rtnf is rtnf}_k) \quad \text{then} \quad \text{rcd is rcd}_{ijk} \\
&\text{If} \ (\text{rfnf is rfnf}_i \text{ and rsnf is rsnf}_j \text{ and rtnf is rtnf}_k) \quad \text{then} \quad \text{rcl is rcl}_{ijk}
\end{aligned}
\tag{4.3}
$$

According to the usual Fuzzy Logic control method (Parhi, 2005), a factor $w_{ijk}$ is defined for the rules as follows

$$w_{ijk} = \mu_{\text{fnf}_i}(\text{freq}_i) \ \wedge \ \mu_{\text{snf}_j}(\text{freq}_j) \ \wedge \ \mu_{\text{tnf}_k}(\text{freq}_k) \tag{4.4}$$

where $\text{freq}_i$, $\text{freq}_j$ and $\text{freq}_k$ are the first, second and third natural frequency of the cantilever beam with a crack, respectively. Applying the composition rule of interference (Parhi, 2005), the membership values of the relative crack location and relative crack depth (location) are given as

$$
\begin{aligned}
&\mu_{\text{rcl}_{ijk}}(\text{location}) = w_{ijk} \ \wedge \ \mu_{\text{rcl}_{ijk}}(\text{location}) \qquad \forall \text{length} \in \text{rcl} \\
&\mu_{\text{rcd}_{ijk}}(\text{depth}) = w_{ijk} \ \wedge \ \mu_{\text{rcd}_{ijk}}(\text{depth}) \qquad \forall \text{depth} \in \text{rcd}
\end{aligned}
\tag{4.5}
$$

The overall conclusion by combining the output can be written as follows

$$
\begin{aligned}
&\mu_{\text{rcl}}(\text{location}) = \mu_{\text{rcl}_{111111}}(\text{location}) \ \vee \ldots \vee \ \mu_{\text{rcl}_{ijk}}(\text{location}) \ \vee \ldots \vee \ \mu_{\text{rcl}_{131313}}(\text{location}) \\
&\mu_{\text{rcd}}(\text{depth}) = \mu_{\text{rcd}_{111111}}(\text{depth}) \ \vee \ldots \vee \ \mu_{\text{rcd}_{ijk}}(\text{depth}) \ \vee \ldots \vee \ \mu_{\text{rcd}_{131313}}(\text{depth})
\end{aligned}
\tag{4.6}
$$

The crisp values of thw relative crack location and relative crack depth are computed using the center of gravity method (Parhi, 2005) as

$$
\begin{aligned}
&\text{Relative crack location} \ = \ \text{rcl} \ = \ \frac{\int \text{location} \, \mu_{\text{rcl}}(\text{location}) \, d\text{location}}{\int \mu_{\text{rcl}}(\text{location}) \, d\text{location}} \\
&\text{Relative crack depth} \ = \ \text{rcd} \ = \ \frac{\int \text{depth} \, \mu_{\text{rcd}}(\text{depth}) \, d\text{depth}}{\int \mu_{\text{rcd}}(\text{depth}) \, d\text{depth}}
\end{aligned}
\tag{4.7}
$$

## 5. Analysis of fault detection using simple differential evolution algorithm (DEA)

Differential Evolution (DE) which utilizes $N_P$ $D$-dimensional vectors of real valued parameters is a parallel direct search method. $P(G)$ is the current population composed of encoded with individuals $X_i$. Figure 4 describes the idea of the Differential Evolution Algorithm which has been used for crack detection in the current research work.

Here $X_i = \{x_1, x_2, x_3, x_4, x_5\}$, where $x_1$ – rfnf, $x_2$ – rsnf, $x_3$ – rtnf, $x_4$ – rcd, $x_5$ – rcl, $G$ – number of generations, $D$ – number of parameters.
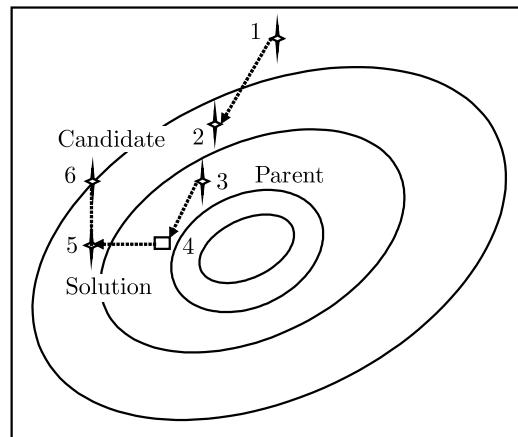


Fig. 4. Differential evolution algorithm

The following steps describe the algorithm for Differential Evolution Algorithm.

1. Read the parameters – scaling factor $F$, crossover constant $C_r$, population size $N_p$, maximum iterations $G_{max}$ and decision variables $D$ (i.e. rfnf, rsnf, rtnf, rcd and rcl).

2. Set the iteration $G = 0$, population index $i = 1$, set the decision variable $j = 1$.

3. Initialise the parent vector uniformly in the random search space. The initial value of the $j$-th parameter in the $i$-th individual at the generation $G = 0$ is given as

$$x_{j,i}^{(0)} = x_j^{min} + \text{rand}_j(0,1)(x_j^{max} - x_j^{min}) \qquad j = 1, \ldots, D \qquad i = 1, \ldots, N_p \qquad (5.1)$$

4. Once initialised, DE mutates the population to produce a population of $N_p$ mutant vectors

$$X_i^{'(G)} = X_a^G + F(X_b^G - X_c^G) \qquad i = 1, \ldots, N_p \qquad (5.2)$$

The indices $a$, $b$ and $c$ are randomly chosen. These indices are different from each other and from the base vector index $i$. The scaling factor $F$ is a real and constant factor $F \in [0, 2]$. As this constant is used in the mutation operator and used to control the rate at which the population evolves, here in the current paper it is taken as 0.3.

5. After mutation, uniform crossover is employed to generate trial vectors $X_i''$ by mixing the mutant vectors and target vectors $X_i$

$$X_{j,i}^{''(G)} = \begin{cases} X_{j,i}^{'(G)} & \text{if} \quad \text{rand}_j(0,1) \leqslant C_r \ \vee \ j = j_{\text{rand}} \\ X_{j,i}^{(G)} & \text{otherwise} \end{cases} \qquad (5.3)$$

The crossover operation is applied to each pair of the target vector $X_i$ and its corresponding mutant vector $X_i'$ to generate the trial vector $X_i''$.

The crossover probability is a user defined value. The crossover probability is defined as $C_r \in (0, 1)$ and in this work it is taken as 0.6. The crossover operator copies the $j$-th parameter of the mutant vector $X_i'$ to the corresponding parameter of the trial vector $X_i''$ if $\text{rand}_j(0,1) \leqslant C_r$, otherwise it is copied from the corresponding target vector $X_i$.

6. Sometimes the upper and lower bounds of the newly generated trial vectors exceed the given value and then they are randomly and uniformly initialised to the initial value given previously. The objective function values of all trial vectors are evaluated. Then the selection operator (according to the fitness rank) determines the population by choosing between the trial vectors and their predecessors (target vectors):

   a) if the trial vector $X_i^{''(G)}$ has an equal or lower fitness function value (optimal) than that of its target vector $X_i^{(G)}$, it replaces the target vector in the next generation,

   b) otherwise, the target vector retains its place in the population for at least one more generation

$$X_i^{(G+1)} = \begin{cases} X_i^{''(G)} & \text{if} \quad f(X_i^{''(G)}) \leqslant f(X_i^{''(G)}) \qquad i = 1, \ldots, N_p \\ X_i^{(G)} & \text{otherwise} \end{cases} \qquad (5.4)$$

7. Once the new population is installed, the process of mutation, crossover and selection is repeated for several generations.

8. The algorithm stops after reaching threshold values for the target vector.

The hybridized methodology consists of three major steps, i.e., preprocessing, processing, postprocessing. In the preprocessing, the individual solutions are fed to the DEA. Then the fuzzy rules using DEA in this step are fed to the Fuzzy Inference System (FIS) for the implementation and aggregation of the fuzzy rules. In the postprocessing, the results from the FIS are defuzzified to give the crisp result (rcd, rcl) from the methodology. Figure 5 describes the proposed methodology in the pictorial form.
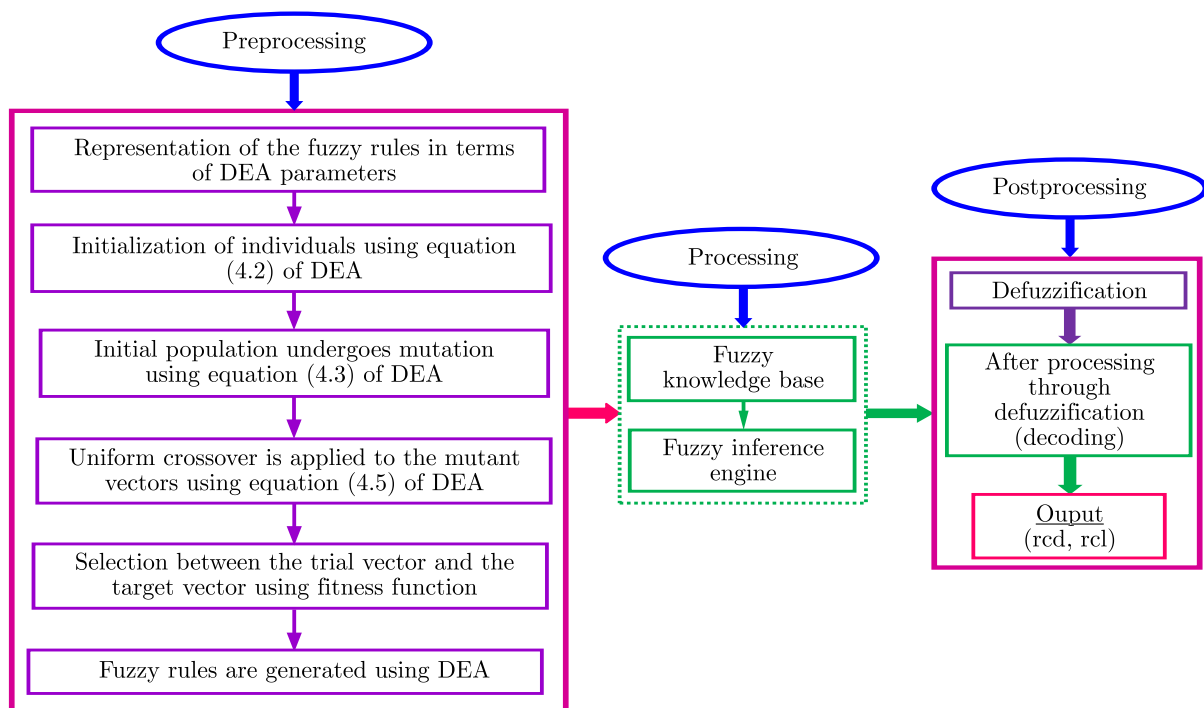


Fig. 5. Pictorial presentation of DEAFL system

Following are the steps used for computation of MF using Differential Evolution Algorithm (DEA) described in detail.

1. In the first step of hybridisation of the DEA and FLS is to represent the fuzzy rules in terms of DEA parameters.

Here $X_i$, which is an individual in the population of DEA, represents the fuzzy rule, where $x_1$, $x_2$, $x_3$, $x_4$, $x_5$ represent the linguistic variables of fuzzy membership functions in the fuzzy rule.

2. Then initialisation takes place using equation (5.1) of DEA.

3. The initial population undergoes mutation using equation (5.2) of DEA.

4. Then uniform crossover is applied to the mutant vectors using equation (5.3) of DEA.

5. A fitness function is used to make selection between the trial vector and the target vector, whichever becomes the best fit replaces the target vector in the next generation. Otherwise, if the stopping criteria are met, the algorithm stops making the current target vector as the best solution (fuzzy rule).

6. Likewise when some (Musmar *et al.*, 2014) fuzzy rules are generated using DEA, they are fed to the Mamdani fuzzy inference system.

7. After the implementation and aggregation of the fuzzy rules in the inference system, the results are defuzzified using centroid defuzzification.

8. The defuzzification process shows the crisp output from the fuzzy inference system.

## 6. Experimental set-up used in the fault detection of the cracked beam

The instruments used in free vibration analysis of the fixed-fixed beam are an impact hammer, vibration pick-up, vibration analyzer and vibration indicator. Using the impact hammer, the cracked fixed-fixed beam is excited in the free vibration mode. The vibration analyzer is PULSE LAB Prolite 3560. The excitation parameters are picked up by the vibration pick-up or accelerometer. Then these parameters are fed to the vibration analyzer, where the parameters are analyzed, and the results are shown in the vibration indicator.

Several tests are conducted using the experimental setup (Fig. 6) on aluminium alloy beam specimens (800 mm×38 mm×6 mm) with a transverse crack for determining the natural frequencies at different crack locations and crack depths. These specimens are given vibration by the impact hammer, and the 1st, 2nd and 3rd natural frequencies are recorded in the vibration indicator. The schematic diagram of the experimental set-up is shown in Fig. 7.
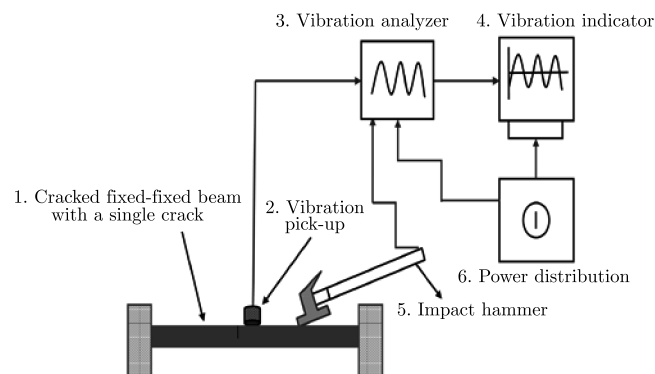


Fig. 6. Schematic diagram of experimental set-up; 1 – cracked fixed-fixed beam with a single crack, 2 – vibration pick-up, 3 – vibration analyzer, 4 – vibration indicator, 5 – impact hammer, 6 – power distribution

## 7. Results and discussion

The results found from the application of the algorithms are given in this Section. The formula used for calculation of the errors is given in Eqs. (7.1) and (7.2).

The percentage error in FEA is calculated using the following formula

$$\frac{\text{FEA result} - \text{Result from the proposed technique}}{\text{F}EA\, result} \cdot 100 \tag{7.1}$$

The percentage error in the experimental work is calculated using the following formula

$$\frac{\text{Exp. result} - \text{Result from the proposed technique}}{\text{E}xp.result} \cdot 100 \tag{7.2}$$

**Table 1.** Comparison of the results from FLS and FEA

| No. | rfnf from FEA | rsnf from FEA | rtnf from FEA | red from FEA | rcl from FEA | red using the FLS technique | rcl using the FLS technique | percent. error rcd | percent. error rcl |
|-----|------|------|------|---------|---------|----------|----------|------|------|
| 1 | 0.9952 | 0.9992 | 0.9944 | 0.28125 | 0.5625 | 0.272194 | 0.543206 | 3.22 | 3.43 |
| 2 | 0.9958 | 0.9998 | 0.9940 | 0.25 | 0.46875 | 0.241275 | 0.451922 | 3.49 | 3.59 |
| 3 | 0.9960 | 0.9999 | 0.9987 | 0.25 | 0.25 | 0.2412 | 0.240325 | 3.52 | 3.87 |
| 4 | 0.9969 | 0.9969 | 0.9952 | 0.1875 | 0.5 | 0.181106 | 0.4817 | 3.41 | 3.66 |
| 5 | 0.9705 | 0.9703 | 0.9700 | 0.2166 | 0.5 | 0.209301 | 0.4811 | 3.37 | 3.78 |

**Table 2.** Comparison of the results from FLS and experimental analysis

| No. | rfnf from FEA | rsnf from FEA | rtnf from FEA | red from FEA | rcl from FEA | red using the FLS technique | rcl using the FLS technique | percent. error rcd | percent. error rcl |
|-----|------|------|------|---------|--------|----------|----------|------|------|
| 1 | 0.9988 | 0.9993 | 0.9976 | 0.15625 | 0.3125 | 0.150703 | 0.300438 | 3.55 | 3.86 |
| 2 | 0.99979 | 0.9960 | 0.9996 | 0.333 | 0.3125 | 0.320712 | 0.300156 | 3.69 | 3.95 |
| 3 | 0.9552 | 0.9551 | 0.9549 | 0.2833 | 0.375 | 0.272025 | 0.362138 | 3.98 | 3.43 |
| 4 | 0.9211 | 0.9219 | 0.9218 | 0.4 | 0.25 | 0.38436 | 0.24055 | 3.91 | 3.78 |
| 5 | 0.9463 | 0.9460 | 0.9458 | 0.367 | 0.3125 | 0.353127 | 0.300969 | 3.78 | 3.69 |

**Table 3.** Comparison of the results from DEAFLS and FEA

| No. | rfnf from FEA | rsnf from FEA | rtnf from FEA | red from FEA | rcl from FEA | red using the FLS technique | rcl using the FLS technique | percent. error rcd | percent. error rcl |
|-----|------|------|------|---------|---------|----------|----------|------|------|
| 1 | 0.9952 | 0.9992 | 0.9944 | 0.28125 | 0.5625 | 0.274753 | 0.549338 | 2.31 | 2.34 |
| 2 | 0.9958 | 0.9998 | 0.9940 | 0.25 | 0.46875 | 0.24365 | 0.458531 | 2.54 | 2.18 |
| 3 | 0.9960 | 0.9999 | 0.9987 | 0.25 | 0.25 | 0.2444 | 0.24395 | 2.24 | 2.42 |
| 4 | 0.9969 | 0.9969 | 0.9952 | 0.1875 | 0.5 | 0.183544 | 0.4871 | 2.11 | 2.58 |
| 5 | 0.9705 | 0.9703 | 0.9700 | 0.2166 | 0.5 | 0.211467 | 0.48635 | 2.37 | 2.73 |

In this paper, the bootstrap method has been adapted to find the average error rates. The bootstrap method is a statistical method for obtaining an estimate of the error. The results of the methods with 95% confidence intervals are provided in Table 5. As the confidence interval is taken as 95%, the formula for determination of the average error rates is

$$\mu - 1.96\frac{s}{\sqrt{n}} < \text{ mean error } < \mu + 1.96\frac{s}{\sqrt{n}} \tag{7.3}$$

where $\mu$ – mean, $s$ – standard deviation, $n$ – sample population.

**Table 4.** Comparison of the results from DEAFLS and Experimental Analysis

| No. | rfnf from FEA | rsnf from FEA | rtnf from FEA | red from FEA | rcl from FEA | red using the FLS technique | rcl using the FLS technique | percent. error rcd | percent. error rcl |
|---|---|---|---|---|---|---|---|---|---|
| 1 | 0.9988 | 0.9993 | 0.9976 | 0.15625 | 0.3125 | 0.152469 | 0.304563 | 2.42 | 2.54 |
| 2 | 0.99979 | 0.9960 | 0.9996 | 0.333 | 0.3125 | 0.324375 | 0.303781 | 2.59 | 2.79 |
| 3 | 0.9552 | 0.9551 | 0.9549 | 0.2833 | 0.375 | 0.275594 | 0.366563 | 2.72 | 2.25 |
| 4 | 0.9211 | 0.9219 | 0.9218 | 0.4 | 0.25 | 0.38936 | 0.242825 | 2.66 | 2.87 |
| 5 | 0.9463 | 0.9460 | 0.9458 | 0.367 | 0.3125 | 0.356247 | 0.303688 | 2.93 | 2.82 |

**Table 5.** Results from the bootstrap method with 95% confidence intervals

| Table 1 | | Table 2 | | Table 3 | | Table 4 | |
|---|---|---|---|---|---|---|---|
| rcd | rcl | rcd | rcl | rcd | rcl | rcd | rcl |
| 3.298398-3.505602 | 3.516654-3.815346 | 3.631526-3.932474 | 3.567417-3.916583 | 2.174495-2.453505 | 2.263439-2.636561 | 2.500648-2.827352 | 2.426724-2.881276 |

The performance of the Fuzzy Logic Controller depends on the fuzzy membership functions and fuzzy rules. So, it is very much needed to optimize or adjust the parameters according to the problem domain. Fuzzy rules are usually generated using linguistic terms in the if-then format, and it largely depends on the human expertise to derive them. In all conditions, the correct choice of the fuzzy membership function with the linguistic variables plays an important role in the performance of the Fuzzy Logic Controller.

It is very difficult to present the expert's knowledge perfectly through the linguistic variables, always. The rule base of the Fuzzy Logic Controller has many parameters which must be adjusted. These parameters are capable to alter or modify the controller performance.

The previous work proposed by different researchers (automatic design of the fuzzy membership function) still required human experts to handle the control system. In those works, only the membership functions were optimized. Fuzzy rules which form the skeleton of the fuzzy rule based system still needs human expertise for its generation. So, in order to overcome the above stated problems, a method to produce fuzzy rules automatically is proposed in this work.

## 8. Conclusion

A method for crack prediction in beam-like structures has been designed and developed using a clonal selection algorithm and fuzzy logic. It is found that the presence of cracks has a remarkable effect on the dynamic characteristics of the beam under consideration. Theoretical, finite element and experimental analysis have been carried out to calculate vibration parameters. These vibration parameters have been used to make a database and subsequent design of the hybrid system. Different operations like crossover and mutation used in the clonal selection algorithm are given in detail. Likewise, different parameters of the fuzzy logic are also discussed.

Table 1 and 3 provide a comparison of the results from FEA with the results from FLS and DEAFLS, respectively. Similarly Table 2 and 4 provide a comparison of the results of the experimental analysis with FLS and DEAFLS, respectively.

The error for FLS is found to be 3.402% and 3.666% in comparison with the results from FEA for rcd and rcl. In comparison with the results of the experimental analysis for rcd and rcl, the errors are found to be 3.782% and 3.742%. While applying DEAFLS to the current problem, the errors are found to be 2.314% and 2.45% in comparison with the results from FEA for rcd and rcl. While comparing with the results of the experimental analysis for rcd and rcl, the errors are

found to be 2.664% and 2.654%, respectively. From the results and errors, it can be concluded that the proposed method of fusion of the fuzzy logic system and the differential evolution algorithm gives better results than the logic system standalone. This improvement occurs due to some automation of generation of fuzzy rules using the differential evolution algorithm. So, this method can be used as a robust tool for online damage detection of cracked structures as well as other engineering applications.

# References

1. AMALI S.M.J., BASKAR S., 2013, Fuzzy logic-based diversity-controlled self-adaptive differential evolution, *Engineering Optimization*, **45**, 8,899-915

2. CADDEMI S., MORASSI A., 2013, Multi-cracked Euler-Bernoulli beams: mathematical modeling and exact solutions, *International Journal of Solids and Structures*, **50**, 944-956

3. DANESHMEHR A.R., NATEGHI A., INMAN D.J., 2013, Free vibration analysis of cracked composite beams subjected to coupled bending-torsion loads based on a first order shear deformation theory, *Applied Mathematical Modelling*, 1-18

4. DASH A.K., PARHI D.R., 2014, Analysis of an intelligent hybrid system for fault diagnosis in cracked structure, *Arabian Journal for Science and Engineering*, **39**, 1337-1357

5. DEWHIRST O.P., SIMPSON D.M., ANGARITA N., ALLEN R., 2010, Wiener-Hammerstein parameter estimation using differential evolution, *International Conference on Bio-inspired Systems and Signal Processing*, 271-276

6. GANGULI R., 2001, A fuzzy logic system for ground based structural health monitoring of a helicopter rotor using modal data, *Journal of Intelligent Material Systems and Structures*, **12**, 397-407

7. JIAO Y.B., LIU H.B., CHENG Y.C., GONG Y.F., 2015, Damage identification of bridge based on Chebyshev polynomial fitting and fuzzy logic without considering baseline model parameters, *Shock and Vibration*, 1-10

8. KHIEM N.T., TRAN H.T., 2013, A procedure for multiple crack identification in beam-like structures from natural vibration mode, *Journal of Vibration and Control*, 1-11

9. MUSMAR M.A., RJOUB M.I., HADI M.A.A., 2014, Nonlinear finite element analysis of shallow reinforced concrete beams using solid 65 element, *ARPN Journal of Engineering and Applied Sciences*, **9**, 2, 85-89

10. NERI F., 2008, On memetic differential evolution frameworks: a study of advantages and limitations in hybridization, *IEEE*, 2135-2142

11. PARANDAMAN P., JAYARAMAN M., 2014, Finite element analysis of reinforced concrete beam retrofitted with different fiber composites, *Middle-East Journal of Scientific Research*, **22**, 7, 948-953

12. PARHI D.R., 2005, Navigation of mobile robot using a fuzzy logic controller, *Journal of Intelligent and Robotic Systems: Theory and Applications*, **42**, 3, 253-273

13. PAWAR R.S., SAWANT S.H., 2014, An overview of vibration analysis of cracked cantilever beam with non-linear parameters and harmonic excitations, *International Journal of Innovative Technology and Exploring Engineering*, **8**, 3, 53-55

14. QIN A.K., SUGANTHAN P.N., 2005, Self-adaptive differential evolution algorithm for numerical optimization, *IEEE Explore 2005*, 1785-1791

15. SINHA J.K., FRISWELL M.I., EDWARDS S., 2002, Simplified models for the location of cracks in beam structures using measured vibration data, *Journal of Sound and Vibration*, **251**, 1, 13-38

16. STORN R., PRICE K., 1997, Differential evolution – a simple and efficient heuristic for global optimization over continuous spaces, *Journal of Global Optimization*, **11**, 341-359

17. Tada H., Paris P.C., Irwin G.R., 1973, *The Stress Analysis of Cracks Handbook*, Del. Research Corporation, Hellertown

18. Tang Y., 2012, Parameter estimation of Wiener model using differential evolution algorithm, *International Journal of Circuits, Systems and Signal Processing*, **6**, 5, 315-323

19. Thangaraj R., Pant M., Abraham A., Bouvry P., 2010, Particle swarm optimization: hybridization perspectives and experimental illustrations, *Applied Mathematics and Computation*, 1-19

20. Thatoi D.N., Choudhury S., Jena P.K., 2014, Fault diagnosis of beam-like structure using modified fuzzy technique, *Advances in Acoustics and Vibration*, 1-18

21. Xue F., Sanderson A.C., Bonissone P.P., Graves R.J., 2005, Fuzzy logic controlled multi-objective differential evolution, *IEEE Conference on Fuzzy Systems*, 720-725

22. Zadeh L.A., 1965, Fuzzy sets, *Information and Control*, **8**, 338-353

# EXPERIMENTAL STUDY OF THE SHEAR RESISTANCE OF GRANULAR MATERIAL: INFLUENCE OF INITIAL STATE

Abdelhamid Flitti, Noureddine Della

*Laboratory of Material Sciences and Environment (LMSE), University Hassiba Benbouali of Chlef (Algeria)*
*e-mail: n.della@univ-chlef.dz*

Ramiro D. Verástegui Flores

*iMMC, Catholic University of Louvain (Belgium)*

The shear strength of sand and its mechanical properties can be affected by numerous parameters. This work presents an experimental investigation which aims to study the influence of the fines content, the depositional method and the grain size on the shear strength of Chlef sand. Tests were conducted with the shear box on two types of soil, the natural sand and the clean sand-silt mixture. Dense samples ($Dr = 88\%$) were reconstituted through dry deposition for each type of the material. An additional series of tests was carried out on a medium dense natural sand ($Dr = 52\%$) prepared by dry and wet ($w = 3\%$) deposition methods. All specimens were subjected to normal stresses of $100\,\mathrm{kPa}$, $200\,\mathrm{kPa}$ and $300\,\mathrm{kPa}$ and there was no immersion of water. The tests results show that the behavior of sand can be affected by three parameters, the fines content, the deposition method and the particle size. The maximum shear stress and the friction angle decrease as the fines content increases, the initial water content increases, the effective grain size diameter decreases and the uniformity coefficient increases. The cohesion intercept increases with the increasing fines content and decreasing initial water content. Overall, the samples prepared by the dry deposition method show more resistance than those prepared by the wet deposition method. The results obtained are generally in agreement with the previous research on drained and undrained saturated sand in the literature.

*Keywords:* dry sand, fine content, water content, grain size, depositional method

## 1. Introduction

Soil of the Chlef region is vulnerable to earthquakes and its mechanical effects as the north of Algeria is a part of the African tectonic plate. On October 10th 1980, the Chlef region was hit by an earthquake of magnitude 7.3 [12], considered the strongest in its history. Much damage occurred due to landslides, pavement deformation and liquefaction [3]. Due to all these facts, the characterization of the mechanical behavior of soil of this region and especially the sand of Chlef river is of relevance to mitigate and prevent similar disaster in the future.

The shear strength of soil was studied through the direct shear test. The experiment showed that very similar shear strength results could be obtained on saturated sand and dry sand, provided that the sand remained saturated and that drainage took place freely during shear, and in both cases the effective stresses were equal to the total stresses (Head and Epps, 2011).

The behavior of saturated Chlef sand is the topic of study of many researchers, but studies conducted on the dry chlef sand are rare in the literature.

The objective of this research was to study the effect of the fines content, the deposition method and the particle size on the shear strength of the dry Chlef sand (without saturation by immersion in water) using the direct shear apparatus.

## 2. Literature review

The effect of the fines content and the sample preparation method on the liquefaction resistance of saturated soil was the subject of some controversial research, because no consensus could be found in the literature.

Researchers who studied the effect of the fines content on the resistance of saturated soils are divided into three groups; some say that an increase in the fines content increases the liquefaction resistance (Chang *et al.*, 1982; Amini and Qi, 2000), others say that it reduces the liquefaction resistance (Shen *et al.*, 1977; Troncosco and Verdugo, 1985; Finn *et al.*, 1994; Vaid, 1994; Zlatovic and Ishihara, 1997; Arab, 2009; Belkhatir *et al.*, 2013, 2014), while the third group of researchers conclude that the liquefaction resistance decreases with an increasing fines content to a minimum value, then it rises (Law and Ling, 1992; Koester, 1994; Bouferra and Shahrour, 2004).

The results obtained on the effect of the depositional method are not all in agreement, some authors found that the samples prepared by the sedimentation method present a higher resistance to liquefaction than the samples prepared by other methods such as the dry funnel pluviation and the wet deposition (Zlatovic and Ishihara, 1997); others found that the liquefaction resistance of the samples prepared by the wet deposition is larger than that of samples prepared by the dry funnel pluviation (Mulilis *et al.*, 1977; Yamamuro and Wood, 2004). Canou (1989), Ishihara (1993), Benahmed *et al.* (2004) found that the resistance of the samples prepared by the dry funnel pluviation is more elevated than by the wet deposition method. The tests performed by Della *et al.* (2009) on saturated Chlef sand confirmed this result, showing that the dry funnel pluviation method gives stable samples (dilating) while the wet deposition method encourages contractance.

It is known in the literature that the particle size significantly affects the resistance to soil liquefaction. Whether from studies conducted in the laboratory (Lee and Fitton, 1968) or in situ observations (Tsuchida, 1970; Seed and Idriss, 1971), many boundaries of particle size distribution curves have been proposed to identify liquefiable soils. To study the effect of grain size, a series of undrained tests were performed by Belkhatir *et al.* (2011). They found that the undrained shear strength at the peak and the undrained residual shear strength decreased as the coefficient of uniformity increased while the average diameter decreased and fines content increased up to 50%.

Due to the lack of studies conducted on the unsaturated sand of Chlef region (Northern Algeria), it was suggested to study the effect of the fines content, the deposition method and the particle size on the shear strength of the dry Chlef sand (without saturation by immersion in water) using the direct shear apparatus.

## 3. Material tested

The tests were realized on sand from the Chlef river (which crosses the city of Chlef to the west of Algiers). However, two types of the Chlef sand were used; the natural sand and the clean sand mixed with different fractions of silt (from 0% to 40%). The Chlef river silt shows low plasticity with a plasticity index equal to 5.81%. Figure 1 shows microphotographs of the natural and the clean sand. The properties of the natural sand, the clean sand-silt mixture and the silt used in this study are illustrated in Table 1. The grain size distribution curves of the tested soils are shown in Fig. 2.

Figure 3 shows the variation of the maximum and the minimum void ratio with the fines content. It is clear that both decrease with the increasing fines content ($Fc$) up to a value $Fc = 30\%$ beyond which they begin to increase following the same trend (similar observation were reported by Belkhatir *et al.* (2013)).
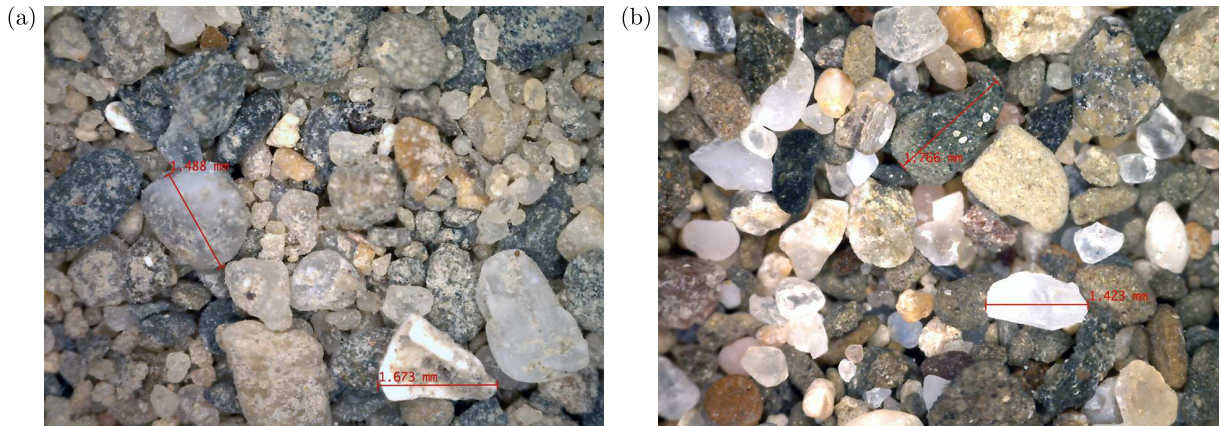
Fig. 1. Microphotographs: (a) Chlef natural and (b) Chlef clean sand (zoom 50x)

**Table 1.** Index properties of materials used

| Material | $Fc$ [%] | $G_S$ [g/cm$^3$] | $e_{min}$ | $e_{max}$ | $D_{10}$ [mm] | $D_{30}$ [mm] | $D_{50}$ [mm] | $D_{60}$ [mm] | $C_U$ | $C_C$ |
|---|---|---|---|---|---|---|---|---|---|---|
| Natural sand | 1 | 2.700 | 0.586 | 0.946 | 0.171 | 0.311 | 0.463 | 0.538 | 3.153 | 1.055 |
| Clean sand | 0 | 2.652 | 0.632 | 0.795 | 0.266 | 0.431 | 0.596 | 0.700 | 2.634 | 0.999 |
| Silty sand | 10 | 2.654 | 0.536 | 0.703 | 0.077 | 0.369 | 0.549 | 0.643 | 8.304 | 2.733 |
| (clean sand | 20 | 2.655 | 0.458 | 0.697 | 0.029 | 0.298 | 0.510 | 0.616 | 21.622 | 5.058 |
| + fines | 30 | 2.657 | 0.449 | 0.687 | 0.017 | 0.087 | 0.420 | 0.535 | 30.630 | 0.811 |
| content) | 40 | 2.658 | 0.504 | 0.759 | 0.011 | 0.057 | 0.307 | 0.437 | 38.305 | 0.662 |
| Silt | 100 | 2.667 | 0.991 | 1.563 | – | 0.015 | 0.029 | 0.036 | – | – |
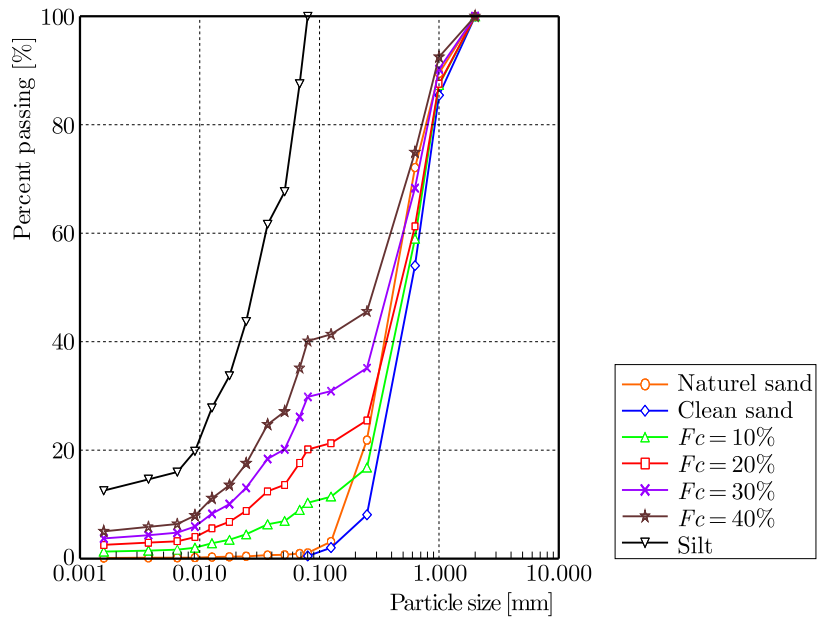


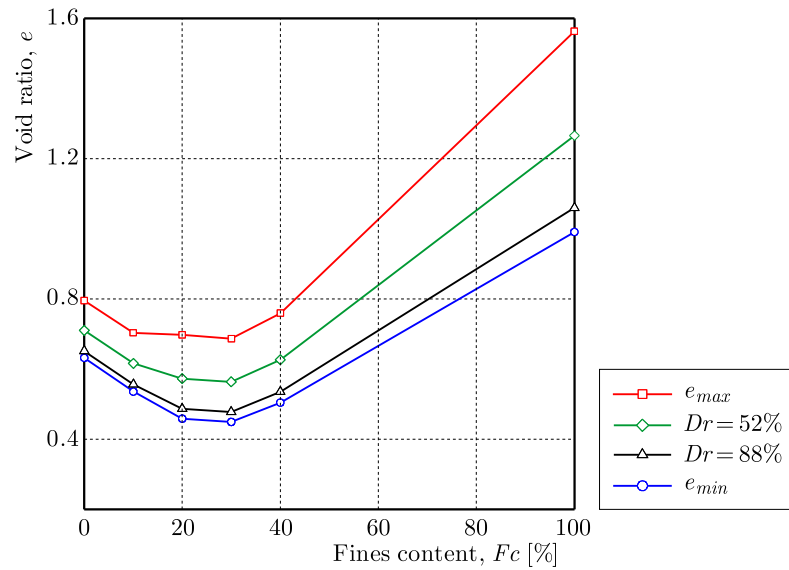Fig. 2. Grain size distributed curves of the tested materials

Fig. 3. Maximum and minimum void ratios versus fines content

## 4.   Experimental program

In this study, a series of tests were performed on the natural sand and the clean sand-silt mixture for a relative density $Dr = 88\%$ (also $Dr = 52\%$ for some tests) under three normal stresses $\sigma_N = 100$ kPa, 200 kPa and 300 kPa. To study the effect of the depositional method, dry or wet, the initial water contents were set to $w = 0\%$ and 3%, respectively.

The tests were performed using a square direct shear box $60 \times 60$ mm². The initial sample height was 25 mm. The test consisted in placing a sample in the shear box and subjecting it to a vertical load $N$ that represented the normal stress applied (100 kPa, 200 kPa, 300 kPa) and a horizontal load $T$ which was gradually increased. The direct shear test allowed measuring the peak and residual shear strength corresponding to every normal stress.

Two methods were used to set-up the sample, the dry deposition and the wet deposition methods. In the wet deposition method, the dry sand was mixed thoroughly with a small quantity of water (3%) until a homogeneous soil sample was obtained. In the dry deposition method, the sand was deposited in the dry state. To achieve the two relative densities, the sample was divided into three layers. Each layer was compacted to achieve the dense state ($Dr = 88\%$), however, no compaction was necessary to achieve the medium dense state ($Dr = 52\%$), so only the sample surface was leveled off. After the set-up, the samples were sheared at a constant speed (1 mm/min).

## 5.   Test results

### 5.1.   Effect of fines content

To study the effect of fines content on the shear strength of dry sand, five samples of sand-silt mixture ($Fc = 0\%$ to 40%) were tested under three normal stresses. Figure 4a shows the effect of the fines content on the shear stress of dry sand ($\sigma_N = 300$ kPa, $Dr = 88\%$). For samples with $Fc = 0\%$ to 20%, the mobilized shear stress increased with the increasing horizontal displacement to reach the maximum value (located between 2 and 3 mm) and then it gradually decreased; whereas the mobilized shear stress of samples with $Fc = 30\%$ and $Fc = 40\%$ did not show the peak value (Fig. 4a).

Figure 4b shows the Mohr-Coulomb failure envelope that represents the relationship between the maximum shear stress $\tau_{max}$ and the normal stress $\sigma_N$ according to the following formula

$$\tau_{max} = C + \sigma_N \tan\varphi \tag{5.1}$$

where $C$ and $\varphi$ are the cohesion intercept and the friction angle, respectively.

Figure 4b shows clearly that the slope of the failure envelope decreases with the increasing fines content. The reliability of these results is high considering the limited spread obtained for each series of tests ($R^2 = 0.97 \sim 0.99$).
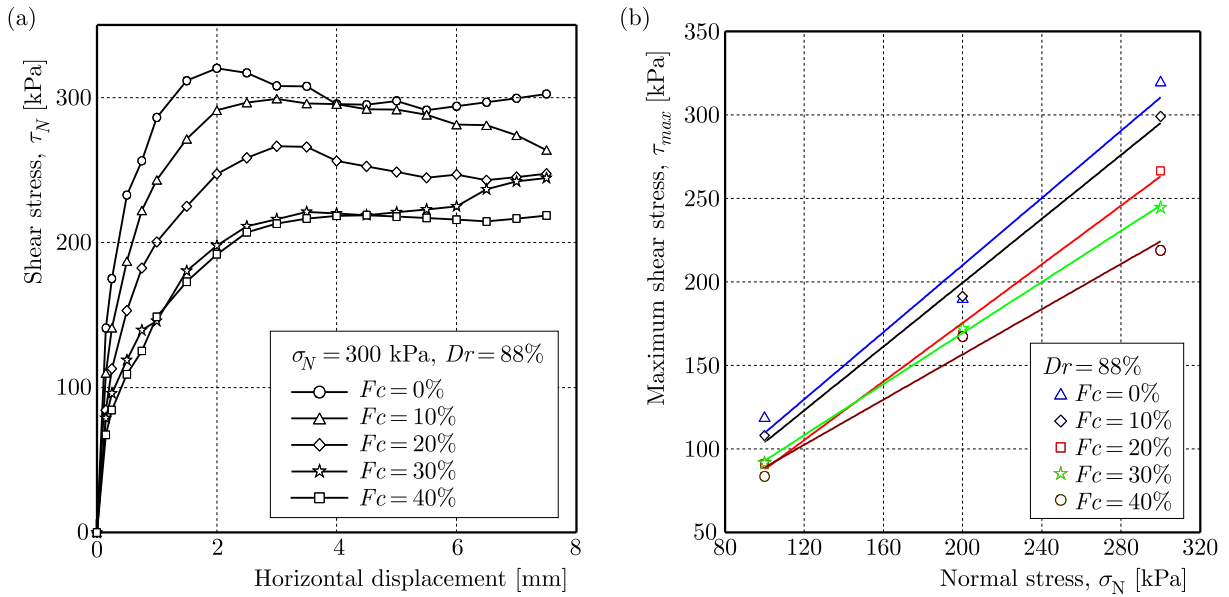


Fig. 4. Effect of the fines content on the strength: (a) shear stress versus horizontal displacement $\sigma_N = 300\,\text{kPa}$, $Dr = 88\%$, (b) maximum shear stress versus normal stress



Fig. 5. Maximum shear stress ($\tau_{max}$) versus fines content ($Fc$), $\sigma_N = 100, 200, 300\,\text{kPa}$, $Dr = 88\%$

The development of the maximum shear stress with the fines content is shown in Fig. 5. It is clear from this figure that the maximum shear stress decreases with the increasing fines content

for the three normal stresses ($\sigma_N = 100, 200, 300\,\text{kPa}$), but the decrease is more pronounced for $\sigma_N = 300\,\text{kPa}$.

Figure 6 shows the effect of the fines content on the mecanical properties (cohesion intercept and friction angle) of the sand-silt mixture for the dense state 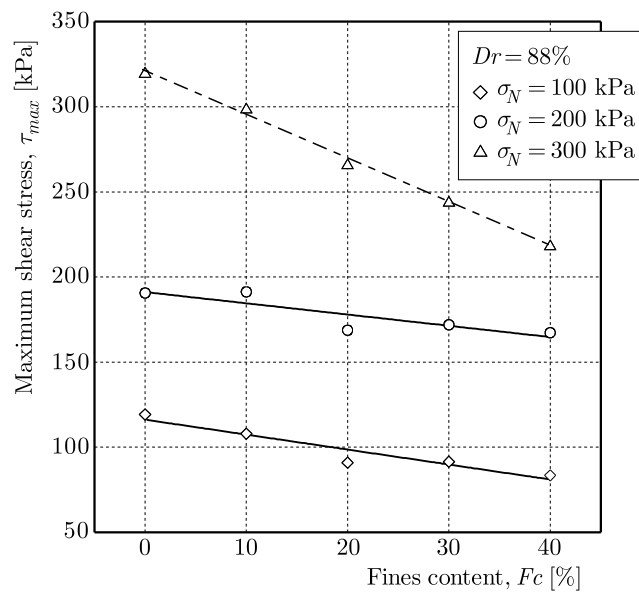($Dr = 88\%$). It can be seen that the cohesion increases with the increasing fines content (Fig. 6a). For the friction angle, it is clear that it decreases lineary with the increasing fines content (Fig. 6b). This decrease in the resistance is probably due to the presence of fine particles between grains of sand that promote reduction in the contact between sand particles. The same effect was found by Arab (2009) on the saturated sand.
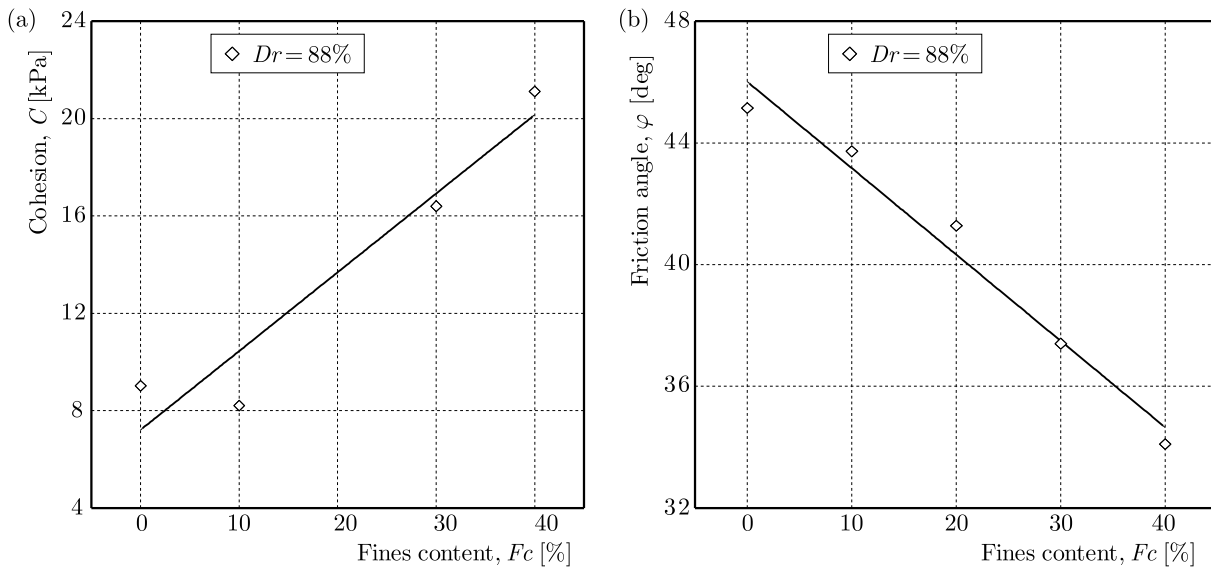


Fig. 6. Variation of mechanical properties with the fines content ($Fc$), $Dr = 88\%$: (a) cohesion versus fines content, (b) friction angle versus fines content

## 5.2. Effect of the mode of deposition

In order to study the effect of the depositional method (dry or wet), a series of tests were performed on the natural sand. Two values of initial water content were used; $w = 0\%$ for the dry case, and $w = 3\%$ for the wet case. Specimens at two relative densities were tested ($Dr = 52\%$, $Dr = 88\%$) subjected to three levels of normal stresses ($\sigma_N = 100, 200$ and $300\,\text{kPa}$).

The relationship between the mobilized shear stress and the horizontal displacement is shown in Fig. 7. For the medium dense state ($Dr = 52\%$), it is clear from Fig. 7a that the shear stress of the dry specimens rapidly increases until a horizontal displacement of about 3 mm occurs. Beyond that, the increase is less significant. The results on the specimens prepared by wet deposition show a mobilized shear stress that increases continuously with the increasing horizontal displacement. In the dense state ($Dr = 88\%$), Fig. 7b shows that the shear stress of the dry method rises to reach a peak value (between 3 mm and 6 mm), while the shear stress of the wet method keeps increasing with the horizontal displacement as in the medium dense specimens.

Figure 8 shows the variation of the maximum shear stress $\tau_{max}$ (deduced from Fig. 7) with the initial water content in the two states, the dense and the medium dense. It is clear that the maximum shear stress of the dry specimens is higher than that of the wet specimens. This result is in agreement with that obtained by Della et al. (2009) on the saturated sand. The difference in the resistance between the dry and wet deposition method is more pronounced in the dense

(a)



(b)
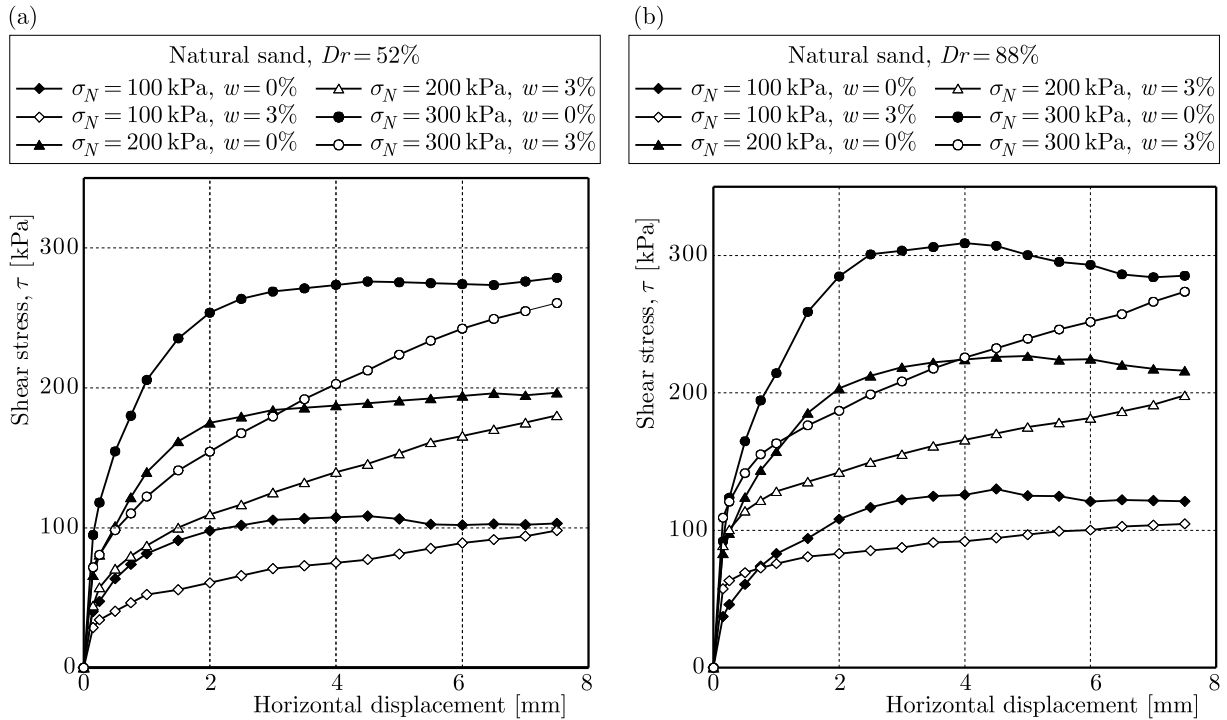
Fig. 7. Shear stress versus horizontal displacement, $\sigma_N = 100, 200$ and $300\,\text{kPa}$: (a) medium dense state $(Dr = 52\%)$, (b) dense state $(Dr = 88\%)$
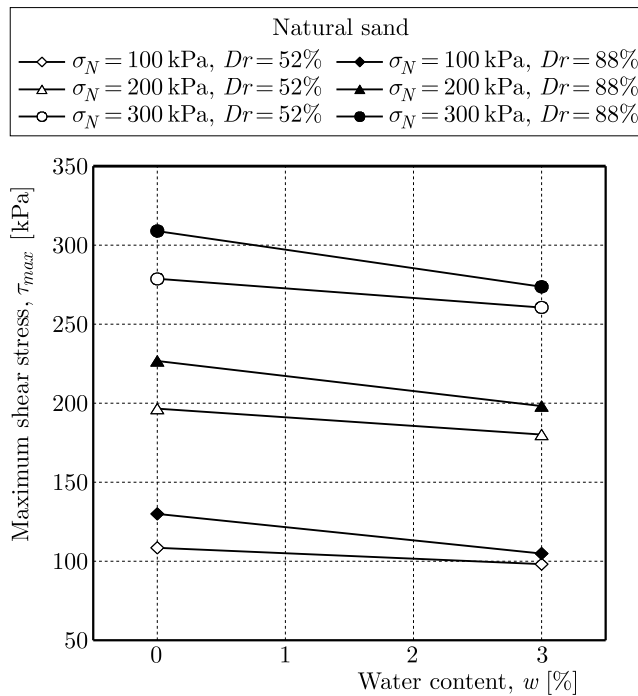


Fig. 8. Maximum shear stress $(\tau_{max})$ versus water content $(w)$, $\sigma_N = 100, 200$ and $300\,\text{kPa}$, $Dr = 52\%$ and $88\%$

state. Furthermore, the difference in the resistance between the dense state and the medium dense state is more apparent in the dry deposited samples than in the wet deposited samples.

The effect of the depositional method in terms of the initial water content on the mechanical properties of sand is shown in Fig. 9. It is clear that the cohesion intercept decreases with the increasing initial water content for both the dense and the medium dense state (Fig. 9a), but

the trend of the decrease is more pronounced in the dense state. Concerning the friction angle, it can be seen from Fig. 9b that it also decreases with the increasing initial water content with the same trend for the two relative densities. This decrease in the friction angle confirms the previous result and allows saying that the dry samples are more resistant than the wet samples.



Fig. 9. Variation of the mechanical characteristics with the initial water content ($w$), $Dr = 52\%$ and 88%: (a) cohesion versus water content, (b) friction angle versus water content

### 5.3. Effect of the particle size

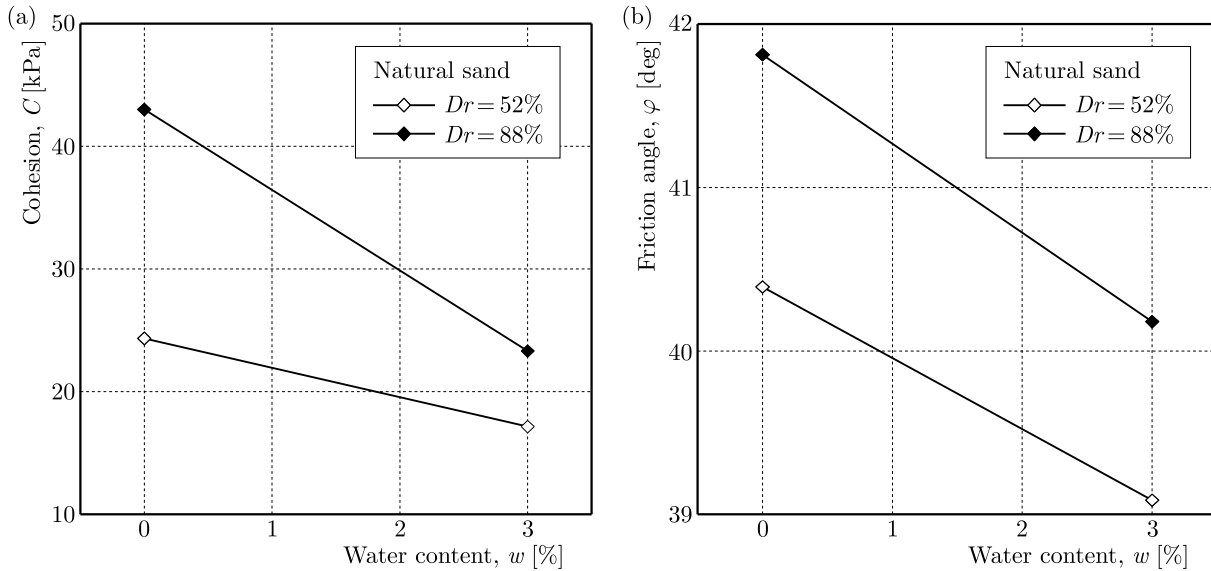Only the effective grain size diameter $D_{10}$ and the uniformity coefficient $Cu$ were chosen as parameters to study the particle size effect on the shear stress and the friction angle of the sand-silt mixture. For each normal stress level ($\sigma_N = 100$, 200 and 300 kPa), it was found that the maximum shear stress increases according to a logarithmic trend with an increasing effective grain size diameter $D_{10}$ (Fig. 10a). About the friction angle, Fig. 10b shows that it increases with the increasing effective grain size diameter and decreasing fines content.

As it is known, the uniformity coefficient ($Cu$) is a crude shape parameter (Holtz and Kovacs, 1981) and it represents the ratio of the 60% particle size ($D_{60}$) to the 10% particle size ($D_{10}$) (Head, 2006). Figure 11 shows the effect of the uniformity coefficient on the mechanical behavior of the sand-silt mixture. By increasing the fines content from 0% to 40%, the uniformity coefficient values range between 2.6 and 38.3, this is why Figs. 11a and 11b present similar tendencies and results with those of Figs. 5 and 6b, respectively showing that the maximum shear stress and the friction angle decrease linearly with the increasing uniformity coefficient. These findings are in agreement with those found by Belkhatir *et al.* (2011) on the saturated sand.

### 6. Conclusion

Results of experimental research on the influence of the fines content, the depositional method in terms of the initial water content and the grain size on the shear stress as well as the mechanical properties of Chlef river sand (natural and clean sand-silt mixture) have been presented.

Shear tests were performed in a direct shear apparatus. Two relative densities were evaluated $Dr = 52\%$ and 88% for the natural sand using two sample preparation methods, the dry deposition and the wet deposition, while only dense ($Dr = 88\%$) specimens of clean sand-silt mixture were tested using the dry deposition. The specimens were sheared dry without water immersion and they were subjected to three levels of normal stresses $\sigma_N = 100$, 200 and 300 kPa.
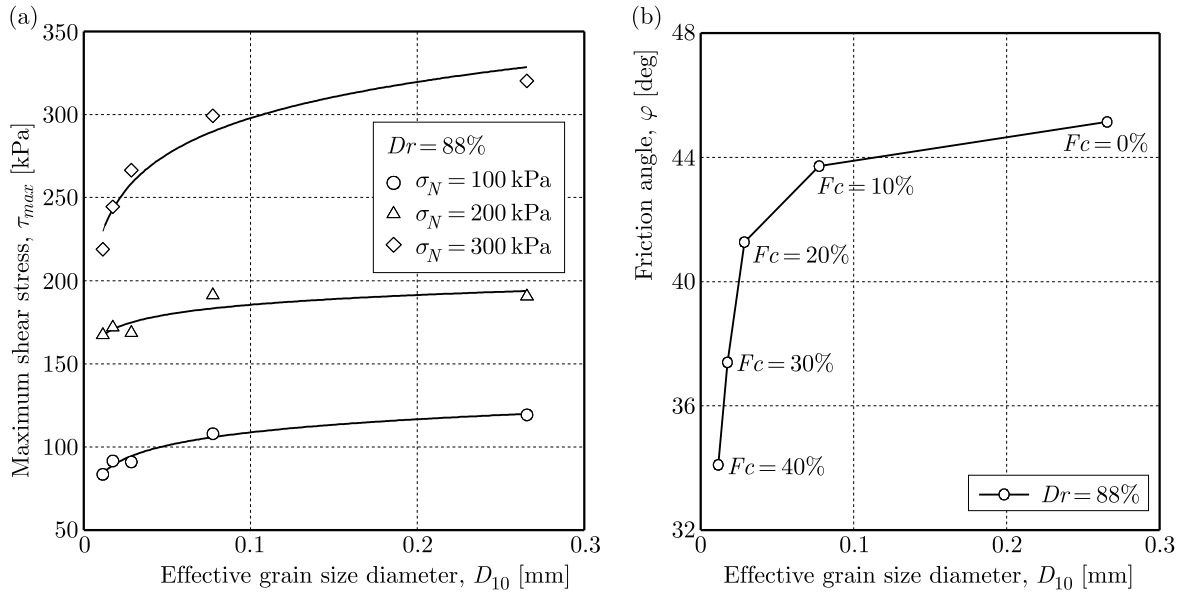
Fig. 10. Effect of the effective grain size diameter $D_{10}$: (a) maximum shear stress ($\tau_{max}$) versus the effective grain size diameter, (b) friction angle versus the effective grain size diameter
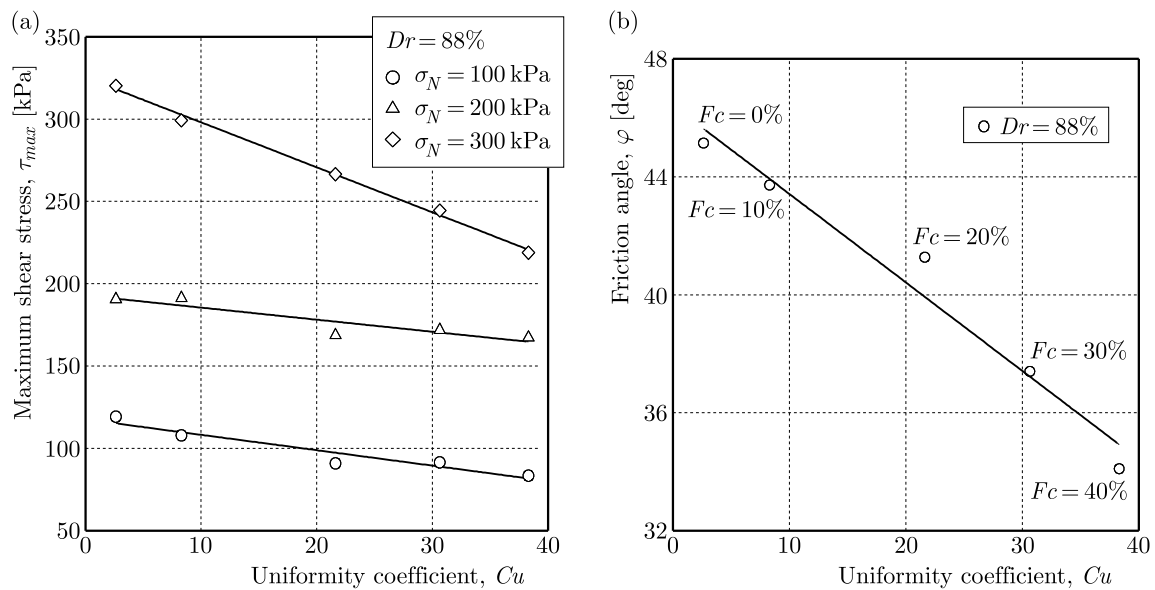


Fig. 11. Effect of the uniformity coefficient $Cu$: (a) maximum shear stress ($\tau_{max}$) versus the uniformity coefficient, (b) friction angle versus the uniformity coefficient

Test results showed that the fines content, the depositional method and the grain size affect the strength of the dry sand. It was found that by increasing the fines content, the strength of the sand-silt mixture decreases, the friction angle decreases and the cohesion increases. Concerning the effect of the depositional method, it was shown that the maximum shear stress of the dry deposited specimens was higher than that of the wet deposited specimens. Also, the friction angle and the cohesion decreased with the increasing initial water content at deposition. About the effect of the grain size, the tests illustrated that the maximum shear stress and the friction angle increased with the increasing grain size diameter $D_{10}$ and the decreasing fines content. Furthermore, the results showed that the maximum shear stress and the friction angle decreased linearly with the increasing uniformity coefficient and the fines content.

The results obtained from this study performed on the dry Chlef river sand are in agreement with those carried out on the saturated sand reported in the literature.

# References

1. AMINI F., QI G.Z., 2000, Liquefaction testing of stratified silty sands, *Journal of Geotechnical and Geoenvironmental Engineering*, **126**, 3, 208-217

2. ARAB A., 2009, Comportement monotone et cyclique dun sable limoneux, *C.R. Mecanique*, **337**, 621-631

3. Assistance pour la réalisation d'une étude de microzonation sismique dans la région de Chlef (Phase II), Résultats et recommandations du projet, Unesco, PNUD, Paris, 1985

4. BELKHATIR M., ARAB A., DELLA N., SCHANZ T., 2014, Laboratory study on the hydraulic conductivity and pore pressure of sand-silt mixtures, *Marine Georesources and Geotechnology*, **32**, 2, 106-122, DOI: 10.1080/1064119X.2012.710712

5. BELKHATIR M., ARAB A., SCHANZ T., MISSOUM H., DELLA N., 2011, Laboratory study on the liquefaction resistance of sand-silt mixtures: effect of grading characteristics, *Granular Matter*, **13**, 599-609

6. BELKHATIR M., SCHANZ T., ARAB A., 2013, Effect of fines content and void ratio on the saturated hydraulic conductivity and undrained shear strength of sand-silt mixtures, *Environmental Earth Sciences*, DOI 10.1007/s12665-013-2289-z, 2469-2479

7. BENAHMED N., CANOU J., DUPLA J.C., 2004, Structure initiale et propriétés de liquéfaction statique d'un sable, *C.R. Mecanique*, **332**, 887-894

8. BOUFERRA R., SHAHROUR I., 2004, Influence of fines on the resistance to liquefaction of a clayey sand, *Ground Improvement*, **8**, 1, 1-5

9. CANOU J., 1989, Contribution à l'étude et à l'évaluation des propriétés de liquéfaction d'un sable, Thèse de Doctorat de l'Ecole Nationale Des Ponts et Chaussées, Paris

10. CHANG N.Y., YEH S.I., KAUFMAN L.P., 1982, Liquefaction potential of clean and silty sands, *Proceedings 3rd International Earthquake Microzonation Conference*, Seattle, Washington, **2**, 1017-1032

11. DELLA N., ARAB A., BELKHATIR M., MISSOUM H., 2009, Identification of the behavior of the Chlef sand to static liquefaction, *C.R. Mecanique*, **337**, 282-290

12. El Asnam Algeria Earthquake of October 10, 1980, A Reconnaissance and Engineering Report, Earthquake Engineering Research Institute, Berkeley, California, January 1983

13. FINN W.L., LEDBETTER R.H., WU G., 1994, Liquefaction in silty soils: design and analysis, *Ground Failures Under Seismic Conditions, Geotechnical Special Publication, ASCE*, **44**, 51-76

14. HEAD K.H., 2006, *Manual of Soil Laboratory Testing, Volume 1: Soil Classification and Compaction Tests*, Third Edition, Whittles Publishing, Scotland, UK, p. 416

15. HEAD K.H., EPPS R.J., 2011, *Manual of Soil Laboratory Testing, Volume 2: Permeability, Shear Strength and Compressibility Tests*, Third Edition, Whittles Publishing, Scotland, UK, p. 499

16. HOLTZ R.D., KOVACS W.D., 1981, *An Introduction to Geotechnical Engineering*, Prentice Hall, Englewood Cliffs, New Jersey, 733 pages

17. ISHIHARA K., 1993, Liquefaction and flow failure during earthquakes, *Géotechnique*, **43**, 3, 351-415

18. KOESTER J.P., 1994, The influence of fines type and content on cyclic strength, *Ground Failures Under Seismic Conditions, Geotechnical Special Publication, ASCE*, **44**, 17-33

19. LAW K.T., LING Y.H., 1992, Liquefaction of granular soils with non-cohesive and cohesive fines, *Proceedings of the Tenth World Conference on Earthquake Engineering*, Rotterdam, 1491-1496

20. LEE K.L., FITTON J.A., 1968, Factors affecting the cyclic loading strength of soil, *Symposium on Vibration Effects of Earthquakes on Soils and Foundations, ASTM STP*, **450**, 71-95

21. MULILIS J.P., SEED H.B., CHAN C.K., MITCHELL J.K., ARULANADAN K., 1977, Effects of sample preparation on sand liquefaction, *Journal of Geotechnical Engineering Division, ASCE*, **103** (GT2), 91-108

22. SEED H.B., IDRISS I.M., 1971, Simplified procedure for evaluating soil liquefaction potential, *Journal of the Soil Mechanics and Foundations Division, ASCE*, **97**, SM9, 1249-1273

23. SHEN C.K., VRYMOED J.L., UYENO C.K., 1977, The effects of fines on liquefaction of sands, *Proceedings of the 9th International Conference on Soil Mechanics and Foundation Engineering*, Tokyo, **2**, 381-385

24. TRONCOSCO J.H., VERDUGO R., 1985, Silt content and dynamic behavior of tailing sands, *Proceedings of the 12th International Conference on Soil Mechanics and Foundation Engineering*, San Francisco, USA, 1311-1314

25. TSUCHIDA H., 1970, Prediction and countermeasure against liquefaction in sand deposits (in Japanese), *Abstract of the Seminar of the Port and Harbour Research Institute*, Ministry of Transport, Yokosuka, Japan, 3.1-3.33

26. VAID V.P., 1994, Liquefaction of silty soils, *Ground Failures Under Seismic Conditions, Geotechnical Special Publication, ASCE*, **44**, 1-16

27. YAMAMURO J.A., WOOD F.M., 2004, Effect of depositional method on the undrained behavior and microstructure of sand with silt, *Soil Dynamics and Earthquake Engineering*, **24**, 751-760

28. ZLATOVIC S., ISHIHARA K., 1997, Normalized behavior of very loose non-plastic soils: effects of fabric, *Soils and Foundations*, **37**, 4, 47-56

# DISPERSION OF SH WAVES IN A VISCOELASTIC LAYER IMPERFECTLY BONDED WITH A COUPLE STRESS SUBSTRATE

Vikas Sharma

*Department of Mathematics, Lovely Professional University, Phagwara, Punjab, India*

*e-mail: vikas.sharma@lpu.co.in; vikassharma10a@yahoo.co.in*

Satish Kumar

*School of Mathematics, Thapar University, Patiala, Punjab, India*

*e-mail: satishk.sharma@thapar.edu*

The paper deals with propagation of SH waves in a viscoelastic layer over a couple stress substrate with imperfect bonding at the interface. A dispersion equation of SH waves in a viscoelastic layer overlying the couple stress substrate with an imperfect interface between them has been obtained. Dispersion equations for propagation of SH waves with perfectly bonded interface and slippage interface between two media are also obtained as particular cases. Effects of the degree of imperfectness of the interface are studied on the phase velocity of SH waves. The dispersion curves are plotted and the effects of material properties of both couple stress substrate and viscoelastic layer are studied. The effects of internal microstructures of the couple stress substrate in terms of characteristic length of the material are presented. The effects of heterogeneity, friction parameter and thickness of the viscoelastic layer are also studied on the propagation of SH waves.

*Keywords:* SH waves, couple stress theory, imperfect bonding, characteristic length, viscoelasticity

## 1. Introduction

The dynamical behaviour of near surface materials is very complicated and could not be explained on the basis of classical continuum mechanics. To explain the relationship between stress and strain at a particular subsurface point, the near surface of earth is modelled as a viscoelastic material (Butler, 2005). Wide variations of rocks erupted from volcanoes and scattering of high frequency seismic waves support the existence of small scale heterogeneity in the earth lithosphere. Hence, heterogeneity and viscoelasticity are to be considered for real characterisation of internal microstructure of solid earth.

Shear horizontal (SH) waves are linearly polarized in the direction normal to the direction of propagation and parallel to the surface. These waves propagate in a layer in contact with an elastic half space. The study of these guided waves has received much attention in the field of seismology for estimating damage capabilities of seismic waves. These waves are also helpful for studying surface mechanical properties of underlying solids in non destructive testing techniques and in electronics industry (Simonetti and Cawley, 2004; Qingzeng *et al.*, 2014). SH waves in a layered structure for a perfectly bonded interface between two media are studied by many researchers, but this condition is rarely achieved in reality. Due to certain reasons like thermal mismatch or some faults in the manufacturing process, cracks or defects may appear at the interface which leads to an imperfect interface. Components of the displacement field are not continuous at the common boundary of two media in the case of an imperfect interface. The difference in displacement fields is assumed to linearly depend upon the traction vector. These imperfections at the common boundary may affect the propagation of SH waves.

Bhattacharya (1970) pointed out some possible exact solutions to the SH-wave equation for inhomogeneous media. Schoenberg (1980) studied elastic wave behaviour across a linear slip interface by assuming that the displacement discontinuity is linearly related to stress traction, which itself is continuous across the interface. He studied the effects of interfacial compliances on reflection and transmission coefficients of plane harmonic waves. Liu *et al.* (2007) studied Love waves in layered graded composite structures with a rigid, slip and imperfectly bonded interface which was described using an interface shear spring model. They showed that for the imperfectly bonded interface, the phase velocity of Love waves changed in the range of velocities for the rigid and slip interface conditions. Nie *et al.* (2009) studied shear horizontal guided waves in a coupled plate consisting of a piezoelectric layer and a piezomagnetic layer. They assumed that both layers are transversely isotropic and are perfectly bonded at the interface. They concluded that phase velocity of SH waves approached the smaller bulk shear wave velocity of the two materials in the system with the increase in the wave number. Borcherdt (2009) studied the propagation of SH waves in viscoelastic media. Kumar and Chawla (2011) studied wave propagation at an imperfect boundary between the transversely isotropic thermodiffusive elastic layer and half space in the context of the Green-Lindsay theory. They presented the effects of various parameters involved in the problem on both phase velocity and attenuation of SH-waves. Singh *et al.* (2011) studied propagation of waves at an imperfectly bonded interface between two monoclinic thermoelastic half-spaces. Otero *et al.* (2011) studied dispersion relations for SH waves on a magnetoelectroelastic heterostructure with imperfect interfaces. They observed that with decreasing values of imperfect bonding parameter, propagation velocity also decreased. Cui *et al.* (2013) studied SH waves in a piezoelectric structure with an imperfectly bonded viscoelastic layer. Sahu *et al.* (2014) studied SH waves in a viscoelastic heterogeneous layer over a half space with self-weight. They studied the effects of gravity, heterogeneity and internal friction on propagation of SH waves in the viscoelastic layer over the half space. They observed that heterogeneity of the medium affected the velocity profile of SH wave significantly. Vardoulakis and Georgiadis (1997) studied SH surface waves in a homogeneous gradient-elastic half space with surface energy. They showed the existence of SH waves in a homogeneous gradient-elastic half space. Recently, Sharma and Kumar (2016) studied propagation of SH waves in layered media consisting of a viscoelastic layer perfectly bonded with a couple stress substrate.

In the classical elasticity, it is assumed that the matter is continuously distributed without any defects, and internal microstructure of the material is also ignored. Experimental results have shown that the materials having inner atomic structure or microstructures behave differently at the micro level as compared to macroscale. Due to these shortcomings of the classical elasticity, size dependent continuum mechanics has been developed, which accounts for the internal microstructure of the material and predicts the dependence of macroscopic response on microstructural parameters of the material. Voigt (1887) was first to generate the idea of couple stresses in the material. Cosserat and Cosserat (1909) gave a mathematical model involving couple stresses in the material but they did not give any specific constitutive relations. Later on, many researchers like Toupin (1962), Mindlin and Tiersten (1962), Koiter (1964), Eringen (1968) and Nowacki (1974) worked on this idea and presented many theories. In these theories, the concept of couple stress was introduced by defining the deformation of the material through displacement and an independent rotation vector, which were associated with stresses and couple stresses through constitutive relations. Due to rotation, the couple stress theory was able to explain the dispersive nature of waves, which was not captured by the classical theory of elasticity.

Many researchers have used couple stress theory to study problems of wave propagation in elastic media under different conditions. Sengupta and Ghosh (1974a,b) studied the effects of couple stresses in elastic media, they deduced the equations of surface waves in elastic media under the influence of couple stresses and observed that the couple stresses affect the velocity

of Rayleigh and Love wave propagation. Das *et al.* (1991) studied thermo-viscoelastic Rayleigh waves under the influence of couple stress and gravity. Debnath and Roy (1988) studied propagation of edge waves in a thinly layered laminated medium with stress couples under initial stresses. They showed that for a specific compression, the presence of couple stresses increase the velocity of wave propagation with an increase in the wave number, whereas the trend was totally reversed when there was no couple stress. Georgiadis and Velgaki (2003) studied the dispersive nature of Rayleigh waves propagating along the surface of a half-space at high frequencies using the couple stress theory.

There were some difficulties with the original couple stress theory like indeterminacy of the spherical part of the couple stress tensor or involvement of separate material length scale parameters. Hadjesfandiari and Dargush (2011) proposed a consistent couple stress theory by considering true continuum kinematical displacement and rotation. In that proposed theory, it was shown that the couple-stress tensor was skew-symmetric and the skew-symmetric part of the gradient of the rotation tensor was the consistent curvature tensor. It is also shown that for an isotropic material two Lamé parameters ($\lambda$ and $\mu$) and one length scale parameter ($\eta = \mu l^2$) completely characterise the behaviour. Here, a length scale parameter $l$ called the characteristic length is relevant for studies conducted at the micro or nano level for the materials which exhibit internal microstructures like composites or cellular solids. It is assumed that the characteristic length is comparable to the average cell size of the material.

Keeping in mind various factors affecting the dispersion of SH waves like nature of the interface between two media, properties of the half space and coated layer, we intend to study SH waves in a viscoelastic layer lying over a couple stress substrate with an imperfect interface between them. To study the effects of microstructures of the substrate on the propagation of SH waves, a model comprising of granular macromorphic rock (Dionysos Marble) exhibiting the properties of a couple stress solid underlying heterogeneous viscoelastic layer is employed. The couple stress theory proposed by Hadjesfandiari and Dargush (2011) is applied for observing the effects of microstructures of the material of the substrate in terms of the characteristic length and other parameters of the viscoelastic layer on the propagation of SH waves.

## 2. Formulation and solution of the problem

Consider a layer of a viscoelastic medium of thickness $H$ lying over a couple stress substrate with microstructures. The interface between two media is assumed to be imperfect. The origin of the coordinate system $O(x, y, z)$ lies on the interfacial surface joining the substrate and layer of the viscoelastic medium. Here, the $z$ axis is pointing vertically downwards into the half space, the interface between the layer and half space is given by $z = 0$ and the free surface of the layer is $z = -H$. For SH waves, displacement components and body forces are independent of the $y$ co-ordinate, so if $(u, v, w)$ are the displacement co-ordinates of a point, then $u = w = 0$ and $v$ is a function of the parameters $x$, $z$ and $t$.
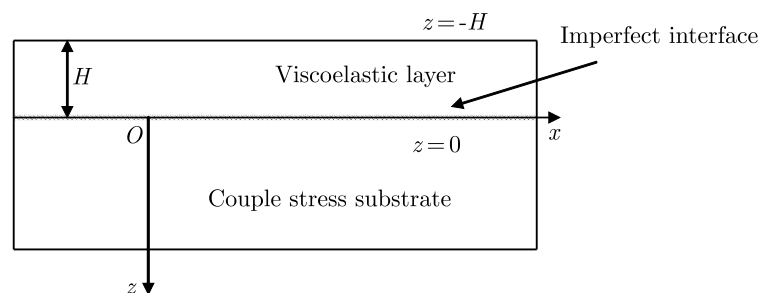


Fig. 1. Geometry of the problem

### 2.1. Couple stress half space

The basic governing equation of motion and constitutive relations of couple stress theory for an isotropic material in the absence of body forces (Hadjesfandiari and Dargush, 2011) are given by

$$(\lambda + \mu + \eta\nabla^2)\nabla(\nabla \cdot \mathbf{u}) + (\mu - \eta\nabla^2)\nabla^2\mathbf{u} = \rho\frac{\partial^2\mathbf{u}}{\partial t^2} \tag{2.1}$$

where $\lambda$ and $\mu$ are Lamé constants, $\eta = \mu l^2$ is the couple-stress coefficient, $l$ is the characteristic length, $\rho$ is density of the material of the half space, and $\mathbf{u}$ is the displacement vector.

Let us assume that $\mathbf{u} = [0, v, 0]$ and $\partial/\partial y \equiv 0$. Under these conditions, the equation of motion becomes

$$\left(\frac{\partial^2 v}{\partial x^2} + \frac{\partial^2 v}{\partial z^2}\right) - l^2\left(\frac{\partial^4 v}{\partial x^4} + \frac{\partial^4 v}{\partial z^4} + 2\frac{\partial^4 v}{\partial x^2\partial z^2}\right) = \frac{1}{C_2^2}\frac{\partial^2 v}{\partial t^2} \tag{2.2}$$

where $C_2^2 = \mu/\rho$.

We assume the solution to Eq. (2.2) to be $v = f(z)\exp[-\mathrm{i}(\omega t - kx)]$, where $k$ is the wave number, $\omega = kc$ is the angular frequency and $c$ is the phase velocity. Using this solution in Eq. (2.2), we get

$$\frac{d^4 f}{dz^4} - S\frac{d^2 f}{dz^2} + Pf = 0 \tag{2.3}$$

where

$$S = 2k^2 + \frac{1}{l^2} \qquad P = k^4 + \frac{k^2}{l^2} - \frac{\omega^2}{l^2 C_2^2}$$

Since in the couple stress elastic half space the amplitude of waves decreases with an increase in depth, so the solution to the above differential equation becomes

$$f(z) = A_1 \mathrm{e}^{-a_1 z} + B_1 \mathrm{e}^{-b_1 z} \tag{2.4}$$

where

$$a_1 = \sqrt{\frac{S + \sqrt{S^2 - 4P}}{2}} \qquad b_1 = \sqrt{\frac{S - \sqrt{S^2 - 4P}}{2}}$$

and

$$v = (A_1 \mathrm{e}^{-a_1 z} + B_1 \mathrm{e}^{-b_1 z})\mathrm{e}^{-\mathrm{i}(\omega t - kx)} \tag{2.5}$$

The constitutive relations in the elastic half space are given by (Hadjesfandiari and Dargush, 2011)

$$\sigma_{ji} = \lambda u_{k,k}\delta_{ij} + \mu(u_{i,j} + u_{j,i}) - \eta\nabla^2(u_{i,j} - u_{j,i})$$
$$\mu_{ji} = 4\eta(\omega_{i,j} - \omega_{j,i}) \qquad \omega_i = \frac{1}{2}\epsilon_{ijk}u_{k,j} \tag{2.6}$$

Here, $u_i$ are displacement components, $\sigma_{ji}$ is the non-symmetric force-stress tensor, $\mu_{ji}$ is the skew symmetric couple-stress tensor, $\delta_{ij}$ is Kronecker's delta, $\epsilon_{ijk}$ is the permutation tensor and $i, j, k = 1, 2, 3$

$$\sigma_{yz} = \mu\frac{\partial v}{\partial z} + \mu l^2\left(\frac{\partial^3 v}{\partial x^2\partial z} + \frac{\partial^3 v}{\partial z^3}\right) \qquad \mu_{xz} = 2\mu l^2\left(\frac{\partial^2 v}{\partial x^2} + \frac{\partial^2 v}{\partial z^2}\right) \tag{2.7}$$

Using Eq. (2.5) in eq. (2.7), we get

$$\sigma_{yz} = \Big[\mu(-a_1 A_1 e^{-a_1 z} - b_1 B_1 e^{-b_1 z}) + \mu l^2 (a_1 A_1 k^2 e^{-a_1 z}$$

$$+ b_1 B_1 k^2 e^{-b_1 z} - a_1^3 A_1 e^{-a_1 z} - b_1^3 B_1 e^{-b_1 z})\Big] e^{-i(\omega t - kx)} \tag{2.8}$$

$$\mu_{xz} = 2\mu l^2 \Big[a_1^2 A_1 e^{-a_1 z} + b_1^2 B_1 e^{-b_1 z} - (A_1 e^{-a_1 z} + B_1 e^{-b_1 z})k^2\Big] e^{-i(\omega t - kx)}$$

### 2.2. Heterogeneous viscoelastic layer

For the heterogeneity of the layer, we assume that properties of the medium change only in the $z$-direction. For SH waves propagating in the $x$-direction and causing displacement in the $y$-direction only, we shall assume that $\mathbf{u}_1 = [0, v_1, 0]$ and $\partial/\partial y \equiv 0$.

The equation of motion in the absence of body forces and under the above mentioned assumptions (Ravinder, 1968) is given by

$$\frac{\partial P_{xy}}{\partial x} + \frac{\partial P_{yz}}{\partial z} = \rho_1 \frac{\partial^2 v_1}{\partial t^2} \tag{2.9}$$

where

$$P_{xy} = \Big(\mu_1 + \eta_1 \frac{\partial}{\partial t}\Big)\frac{\partial v_1}{\partial x} \qquad P_{yz} = \Big(\mu_1 + \eta_1 \frac{\partial}{\partial t}\Big)\frac{\partial v_1}{\partial z}$$

In the upper viscoelastic layer $\mu_1$, $\eta_1$ and $\rho_1$ are assumed to be function of depth only and are given by

$$\mu_1 = \mu_0(1 - \sin \alpha z) \qquad \eta_1 = \eta_0(1 - \sin \alpha z) \qquad \rho_1 = \rho_0(1 - \sin \alpha z) \tag{2.10}$$

where $\mu_0$, $\eta_0$, $\rho_0$ are the constant values of $\mu_1$, $\eta_1$ and $\rho_1$ at the interface of the layer and half space, and $\alpha$ is an arbitrary constant having dimensions of the inverse of length.

For the heterogeneous viscoelastic layer, Eq. (2.9) becomes

$$\Big(\mu_1 + \eta_1 \frac{\partial}{\partial t}\Big)\frac{\partial^2 v_1}{\partial x^2} + \frac{\partial}{\partial z}\Big[\Big(\mu_1 + \eta_1 \frac{\partial}{\partial t}\Big)\frac{\partial v_1}{\partial z}\Big] = \rho_1 \frac{\partial^2 v_1}{\partial t^2} \tag{2.11}$$

Now, assuming the solution $v_1 = v_L(z) \exp[-i(\omega t - kx)]$, the equation of motion becomes

$$\frac{d^2 v_L}{dz^2} + \frac{1}{\overline{\mu}_1}(\overline{\mu}_1)'\frac{dv_L}{dz} + \Big(\frac{\rho_1 \omega^2}{\overline{\mu}_1} - k^2\Big)v_L = 0 \tag{2.12}$$

where $\overline{\mu}_1 = \mu_1 - i\omega \eta_1$ and $(\overline{\mu}_1)' = d\overline{\mu}_1/dz$. Taking $v_L(z) = Y_1(z)/\sqrt{\overline{\mu}_1}$, Eq. (2.12) reduces to

$$\frac{d^2 Y_1}{dz^2} + \Big[\frac{1}{4(\overline{\mu}_1)^2}\Big(\frac{d\overline{\mu}_1}{dz}\Big)^2 - \frac{1}{2\overline{\mu}_1}\frac{d^2\overline{\mu}_1}{dz^2} + \frac{\rho_1 \omega^2}{\overline{\mu}_1} - k^2\Big]Y_1 = 0 \tag{2.13}$$

Solving this equation further, gives

$$\frac{d^2 Y_1}{dz^2} + \Big[\frac{\alpha^2}{4} + \frac{\rho_0 \omega^2}{\overline{\mu}_0} - k^2\Big]Y_1 = 0 \tag{2.14}$$

where $\overline{\mu}_0 = \mu_0 - i\omega \eta_0$.

The solution to the above differential equation is

$$Y_1 = A\cos(mz) + B\sin(mz)$$

where $A$ and $B$ are arbitrary constants and

$$m^2 = \frac{\alpha^2}{4} + \frac{\rho_0 \omega^2}{\overline{\mu}_0} - k^2$$

Hence $v_1 = v_L(z)\exp[-i(\omega t - kx)] = (Y_1(z)/\sqrt{\overline{\mu}_1})\exp[-i(\omega t - kx)]$, that

$$v_1 = \frac{1}{\sqrt{\overline{\mu}_0}}\frac{1}{\sqrt{1 - \sin \alpha z}}[A\cos(mz) + B\sin(mz)]e^{-i(\omega t - kx)} \tag{2.15}$$

## 3. Boundary conditions

Boundary conditions to be satisfied at the free surface of the viscoelastic layer and at the interfacial surface between the viscoelastic layer and the couple stress half space are:

(i) The top surface of the viscoelastic layer should be stress free, so $P_{yz} = (\mu_1 + \eta_1 \partial/\partial t)(\partial v_1/\partial z) = 0$ at $z = -H$.

(ii) The difference in displacement fields is assumed to depend linearly upon the traction vector, that is $P_{yz} = G(v - v_1)$ at $z = 0$, where $G$ measures the degree of imperfectness at the interface.

(iii) The magnitude of shear stresses of both the couple stress substrate and the viscoelastic layer should be equal at the interface, that is $P_{yz} = \sigma_{yz}$ at $z = 0$.

(iv) The couple stress tensor $\mu_{xz}$ should vanish at the interface, that is $\mu_{xz} = 0$ at $z = 0$.

## 4. Derivation of secular equation

### 4.1. SH waves in the viscoelastic layer over the couple stress half space with an imperfect interface

Using the above mentioned boundary conditions, we get following four equations

$$
\begin{aligned}
&\sqrt{\overline{\mu}_0}[2m(1 + \sin(\alpha H))\sin(mH) + \alpha \cos(\alpha H)\cos(mH)]A \\
&\quad + \sqrt{\overline{\mu}_0}[2m(1 + \sin(\alpha H))\cos(mH) - \alpha \cos(\alpha H)\sin(mH)]B = 0
\end{aligned}
$$

$$
\begin{aligned}
&-\left(\frac{\sqrt{\overline{\mu}_0}\alpha}{2} + \frac{G}{\sqrt{\overline{\mu}_0}}\right)A - \sqrt{\overline{\mu}_0}mB + GA_1 + GB_1 = 0 \\
&\frac{\alpha\sqrt{\overline{\mu}_0}A}{2} + \sqrt{\overline{\mu}_0}mB + \mu a_1[1 + (a_1^2 - k^2)l^2]A_1 + \mu b_1[1 + (b_1^2 - k^2)l^2]B_1 = 0 \\
&(a_1^2 - k^2)A_1 + (b_1^2 - k^2)B_1 = 0
\end{aligned} \tag{4.1}
$$

Equations (4.1) will have a non-trivial solution if the determinant of coefficients of the unknowns $A$, $B$, $A_1$, $B_1$ vanishes. Applying this condition to the above system of equations, we obtain the following secular equation for the SH waves in the heterogeneous viscoelastic layer imperfectly bonded to a couple stress half space with microstructures as

$$
(-2T_1\overline{\mu}_0 m + T_2\overline{\mu}_0\alpha)[Q + G(b_1^2 - a_1^2)] + 2T_2 QG = 0 \tag{4.2}
$$

where

$$
\begin{aligned}
T_1 &= 2m[1 + \sin(\alpha H)]\sin(mH) + \alpha \cos(\alpha H)\cos(mH) \\
T_2 &= 2m[1 + \sin(\alpha H)]\cos(mH) - \alpha \cos(\alpha H)\sin(mH) \\
Q &= \mu(k^2 - a_1^2)(k^2 - b_1^2)(a_1 - b_1)l^2 + \mu b_1(k^2 - a_1^2) - \mu a_1(k^2 - b_1^2)
\end{aligned}
$$

Now, separating the real and imaginary parts of eq. (4.2), we get a dispersion equation of SH waves as

$$
\begin{aligned}
&[-2R_1\mu_0 m_1 - 2R_1\omega\eta_0 m_2 - 2I_1\omega\eta_0 m_1 + 2I_1\mu_0 m_2 \\
&\quad + \alpha(R_2\mu_0 + \omega\eta_0 I_2)][Q + G(b_1^2 - a_1^2)] + 2R_2 QG = 0
\end{aligned} \tag{4.3}
$$

and the imaginary part gives us the damping equation of SH waves as

$$
\begin{aligned}
&[2R_1\omega\eta_0 m_1 - 2R_1\mu_0 m_2 - 2I_1\mu_0 m_1 - 2I_1\omega\eta_0 m_2 \\
&\quad + \alpha(I_2\mu_0 - R_2\omega\eta_0)][Q + G(b_1^2 - a_1^2)] + 2I_2 QG = 0
\end{aligned} \tag{4.4}
$$

### 4.2. SH waves in the viscoelastic layer over the couple stress half space with a perfectly bonded interface

If in Eq. (4.2) $G \to \infty$, we get a secular equation for SH waves in the viscoelastic layer over the couple stress half space with a perfectly bonded interface. It is the same as that obtained by Sharma and Kumar (2016)

$$(-2T_1\overline{\mu}_0 m + T_2\overline{\mu}_0\alpha)(b_1^2 - a_1^2) + 2T_2 Q = 0 \tag{4.5}$$

### 4.3. SH waves in the viscoelastic layer over the couple stress half space with a slip interface

If in Eq. (4.2), $G \to 0$, the secular equation for SH waves in the viscoelastic layer over the couple stress half space for a slippage interface is given by

$$(-2T_1\overline{\mu}_0 m + T_2\overline{\mu}_0\alpha)Q = 0 \tag{4.6}$$

where

$$T_1 = R_1 + \mathrm{i}I_1 \qquad T_2 = R_2 + \mathrm{i}I_2$$

$$m = m_1 + \mathrm{i}m_2 \qquad m_1 = \sqrt{r}\cos\frac{\theta}{2} \qquad m_2 = \sqrt{r}\sin\frac{\theta}{2}$$

$$R_1 = 2[1 + \sin(\alpha H)](m_1 S_1 - m_2 S_2) + \alpha\cos(\alpha H)E_1$$

$$I_1 = 2[1 + \sin(\alpha H)](m_1 S_2 + m_2 S_1) - \alpha\cos(\alpha H)E_2$$

$$R_2 = 2[1 + \sin(\alpha H)](m_1 E_1 + m_2 E_2) - \alpha\cos(\alpha H)S_1$$

$$I_2 = 2[1 + \sin(\alpha H)](m_2 E_1 - m_1 E_2) - \alpha\cos(\alpha H)S_2$$

$$S_1 = \sin(m_1 H)\cosh(m_2 H) \qquad S_2 = \cos(m_1 H)\sinh(m_2 H)$$

$$E_1 = \cos(m_1 H)\cosh(m_2 H) \qquad E_2 = \sin(m_1 H)\sinh(m_2 H)$$

$$F_1 = \frac{\rho_0\omega^3\eta_0}{\mu_0^2 + \omega^2\eta_0^2} \qquad F_2 = \frac{\alpha^2}{4} - k^2 + \frac{\rho_0\omega^2\mu_0}{\mu_0^2 + \omega^2\eta_0^2}$$

$$r = \sqrt{F_1^2 + F_2^2} \qquad \tan\theta = \frac{F_1}{F_2}$$

## 5. Numerical results and discussion

(i) For the viscoelastic layer, various material parameters (Gubbins, 1990) are taken as $\rho_0 = 4705\,\mathrm{kg/m^3}$, $\mu_0 = 1.987 \cdot 10^{10}\,\mathrm{N/m^2}$, $\mu_0/\eta_0 = 10^6\,\mathrm{s^{-1}}$, $\beta_1 = \sqrt{\mu_0/\rho_0} = 2055\,\mathrm{m/s}$.

(ii) The material parameters for the couple stress half space which is made of Dionysos Marble (Vardoulakis and Georgiadis, 1997) are $\rho = 2717\,\mathrm{kg/m^3}$, $\mu = 30.5 \cdot 10^9\,\mathrm{N/m^2}$, $C_2 = \sqrt{\mu/\rho} = 3350\,\mathrm{m/s}$.

Dionysos Marble is a white fine-grained metamorphic marble with saccharoidal microstructure. To find the impact of characteristic length, different cases of characteristic length $l$ comparable with the internal cell size of granular macromorphic rock $O(10^{-4})$ such as $l = 0.0001\,\mathrm{m}$, $l = 0.0004\,\mathrm{m}$, $l = 0.0008\,\mathrm{m}$ are considered. In all the figures, phase velocity is plotted using Eq. (4.3) and the real part of Eq. (4.5). Graphs of damping velocity are plotted using Eq. (4.4) and the imaginary part of Eq. (4.5).

### 5.1. Effects of degree of imperfectness at the interface

To study the role of degree of imperfectness of the interface on the propagation of SH waves in the viscoelastic layer over the couple stress substrate, curves are provided in Figs. 2a and 2b. Here, we have considered fixed values of other parameters as $\alpha H = 0.54$, characteristic length $l = 0.0004\,\mathrm{m}$ and friction parameter $\mu_1/\eta_1 = 10^6$. It can be observed in Fig. 2a that SH waves are dispersive, and the non dimensional phase velocity $c/\beta_1$ of SH waves decreases sharply with an increase in the non dimensional wave number $kH$ before becoming asymptotically constant. It can also be observed from the profiles in Fig. 2a that an increase in the value of parameter $G$ leads to an increase in the phase velocity of SH waves for any fixed value of the dimensionless wave number $kH$. Since the imperfectness is inversely proportional to $G$, so an increase in the imperfectness adversely affects the phase velocity, and the phase velocity is maximum when the interface is perfectly bonded $G \to \infty$. Figure 2b shows the variation in non dimensional damping velocity of SH waves with the non dimensional wave number for different values of the parameter $G$. It can be observed that the damping velocity increases with an increase in the parameter $G$. The damping velocity is also maximum when the interface is perfectly bonded.
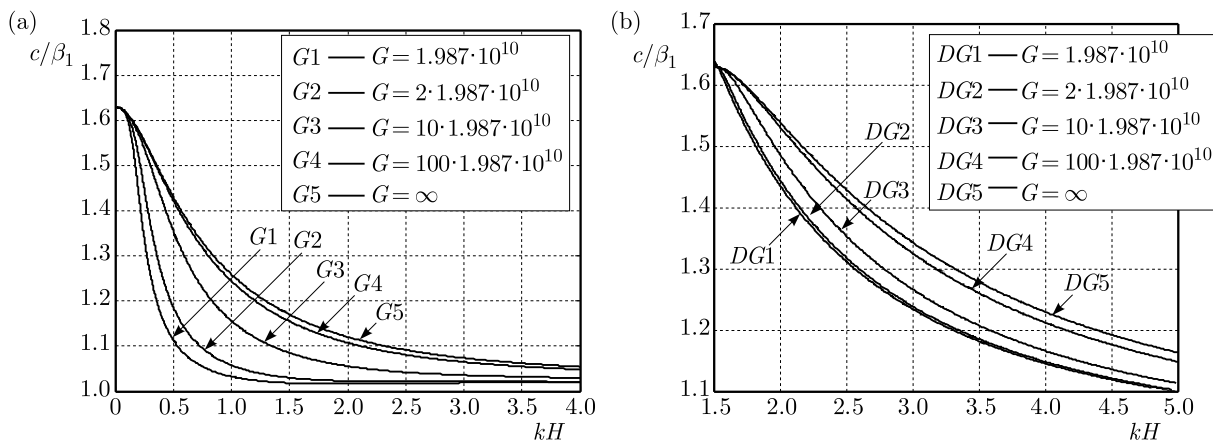


Fig. 2. (a) Phase and (b) damping velocity profiles of SH waves with the wave number for different values of $G$

### 5.2. Effects of the heterogeneity parameter

The role of the heterogeneity parameter on both the phase and damping velocities of SH waves is studied in Figs. 3a and 3b. Dispersion curves are provided for three different values of the heterogeneity parameter $\alpha H = 0.18$, $0.54$ and $0.72$. We have considered values of other parameters as $H = 0.09\,\mathrm{m}$, characteristic length $l = 0.0004\,\mathrm{m}$ and friction parameter $\mu_1/\eta_1 = 10^6$ and the value of $G = 2 \cdot 1.987 \cdot 10^{10}$. It can be observed that with the increasing value of the heterogeneity parameter $\alpha H$, the phase velocity of SH waves decreases. Figure 3b shows variation of the damping velocity with the wave number for different values of the heterogeneity parameter. It can be seen that the damping velocity of SH waves increases with an increase in the heterogeneity parameter.

### 5.3. Effects of the friction parameter

Dispersion curves to demonstrate the role of the friction parameter on SH waves in the viscoelastic layer are provided in Figs. 4a and 4b for three different values of the friction parameter $\mu_1/\eta_1 = 7 \cdot 10^5\,\mathrm{s}^{-1}$, $10 \cdot 10^5\,\mathrm{s}^{-1}$, $80 \cdot 10^5\,\mathrm{s}^{-1}$. We have considered the values of other parameters as $\alpha H = 0.54$, characteristic length $l = 0.0004\,\mathrm{m}$ and $G = 2 \cdot 1.987 \cdot 10^{10}$. It can be observed from these figures that both the phase velocity and damping velocity of SH waves decrease with an increase in the value of the friction parameter $\mu_1/\eta_1$.
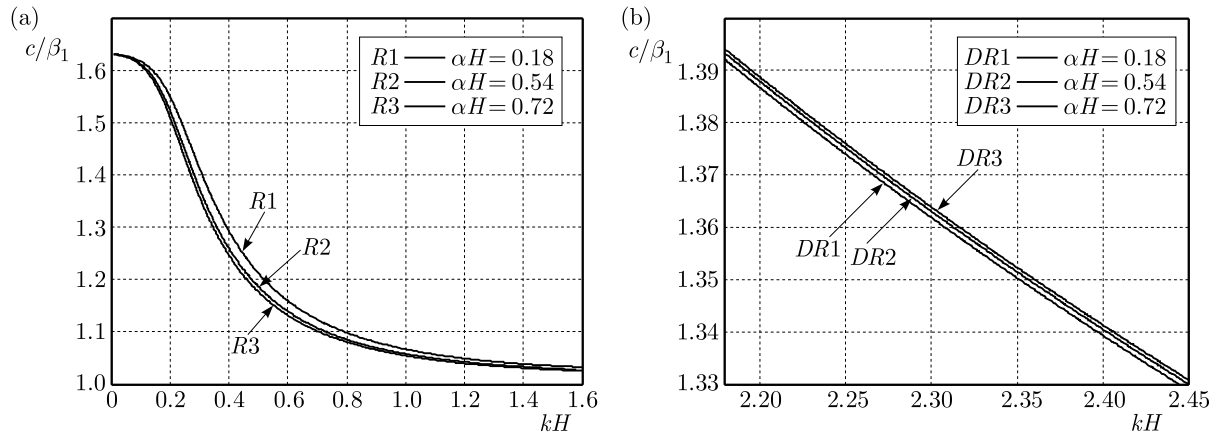
(a)



(b)

Fig. 3. (a) Phase and (b) damping velocity profiles of SH waves with the wave number for different values of $\alpha H$
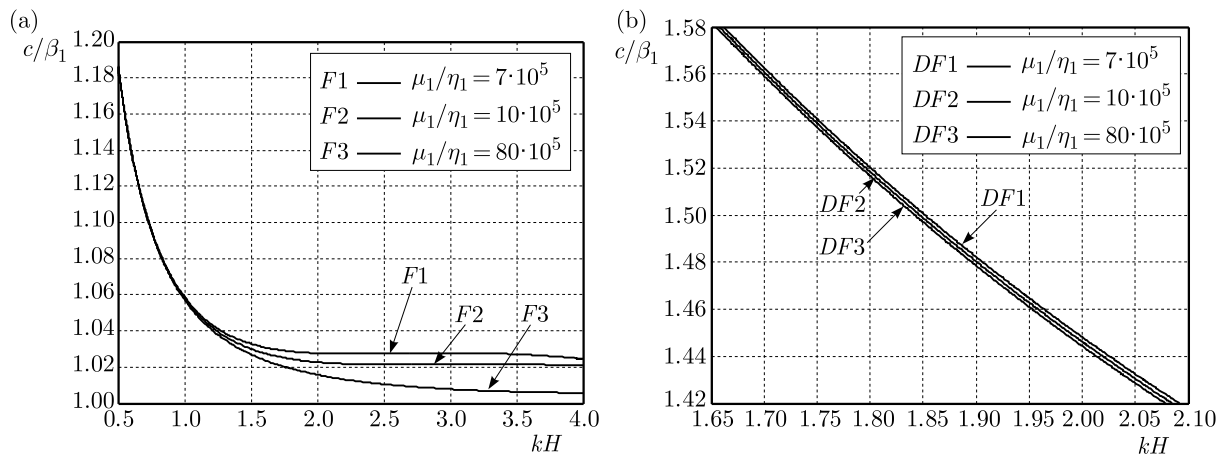
(a)



(b)

Fig. 4. (a) Phase and (b) damping velocity profiles of SH waves with the wave number for different values of $\mu_1/\eta_1$

## 5.4. Effects of the thickness of the viscoelastic layer

Figure 5a shows variation in the phase velocity $c/\beta_1$ against the wave number $kH$ for three different values of thickness, $H = 0.04$ m, $0.06$ m, $0.09$ m. The values of other fixed parameters are $\alpha H = 0.54$, $\mu_1/\eta_1 = 10^6$, $l = 0.0004$ and $G = 2 \cdot 1.987 \cdot 10^{10}$. It is observed that with the increasing value of thickness of the viscoelastic layer over the couple stress substrate, the phase velocity of SH waves also increases. Figure 5b shows variation of the damping velocity of SH waves with the wave number for different values of thickness of the viscoelastic layer. It can be seen that the damping velocity of SH waves decreases with an increase in thickness of the layer.

## 5.5. Effects of the internal microstructure of the substrate

For observing the effects of internal microstructure of the underlying substrate, variation in the phase velocity and damping velocity is shown against the wave number in Figs. 6a and 6b for three different values of the characteristic length $l = 0.0001$ m, $0.0004$ m, $0.0008$ m. The values of other fixed parameters are taken as $\alpha H = 0.54$, $\mu_1/\eta_1 = 10^6$ and $G = 2 \cdot 1.987 \cdot 10^{10}$. It can be observed that both the phase velocity and damping velocity of SH waves increase with an increase in the characteristic length $l$ of the material.
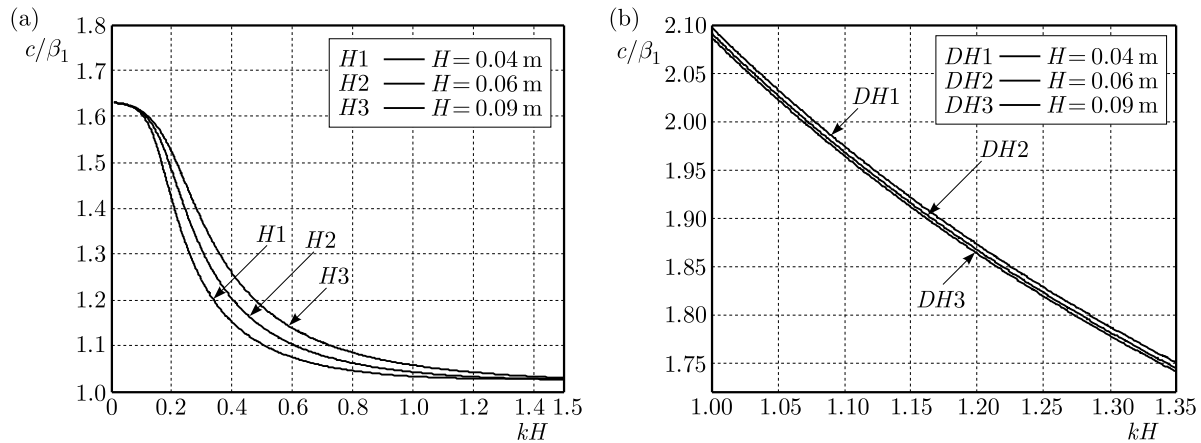
Fig. 5. (a) Phase and (b) damping velocity profiles of SH waves with the wave number for different values of $H$
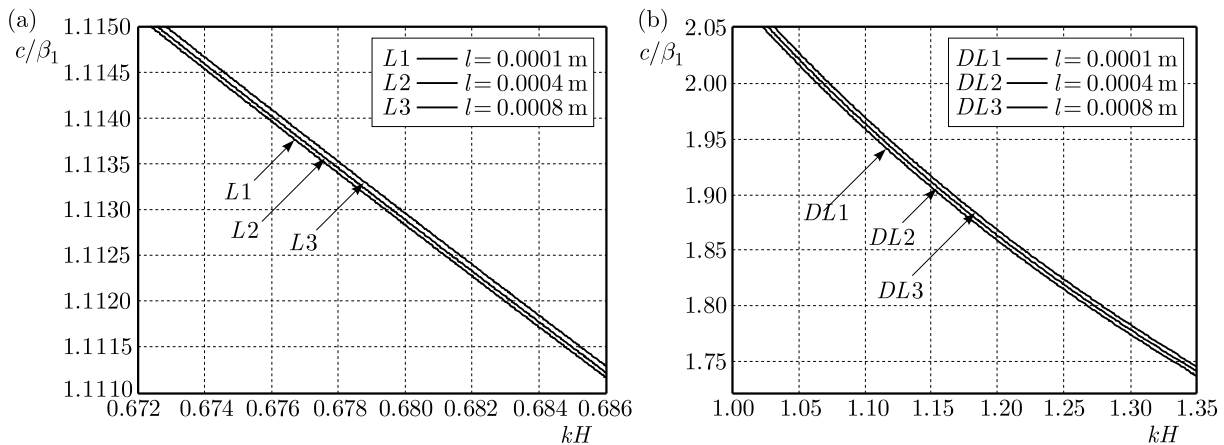


Fig. 6. (a) Phase and (b) damping velocity profiles of SH the waves with wave number for different values of $l$

## 6. Conclusion

Propagation of SH waves is studied in a viscoelastic layer bonded imperfectly with a couple stress substrate. Dispersion equations for propagation of SH waves with a perfectly bonded interface and a slippage interface between two media are also obtained as particular cases. The numerical results are presented graphically. Following major conclusions are drawn from the present study:

- SH waves show dispersion in the considered model. Initially, the phase velocity of SH waves decreases sharply with an increase in the wave number, then it becomes asymptotically constant for higher wave numbers.

- Imperfectness at the interface between two media has a significant effect on the phase and damping velocities of SH waves. It is observed that with the decreasing value of imperfectness at the interface, both the phase and damping velocities of SH waves increase. The phase and damping velocities are highest when the interface is perfectly bonded.

- The heterogeneity parameter of the viscoelastic layer has an adverse effect on the phase velocity but it favours the damping velocity. So, the phase velocity decreases and the damping velocity increases with an increase in the heterogeneity parameter.

- The friction parameter of the viscoelastic layer has an adverse effect on both the phase and damping velocities. Both of them decrease with the increasing value of this parameter.

- It is observed that with the increasing value of thickness of the viscoelastic layer over the couple stress substrate, the phase velocity of SH waves increases. The increasing value of thickness of the viscoelastic layer does not favour damping velocity.

- Characteristic length $l$ which measures internal microstructure of the material of the underlying substrate favours both the phase and damping velocities of SH waves. These velocities increase with the increasing value of characteristic length of the underlying couple stress substrate.

The consideration of microstructural effects on the propagation of SH waves in this realistic model may provide possible applications to non-destructive testing techniques and other engineering fields. The results presented in this work may be applied to the designing of liquid viscosity sensors and biosensors. As the model is considered to replicate the internal structure of earth, so it may also find possible application to seismology or geomechanics engineering.

## References

1. BHATTACHARYA S.N., 1970, Exact solution of SH-wave equation for inhomogeneous media, *Bulletin of Seismological Society of America*, **60**, 6, 1847-1859

2. BORCHERDT R.D., 2009, *Viscoelastic Waves in Layered Media*, Cambridge University Press, New York

3. BUTLER D.K., 2005, *Near-Surface Geophysics*, Society of Exploration Geophysicists, Tulsa, Okla

4. COSSERAT E., COSSERAT F., 1909, *Théorie des corps deformables*, A. Hermann et Fils, Paris

5. CUI J., DU J., WANG J., 2013, Study on SH waves in piezoelectric structure with an imperfectly bonded viscoelastic layer, *Joint UFFC, EFTF and PFM Symposium*, 1017-1020

6. DAS T.K., SENGUPTA P.R., DEBNATH L., 1991, Thermo-visco-elastic Rayleigh waves under the influence of couple stress and gravity, *International Journal of Mathematics and Mathematical Sciences*, **14**, 3, 553-560

7. DEBNATH L., ROY P.P., 1988, Propagation of edge waves in a thinly layered laminated medium with stress couples under initial stresses, *Journal of Applied Mathematics and Simulation*, **1**, 271-286

8. ERINGEN A.C., 1968, Theory of micropolar elasticity, [In:] *Fracture*, H. Liebowitz (Edit.), Academic Press, New York, 2, 662-729

9. GEORGIADIS H.G., VELGAKI E.G., 2003, High-frequency Rayleigh waves in materials with microstructure and couple-stress effects, *International Journal of Solids and Structures*, **40**, 2501-2520

10. GUBBINS D., 1990, *Seismology and Plate Tectonics*, Cambridge University Press, Cambridge

11. HADJESFANDIARI A.R., DARGUSH G.F., 2011, Couple stress theory for solids, *International Journal of Solids and Structures*, **48**, 2496-2510

12. KOITER W.T., 1964, Couple stresses in the theory of elasticity I and II, *Proceedings of the Koninklijke, Nederlandse Akademie van Wetenschappen B*, **67**, 17-44

13. KUMAR R., CHAWLA V., 2011, Wave propagation at the imperfect boundary between transversely isotropic thermodiffusive elastic layer and half-space, *Journal of Engineering Physics and Thermophysics*, **84**, 5, 1192-2000

14. LIU H., YANG J.L., LIU K., 2007, Love waves in layered graded composite structures with imperfectly bonded interface, *Chinese Journal of Aeronautics*, **20**, 210-214

15. MINDLIN R.D., TIERSTEN H.F., 1962, Effects of couple-stresses in linear elasticity, *Archive for Rational Mechanics and Analysis*, **11**, 415-488

16. Nie G., An Z., Liu J., 2009, SH-guided waves in layered piezoelectric/piezomagnetic plates, *Progress in Natural Science*, **19**, 811-816

17. Nowacki W., 1974, *Micropolar Elasticity*, International Center for Mechanical Sciences, Courses and Lectures No: 151, Udine, Springer-Verlag, Wien-New York

18. Otero J.A., Calas H., Rodrguez-Ramos R., Bravo-castillero J., Aguiar A.R., Monsivais G., 2011, Dispersion relations for SH waves on a magnetoelectroelastic heterostructure with imperfect interfaces, *Journal of Mechanics of Materials and Structures*, **6**, 7/8, 969-994

19. Qingzeng M.A., Jingpin J.,Ping H.U., Xi Z., Bin W.U., Cunfu H.E., 2014, Excitation and detection of shear horizontal waves with electromagnetic acoustic transducers for nondestructive testing of plates, *Chinese Journal of Mechanical Engineering*, **27**, 2, 428-436

20. Ravindra R., 1968, Usual assumptions in the treatment of wave propagation in heterogeneous elastic media, *Pure and Applied Geophysics*, **70**, 1, 12-17

21. Sahu S.A., Saroj P.K., Dewangan N., 2014, SH-waves in viscoelastic heterogeneous layer over half-space with self-weight, *Archive of Applied Mechanics*, **84**, 235-245

22. Schoenberg M., 1980, Elastic wave behavior across linear slip interfaces, *Journal of the Acoustical Society of America*, **68**, 5, 1516-1521

23. Sengupta P.R., Ghosh B., 1974a, Effects of couple stresses on the propagation of waves in an elastic layer, *Pure and Applied Geophysics*, **112**, 331-338

24. Sengupta P.R., Ghosh B., 1974b, Effects of couple stresses on the surface waves in elastic media, *Gerlands Beitrage zur Geophysik, Leipzig*, **83**, 309-318

25. Sharma V., Kumar S., 2016, Influence of microstructure, heterogeneity and internal friction on SH waves propagation in a viscoelastic layer overlying a couple stress substrate, *Structural Engineering and Mechanics*, **57**, 4, 703-716

26. Simonetti F., Cawley P., 2004, On the nature of shear horizontal wave propagation in elastic plates coated with viscoelastic materials, *Proceedings of Royal Society – A*, **460**, 2197-2221

27. Singh J., Singh B., Ailawalia P., 2011, Propagation of waves at an imperfectly bonded interface between two monoclinic thermoelastic half-spaces, *Journal of Theoretical and Applied Mechanics*, **41**, 3, 77-92

28. Toupin R.A., 1962, Elastic materials with couple-stresses, *Archive for Rational Mechanics and Analysis*, **11**, 385-414

29. Vardoulakis I., Georgiadis H.G., 1997, SH surface waves in a homogeneous gradient-elastic half-space with surface energy, *Journal of Elasticity*, **47**, 147-165

30. Voigt W., 1887, Theoretische Studien fiber die Elastizitatsverhiltnisse der Kristalle, *Abh. Geschichte Wissenschaften*, **34**

# SIZE OPTIMIZATION OF RECTANGULAR CROSS-SECTION MEMBERS SUBJECT TO FATIGUE CONSTRAINTS

Juan M. González Mendoza, Samuel Alcántara Montes

*Department of Graduate Studies and Research, National Polytechnic Institute, Mexico*

*e-mail: johann009@yahoo.com; sammotion@yahoo.com.mx*

José De J. Silva Lomelí, Juan A. Flores Campos

*UPIITA, National Polytechnic Institute, Mexico; e-mail: jsilval@ipn.mx; jaflores@ipn.mx*

Although in the scientific literature there are studies regarding optimization of structural members subject to static loads or even cyclic in-phase loads, the optimization of structures subject to cyclic, out-of-phase multiaxial loads is still an unexplored issue. In this paper, we present an approach to the problem of size optimization of rectangular cross-section members subject to multiaxial in-phase and out-of-phase cyclic loads. The objective of the optimization is to minimize the cross sectional area of such elements while retaining their fatigue endurance. Under the proposed methodology, optimum values of the area are achieved for six loading cases and for three values of the height to width ratio of the cross section, and these values are reported. The novelty of the approach lies in the inclusion of two multiaxial high cycle fatigue criteria, i.e., Dang Van and Vu-Halm-Nadot ones, as constraints for size optimization problems, fully integrated within an in-house developed tool, capable of handling non-proportional stresses. A plot of the feasible solution space for this optimization problem is also obtained.

*Keywords:* size optimization, multiaxial fatigue, non-proportional

## Nomenclature

| | | |
|---|---|---|
| $u_1, u_2$ | – | design variables |
| $M_t, M_b$ | – | applied torsional and bending moment, respectively |
| $f_{-1}, t_{-1}$ | – | fatigue limit in fully reversed bending and torsion, respectively |
| $S_u$ | – | ultimate strength |
| $\sigma_{ij}$ | – | macroscopic stress tensor |
| $\sigma_H$ | – | hydrostatic stress |
| $S_{ij}, s_{ij}$ | – | macroscopic and mesoscopic deviatoric stress tensor, respectively |
| $\text{dev}\, \rho_{ij}^*$ | – | deviatoric local residual stress tensor |
| $I_{1a}, I_{1m}$ | – | amplitude and mean value of first invariant of stress tensor, respectively |
| $J_{2a}$ | – | amplitude of second invariant of deviatoric stress tensor |
| $\phi$ | – | phase angle |

## 1. Introduction

Optimization of structural elements is an important problem in engineering design, and rectangular cross-section members are widely used in engineering applications for machine components.

Many authors have applied size, shape and topology optimization techniques to structural elements as diverse as beams, test specimens, or notched elements subject generally to static loads or proportional cyclic loads.

Baptista *et al.* (2014) optimized the geometry of cruciform specimens for biaxial fatigue testing machines in order to obtain maximum and uniform stress values in the gauge area of such specimens, where the fatigue damage was supposed to initiate. Ghelichi *et al.* (2011) optimized the shape of the notches in components subject to multiaxial cyclic loads using the Liu-Zenner criterion and decreasing the stress concentration at the notch.

Andjelić and Milosević-Mitić (2012) solved the problem of optimization of thin walled I-beams loaded in static bending and torsion. They determined the minimum mass of the I-beam subject to stress constraints.

Mrzygłód (2010) and Mrzygłód and Zieliński (2006) made remarkable contributions by implementing multiaxial, high cycle fatigue criteria as constraints in the structural optimization of vehicle parts on the assumption of in-phase loadings. The goal of their optimization was to decrease the mass of the parts while retaining their fatigue endurance.

Holmberg *et al.* (2014) explored the problem of topology optimization with fatigue constraints. Their objective was to find the design with the minimum mass that could still withstand a specific life time. They tested their methodology with some examples involving only one load direction on models such as L-shaped beams.

Jeong *et al.* (2015) should be mentioned for developing a topology optimization method that included static stress and fatigue constraints, the aim of which was to minimize the mass of structures under the effect of constant amplitude proportional loads. They proved the applicability of their approach to two-dimensional continuum structures.

In the experimental field, the work by Rozumek *et al.* (2010) has to be noticed as they conducted tests on rectangular cross-section specimens subject to combined cyclic loadings and recorded their lives to crack initiation.

However, there is little research related to the optimization of structural elements subject to fatigue constraints, much less multiaxial fatigue constraints for problems involving in-phase as well as out-of-phase cyclic loads.

Therefore, the main problem to be addressed in this paper is to present an approach to the size optimization of structural members including multiaxial fatigue criteria as constraints, when the structural member under consideration is subject to biaxial proportional and non-proportional loads, using in-house developed tools.

## 2. Description of geometry, stresses and loads applied

The objective of the optimization is to minimize the area of rectangular cross-section members subject to biaxial cyclic loading, i.e., combined in-phase and out-of-phase bending with torsion while retaining their fatigue endurance. Therefore, it is necessary to analyze briefly the relationships between the loads being applied to such members and the resulting normal and shear stresses.

Let us consider a rectangular cross-section member subject to a torsional moment as well as to a bending moment as shown in Fig. 1. The maximum shear stress at the center of the long side due to the torsional moment is given by equation $(2.1)_1$ (Boresi, 2002). Meanwhile, the stress on the short side is given by equation $(2.1)_2$, point $A$. In Fig. 1, as in the optimization process, the width and height of the cross section are identified as $u_1$, $u_2$, respectively

$$\tau_{max} = \sigma_{13} = \frac{M_t}{k_2 u_2 u_1^2} \qquad \sigma_{12} = k_3 \tau_{max} \tag{2.1}$$

Factors $k_2$, $k_3$ are shown in Table 1 for several values of the height to width ratio $u_2/u_1$ assuming the case where $u_2 > u_1$.
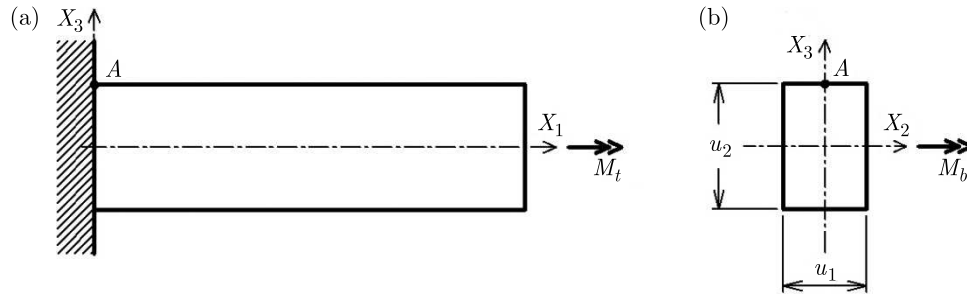
Fig. 1. Rectangular cross-section cantilever beam subjected to combined bending with torsion:
(a) left view, applied torsional moment, (b) front view, applied bending moment

**Table 1.** Factors $k_2$, $k_3$. Data from Timoshenko and Goodier (1951) and from Gasiak and Robak (2010)

| $u_2/u_1$ | 1.0 | 1.5 | 2.0 | 3.0 | 4.0 | 6.0 | 10.0 |
|---|---|---|---|---|---|---|---|
| $k_2$ | 0.208 | 0.231 | 0.246 | 0.267 | 0.282 | 0.299 | 0.312 |
| $k_3$ | 1.000 | 0.859 | 0.795 | 0.753 | 0.745 | 0.743 | 0.742 |

With regard to the normal stress, owing to the bending moment, it reaches its maximum value at point $A$ calculated using equation

$$\sigma_{11} = \frac{6M_b}{u_1 u_2^2} \tag{2.2}$$

We consider the normal and shear stresses at point $A$ and also make the following assumptions:

- Bending and torsional moments are applied in a cyclic, fully reversible manner, under the high cycle fatigue regime.

- With loads applied in a synchronous and sinusoidal way, the normal and shear stresses change along one loading cycle according to equations

$$\sigma_{11}(t) = \sigma_{11,m} + \sigma_{11,a} \sin \frac{2\pi t}{T} \qquad \sigma_{12}(t) = \sigma_{12,m} + \sigma_{12,a} \sin\left(\frac{2\pi t}{T} - \phi\right) \tag{2.3}$$

## 3. Fatigue criteria included as constraints

The fatigue criteria selected to be included as constraints, i.e., Dang Van, Vu-Halm-Nadot ones, show good agreement with experimental results. They have been selected such that a comparative base for the obtained results can be established with the fatigue criteria based on different methods, i.e., a multi-scale method or stress invariant method.

Although further explanation of these criteria can be found respectively in (Dang Van *et al.*, 1989; Vu *et al.*, 2010), we make a short review of the stresses to be calculated for each of them.

### 3.1. Dang Van criterion

This criterion evaluates an equivalent stress resulting from the linear combination of mesoscopic shear and hydrostatic stresses. Then it compares this equivalent stress against the fatigue limit in fully reversed torsion $t_{-1}$, see equation $(3.3)_1$. As a previous step to the calculation

of mesoscopic stresses, it is mandatory to obtain quantities such as components of the macroscopic stress tensor $\sigma_{ij}(t)$, the hydrostatic stress $\sigma_H(t)$, and the macroscopic deviatoric stress tensor $S_{ij}(t)$ all of them acting throughout one loading cycle

$$\sigma_H(t) = \frac{\sigma_1(t) + \sigma_2(t) + \sigma_3(t)}{3} \qquad\qquad S_{ij}(t) = \sigma_{ij}(t) - \sigma_H(t)I_{ij} \tag{3.1}$$

The calculation of the deviatoric local residual stress tensor $\operatorname{dev}\rho_{ij}^*$, is not a trivial task when loads are non-proportional, but it is a fundamental step to the calculation of mesoscopic stresses

$$s_{ij}(t) = S_{ij}(t) + \operatorname{dev}\rho_{ij}^* \qquad\qquad \tau(t) = \frac{s_1(t) - s_3(t)}{2} \tag{3.2}$$

The value of $\overline{\alpha}$ is defined in equation $(3.3)_2$, and for both criteria $\overline{\beta} = t_{-1}$

$$\max[\tau(t) + \overline{\alpha}\sigma_H(t)] \leqslant \overline{\beta} \qquad\qquad \overline{\alpha} = \frac{3t_{-1}}{f_{-1}} - \frac{3}{2} \tag{3.3}$$

### 3.2. Vu-Halm-Nadot criterion

This multiaxial fatigue criterion is based on invariants of the macroscopic stress tensor and it has an advantage of low-computation time. Its evaluation requires, in the first place, calculation of the amplitude of the second invariant of the macroscopic deviatoric stress tensor

$$J_2'(t) = \sqrt{J_{2a}(t)} = \sqrt{\frac{1}{2}[S_a(t) \cdot S_a(t)]} \tag{3.4}$$

after which their authors propose to introduce the mean value of the second invariant of the deviatoric stress tensor along one loading cycle

$$J_{2,mean} = \frac{1}{T} \int_0^T J_2'(t) \, dt \tag{3.5}$$

Once these quantities are obtained, the Vu-Halm-Nadot criterion is expressed as

$$\sqrt{\gamma_1 J_2'^2(t) + \gamma_2 J_{2,mean}^2 + \gamma_3 I_f(I_{1a}, I_{1m})} \leqslant \overline{\beta} \tag{3.6}$$

where $I_f$ is a function of $I_{1a}$ and $I_{1m}$

$$\begin{aligned}
I_{1a} &= \frac{1}{2}\Big\{\max_{t \in T} I_1(t) - \min_{t \in T} I_1(t)\Big\} \\
I_{1m} &= \frac{1}{2}\Big\{\max_{t \in T} I_1(t) + \min_{t \in T} I_1(t)\Big\}
\end{aligned} \tag{3.7}$$

While using this criterion, the ultimate strength is employed to distinguish between two classes of metals, i.e., low-strength with $S_u < 750\,\text{MPa}$, and for which $I_f$ is given by

$$I_f(I_{1a}, I_{1m}) = I_{1a} + I_{1m} \tag{3.8}$$

and high-strength with $S_u > 750\,\text{MPa}$, and for which $I_f$ is given by

$$I_f(I_{1a}, I_{1m}) = I_{1a} + \frac{f_{-1}}{t_{-1}}I_{1m} \tag{3.9}$$

where $\gamma_1$, $\gamma_2$ are material parameters dependent on the ultimate strength of the material. The value of $\gamma_3$ is given by

$$\gamma_3 = \frac{1}{f_{-1}}\Big(t_{-1}^2 - \frac{f_{-1}^2}{3}\Big) \tag{3.10}$$

For low-strength metals: $\gamma_1 = 0.65$, $\gamma_2 = 0.8636$; for high-strength metals: $\gamma_1 = 0.3$, $\gamma_2 = 1.7272$.

An in-house tool has been developed for the use of such criteria as fatigue constraints on size optimization problems for both proportional and non-proportional loads. This in-house tool has been developed using the commercial software Matlab (MATLAB Optimization Toolbox User's Guide, 2013).

## 4. Formulation of the optimization problem

The size optimization problem can be expressed as finding the set of design variables $\{u\}$ that minimize the objective function, i.e., the area of the rectangular cross-section members subject to biaxial bending with torsion

$$\min f(u_1, u_2) = u_1 u_2 \tag{4.1}$$

while keeping the state variable, i.e., their fatigue endurance under the value of $\overline{\beta}$ (Christensen and Klarbring, 2009), selecting one of the equations

$$\begin{aligned} \max[\tau(t) + \overline{\alpha}\sigma_H(t)] &\leqslant \overline{\beta} \\ \sqrt{\gamma_1 J_2'^2(t) + \gamma_2 J_{2,mean}^2 + \gamma_3 I_f(I_{1a}, I_{1m})} &\leqslant \overline{\beta} \end{aligned} \tag{4.2}$$

We also add a linear constraint to this problem, representing a specific height to width ratio of the cross section

$$u_2 \leqslant c_1 u_1 \tag{4.3}$$

This optimization problem is solved using our in-house tool developed in Matlab. The optimization method used is the Sequential Quadratic Programming algorithm (SQP), a gradient based algorithm that can handle constrained nonlinear programming problems.

The Sequential Quadratic Programming algorithm works by solving in an iterative manner a series of quadratic programming sub-problems which are based on the expansion about the current design point of both the objective and the constraint functions using the Taylor series. Although the full description of this algorithm is out of the scope of this paper, a detailed description of it can be found in Venkataraman (2002).

The SQP algorithm is implemented within the optimization function *fmincon* of Matlab and, in turn, this function is coded in our tool, which invokes the constraint functions (which are not explicit functions of the design variables $u_1$, $u_2$), and the objective function in every iteration.

A flowchart of the optimization approach is presented in Fig. 2. The design variables $\{u\}$ are changed throughout the optimization process while keeping the values of the applied bending and torsional moments. Thus, as geometry changes, the applied stresses are updated in every iteration as well as the equivalent stress calculated according to the multiaxial high cycle fatigue criterion. The latter is then compared against the permissible value of $\overline{\beta}$ that is $t_{-1}$. New values of $u_1$, $u_2$ are set and the iterative process continues until the objective function, i.e., the cross sectional area achieves the conditions of convergence and the solution still satisfies the fatigue constraints.

## 5. Numerical examples

As a numerical example of the size optimization approach presented here, we use a rectangular cross-section beam model as the one depicted in Fig. 1, under biaxial in-phase and out-of-phase loads.
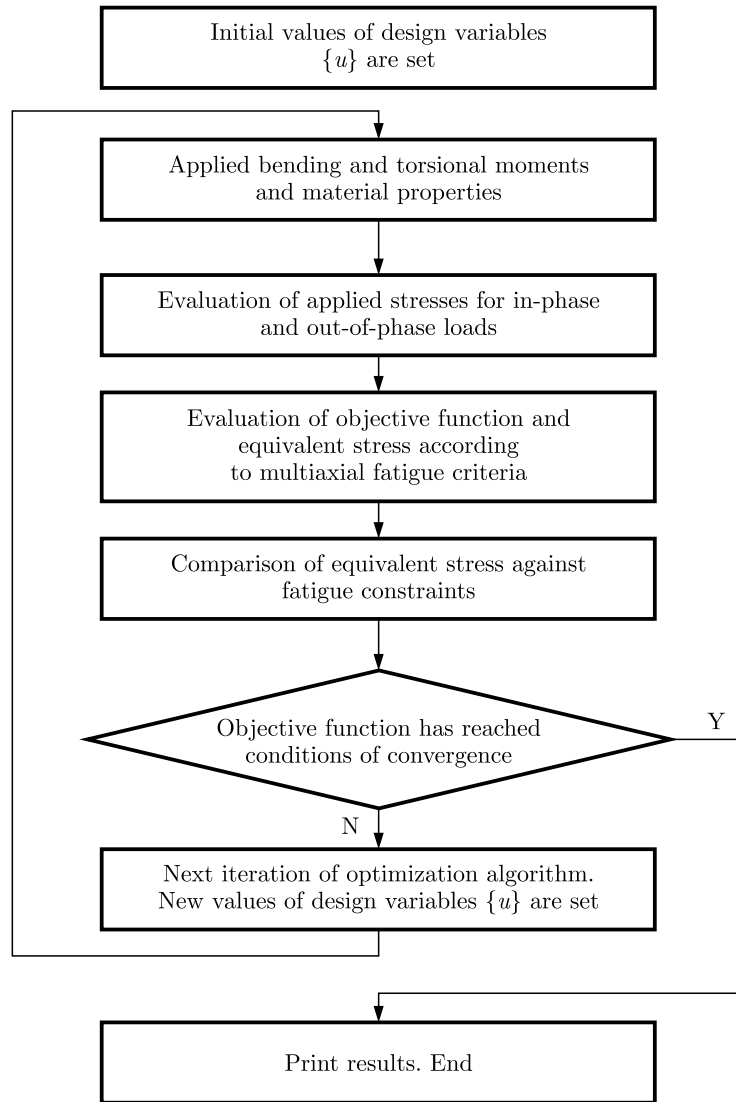
Fig. 2. Flowchart of the implemented optimization approach

We define six loading cases acting over this model representing cyclic, fully reversible, bending and torsional moments. These combinations appear in Table 2. For the first three loading cases, bending and torsional moments are applied in phase, therefore $\phi$, the phase angle, equals zero. For the last three loading cases, bending and torsional moments are applied out of phase, and $\phi$ equals 90°. Examples of the resulting stress histories are seen in Fig. 3.

**Table 2.** Loading cases acting over the rectangular cross-section model. Applied bending moment $M_{b,a}$, applied torsional moment $M_{t,a}$, phase angle $\phi$

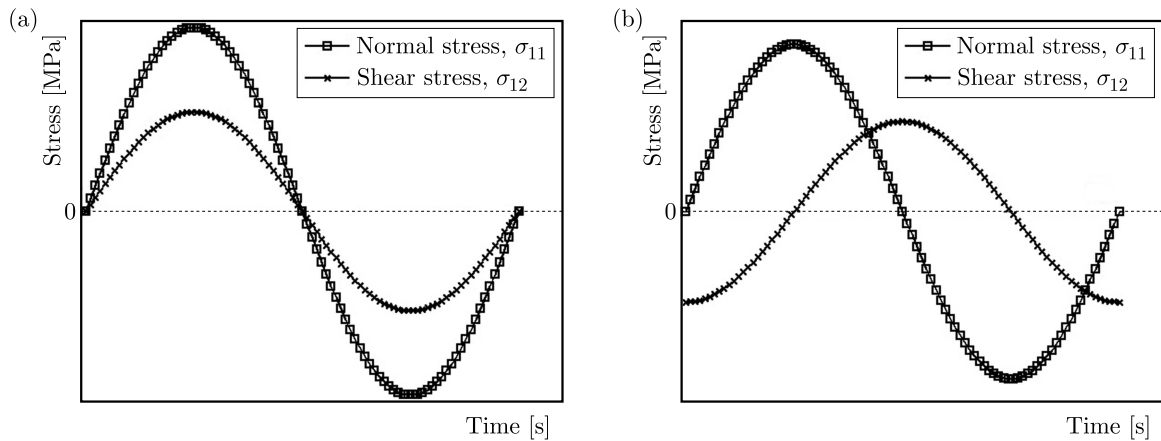| Loading case | $M_{b,a}$ [Nm] | $M_{t,a}$ [Nm] | $\phi$ [deg] |
|:---:|:---:|:---:|:---:|
| 1 | 20 | 10 | 0 |
| 2 | 25 | 12.5 | 0 |
| 3 | 30 | 15 | 0 |
| 4 | 20 | 10 | 90 |
| 5 | 25 | 12.5 | 90 |
| 6 | 30 | 15 | 90 |

Fig. 3. Stress histories acting over the model: (a) in-phase loads, (b) out-of-phase loads

The material employed in the analyses is hard steel. It has the following properties relevant for fatigue design: ultimate strength $S_u = 680$ MPa, fatigue limit in fully reversed bending $f_{-1} = 313.9$ MPa, fatigue limit in fully reversed torsion $t_{-1} = 196.2$ MPa. Data are taken from Nishihara and Kawamoto reported in (Papadopoulos *et al.*, 1997).

As stated earlier, the objective of the optimization is to minimize the area of the rectangular cross section member for each loading case and for three different height to width ratios of the section (1.50, 1.75, and 2.00). This is accomplished while keeping the values of the applied bending and torsional moments, and also while keeping the fatigue endurance of the model. The initial values of the design variables are set as: $u_1 = 8$ mm, $u_2 = 10$ mm for all loading cases. This point is selected from within the feasible region, which we explain in detail in the next Section.

## 6.    Results and discussion

The optimum values of area of the rectangular cross-section members have been calculated for each loading case of Table 2, using the Dang Van and Vu-Halm-Nadot multiaxial high cycle fatigue criteria as constraints. This means finding the minimum cross sectional area that will withstand the applied loads, and will do it with an equivalent stress below the fatigue limit in fully reversed torsion, or in other words, will be able to resist infinite life.

These results are shown in tables 3, 4 and 5 for three different height to width ratios of the section, respectively. We will explain our results throughout an example. Let us refer to loading case six for which: $M_{b,a} = 30$ Nm, $M_{t,a} = 15$ Nm, $\phi = 90°$. The initial values of the design variables selected from within the feasible region are: $u_1 = 8$ mm, $u_2 = 10$ mm. The height to width ratio is 1.50, and the Dang Van fatigue criterion is used. After application of the size optimization, the optimum value of area found is $60.29$ mm$^2$. For the same loading conditions but using a $H/W$ ratio of 1.75, the optimum value is $57.27$ mm$^2$. Finally, for a $H/W$ ratio of 2.00, the optimum value is $54.78$ mm$^2$.

We use the feasible solution space for the same loading case as a graphical representation of the optimization problem. It is shown in Figs. 4 and 5 for both fatigue criteria, respectively.

The points on any curve of this diagram have the same value. Therefore, we observe contour curves of a constant area representing the objective function, to decrease from the upper right corner to the down left corner of the picture. Three dotted lines represent the values of the height to width ratio of the cross section. The remaining solid curve represents the value of the fatigue limit for each criterion. The initial values of the design variables are selected from within the feasible region, i.e., the region beneath the specific line of $H/W$ ratio and above the curve

**Table 3.** Optimum values of the area for $1.0 \cdot 10^6$ cycles. Height to width ratio: 1.50

| Loading case | $M_{b,a}$ [Nm] | $M_{t,a}$ [Nm] | $\phi$ [deg] | $A_{optim}$ [mm$^2$] | |
|---|---|---|---|---|---|
| | | | | Dang Van | VHN |
| 1 | 20 | 10 | 0 | 54.70 | 52.70 |
| 2 | 25 | 12.5 | 0 | 63.47 | 61.15 |
| 3 | 30 | 15 | 0 | 71.68 | 69.05 |
| 4 | 20 | 10 | 90 | 46.01 | 50.49 |
| 5 | 25 | 12.5 | 90 | 53.39 | 58.58 |
| 6 | 30 | 15 | 90 | 60.29 | 66.16 |

**Table 4.** Optimum values of the area for $1.0 \cdot 10^6$ cycles. Height to width ratio: 1.75

| Loading case | $M_{b,a}$ [Nm] | $M_{t,a}$ [Nm] | $\phi$ [deg] | $A_{optim}$ [mm$^2$] | |
|---|---|---|---|---|---|
| | | | | Dang Van | VHN |
| 1 | 20 | 10 | 0 | 52.98 | 50.99 |
| 2 | 25 | 12.5 | 0 | 61.48 | 59.17 |
| 3 | 30 | 15 | 0 | 69.43 | 66.82 |
| 4 | 20 | 10 | 90 | 43.71 | 48.49 |
| 5 | 25 | 12.5 | 90 | 50.72 | 56.27 |
| 6 | 30 | 15 | 90 | 57.27 | 63.54 |

**Table 5.** Optimum values of the area for $1.0 \cdot 10^6$ cycles. Height to width ratio: 2.00

| Loading case | $M_{b,a}$ [Nm] | $M_{t,a}$ [Nm] | $\phi$ [deg] | $A_{optim}$ [mm$^2$] | |
|---|---|---|---|---|---|
| | | | | Dang Van | VHN |
| 1 | 20 | 10 | 0 | 51.78 | 49.77 |
| 2 | 25 | 12.5 | 0 | 60.08 | 57.76 |
| 3 | 30 | 15 | 0 | 67.85 | 65.22 |
| 4 | 20 | 10 | 90 | 41.80 | 46.95 |
| 5 | 25 | 12.5 | 90 | 48.51 | 54.49 |
| 6 | 30 | 15 | 90 | 54.78 | 61.53 |

of fatigue endurance. The optimum values are at the intersection of a $H/W$ ratio line and the fatigue curve, see Figs. 4 and 5. They correspond to those reported in Tables 3-5.

In Figs. 6a and 6b, the convergence histories for loading case 6 using both criteria are shown. As it can be seen, after the initial value of the objective function is set, the Sequential Quadratic Programming algorithm quickly converges to the minimum point within just four iterations.

In order to establish a comparative base for the results obtained and to check their effectiveness, we have arrived at similar optimum values of the objective function by means of fatigue criteria based on two different methods, i.e., multi-scale and stress-invariants.

Furthermore, the results from Tables 3-5 and Figs. 4 and 5 show that amongst the optimum values, less amount of material is needed to withstand the applied loads when the $H/W$ ratio is increased, see Table 6. Finally, with regard to the fatigue criteria included as constraints, the Vu-Halm-Nadot criterion has an advantage of faster computing times.

## 7. Conclusion

Little research has been devoted to the problem of size optimization of structural members subject to non-proportional cyclic stresses. Therefore, we present an approach aimed at minimizing
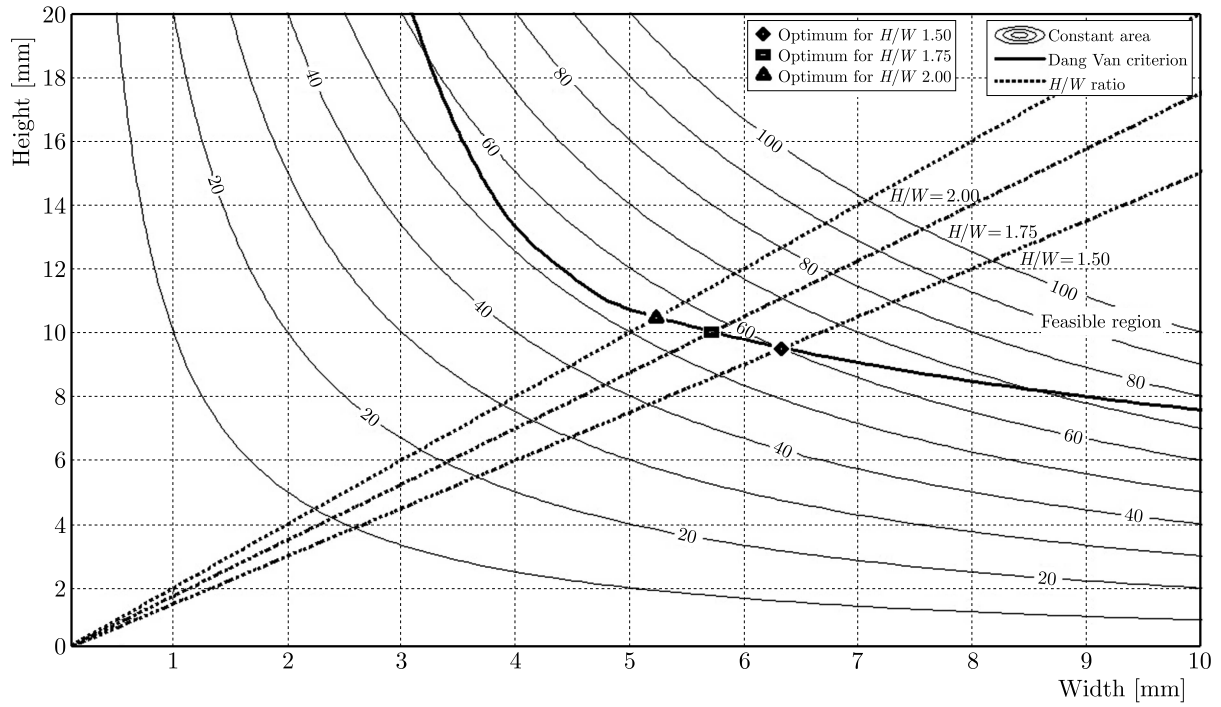
Fig. 4. Feasible solution space using the Dang Van criterion as a constraint, loading case 6. Contour curves of a constant area in mm$^2$
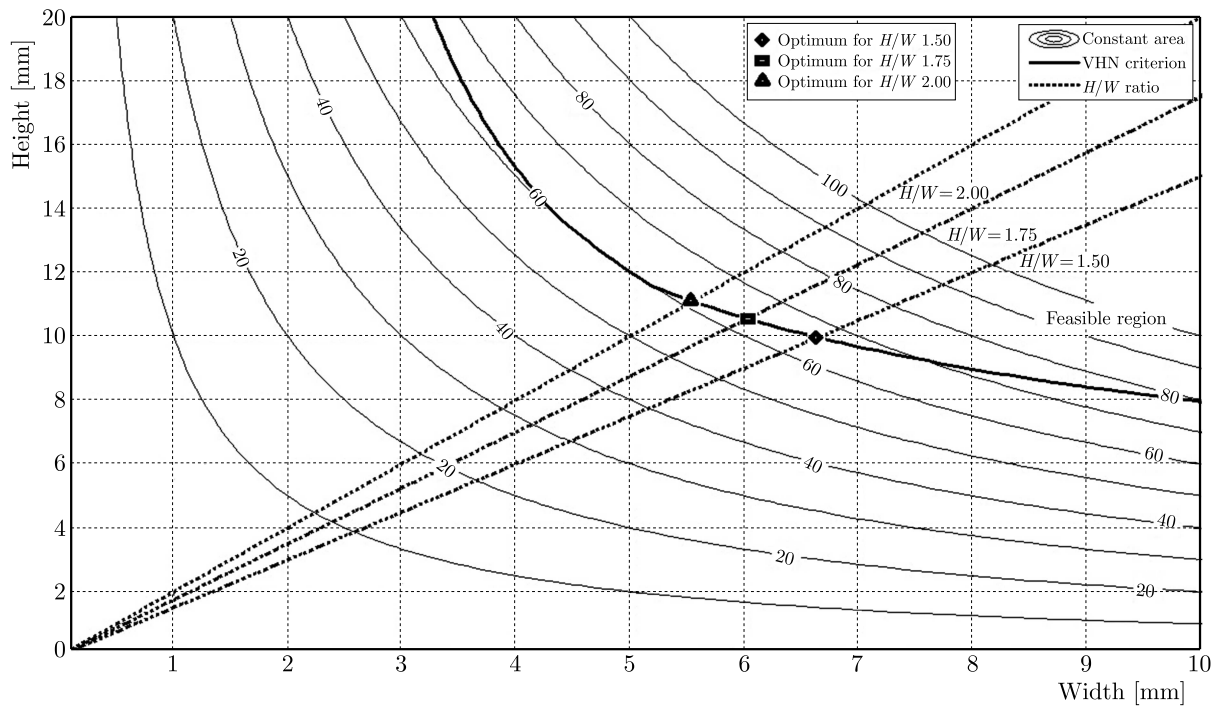


Fig. 5. Feasible solution space using the Vu-Halm-Nadot criterion as a constraint, loading case 6. Contour curves of a constant area in mm$^2$

the area of rectangular cross-section members under multiaxial in-phase and out-of-phase cyclic loadings while retaining their fatigue endurance.

This approach is based on the use of an in-house developed tool, in which two multiaxial high cycle fatigue criteria have been included as constraints, i.e., the Dang Van and Vu-Halm-Nadot criteria, coded as nonlinear constraints within the *fmincon* optimization function in Matlab.
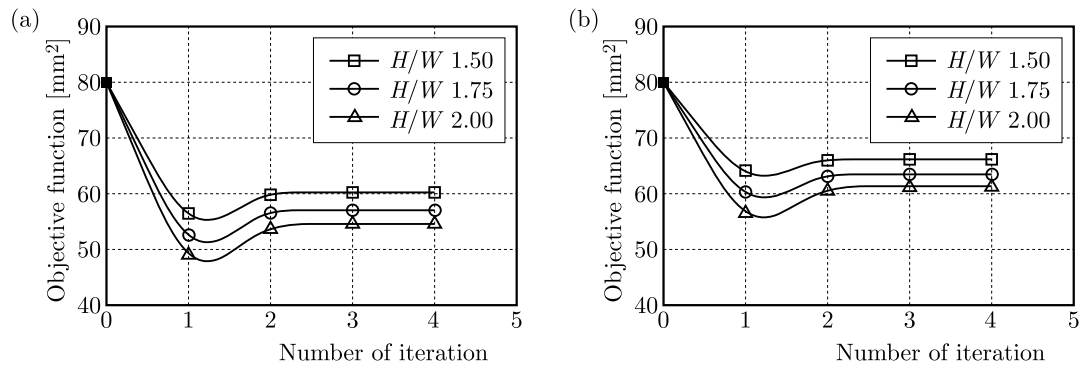
Fig. 6. Convergence diagram, loading case 6. Initial value of the objective function in all cases: $80\,\mathrm{mm}^2$. Fatigue criterion: (a) Dang Van, (b) Vu-Halm-Nadot

**Table 6.** Reduction of optimum values of the area as the height to width ratio increases, for both criteria

| Loading case | Increase of the height to width ratio | Reduction of area [%] Dang Van criterion | Reduction of area [%] VHN criterion |
|---|---|---|---|
| 1, 2, 3 | 1.50 to 1.75 | 3.14 | 3.24 |
| 4, 5, 6 | 1.50 to 1.75 | 5.01 | 3.95 |
| 1, 2, 3 | 1.75 to 2.00 | 2.28 | 2.39 |
| 4, 5, 6 | 1.75 to 2.00 | 4.35 | 3.17 |

In the numerical examples given as the reference, optimum values of the area are obtained for each loading case and for three values of the height to width ratio of the cross section. If we consider mass of an element to be proportional to its cross-sectional area, minimizing this area would mean a reduction of mass.

The novelty of the approach lies in the inclusion of multiaxial high cycle fatigue criteria as constraints for structural optimization problems capable of handling non-proportional loads, and the obtainment of the feasible solution space, including these fatigue constraints, which is a visual aid for verifying the viability of the solution for each loading case. The results of the applied approach are encouraging, since it can be useful for experimental work in which rectangular cross-section specimens are used, or as a base for methods focused on size optimization using the Sequential Quadratic Programming algorithm.

# References

1. ANDJELIĆ N., MILOSEVIĆ-MITIĆ V., 2012, Optimum design of thin-walled I-beam subjected to stress constraint, *Journal of Theoretical and Applied Mechanics*, **50**, 4, 987-999

2. BAPTISTA R., CLAUDIO R.A., REIS L., GUELHO I., FREITAS M., MADEIRA J.F.A., 2014, Design optimization of cruciform specimens for biaxial fatigue loading, *Frattura ed Integritá Strutturale*, **30**, 118-126

3. BORESI A.P., 2002, *Advanced Mechanics of Materials*, 6th edition, Wiley

4. CHRISTENSEN P., KLARBRING A., 2009, *An Introduction to Structural Optimization*, Springer

5. Dang Van K., Griveau B., Message O., 1989, On a new multiaxial fatigue limit criterion: theory and applications, [In:] *Biaxial and Multiaxial Fatigue*, EGF 3, M.W. Brown and K.J. Miller (Edit.), Mechanical Engineering Publications, London, 479-496

6. Gasiak G., Robak G., 2010, Simulation of fatigue life of constructional steels with the mixed modes I and III loading, *Fatigue and Fracture of Engineering Materials and Structures*, **34**, 389-402

7. Ghelichi R., Bernasconi A., Guagliano M., 2011, Geometrical optimization of notches under multiaxial fatigue loading, *International Journal of Fatigue*, **33**, 985-991

8. Holmberg E., Torstenfelt B., Klarbring A., 2014, Fatigue constrained topology optimization, *Structural Multidisciplinary Optimization*, **50**, 207-219

9. Jeong S.H., Choi D.H., Yoon G.H., 2015, Fatigue and static failure considerations using a topology optimization method, *Applied Mathematical Modelling*, **39**, 1137-1162

10. MATLAB. R2013b documentation. The MathWorks, Inc.; 2013

11. Mrzygłód M., 2010, Two-stage optimization method with fatigue constraints for thin-walled structures, *Journal of Theoretical and Applied Mechanics*, **48**, 3, 567-578

12. Mrzygłód M., Zieliński A.P., 2006, Numerical implementation of multiaxial high-cycle fatigue criterion to structural optimization, *Journal of Theoretical and Applied Mechanics*, **44**, 3, 691-712

13. Papadopoulos I.V., Davoli P., Gorla C., Filippini M., Bernasconi A., 1997, A comparative study of multiaxial high-cycle fatigue criteria for metals, *International Journal of Fatigue*, **19**, 3, 219-235

14. Rozumek D., Marciniak Z., Macha E., 2010, Fatigue life of specimens with round and rectangular cross-sections under out-of-phase bending and torsional loading, *The Ninth International Conference on Multiaxial Fatigue and Fracture (ICMFF9)*, Parma (Italy), 75-85

15. Timoshenko S., Goodier J.N., 1951, *Theory of Elasticity*, 2nd edition, McGraw-Hill

16. Venkataraman P., 2002, *Applied Optimization with MATLAB Programming*, Wiley

17. Vu Q.H., Halm D., Nadot Y., 2010, Multiaxial fatigue criterion for complex loading based on stress invariants, *International Journal of Fatigue*, **32**, 1004-1014

# THE INFLUENCE OF VARIATIONS OF GEOMETRICAL PARAMETERS ON THE NOTCHING STRESS INTENSITY FACTORS OF CYLINDRICAL SHELLS

Hassane Moustabchir, Moulay A. Hamdi Alaoui, Abdelhak Babaoui

*Équipe Science et Ingénierie des Matériaux (ESIM), Département de Physique Faculté des Sciences et Techniques Errachidia, Université My Ismaıl, Boutalamine, Errachidia, Morocco*

Karl D. Dearn, Catalin I. Pruncu

*School of Mechanical Engineering, University of Birmingham, United Kingdom*

*e-mail: c.i.pruncu@bham.ac.uk*

Zitoune Azari

*LaBPS, Ecole Nationale d'Ingénieurs de Metz, Ile du Saulcy, Metz, France*

The modern approach of Virtual Engineering allows one to detect with some accuracy the residual life of components especially free of cracks. The life estimation becomes cumbersome when the components contain a crack. A straightforward formulation requires a parameter that considers geometrical constraints and materials properties. The magnitude of the stress singularity developed by the tip of a crack, needs to be expressed by the Stress Intensity Factors (SIF). In order to prove the validity of the results, calibration by experimental and/or analytical technique is required. To have a better understanding of this parameter, in the first part of this paper an analytical model to compute the SIF connected to crack propagation into Mode I has been implemented. The case study displays a pipeline component with a crack defect submitted to internal pressure. Therefore, an appropriate correlation between the analytical approach and numerical simulation has been established embedded.

*Keywords:* crack, Finite Element (FE), internal pressure, Stress Intensity Factors (SIF)

## 1. Introduction

Mechanical engineering, manufacturing and/or materials performance are still attractive fields of research because of the existence of imperfections in the material components. This open question is notable on pipeline structures that seem to impose an effective challenge due to cumulative price between residual life estimation and capital costs (Schoots *et al.*, 2011). The future development of manufacturing capabilities and the industrial applications of steel cylinders, tailored in this field, is recognized to be very sensitive to the defects occurrence.

The sizes of defects deal with the magnitude of industrial accidents in such cylinders (Staat and Duc, 2007). In technological product innovation, the fracture properties of steel cylinders with defects are very important for their engineering design and application. In the final product, defects may arise in different ways because of cumulative loading action (i.e. internal pressure, temperature gradient, friction between soil/pipes interface and so on, see in Fig. 1).

The crack like "cavities" in Buried Pipeline was determined in (Lee and Choi, 1999) using the maximum equivalent stresses. The simplified approach show the effects of cavities on maximum equivalent stresses of the buried pipeline, and the stresses associated of two main factors such as size and location. Here, may be worth to note that there is a link between the effects of location while the cavities are at the same depth. It was observed when the cavities develop larger than
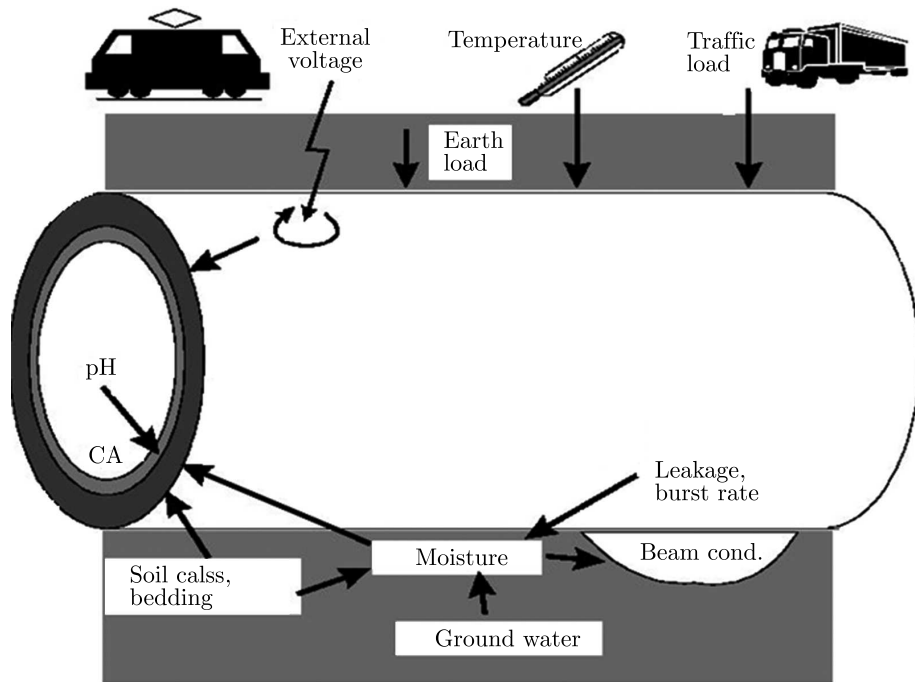
Fig. 1. Example of loads generated in a pipe section

pipeline diameter, the effects of cavities located below the pipeline are found to be larger than those located above the pipeline.

A method to solve the fracture behavior of cracked pipes can be settled using the $J$-$Q$ approach, by using a plane-strain constrain to characterize the effects of control on cleavage fracture behavior. This method allows good assessment for material with cleavage fracture behavior, because the toughness data appear more applicable for cleavage fracture predictions. The approach works well on pressurized pipelines and cylindrical vessels compared to standard methods with an assumption valid on deep notch fracture specimens under bend loading (Cravero and Ruggieri, 2005).

The impact of geometric parameters as well as the crack-tip opening displacement (CTOD) and the crack tip opening angle (CTOA) allows accurate solution in the case of a dam aged pipeline. A digital camera and image analysis software may offer evidence of the progression of the crack tip and may estimate accurately the CTOA (Darcis $et$ $al.$, 2008). This consideration became effective for the fracture evaluation in a particular case of ductile behavior. However, this imposes some limitation in a distinct type of engineering situations, namely situations in which ductile fracture can develop quantitatively $a$ $priori$ and occur in mode I, as it is frequently in the case of pipelines and pressure vessels (Corigliano $et$ $al.$, 1999). To predict experimentally the activity of burst pressures in a thin-walled gas pipeline containing longitudinal cracks, a micromechanics approach based upon the computational cell methodology enclosed in the Gurson-Tvergaard model and a deformation-based approach settled on the CTOA criterion may be relevant. The verification methodology shows the potential predictive capability of the cell approach incorporating the GT model, particularly for moderate to deep crack size to pipe thickness ratios $(a/t)$. However, burst pressure predictions for a shallow crack pipe specimen displayed poor agreement with experiments and largely overestimated the measured failure pressures (Rugieri and Dotta, 2011).

By using the constraint $R^*$, the effects of geometries and crack dimensions was determined on axially cracked pipes and SENT (Single Edge Notched Tension) specimens (Tan $et$ $al.$, 2015). The creep crack-tip constraint are significant when changes are made to some parameters, for

examples, by increasing crack depth, crack length linked to $D/t$ (diameter/thickness). A constraint level as a function of test specimens from high to low may be ordered in the following manner: CT (Compact Tension), CST (C-Shaped Tension), SENB (Single-Edge Notched Bend), SENT and CCT (Center-Cracked Tension). It was observed that the constraint developed by the pin-loaded SENT specimen was almost the same as that of the clamped SENT specimen. Besides, the creep constraint $R^*$ of SENT specimen increases with increasing crack depth $a/W$ (crack depth/specimen width) and specimen width $W$.

At low temperature ($-40°$C to $-60°$C), crack extension vs. time is a critical importance situation because the dynamic crack propagation is very often encountered. To determine fitness for service of arctic pipelines, bursting tests of line pipes samples at low temperature were carried out within a reasonable uncertainty by using timing wires. The determination highlights the axial crack fracture mechanism in a quasi-cleavage manner in the center of the pipe wall showing width of the shear lips be positively correlated with test temperature and burst pressure (Murtagian *et al.*, 2005). Recently, Nordhagen *et al.* (2014) proposed a numerical solution using a simple artificial fluid-structure interaction model validated using an advanced ideal fluid-structure interaction proposal. It appears that average crack speed is most sensitive to pipe thickness, followed by initial pressure, Cockcroft-Latham fracture parameter, decay length, yield strength, pipe diameter and work-hardening.

In order to ensure safe design of pipelines, new methods are compulsory; they can be based on depth knowledge and appropriate characterization of material resistance. However, it is necessary to find a combination between quasi-static test and dynamic drop weight tear testing (DWTT) on modified specimens with pre-fatigued crack where the application of the cohesive zone (CZ) and Gurson-Tveergard-Needleman (GTN) models to describe ductile material damage may be applied. This approach contributes to an increase in the understanding of major parameters controlling ductile fracture propagation and helping to establish a reliable procedure for safe design of new high-capacity pipelines with regard to crack arrest (Scheider *et al.*, 2014).

In this paper, steel cylinders submitted to internal pressure with longitudinal surface defects are evaluated. This kind of longitudinal defects develop, usually, on the external part of the pipe surface in the axial way. The major consideration is dedicated to calculating contributions of the SIF in the steel cylinders submitted to different levels of loading.

To be noted, this survey attempts to confront also the solutions proposed in literature (Heliot *et al.*, 1997; McGowan and Raymund, 1997; Shin and Cai, 2004; You *et al.*, 2007) devoted to calculation of SIFs of pressurized cylinders with longitudinal cracks. In fact, this paper permits one to consolidate a robust strategy, suitable for designing industrial components by using the Finite Element Methods (FEM) confidently. So, using the analytical models cited in the literature allows eliminating "the industrial fear" that appears while an industrial user comes in the contact with "the black box" approach of the FEM tools.

In Fig. 2, we present respectively a physical problem where the SIFs can be applied successfully along the crack front, the component from a steel cylinder with different external surface crack sizes. The internal pressure enforced to fracture the wall size was $P = 1.5$ MPa that corresponded to a working pressure of a pipeline platform. In the present configuration (i.e. sketched in Fig. 2a and 2b), it is assumed that both values of the SIF for Mode I, namely, $K_I$ parameter reach the largest values at the deepest points of different external surface cracks and, besides, decrease from the deepest point down to the surface point along the crack front. A mathematical formulation of SIFs values along the axial external surface cracks can be very well expressed by a polynomial equation following the point locations along the crack fronts by using six order polynomials

$$K_I = \sum_{i=0}^{6} A_i \left(\frac{2\phi}{\pi}\right)^i \qquad (1.1)$$

where $A_i$ are constants that depend on the crack type, crack size, internal pressure, dimensions and of course the material of the cylinder. Details on the conditions of the present formulations (i.e. while the internal pressure is imposed) and all constants for different axial external surface cracks are listed in (Su and Gouri, 1999).
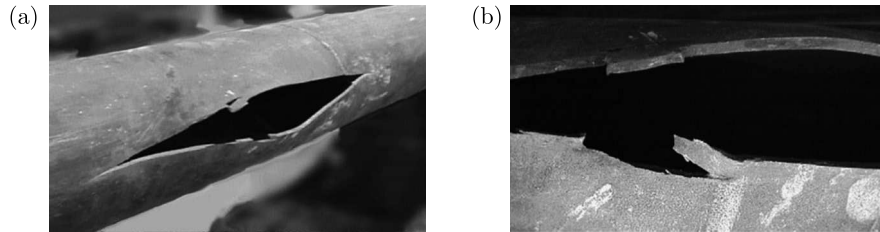


Fig. 2. Photographs of an axial crack in an engineering-structure caused by the applied load (the case of a steel gas cylinder)

## 2. Stress intensity factors (SIF) for pipes in service section

Critical temperature, pressure and the fluid stream can activate together a complex mechanism in the materials behavior while flaw geometries (having different shape) can easily initiate and propagate. To easy solve this challenge, we only consider a hypothetical case of axial flaws at the surface of a pipe (Fig. 3).
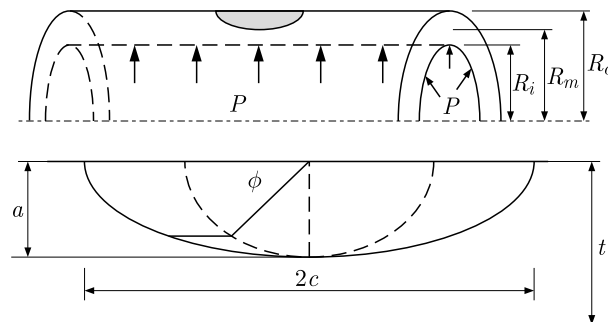


Fig. 3. Pipe geometry containing longitudinal surface flaw

Thus, in the simplified approach connected to the above flow configuration, a symmetry dimension of the structure may require. Once established a convenient methodology to run typical experimental processes, such as this symmetrical geometry, allows detecting accurately the values of $K_I$. The computation technique needs to sustain this strategy. There, dynamic loading events such as pressure surges and external impact are ignored, and the expected operating conditions of the buried pipeline are split into static contributions from the internal pressure, loading moment and tension stress.

Since each of these stress components creates mode-I opening of the flaw, individual SIF can be superposed to give a net value of $K_I$

$$K_{I\,NETT} \approx K_{IP} + K_{IM} + K_{IT} \tag{2.1}$$

with: $K_{IP}$ a factor of internal pressure, $K_{IM}$ a factor of bending load, $K_{IT}$ a factor tension loading.

A minimum assumption to avoid crack propagation, denoted by as well as the material fracture toughness ($K_{IC}$), must be sufficient to overcome the combined constraints of other factors. The embedded formulation of the cumulative action of these "external" SIFs allows

propagation of the cracks, when the critical Stress Intensity Factors SIF's(crit) (i.e. $K_{IC}$) become lower with respect to the net value of $K_I$

$$K_{IP} + K_{IM} + K_{IT} \geqslant K_{IC} \tag{2.2}$$

So, we notice the primary and most important problem in fracture analysis that the pressure vessel requires determination of the nett value of the SIF of the crack surface. The approach presented in this survey provides a comprehension range of results of SIFs for external surface cracks in a cylindrical fissure vessel.

A pipeline structure submitted to internal loading situations may develop the following state that is displayed in Figs. 4a-4c, where the effect of internal pressure can be examined for three different conditions. In the first case (i.e. Fig. 4a), we may consider only the pressure loading condition. In the second case (i.e. Fig. 4b), the pipe segment is assumed to have 'open ends' (i.e. the axial force at the ends due to pressure is zero). Thirdly, a 'closed end' situation is exhibited by applying the corresponding axial force (end-load) to the ends due to the applied pressure. In reality, the net axial force in a pipeline section may change from tensile to compressive loading. These loading sequences correspond to realistic situations encountered in pipelines. However, differences between the results obtained by the applied loads in a proportional or non-proportional manner could be another problem.
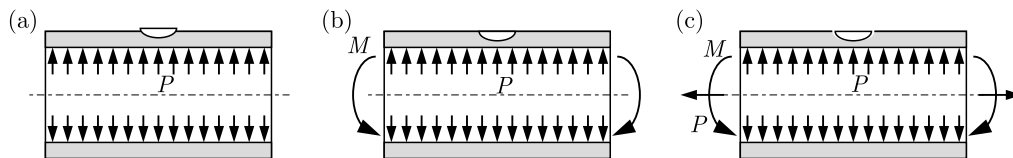


Fig. 4. Different load situations embedded into pipe configuration

When the pipe is loaded under bending routine along with internal pressure, a varying bending moment distribution along the length may be noted. This is caused by nonlinear geometry effects. Hence, in simulations with internal pressure, symmetry boundary conditions at the mid--length of the pipe are imposed through another set of MPC's. This facilitates direct calculation of the resisting moment at the mid-section.

However, has been it verified that the computed fracture parameters are not affected by these MPC's at the mid-section. Numerical analyses (i.e. based on the Finite Element Method (FEM) approach) could be a better tool to simulate the real life of pipe structures (containing flow) and, besides, to corroborate the analytical results with the numerical approximation.

## 3. Stress Intensity Factor (SIF) evaluation

The state of crack growth from a given longitudinal notch in a pipe depends somehow on the nature of the dominant stress state in the component. This reflects the nature of stress intensity ahead of the crack tip. In this specific case of a cracked component, the available evaluation routes for determination of the SIFs have been derived by using both analytical and numerical techniques. The introduction of the $K$ concept (link to the toughness in terms of critical values) proves to be a special value for studies on fracture and/or fatigue cracking (Tada *et al.*, 2000).

A number of researchers have published particular solutions of SIFs for a great range of notch profiles and loading conditions. Raju and Newman (1982) and Anderson (1999), in particular, developed numerical solutions for internally pressurized components containing semi-elliptical shapes with the aspect ratio $\alpha = a/b$ and relative depth $\xi = a/t$ of the deepest point $A$ on the defect front, where $a$ is the maximum crack depth. The fracture analysis of the above cracked

shell is very useful because some recommendations propose replacing the actual surface defect by an equivalent semi-elliptical crack.

The approach of SIF derived by Raju and Newman (1982) has been taken as the base framework for semi-elliptical cracks. The crack profile has been defined in terms of the shape factor $Q$ approximated by the following expressions

$$Q = \begin{cases} 1 + 1.464\left(\dfrac{a}{c}\right)^{1.65} & \text{for} \quad \dfrac{a}{c} < 1 \\[3mm] 1 + 1.464\left(\dfrac{c}{a}\right)^{1.65} & \text{for} \quad \dfrac{a}{c} > 1 \end{cases} \tag{3.1}$$

This approximation permits accurate estimation even in a particular case, where the correction factor developed in (ASME, 1981) works as a general model requiring only the first part of equation (3.1). The general hypothesis is

$$Q = 1 + 1.464\left(\frac{a}{c}\right)^{1.65} \tag{3.2}$$

Further, the SIF $K_I$ is evaluated in terms of the Lamé average hoop stress as

$$K_{IP} = \frac{PR_m}{t}\sqrt{\frac{\pi a}{Q}}Y\left(\frac{a}{t}, \frac{a}{2c}, \frac{R_0}{t}\right) \tag{3.3}$$

where $P$ is the internal pressure, $R_m$ and $R_0$ are the mean and outer radii of the pipe, respectively, $t$ is pipe thickness, $a$ is depth and $2c$ is crack length.

The formulation expressed in equation (3.3) covers the range of pipes with $R/t \leqslant 10$, considered in the present survey. It is believed that the approximation is quite good. However, to check the result, an interpolation between the previous solution and the numerical results presented by Stonesifer *et al.* (1992) for the geometrical correction $Y$ has been made. We noticed that equation (3.3) is valid in the case of pipes with ratios up to $R/t = 40$. Finally, for consistent results, the stress intensity factor has been evaluated by the formula presented in (Zahor, 1991) that partially agree with (Raju and Newman, 1982) and with the same limitations on the $R/t$ ratio. The formulation is expressed in the following manner

$$K_{IP} = PR_i\sqrt{\frac{\pi}{t}}\left(0.25 + \frac{0.42\alpha + 0.21\alpha^2}{[0.11(R/t) - 0.1]^{0.16}}\right) \tag{3.4}$$

where the shape factor $\alpha$ is defined

$$\alpha = \frac{a}{t}\left(\frac{c}{a}\right)^{0.58}$$

Subsequently, the stress intensity factor has been determined for a through wall crack, adopting two different expressions. The first agrees with (Zahor, 1991), described as

$$K_{IP} = \frac{PR_i}{t}\sqrt{\pi a}(1 + 0.0724\rho + 0.649\rho^2 - 0.233\rho^3 + 0.0382\rho^4 - 0.00235\rho^5) \tag{3.5}$$

with $\rho = c/\sqrt{R_i t}$.

In SAQ Handbook (Anderson, 1999), the Stress Intensity Factor $K$ is defined as

$$K_{IP} = \sqrt{\pi a}\sum_{i=0}^{3}\sigma_i Y_i\left(\frac{a}{t}, \frac{a}{2c}, \frac{R_m}{t}\right) \tag{3.6}$$

where $\sigma_i$ are the components which define the stress distribution though the cylinder wall, according to

$$\sigma_u = \sum_{i=0}^{3}\sigma_i\left(\frac{u^i}{a}\right) \tag{3.7}$$

The co-ordinate $u$ is defined through the remaining wall thickness ($u$ varies from the crack depth $a$ to the wall thickness $t$). The geometrical functions $Y_i$ are tabulated in (Raju and Newman, 1982).

This analytical correction has been confronted to the particular solution of (Zahoor, 1991). By using this formulation, the key form expression can be settled following the boundary correction factor $Y$ applied in Eq. (3.3)

$$Y = 1.12 + 0.053\xi + \frac{1 + 0.02\xi + 0.0191\xi^2}{1400}\Big(20 - \frac{R_m}{t}\Big)^2 \tag{3.8}$$

with

$$\xi = \frac{a}{t} \cdot \frac{a}{2c}$$

The outcomes derived from equation (3.8) are plotted in Fig. 5.
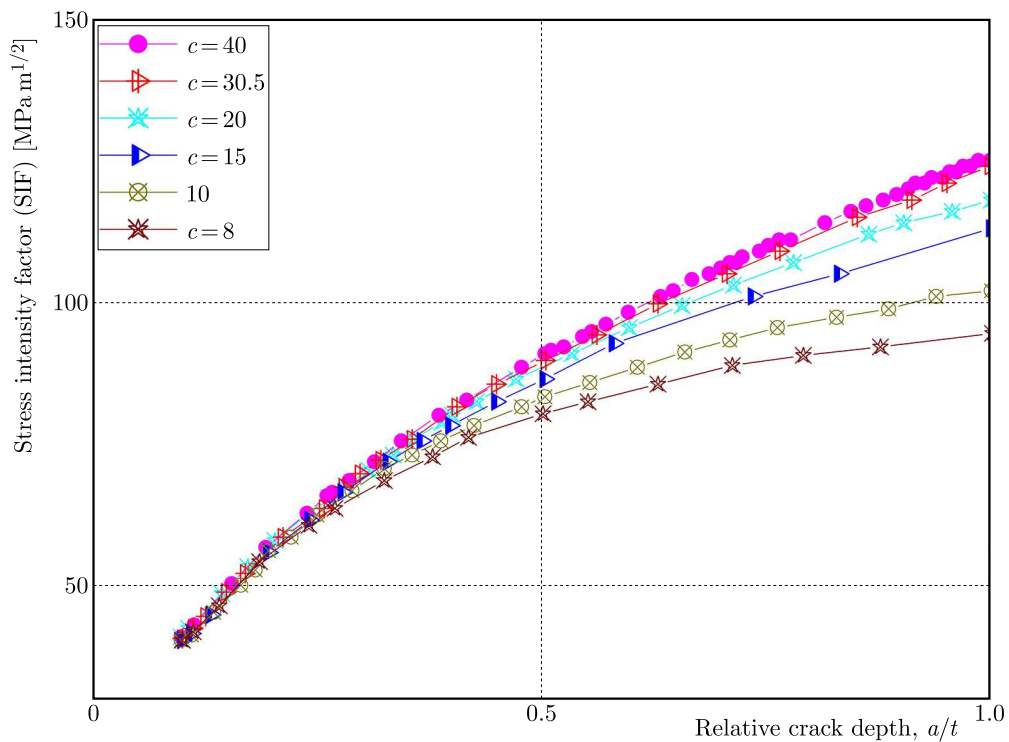


Fig. 5. Variations of $K_I$ with relative crack depth determined by Eq. (3.8)

Figure 5 displays the SIFs of steel cylinders with axial surface cracks (considering different lengths of flow), respecting the condition entailed in (Su and Bhuyan Gouri, 1999; Anderson, 1994). In a particular state (depending on cylinders with axial cracks), the stress intensity factor can be expressed respecting the following state of different relative crack sizes $2c/t$

$$K_{IP} = 0.4294\Big(\frac{2c}{t}\Big)^3 - 6.1122\Big(\frac{2c}{t}\Big)^2 + 49.489\frac{2c}{t} - 4.1444 \tag{3.9}$$

This expression is valid only in the range of $2.6 < 2c/t < 10.4$.

Vis a vis DN100 ABS pipe, in the case when the internal pressure is imposed, the SIF aroused can be calculated using the FE data considering different flaw depths. The accuracy of the results may be enhanced using a polynomial approximation as stated below

$$K_{IP} = 32.149 - 82.294\sqrt{a}\frac{a}{t} + 263.661\sqrt{a}\Big(\frac{a}{t}\Big)^2 - 111.753\sqrt{a}\Big(\frac{a}{t}\Big)^3 \tag{3.10}$$

In this configuration, the geometric correction factor have the form

$$Y = \frac{K_{IP}}{\sigma_{IP}\sqrt{\pi a}} = 1.824 - 4.669\frac{a}{t} + 14.959\left(\frac{a}{t}\right)^2 - 6.341\left(\frac{a}{t}\right)^3 \tag{3.11}$$

where $\sigma_{IP}$ is the membrane hoop stress of the pipe bore surface derived from the Lamé equation for a thick-walled cylinder

$$\sigma_{IP} = \frac{P(R_i^2 + R_0^2)}{R_0^2 - R_i^2} \tag{3.12}$$

where $R_0$ and $R_i$ are the outer and internal radii of the pipe, respectively.

## 4. FE analysis

The particular model depicted in Fig. 3 highlights a longitudinal crack surface in a pipe under internal pressure $P$ with configuration translated into numerical computation. The labels in the above sketch represent the characteristics of the pipe studied, which matches with a real situation. There, the mean radius and thickness of the pipe are denoted by $R_m$ and $t$, respectively. The crack length is characterized by $2c$ and the geometry is defined such that the depth of the crack is $a$. Four different values of $R_m/t$ are employed in the present work and different values of $2c$ are considered, namely, $2c = 16, 20, 30, 40, 61$ and $80$ mm. In this configuration, the internal pressure is settled $P = 1.5$ MPa. The 3D elastic computation approach under FE strategy has been implemented for this case of a longitudinal crack surface. Figure 6 shows details of the configuration. The methodology has been performed using a general-purpose FE program (CASTEM, 2014). The material tensile properties introduced in the FE analysis are assumed to obey the Ramberg-Osgood (R-O) equation

$$\frac{\varepsilon}{\varepsilon_0} = \frac{\sigma}{\sigma_y} + \alpha\frac{\sigma}{\sigma_y} \tag{4.1}$$

where $\varepsilon_0$, $\sigma_y$, and $\alpha$ are constants, $E\varepsilon_0 = \sigma_y$ , where $E$ is Young's modulus.

In Table 1, mechanical properties of the material evaluated in this paper which is steel P264GH are given.

**Table 1**

| Characteristic | Values |
|---|---|
| Elastic strain | $\varepsilon_0 = 0.0016$ |
| $\alpha = 1.86$ | constant |
| Modulus of elasticity | $E = 207000$ MPa |
| Poisson's ratio | $\nu = 0.3$ |
| Yield strength | $\sigma_y = 340$ MPa |
| Ultimate tensile strength | $R_m = 440$ MPa |
| Elongation to fracture | $A = 35\%$ |

The shape of the crack embedded in the pipe configuration during simulation is sketched in Fig. 6. In the programing procedure, only a half of the structure has been taken in account to reduce the resources needed for simulation. The structural mesh, having a progressive density of the mesh in front of the crack, has been embedded in order to stimulate the stress singularity. This technique of mesh densities near the notch in the pipeline network was considered with success in the particular case of fracture defect assessment in (Moustabchir et al.. 2015).
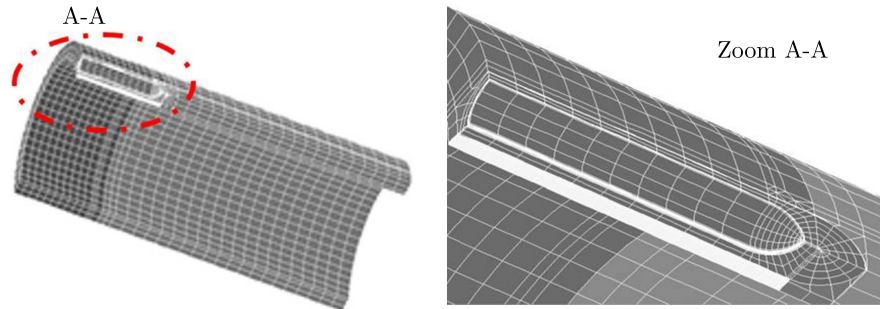
Fig. 6. Finite element configuration of a half of pipe with a longitudinal flaw

## 5.    Discussions

In this paper, the engineering $K_I$ parameter equations for an axial crack surface located in a pipe under internal pressure are throughly considered. The proposed approach offers details concerning the results obtained using an analytical method and a 3D computation technique. The $K_I$ parameter determined obeys R-O materials laws in the case of plastic deformation in a partially and fully plastic situation.

The values of the $K_I$ parameter have been determined considering a cylinder containing a defined crack size (i.e. crack surface). A summary regarding the results obtained using these methods of different axial crack surfaces are shown in Figs. 7a and 7b.

Figure 7a presents variations of the SIF values at the deepest points (i.e. crack fronts linked to the wall structure) of the external axial crack surface in the cylinders of different relative crack depths $a/t$ (crack). The results determined here prove a good approximation between the FE outcome and literature determinations.
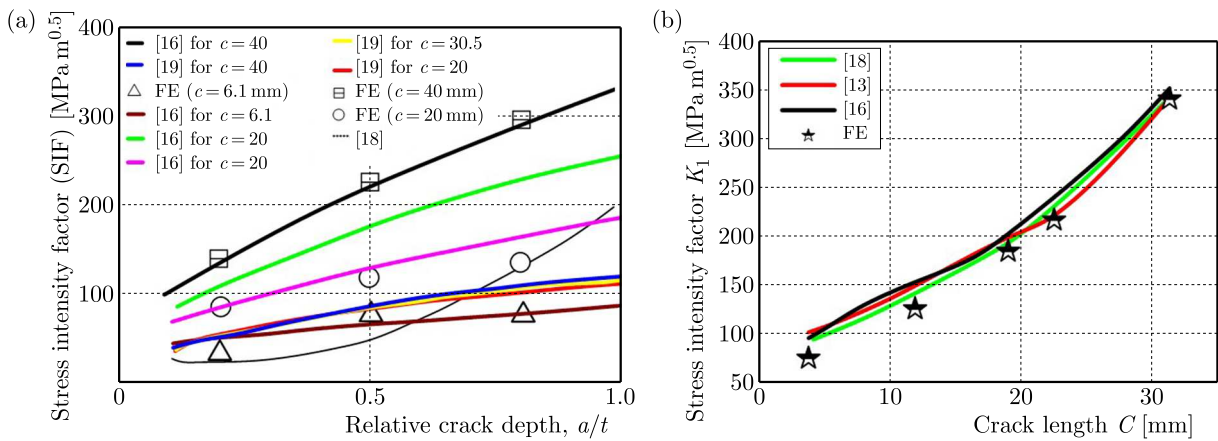


Fig. 7. (a) Variations of the $K_I$ parameter at the deepest point for a relative crack depth, (b) variations of $K_I$ parameter versus length of the crack; [13] – Nordhagen *et al.* (2014), [16] – Scheider *et al.* (2014), [18] – Schin and Cai (2004), [19] – Staat and Duc (2007)

Figure 7b deals with the effect of crack length, determining the evolution of SIF values. These results correspond to a certain situation, where the axial crack surface is characterized by the following dimensions $a/t = 0.2$, $D/t = 17$ and $n = 0.0446$. To be noted, the effects of SIF associated to the dimensions of the crack (as well as for different crack lengths) have also been considered. Figure 7a highlights the activity of the SIF. It increases with an increase in the crack length, and more particularly, the effects of crack length are observed more pronounced for short cracks.

These results confirm that the deepest points (linked to crack front) in a pipe structure are the most dangerous locations in the cylinders with slender axial surface defects, conforming to $a/t < 1$ (crack depth/cylinder thickness).

Besides, Fig. 7b proves the ascendant trend of the SIF values with respect to the crack size occurred in the pipe, crack dimensions as well as the record of $a/t$ for the external crack surface in the steel cylinder.

## 6.    Conclusions

Based on the results of this paper, the following conclusions can be drawn:

- The analytical results presented in Figs. 7a and 7b are found to be in good agreement with numerical results.

- A pipe with an axial external crack surface can be very well modelled using FE, as a three-dimensional finite element method, starting from a determined assumption. The FE modelling considers not only the cylindrical body but also the neck and transition areas of the cylinders, so the modelling process yields accurate results.

- The cylinder dimensions and crack size range are based directly on practically-applied steel gas cylinders, so the results are of greater practical value and can be applied to steel gas cylinders. The present results agree well with the results found in the literature.

- The Stress Intensity Factors associated with the axial crack surface are determined for different sizes. It has also been revealed that it is possible to describe the Stress Intensity Factor along the crack front of cylinders with axial external cracks by a six-order polynomial of the point of location. In short terms, this approach can be verified very well involving a second-order polynomial relative to the crack length $2c/t$, and a third-order polynomial relative to the crack depth $a/t$.

## References

1. ANDERSON P., 1999, *Procedure for Safety Assessment of Component with Cracks, Handbook Swedish Nuclear Power Institute*, Publication 99:49, SAQ/FOU Report 96/8. 3rd revised Ed.

2. ANDERSON T.L., 1884, *Fracture Mechanics Fundamentals and Application*, Chapter 12, Boca Raton, FL: CRC Press

3. *ASME Boiler and Pressure Vessel Code, Section XI*, 1981, Rules for in-service inspection of nuclear power plant components, American Soc. Mechanical Engineers, USA

4. CASTEM, 2014, http://www-cast3m.cea.fr/

5. CORIGLIANO A., MAIER G., MARIANI S., 1999, Analysis of ductile fracture in damaged pipelines by a geometric parameter method, *Engineering Structures*, **21**, 924-936

6. CRAVERO S., RUGGIERI C., 2005, Correlation of fracture behavior in high pressure pipelines with axial flaws using constraint designed test specimens. Part I: Plane-strain analyses, *Engineering Fracture Mechanics*, **72**, 1344-1360

7. DARCIS P.P., McCOWAN C.N., WINDHOFF H., McCOLSKEY J.D., SIEWERT T.A., 2008, Crack tip opening angle optical measurement methods in five pipeline steels, *Engineering Fracture Mechanics*, **75**, 2453-2468

8. Heliot J., Labbens R.C., Pellissier-Tanon A., 1997, Semi-elliptical cracks in a cylinder subjected to stress gradients, *Fracture Mechanics, ASTM STP 677*, 341-364

9. Lee O.S., Choi S.S., 1999, Effect of circular cavity on maximum equivalent stress and stress intensity factor at a crack in buried pipeline, *KSME International Journal*, **13**, 350 357

10. McGowan J.J., Raymund M., 1997, Stress intensity factor solutions for internal longitudinal semi-elliptical surface flaws in a cylinder under arbitrary loading, *Fracture Mechanics, ASTM STP 677*, 365-380

11. Moustabchir H., Pruncu C.I., Azari Z., Hariri S., Dmytrakh I., 2015, Fracture mechanics defect assessment diagram on pipe from steel P264GH with a notch, *International Journal of Mechanics and Materials in Design*, DOI 10.1007/s10999-015-9296-z

12. Murtagian G.R., Johnson D.H., Ernst H.A., 2005, Dynamic crack propagation in steel line pipes. Part I: Experimental investigation, *Engineering Fracture Mechanics*, **72**, 2519-2534

13. Nordhagen H., Dumoulin S., Gruben G., 2014, Main properties governing the ductile fracture velocity in pipelines: a numerical study using an (artificial fluid)-structure interaction model, *20th European Conference on Fracture (ECF20), Procedia Materials Science*, **3**, 1650-1655

14. Raju I.S., Newman Jr J.C., 1982, Stress intensity factors for internal and external surface cracks in cylindrical vessels, *Journal of Press Vessel Technology*, **104**, 293-308

15. Ruggieri C., Dotta F., 2011, Numerical modeling of ductile crack extension in high pressure pipelines with longitudinal flaws, *Engineering Structures*, **33**, 1423-1438

16. Scheider I., Nonn A., Völling A., Mondry A., Kalwa C., 2014, A damage mechanics based evaluation of dynamic fracture resistance in gas pipelines, *20th European Conference on Fracture (ECF20), Procedia Materials Science*, **3**, 1956-1964

17. Schoots K., Rivera-Tinoco R., Verbong G., Van der Zwaan B., 2011, Historical variation in the capital costs of natural gas, carbon dioxide and hydrogen pipelines and implications for future infrastructure, *International Journal of Greenhouse Gas Control*, **5**, 1614-1623

18. Shin C.S., Cai C.Q., 2004, Experimental and finite element analyses on stress intensity factors of an elliptical surface crack in a circular shaft under tension and bending, *International Journal of Fracture*, **129**, 239-264

19. Staat M., Duc K.V., 2007, Limit analysis of flaws in pressurized pipes and cylindrical vessels. Part I: Axial defects, *Engineering Fracture Mechanics*, **74**, 431-450

20. Stonesifer R.B., Brust F.W., Leis B.N., 1992, Stress intensity factors for long axial outer surface cracks in large $R/t$ pipes, *Fracture Mechanics: Twenty-Second Symposium, ASTM STP 1131*, **11**, 29-45

21. Su B., Bhuyan Gouri S., Elastic fracture properties of all-steel gas cylinders with different axial crack types, *International Journal of Pressure Vessels and Piping*, **76**, 23-33

22. Tada H., Paris P.C., Irwin G.R., 2000, *Stress Analysis of Cracks Handbook*, Third Edition, ASME Press

23. Tan J.P., Tu S.T., Wang G.Z., Xuan F.Z., 2015, Characterization and correlation of 3-D creep constraint between axially cracked pipelines and test specimens, *Engineering Fracture Mechanics*

24. You L.H., Ou H., Zheng Z.Y., 2007, Creep deformations and stresses in thick-walled cylindrical vessels of functionally graded materials subjected to internal pressure, *Composite Structures*, **78**, 2285-2291

25. Zahoor A., 1991, *Ductile Fracture Handbook*, Research project 1757-69, Vol. 3, Electric Power Research Institute

# MESHLESS LOCAL RADIAL POINT INTERPOLATION (MLRPI) FOR GENERALIZED TELEGRAPH AND HEAT DIFFUSION EQUATION WITH NON-LOCAL BOUNDARY CONDITIONS

Elyas Shivanian, Arman Khodayari

*Imam Khomeini International University, Department of Mathematics, Qazvin, Iran*

*e-mail address: shivanian@sci.ikiu.ac.ir*

In this paper, the meshless local radial point interpolation (MLRPI) method is formulated to the generalized one-dimensional linear telegraph and heat diffusion equation with non-local boundary conditions. The MLRPI method is categorized under meshless methods in which any background integration cells are not required, so that all integrations are carried out locally over small quadrature domains of regular shapes, such as lines in one dimensions, circles or squares in two dimensions and spheres or cubes in three dimensions. A technique based on the radial point interpolation is adopted to construct shape functions, also called basis functions, using the radial basis functions. These shape functions have delta function property in the frame work of interpolation, therefore they convince us to impose boundary conditions directly. The time derivatives are approximated by the finite difference time--stepping method. We also apply Simpson's integration rule to treat the non-local boundary conditions. Convergency and stability of the MLRPI method are clarified by surveying some numerical experiments.

*Keyword:* non-local boundary condition, meshless local radial point interpolation (MLRPI) method, local weak formulation, radial basis function, telegraph equation

## 1. Introduction

The telegraph equation is one of the important equations of mathematical physics with applications to many different fields such as transmission and propagation of electrical signals (Gonzalez-Velasco, 1995; Jordan and Puri, 1999), vibrational systems (Boyce and DiPrima, 1977), random walk theory (Banasiak and Mika, 1998) and mechanical systems (Tikhonov and Samarskii, 1990), etc. The heat diffusion and wave propagation equations are particular cases of the telegraph equation. Recently, increasing attention has been paid to the development, analysis and implementation of stable methods for numerical solutions of second-order hyperbolic equations. There have been many numerical methods for hyperbolic equations, such as the finite difference, the finite element, and the collocation methods, etc. (see Almenar *et al.*, 1997; Ciment and Leventhal, 1978) and literatures therein.

On the other hand, many of natural phenomena in science and engineering have been modelled by non-local boundary value problems. In these non-local problems, some integral terms often appear in the boundary conditions. These types of problems constitute a special class of boundary value problems which widely appear in mathematical modelling of various processes of physics, heat transfer, ecology, thermoelasticity, chemistry, biology and industry.

According to the numerical results obtained, the present methods can be considered as practical and effective numerical techniques to solve telegraph equations with non-local boundary conditions.

Let $\Omega = [0,1]$. Consider the 1D linear telegraph equation

$$\frac{\partial^2 u}{\partial t^2} + c\frac{\partial u}{\partial t} + bu - p\frac{\partial^2 u}{\partial x^2} = f(x,t) \qquad (x,t) \in \Omega \times [0,T] \tag{1.1}$$

with the initial and non-local boundary conditions

$$u(x,0) = u_0(x) \qquad \frac{\partial u}{\partial t}(x,0) = \psi(x)$$

$$u(0,t) = \gamma_1 \int_0^1 u(x,t)\, dx + \mu_1(t) \tag{1.2}$$

$$u(1,t) = \gamma_2 \int_0^1 u(x,t)\, dx + \mu_2(t)$$

where $c$, $b$ and $p$ are positive constants, $\gamma_1$ and $\gamma_2$ are constants and the functions $f$, $\psi$, $\mu_1(t)$ and $\mu_2(t)$ are assumed to be sufficiently smooth. Many partial differential equations are too complex to be solved by analytical methods. This caused mathematicians and engineers to come up with numerical methods such as the finite difference method (FDM) and the finite element method (FEM) to solve the equations. Although, these methods have been successfully applied to computational fluid dynamics problems, their accuracy depends critically on mesh quality and they have many difficulties in dealing with some complex problems. These difficulties can be overcome by meshless methods which have attracted considerable interest over the past few years (Kochmann and Venturini, 2014; Liu and Gu, 2005; Pan and Yuan, 2009; Sladek et al., 2006). These meshless methods do not require mesh for discretisation of the problem domain, and they construct approximate functions only via a set of nodes, so-called field nodes. In general, the meshless methods can be grouped into two categories. The first category is based on weak forms such as the element free Galerkin (EFG) method (Belytschko et al., 1995; Singh et al., 2007), the second category is based on strong forms such as meshless methods based on the radial basis functions (RBFs) (Dehghan and Shokri, 2008; Kansa, 1990). In addition, a meshless method based on combination of the strong and weak form has also been developed and is known as the meshless weak strong (MWS) form method. Due to the ill-conditioning of the resultant linear systems in the RBF-collocation method, various approaches are proposed to circumvent this problem (Libre et al., 2008; Ling and Schaback, 2008), being among them. The weak forms are used to derive a set of algebraic equations through a numerical integration process using a set of quadrature domain that may be constructed globally or locally in the domain of the problem. In the global formulation, background cells are required for the integration of the weak form. Strictly speaking, these meshless methods are not truly meshless methods. But in methods based on the local weak form formulation, numerical integrations are carried out over a local quadrature domains, therefore, no cells are required. As a result, they are referred to as truly meshless methods such as the meshless local Petrov-Galerkin (MLPG) method (Atluri and Zhu, 1998; Dehghan and Mirzaei, 2008; Shirzadi, 2014; Shivanian, 2015b). In the literature, several meshless weak form methods have been proposed such as the diffuse element method (DEM) (Nayroles et al., 1992), smooth particle hydrodynamic (SPH) (Bratsos, 2008; Dashtimanesh and Ghadimi, 2013), reproducing kernel particle method (RKPM) (Liu et al., 1995), boundary node method (BNM) (Mukherjee and Mukherjee, 1997), partition of unity finite element method (PUFEM) (Melenh and Babuska, 1996), finite sphere method (FSM) (De and Bathe, 2000), boundary point interpolation method (BPIM) (Gu and Liu, 2002) and boundary radial point interpolation method (BRPIM) (Gu and Liu, 2003). Liu applied the concept of MLPG and developed the meshless local radial point interpolation (MLRPI) method (Hosseini et al., 2015; Liu and Gu, 2001; Shivanian, 2013, 2015a; Shivanian and khodabandehlo, 2014). In this paper,

we concentrate on the numerical solution of Eqs. (1.1) and (1.2) using the meshless local radial point interpolation (MLRPI) method. Besides, we use Simpson's integration rule to impose the non-local boundary condition.

## 2. Approximation of field variables using the radial point interpolation method

Consider a continuous function $u(x)$ defined in a domain $\Omega$, which is represented by a set of field nodes. The $u(x)$ at the point of interest $x$ is approximated as follows

$$u(\mathbf{x}) = \sum_{i=1}^{n} R_i(\mathbf{x})a_i + \sum_{j=1}^{m} p_j(\mathbf{x})b_j = \mathbf{R}^{\mathrm{T}}(\mathbf{x})\mathbf{a} + \mathbf{P}^{\mathrm{T}}(\mathbf{x})\mathbf{b} \qquad (2.1)$$

where $R_i(\mathbf{x})$ is thea radial basis function (RBF), $n$ is the number of RBFs, $p_j(\mathbf{x})$ is the monomial in the 1-D space $x$ and $m$ is the number of the monomials. In the present work, we have applied thin plate spline (TPS) multiquadrics (MQ) as the radial basis functions in Eq. (2.1). In order to determine $a_i$ and $b_j$ in Eq. (2.1), a support domain is needed for the point of interest at $x$ so that $n$ field nodes are included in the support domain. Then, coefficients $a_i$ and $b_j$ in Eq. (2.1) can be determined by the following system of $n$ linear equations

$$\mathbf{U}_s = \mathbf{R}_n\mathbf{a} + \mathbf{P}_m\mathbf{b} \qquad (2.2)$$

in which the vector $U_s$ is

$$\mathbf{U}_s = \{u_1, u_2, u_3, \ldots, u_n\}^{\mathrm{T}} \qquad (2.3)$$

moreover, $\mathbf{R}_n$ and $\mathbf{P}_m$ are the RBFs and polynomial moment matrices, respectively. On the other hand, Eq. (2.1) can be rewritten as

$$u(\mathbf{x}) = \mathbf{R}^{\mathrm{T}}(\mathbf{x})\mathbf{a} + \mathbf{P}^{\mathrm{T}}(\mathbf{x})\mathbf{b} = \left\{\mathbf{R}^{\mathrm{T}}(\mathbf{x}), \mathbf{P}^{\mathrm{T}}(\mathbf{x})\right\} \begin{bmatrix} \mathbf{a} \\ \mathbf{b} \end{bmatrix} \qquad (2.4)$$

and then, by using that, we obtain

$$\begin{aligned} u(\mathbf{x}) &= \left\{\mathbf{R}^{\mathrm{T}}(\mathbf{x}), \mathbf{P}^{\mathrm{T}}(\mathbf{x})\right\} \begin{bmatrix} \mathbf{R}_n & \mathbf{P}_m \\ \mathbf{P}_m^{\mathrm{T}} & \mathbf{0} \end{bmatrix}^{-1} \widetilde{\mathbf{U}}_s \\ &= \left\{\mathbf{R}^{\mathrm{T}}(\mathbf{x}), \mathbf{P}^{\mathrm{T}}(\mathbf{x})\right\} \mathbf{G}^{-1}\widetilde{\mathbf{U}}_s = \widetilde{\mathbf{\Phi}}^{\mathrm{T}}(\mathbf{x})\widetilde{\mathbf{U}}_s \end{aligned} \qquad (2.5)$$

where $\widetilde{\mathbf{\Phi}}^{\mathrm{T}}(\mathbf{x})$ can be be introduced by

$$\widetilde{\mathbf{\Phi}}^{\mathrm{T}}(\mathbf{x}) = \left\{\mathbf{R}^{\mathrm{T}}(\mathbf{x}), \mathbf{P}^{\mathrm{T}}(\mathbf{x})\right\} \mathbf{G}^{-1} = \{\phi_1(\mathbf{x}), \phi_2(\mathbf{x}), \ldots, \phi_n(\mathbf{x}), \phi_{n+1}(\mathbf{x}), \ldots, \phi_{n+m}(\mathbf{x})\} \qquad (2.6)$$

The first $n$ functions of the above vector function are called the RPIM shape functions corresponding to the nodal displacements. We show them by the vector $\widetilde{\mathbf{\Phi}}^{\mathrm{T}}(\mathbf{x})$, so that it is

$$\widetilde{\mathbf{\Phi}}^{\mathrm{T}}(\mathbf{x}) = \{\phi_1(\mathbf{x}), \phi_2(\mathbf{x}), \ldots, \phi_n(\mathbf{x})\} \qquad (2.7)$$

Equation (2.5) is then transformed into

$$u(\mathbf{x}) = \widetilde{\mathbf{\Phi}}^{\mathrm{T}}(\mathbf{x})\mathbf{U}_s = \sum_{i=1}^{n} \phi_i(\mathbf{x})u_i \qquad (2.8)$$

## 3. Finite differences approximation

The following finite difference approximations of the order $O(\Delta t)^2$ are used for time discretization

$$
\begin{aligned}
\frac{\partial^2 u(\mathbf{x},t)}{\partial t^2} &\cong \frac{1}{\Delta t^2}\big(u^{(k+1)}(\mathbf{x}) - 2u^{(k)}(\mathbf{x}) + u^{(k-1)}(\mathbf{x})\big) \\
\frac{\partial u(\mathbf{x},t)}{\partial t} &\cong \frac{1}{2\Delta t}\big(u^{(k+1)}(\mathbf{x}) - u^{(k-1)}(\mathbf{x})\big)
\end{aligned}
\tag{3.1}
$$

Also, we employ the following approximation using the Crank-Nicolson technique

$$
\begin{aligned}
u(\mathbf{x},t) &\cong \frac{1}{3}\big(u^{(k+1)}(\mathbf{x}) + u^{(k)}(\mathbf{x}) + u^{(k-1)}(\mathbf{x})\big) \\
\frac{\partial^2 u(\mathbf{x},t)}{\partial \mathbf{x}^2} &\cong \frac{1}{3}\Big(\frac{\partial^2 u^{(k+1)}(\mathbf{x},t)}{\partial \mathbf{x}^2} + \frac{\partial^2 u^{(k)}(\mathbf{x},t)}{\partial \mathbf{x}^2} + \frac{\partial^2 u^{(k-1)}(\mathbf{x},t)}{\partial \mathbf{x}^2}\Big)
\end{aligned}
\tag{3.2}
$$

where $u^k(\mathbf{x}) = u(\mathbf{x}, k\Delta t)$.

Using the above approximations, Eq. (1.1) can be written as

$$
\begin{aligned}
&\frac{1}{\Delta t^2}\big(u^{(k+1)}(\mathbf{x}) - 2u^{(k)}(\mathbf{x}) + u^{(k-1)}(\mathbf{x})\big) + \frac{c}{2\Delta t}\big(u^{(k+1)}(\mathbf{x}) - u^{(k-1)}(\mathbf{x})\big) \\
&+ \frac{b}{3}\big(u^{(k+1)}(\mathbf{x}) + u^{(k)}(\mathbf{x}) + u^{(k-1)}(\mathbf{x})\big) \\
&- \frac{p}{3}\Big(\frac{\partial^2 u^{(k+1)}(\mathbf{x})}{\partial \mathbf{x}^2} + \frac{\partial^2 u^{(k)}(\mathbf{x})}{\partial \mathbf{x}^2} + \frac{\partial^2 u^{(k-1)}(\mathbf{x})}{\partial \mathbf{x}^2}\Big) = \frac{1}{3}\big(f^{(k+1)}(\mathbf{x}) + f^{(k)}(\mathbf{x}) + f^{(k-1)}(\mathbf{x})\big)
\end{aligned}
\tag{3.3}
$$

Supposing the notations $\lambda = 1/\Delta t^2$ and $\mu = c/(2\Delta t)$, we obtain

$$
\begin{aligned}
&\Big(\lambda + \mu + \frac{b}{3}\Big)u^{(k+1)} - \frac{p}{3}\frac{\partial^2 u^{(k+1)}(\mathbf{x})}{\partial \mathbf{x}^2} = \Big(2\lambda - \frac{b}{3}\Big)u^{(k)} + \frac{p}{3}\frac{\partial^2 u^{(k)}(\mathbf{x})}{\partial \mathbf{x}^2} \\
&+ \Big(-\lambda + \mu - \frac{b}{3}\Big)u^{(k-1)} + \frac{p}{3}\frac{\partial^2 u^{(k-1)}(\mathbf{x})}{\partial \mathbf{x}^2} + \frac{1}{3}\big(f^{(k+1)}(\mathbf{x}) + f^{(k)}(\mathbf{x}) + f^{(k-1)}(\mathbf{x})\big).
\end{aligned}
\tag{3.4}
$$

## 4. The meshless local weak form formulation

Instead of setting the global weak form, the MLRPI method sets up the weak form over the local quadrature cell such as $\Omega_q$, which is a small region taken for each node in the global domain $\Omega$. The local quadrature cells overlap with each other and cover the whole global domain $\Omega$. The local quadrature cells could be of any geometric shape and size. In one dimensional problems, they are lines (intervals). The local weak form of Eq. (3.4) for $\mathbf{x}_i \in \Omega_q^i = (x_i - r_q, x_i + r_q)$ can be constructed as

$$
\begin{aligned}
&\int_{\Omega_q^i}\Big[\Big(\big(\lambda + \mu + \frac{b}{3}\big)u^{(k+1)} - \frac{p}{3}\frac{\partial^2 u^{(k+1)}(\mathbf{x})}{\partial \mathbf{x}^2}\Big]\nu(\mathbf{x})\,dx = \int_{\Omega_q^i}\Big[\big(2\lambda - \frac{b}{3}\big)u^{(k)} + \frac{p}{3}\frac{\partial^2 u^{(k)}(\mathbf{x})}{\partial \mathbf{x}^2}\Big]\nu(\mathbf{x})\,dx \\
&+ \int_{\Omega_q^i}\Big[\big(\big(-\lambda + \mu - \frac{b}{3}\big)u^{(k-1)} + \frac{p}{3}\frac{\partial^2 u^{(k-1)}(\mathbf{x})}{\partial \mathbf{x}^2}\Big]\nu(\mathbf{x})\,dx \\
&+ \int_{\Omega_q^i}\Big[\frac{1}{3}\big(f^{(k+1)}(\mathbf{x}) + f^{(k)}(\mathbf{x}) + f^{(k-1)}(\mathbf{x})\big)\Big]\nu(\mathbf{x})\,dx
\end{aligned}
\tag{4.1}
$$

where $\Omega_q^i$ is the local quadrature domain corresponding to the point $i$, and $\nu(\mathbf{x})$ is the Heaviside step function defined by (Hu *et al.*, 2006; Liu *et al.*, 2006)

$$\nu(\mathbf{x}) = \begin{cases} 1 & x \in \Omega_q \\ 0 & x \notin \Omega_q \end{cases} \tag{4.2}$$

as the test function in each local quadrature domain. Hence, we obtain

$$\left(\lambda + \mu + \frac{b}{3}\right) \int\limits_{\Omega_q^i} u^{(k+1)}\nu(\mathbf{x})\, dx - \frac{p}{3} \int\limits_{\Omega_q^i} \frac{\partial^2 u^{(k+1)}(\mathbf{x})}{\partial \mathbf{x}^2}\nu(\mathbf{x})\, dx$$

$$= \left(2\lambda - \frac{b}{3}\right) \int\limits_{\Omega_q^i} u^{(k)}\nu(\mathbf{x})\, dx + \frac{p}{3} \int\limits_{\Omega_q^i} \frac{\partial^2 u^{(k)}(\mathbf{x})}{\partial \mathbf{x}^2}\nu(\mathbf{x})\, dx$$

$$+ \left(-\lambda + \mu - \frac{b}{3}\right) \int\limits_{\Omega_q^i} u^{(k-1)}\nu(\mathbf{x})\, dx + \frac{p}{3} \int\limits_{\Omega_q^i} \frac{\partial^2 u^{(k-1)}(\mathbf{x})}{\partial \mathbf{x}^2}\nu(\mathbf{x})\, dx \tag{4.3}$$

$$+ \frac{1}{3} \int\limits_{\Omega_q^i} (f^{(k+1)}(\mathbf{x}) + f^{(k)}(\mathbf{x}) + f^{(k-1)}(\mathbf{x}))\nu(\mathbf{x})\, dx$$

Using integration by parts, one obtains

$$\int\limits_{\Omega_q^i} \frac{\partial^2 u^{(k)}(\mathbf{x})}{\partial \mathbf{x}^2}\nu(\mathbf{x})\, dx = \nu(\mathbf{x})\frac{\partial u^{(k)}(\mathbf{x})}{\partial \mathbf{x}}\Big|_{\mathbf{x}=x_i-r_q}^{\mathbf{x}=x_i+r_q} - \int\limits_{\Omega_q^i} \frac{\partial u^{(k)}(\mathbf{x})}{\partial \mathbf{x}}\frac{\partial \nu(\mathbf{x})}{\partial x}\, dx \tag{4.4}$$

Then, by applying the test function, the following local weak equation is obtained

$$\left(\lambda + \mu + \frac{b}{3}\right) \int\limits_{\Omega_q^i} u^{(k+1)}\, dx - \frac{p}{3}\left(\frac{\partial u^{(k+1)}(\mathbf{x})}{\partial \mathbf{x}}\Big|_{\mathbf{x}=x_i-r_q}^{\mathbf{x}=x_i+r_q}\right)$$

$$= \left(2\lambda - \frac{b}{3}\right) \int\limits_{\Omega_q^i} u^{(k)}\, dx + \frac{p}{3}\left(\frac{\partial u^{(k)}(\mathbf{x})}{\partial \mathbf{x}}\Big|_{\mathbf{x}=x_i-r_q}^{\mathbf{x}=x_i+r_q}\right)$$

$$+ \left(-\lambda + \mu - \frac{b}{3}\right) \int\limits_{\Omega_q^i} u^{(k-1)}\, dx + \frac{p}{3}\left(\frac{\partial u^{(k-1)}(\mathbf{x})}{\partial \mathbf{x}}\Big|_{\mathbf{x}=x_i-r_q}^{\mathbf{x}=x_i+r_q}\right) \tag{4.5}$$

$$+ \frac{1}{3} \int\limits_{\Omega_q^i} (f^{(k+1)}(\mathbf{x}) + f^{(k)}(\mathbf{x}) + f^{(k-1)}(\mathbf{x}))\, dx$$

## 5.  Discretization in the MLRPI method

In this Section, we consider Eq. (4.5) to see how to obtain discrete equations. Consider $N$ regularly located points on the boundary and domain of the problem, i.e. interval $[0,1]$, so that the distance between two consecutive nodes in each direction is constant and equal to $h$. Assuming that $u(\mathbf{x}_i, k\Delta t)$, $i = 1, 2, \ldots, N$ are known, our aim is to compute $u(\mathbf{x}_i, (k+1)\Delta t)$, $i = 1, 2, \ldots, N$. So, we have $N$ unknowns and to compute these unknowns, we need $N$ equations. To obtain the discrete equations from locally weak forms (4.5) for the nodes located in the interior of the domain, i.e., for $\mathbf{x}_i \in$ interior $\Omega$, we substitute approximation formulas (2.8) into local integral equations (4.5) to have

$$\left[\left(\lambda+\mu+\frac{b}{3}\right)\sum_{j=1}^{N}\left(\int_{\Omega_q^i}\phi_j(\mathbf{x})\,dx\right)-\frac{p}{3}\sum_{j=1}^{N}\left(\frac{\partial\phi_j(\mathbf{x})}{\partial\mathbf{x}}\Big|_{\mathbf{x}=x_i+r_q}-\frac{\partial\phi_j(\mathbf{x})}{\partial\mathbf{x}}\Big|_{\mathbf{x}=x_i-r_q}\right)\right]u_j^{(k+1)}$$

$$=\left[\left(2\lambda-\frac{b}{3}\right)\sum_{j=1}^{N}\left(\int_{\Omega_q^i}\phi_j(\mathbf{x})\,dx\right)+\frac{p}{3}\sum_{j=1}^{N}\left(\frac{\partial\phi_j(\mathbf{x})}{\partial\mathbf{x}}\Big|_{\mathbf{x}=x_i+r_q}-\frac{\partial\phi_j(\mathbf{x})}{\partial\mathbf{x}}\Big|_{\mathbf{x}=x_i-r_q}\right)\right]u_j^{(k)}$$

$$+\left[\left(-\lambda+\mu-\frac{b}{3}\right)\sum_{j=1}^{N}\left(\int_{\Omega_q^i}\phi_j(\mathbf{x})dx\right)+\frac{p}{3}\sum_{j=1}^{N}\left(\frac{\partial\phi_j(\mathbf{x})}{\partial\mathbf{x}}\Big|_{\mathbf{x}=x_i+r_q}-\frac{\partial\phi_j(\mathbf{x})}{\partial\mathbf{x}}\Big|_{\mathbf{x}=x_i-r_q}\right)\right]u_j^{(k-1)}$$

$$+\frac{1}{3}\int_{\Omega_q^i}\left(f^{(k+1)}(\mathbf{x})+f^{(k)}(\mathbf{x})+f^{(k-1)}(\mathbf{x})\right)\,dx \tag{5.1}$$

## 6.    Numerical implementation of the MLRPI method

By using Simpson's integration rule for nodes which are located on the boundary, we have for all $k$

$$u^{(k)}(x_1)=\gamma_1\frac{h}{3}\left[u^{(k)}(x_1)+4u^{(k)}(x_2)+2u^{(k)}(x_3)+\ldots+4u^{(k)}(x_{N-1})+u^{(k)}(x_N)\right]+\mu_1(k\Delta t)$$

$$u^{(k)}(x_N)=\gamma_2\frac{h}{3}\left[u^{(k)}(x_1)+4u^{(k)}(x_2)+2u^{(k)}(x_3)+\ldots+4u^{(k)}(x_{N-1})+u^{(k)}(x_N)\right]+\mu_2(k\Delta t) \tag{6.1}$$

where $x_1=0$ and $x_N=1$.

The matrix forms of Eqs. (5.1) and (6.1) for all $N$ nodal points in the domain and the boundary of the problem are given below

$$\left[\left(\lambda+\mu+\frac{b}{3}\right)\sum_{j=1}^{N}A_{i,j}-\frac{p}{3}\sum_{j=1}^{N}B_{i,j}\right]u_j^{(k+1)}=\left[\left(2\lambda-\frac{b}{3}\right)\sum_{j=1}^{N}A_{i,j}+\frac{p}{3}\sum_{j=1}^{N}B_{i,j}\right]u_j^{(k)}$$

$$+\left[\left(-\lambda+\mu-\frac{b}{3}\right)\sum_{j=1}^{N}A_{i,j}+\frac{p}{3}\sum_{j=1}^{N}B_{i,j}\right]u_j^{(k-1)}+E_i(k-1,k,k+1) \tag{6.2}$$

where

$$A_{i,j}=\int_{\Omega_q^i}\phi_j(\mathbf{x})\,dx$$

$$B_{i,j}=\left(\frac{\partial\phi_j(\mathbf{x})}{\partial\mathbf{x}}\Big|_{\mathbf{x}=x_i+r_q}-\frac{\partial\phi_j(\mathbf{x})}{\partial\mathbf{x}}\Big|_{\mathbf{x}=x_i-r_q}\right) \tag{6.3}$$

$$E_i(k-1,k,k+1)=\frac{1}{3}\int_{\Omega_q^i}\left(f^{(k+1)}(\mathbf{x})+f^{(k)}(\mathbf{x})+f^{(k-1)}(\mathbf{x})\right)\,dx$$

Assuming

$$\mathbf{A}_{i,j}=\left(\lambda+\mu+\frac{b}{3}\right)A_{i,j}-\frac{p}{3}B_{i,j} \qquad \mathbf{B}_{i,j}=\left(2\lambda-\frac{b}{3}\right)A_{i,j}+\frac{p}{3}B_{i,j}$$

$$\mathbf{C}_{i,j}=\left(-\lambda+\mu-\frac{b}{3}\right)A_{i,j}+\frac{p}{3}B_{i,j} \qquad \mathbf{U}=\{u_i\}_{N\times1} \tag{6.4}$$

$$\mathbf{E}^k=[E_1(k-1,k,k+1),E_2(k-1,k,k+1),\ldots,E_N(k-1,k,k+1)]^{\mathrm{T}}$$

yields

$$\mathbf{A}\mathbf{U}^{(k+1)} = \mathbf{B}\mathbf{U}^{(k)} + \mathbf{C}\mathbf{U}^{(k-1)} + \mathbf{E}^k \tag{6.5}$$

Furthermore, to satisfy Eqs. (6.1), for both nodes belong to the boundary, i.e., $\{x_1, x_N\}$, we set

$$
\begin{aligned}
\mathbf{E}_i^k &= \begin{cases} \mu_1(k\Delta t) & i = 1 \\ \mu_2(k\Delta t) & i = N \end{cases} \\
\forall j: \quad \mathbf{B}_{i,j} &= \mathbf{C}_{i,j} = \mathbf{0} \qquad i = 1, N \\
\mathbf{A}_1 &= \left[1 - \gamma_1 \frac{h}{3}, -4\gamma_1 \frac{h}{3}, -2\gamma_1 \frac{h}{3}, \dots, -4\gamma_1 \frac{h}{3}, -\gamma_1 \frac{h}{3}\right] \\
\mathbf{A}_N &= \left[-\gamma_2 \frac{h}{3}, -4\gamma_2 \frac{h}{3}, -2\gamma_2 \frac{h}{3}, \dots, -4\gamma_2 \frac{h}{3}, 1 - \gamma_2 \frac{h}{3}\right]
\end{aligned}
\tag{6.6}
$$

where $\mathbf{A}_1$ and $\mathbf{A}_N$ are the first and $N$-th rows of the matrix $\mathbf{A}$, respectively.

At the first time level, when $n = 0$, according to the initial conditions that are introduced in Eq. (1.2), we apply the following assumptions

$$u^{(0)} = u_0 \qquad u^{(-1)} \cong u^{(1)} - 2\Delta t \psi(x)$$

where

$$u_0 = [u_0(x_1), u_0(x_2), \dots, u_0(x_N)]^{\mathrm{T}} \qquad \psi = [\psi(x_1), \psi(x_2), \dots, \psi(x_N)]^{\mathrm{T}}$$

## 7. Numerical experiments

In this Section, two numerical expriments for application of the meshless local radial point interpolation method (MLRPI) in solving the one-dimensional linear telegraph equation with non-local boundary conditions are presented. In both examples, the domain integrals are evaluated with 3 points Gaussian quadrature rule. In these problems, the regular distributed nodal points are used. Also, in order to implement the meshless local weak form in these cases, the radius of the local quadrature domain $r_q = 0.8h$ is selected, where $h$ is the distance between the nodes in the $x$ direction ($h = \Delta x$). The size of $r_q$ is such that the union of these sub-domains must cover the whole global domain. The radius of the support domain to the local radial point interpolation method is $r_s = 4r_q$. This size is significant enough to have a sufficient number of nodes ($n$) to give appropriate shape functions. Also, in Eq. (2.1), we set $m = 5$.

**Example 1.** We set $c = 20$, $b = 25$ and $p = 1$. The exact solution of the first example is taken as $u(x, t) = t^3(2x^3 - x + 4)$, $(x, t) \in [0, 1] \times [0, 1]$. According to this exact solution, $f(x, t)$ is given by

$$f(x, t) = (6t + 3ct^2)(2x^3 - x + 4) + bt^3(2x^3 - x + 4) - 12pxt^3$$

the initial conditions are

$$u(x, 0) = 0 \qquad \frac{\partial u}{\partial t}(x, 0) = 0$$

and the non-local boundary conditions take the form

$$u(0, t) = \int_0^1 u(x, t)\, dx \qquad t \geqslant 0$$

$$u(1, t) = \frac{5}{4} \int_0^1 u(x, t)\, dx \qquad t \geqslant 0$$

Tables 1 and 2 as well as Fig. 1a show the results of the MLRPI method to solve Example 1 using TPS as the radial basis function. Also, Tables 3 and 4 as well as Fig. 1b illustrate the results of the current method to solve Example 1 using MQ as the radial basis function. As it is seen, the MLRPI method is of high accuracy. Furthermore, it is seen that the method is convergent with respect to the spatial and time variable using both TPS and MQ.
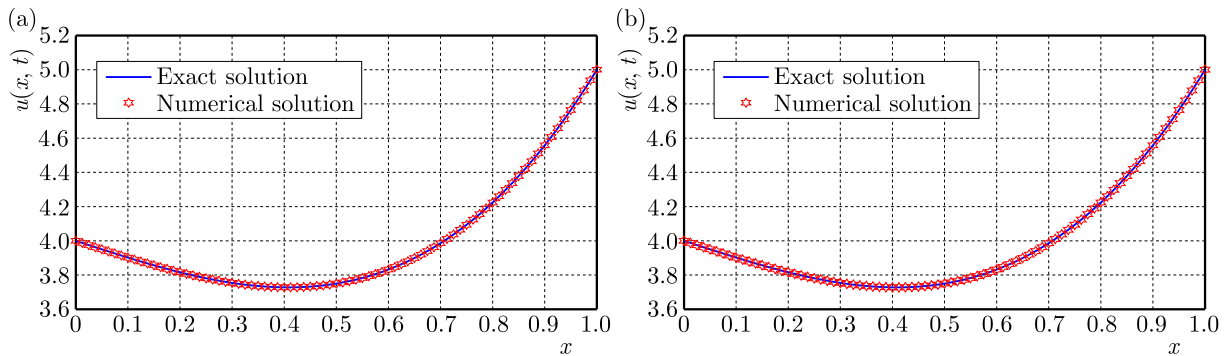


Fig. 1. Numerical solutions and the exact solution at time $t = 1.0$ for Example 1: (a) using TPS, (b) using MQ. The solid line corresponds to the exact solution, the starred line corresponds to the numerical solution of the MLRPI with $\Delta t = 0.0001$ and $\Delta x = 0.0125$

**Table 1.** The $L^1$, $L^2$ and $L^\infty$ errors calculated by MLRPI for Example 1 with different $\Delta x$ and $\Delta t$ at time $t = 1.0$ (using TPS)

| $\Delta t$ | $\Delta x$ | $\|E\|_1$ | $\|E\|_2$ | $\|E\|_\infty$ |
|---|---|---|---|---|
| 0.001 | 0.25 | 4.070835E-03 | 2.136594E-03 | 1.508984E-03 |
| 0.001 | 0.125 | 3.470766E-04 | 1.792837E-04 | 1.587210E-04 |
| 0.001 | 0.1 | 1.718355E-04 | 7.995307E-05 | 6.922815E-05 |
| 0.001 | 0.05 | 6.156571E-05 | 1.401474E-05 | 5.949385E-06 |

**Table 2.** The $L^1$, $L^2$ and $L^\infty$ errors calculated by MLRPI for Example 1 with different $\Delta x$ and $\Delta t$ at time $t = 1.0$ (using TPS)

| $\Delta t$ | $\Delta x$ | $\|E\|_1$ | $\|E\|_2$ | $\|E\|_\infty$ |
|---|---|---|---|---|
| 0.001 | 0.0125 | 1.945099E-04 | 2.169317E-05 | 2.997031E-06 |
| 0.0005 | 0.0125 | 4.863614E-05 | 5.424111E-06 | 7.494035E-07 |
| 0.00025 | 0.0125 | 1.217382E-05 | 1.357562E-06 | 1.875924E-07 |
| 0.0001 | 0.0125 | 1.964876E-06 | 2.192364E-07 | 3.026972E-08 |

**Table 3.** The $L^1$, $L^2$ and $L^\infty$ errors calculated by MLRPI for Example 1 with different $\Delta x$ and $\Delta t$ at time $t = 1.0$ (using MQ)

| $\Delta t$ | $\Delta x$ | $\|E\|_1$ | $\|E\|_2$ | $\|E\|_\infty$ |
|---|---|---|---|---|
| 0.001 | 0.25 | 4.070835E-03 | 2.136594E-03 | 1.508984E-03 |
| 0.001 | 0.125 | 3.459171E-04 | 1.780828E-04 | 1.575668E-04 |
| 0.001 | 0.1 | 1.715535E-04 | 7.972770E-05 | 6.898580E-05 |
| 0.001 | 0.05 | 6.154538E-05 | 1.401788E-05 | 5.974310E-06 |

**Table 4.** The $L^1$, $L^2$ and $L^\infty$ errors calculated by MLRPI for Example 1 with different $\Delta x$ and $\Delta t$ at time $t = 1.0$ (using MQ)

| $\Delta t$ | $\Delta x$ | $\|E\|_1$ | $\|E\|_2$ | $\|E\|_\infty$ |
|---|---|---|---|---|
| 0.001 | 0.0125 | 1.942840E-04 | 2.166659E-05 | 2.993550E-06 |
| 0.0005 | 0.0125 | 4.841030E-05 | 5.397581E-06 | 7.459259E-07 |
| 0.00025 | 0.0125 | 1.194834E-05 | 1.331264E-06 | 1.841192E-07 |
| 0.0001 | 0.0125 | 1.740619E-06 | 1.944979E-07 | 2.682201E-08 |

**Example 2.** We set $c = 20$, $b = 25$ and $p = 1$. The exact solution of the this example is taken as $u(x,t) = t^3 \sin(x+1)$, $(x,t) \in [0,1] \times [0,1]$. According to this exact solution, $f(x,t)$ is given by

$$f(x,t) = (6t + 3ct^2)\sin(x+1) + bt^3\sin(x+1) + pt^3\sin(x+1)$$

the initial conditions are

$$u(x,0) = 0 \qquad \frac{\partial u}{\partial t}(x,0) = 0$$

and the non-local boundary conditions take the form

$$u(0,t) = 0.8797864387 \int_0^1 u(x,t)\,dx \qquad t \geqslant 0$$

$$u(1,t) = 0.950701283 \int_0^1 u(x,t)\,dx \qquad t \geqslant 0$$

Tables 5 and 6 as well as Fig. 2a show the results of the MLRPI method to solve Example 2 using TPS as the radial basis function. Besides, Tables 7 and 8 as well as Fig. 2b demonstrate the results of the present method to solve Example 2 using MQ as the radial basis function. As it is seen, the MLRPI method is of high accuracy. Moreover, we see that the convergence with respect to both the time step ($\Delta t$) and the number of nodal points ($N$) are hold, no matter which kind of RBF we use.
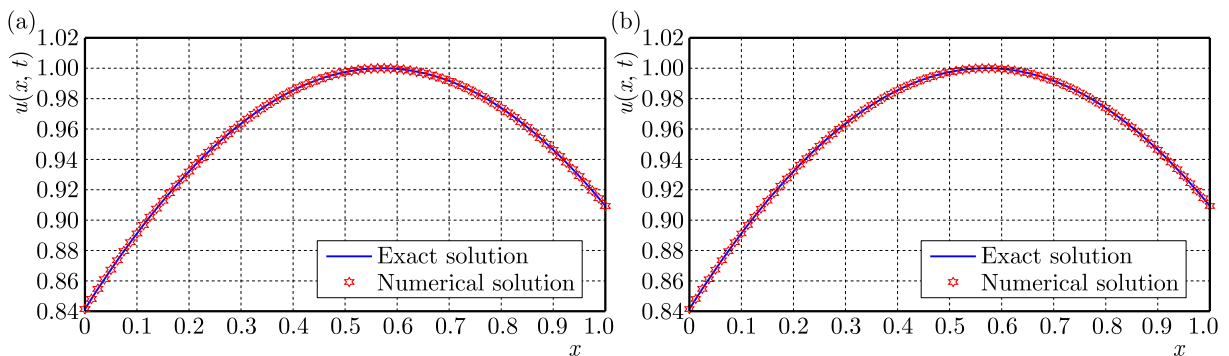


Fig. 2. Numerical solutions and the exact solution at time $t = 1.0$ for Example 2: (a) using TPS, (b) using MQ. The solid line corresponds to the exact solution, the starred line corresponds to the numerical solution of the MLRPI with $\Delta t = 0.0001$ and $\Delta x = 0.0125$

On the top of that, the MLRPI method can be used to solve complex engineering problems with lower computational cost, higher accuracy, simpler construction of higher-order shape functions and easier handling of large deformation problems.

**Table 5.** The $L^1$, $L^2$ and $L^\infty$ errors calculated by MLRPI for Example 2 with different $\Delta x$ and $\Delta t$ at time $t = 1.0$ (using TPS)

| $\Delta t$ | $\Delta x$ | $\|E\|_1$ | $\|E\|_2$ | $\|E\|_\infty$ |
|---|---|---|---|---|
| 0.001 | 0.25 | 4.467206E-04 | 2.263494E-04 | 1.434185E-04 |
| 0.001 | 0.125 | 2.548359E-05 | 1.304920E-05 | 1.148951E-05 |
| 0.001 | 0.1 | 1.502825E-05 | 6.430589E-06 | 5.320887E-06 |
| 0.001 | 0.05 | 1.175112E-05 | 2.629557E-06 | 8.956239E-07 |

**Table 6.** The $L^1$, $L^2$ and $L^\infty$ errors calculated by MLRPI for Example 2 with different $\Delta x$ and $\Delta t$ at time $t = 1.0$ (using TPS)

| $\Delta t$ | $\Delta x$ | $\|E\|_1$ | $\|E\|_2$ | $\|E\|_\infty$ |
|---|---|---|---|---|
| 0.001 | 0.0125 | 4.418773E-05 | 4.914641E-06 | 5.709157E-07 |
| 0.0005 | 0.0125 | 1.104494E-05 | 1.228475E-06 | 1.426643E-07 |
| 0.00025 | 0.0125 | 2.7603974E-06 | 3.070796E-07 | 3.561701E-08 |
| 0.0001 | 0.0125 | 4.405399E-07 | 4.920947E-08 | 6.985131E-09 |

**Table 7.** The $L^1$, $L^2$ and $L^\infty$ errors calculated by MLRPI for Example 2 with different $\Delta x$ and $\Delta t$ at time $t = 1.0$ (using MQ)

| $\Delta t$ | $\Delta x$ | $\|E\|_1$ | $\|E\|_2$ | $\|E\|_\infty$ |
|---|---|---|---|---|
| 0.001 | 0.25 | 4.467206E-04 | 2.263494E-04 | 1.434185E-04 |
| 0.001 | 0.125 | 2.542164E-05 | 1.296910E-05 | 1.140565E-05 |
| 0.001 | 0.1 | 1.500617E-05 | 6.414381E-06 | 5.302278E-06 |
| 0.001 | 0.05 | 1.174746E-05 | 2.629195E-06 | 8.987330E-07 |

**Table 8.** The $L^1$, $L^2$ and $L^\infty$ errors calculated by MLRPI for Example 2 with different $\Delta x$ and $\Delta t$ at time $t = 1.0$ (using MQ)

| $\Delta t$ | $\Delta x$ | $\|E\|_1$ | $\|E\|_2$ | $\|E\|_\infty$ |
|---|---|---|---|---|
| 0.001 | 0.0125 | 4.413908E-05 | 4.909225E-06 | 5.701902E-07 |
| 0.0005 | 0.0125 | 1.099625E-05 | 1.223055E-06 | 1.419426E-07 |
| 0.00025 | 0.0125 | 2.711815E-06 | 3.016704E-07 | 3.548134E-08 |
| 0.0001 | 0.0125 | 3.928077E-07 | 4.390304E-08 | 5.957403E-09 |

## 8.  Conclusions

In the aforementioned discussion, we applied the meshless local radial point interpolation (MLRPI) method to solve the linear telegraph equation with non-local boundary conditions. The radial point interpolation method is adopted for approximating the field variable. Also the weak form of the discretized equations has been constructed on local subdomains. So, this method requires neither domain element nor background cells in either the interpolation or the intergration. It means this method is a truly meshless method. Furthermore, time discretization has been done using finite difference techniques. The principal benefit of the method is to capture the behavior of the solution for similar problems with non-local boundary conditions where most of schemes fail. Also, the MLRPI method can easily handle the damage of the components, such as fracture which is very useful to simulate material breakage. Finally, accuracy and usefulness of the proposed method are illustrated by two examples.

# References

1. ALMENAR P., JODAR L., MARTIN J.A., 1997, Mixed problems for the time-dependent telegraph equation: Continuous numerical solutions with a priori error bounds, *Mathematical and Computer Modelling*, **25**, 11, 31-44

2. ATLURI S., ZHU T., 1998, A new meshless local Petrov-Galerkin (MLPG) approach in computational mechanics, *Computational Mechanics*, **22**, 117-127

3. BANASIAK J., MIKA J.R., 1998, Singularly perturbed telegraph equations with applications in the random walk theory, *Journal of Applied Mathematics and Stochastic Analysis*, **11**, 1, 9-28

4. BELYTSCHKO T., LU Y.Y., GU L., 1995, Element free Galerkin methods for static and dynamic fracture, *International Journal of Solids and Structures*, **32**, 2547-2570

5. BOYCE W.E., DIPRIMA R.C., 1977, *Differential Equations Elementary and Boundary Value Problems*, Wiley, New York

6. BRATSOS A.G., 2008, An improved numerical scheme for the sine-Gordon equation in 2+1 dimensions, *International Journal for Numerical Methods in Engineering*, **75**, 787-799

7. CIMENT M., LEVENTHAL S.H., 1978, A note on the operator compact implicit method for the wave equation, *Mathematics of Computation*, **32**, 143-147

8. DASHTIMANESH A., GHADIMI P., 2013, A three-dimensional SPH model for detailed study of free surface deformation, just behind a rectangular planing hull, *Journal of the Brazilian Society of Mechanical Sciences and Engineering*, **35**, 4, 369-380

9. DE S., BATHE K.J., 2000, The method of finite spheres, *Computational Mechanics*, **25**, 329-345

10. DEHGHAN M., MIRZAEI D., 2008, The meshless local Petrov-Galerkin (MLPG) method for the generalized two-dimensional non-linear Schrödinger equation, *Engineering Analysis with Boundary Elements*, **32**, 747-756

11. DEHGHAN M., SHOKRI A., 2008, A numerical method for solution of the two dimensional sine-Gordon equation using the radial basis functions, *Mathematics and Computers in Simulation*, **79**, 700-715

12. GONZALEZ-VELASCO E.A., 1995, *Fourier Analysis and Boundary Value Problems*, Academic Press, New York

13. GU Y., LIU G., 2002, A boundary point interpolation method for stress analysis of solids, *Computational Mechanics*, **28**, 47-54

14. GU Y.T., LIU G.R., 2003, A boundary radial point interpolation method (BRPIM) for 2-D structural analyses, *Structural Engineering and Mechanics*, **15**, 535-550

15. HOSSEINI V.R., SHIVANIAN E., CHEN W., 2015, Local integration of 2-D fractional telegraph equation via local radial point interpolant approximation, *European Physical Journal Plus*, **130**, 33-54

16. HU D., LONG S., LIU K., LI G., 2006, A modified meshless local Petrov-Galerkin method to elasticity problems in computer modeling and simulation, *Engineering Analysis with Boundary Elements*, **30**, 399-404

17. JORDAN P.M., PURI A., 1999, Digital signal propagation in dispersive media, *Journal of Applied Physics*, **85**, 3, 1273-1282

18. KANSA E., 1990, Multiquadrics-a scattered data approximation scheme with applications to computational fluid-dynamics. I. Surface approximations and partial derivative estimates, *Computers and Mathematics with Applications*, **19**, 8/9, 127-145

19. KOCHMANN D.M., VENTURINI G.N., 2014, A meshless quasicontinuum method based on local maximum-entropy interpolation, *Modelling and Simulation in Materials Science and Engineering*, **22**, 3, 034007

20. LIBRE N., EMDADI A., KANSA E., SHEKARCHI M., RAHIMIAN M., 2008, A fast adaptive wavelet scheme in RBF collocation for nearly singular potential PDEs, *Computer Modeling in Engineering and Sciences*, **38**, 3, 263-284

21. LING L., SCHABACK R., 2008, Stable and convergent unsymmetric meshless collocation methods, *SIAM Journal of Numerical Analysis*, *46*, 3, 1097-1115

22. LIU G.R., GU Y.T., 2001, A local radial point interpolation method (LR-PIM) for free vibration analyses of 2-D solids, *Journal of Sound and Vibration*, **246**, 1, 29-46

23. LIU G., GU Y., 2005, *An Introduction to Meshfree Methods and their Programing*, Springer

24. LIU K., LONG S., LI G., 2006, A simple and less-costly meshless local Petrov-Galerkin (MLPG) method for the dynamic fracture problem, *Engineering Analysis with Boundary Elements*, **30**, 72-76

25. LIU W.K., JUN S., ZHANG Y.F., 1995, Reproducing kernel particle methods, *International Journal for Numerical Methods in Engineering*, **20**, 1081-1106

26. MELENK J.M., BABUSKA I., 1996, The partition of unity finite element method: Basic theory and applications, *Computer Methods in Applied Mechanics and Engineerin*, **139**, 289-314

27. MUKHERJEE Y.X., MUKHERJEE S., 1997, Boundary node method for potential problems, *International Journal for Numerical Methods in Engineering*, **40**, 797-815

28. NAYROLES B., TOUZOT G., VILLON P., 1992, Generalizing the finite element method: diffuse approximation and diffuse elements, *Computational Mechanics*, **10**, 307-318

29. PAN X., YUAN H., 2009, Applications of meshless methods for damage computations with finite strains, *Modelling and Simulation in Materials Science and Engineering*, **17**, 4, 045005

30. SHIRZADI A., 2014, Solving 2D reaction-diffusion equations with nonlocal boundary conditions by the RBF-MLPG method, *Computational Mathematics and Modeling*, **25**, 4, 521-529

31. SHIVANIAN E., 2013, Analysis of meshless local radial point interpolation (MLRPI) on a nonlinear partial integro-differential equation arising in population dynamics, *Engineering Analysis with Boundary Elements*, **37**, 1693-1702

32. SHIVANIAN E., 2015a, A new spectral meshless radial point interpolation (SMRPI) method: A well-behaved alternative to the meshless weak forms, *Engineering Analysis with Boundary Elements*, **54**, 1-12

33. SHIVANIAN E., 2015b, Meshless local Petrov-Galerkin (MLPG) method for three-dimensional nonlinear wave equations via moving least squares approximation, *Engineering Analysis with Boundary Elements*, **50**, 249-257

34. SHIVANIAN E., KHODABANDEHLO H.R., 2014, Meshless local radial point interpolation (MLRPI) on the telegraph equation with purely integral conditions, *European Physical Journal Plus*, **129**, 241-251

35. SINGH I.V., TANAKA M., ENDO M., 2007, Meshless method for nonlinear heat conduction analysis of nano-composites, *Heat and Mass Transfer*, **43**, 10, 1097-1106

36. SLADEK J., SLADEK V., ZHANG C., TAN C.L., 2006, Evaluation of fracture parameters for crack problems in FGM by a meshless method, *Journal of Theoretical and Applied Mechanics*, **44**, 3, 603-636

37. TIKHONOV A.N., SAMARSKII A.A., 1990, *Equations of Mathematical Physics*, Dover, New York

# PREPARATION WITH MODELING AND THEORETICAL PREDICTIONS OF MECHANICAL PROPERTIES OF FUNCTIONALLY GRADED POLYETHYLENE/CLAY NANOCOMPOSITES

Mohhamad H. Yas, Mahdi K. Khorramabadi

*Department of Mechanical Engineering, Razi University, Kermanshah, Iran*

*e-mail: yas@razi.ac.ir; mehdi_karami2001@yahoo.com*

This paper presents preparation with modeling and theoretical predictions of mechanical properties of compatibilized functionally graded and uniform distribution polyethylene/modified montmorillonite nanocomposites manufactured by solution and melt mixing techniques. The morphology is studied by Scanning Electron Microscopy (SEM) and comparisons are made between two techniques. Young's modulus of nanocomposites for functionally graded and uniform distributions is calculated using a genetic algorithm and is then compared with the results of other theoretical prediction models mentioned in the literature as well as experimental results. It is found that the melt mixing technique is the preferred preparation method, and the results obtained from the theoretical predictions of genetic algorithm procedure are in good agreement with the experimental ones.

*Keywords:* functionally graded material, nanocomposites, solution technique, melt mixing technique, genetic algorithm theory

## 1. Introduction

Nanocomposites have attracted attention in the recent years because of their improved mechanical, thermal, solvent resistance and fire retardant properties compared to the pure or conventional composite materials. There has been growing interest in polymer/nanoclay nanocomposites in recent years because of their outstanding properties at low loading levels as compared with conventional composites. It has been observed that adding small quantities of nanoclay to some thermoplastics as a reinforcing filler to form nanocomposite materials has not only led to more improved mechanical and thermal properties, but also to enhancement of dielectric strength and partial discharge resistance (Kawasumi *et al.*, 1997; Tan and Yang, 1998; Han *et al.*, 2001; Kornmann *et al.*, 2001; Utracki and Kamal, 2002; Hotta and Paul, 2004; Zhao and He, 2006; Awaji *et al.*, 2009; Chen and Chen, 2009; Kim *et al.*, 2009). As reported in several previous papers (Avila *et al.*, 2008; Nam *et al.*, 2001; Hrachova *et al.*, 2013; Pakdaman *et al.*, 2013; Grigoriadi *et al.*, 2012), some continuum-mechanics based theoretical models have been proposed to predict mechanical properties of polymer/clay nanocomposites. Fornes and Paul (2003) applied the Halpin-Tsai and Mori-Tanaka reinforcement theories to predict the modulus of nylon based nanocomposites. The modulus obtained using Mori-Tanaka calculation increased with nanoclay reinforcement as predicted. The Halpin-Tsai formula gave higher values to the modulus but could still be used to predict its magnitude.

Some efforts have been focused on the modeling of mechanical properties of nanoclay-reinforced polymer composites (Sheng *et al.*, 2004) and nanoparticle-reinforced polymer composites (Smith *et al.*, 2002; Brown *et al.*, 2003). Those modeling efforts have demonstrated the need for the development of a model that would predict mechanical properties of nanoparticle/polyimide composites as a function of nanoparticle size and weight fraction as well as the molecular structure of the nanoparticle/polyimide interface. Although experimental-based research

can ideally be used to determine structure-property relationships of nanostructured composites, experimental synthesis and characterization of nanostructured composites demands making use of sophisticated processing methods and testing equipment, which may result in exorbitant costs. To this end, computational modeling techniques for determination of the mechanical properties of nanocomposites have proven to be very effective (Liu and Chen, 2003; Chen and Liu, 2004; Avila *et al.*, 2006; Haque and Shamsuzzoha, 2003; Isik *et al.*, 2003; Thilly *et al.*, 2009; Dong *et al.*, 2008; Song and Youn, 2006). Genetic algorithms are a family of computational models inspired by evolution. These algorithms encode a potential solution or a specific problem on a simple chromosome-like data structure and apply recombination operators to these structures so as to preserve critical information. Genetic algorithms are often viewed as function optimizers, although the range of problems to which genetic algorithms have been applied is quite broad.

Functionally Graded Materials (FGMs) are inhomogeneous composite materials with gradient compositional variation of the constituents (e.g., metal and ceramic) from one surface of the material to the other, which results in continuously varying material properties. The materials are intentionally designed in such a way that they possess desirable properties for specific applications. Shen (2009, 2011) suggested that the interfacial bonding strength can be improved through the use of a graded distribution of CNTs in the matrix and examined nonlinear bending behavior of simply supported, functionally graded nanocomposite plates reinforced by single walled carbon nanotubes subjected to a transverse uniform or sinusoidal loading in thermal environment. He also investigated post-buckling of nanocomposite cylindrical shells reinforced by SWCNTs subjected to axial compression in thermal environment and showed that the linear functionally graded reinforcements can increase the buckling load. Shen and Xiang (2012) investigated large amplitude vibration behavior of FG-CNTRC cylindrical shells in thermal environments. They assumed that the material properties of CNTRCs were temperature-dependent and solved the equations of motion by an improved perturbation technique to determine nonlinear frequencies of the CNTRC shells.

The present work deals with the preparation and modeling with theoretical predictions of mechanical properties of compatibilized functionally graded and uniform distribution polyethylene/low density polyethylene (LDPE)/modified montmorillonite (MMT) nanocomposites prepared by both solution and melt mixing techniques. The morphology is studied by Scanning Electron Microscopy (SEM) and comparisons are made between the two techniques and then between functionally graded polyethylene/clay nanocomposites with the uniform ones. By using the genetic algorithm procedure, Young's modulus of nanocomposites for functionally graded and uniform distributions is calculated and then is compared with the results of other theoretical predictions models mentioned in the literature and the experimental results. It is found that the melt mixing technique is the preferred method for preparation the functionally graded and uniform distribution polyethylene/clay nanocomposites. Finally, it is shown that the results obtained from the genetic algorithm approach are in good agreement with the experimental ones.

## 2. Experimental

### 2.1. Materials

The polymer matrix used in this study was a linear low-density polyethylene with the trade name LL209AA from Arak Petrochemical Co. (Iran), with melt flow index (MFI) of $0.9\,\mathrm{g}/10\,\mathrm{min}$ and density of $\rho = 0.92\,\mathrm{g/cm}s$. The nanofiller were K10 montmorillonite from Sigma-Aldrich, Germany. Also, the polyethylenglycol employed in this study was polyethylenglycol 40 from Merk-KGaA, Germany.

## 2.2. Processing

### 2.2.1. Melt mixing technique for uniformed distribution (UD)

An internal mixer from Brabender, Germany (model WHT 55), with roller type rotors and mixer capacity of $55\,cm^3$ was used for preparing nanocomposites samples. The nano clay (MMT) was dried at $40°C$ in a vacuum oven for a minimum of $48\,h$. Low density polyethylene (LDPE) and polyethylenglycol were added to the nanoclay. All materials were manually premixed before introduction into the mixer. The extrusion temperature was set at $140\text{-}180°C$ from the feeder to the die.

### 2.2.2. Solution technique for uniformed distribution (UD)

The nanoclay (MMT) was dried at $40°C$ in the vacuum oven for a minimum of $48\,h$. Low density polyethylene (LDPE) and toluene solution were added to the nanoclay. The mechanical mixture was stirred for $30\,min$ at room temperature. After $30$ min of mechanical stirring, the suspension was treated with ultrasound for $20\,min$. After stirring, the suspension was distilled. The ultrasonic stirring from Hielscher, Germany (model UP400S), was used to ultrasound the suspension.

### 2.2.3. Melt mixing technique for functionally graded distribution (FGD)

After the melt mixing procedure, the products were then compressed and molded into sheets by an electrically heated hydraulic press. The thickness of every sheet was $1\,mm$ and four sheets with different nanoparticles weight fractions (pure, $1\,wt.\%$, $3\,wt.\%$ and $5\,wt.\%$) were employed to form functionally graded nanocomposite. The processing of melt mixing technique for functionally graded distribution is presented in Fig. 1.
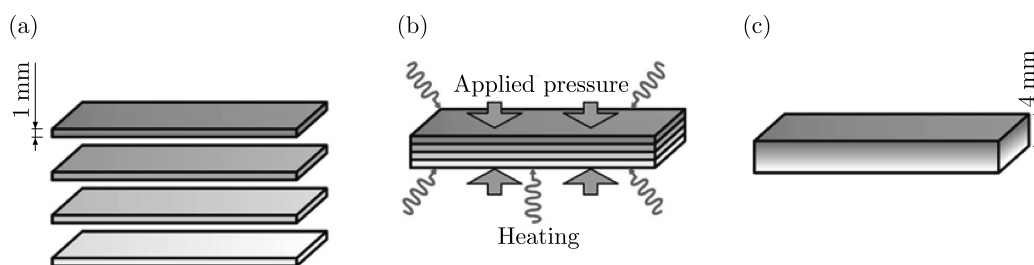


Fig. 1. Processing of melt mixing technique for functionally graded distribution: (a) primary set of nanocomposite sheets with different nanoparticle fractions, (b) processing the FG nanocomposite, (c) fabricated FG nanocomposite

## 2.3. Scanning electron microscopy (SEM) analysis

The morphology of nanocomposite cross section samples was investigated using a SERON AIS2300C scanning electron microscope. The initial sample preparing process was carried out by a gold-coater chamber. Figure 2a is the SEM photography of the nanocomposite for uniform distribution prepared by the solution technique and Fig. 2b is the SEM image of the nanocomposite for uniform distribution prepared by the melt mixing technique.

Figure 2a shows that the morphology for the solution technique is not homogeneous, which reveals a poor intercalated/exfoliated structure. However, when the melt mixing technique was employed and a compatibilizer was added (Fig. 2b), it was observed that the density and size of the aggregates decreased, which indicated that the dispersion of nanoclays within the polymer matrix was much better. The comparisons between Fig. 2a and Fig. 2b show that the adhesion of the particles of nanoclay and polymer in the presence of the compatibilizer is improved. The
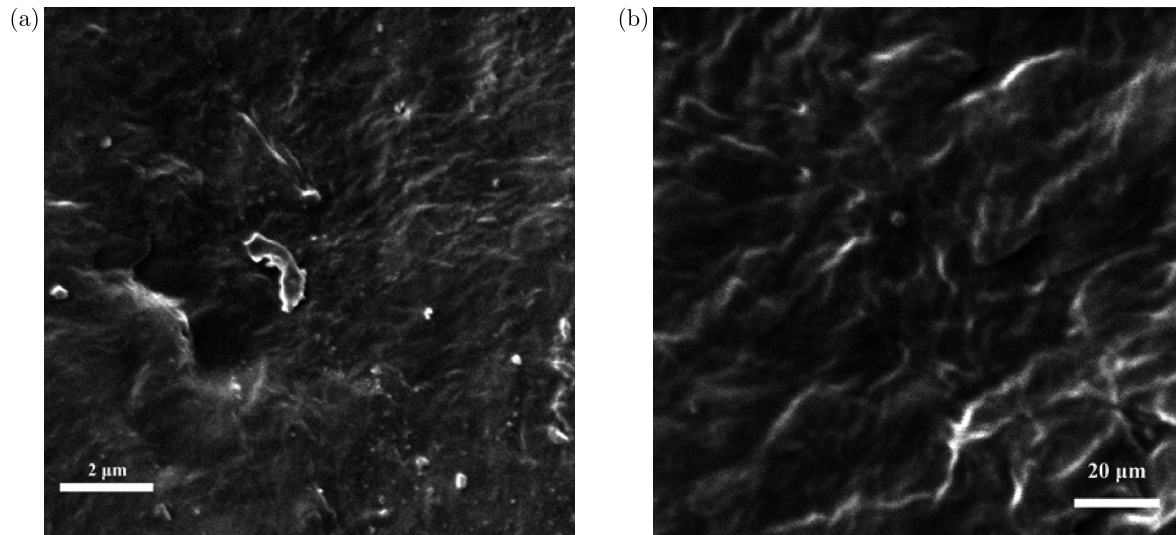
Fig. 2. SEM image of nanocomposite prepared by (a) solution technique and (b) melt mixing technique for uniform distribution
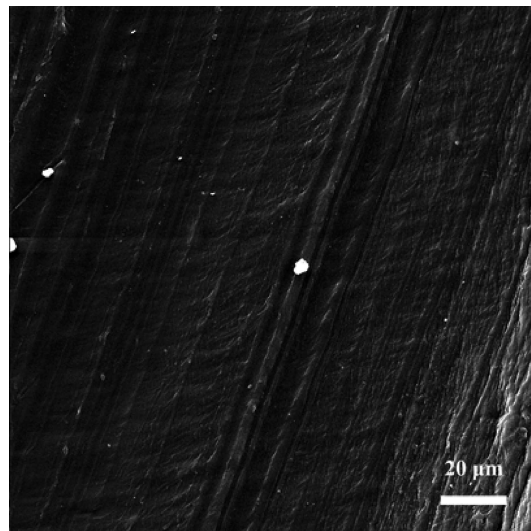


Fig. 3. SEM image of nanocomposite prepared by melt mixing technique for functionally graded distribution

morphology of nanocomposites cross section samples for functionally graded distribution was investigated by a TESCAN MRIA3 SEM after being coated with gold. Figure 3 is the SEM image of the nanocomposite for functionally graded distribution prepared by the melt mixing technique. It seems that the dispersion of nanoclay varies smoothly and continuously from one surface to the other.

## 2.4. Mechanical properties

The tensile properties were evaluated according to ASTM D638 using dumbbell-shaped samples and a Gotech universal testing machine (Model GT-AI5000L) tensile tester with a crosshead speed of 50 mm/min. The material compositions of the nanocomposites are listed in Table 1.

Figure 4a illustrates the effect of nanoparticles with different weight fractions on the elastic modulus. As noticed, the elastic modulus begins to increase up to 5 wt.% of nanoclay. As the

**Table 1.** Sample compositions

| Sample | LDPE [wt%] | Compatibilizer [wt%] | MMT [wt%] |
|--------|------------|----------------------|-----------|
| 1 | 85 | 15 | – |
| 2 | 82 | 15 | 3 |
| 3 | 80 | 15 | 5 |
| 4 | 78 | 15 | 7 |

clay weight fraction exceeds 5 wt.%, the elastic modulus levels off, but for functionally graded distribution, the elastic modulus is generally larger than the corresponding values for uniformed distribution of the nanoclay.
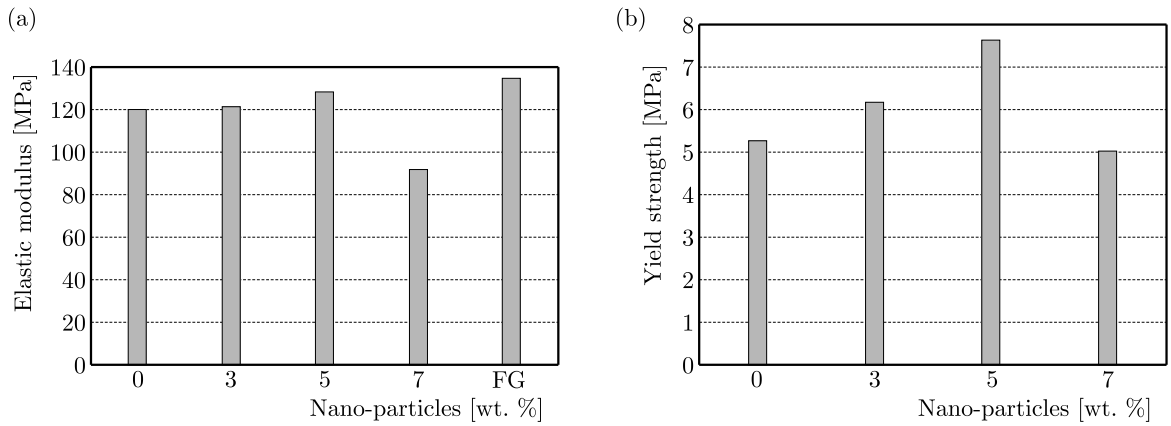


Fig. 4. The effect of nanoparticles with different weight fractions on (a) elastic modulus and (b) yield strength

Figure 4b illustrates the effect of nanoparticles with different weight fractions on yield strengths. As observed, the yield strengths begin to increase up to 5 wt.% of nanoclay. As the weight fraction of clay exceeds 5 wt.%, the yield strengths level off.

## 3. Modeling

### 3.1. Theoretical predictions

GA is an unorthodox search or optimization algorithm which was first suggested by John Holland in his book *Adaptation and Artificial Systems* (Holland, 1975). As the name suggests, the GA was inspired by processes observed in natural evolution. The GA method searches for the best alternative (in the sense of a given fitness function) through chromosome evolution. In this paper, the $1 - R^2_{adj}$ is introduced as the fitness function which is to be minimized. $R^2_{adj}$ is the accuracy criterion of an arbitrary mechanical property function (such as Young's modulus). $R^2_{adj}$ is defined as a process which is demonstrated below. The mechanical property is a function of nanoclay weight percent and $R^2_{adj}$ is a function of coefficients which are introduced below. $M_i$ is considered as the mechanical properties and $W$ as the nano clay weight percent. $M_1$, $M_2$, $M_3$ and $M_4$ are Young's modulus, yield stress, ultimate strength and elongation at break, respectively. The $M_i$ is expressed as a polynomial function of $W$ as follows

$$M_i = \sum_{j=0}^{4} a_{ji} W^j \tag{3.1}$$

Now, the coefficients $a_{ji}$ are found by maximizing the accuracy of the polynomial function. The equations can be written as:

$$R^2_{adj} = 1 - \frac{VAR_E}{VAR_T} \tag{3.2}$$

in which

$$\begin{aligned}
VAR_E &= \frac{SS_{Err}}{n-k-1} & VAR_T &= \frac{SS_{Tot}}{n-1} \\
SS_{Tot} &= \sum_{i=1}^{n}(y_i - \overline{y})^2 & SS_{Err} &= \sum_{i=1}^{n}(y_i - M_i)^2 \quad \overline{y} = \tfrac{1}{n}\sum_{i=1}^{n} y_i
\end{aligned} \tag{3.3}$$

and

$$M_i(W) = a_{0i} + a_{1i}W + a_{2i}W^2 + a_{3i}W^3 \tag{3.4}$$

In these equations, $n = 4$ is the number of experiments and $k = 0$ is the number of duplicated experiments and $y_i$ show the experimentally measured mechanical properties. After minimization of $1 - R^2_{adj}$ via MATLAB, the factors $a_{ji}$ are obtained after approximately 40 generations.

### 3.2. Einstein's model

One of the earliest models developed to predict mechanical properties of composites is Einstein's model (Einstein, 1956)

$$\frac{E_c}{E_m} = 1 + 2.5\phi_f \tag{3.5}$$

where $E_c$ and $E_m$ are the moduli of the composite and matrix, respectively. $\phi_f$ is the volume fraction of the filler in the matrix.

### 3.3. Guth and Gold model

The reinforcing effect of spherical colloidal fillers on elastomers was studied by Guth and Gold, and the modulus is given by equation (Guth, 1945)

$$E_c = E_m(1 + 2.5\phi_f + 14.1\phi_f^2) \tag{3.6}$$

where $E_c$ and $E_m$ are the moduli of the composite and matrix, respectively. $\phi_f$ is the volume fraction of the filler in the matrix. The conversion of weight fractions of nanoclay to volume fractions is shown in Table 2.

**Table 2.** Conversion of weight fractions of nanoclay to volume fractions

| Volume fraction of nanoclay | Weight fraction of nanoclay |
|---|---|
| 3% | 1.44% |
| 5% | 2.4% |
| 7% | 3.36% |

### 3.4. Mori-Tanaka model

A combination of the Mori-Tanaka mean stress concept and the eigenstrain idea of Eshelby's inclusion model was used by Tandon and Weng (1984) to determine the overall elasticity tensor of the nanocomposite materials, assuming that either of the mixture and inclusions (e.g., discontinuous fibers/flakes/nanoparticles) are isotropic or transversely isotropic. For a material reinforced by ellipsoidal particles aligned in the longitudinal direction, the longitudinal modulus may be determined as

$$\frac{E_1 1}{E_m} = \frac{1}{1 + \frac{1}{A} f_p (A_1 + 2\nu_m A_2)} \tag{3.7}$$

where the subscripts $p$ and $m$ stand for the particles and the matrix, respectively. $\nu_m$ is Poisson's ratio of the matrix and $f_p$ are the inclusion particles volume fraction. The constants $A$ and $A_i$ can be calculated from the matrix/particle properties and components of Eshelby's tensor $H_{ijkl}$ (Sheng *et al.*, 2004; Eshelby, 1961; Taya, 1981; Taya and Mura, 1981) which depend on the particle aspect ratio and dimensionless elastic constants of the matrix.

## 4. Results and discussion

Obtaining the $a_{ji}$ coefficients, Young's modulus can be expressed as a function of the nanoclay weight percent as follows

$$E = -3.401w + 4.97w^2 - 0.677w^3 + 105.338 \tag{4.1}$$

Here, $w$ is the nanoclay weight percent. To investigate correctness of the present results, comparison studies are carried out for Young's modulus of uniform distribution nanocomposites which are presented in Table 3.

**Table 3.** Comparison of Young's modulus for uniform distribution nanocomposites

| Nano clay weight percent | Einstein's predictions [Mpa] | Guth and Gold's predictions [Mpa] | Mori-Tanaka predictions [Mpa] | Theoretical predictions [Mpa] | Experimental results [Mpa] |
|---|---|---|---|---|---|
| pure | 105.338 | 105.338 | 105.338 | 105.338 | 105.338 |
| 3% | 109.130 | 109.438 | 126.362 | 121.586 | 121.582 |
| 5% | 111.658 | 112.513 | 132.715 | 127.958 | 127.939 |
| 7% | 114.186 | 115.863 | 139.412 | 92.850 | 92.795 |

The compression between theoretical predictions and the experimental data shows high accuracy of the present analysis. Equation (4.1) can be used to derive the suitable relation for Young's modulus of the functionally graded distribution. The specimen with functionally graded distribution consists of four perfectly bonded sheets with a total thickness of 4 mm. Each sheet has 1 mm thickness with different nanoparticles weight fractions (pure, 1 wt.%, 3 wt.% and 5 wt.%). Young's modulus can be written as

$$E(z) = -3.401(2z + \text{sgn}\,[z]) + 4.97(2z + \text{sgn}\,[z])^2 - 0.677(2z + \text{sgn}\,[z])^3 + 105.338 \tag{4.2}$$

As mentioned before, Young's modulus is assumed to vary as a function of the thickness coordinate $z$ ($0 \leqslant z \leqslant 4$). Equation (4.2) can be verified via employing static analysis of the functionally graded nanocomposite beam under a transverse load. It is considered as a functionally graded nanocomposite beam as shown in Fig. 5.
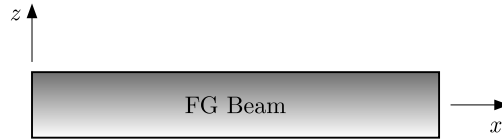
Fig. 5. Schematic of the problem studied

The thickness, length, and width of the beam are denoted, respectively, by $h$, $L$, and $b$. The position of neutral surface can be determined as (Yaghoobi and Fereidoon, 2010):

$$h_0 = \frac{\int\limits_{-h/2}^{h/2} E(z)z \, dz}{\int\limits_{-h/2}^{h/2} E(z) \, dz} \tag{4.3}$$

In the Euler-Bernoulli theory, the differential equation of deflection can be expressed as (Yaghoobi and Fereidoon, 2010)

$$\frac{d^2w}{dx^2} = \frac{M(x)}{D} \tag{4.4}$$

where $D$ denotes bending rigidity of the FG nanocomposite beam defined by (Yaghoobi and Fereidoon, 2010)

$$D = \int\limits_{-h/2}^{h/2} bE(z)(z - h_0)^2 \, dz \tag{4.5}$$

Boundary conditions for simply supported and cantilever beams are

$$\begin{aligned} w = 0 \quad &\text{at} \quad x = 0, l \\ w = 0 \quad \wedge \quad \frac{dw}{dx} = 0 \quad &\text{at} \quad x = 0, l \end{aligned} \tag{4.6}$$

By integrating Eq. (4.4) and then applying boundary conditions, Eqs. (4.6), one can easily obtain deflection of the beam under the transverse load. For static analysis of the functionally graded nanocomposite beam under the transverse load, the beam apparatus from TQ, England (Model SM1004), was used for deflection test. The test specimen had a rectangular cross section $(20 \times 4)\,\text{mm}^2$ and a length of 15 cm. The load magnitude for both boundary conditions was 0.54 N. The comparison between theoretical and experimental data for the deflection of the functionally graded distribution nanocomposites is shown in Table 4.

**Table 4.** Compression between theoretical and experimental data for deflection

| Boundary condition | Load position $x$ [cm] | Deflection measuring position $x$ [cm] | Theoretical deflection [mm] | Experimental deflection [mm] |
|---|---|---|---|---|
| Simply support | 5.5 | 7.5 | 3.82 | 3.65 |
| Cantilever | 7 | 15 | 5.87 | 5.59 |

As observed, there is a good agreement between the results. Thus the presented approach for modeling of Young's modulus of functionally graded distribution nanocomposites has high accuracy.

## 5. Conclusions

This paper presents the preparation with modeling and theoretical predictions of mechanical properties of functionally graded and uniform distribution polyethylene/low density polyethylene (LDPE)/modified montmorillonite (MMT) nanocomposites prepared by both solution and melt mixing techniques. From this study, the following conclusions can be made:

- The mixing technique is generally better than the solution one for preparation of the polyethylene/low density polyethylene (LDPE)/modified montmorillonite (MMT) nanocomposites.
- The compatibilizer plays an important role in improving the properties of polyethylene/low density polyethylene (LDPE)/modified montmorillonite (MMT) nanocomposites.
- By increasing weight fractions of the nanoparticles, the mechanical properties increase up to 5 wt.% nanoclay.
- The elastic modulus for FG distribution of the nanoclay is generally larger than the corresponding value for the uniform distribution of the nanoclay.
- GA is an acceptable optimization research technique which can be used with confidence to identify mechanical properties of nanocomposites with maximum accuracy.

## References

1. Avila A.F., Donadon L.V., Duarte H.V., 2008, A modal analysis of nanoclay-epoxy-fiber glass composite, *Composite and Structure*, **83**, 324-333

2. Avila A.F., Duarte H.V., Soares M.I., 2006, The nanoclay influence on impact response of laminate plates, *American Journal of Solids and Structures*, **37**, 3-20

3. Awaji H., Nishimura Y., Choi S., Takahashi Y., Goto T., Hashimoto S., 2009, Toughening mechanism and frontal process zone size of ceramics, *Journal of the Ceramic Society of Japan*, **117**, 623-629

4. Brown D., Mele P., Marceau S., 2003, A molecular dynamics study of a model nanoparticle embedded in a polymer matrix, *Macromolecules*, **36**, 1395-1406

5. Chen L., Chen G., 2009, Relaxation behavior study of silicone rubber crosslinked network under static and dynamic compression by electric response, *Polymer Composites*, **30**, 101-106

6. Chen X.L., Liu Y.J., 2004, Square representative volume elements for evaluating the effective material properties of carbon nanotube-based composites, *Computational Materials Science*, **29**, 1-11

7. Dong Y., Bhattacharyya D., Hunter P.J., 2008, Experiental characterisation and object-oriented finite element modeling of polypropylene/organoclay nanocomposites, *Composite Science Technology*, **68**, 2864-2875

8. Einstein A., 1956, *Investigation on Theory of Brownian Motion*, New York, Dover

9. Eshelby J.D., 1961, Elastic inclusions and inhomogeneities, *Progress in Solid Mechanics*, **2**, 89-140

10. Fornes T.D., Paul D.R., 2003, Modeling properties of nylon 6/clay nanocomposites using composite theories, *Polymer*, **44**, 4993-5013

11. Grigoriadi K., Giannakas A., Ladavos A., 2012, Thermomechanical behavior of polymer/layered silicate clay nanocomposites based on unmodified low density polyethylene, *Polymer Engineering Science*, **51**, 301-308

12. Guth E., 1945, Theory of filler reinforcement, *Journal of Applied Physics*, **16**, 20-25

13. HAN Y., WANG Z., LI X., FU J., CHENG Z., 2001, Polymer-layered silicate nanocomposites: synthesis, characterization, properties and applications, *Current Trends in Polymer Science*, **6**, 1-16

14. HAQUE A., SHAMSUZZOHA M., 2003, S2-glass/epoxy polymer nanocomposites manufacturing, structures, thermal and mechanical properties, *Journal of Composite Materials*, **37**, 1821-1837

15. HOLLAND J.H., 1975, *Adaptation in Natural and Artificial Systems*, University of Michigan press, Ann Arbor

16. HOTTA S., PAUL D.R., 2004, Nanocomposites formed from linear low density polyethylene and organoclays, *Polymer*, **45**, 7639-7654

17. HRACHOVA J., KOMADEL P., MOSKOVA D.J., 2013, Properties of organo-clay/natural rubber nanocomposites, *Journal of Apply Polymer Science*, **127**, 3447-3455

18. ISIK I., YILMAZER U., BAYRAM G., 2003, Impact modified epoxy/montmorillonite nanocomposites, synthesis and characterization, *Polymer*, **44**, 6371-6377

19. KAWASUMI M., HASEGAWA N., KATO M., USUKI A., OKADA A., 1997, Preparation and mechanical properties of polypropylene-clay hybrids, *Macromolecules*, **30**, 6333-6338

20. KIM P.N., DOSS M., TILLOTSON J.P., 2009, High energy density nanocomposites based on surface-modiied BaTiO3 and a ferroelectric polymer, *ACS Nano*, **3**, 2581-2592

21. KORNMANN X., LINDBERG H., BERGLUND L.A., 2001, Synthesis of epoxy-clay nanocomposites: inluence of the nature of the clay on structure, *Polymer*, **42**, 1303-1310

22. LIU Y.J., CHEN X.L., 2003, Evaluations of the effective material properties of carbon nanotube-based composites using a nanoscale representative volume element, *Mechanics of Materials*, **35**, 69-81

23. NAM P.H., MAITI P., OKAMOTO M., 2001, Hierarchical structure and properties of intercalated polypropylene/clay nanocomposite, *Polymer*, **42**, 9633-9640

24. PAKDAMAN A.S., MORSHEDIAN J., JAHANI Y., 2013, Effect of organoclay and silane grafting of polyethylene on morphology, barrierity, and rheological properties of HDPE/PA6 blends, *Journal of Apply Polymer Science*, **127**, 1211-1220

25. SHEN H.S., 2009, Nonlinear bending of functionally graded carbon nanotube reinforced composite plates in thermal environments, *Composite Structures*, **91**, 9-19

26. SHEN H.S., 2011, Postbuckling of nanotube-reinforced composite cylindrical shells in thermal environments. Part I: Axially-loaded shells, *Composite Structures*, **93**, 2096-2108

27. SHEN H.S., XIANG Y., 2012, Nonlinear vibration of nanotube-reinforced composite cylindrical shells in thermal environments, *Computer Methods in Applied Mechanics and Engineering*, **213**, 196-205

28. SHENG N., BOYCE M.C., PARKS D.M., RUTLEDGE G.C., ABES J.I., COHEN R.E., 2004, Multiscale micromechanical modeling of polymer/clay nanocomposites and the effective clay particle, *Polymer*, **45**, 487-506

29. SMITH G.D., BEDROV D., LI L., 2002, A molecular dynamics simulation study of the viscoelastic properties of polymer nanocomposites, *Journal of Chemical Physics*, **117**, 9478-9489

30. SONG S.Y., YOUN J.R., 2006, Modelling of effective elastic properties of polymer based carbon nanotube composites, *Polymer*, **47**, 1741-1748

31. TAN H., YANG W., 1998, Toughening mechanisms of nano-composite ceramics, *Mechanics of Materials*, **30**, 111-123

32. TANDON G.P., WENG G.J., 1984, The effect of aspect ratio of inclusions on the elastic properties of unidirectionally aligned composites, *Polymer Composites*, **5**, 327-333

33. TAYA M., 1981, On stiffness and strength of an aligned short-fiber reinforced composite containing penny- shaped cracks in the matrix, *Journal of Composite Materials*, **15**, 198-210

34. TAYA M., MURA T., 1981, On stiffness and strength of an aligned short-fiber reinforced composite containing fiber-end cracks under uni-axial applied stress, *ASME Journal of Applied Mechanics*, **48**, 361-367

35. THILLY L., PETEGEM S.V., RENAULT P.O., 2009, A new criterion for elastio-plastic transition in nanomaterials. Application to size and composite effects on Cu-Nb nanocomposite wires, *Acta Materialia*, **57**, 3157-3169

36. UTRACKI L.A., KAMAL M.R., 2002, Clay-containing polymeric nanocomposites, *Arabian Journal for Science and Engineering*, **27**, 43-67

37. YAGHOOBI H., FEREIDOON A., 2010, Influence of neutral surface position on deflection of functionally graded beam under uniformly distributed load, *World Applied Sceince Journal*, **10**, 337-341

38. ZHAO K., HE K., 2006, Dielectric relaxation of suspensions of nanoscale particles surrounded by a thick electric double layer, *Physical Review B*, **74**, 1-10

# MODELING OF CYCLIC THERMO-ELASTIC-PLASTIC BEHAVIOUR OF P91 STEEL

Piotr Sulich, Władysław Egner

*Cracow University of Technology, Faculty of Mechanical Engineering, Institute of Applied Mechanics, Kraków, Poland*
*e-mail: piotrjansulich@gmail.com; wladyslaw.egner@pk.edu.pl*

Stanisław Mroziński

*UTP University of Science and Technology, Faculty of Mechanical Engineering, Bydgoszcz, Poland*
*e-mail: stanislaw.mrozinski@utp.edu.pl*

Halina Egner

*Cracow University of Technology, Faculty of Mechanical Engineering, Institute of Applied Mechanics, Kraków, Poland*
*e-mail: halina.egner@pk.edu.pl*

Thermomechanical low cycle fatigue behaviour of P91 steel used in power industry applications has been extensively investigated. The constitutive model of Armstrong-Frederick, extended with temperature rate effects, has been applied to describe the behaviour of the thermo-elastic-plastic material. The proposed model has been successfully implemented in simulation of low cycle fatigue of the examined steel in two different temperatures.

*Keywords:* constitutive modeling, low cycle fatigue, identification of material parameters

## 1. Introduction

Thermomechanical low cycle fatigue accompanied by elastic-plastic strains is one of the dominant failure modes in high temperature structural components such as electric power boilers, boiler pipes, engine elements, etc. Extensive research on the behaviour of various engineering materials under low cycle fatigue conditions has been carried out for the last 50 years in order to develop the adequate constitutive modeling as well as the appropriate predictions of the fatigue lifetime (Taleb *et al.*, 2006; Zhang *et al.*, 2008; Ganczarski and Skrzypek, 2009; Taleb and Cailletaud, 2010; Skrzypek and Ganczarski, 2015).

The aim of this paper is to work out a procedure of comprehensive analysis of thermomechanical low-cycle fatigue behaviour on the example of P91 steel, widely used in power industry applications (Duda *et al.*, 2016). Firstly, the material is tested experimentally in two test temperatures, then the material behaviour is described by a constitutive model implemented into a numerical procedure. Next, the material characteristics are identified in different test temperatures. Finally, the numerical simulations of fatigue tests are performed and compared with the experimental results.

To reduce the number of material parameters for identification, the Armstrong and Frederick constitutive model extended with temperature rate effects is here applied.

The present work is treated as an initial step in the comprehensive analysis of P91 steel behaviour in thermomechanical fatigue conditions. For this reason, classical Armstrong and Frederick constitutive model and only two testing temperatures for parameter identification are considered. However, the procedure of analysis is general and can be applied to a more complex modeling.

## 2. Behaviour of P91 steel

### 2.1. Experimental equipment and material investigated

Tested specimens (see Fig. 1) were cut out of a boiler pipe of diameter $d = 200$ mm and wall thickness $t = 20$ mm (see Fig. 2). The chemical composition of steel is shown in Table 1. Low cycle fatigue tests were strain controlled with constant total strain amplitude ($\varepsilon_{ac} = $ const, frequency of loading $0.2$ Hz) and constant temperature in each test.
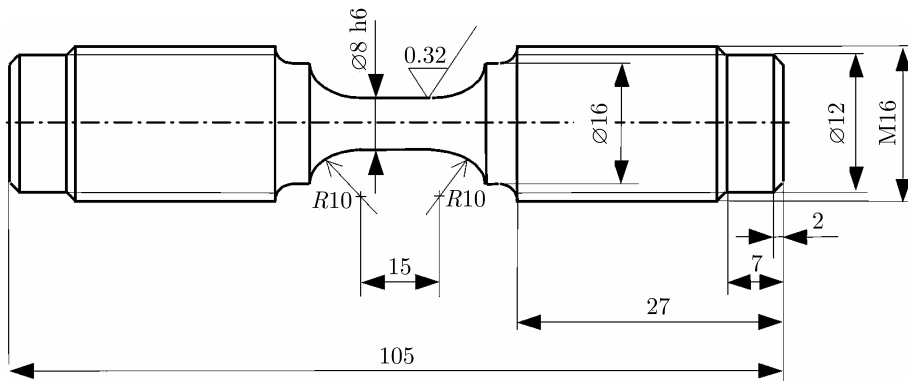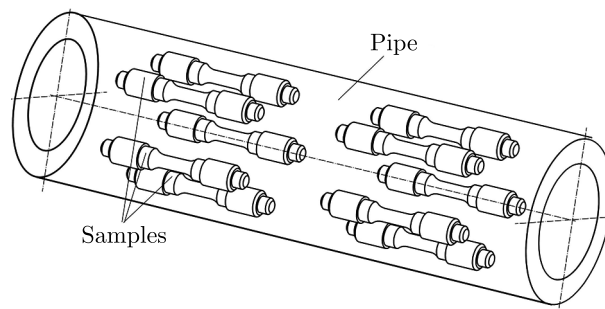


Fig. 1. Shape and dimensions of the tested specimen



Fig. 2. Sampling procedure

**Table 1.** Chemical composition of the steel

| C | Si | Mn | P | S | Cr | Mo | Ni | Al | Co | Cu | Nb | Ti | V | W |
|---|----|----|----|----|----|----|----|----|----|----|----|----|----|----|
| 0.197 | 0.442 | 0.489 | 0.017 | 0.005 | 8.82 | 0.971 | 0.307 | 0.012 | 0.017 | 0.036 | 0.074 | 0.004 | 0.201 | 0.02 |

**Table 2.** Loading scheme, strain amplitude and temperature

| Loading scheme | $\varepsilon_{aci}$ [%] | $T_i$ [°C] |
|---|---|---|
|  | $\varepsilon_{ac1} = 0.25$ <br> $\varepsilon_{ac2} = 0.30$ <br> $\varepsilon_{ac3} = 0.35$ <br> $\varepsilon_{ac4} = 0.50$ <br> $\varepsilon_{ac5} = 0.60$ | $T_1 = 20$ <br> $T_2 = 600$ |

Five levels of the total strain amplitude, and two levels of temperature were applied (see Table 2). Experiments were performed on the testing machine Instron 8502 equipped with a heating chamber.

The temperature was controlled by the use of a thermocouple attached to the sample measuring section. The material deformation was determined by means of a strain gauge extensometer (gauge length 12.5 mm) (see Fig. 3).
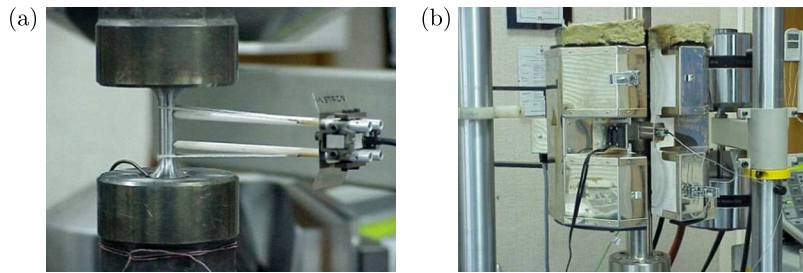


Fig. 3. The test stand: (a) ekstensometer mounting, (b) heating chamber

## 2.2. Material behaviour

The tested steel exhibits cyclic softening, regardless of the testing temperature (half-stress amplitude decreases with increasing cumulated plastic strain, cf. Golański and Mroziński (2013)). This softening could be divided into three phases, which are: the rapid softening phase during the initial few hundred cycles followed by a slow quasi-linear softening phase, and finally again fast softening till rupture (see Fig. 4) (cf. Bernhart *et al.*, 1999; Mebarki *et al.*, 2004). The first phase is generally explained by a rapid change in the dislocation density inherited from the quench treatment, the second is related to the formation of dislocation sub-structure and carbide coarsening under the action of time, temperature and cyclic load, while the third phase is a consequence of micro-damage development in the material that ultimately causes failure of the tested sample (cf. Seweryn *et al.* 2008; Szusta and Seweryn, 2010).

## 3. Constitutive model of a thermo-elastic-plastic material

### 3.1. Basic assumptions

In constitutive modeling, the well-known formalism of thermodynamics of irreversible processes with internal state variables and the local state method are often adopted (Maugin, 1999; Ottosen and Ristinmaa, 2005; Chaboche, 1997a,b, 1986; Skrzypek and Kuna-Ciskał, 2003; Egner, 2012). In this approach, we consider a material as a specific portion of the physical universe, called a system. The current state of a system is entirely determined by certain values of some independent variables, called variables of state, which can be scalars, vectors, or tensors (matrices), such as temperature (scalar) or strain (second order tensor). For a thermo-elastic-plastic material exhibiting mixed hardening the following set of state variables is defined

$$\{V_\alpha^{st}\} = \{\varepsilon_{ij}^e; \alpha_{ij}, p; \theta\} \tag{3.1}$$

where $\varepsilon_{ij}^e$ are components of the reversible (elastic) strain tensor, $\alpha_{ij}$ corresponds to kinematic plastic hardening, $p$ is the accumulated plastic strain

$$p = \int\limits_0^t \sqrt{\frac{2}{3}\dot{\varepsilon}_{ij}^p \dot{\varepsilon}_{ij}^p}\, dt \tag{3.2}$$

and $\theta$ is the absolute temperature in Kelvins.
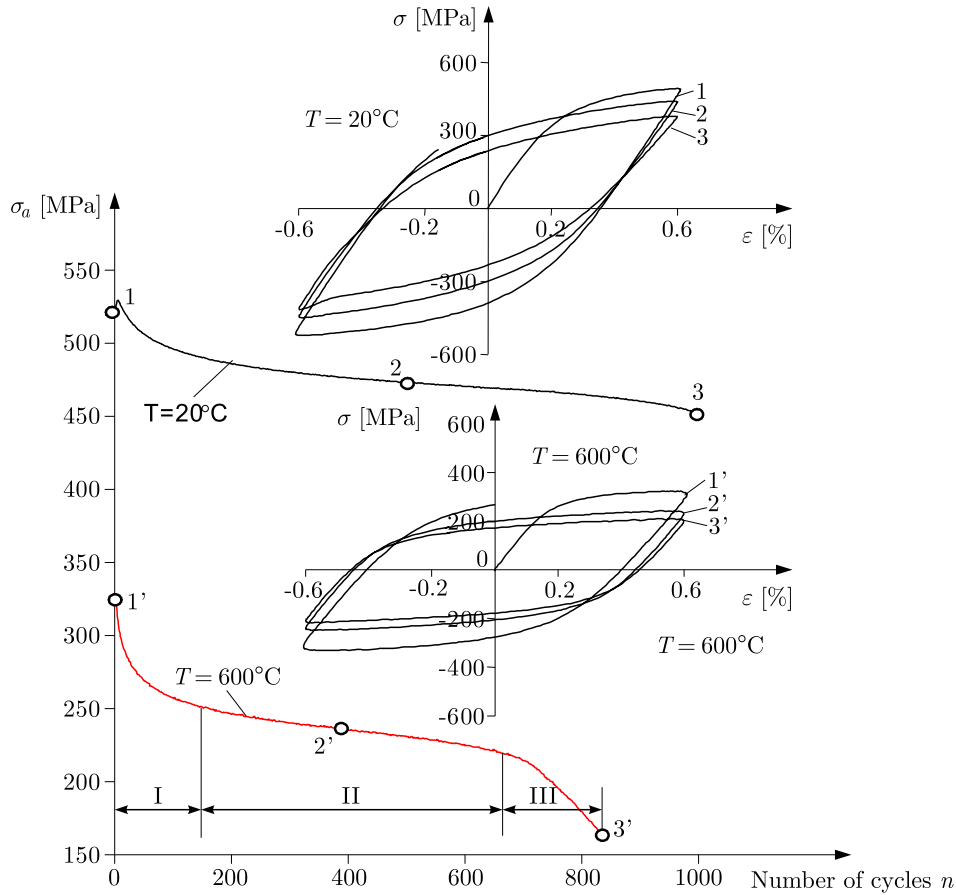
Fig. 4. Cyclic softening of the steel at a constant total strain amplitude $\varepsilon_{ac} = 0.6\%$

In the case of infinitesimal deformation, the total strain tensor components $\varepsilon_{ij}$ are expressed as the sum of the elastic (reversible) $\varepsilon_{ij}^e$, plastic (irreversible) $\varepsilon_{ij}^p$ and thermal $\varepsilon_{ij}^\theta$ strains

$$\varepsilon_{ij} = \varepsilon_{ij}^e + \varepsilon_{ij}^p + \varepsilon_{ij}^\theta \tag{3.3}$$

while thermal strain is expressed as

$$\varepsilon_{ij}^\theta = \alpha_{ij}^\theta(\theta)(\theta - \theta_0) \tag{3.4}$$

with $\alpha_{ij}^\theta(\theta)$ standing for components of the thermal expansion tensor, and $\theta_0$ for the reference temperature at which no thermal strains exist.

### 3.2. State potential and equations of the state

The constitutive behaviour is defined by the specification of two potentials: energy potential and dissipation potential. The state potential is a closed, convex, and scalar-valued function of the overall state variables. The Helmholtz free energy $\psi$ is here used, decomposed into thermo-elastic $\rho\psi^{te}$ and thermo-plastic $\rho\psi^{tp}$ terms ($\rho$ is mass density)

$$\rho\psi(V_\alpha^{st}) = \rho\psi^{te}(\varepsilon_{ij}^e; \theta) + \rho\psi^{tp}(\alpha_{ij}, p; \theta) \tag{3.5}$$

The following classical functions are here adopted (cf. for ex. Ottosen and Ristinmaa, 2005; Egner and Egner, 2015)

$$\rho\psi^{te} = \rho h(\theta) + \frac{1}{2}(\varepsilon_{ij} - \varepsilon_{ij}^p)E_{ijkl}(\theta)(\varepsilon_{kl} - \varepsilon_{kl}^p) - \beta_{ij}(\theta)(\varepsilon_{ij} - \varepsilon_{ij}^p)(\theta - \theta_0)$$

$$\beta_{ij} = E_{ijkl}(\theta)\alpha_{kl}^{\theta}(\theta) \tag{3.6}$$

$$\rho\psi^{tp} = \frac{1}{3}C(\theta)\alpha_{ij}\alpha_{ij} + Q(\theta)\Big[p + \frac{1}{b(\theta)}\mathrm{e}^{-b(\theta)p}\Big]$$

where $h(\theta)$ is a function of temperature, $E_{ijkl}(\theta)$ denote components of the elastic stiffness tensor, and $C(\theta)$, $Q(\theta)$, $b(\theta)$ stand for temperature dependent material parameters.

The thermodynamic forces conjugated to state variables (3.1) result from the assumed form of state potential (3.5) and are defined by the following state equations

$$\sigma_{ij} = E_{ijkl}(\theta)(\varepsilon_{kl} - \varepsilon_{kl}^p) - \beta_{ij}(\theta)(\theta - \theta_0) \qquad X_{ij} = \frac{2}{3}C(\theta)\alpha_{ij}$$

$$R = Q(\theta)(1 - \mathrm{e}^{-b(\theta)p}) \tag{3.7}$$

$\sigma_{ij}$ is here the stress tensor (thermodynamic force conjugated to elastic strain $\varepsilon_{ij}^e$), $X_{ij}$ denotes the back stress (conjugated to plastic hardening variable $\alpha_{ij}$), and $R$ is the drag stress (conjugated to accumulated plastic strain $p$).

If we now define the components of the thermodynamic conjugate force vector $\{J_\alpha\}$ and the flux vector components $\{\dot{P}_\alpha\}$ as

$$\{J_\alpha\} = \{J_\alpha^{mech}; J_\alpha^{\theta}\} = \Big\{\sigma_{ij}, X_{ij}, R; \frac{\theta_{,i}}{\theta}\Big\}$$

$$\{\dot{P}_\alpha\} = \{\dot{P}_\alpha^{mech}; \dot{P}_\alpha^{\theta}\} = \{\dot{\varepsilon}_{ij}^p, -\dot{\alpha}_{ij}, -\dot{p}; -q_i\} \tag{3.8}$$

then the dissipation inequality can be expressed as the scalar product of $J_\alpha$ and $\dot{P}_\alpha$ as follows (Krajcinovic, 1996)

$$\pi = J_\alpha\dot{P}_\alpha \geqslant 0 \tag{3.9}$$

where $\pi$ is the dissipation function.

### 3.3. Dissipation potential and evolution equations

A constitutive model that fulfills the Clausius-Duhem inequality fulfills all formal requirements. However, this does not guarantee that the model provides a good approximation of the real material behaviour. If the internal state variables chosen in the modeling are not identified with underlying physical mechanisms responsible for dissipation, the theory may be physically empty (Maugin, 1999). There are various approaches for the establishment of the rate laws, so that the dissipation inequality is fulfilled. The most often used is the potential approach based on the assumption of the existence of a dissipation potential $F$, being a closed, convex, and scalar-valued function of thermodynamic forces $(3.8)_1$, and some other possible variables. The potential of dissipation $F$ is here assumed not equal to plastic yield surface and dependent on temperature (non-associated thermo-plasticity). This allows obtaining non-linear plastic hardening rules (cf. Ganczarski *et al.*, 2010)

$$F(J_\alpha, \theta) = f(J_\alpha, \theta) + \frac{3\gamma(\theta)}{4C(\theta)}X_{ij}(\alpha_{ij}, \theta)X_{ij}(\alpha_{ij}, \theta)$$

$$f(J_\alpha, \theta) = \sqrt{\frac{3}{2}[s_{ij} - X_{ij}(\alpha_{ij}, \theta)][s_{ij} - X_{ij}(\alpha_{ij}, \theta)]} - [\sigma_y(\theta) + R(p, \theta)] \tag{3.10}$$

where $f(J_\alpha, \theta)$ is the von Mises plastic yield surface, $s_{ij}$ is the stress deviator, $\sigma_y(\theta)$ denotes the yield stress, and $\gamma(\theta)$ is another temperature dependent material parameter.

According to the generalized normality rule (cf. Chaboche, 2008), the following classical rate equations are obtained

$$\dot{\varepsilon}_{ij}^p = \dot{\lambda}^p \frac{s_{ij} - X_{ij}}{\sqrt{\frac{3}{2}[s_{ij} - X_{ij}(\alpha_{ij}, \theta)][s_{ij} - X_{ij}(\alpha_{ij}, \theta)]}} \tag{3.11}$$

$$\dot{\alpha}_{ij} = \dot{\varepsilon}_{ij}^p - \frac{3\gamma}{2C} X_{ij}\dot{p} \qquad \dot{p} = \dot{\lambda}^p$$

The kinetic equations of force-like variables are obtained by taking time derivatives of functions (3.7)

$$\dot{\sigma}_{ij} = E_{ijkl}(\theta)(\dot{\varepsilon}_{kl} - \dot{\varepsilon}_{kl}^p) - P_{ij}\dot{\theta} \tag{3.12}$$

where

$$P_{ij} = -\frac{\partial E_{ijkl}(\theta)}{\partial\theta}(\varepsilon_{kl} - \varepsilon_{kl}^p) + \frac{\partial\beta_{ij}(\theta)}{\partial\theta}(\theta - \theta_0) + \beta_{ij}(\theta)$$

$$\dot{X}_{ij} = \frac{2}{3}C(\theta)\dot{\alpha}_{ij} + \frac{2}{3}\frac{dC(\theta)}{d\theta}\alpha_{ij}\dot{\theta} \tag{3.13}$$

$$\dot{R} = Q(\theta)b(\theta)\mathrm{e}^{-b(\theta)p}\dot{p} + \Big[\frac{dQ(\theta)}{d\theta}(1 - \mathrm{e}^{-b(\theta)p}) + Q(\theta)\frac{db(\theta)}{d\theta}\mathrm{e}^{-b(\theta)p}p\Big]\dot{\theta}$$

### 3.4. Consistency condition

Calculation of the Lagrange multiplier $\dot{\lambda}^p(\theta)$ for rate-independent material needs making use of the consistency condition

$$\dot{f}(J_\alpha, \theta) = \frac{\partial f}{\partial\sigma_{ij}}\dot{\sigma}_{ij} + \frac{\partial f}{\partial X_{ij}}\dot{X}_{ij} + \frac{\partial f}{\partial R}\dot{R} + \frac{\partial f}{\partial\theta}\dot{\theta} = 0 \tag{3.14}$$

The classical Kuhn-Tucker loading/unloading conditions have the form

$$f \leqslant 0 \quad \text{and} \quad \dot{f} \begin{cases} < 0 & \text{and} \quad \dot{\lambda}^p = 0 \Rightarrow \quad \text{passive loading} \\ = 0 & \text{and} \quad \dot{\lambda}^p = 0 \Rightarrow \quad \text{neutral loading} \\ = 0 & \text{and} \quad \dot{\lambda}^p > 0 \Rightarrow \quad \text{active loading} \end{cases} \tag{3.15}$$

Substituting equations (3.7) and (3.11) into equation (3.14) leads to the following

$$\dot{f} = \frac{\partial f}{\partial\sigma_{ij}}\dot{\sigma}_{ij} - \dot{\lambda}^p\Big[\frac{2}{3}C\frac{\partial f}{\partial\sigma_{ij}}\Big(\frac{\partial f}{\partial\sigma_{ij}} - \gamma\alpha_{ij}\Big) - \frac{\partial f}{\partial R}Q b\mathrm{e}^{-bp}\Big] - \Big\{\frac{2}{3}\frac{dC}{d\theta}\frac{\partial f}{\partial\sigma_{ij}}\alpha_{ij}$$

$$- \frac{\partial f}{\partial R}\Big[\frac{dQ}{d\theta}(1 - \mathrm{e}^{-bp}) + Q\frac{db}{d\theta}\mathrm{e}^{-bp}p\Big] - \frac{\partial f}{\partial\theta}\Big\}\dot{\theta} = \frac{\partial f}{\partial\sigma_{ij}}\dot{\sigma}_{ij} - \dot{\lambda}^p H - \dot{\theta}S = 0 \tag{3.16}$$

In the above equation, $H$ is the generalized hardening modulus

$$H = \frac{2}{3}C\frac{\partial f}{\partial\sigma_{ij}}\Big(\frac{\partial f}{\partial\sigma_{ij}} - \gamma\alpha_{ij}\Big) - \frac{\partial f}{\partial R}Q b\mathrm{e}^{-bp} \tag{3.17}$$

and $S$ reflects the sensitivity of the yield surface on temperature changes (cf. Egner, 2012)

$$S = \frac{2}{3}\frac{dC}{d\theta}\frac{\partial f}{\partial\sigma_{ij}}\alpha_{ij} - \frac{\partial f}{\partial R}\Big[\frac{dQ}{d\theta}(1 - \mathrm{e}^{-bp}) + Q\frac{db}{d\theta}\mathrm{e}^{-bp}p\Big] - \frac{\partial f}{\partial\theta} \tag{3.18}$$

Expression (3.16) determines the consistency multiplier

$$\dot{\lambda}^p(\theta) = \frac{1}{w}\Big[\frac{\partial f}{\partial\sigma_{ij}}E_{ijkl}\dot{\varepsilon}_{kl} - \Big(\frac{\partial f}{\partial\sigma_{ij}}P_{ij} + S\Big)\dot{\theta}\Big] \tag{3.19}$$

where

$$w = \frac{\partial f}{\partial\sigma_{ij}}E_{ijkl}\frac{\partial f}{\partial\sigma_{kl}} + H \tag{3.20}$$

### 3.5. Heat balance equation

To determine the temperature distribution within the body, the heat balance equation is used, derived from the first law of thermodynamics by substituting into it the internal energy density together with Fourier's law. The heat balance equation takes the form ($c_\varepsilon^\theta$ is the specific heat capacity at a constant strain and $r$ is the distributed heat source per unit volume)

$$\rho c_\varepsilon^\theta \dot{\theta} = -q_{i,i} + r - \theta P_{ij}(\dot{\varepsilon} - \dot{\varepsilon}_{ij}^I) + \sigma_{ij}\dot{\varepsilon}_{ij}^p - \left(R - \theta \frac{\partial R}{\partial \theta}\right)\dot{p} - \left(X_{ij} - \theta \frac{\partial X_{ij}}{\partial \theta}\right)\dot{\alpha}_{ij} \qquad (3.21)$$

## 4. Numerical implementation and results

### 4.1. Numerical algorithm

In the case of uniaxial loading (tension/compression), the tensorial quantities: stress tensor, strain tensor and back stress tensor may be presented in the following matrix forms

$$[\sigma_{ij}] = \sigma \begin{bmatrix} 1 & 0 & 0 \\ 0 & 0 & 0 \\ 0 & 0 & 0 \end{bmatrix} \qquad [s_{ij}] = \sigma \begin{bmatrix} \frac{2}{3} & 0 & 0 \\ 0 & -\frac{1}{3} & 0 \\ 0 & 0 & -\frac{1}{3} \end{bmatrix}$$

$$[\varepsilon_{ij}] = \varepsilon^e \begin{bmatrix} 1 & 0 & 0 \\ 0 & -\nu & 0 \\ 0 & 0 & -\nu \end{bmatrix} + \varepsilon^p \begin{bmatrix} 1 & 0 & 0 \\ 0 & -\frac{1}{2} & 0 \\ 0 & 0 & -\frac{1}{2} \end{bmatrix} + \alpha^\theta(\theta - \theta_0) \begin{bmatrix} 1 & 0 & 0 \\ 0 & 1 & 0 \\ 0 & 0 & 1 \end{bmatrix} \qquad (4.1)$$

$$[X_{ij}] = X \begin{bmatrix} \frac{2}{3} & 0 & 0 \\ 0 & -\frac{1}{3} & 0 \\ 0 & 0 & -\frac{1}{3} \end{bmatrix} \qquad [\alpha_{ij}] = \alpha \begin{bmatrix} 1 & 0 & 0 \\ 0 & -\frac{1}{2} & 0 \\ 0 & 0 & -\frac{1}{2} \end{bmatrix}$$

The numerical procedure implementing EAF model has been built by the use of Mathematica 10 software according to the algorithms based on the classical backward Euler scheme and the Newton-Raphson method (cf. Chaboche and Cailletaud, 1996) (see Fig. 5). The vector $\Delta S = [\Delta\lambda, \Delta\varepsilon^e, \Delta\theta, \Delta\alpha]^{\mathrm{T}}$ contains increments of the unknowns, and is iteratively calculated according to

$$\Delta S_{(k+1)} = \Delta S_{(k)} - [J_{(k)}]^{-1} R(\Delta S_{(k)}) \qquad (4.2)$$

In the above equation $[J] = \partial R/\partial \Delta S$ is the Jacobian matrix and $R(\Delta S)$ is the residual vector containing the components $R_i = \Delta S_i - \widehat{\Delta S_i}$, where $\Delta S_i$ is a variable while $\widehat{\Delta S_i}$ denotes the function resulting from the evolution rule for the $i$-th variable $S_i$. It is evident that the condition $R(\Delta S) = 0$ defines the solution. If we expand this condition into a Taylor series, we obtain (4.2). The iteration procedure is stopped when the norm of $R$ is sufficiently small.

### 4.2. Identification of model parameters

The identification of model parameters has been performed with the application of SIMULIA--Isight package (cf. SIMULIA Abaqus Extended Products, 2014), which provides a platform for automatic optimal selection of material parameters. For this purpose, two components offered by the program: "Data Matching" and "Optimization" have been used. "Data Matching" component allows one to calibrate the model by analyzing different error measures between the experimental data and numerical simulation results. The following vector of material parameters $P_i$ is searched

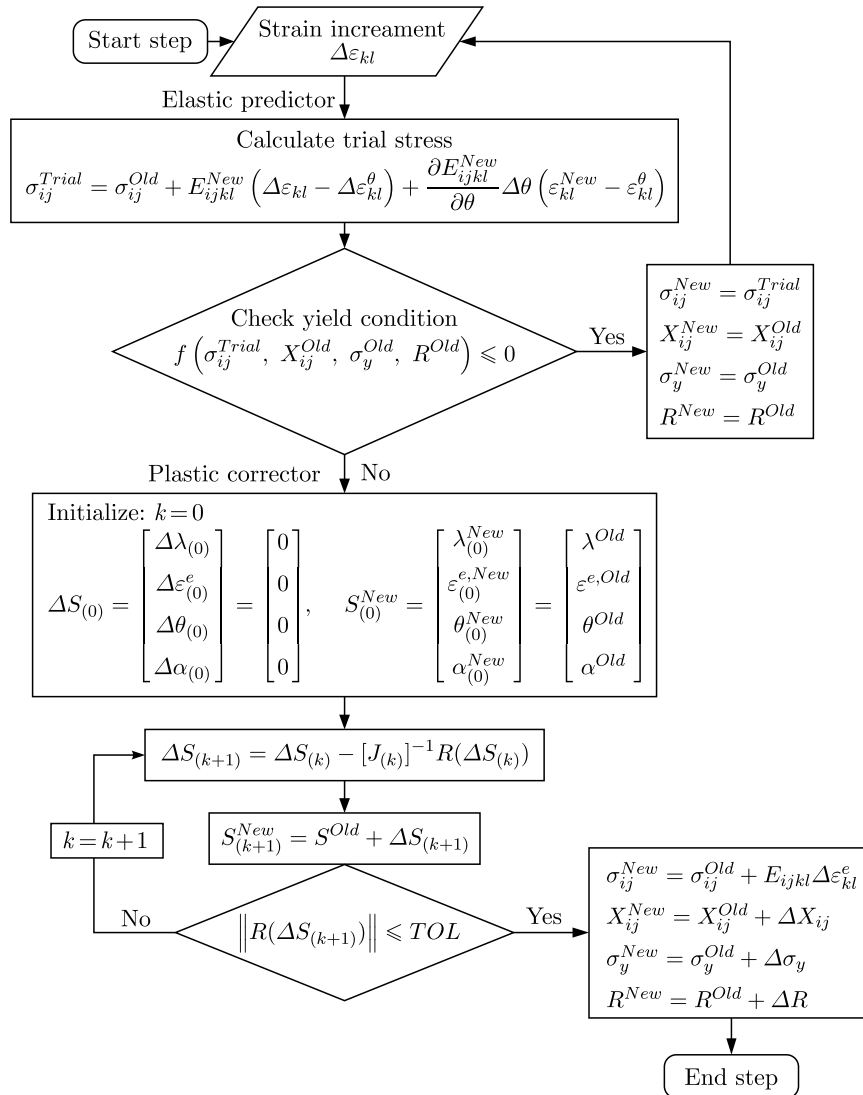$$\{P_i\} = \{\sigma_y, E, \gamma, C, b, Q\} \qquad P_i \in \langle L_i, U_i \rangle \qquad (4.3)$$

Fig. 5. Numerical algorithm

The parameters are bounded between their respective lower bounds $L_i$ and upper bounds $U_i$. Before the identification starts, the parameters are subjected to normalization, so that

$$\overline{P}_i \in \langle -1, 1+ \rangle \qquad P_i = \frac{1}{2}[(1 - \overline{P}_i)L_i + (1 + \overline{P}_i)U_i] \qquad (4.4)$$

In the present analysis, the error measure used is the square root of the sum of squared deviations

$$F_{obj}(\overline{P}_i) = \sum_{k=1}^{m} [\sigma_k(P_i) - \sigma_k^e]^2 \qquad (4.5)$$

where $\sigma_k^e$ denote the experimental stress data and $\sigma_k(P_i)$ are the stress data calculated numerically by the use of current values of the model parameters $P_i$.

The "optimization" component is applied to find an optimal solution in the user-defined field, with the assumed constraints and the objective function defined by (4.5). The constraints limit the search field to the range of acceptable physical values. To reduce the dimension of the field in which the optimal solution is searched, the following procedure has been applied: the initial yield stress $\sigma_y$ and the elastic modulus $E$ are identified manually, considering the

monotonic tensile part of the first hysteresis loop. Next, considering the whole first hysteresis loop, the approximate values of kinematic hardening parameters ($\gamma$ and $C$) are looked for on the assumption that the isotropic hardening is negligible ($b = 0$ and $Q = 0$)

$$\min\{F_{obj}(\overline{P}_i): \quad E = \text{const} \ \wedge \ \sigma_y = \text{const} \ \wedge \ b = 0 \ \wedge \ Q = 0\} \tag{4.6}$$

Then the parameters related to the isotropic hardening are searched with the use of several chosen hysteresis loops (loop 2 to 20)

$$\min\{F_{obj}(\overline{P}_i): \quad E = \text{const} \ \wedge \ \sigma_y = \text{const} \ \wedge \ \gamma = \text{const} \ \wedge \ C = \text{const}\} \tag{4.7}$$

As a result, the approximate values of material parameters, constituting the starting point for optimization are set, and the identification of all the unknown material parameters $(E, \sigma_y, \gamma, C, b, Q)$ is performed once again, but in a substantially limited range around the initial point. The results of the applied identification procedure are presented in Table 3. Please note that these data ensure the best fit of the results simulated numerically into the experimental results for the chosen objective function $F_{obj}(\overline{P}_i)$. However, the constitutive model does not account for nonlinear elastic effects, therefore the yield stress is clearly underestimated relative to the offset yield stress $R_{p02}$ for the considered material (cf. Mroziński and Piotrowski, 2013).

**Table 3.** Material parameters ($\varepsilon_{ac} = 0.60\%$)

|  | 20°C | 600°C |
|---|---|---|
| $\sigma_y$ [MPa] | 278 | 184 |
| $E$ [MPa] | 198 000 | 159 000 |
| $\gamma$ | 595 | 752 |
| $C$ [MPa] | 130 420 | 89 120 |
| $b$ | 1.02 | 1.88 |
| $Q$ [MPa] | −39 | −69 |

The experimental observations indicate that steel is not stable during fatigue, and that the microstructure can be modified by the thermal cycle. However, such a case takes place when temperatures reach or exceed the tempering temperatures, even for a short time (cf. Zhang *et al.*, 2008). In other words, there are two ranges of temperature, in which the fatigue behaviour of the steel is different:

(1) Above the tempering temperature, a sharp ageing is observed while the fatigue test additionally enhances the microstructural evolutions related to ageing. In such a case, changes of mechanical properties of the steel are induced by factors related independently to the history of temperature. As a consequence, it is necessary to include additional parameters (state variables) for correct description of such an influence of temperature in a constitutive model. The identification of model parameters, being temperature history dependent, should be done for all temperatures by identifying with all tests together with the chosen material functions of temperature (cf. Cailletaud *et al.*, 2000). For this purpose, an experimental thermomechanical fatigue tests should be performed and used for parameter identification.

(2) On the other hand, below the tempering temperature (the case considered in the present analysis) the ageing remains nearly constant, so that the mechanical properties depend on the current temperature and not on the history of temperature. In such a case, there is no need to include in the identification procedure all temperatures together, but to use several isothermal tests in different temperatures, and introduce the influence of temperature on the material parameters by interpolation techniques with polynomial or spline functions.

### 4.3. Simulation of the tests under strain control

Kinematic hardening equations $(3.11)_2$ and $(3.13)_2$, proposed by Armstrong and Frederick (1996), introduce a recall term, which is collinear with the back stress $X_{ij}$. For a monotonic uniaxial loading, the evolution of $X_{ij}$ becomes exponential with a saturation value $C/\gamma$. Integration of $(3.13)_2$ with respect to $\varepsilon_{ij}^p$ (for the isothermal case) yields

$$X_{ij} = \nu \frac{C}{\gamma} \big(1 - \mathrm{e}^{-\nu\gamma\varepsilon_{ij}^p}\big) \tag{4.8}$$

where $\nu = \pm 1$ indicates the flow direction. Function (4.8) is shown in Fig. 6a for two testing temperatures. It can be seen that the translation of the yield surface for the same strain level is more pronounced in lower temperatures.
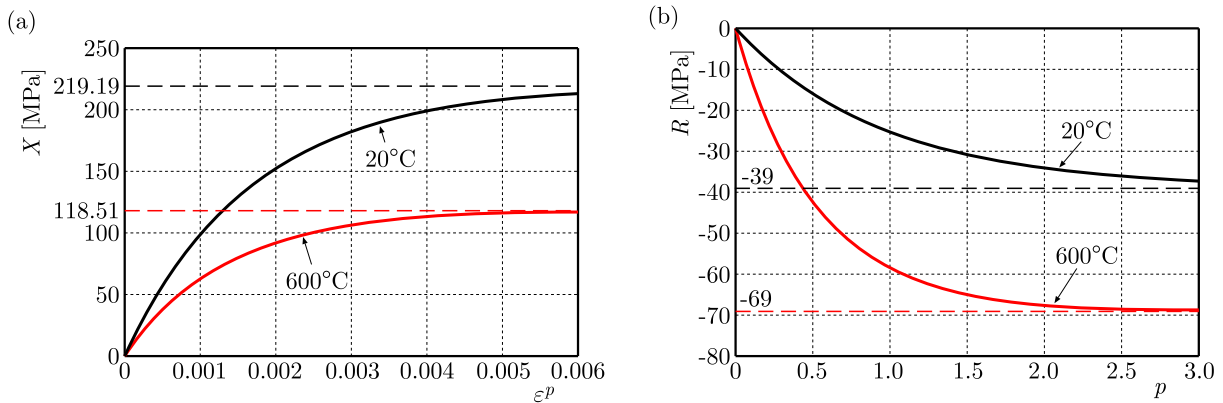


Fig. 6. (a) Evolution of back stress versus plastic strain. (b) Evolution of $R$ versus accumulated plastic strain

The $R$-$p$ curve obtained on the basis of Eq. $(3.7)_3$ is shown in Fig. 6b. The parameters $Q$ and $b$ depend on the material and temperature. For cyclic loading, the value of $b$ is usually placed in the range between 0.5 and 50. In the context of monotonic loading, the value of $b$ should be much higher (cf. Chaboche, 2008).
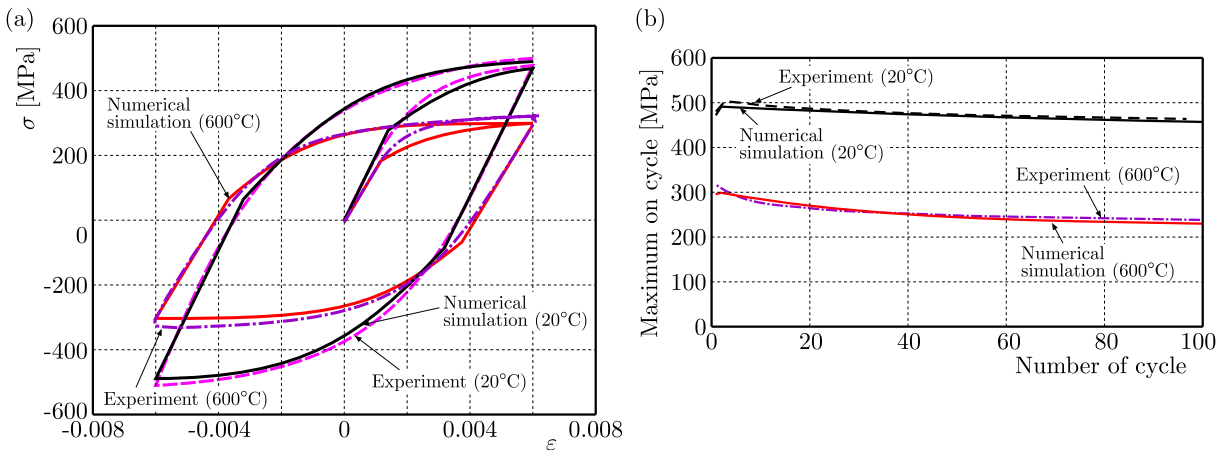


Fig. 7. Comparison between experimental and calculated (a) responses with a strain rate of $10^{-2}$ and (b) maximum stress vs. cycles at temperatures of 20°C and 600°C

Figure 7a presents a comparison between the test results used in the identification process and their simulations by the described model using the material parameters for Table 3. As shown in Fig. 7a, the model simulates the first hysteresis loop with a very good accuracy. Also, stage I of the tests used in the identification process (the rapid softening phase during the initial few hundred cycles) is well reflected, see Fig. 7b.

The identification is performed with the use of chosen hysteresis loops only, and not with the whole fatigue curve. However, when the optimal values of model parameters are obtained, the (numerically obtained) maximum stress on cycle versus cycle number exhibits a good agreement with the results of all the first 100 cycles of the experiment (see Fig. 7b).

## 5.   Conclusions

In the present paper, the algorithm for a comprehensive analysis of thermomechanical fatigue behaviour is presented. Such an analysis consists of five main steps: (1) experimental testing in several test temperatures, (2) constitutive modeling of material behaviour regarding the efects of temperature change, (3) numerical implementation of the mathematical model, (4) identification of model parameters in different test temperatures to obtain temperature-dependent material characteristics, and (5) validation of the analysis by comparison between the experimental and numerical results.

The classical Armstrong and Frederick constitutive model used in the presented analysis is not capable of describing different physical mechanisms able to produce material nonlinearities on a macro-scale. For this reason, a more advanced constitutive model should be adopted to properly refelect the material behaviour under different loading paths (cf. Besson *et al.*, 2009; Saanouni, 2012; Egner and Egner, 2014). However, such advanced models involve many material parameters that need to be identified. This is why in this research a simple model is considered, but the described procedure is general and can be applied also to a more compehensive modeling (cf. Velay *et al.*, 2006; Saï, 2011).

## References

1. ARMSTRONG P.J., FREDERICK C.O., 1966, A mathematical representation of the multiaxial Bauschinger effect, Report RD/B/N731, CEGB, Central Electricity Generating Board, Berkeley, UK

2. BERNHART G., MOULINIER G., BRUCELLE O., DELAGNES D., 1999, High temperature low cycle fatigue behaviour of a martensite forging tool steel, *International Journal of Fatigue*, **21**, 2, 179-186

3. BESSON J., CAILLETAUD G., CHABOCHE J.L., FOREST S., BLÉTRY M., 2009, *Non-Linear Mechanics of Materials*, Springer

4. CHABOCHE J.L., 1997a, Thermodynamic formulation of constitutive equations and application to the viscoplasticity and viscoelasticity of metals and polymers, *International Journal of Solids and Structures*, **34**, 18, 2239-2254

5. CHABOCHE J.L., 1997b, Viscoplastic constitutive equations for the description of cyclic and anisotropic behaviour of metals, *Bulletin de L'Academie Polonaise des Sciences, Série des Sciences Techniques*, **XXV**, 1, 33-39

6. CHABOCHE J., 1986, Time independent constitutive theories for cyclic plasticity, *International Journal of Plasticity*, **2**, 2, 149-188

7. CHABOCHE J.L., 2008, A review of some plasticity and viscoplasticity constitutive theories, *International Journal of Plasticity*, **24**, 1642-1693

8. CHABOCHE J.L., CAILLETAUD, G., 1996, Integration methods for complex plastic constitutive equations, *Computer Methods in Applied Mechanics and Engineering*, **133**, 125-155

9. CAILLETAUD G., DEPOID C., MASSINON D., NICOULEAU-BOURLES E., 2000, Elastoviscoplasticity with aging in aluminium alloys, [In:] *Continuum Thermomechanics: The Art and Science of Modelling Material Behaviour (Paul Germain's Anniversary Volume)*, Solid Mechanics and Its Applications, Kluwer Academic Publishers, 75-86

10. DUDA P., FELKOWSKI Ł., DOBRZAŃSKI J., PURZYŃSKA H., 2016, Modelling the strain and stress state under creep conditions in P91 steel, *Materials at High Temperatures*, **33**, 85-93

11. EGNER H., 2012, On the full coupling between thermo-plasticity and thermo-damage in thermo-dynamic modeling of dissipative materials, *International Journal of Solids and Structures*, **49**, 279-288

12. EGNER H., EGNER W., 2015, Classification of constitutive equations for dissipative materials-general review, [In:] *Mechanics of Anisotropic Materials*, J.J. Skrzypek and A.W. Ganczarski (Edit.), 247-294, Springer

13. EGNER H., EGNER W., 2014, Modeling of a tempered martensitic hot work tool steel behavior in the presence of thermo-viscoplastic coupling, *International Journal of Plasticity*, **57**, 77-91

14. GANCZARSKI A.W., EGNER H., MUC A., SKRZYPEK J.J., 2010, Constitutive models for analysis and design of multifunctional technological materials, [In:] *Innovative Technological Materials. Structural Properties by Neutrons, Synchrotron Radiation and Modelling*, F. Rustichelli and J.J. Skrzypek (Edit.), 179-220, Springer

15. GANCZARSKI A., SKRZYPEK J., 2009, A study on coupled thermo-elasto-plastic-damage dissipative phenomena: models and application to some innovative materials, *Journal of Thermal Stresses*, **32**, 698-751

16. GOLAŃSKI G., MROZIŃSKI S., 2013, Low cycle fatigue and cyclic softening behavior of martensitic cast steel, *Engineering Failure Analysis*, **12**, 35, 692-702

17. KRAJCINOVIC D., 1996, *Damage Mechanics*, Elsevier

18. MAUGIN G. A., 1999, *The Thermomechanics of Nonlinear Irreversible Behaviors. An Introduction*, World Scientific Series on Nonlinear Science, Series A, Vol. 27

19. MEBARKI N., DELAGNES D., LAMESLE P., DELMAS F., LEVAILLANT C., 2004, Relationship between microstructure and mechanical properties of a 5%Cr tempered martensitic tool steel, *Materials Science and Engineering A*, **387-389**, 1/2, 171-175

20. MROZIŃSKI S., PIOTROWSKI M., 2013, Influence of temperature and loading program on the fatigue life of steel P91, *Acta Mechanica et Automatica*, **7**, 2, 93-98

21. OTTOSEN N. S., RISTINMAA M., 2005, *The Mechanics of Constitutive Modeling*, Elsevier

22. SAANOUNI, K., 2012, *Damage Mechanics in Metal Forming: Advanced Modeling and Numerical Simulation*, ISTE/Wiley, London.

23. SAÏ K., 2011, Multi-mechanism models: Present state and future trends, *International Journal of Plasticity*, **27**, 250-281

24. SEWERYN A., BUCZYŃSKI A., SZUSTA J., 2008, Damage accumulation model for low cycle fatigue, *International Journal of Fatigue*, **30**, 756-765

25. SIMULIA Abaqus Extended Products, Abaqus 6.14-AP Isight 5.9, Dassault Systemes 1994-2014, http://www.3ds.com/products/simulia

26. SKRZYPEK J., GANCZARSKI A., 2015, *Mechanics of Anisotropic Materials*, Springer

27. SKRZYPEK J., KUNA-CISKAŁ H., 2003, Anisotropic elastic-brittle-damage and fracture models based on irreversible thermodynamics, [In:] *Anisotropic Behaviour of Damaged Materials*, J. Skrzypek and A. Ganczarski (Edit.), Lecture Notes in Applied and Computational Mechanics, vol. 9, 143-184, Springer

28. SZUSTA J., SEWERYN A., 2010, Low-cycle fatigue model of damage accumulation – The strain approach, *Engineering Fracture Mechanics*, **77**, 1604-1616

29. TALEB L., CAILLETAUD G., 2010, An updated version of the multimechanism model for cyclic plasticity, *International Journal of Plasticity*, **26**, 859-874

30. TALEB L., CAILLETAUD G., BLAJ L., 2006, Numerical simulation of complex ratcheting tests with a multi-mechanism model type, *International Journal of Plasticity*, **22**, 724-753

31. VELAY V., BERNHART G., PENAZZI L., 2006, Cyclic behavior modeling of a tempered martensitic hot work tool steel, *International Journal of Plasticity*, **22**, 459-496

32. ZHANG Z., BERNHART G., DELAGNES D., 2008, Cyclic behavior constitutive modeling of a tempered martensitic steel including ageing effect, *International Journal of Fatigue*, **30**, 706-716

# THE FRACTURE MECHANICS FORMULAS FOR SPLIT-TENSION STRIPS

RAGIP INCE

*Firat University, Engineering Faculty, Civil Engineering Department, Elazig, Turkey*

*e-mail: rince@firat.edu.tr*

The notched beams have been commonly used in concrete fracture. In this study, the splitting-strip specimens, which have some advantages – compactness and lightness – compared to beams, are analyzed for effective crack models. Using the Fourier integrals and Fourier series, a formula for the maximum tensile strength of concrete is first derived for an un-notched splitting-strip in the plane of loading. Subsequently, the linear elastic fracture mechanics formulas of the splitting-strip specimens, namely the stress intensity factor $K_I$, the crack mouth opening displacement $CMOD$, and the crack opening displacement profile $COD$, are determined for different load-distributed widths via the weight function.

*Keywords:* concrete, Fourier integrals, fracture mechanics, splitting test, weight functions

## 1. Introduction

The split-tension specimens are frequently used to determine tensile strength of materials, such as concrete and rock (Neville, 2011). The split-cylinder test, which is also called the Brazilian split test, was proposed by Carneiro and Barcellos (1949). This test was successfully applied to cubes by Nilsson (1961). However, split-tension test specimens, namely, cylinders, cubes and diagonal cubes, have also been successfully used in concrete fractures over the last decade (Modeer, 1979; Tang, 1994; Rocco *et al.*, 1995; Tang *et al.*, 1996; Ince, 2010, 2012a,b). The splitting concrete specimens exhibit several advantages, e.g., compactness and lightness, and the weight of the specimen can be disregarded in calculation of fracture parameters.

The experimental investigations on fracture mechanics of cement-based materials conducted until the 1970s indicated that classical linear elastic fracture mechanics (LEFM) was no longer valid for quasi-brittle materials such as concrete. This inapplicability of LEFM was due to the existence of a relatively large inelastic zone in the front and around the tip of the main cracks in concrete. This so-called fracture process zone (FPZ) was ignored by LEFM. Consequently, several investigators have developed deterministic fracture-mechanics approaches to describe fracture--dominated failure of concrete structures. These models could be classified as cohesive crack models and effective crack models. Contrary to LEFM, in which a single fracture parameter was used such as the critical stress intensity factor, those models needed at least two experimentally determined fracture parameters to characterize failure of concrete structures. These models could be classified as cohesive crack models and effective crack models: namely the two-parameter model (Jenq and Shah, 1985), the effective crack model (Nallathambi and Karihaloo, 1986), the size effect model (Bazant and Kazemi, 1990) and the double-K model (Xu and Reinhardt, 1999).

Analytical and numerical studies on split-tension specimens (Modeer, 1979; Tang, 1994; Rocco *et al.*, 1995; Tang *et al.*, 1996; Ince, 2010, 2012a,b; Ince *et al.*, 2015, 2016) have revealed that nominal strength is highly affected by the width of the distributed load and the specimen size. The existing design codes have not considered these effects in the determination of the split-tensile strength of concrete. On the other hand, theoretical and experimental studies with

splitting strip specimens (Davies and Bose, 1968; Filon, 1903; Schleeh, 1978) are limited when compared to those of other splitting specimens.

For this purpose, LEFM formulas for the stress intensity factor $K_I$, the crack mouth opening displacement ($CMOD$), and the crack opening displacement profile ($COD$) of splitting strip specimens have been evaluated for different load-distributed widths and initial crack lengths utilizing the weight function in this study. In addition, the maximum tensile stresses in the un-notched split-tension strips have also been determined for different load-distributed widths.

## 2.  A historical overview of splitting tests

As indicated in Fig. 1a, a split-tension specimen is placed between the platens of the test machine and the load is subsequently applied until failure, which is caused by splitting along the vertical diameter due to the lateral tensile stress that has occurred (Neville, 2011). According to elasticity theory (Timoshenko and Godier, 1970), the nominal tensile strength of split-tension specimens is defined as

$$\sigma_{Nc} = \frac{2P_c}{\pi bh} \tag{2.1}$$

where $P_c$ is the ultimate load, $b$ is the specimen width and $h$ is the specimen depth. However, Eq. (2.1) is only valid for the concentrated loading condition shown in Fig. 1a. In practice, the applied load is distributed on the specimens over a finite width ($2t$) using soft materials, such as hard cardboard and plywood, as indicated in Fig. 1b (Neville, 2011; Davies and Bose, 1960). Tang et al. (1992) investigated the effect of distributed load in three-point bending beams and split--tension cylinders. The nominal strength decreased with the increasing width of the distributed load in the split-tension cylinder, whereas this effect was not significant in the bending specimens. According to Tang (1994), the maximum tensile stress value of the un-notched cylinder specimens at the plane of loading could be calculated as

$$\sigma_{max} = \frac{2P}{\pi bh} \sqrt{(1 - \beta^2)^3} \tag{2.2}$$

where $P$ is the total compressive load and $\beta = 2t/h = t/d$ is the ratio of the distributed-load width to the specimen depth (d is the characteristic specimen size), as depicted in Fig. 1. Rocco et al. (1995) examined the cylinder and cube specimens and proposed that the maximum tensile stress could be calculated for the un-notched cube specimens at the plane of loading as follows

$$\sigma_{max} = \frac{2P}{\pi bh} \left[ \sqrt[3]{(1 - \beta^2)^5} - 0.0115 \right] \qquad \beta \leqslant 0.20 \tag{2.3}$$

Using the boundary element method, a formula for the maximum tensile strength of concrete was similarly derived for un-notched diagonal cubes in the plane of loading by Ince (2012a) as follows

$$\sigma_{max} = \frac{2P}{\pi bh} \frac{1}{0.931 + 38.931 \beta^{4.778}} \qquad \beta \leqslant 0.25 \tag{2.4}$$

One of the advantages of diagonal splitting-cube specimens is nearly const $= 1/0.931 = 1.074$ maximum stress in the plane of loading for $\beta \leqslant 0.15$, which differs from other splitting specimens.

Approaches based on fracture mechanics and using notched split cylinder specimens were first performed by Tweed et al. (1972). They developed a closed-form expression for the geometry factor of the notched split-tension cylinder. Tang (1994) also used the finite element method
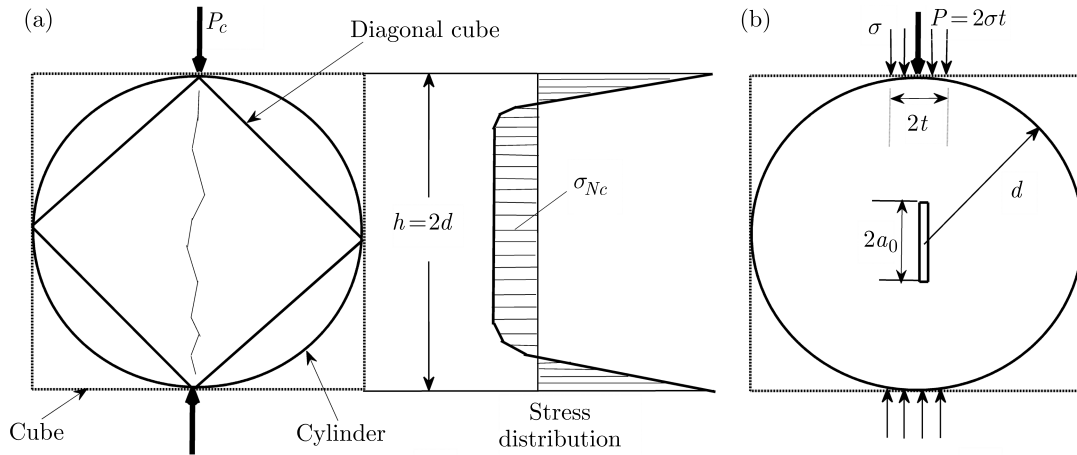
Fig. 1. Splitting tension test: (a) geometry and stress distribution, (b) notched specimen and distributed loading case

to study notched cylinder specimens under the opposite distributed loading and the developed LEFM formulas (Fig. 1b). Cubical and diagonal cubic specimens with a central notch were investigated using effective crack models by Ince (2010, 2012a) who evaluated LEFM formulas with those split-tension specimens for various load-distributed widths and initial crack lengths using the finite element and boundary element method. A series of experimental studies with split-tension and beam specimens were also performed. The results were discussed based on two most popular fracture models: the two-parameter and the size effect models. The results of the tests revealed that the notched cube and diagonal cube tests can be utilized successfully for determining the fracture parameters of concrete. Subsequently, Ince (2012b) derived an improved version of LEFM formulas for splitting cylinder and cube specimens and then computed the four-term universal weight functions of the split-tension specimens such as cylinder, cube and diagonal cube by using the boundary element method to simulate the double-K concrete fracture model.

The numbers of theoretical and experimental studies with splitting strip specimens (Davies and Bose, 1968; Filon, 1903; Schleeh, 1978) were limited when compared to studies conducted with other splitting specimens. For instance, a formula similar to equations (2.2)-(2.4) was not developed. Therefore, in the present research, both un-notched and notched splitting strip specimens have been analyzed using analytical and numerical methods.

## 3. Deriving LEFM formulas for split-tension strip

In this study, split-tension strip specimens have been simulated for the use in effective crack fracture models based on earlier studies of split-tension tests for concrete fracture. The weight function approach was used to determine the LEFM formulas for split-tension strip specimens with the central initial notch.

The weight function method was originally suggested by Bueckner (1970) and Rice (1972) to evaluate the stress intensity factor using a simple integration. When a weight function is determined for a notched body, the stress intensity factors could be calculated for arbitrary loadings on the same body. For the case of mode I, the stress intensity factors can be expressed as follows

$$K_I = \int_0^a \sigma(y) m(y, a) \, dy \tag{3.1}$$

where $a$ is the crack length, $\sigma(y)$ is the normal stress along the crack line in the un-cracked body, and $m(y, a)$ is the weight function (or Green's functions which are essentially equivalent to the weight functions) (Gdoutos, 1990).

For the central notch, an infinite strip subjected to four equal point loads on the notch, as shown in Fig. 2, the Green function was derived by Tada *et al.* (2000) as follows

$$K_I = \frac{2F}{\sqrt{2d}}\left[+0.297\sqrt{1 - \left(\frac{y}{a}\right)^2}\left(1 - \cos\frac{\pi a}{2d}\right)\right]\sqrt{\tan\frac{\pi a}{2d}}\left[1 - \left(\cos\frac{\pi a}{2d}\Big/\cos\frac{\pi y}{2d}\right)^2\right]^{-\frac{1}{2}} \quad (3.2)$$
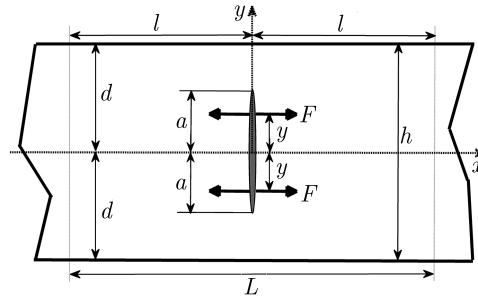


Fig. 2. A center-cracked infinite strip subjected to four equal point loads

The accuracy of Eq. (3.2) is better than 1% for all $a/d$ and $y/a$ (Tada *et al.*, 2000). The normal stresses along the crack line in the un-cracked body must be first computed to determine the stress intensity factor according to the weight function method.

### 3.1. Determination of normal stresses along the crack line in the un-cracked body

In this study, a rectangular plate $-l < x < l$ and $-d < y < d$ with unit width is only loaded by a uniform compressive traction $p_0$ in the central region $-t < x < t$ of both boundaries $y = \pm d$. It is modeled by considering earlier studies on split-tension tests (Ince, 2010, 2012a,b), as depicted in Fig. 3a. In the plane elasticity problems not including body forces, the stress components can be expressed via the following equations (Barber, 2004; Timoshenko and Godier, 1970)

$$\sigma_x = \frac{\partial^2 \Phi}{\partial y^2} \qquad\qquad \sigma_y = \frac{\partial^2 \Phi}{\partial x^2} \qquad\qquad \tau_{xy} = -\frac{\partial^2 \Phi}{\partial x \partial y} \qquad\qquad (3.3)$$

in which $\Phi$ is the so-called Airy's stress function of $x$ and $y$. This function also satisfies the following bi-harmonic equation

$$\frac{\partial^4 \Phi}{\partial x^4} + 2\frac{\partial^4 \Phi}{\partial x^2 \partial y^2} + \frac{\partial^4 \Phi}{\partial y^4} = 0 \qquad\qquad (3.4)$$

A stress function based on a polynomial can be utilized for some simple cases such as a continuously distributed loading on the boundaries of the elastic body. However, a more useful solution for discontinuous loading, as shown in Fig. 3a, may be derived by using Fourier series (Barber, 2004; Timoshenko and Godier, 1970; Mirsalimov and Hasanov, 2015; Basu and Mandal, 2016). The following equation has commonly been used as the stress function in such cases

$$\Phi = \sin(\lambda x)f(y) \qquad\qquad \lambda = \frac{n\pi}{l} \qquad\qquad (3.5)$$

where $n$ is an integer and $f(y)$ is only a function of $y$. When Eq. (3.5) is substituted into Eq. (3.4) in order to determine $f(y)$, the following ordinary differential equation is obtained

$$f^{(4)}(y) - 2\lambda^2 f''(y) + \lambda^4 f(y) = 0 \qquad\qquad (3.6)$$
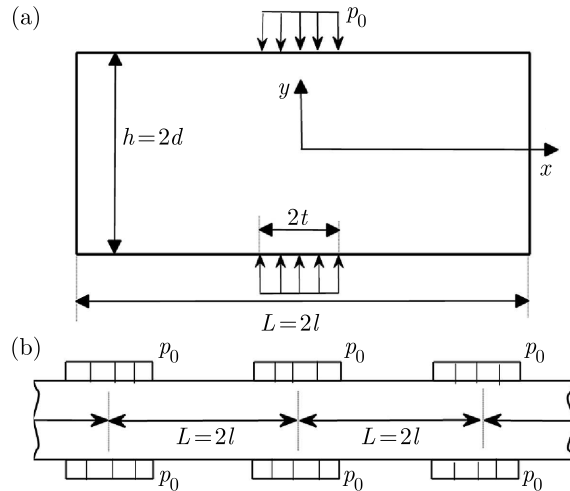
Fig. 3. (a) Base problem for split-tension strip, (b) case of periodic loading

The general solution to the above equation can be written as

$$f(y) = C_1 \cosh(\lambda y) + C_2 \sinh(\lambda y) + C_3 y \cosh(\lambda y) + C_4 y \sinh(\lambda y) \tag{3.7}$$

Consequently, the stress function of the given problem is

$$\Phi = \sin(\lambda x)[C_1 \cosh(\lambda y) + C_2 \sinh(\lambda y) + C_3 y \cosh(\lambda y) + C_4 y \sinh(\lambda y)] \tag{3.8}$$

in which $C_1$, $C_2$, $C_3$ and $C_4$ are arbitrary constants. Since the loading and geometry of the plate in Fig. 3a are symmetric in both axes, and $\sinh(\lambda y)$ and $y \cosh(\lambda y)$ are odd functions, the constants $C_2$ and $C_3$ are equal to zero (Barber, 2004). Therefore, the stress components can be determined from Eq. (3.3) as follows

$$\begin{aligned}
\sigma_x &= \sin(\lambda x)\{C_1 \lambda^2 \cosh(\lambda y) + C_4 \lambda[2 \cosh(\lambda y) + \lambda y \sinh(\lambda y)]\} \\
\sigma_y &= -\lambda^2 \sin(\lambda x)\{C_1 \cosh(\lambda y) + C_4 y \sinh(\lambda y)\} \\
\tau_{xy} &= -\lambda \cos(\lambda x)\{C_1 \lambda \sinh(\lambda y) + C_4[\sinh(\lambda y) + \lambda y \cosh(\lambda y)]\}
\end{aligned} \tag{3.9}$$

When the loading given in Fig. 3a is expanded into the Fourier series, the following equation can be obtained

$$p(x) = \frac{p_0 t}{l} + \frac{2 p_0}{l} \sum_{n=1}^{\infty} \frac{1}{\lambda} \sin(\lambda t) \cos(\lambda x) \tag{3.10}$$

where the first term gives the mean load. The constants $C_1$ and $C_4$ in Eqs. (3.8) and (3.9) can be determined from the following boundary conditions

$$\begin{aligned}
y = \pm d &\quad \Rightarrow \quad \tau_{xy} = 0 \\
y = \pm d &\quad\quad\quad\quad\quad \Rightarrow \quad \sigma_y = p(x)
\end{aligned} \tag{3.11}$$

Substituting the first boundary condition in Eq. $(3.9)_3$, the following equation can be written as

$$C_4 = -C_1 \frac{\lambda \sinh(\lambda d)}{\sinh(\lambda d) + \lambda d \cosh(\lambda d)} \tag{3.12}$$

A similar procedure with Eq. $(3.9)_2$ and the second boundary conditions can be carried out for the corresponding constants as

$$\begin{aligned}
C_1 &= \frac{p(x)}{\lambda^2 \sin(\lambda x)} \frac{\sinh(\lambda d) + \lambda d \cosh(\lambda d)}{\cosh(\lambda d) \sinh(\lambda d) + \lambda d} \\
C_4 &= -\frac{p(x)}{\lambda^2 \sin(\lambda x)} \frac{\lambda \sinh(\lambda d)}{\cosh(\lambda d) \sinh(\lambda d) + \lambda d}
\end{aligned} \tag{3.13}$$

Consequently, the normal stress $\sigma_x$ can be derived from Eq. $(3.9)_1$ as

$$\sigma_x = \frac{2p_0}{\pi} \sum_{n=1}^{\infty} \frac{\psi_n(\lambda, y)}{n} \sin(\lambda t) \cos(\lambda x)$$

$$\psi_n(\lambda, y) = \frac{\cosh(\lambda y)[\lambda d \cosh(\lambda d) - \sinh(\lambda d)] - \lambda y \sinh(\lambda d) \sinh(\lambda y)}{\cosh(\lambda d) \sinh(\lambda d) + \lambda d}$$

(3.14)

For the case of the concentrated load, the above equation can be converted into the following form since $2p_0 t = P = \text{const}$ and $\lim_{\lambda \to 0} \sin(\lambda)/\lambda = 1$ in which $\lambda = n\pi/l$

$$\sigma_x = \frac{P}{l} \sum_{n=1}^{\infty} \psi_n(\lambda, y) \cos(\lambda x)$$

(3.15)

Nevertheless, Equations $(3.14)_1$ and $(3.15)$ are indeed valid for the periodic loadings as indicated in Fig. 3b. For this reason, the residual stresses may naturally occur on the boundaries $x = \pm l$. On the other hand, these series transform the Fourier integrals in the case of $l \to \infty$ in $\lambda = n\pi/l$ and then they can be used for the non-periodic loadings (Girkmann, 1959). By considering $\Delta\lambda = (\pi/l)\Delta n$, Eqs. $(3.14)_1$ and $(3.15)$ can be written respectively, as

$$\sigma_x = \lim_{l \to \infty} \left[ \frac{2p_0}{\pi} \sum_{\lambda = \pi/l}^{\infty} \frac{\psi(\lambda, y)}{\lambda} \sin(\lambda t) \cos(\lambda x) \Delta\lambda \right] = \frac{2p_0}{\pi} \int_0^\infty \frac{\psi(\lambda, y)}{\lambda} \sin(\lambda t) \cos(\lambda x) \, d\lambda$$

$$\sigma_x = \lim_{l \to \infty} \left[ \frac{P}{\pi} \sum_{\lambda = \pi/l}^{\infty} \psi(\lambda, y) \cos(\lambda x) \Delta\lambda \right] = \frac{P}{\pi} \int_0^\infty \psi(\lambda, y) \cos(\lambda x) \, d\lambda$$

(3.16)

in which, the function $\psi(\lambda, y)$ in Eqs. (3.16) is the same as $\psi_n(\lambda, y)$ in Eq. $(3.14)_2$.

From the above discussion, the following data would be the inputs in the analysis: $h = 2d = 1\,\text{mm}$ and $P = 1\,\text{N}$ in the subsequent analysis. The stress analyses have been performed for the load-distributed width-to-specimen depth ratios $\beta = 2t/h = t/d = 0$, 0.05, 0.1, 0.15, 0.20, 0.25, and 0.29. Figure 4 indicates the elastic stress distribution of $\sigma_x$ at $x/d = 0$, 1, 2 and 3 for $\beta = 0$ and 0.25 obtained from Eqs. (3.16) based on the Fourier integrals (the case of the infinitely long strip). In the analysis, the Gauss-Lagurre method with 100 points has been used for the integration procedure since the analytical solution of Eqs. (3.16) might not be available. It is seen from this figure that $\sigma_x$ decreases very rapidly with the increasing $x$ and it becomes approximately zero at $x/d = 3$ for any $\beta$ value. A similar result for the elastic stress distribution of $\sigma_y$ in the middle plane $y = 0$ was obtained using a different method based on the Fourier integrals by Filon (1903) again for an infinite beam subjected to two equal and opposite concentrated loads (Girkmann, 1959). In addition, Davies and Bose (1968) simulated the splitting beams with the length/depth= $L/h = 3$ by using the finite element method for $\beta = 0$ and 1/12.

On the other hand, in the splitting strip specimens, the maximum tensile stress in the plane of loading does not occur at the midpoint ($x = y = 0$), unlike in other splitting specimens. The relative maximum tensile strength values of the splitting strip specimens and other splitting specimens are given for different $\beta$ values in Fig. 5, comparatively. In this figure, the relative location values $(y/d)$ of the maximum tensile stresses are also given for the infinite strip specimens. As shown in Fig. 5, the maximum tensile stress of the strip specimens occurs at the midpoint for $\beta \geqslant 0.29$. Similar to the maximum tensile stress value of the un-notched diagonal splitting-cube specimen, Eq. (3.17) is proposed for the maximum tensile stress value of an un-notched splitting strip specimen in the plane of loading

$$\sigma_{max} = \frac{2P}{\pi bd} \left( \frac{1}{0.7 + 1.685\beta^{0.617}} \right) \qquad \beta \leqslant 0.29$$

(3.17)

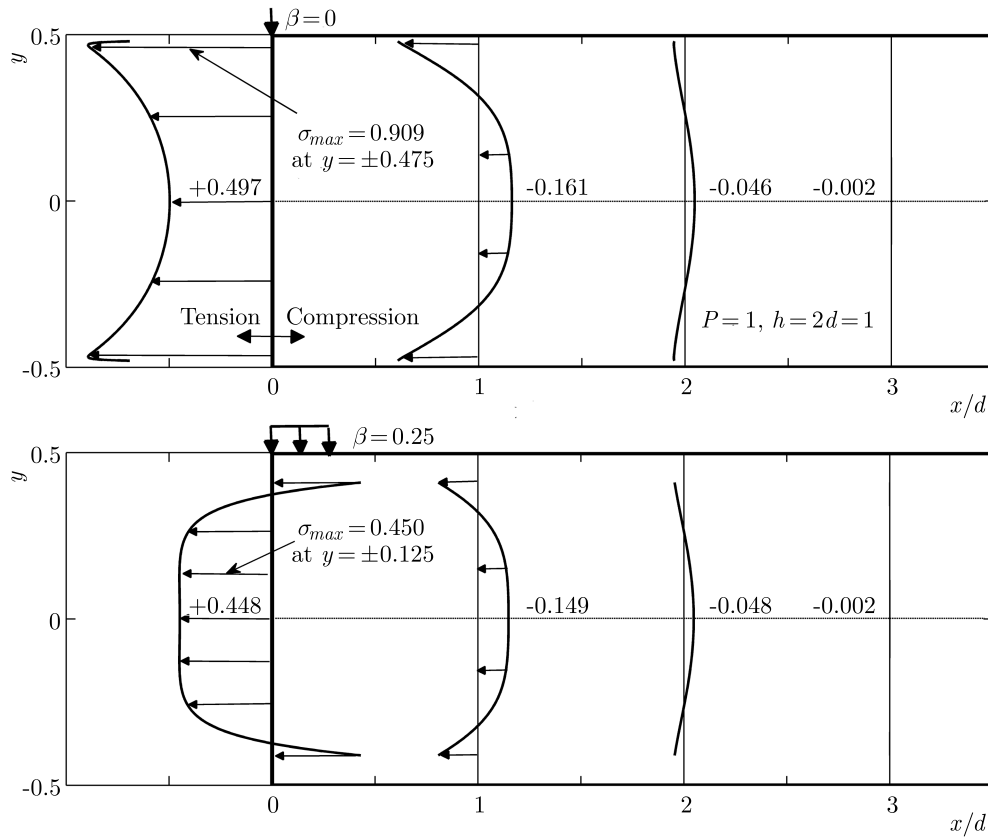The accuracy of Eq. (3.17) is 0.5% for the particular data given in Fig. 5.

Fig. 4. Stress distribution of $\sigma_x$ at $x/d = 0$, 1, 2 and 3 for $\beta = 0$ and 0.25 in infinitely long strip
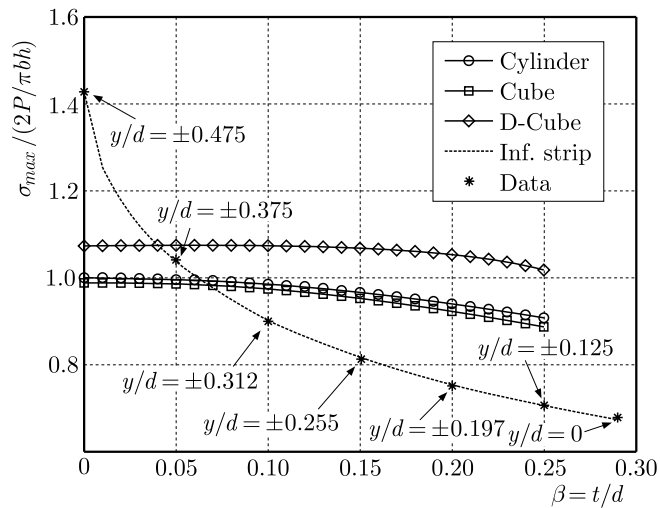


Fig. 5. Comparison of the nominal strengths of split-tension specimens

### 3.2. LEFM formulas

Using the boundary collocation method, Isida (1971) proved that the central cracked plate could be practically regarded as an infinite strip when the length/depth= $L/h$ ratio of a plate is $\geqslant 3$. Nevertheless, it was indicated in the analysis for Eqs. $(3.14)_1$ and (3.15) based on the Fourier series for the finite strip with $L/h = 2$ (Fig. 3b) that the stress distribution of $\sigma_x$ on the vertical axis at $x = 0$ was exactly the same as in the case of the infinitely long strip for $\beta = 0$ to 0.25. This may be explained by Saint-Venant's principle. The sums of the series were continued to be

taken until the absolute value of the $n$-th term was less than 1e-100. Consequently, the number of terms ranged from 192 (small $y$ values) to 340 (large $y$ values). Meanwhile, similar results were found for certain $\beta$ values (0.05, 0.10 and 0.20) by Schleeh (1978) who studied on a plate with $L/h = 2$ using the Fourier series. Additionally, in this study, it has also been observed that for $\sigma_x$ stress distribution along the plane $x = 0$, the maximum difference between the solution with $L/h = 2$ and that of $L/h = 1.5$ was 0.1%. Nevertheless, it will be seen in the following Sections of this work that this difference is much more significant for a cracked body.

In this study, the analysis of the split-tension strip specimens based on fracture mechanics has been performed for all cases including combinations obtained with $\alpha$ values of 0.1, 0.2, 0.3, 0.4, 0.5, 0.6, 0.7 and 0.8 and load-distributed width-to-specimen depth ratio values of $\beta = 0$, 0.05, 0.1, 0.15, 0.2, and 0.25. A parallel analysis was also performed using the boundary element program (BEM). In all analyses, the stress intensity factor $K_I$ was computed using Eq. (3.1). In practice, the polynomial approach was commonly utilized to interpret normal stresses along the crack line $\sigma(y)$ in Eq. (3.1) (Anderson 2005). Therefore, in this study, the function of $\sigma(y)$ was computed at specific points including 0, 0.05, 0.1, 0.15, 0.2, 0.25, 0.3, 0.35 and 0.4 mm on the infinitely long strip with $h = 2d = 1$ mm and then expressed as the 8th degree polynomial by using the least squares method for each $\beta$ value. Green's function in Eq. (3.2) was used as the weight function $m(y, a)$ in Eq. (3.1), since it was essentially equivalent to the weight function, as discussed above. The integration procedures were achieved by means of the Gauss-Chebyshev method.

In this study, the stress intensity factor is defined as follows for the splitting strip specimens

$$K_I = \sigma_N \sqrt{\pi a}\, Y(\beta, \alpha) \tag{3.18}$$

where $\sigma_N$ is the nominal stress according to Eq. (2.1), a is half length of the notch, and $Y(\beta, \alpha)$ is the geometry factor, where $\beta$ is the relative load-distributed width $(t/d)$ and $\alpha$ is the relative crack length $(a/d)$. The $Y(\beta, \alpha)$ geometry factors of the splitting specimens are obtained as $Y(\beta, \alpha) = K_I/(\sigma_N \sqrt{\pi a})$, where $K_I$ is calculated from Eq. (3.1).
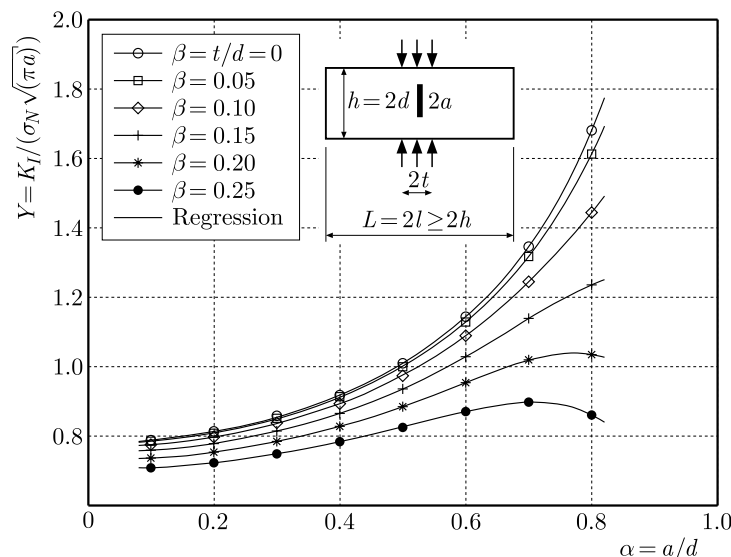


Fig. 6. Geometry factor $Y(\beta, \alpha)$ values for split-strip specimens

Figure 6 shows the individual geometry factors obtained from the analytical solution; these factors are presented as symbols for each $\alpha$ and $\beta$ value. The geometry factors have been generated with the least square method for each $\beta$ value, as indicated by the curved solid line in Fig. 6. The general form of the selected function is

$$Y(\beta, \alpha) = A_0(\beta) + A_1(\beta)\alpha + A_2(\beta)\alpha^2 + A_3(\beta)\alpha^3 + A_4(\beta)\alpha^4 + A_5(\beta)\alpha^5 \tag{3.19}$$

where the coefficients $A_i$ ($i = 0$ to $5$) are functions of $\beta$, as summarized in Table 1. Equation (3.19) fits all the results from the analytical solutions with an accuracy of 0.1% for $0.1 \leqslant \alpha \leqslant 0.8$ and any $\beta$ value. It is emphasized that this accuracy is valid for the strips with $L/h \geqslant 2$, as discussed above.

**Table 1.** Ai and Bi coefficients for split-strip specimen

| Coefficient | $\beta = t/d$ | | | | | |
|:---:|:---:|:---:|:---:|:---:|:---:|:---:|
| | 0 | 0.05 | 0.10 | 0.15 | 0.20 | 0.25 |
| $A_0$ | 0.7570 | 0.7656 | 0.7781 | 0.7751 | 0.7534 | 0.7200 |
| $A_1$ | 0.5009 | 0.2618 | $-0.1872$ | $-0.4591$ | $-0.4724$ | $-0.3435$ |
| $A_2$ | $-2.8063$ | $-1.1558$ | 1.9581 | 3.8574 | 3.9428 | 2.9948 |
| $A_3$ | 11.4780 | 6.2913 | $-3.6245$ | $-9.9595$ | $-10.7060$ | $-8.1581$ |
| $A_4$ | $-16.6660$ | $-9.2409$ | 5.1032 | 14.5480 | 16.0060 | 12.5460 |
| $A_5$ | 9.9819 | 5.9303 | $-2.0490$ | $-7.6288$ | $-8.9671$ | $-7.5169$ |
| $B_0$ | 0.8882 | 0.8883 | 0.8851 | 0.8733 | 0.8515 | 0.82158 |
| $B_1$ | 1.5494 | 1.4740 | 1.3054 | 1.1399 | 1.0223 | 0.94892 |
| $B_2$ | $-6.0402$ | $-5.5487$ | $-4.4507$ | $-3.3906$ | $-2.6901$ | $-2.3399$ |
| $B_3$ | 16.806 | 15.2700 | 11.8060 | 8.4028 | 6.0978 | 4.9091 |
| $B_4$ | $-21.027$ | $-18.8330$ | $-13.8580$ | $-8.9269$ | $-5.5668$ | $-3.8579$ |
| $B_5$ | 11.503 | 10.2930 | 7.5156 | 4.6857 | 2.6659 | 1.5512 |
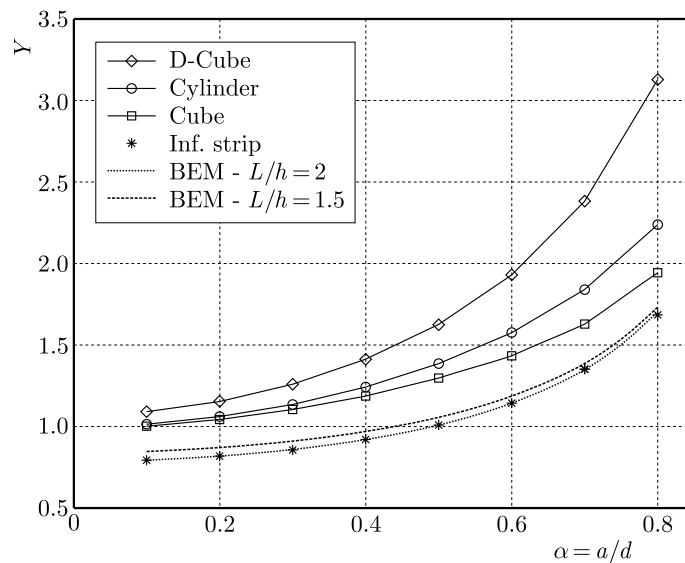


Fig. 7. Comparison of geometry factor $Y$ values of split-tension specimens for $\beta = 0$

The variation of the geometry factors is summarized for the splitting specimens, namely: cylinder, cube, diagonal cube and infinite strip for the case of concentrated loading in Fig. 7. The $Y$ functions of cylindrical and cubical specimens have been obtained from the BEM solutions found in the literature. The BEM solutions for splitting strip specimens with $L/h = 1.5$ and $2$ are also given in Fig. 7. A one-quarter model has been used for the plain strain conditions, because of its symmetry in the BEM study. Similar to earlier studies of the author, 250 boundary elements, including 2 crack tip elements, provided reliable results for the crack tip singularity in a one-quarter specimen. The following factors have been the inputs in the analysis: Young's modulus $E = 1\,\mathrm{MPa}$, Poisson's ratio $\nu = 0.2$, $h = 2d = 200\,\mathrm{mm}$, and $P = 100\,\mathrm{N}$. A detailed explanation of the BEM simulations may be seen elsewhere (Ince, 2012a,b). The accuracies of BEM solutions

of the strip specimens are greater than 1.2% for $L/h = 2$ and better than 7.5% for $L/h = 1.5$ in comparison with the solution of the infinitely long strip in Fig. 7. On the other hand, the behavior of splitting strips is very different from other splitting specimens, as is clearly shown in Fig. 7. For $\alpha = 0$, the value of $Y$ of strip specimens approach approximately to 0.75, while that of the other specimens approach to 1. Furthermore, the $Y$ function of the strip is approximately parallel to that of the cube.

Tada *et al.* (2000) proposed that Castigliano's theorem may be used for calculating opening displacements of the crack surface in a cracked body, as follows

$$COD(y) = \frac{2}{E'} \int\limits_{a_F}^{a} K_{IP} \frac{\partial K_{IF}}{\partial F} \, da \tag{3.20}$$

where $K_{IP}$ is the stress intensity factor due to loading forces, $K_{IF}$ is the stress intensity factor due to virtual forces and $E' = E/(1 - \nu^2)$ for plane strain and $E' = E$ for plane stress. In Eq. (3.20), $a$ is length of the notch and $a_F$ is location of the virtual force in the vertical distance from the center of the specimen, in which the $COD$ value is computed (Fig. 2). In this study, Equations (3.18) and (3.1) are used for $K_{IP}$ and $K_{IF}$, respectively. From Eq. (3.20), $CMOD$ values are computed as follows

$$CMOD = COD(y = 0) = \frac{2}{E'} \int\limits_{0}^{a} K_{IP} \frac{\partial K_{IF}}{\partial F} \, da \tag{3.21}$$

The $CMOD$ includes not only the elastic constants but also the size of the specimens. The general forms of the specimens are usually described in a polar coordinate system (Tang 1994). Therefore, the $CMOD$ is defined as follows in this study

$$CMOD = \frac{\pi \sigma_N a}{E'} V_1(\beta, \alpha) \tag{3.22}$$

$V_1(\beta, \alpha)$ dimensionless function in Eq. (3.22) is calculated by normalizing $CMOD$ values obtained from Eq. (3.21) with $\pi \sigma_N a/E'$ values. Figure 8 indicates individual $V_1$ values for each $\alpha$ and $\beta$.
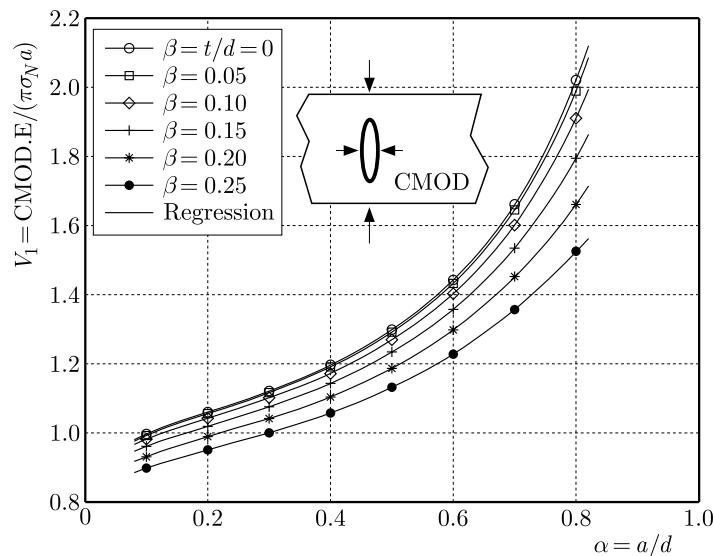


Fig. 8. Non-dimensional $V_1(\beta, \alpha)$ values for split-strip specimens

The $V_1(\beta, \alpha)$ values are generated by the least squares method for each $\beta$, as depicted in Fig. 8. Similar to Eq. (3.19), the following equation is chosen for the general form of the $V_1(\beta, \alpha)$ function

$$V_1(\beta, \alpha) = B_0(\beta) + B_1(\beta)\alpha + B_2(\beta)\alpha^2 + B_3(\beta)\alpha^3 + B_4(\beta)\alpha^4 + B_5(\beta)\alpha^5 \qquad (3.23)$$

where the coefficients $B_i$ $(i = 0, 1, \ldots, 5)$ are functions of $\beta$ that are listed in Table 1. Equation (3.23) fits all the results from the analytical solutions with an accuracy of 0.2% for $0.1 \leqslant \alpha \leqslant 0.8$ and any $\beta$ value.

In practice, *COD* values in a cracked body normalize the *CMOD* value to determine the profile of the crack surface. Consequently, the *COD/CMOD* ratio is independent of the specimen size, but does depend on the specimen geometry and loading type (Tang 1994). In this study, the normalized crack profile of the strip specimen is described by means of regression analysis via a formula similar to the earlier form for the cylindrical and cubical specimens proposed by Ince (2012b) as follows

$$\frac{COD(\beta, y, a)}{CMOD} = \sqrt{\left(1 - \frac{y}{a}\right)^2 + \left[2.367 - 0.038(1 + \beta)^{15.9}\alpha^{1.17}\left(\frac{y}{a}\right)^{0.961}\right]\left[\frac{y}{a} - \left(\frac{y}{a}\right)^2\right]} \qquad (3.24)$$

in which $y$ is the vertical distance from the center of the specimen as shown in Fig. 2. The accuracy of the equation is greater than 3.3% for $0.1 \leqslant \alpha \leqslant 0.8$ and any $\beta$ value.

Equations (3.18) to (3.24) are based on LEFM for split-tension strip specimens. The concrete fracture parameters for effective crack models (two-parameter model, size effect model and double-K model) could easily be calculated using these equations. The coefficients $A_i$ and $B_i$ for $\beta$ values, which are not given in Table 1, could be derived by interpolation.

## 4. Summary and conclusion

Recently, split-tension specimens such as cylinders, cubes and diagonal cubes have been commonly used to determine the tensile strength of cement-based materials. The split-tension strips have been used to determine the fracture parameters of concrete using the effective crack models such as the two-parameter model, the size effect model and the double-K in this article. Based on these theoretical and numerical investigations, the following conclusions can be drawn:

- The number of theoretical and experimental studies on split-tension strip specimens is limited. Therefore, in this study, a formula for the maximum tensile strength of concrete has been developed for un-notched strip specimens. The results of the analysis reveal that the derived formula is valid for strips with the ratio of length/depth= $L/h \geqslant 2$ both for the Fourier integral (the case of the infinite long strip) and the Fourier series (the case of the finite strip). Similarly, it has been indicated from the parallel analysis, which was based on the boundary element method, that the LEFM formulas of cracked strip specimens are valid for strips with $L/h \geqslant 2$.

- The initial crack of the splitting strip specimens starts at about the location of the loading point, while the initial crack in other splitting specimens starts at the center of the section. However, the initial crack location approximates to the center of the section with the increasing load-distributed width-to-specimen depth ratios $\beta$, and it is in the center of the section for $\beta \geqslant 0.29$.

- In this study, only double symmetrical strips have been analyzed and they have no vertical displacement and no shear stress at the middle line $y = 0$, as is clearly shown in Fig. 3. Consequently, by considering the upper half of the strip ($L/d \geqslant 4$), the results of this study may also be utilized in the analysis of a cracked elastic layer resting on a rigid smooth base in soil and rock mechanics. This problem was investigated by Marguerre (1931) for uncracked elastic layers.

## References

1. ANDERSON T.L., 2005, *Fracture Mechanics: Fundamentals and Applications*, CRC Press, Boca Raton

2. BARBER J.R., 2002, *Elasticity*, Kluwer Academic Publishers, Dordrecht

3. BASU S., MANDAL S.C., 2016, P-wave interaction with a pair of rigid strips embedded in an orthotropic strip, *Journal of Theoretical and Applied Mechanics*, **54**, 2, 579-592

4. BAZANT Z.P., KAZEMI M.T., 1990, Determination of fracture energy, process zone length, and brittleness number from size effect with application to rock and concrete, *International Journal of Fracture*, **44**, 2, 111-131

5. BUECKNER H.F., 1970, A novel principle for the computation of stress intensity factors, *Zeitschrift für Angewandte Mathematik and Mechanik*, **50**, 9, 529-546

6. CARNEIRO F.L., BARCELLOS A., 1949, Tensile strength of concrete (in French), *RILEM Bulletin*, **13**, 98-125

7. DAVIES J.D., BOSE D.K., 1968, Stress distribution in splitting tests, *ACI Journal*, **65**, 662-669

8. FILON L.N.G., 1903, On the approximate solution of the bending of a beam of rectangular section, *Transaction of the Royal Society of London Series (A)*, **201**, 63-155

9. GDOUTOS E.E., 1990, *Fracture Mechanics Criteria and Applications*, Kluwer Academic Publishers, London

10. GIRKMANN K., 1959, *Plate and Shell Structures* (in German), Springer-Verlag Wien

11. INCE R., 2010, Determination of concrete fracture parameters based on two-parameter and size effect models using split-tension cubes, *Engineering Fracture Mechanics*, **77**, 2233-2250

12. INCE R., 2012a, Determination of concrete fracture parameters based on peak-load method with diagonal split-tension cubes, *Engineering Fracture Mechanics*, **82**, 100-114

13. INCE R., 2012b, Determination of the fracture parameters of the double-K model using weight functions of split-tension specimens, *Engineering Fracture Mechanics*, **96**, 416-432

14. INCE R., GÖR M., EREN M.E., ALYAMAÇ K.E., 2016, The effect of size on the splitting strength of cubic concrete members, *Strain*, **51**, 2, 135-146

15. INCE R., GÖR M., ALYAMAÇ K.E., EREN M.E., 2016, Multi-fractal scaling law for split strength of concrete cubes, *Magazine of Concrete Research*, **68**, 3, 141-150

16. ISIDA M., 1971, Effect of width and length on stress intensity factors of internally cracked plates under various boundary conditions, *International Journal of Fracture*, **7**, 3, 301-316

17. JENQ Y.S., SHAH S.P., 1985, Two-parameter fracture model for concrete, *Journal of Engineering Mechanics, ASCE*, **111**, 10, 1227-1241

18. MARGUERRE K., 1931, Pressure distribution by an elastic layer on a rigid rough layer (in German), *Ingenieur-Archiv*, **2**, 108-117

19. MIRSALIMOV V.M., HASANOV S.G., 2015, Effect of damages on crack development in coating on elastic foundation, *Journal of Theoretical and Applied Mechanics*, **53**, 4, 823-836

20. MODEER M., 1979, A fracture mechanics approach to failure analyses of concrete materials, Report TVBM-1001, Division of Building Materials, University of Lund, Sweden

21. NALLATHAMBI P., KARIHALOO B.L., 1986, Determination of the specimen size independent fracture toughness of plain concrete, *Magazine of Concrete Research*, **38**, 135, 67-76

22. NEVILLE A.M., 2011, *Properties of Concrete*, Pearson Education Limited, Essex, UK.

23. NILSSON S., 1961, The tensile strength of concrete determined by splitting tests on cubes, *RILEM Bulletin*, **11**, 63-67

24. RICE J.R., 1972, Some remarks on elastic crack-tip stress fields, *International Journal of Solid Structures*, **8**, 751-758

25. ROCCO C., GUINEA G.V., PLANAS J., ELICES M., 1995, The effect of the boundary conditions on the cylinder splitting strength, *Proceedings of FRAMCOS-2: Aedificatio Publishers*, 75-84, Freiburg, Germany

26. SCHLEEH W.S., 1978, Determination of the tensile strength of concrete (in German), *Beton*, **28**, 2, 57-62

27. TADA H., PARIS P.C., IRWIN G.R., 2000, *Stress Analysis of Cracks Handbook*, ASME Press, New York

28. TANG T., 1994, Effect of load-distributed width on split tension of unnotched and notched cylindrical specimens, *Journal of Testing and Evaluation, ASTM*, **22**, 401-409

29. TANG T., OUYANG C., SHAH S.P., 1996, A simple method for determining material fracture parameters from peak loads, *ACI Materials Journal*, **93**, 2, 147-157

30. TANG T., SHAH S.P., OUYANG C., 1992, Fracture mechanics and size effect of concrete in tension, *Journal of Structural Engineering, ASCE*, **118**, 3169-3185

31. TIMOSHENKO S.P., GODIER J.N., 1970, *Theory of Elasticity*, Mc-Graw Hill, New York, USA

32. TWEED J., DAS S.C., ROOKE D.P., 1972, The stress intensity factor of a radial crack in a finite elastic disc, *International Journal of Engineering Science*, **10**, 323-335

33. XU S., REINHARDT H.W., 1999, Determination of double-K criterion for crack propagation in quasi-brittle fracture, Part I: Experimental investigation of crack propagation, *International Journal of Fracture*, **98**, 2, 111-149

# A STUDY ON TRANSIENT WEAR BEHAVIOR OF NEW FREIGHT WHEEL PROFILES DUE TO TWO POINTS CONTACT IN CURVE NEGOTIATION

Morad Shadfar, Habibollah Molatefi

*School of Railway Engineering, Iran University of Science and Technology, Tehran, Iran*

*e-mail: morad.shadfar@gmail.com; molatefi@iust.ac.ir*

Systematic examinations on wear behavior of stick/slip contact around metal on metal have shown that the dissipated energy and contact forces are two important parameters of wear of wheels and rails. Nevertheless, an accurate estimation of these parameters is still a great challenge. Recent developments of non-linear dynamical models and simulation of operational conditions have tried to find a solution of this challenge. These results are used as the input to calculations of wear propagation. Though, the dynamic model should be able to predict wheel-rail interaction with high accuracy. In addition, wheel-rail wear is a function of several other parameters whose their integrated influence becomes more than the main discussed ones. In this study, with the help of multi-body dynamics (MBD), an open wagon equipped with three pieces bogies, considering non-linear effects of friction wedges and structural clearances is modeled in Universal Mechanism. Tangent and curved sections of the track considering random vertical and lateral irregularities are simulated. The simulation results are used to calculate wear of both left and right wheels separately. Specht's wear model based on Archard's wear model is used. The studied parameters are the rail side coefficient of friction, track quality, track curvature, velocity and rail side wear. Finally, the effects of mentioned parameters are studied on wear depth and wear pattern of new wheel profiles under incompatible contact (which occurs in Iran railway network). The results show different wear volume and wear pattern compared to compatible contact.

*Keywords:* three pieces bogie, Specht wear theory, wear depth, incompatible contact, rail side wear

## 1. Introduction

Scientific investigations on the rolling contact problem were begun in early of the 20'th century. The primary results showed the dependency of motion state on the wheel-rail contact forces. A practical progress was made in the late sixties and early seventies. In 1967, the computer based theory of Kalker was known by railway experts and as a consequence, this theory found practical applications in railway industries.

The first investigation on wear of railway wheel profiles was based on computer simulations with simple and steady state considerations, like constant velocity on ideal tangent track (Zobory, 1997). Sherrat and Pearce (1991) presented a very simple model. In their model after calculation of contact forces and creepages, the volume of removal mass was calculated with a wear index. They also considered one $S$ track followed by a tangent track (Braghin *et al.*, 2006). In some works, there is an emphasis on the relation between the maximum contact pressure and removal mass which sometimes considered coefficients as the effects of energy (Zobory, 1997; Telliskiv and Olofsson, 2004). Nevertheless, most assumptions in wear are used in the correspondence of dissipated energy in the slip area and special removed mass per unit distance ([5], Jendel, 2002; Enblom and Berg, 2005; Pombo *et al.*, 2011; Jin *et al.*, 2011; [13]).

Most of the researchers consider that the wear phenomenon occurs only in the wheel, not in the rail. Also in the models, a linear relation between wear and friction work is usually assumed

(Zakharov and Zharov, 2002). Examination of changes in the contact point could lead to predict catastrophic wear which has great importance for increasing velocity (Telliskiv and Olofsson, 2004). Zobory used two different wear regimes: mild wear on the wheel tread and severe wear in the flange (Braghin *et al.*, 2006).

Recent investigations give us an ability to predict wear of the wheel-rail system under specified operation with reasonable accuracy. As a consequence, one can model tangent and curve sections of the track and simulate passage frequency in numerical analysis of railway operation. This process could be done on tracks with random irregularities. With the help of simulation results, the wear volume of the rail and wheel can be calculated on different sections of the track. It is common to use contact codes like CONTACT, FASTSIM or other innovative codes in such works (Braghin *et al.*, 2006). For example, Iwnicki and Xie (2008) considered a 3D wheel-rail system for calculation of the rail head wear in the presence of short pitch irregularity, considering non-Hertzian and non-steady contact based on Kalker's method (Xie and Iwnicki, 2008a,b).

In this study, with the use of a 3D non-linear dynamic model in the presence of random irregularities, sensitivity analysis of the wear pattern for different parameters is performed. The innovation in this paper is the examination of wear in presence of two point contact due to incompatible contact. As it is seen later, the effects of operational parameters would be different compared to compatible, one point contact.

## 2.   Iran railway network

Iran geographic location in the Middle East caused freight mass transit development in comparison to passenger transportating. In the recent years, with respect to an increase in the transit volume and vehicle ages, variant wheel defects are reported by National Railway Administration [1]. These defects are different from one vehicle type and age to another, but most of the wheels show 1 mm hollow tread at early passages.

Although wheels show little hollow tread on early service life, but these hollows do not fall into repair regulations. With the use of these wheels in service, finally thin flanges would cause the wheels to reject. By considering harmful effects of the hollow tread especially in lubricated curves [5], there is a necessity for a comprehensive study around dynamic performance and energy consumption of vehicles. Figure 1 shows a 1 mm hollow tread after 10 000 km passage. Table 1 shows total repaired wheel defects in a range of 14 months [1].



Fig. 1. Tread defects after 10 000 km passage

**Table 1.** Total repaired wheel defects (April 2010 – June 2011) [1]

| Defect type | No. of recorded wheels |
|---|---|
| Hollow tread | 104 |
| Un-conical wheel | 58 |
| Sharp flange | 847 |
| Thin flange | 2085 |
| Total wheel defects | 5612 |

## 3. Wear

According to Zakharov's theory, wear of the wheel and rail are generally proportional to the energy used to overcome the rolling resistance of the wheels and rails [5]. Wear of the wheels and rails is defined with the stress $P$ and relative slip in contact area. Wear is also dependent on the third layer properties which depend, in turn, on lubrication, environment conditions and sand. On the basis of laboratory tests under un-lubricated conditions, three different wear regimes are defined: mild, severe and catastrophic. Figure 2 shows a shakedown diagram. It determines areas of normal and un-normal performance. $P$ is the maximum contact pressure and $\lambda$ is creepage. The curve $P\lambda = 40$ determines changes in the wear regime from mild to severe while $P\lambda = 120$ is the change between severe to catastrophic wear [5].
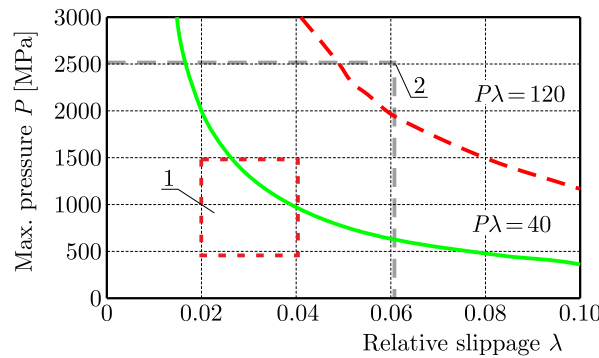


Fig. 2. Shakedown diagram for steel wheels and rails: normal area (1) and abnormal area (2)

### 3.1. Mathematical description of wear

For mild and severe modes of wear, the wear rate can be defined as a linear function of friction work [5]. The friction work can be defined as

$$A = \int_0^t v(t)(F_x \zeta_x + F_y \zeta_y)\, dt \tag{3.1}$$

where $A$ is the friction work, $v$ stands for velocity, $F_x$ and $F_y$ are longitudinal and lateral contact forces, and $\zeta_x$ and $\zeta_y$ are creepages which are defined

$$\boldsymbol{\xi} = \frac{r\boldsymbol{\omega} - \mathbf{V}}{\mathbf{V}} \tag{3.2}$$

where $r$ is wheel radius and $\omega$ is angular velocity of the wheel. All dimensions are in SI.

One of the most applicable wear theories was presented by Archard (Jendel, 2002). He considered a linear relation between the wear volume and friction work. Acordingly

$$I = K_v A \tag{3.3}$$

where $I$ is in m$^3$ and $K_v$ is the wear volume coefficient [m$^3$/J].

For the use of this model, it is necessary to determine the coefficient $K_v$ at any instance. Specht suggested a jumping factor $\alpha$ for every wear regime, therefore $K_v$ can be assumed constant. By implementing the jumping factor into Archard's equation, it can be rewritten as follows

$$I = \begin{cases} K_v A & \text{for} \quad w < w_{cr} \\ K_v \alpha A & \text{for} \quad w \geqslant w_{cr} \end{cases} \tag{3.4}$$

where $w$ is the friction power [s/m$^2$] (friction work per second per contact area) and $w_{cr}$ is the critical friction power which defines the wear regime and changing condition from mild to severe. Equation (3.4) is known as Specht wear model [13].

### 3.2. Determination of the wear coefficient

Several experiments for determining the coefficient $K_v$ has been performed. As a result, a step change in the wear coefficient was obtained by deferent researchers.

The magnitude of $K_v$ has a dependency in the wheel-rail material and its mechanical property. A typical magnitude for common wheels and rail is $10^{-13}$ m$^3$/J and 10 for the jumping factor. By consideration of a mild wear amplitude, it can be reasonable to assume that the most part of the removed mass in the railway is due to the severe wear mode.

### 3.3. Wear calculation algorithm

For calculation of wear of the wheel and rail and its pattern, a sophisticated dynamic model is required. So it is possible to determine accurately shear forces and creepages in contact area at any instance. Zobory with the help of Medyna software calculated wear of wheels and rails in a specific track. The results showed a 5% difference compared to the final field test. The reason was neglecting the effects of switches. Lewis and Olofsson (2009) calculated wear of wheels with ADAMS/RAIL. Similar works were performed by Malvezzi with the help of Simpack and MATLAB and Pombo by Vampire software. In spite of differences in the software, all the works followed the same algorithm presented in Fig. 3. Global parameters contain contact forces, points, area, creepages calculated in time domain and imported into wear calculation. With the use of the wear model wear, depth at any point is calculated, the wheel and rail profile is updated and analysis continued to the next iteration. In this paper, Universal Mechanism software is used for both dynamic and wear modeling.
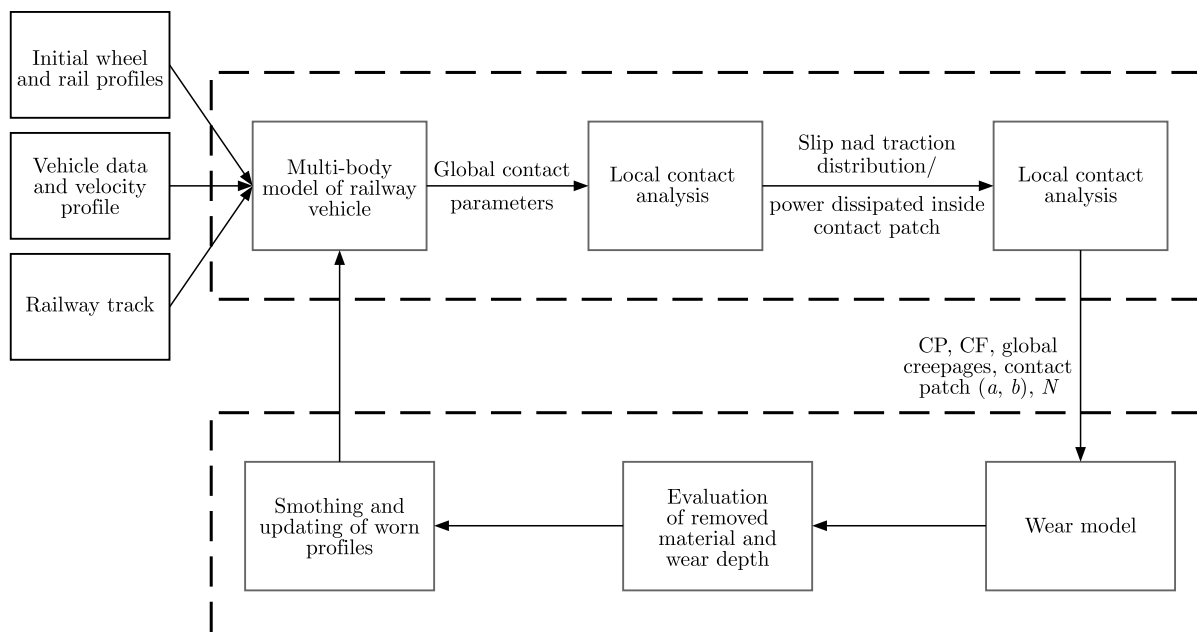


Fig. 3. Wear algorithm

## 4. Dynamic model requirements for the train-track system

The process of wheel-rail wear simulation always needs a proper dynamic environment which is able to make an access to real load and motion data (that show the operation conditions of the train-track system) for analysis of the removed mass. This dynamic model can be defined in deferent levels of detail but it should be able to calculate contact forces and creepages with a high accuracy.

### 4.1. Three pieces bogie

Three pieces bogies have been used in deferent railway networks for more than 60 years. In Iran, Russian bogies are widely used in mass transportation. Iran railway equipped 7100 wagons with these bogies [1]. Table 2 shows types and number of Iran railway wagons equipped with 18100 bogie.

**Table 2.** Iran wagons equipped with 18100 bogies [1]

| Wagon type | Number of wagons |
|---|---|
| Low-sided wagon | 1653 |
| Open wagon | 3716 |
| Flat wagon | 231 |
| Tank car | 461 |
| Hooper ballast wagon | 200 |
| Hooper wagon | 746 |

These bogies use S1002 wheel profile running on the rail UIC60 with rail inclination 1:20 which leads to two point contact as it is shown in the results. This wheel-rail arrangement is not suggested in the standard operation [11]. This arrangement results in improper steering and severe wear during curve negotiation. It also applies different wear pattern for both the wheel and rail. In such conditions, effects of parameters like rail side lubrication, velocity and track quality could be different.

A typical three pieces bogie consists of two side frames which are attached each other with the help of secondary suspension system and a bolster. Damping is provided with 4 friction wedges which move in vertical and lateral directions.

The wheels with the use of adapters are directly connected to side frames (Fig. 4). The friction force between adapters and side frames are modeled considering clearances in the UM template. Direct connection between the adapters and side frames results in high un-sprung mass and high dynamic loads. Low adapter clearances in both vertical and lateral directions lead to high bending and shear stiffness of the bogie. This causes imperfect curving of the wheels.
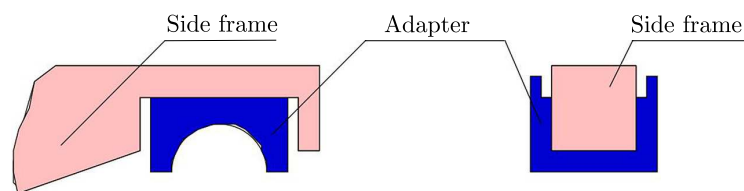


Fig. 4. Connection between an adapter and a side frame

A very unique phenomenon in the three pieces bogie is warping. It usually happens in curves and also some defects like hollow tread could intensify that. As a consequence of warping, high angle of attack and flange contact in both left and right wheels occurrs. This results in flange wear

in both left and right wheels simultaneously. Warping makes 18100 bogie unfair for non-straight corridors. Figure 5 shows a schematic warping of the three pieces bogie.
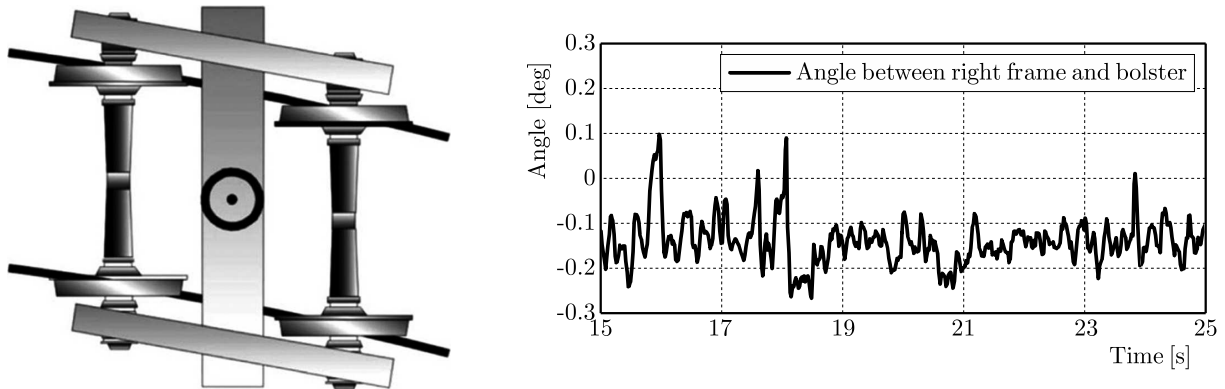


Fig. 5. Warping of the three pieces bogie

Two dimensional wedges let the bolster to damp vibrations in both vertical and lateral directions but implement nonlinearity into the model. Pivot friction and side bearers are also considered in the UM template. Tables 3 to 5 describe parameters of the three pieces bogie which is avaliable in Universal Mechanism software.

**Table 3.** Inertial parameters of the train

| Part | Mass [kg] | CG [m] (from rail surface) | $I_{xx}$ [kg·m$^2$] | $I_{yy}$ [kg·m$^2$] | $I_{zz}$ [kg·m$^2$] |
|---|---|---|---|---|---|
| Wheelset | 1500 | 0.475 | 925 | 200 | 925 |
| Axle box | 11 | 0.475 | 0.04 | 0.157 | 0.16 |
| Side frame | 526.3 | 0.525 | 13.96 | 175.8 | 161.8 |
| Bolster | 682.6 | 0.649351 | 412.609 | 11.06 | 415.909 |
| Carbody | 90000 | 1.4 | 21840 | 53919 | 66800 |

**Table 4.** Parameters of the suspension system

| Part | $K_x$ [N/m] | $K_y$ [N/m] | $K_z$ [N/m] | $K_t$ [Nm/rad] | Coefficient of friction |
|---|---|---|---|---|---|
| Secondary suspension | $8 \cdot 643000$ | $8 \cdot 643000$ | $8 \cdot 632000$ | $8 \cdot 3325000$ | – |
| Wedges | 710000 | 100000 | $2 \cdot 632000$ | – | 0.3 |

**Table 5.** Wheelset parameters

| | |
|---|---|
| Wheel bases space [m] | 1.85 |
| Tap circle distance [m] | 1.5 |
| Longitudinal clearance [mm] | 5 |
| Lateral clearance [mm] | 5 |
| Wheel profile | S1002 |

In order to verify the model, non-linear hunting velocity of the bogie is extracted. This velocity is calculated about 95 km/h (26.3 m/s). In the next step, vertical acceleration of the model is compared with the field test mentioned in (Hosein Nia, 2011). The track consists of a tangent track followed by a curve.

Figure 6 shows vertical acceleration of the measured data and simulated one. The measured acceleration is in the range of $\pm 0.5\,\text{m/s}^2$ and, the MBD model shows a good agreement in both frequency and amplitude.
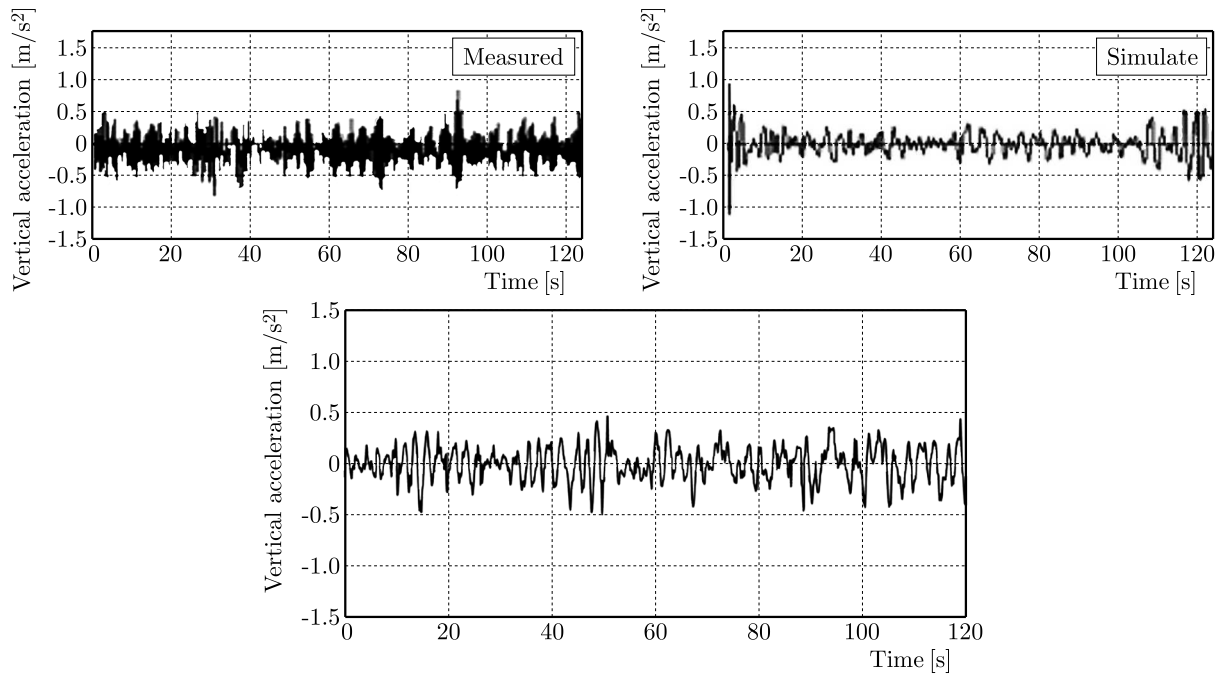


Fig. 6. Comparison between the measured and simulated vertical acceleration (Hosein Nia, 2011) (up) and simulated model in UM (down)

## 5. Analysis assumptions

This part includes wear analysis results by running a train on different tracks and rail profiles. The parameters are rail-side coefficient of friction, velocity, track curvature and quality. Table 6 describes the change in each parameter. These analyses are performed for each rail profile.

**Table 6.** Studied range for parameters

| Case number | Cant [mm] | Radius of curvature [m] | Velocity [m/s] | Rail side coefficient of friction | Class (FRA) |
|---|---|---|---|---|---|
| 1 | 150 | 600 | 25 | 0.1 | 3 |
| 2 | 150 | 600 | 25 | 0.2 | 3 |
| 3 | 150 | 600 | 25 | 0.3 | 3 |
| 4 | 100 | 500 | 25 | 0.2 | 3 |
| 5 | 100 | 700 | 25 | 0.2 | 3 |
| 6 | 100 | 1000 | 25 | 0.2 | 3 |
| 7 | 150 | 600 | 25 | 0.2 | 3 |
| 8 | 150 | 600 | 25 | 0.2 | 6 |
| 9 | 100 | 600 | 16 | 0.2 | 3 |
| 10 | 100 | 600 | 20 | 0.2 | 3 |
| 11 | 100 | 600 | 25 | 0.2 | 3 |

The rail profiles are considered in four different forms as it shown in Fig. 7. The rail profiles are called new profile, worn 1, worn 2 and worn 3, where worn 1 has the least and worn 3 has the most side wear. It should be noted that high and low rails have different profiles in their

worn shapes. All the wheel profiles are considered to be new at the beginning of analysis. The rail profiles are also considered to be constant in the whole track.
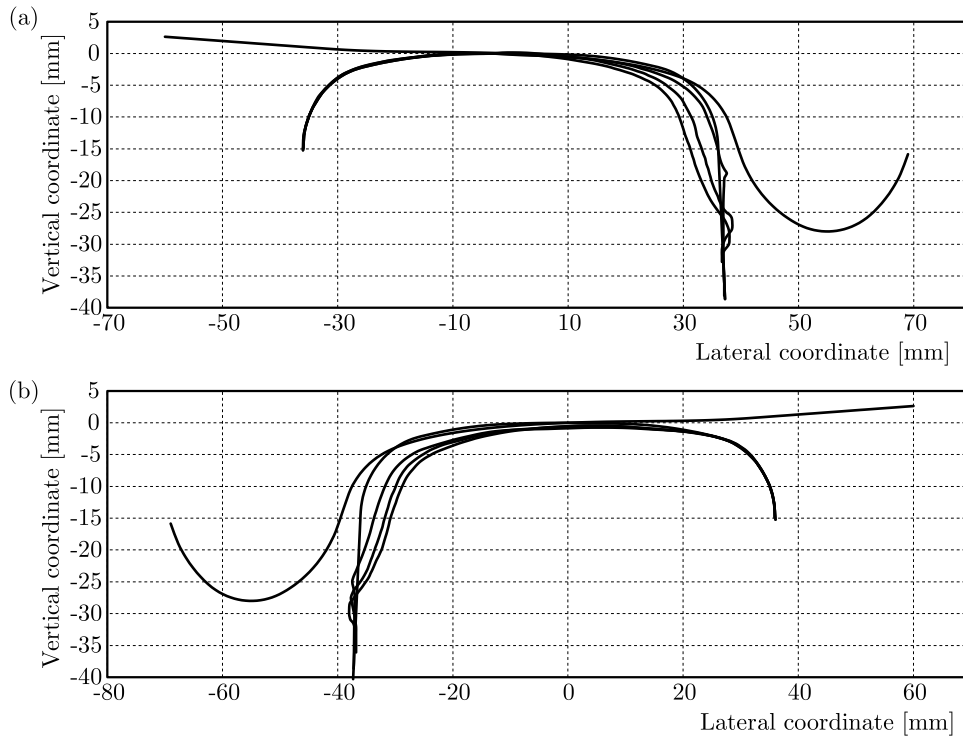


Fig. 7. Worn rail profiles (Lewis and Olofsson, 2009): high rail (left) and low rail (right)

The simulated train consists of 4 wagons as a typical example of a complete train including locomotive, first wagon, middle wagons and the last wagon. The results are gathered from wagon 3 as it is shown in Fig. 8.
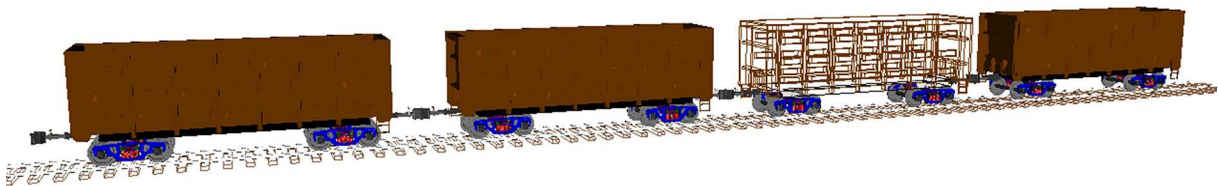


Fig. 8. Simulated 3D train

The train passee over a track and the results are saved at every passage. The track consists of a 40 m tangent track, 130 m spiral, 500 m curve section and the final 130 m spiral.

This analysis is done 15 times.

## 6. Results

Figure 9 shows rolling radius difference (RRD) against lateral displacement of the wheel. The rail profile is UIC 60 and rail inclinations of 1:20 and 1:40, and the wheel profile is S1002. In the rail inclination 1:40, there is a rolling difference for every lateral displacement. So, for each lateral displacement, there is a different point on the wheel. This causes uniform wear along the wheel profile and prevents local wear like hollow tread. In contrast to 1:40, in 1:20 inclination, there is no significant distribution and the contact point remains constant at the first 6 mm of

wheel lateral displacement. As a result, for each curve, the wheel has to make a flange contact, so high flange wear occurs.
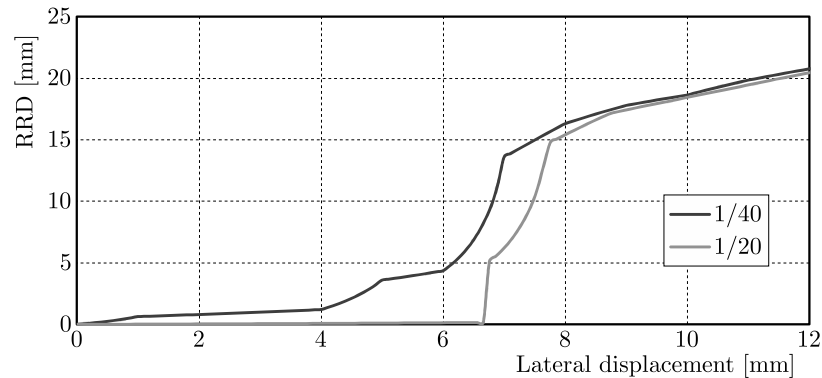


Fig. 9. Effects of rail inclination on rolling radius difference (RRD) in right and left wheels

### 6.1. Wheel-rail compatibility

Figure 10 (left) shows all possible contact points between the wheel and rail. From the top to down side, wear of the rail profiles increases. For a new rail (up) there are two discrete contact zones. So, local wear in this arrangement is expected. With an increase in rail wear, these two zones merge together in order to make a united zone, so a more uniform rate of the contact point change occurrs.
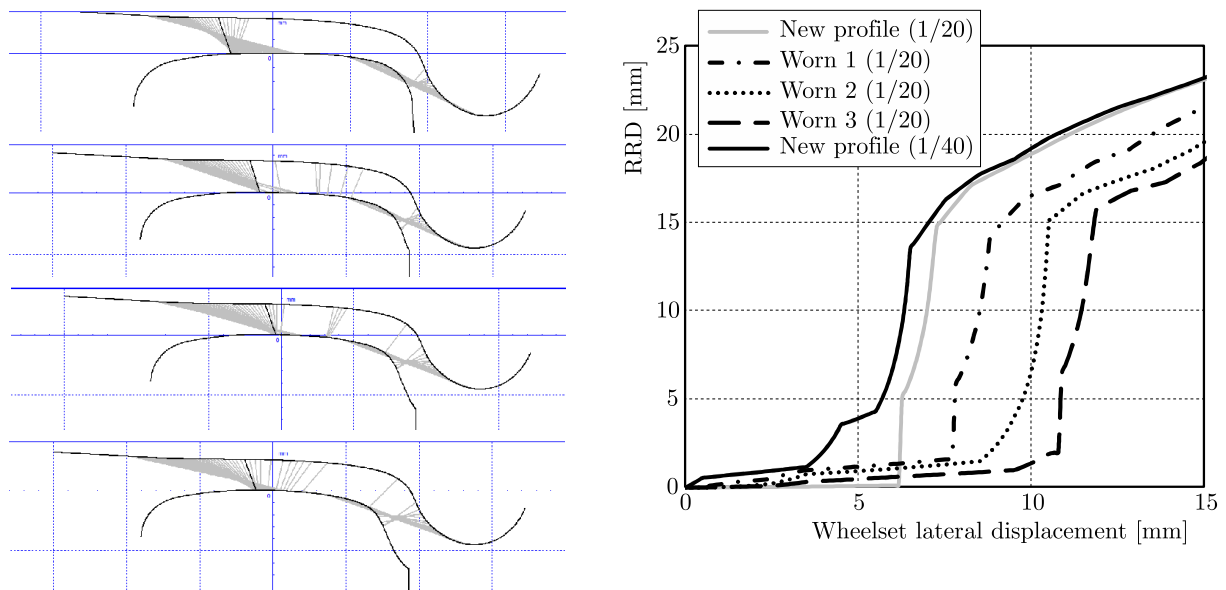


Fig. 10. Contacts for each profile pair (new wheel and worn rails) (left) and RRD diagrams for each profile pair (right)

Figure 10 (right) shows an RRD diagram for profile pairs in Fig. 10 (left). It also includes new wheel and rail profiles in the standard arrangement (rail inclination 1:40). If 1:40, the diagram is considered as standard dynamic performance, so the wear pattern tends to move toward standard at worn rail 1. But with an increase in the rail-side wear and material loss, this dynamic performance descends. So, as a very important result in this part, in sn incompatible or non-standard arrangement the wear pattern tends to move towards the standard performance,

but this balance will never get completed. With an increase in the material loss, the dynamic performance becomes much like a non-standard one again.

The analysis is performed and wear depth for each scenario is calculated. Figure 11 shows wear depth of the outer wheels. The wear pattern and wear amplitude in two bogies were the same, so only the outer wheels of the front bogie is plotted. As it is expected, wear of the wheels in contact with the new rail is more than the worn ones. In ideal, the wear pattern and depth of all wheels should be the same, so more differences in the wear pattern and more imperfect curving behavior could be concluded. In Fig. 11, the leading wheels experience flange wear while the trailing wheels tend to have tread wear. The trailing wheel with the new rail profile shows flange wear, too. The reason is sharp negative angle of attack and this, as it is shown in Fig. 11, is eliminated with an increase in the wheel-rail clearance (increase in rail side wear). The train passes over a simple curve, so discrete flange and treads wear shows two points contact. This phenomenon due to the incompatible arrangement happens in all cases. Discrete wear of 18100 wheels and hollow tread of new wheel profiles are discussed in Section 2. Kalousek (2005) also reported discrete wear of 18100 wheel profiles.
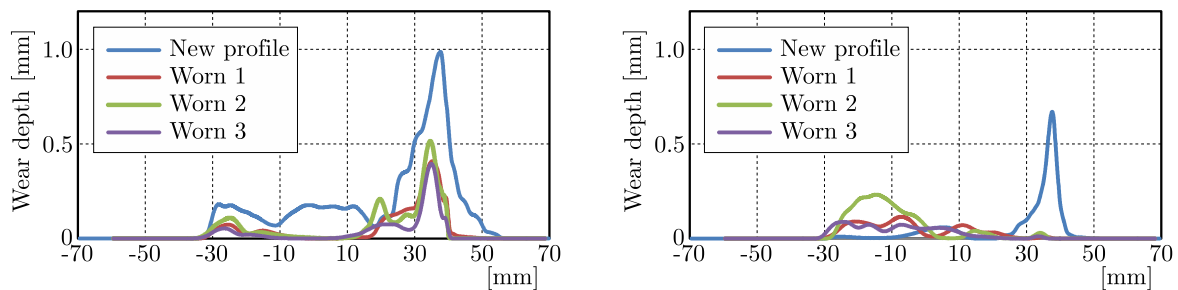
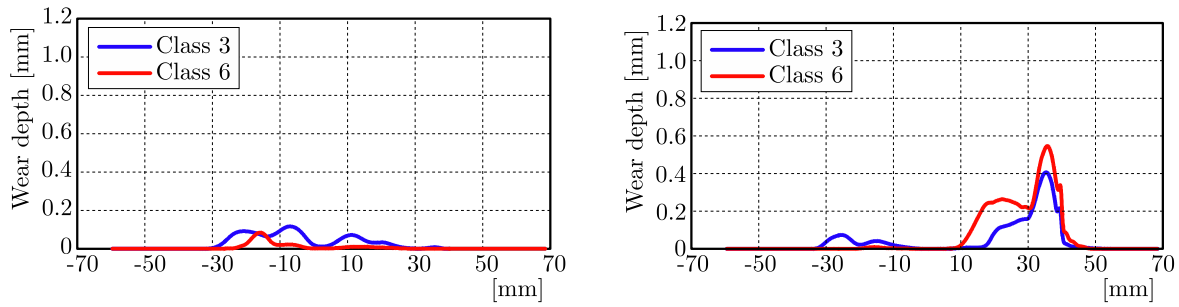

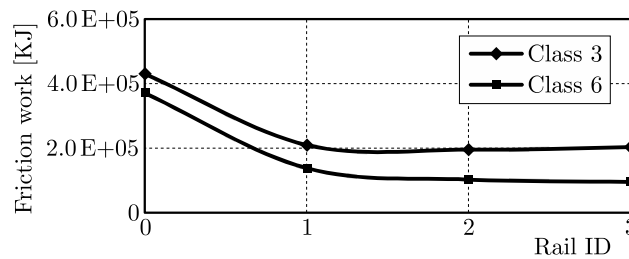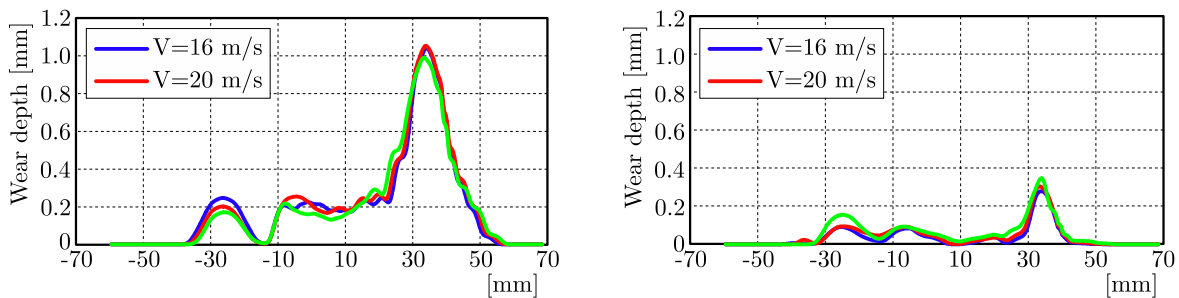Fig. 11. Wear depth diagram for the outer wheels of the front bogie, leading wheel (left) and trailing wheel (right). Rail-side coefficient of friction is 0.1

Figure 12 shows a change in the RRD diagram of worn wheel profiles compared to the new one. For all rail profiles (new, worn 1 to 3), wheel wear approaches the standard mode. This change is negligible for the new rail but worn rail 1 exhibits biggest change in dynamic behavior. As it was mentioned before, RRD changes from worn rail 1 to 3 decrease because of too much material loss and the loss of system balance.
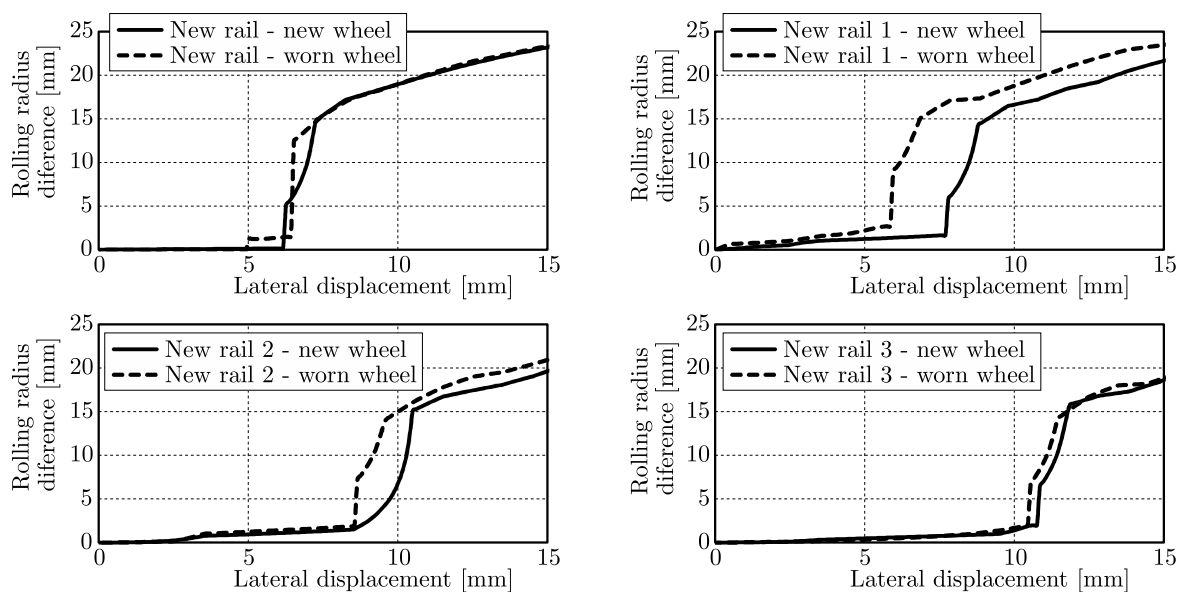


Fig. 12. Comparison of RRD diagrams for worn and new wheel profiles

**6.2. Effect of operational parameters**

*6.2.1. Effect of rail-side friction*

With a decrease in rail-side lubrication, the total friction work reduces, but too much reduction will cause an increase of the work in new rail profile. The reason is the harmful effect in bogie steering and creepages which decrease significantly. Figure 13 shows a comparison between wear depth for rail inclinations 1:20 and 1:40. The wear pattern becomes continuous along the wheel profile. The reason is the one point contact which results in a continuous and smooth change in the contact point. A change in the rail side coefficient of friction results in a very clear pattern of wear of the wheels. On the other side (incompatible wheel-rail arrangement), wear depth is discrete due to two point contact and a sudden change in the contact point from tread to flange. In contrast to 1:40 ones, the change in the coefficient of friction results in a no clear pattern. The wear depth amplitude increases in unfair arrangement and it can be concluded that two the point contact reduced the efficiency of rail side lubrication. From the results for both 1:40 and 1:20 inclinations, wear depth of 0.8-1.0 mm in only 12 km curve passage is not economical. This determines that the three pieces bogie is not suitable for non-straight corridors.
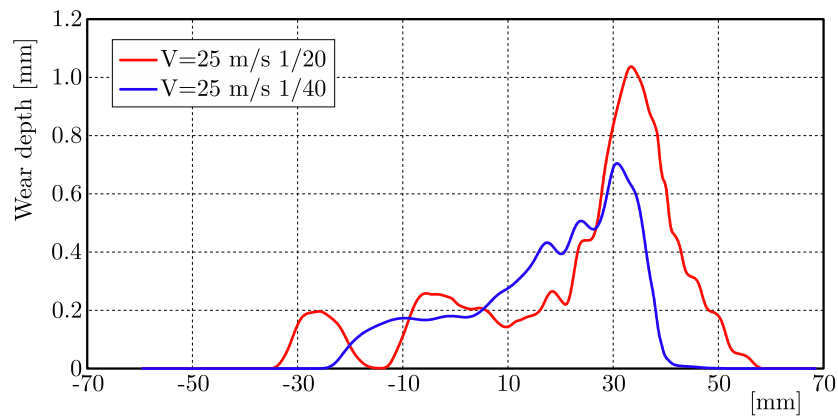


Fig. 13. Comparison of wear depth for the leading wheel (1:20 and 1:40 rail inclination and a new rail profile)

*6.2.2. Effect of track quality*

The change in the track class results in a very clear pattern in wheels though the irregularities are random (Fig. 14). In the new rail profile, wear decreases with an increment of track quality. But this pattern is changed in worn rails. The leading wheel shows more wear in class 6 but the trailing wheels have less wear when compare to class 3. Imperfect curving is still the key parameter for non-uniform wear of the wheels. Also two the point contact can be concluded from the diagrams.

Figure 15 shows the total friction work during analysis. On the basis of this diagram, track quality has a noticeable effect on the rolling resistance of the wheels and, consequently, noticeable effect on energy consumption of the vehicles.

*6.2.3. Effect of velocity*

Velocity is the most important parameter in wear. Figure 16 shows wear depth of the wheel profile passing over a new rail. Wheel tread is more sensible to a change in velocity. With an increase in speed, the leading wheels have less wear in their tread while the trailing ones experience more. On the other hand, an increase in velocity results in better steering and more uniform wear in all wheels.

Fig. 14. Wear depth diagram for the outer wheels of the front bogie, leading wheel (left) and trailing wheel (right) (worn rail No. 1)



Fig. 15. Friction work for different rail profiles and track quality



Fig. 16. Wear depth diagram for the outer wheels of the front bogie, leading wheel (left) and trailing wheel (right) (new rail profile)
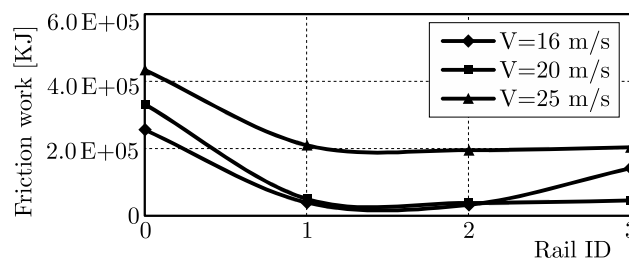


Fig. 17. Friction work for different rail profiles and velocities

Figure 17 also shows the total friction work during analysis. With an increase in speed, the friction work increases while in the wear depth, volume of the removed mass is not changed noticeably. The reason is better steering of bogies, so the bogie spends shorter time in the severe wear mode. All worn rails show a lower friction work compared to the new rail profile as it is expected.

## 7. Conclusion

In this study, the effect of rail side wear on the wear pattern of new wheel profiles is examined. The parameters are the rail side coefficient of friction, track quality, track curvature and velocity. With respect to the analysis conditions, the effects of wheel-rail clearance and curving behavior of a selected bogie (pivot friction) are taken into account.

The results show that imperfect curving of the bogie is the key parameter for non-uniform wear of wheels. Non-uniform wear may result from the tangential force. The wheel-rail clearance also has great influence in the new wheel wear pattern. The results can be summarized as follows:

- Contact analysis of new wheel profiles with different worn rails show discrete contact zones along new wheel and new rail profiles. These zones are merged with an increase in the rail wear.

- The wear pattern of new wheels approaches the standard mode. The change in an RRD diagram is the most for worn rail 1 and descends to worn rail 3.

- Rail-side lubrication is a common way for reducing lateral forces. But the two point contact could easily undo the advantages of lubrication.

- The track class has a very clear effect on the wheels, though the irregularities are random. In the new rail profile, wear decreases with an increase in track quality.

- Track curvature effects become eliminated by the increase in the wheel-rail clearance. This parameter needs more detailed investigation.

- Velocity has the most effect on the wear pattern for new wheel profiles.

- The importance of compatible contact becomes high for changing velocity conditions.

- With an increase in velocity under incompatible contact, wear of wheels becomes more uniform.

Based on the results, Iran Railway Research Center organized a field test for calibrations of the results in wear depth. The wheel and rail wear will be monitored the during following year, and the results will be used in order to optimize the wheel-rail contact quality.

## References

1. Archives of the National Railway Organization of I.R.Iran, Freight Wagons Division

2. BRAGHIN F., LEWIS R., DWYER-JOYCE R.S., BRUNI S., 2006, A mathematical model to predict railway wheel profile evolution due to wear, *Wear*, **261**, 1253-1264

3. ENBLOM R., BERG M., 2005, Simulation of railway wheel profile development due to wear-influence of disc braking and contact environment, *Wear*, **258**, 1055-1063

4. HOSEIN NIA S., 2011, *Dynamics Modeling of Freight Wagons*, Master's Degree Thesis, Department of Mechanical Engineering, Blekinge Institude of Technology, Karlskrona, Sweden

5. International Heavy Haul Association (2001), *Guidelines to best practices for heavy haul railway operations: wheel and rail interface issues*, 2808 Forest Hills Court Virginia Beach, Virginia 23454 USA

6. JENDEL T., 2002, Prediction of wheel profile wear-comparisons with field measurements, *Wear*, **253**, 89-99

7. JIN Y., ISHIDA M., NAMURA A., 2011, Experimental simulation and prediction of wear of wheel flange and rail gauge corner, *Wear*, **271**, 259-267

8. KALOUSEK J., 2005, Wheel/rail damage and its relationship to track curvature, *Wear*, **258**, 1330-1335

9. LEWIS R., OLOFSSON U., 2009, *Wheel-Rail Interface Handbook*, CRC Press, Boca Raton, Boston, New York, Washington, DC

10. POMBO J., AMBROSIO J., PEREIRA M., LEWIS R., DWYER-JOYCE R., ARIAUDO C., KUKA N., 2011, Development of a wear prediction tool for steel railway wheels using three alternative wear functions, *Wear*, **271**, 238-245

11. Rail Safety and Standards Board (2002), *Feasibility of reducing the number of standard wheel profile designs*, Report No. ITLR/T11299/001

12. TELLISKIVI T., OLOFSSON U., 2004, Wheel/rail wear simulation, *Wear*, **257**, 1145-1153

13. Universal Mechanism User's Manual (2012), *Railway wheel and rail profile wear prediction module*, UM Laboratory

14. XIE G., IWNICKI S.D., 2008a, Calculation of wear on a corrugated rail using a three-dimensional contact model, *Wear*, **265**, 1238-1248

15. XIE G., IWNICKI S.D., 2008b, Simulation of wear on a rough rail using a time-domain wheel-track interaction model, *Wear*, **265**, 11/12, 1572-1583

16. ZAKHAROV S., ZHAROV I., 2002, Simulation of mutual wheel/rail wear, *Wear*, **253**, 100-106

17. ZOBORY I., 1997, Prediction of wheel/rail profile wear, *Vehicle System Dynamics*, **28**, 221-259

# A NUMERICAL APPROACH TO PREDICT THE ROTATING STALL IN THE VANELESS DIFFUSER OF A CENTRIFUGAL COMPRESSOR USING THE EIGENVALUE METHOD

Chenxing Hu, Pengyin Liu, Xiaocheng Zhu

*Co-Innovation Center for Advanced Aero-Engine, Shanghai Jiao Tong University, Shanghai, China*
*e-mail: ryanhu@sjtu.edu.cn; pengyinliu@163.com; zhxc@sjtu.edu.cn*

Hua Chen

*National Laboratory of Engine Turbocharging Technology, Tianjin, China*
*e-mail: huachen204887@163.com*

Zhaohui Du

*Co-Innovation Center for Advanced Aero-Engine, Shanghai Jiao Tong University, Shanghai, China*
*e-mail: zhdu@sjtu.edu.cn*

A two-dimensional incompressible flow model is presented to study the occurrence of rotating stall in vaneless diffusers of centrifugal compressors. The diffuser considered has two parallel walls, and the undisturbed flow is assumed to be circumferentially uniform, isentropic, and to have no axial velocity. The linearized 2D Euler equations for an incompressible flow in a fixed frame of the coordinate system are considered. After discretization by a spectral collocation method based on Chebyshev-Gauss-Lobatto points, the generalized eigenvalue problem is solved through the QZ algorithm. The compressor stability is judged by the imaginary part of the eigenvalue obtained. Based on the 2D stability analysis, the influence of inflow angle, radius ratio and wave number are studied. The results from the present stability analysis are compared with some experimental measurement and Shen's model. It is showed that diffuser instability increases rapidly and the stall rotational speed decreases quickly with an increase in the diffuser radius ratio. The largest critical inflow angle can be obtained when the wave number is around $3 \sim 5$ for the radius ratio between 1.5 to 2.2. It is also verified that the stability model proposed in this paper agrees well with experimental data and has the capability to predict the onset of rotating stall, especially for wide diffusers.

*Keywords:* instability, vaneless diffuser, eigenvalue problem, spectral method

## 1. Introduction

Rotating stall in radial vaneless diffuser is one of the most common flow instabilities in centrifugal compressors and it can significantly influence the performance of the compressors. The nature of flow instability, especially rotating stall associated with vaneless diffusers have been extensively investigated by numerous researchers (Day, 2016; Everitt and Spakovszky, 2013; Spakovszky and Roduner, 2009; Ubben and Niehuis, 2015).

For decades, efforts have been made by researchers to explain the mechanism and predict the occurrence of rotating stall within the vaneless diffuser. Quantities of theoretical methodologies based on different assumptions and simplifications on the base flow have been proposed during that time. Generally speaking, one of the basic distinctions between the theoretical models on vaneless diffusers is whether the influence of the boundary layer is taken into consideration. The first type of approaches which was adopted by Jansen (1964), Senoo and Kinoshita (1977) and Frigne and Braembussche (1985) is that the three-dimensional wall boundary layer

is supposed to be responsible for the occurrence of rotating stall in a narrow vaneless diffuser. According to the experimental and theoretical study of Jansen (1964), the flow was assumed to be symmetric with respect to the diffuser depth and the local inward radial velocity component was treated as the inception of rotating stall. While in Senoo's vaneless diffuser model, the flow was no longer assumed to be symmetric and a non-uniform distribution of inlet velocity along the axial direction was taken into account. In his calculations, the critical velocity angle was defined for which reverse flow started in the vaneless diffuser (Senoo and Kinoshita, 1978).

On the other hand, an other theory for the occurrence of rotating stall in a vaneless diffuser, which was employed by Abdelhamid (1980) and Moore (1989), indicates that the stall is associated with two-dimensional core flow instability in vaneless diffusers which usually have the width radius ratio above 0.1. The two-dimensional numerical model developed by Moore is based on calculation of 2D incompressible Euler's equations. Neutrally stable rotating disturbances with low speed were found and a dense set of resonant solutions in which large pressure perturbations were taken as the criterion of rotating stall in Moore's work. Chen *et al.* (2011) extended the 2 dimensional model of Moore into a 3 dimensional model with consideration of the distribution of inlet velocity along the axial direction. Sun *et al.* (2013, 2016) proposed stability models for axial and centrifugal compressors on the basis of the eigenvalue approach. The comparisons with the results from experiments validated the effectiveness and accuracy of their models.

In addition, the significant influence of diffuser geometry and flow parameters on the vaneless diffuser performance and structure of the stall pattern have been also numerically and experimentally investigated in the recent years. The experiments carried out by Abdelhamid (1983) and Bianchini *et al.* (2013) confirmed that the local reverse flow did not necessarily lead to stall. The dependency of flow instability on the diffuser width ratios and diameter were also verified. The critical flow coefficient becomes larger with a decrease in diffuser width according to experiments of Abidogun (2002). Besides those experimental researches, the diffuser stability was also numerically investigated by Everitt (2010) through conducting isolated diffuser simulations, and the volute was found to have potential in delaying the onset of diffuser instability. Although the CFD method has an advantage over theoretical methods by providing a direct and vivid flow field with a relatively high accuracy, there is no a certain way for numerical simulation to capture the complicated disturbance with different frequency, amplitude and length scale due to unsteadiness and complexity of the flow field.

According to Jansen (1964), unsteady inviscid motion of the fluid is analyzed with the assumption that the disturbances can be expressed in terms of periodic waves. The equations are then reduced and solutions are sought for the resulting eigenvalue problem. However, it is mentioned in his paper that the prediction of the number of stall cells and the determination of the constant in the velocity equation requires a subsequentstudy.

In the present paper, firstly a 2D vaneless diffuser theoretical model based on stability analysis of an incompressible base flow is established and the full eigenvalue spectrum is obtained. Then the influence of collocation points and geometric parameters of the vaneless diffuser on the stability is investigated. Finally, the comparison between the results obtained from the present stability model and those from several experiments and models reported previously is performed. Compared to unsteady CFD simulations which are quite time and resources consuming and Senoo's stability model, which is unable to provide the stall number, the present analysis is able to predict the occurrence and stall number cheaply and quickly. And compared to Shen's model, the present model is easier to be extended to the stability problem concerning the sensitivity.

## 2. Theoretical model

### 2.1. Numerical methodology

In the present analysis, the stability discussed here is assessed by linearizing 2D Euler's equations for a base flow and determined by an operator that describes the evolution of small perturbations superposed on the base flow. The eigenvalues of this operator give the frequency and time growth rate of the perturbations. The corresponding eigenfunctions yield the mode shapes. The perturbation with the largest growth rate is the one that dominates the stability in the long term, and the positive growth rate means the occurrence of instability.

The diffuser considered has two parallel walls, and the undisturbed flow is assumed to be circumferentially uniform, isentropic, and to have no axial velocity. To further simplify the calculation, the perturbations and velocity distribution of the base flow along the axial direction are neglected. The flow sketch is shown in Fig. 1. The inflow circumferential angle $\alpha$ is defined at the diffuser inlet as illustrated in Fig. 1b. Then, a 2D flow model for study of the flow stability in the vaneless diffuser can be developed.
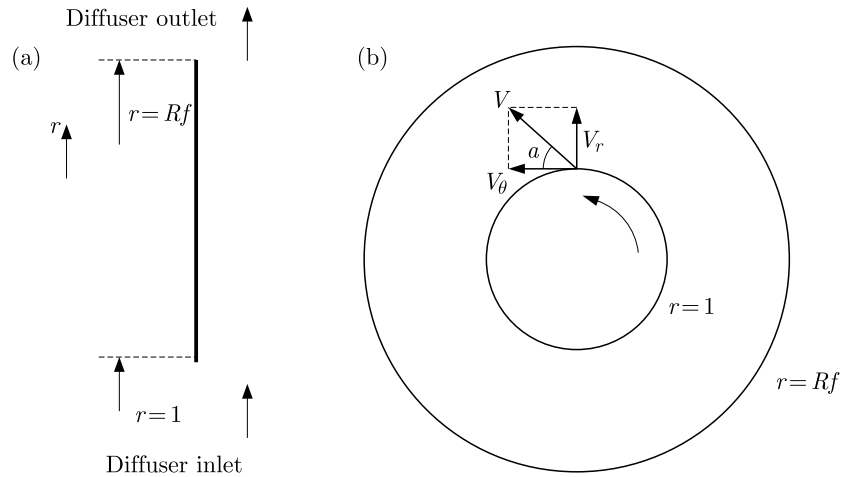


Fig. 1. Sketch of a vaneless diffuser: (a) base flow, (b) inflow angle

### 2.2. Implementation of the numerical model

#### 2.2.1. Linearization of Euler's equations

To begin with, viscosity and compressibility are neglected in our study. The flow field is described by non-dimensionalized 2-D unsteady incompressible Euler's equations as shown

$$
\frac{v_r}{r} + \frac{\partial v_r}{\partial r} + \frac{1}{r}\frac{\partial v_\theta}{\partial \theta} = 0
$$
$$
\frac{\partial v_r}{\partial t} + v_r\frac{\partial v_r}{\partial r} + \frac{v_\theta}{r}\frac{\partial v_r}{\partial \theta} - \frac{v_\theta^2}{r} = -\frac{\partial p}{\partial r} \tag{2.1}
$$
$$
\frac{\partial v_\theta}{\partial t} + v_r\frac{\partial v_\theta}{\partial r} + \frac{v_\theta}{r}\frac{\partial v_\theta}{\partial \theta} + \frac{v_\theta v_r}{r} = -\frac{\partial p}{r\partial \theta}
$$

Here, the velocity is non-dimensionalized by the impeller tip velocity $U$. The length is non-dimensionalized by the corresponding inlet radius $r_1$ and the time $t$ is non-dimensionalized by $r_1/U$. Thus, $v_r$ and $v_\theta$ mean the non-dimensionalized radial and circumferential velocities. In the stability analysis, the flow field is assumed to consist of the base flow and a small disturbance. Then, the velocity and pressure can be rewritten as follows

$$
p = \overline{p} + p' \qquad v_r = \overline{v}_r + v_r' \qquad v_\theta = \overline{v}_\theta + v_\theta' \tag{2.2}
$$

where $\overline{p}$ represents base flow pressure and $p'$ are small disturbances of pressure. For the base flow, $V_r$ and $V_\theta$ represent the inlet radial and circumferential velocity of the base flow, respectively.

Before Eqs. (2.2) are substituted into Eqs. (2.1), emphasis on the small perturbation theory is made: 1) any disturbances of the 2nd and higher orders are neglected, 2) the base flow is treated as steady, so $\partial\overline{\bullet}/\partial t = 0$, c) since the mean flow is circumferentially symmetric, $\partial\overline{\bullet}/\partial\theta = 0$. And Eqs. (2.1) are still appropriate for the base flow. Then the linearized non-dimensional Euler's equations can be derived as follows

$$
\begin{aligned}
&\frac{v'_r}{r} + \frac{\partial v'_r}{\partial r} + \frac{1}{r}\frac{v'_\theta}{\theta} = 0 \\
&\frac{\partial v'_r}{\partial t} + \frac{\partial \overline{v}_r}{\partial r v'_r} + \left(\overline{v}_\theta\frac{\partial v'_r}{r\partial\theta} + \overline{v}_r\frac{\partial v'_r}{\partial r}\right) - \frac{2\overline{v}_\theta v'_\theta}{r} + \frac{\partial p'}{\partial r} = 0 \\
&\frac{\partial v'_\theta}{\partial t} + v'_r\left(\frac{\partial \overline{v}_\theta}{\partial r} + \frac{\overline{v}_\theta}{r}\right) + \left(\overline{v}_\theta\frac{\partial v'_\theta}{r\partial\theta} + \overline{v}_r\frac{\partial v'_\theta}{\partial r}\right) + \frac{\overline{v}_r v'_\theta}{r} + \frac{\partial p'}{r\partial\theta} = 0
\end{aligned}
\tag{2.3}
$$

### 2.2.2. Establishment of the eigenvalue problem

In general, the separation between spatial and temporal coordinates allows making use of Fourier modes in time when the variables are homogeneous. Then the perturbations can be written in form of $e^{i\theta}$ where the homogeneous variables (including time) are taken into account and the inhomogeneous variables are taken as the amplitude function. The specific form of the Fourier mode assumed is that the disturbances are normal modes in the circumferential direction, the disturbances can be written as follows

$$
p' = P(r)e^{i(-\omega t+m\theta)} \qquad v'_r = A(r)e^{i(-\omega t+m\theta)} \qquad v'_\theta = W(r)e^{i(-\omega t+m\theta)}
\tag{2.4}
$$

where $m$ is the azimuthal wavenumber and $\omega = \omega_r + i\omega_i$. Taking $p'$ for instance as

$$
p' = P(r)e^{im\theta}e^{(-i\omega_r+\omega_i)t}
\tag{2.5}
$$

it can be seen that corresponding to $e^{\omega_i t}$ dominates the growth rate of disturbances with time. Namely, if the imaginary part $\omega_i > 0$, the disturbances will grow exponentially with time, and the mode will be unstable. If $\omega_i < 0$, the disturbances will decay with time and the mode will be stable. And is the angular frequency.

The rotational speed of the disturbances in the circumferential direction non-dimensionlized by the impeller rotational speed is

$$
f = \frac{-\omega_r}{m}
\tag{2.6}
$$

Substituting equations (2.4) into (2.3), the ordinary differential equations for $A$, $W$, $P$ which represent $A(r)$, $W(r)$ and $P(r)$ with the subscript omitted, can be obtained as follows ($A'_r = dA/dr$ etc.)

$$
\begin{aligned}
&A'_r + \frac{A}{r} + \frac{im}{r}W = 0 \\
&-i\omega A + \frac{\partial \overline{v}_r}{\partial r}A + \overline{v}_r A'_r + \frac{im\overline{v}_\theta A}{r} - \frac{2\overline{v}_\theta}{r}W + P'_r = 0 \\
&-i\omega W + A\left(\frac{\partial \overline{v}_\theta}{\partial r} + \frac{\overline{v}_\theta}{r}\right) + \overline{v}_r W'_r + \frac{im\overline{v}_\theta W}{r} + \frac{\overline{v}_r}{r}W + \frac{im}{r}P = 0
\end{aligned}
\tag{2.7}
$$

Since there is no inlet disturbances coming from the outside of the system, homogeneous ordinary differential equations (2.7) can also expressed as

$$
\mathbf{M}\phi = \omega\mathbf{J}\phi
\tag{2.8}
$$

where $\phi = [A, W, P]^{\mathrm{T}}$, and $\mathbf{M}$ and $\mathbf{J}$ are the corresponding coefficient matrices

$$\mathbf{M} = \begin{bmatrix} \dfrac{1}{r} + \dfrac{\partial}{\partial r} & \dfrac{im}{r} & 0 \\[2mm] \dfrac{d\overline{v}_r}{dr} + \overline{v}_r\dfrac{\partial}{\partial r} + \dfrac{im\overline{v}_\theta}{r} & -\dfrac{2\overline{v}_\theta}{r} & \dfrac{\partial}{\partial r} \\[2mm] \dfrac{d\overline{v}_\theta}{dr} + \dfrac{\overline{v}_\theta}{r} & \overline{v}_r\dfrac{\partial}{\partial r} + \dfrac{im\overline{v}_\theta}{r} + \dfrac{\overline{v}_r}{r} & \dfrac{im}{r} \end{bmatrix} \qquad \mathbf{J} = \begin{bmatrix} 0 & 0 & 0 \\ i & 0 & 0 \\ 0 & i & 0 \end{bmatrix} \tag{2.9}$$

Solving equation (2.8) leads to a generalized eigenvalue problem, and the eigenvalue is used to determine the instability of the vaneless diffuser.

### 2.2.3. Establishment of the base flow

According to conservation of angular momentum and mass, the circumferential and radial velocity can be expressed as follows

$$\overline{v}_{r1}2\pi r_1 = \overline{v}_r 2\pi r \qquad \overline{v}_{\theta 1} r_1 = \overline{v}_\theta r \tag{2.10}$$

Therefore, the expressions of circumferential and radial velocity can be obtained as

$$\overline{v}_r = \frac{V_r}{r} \qquad \overline{v}_\theta = \frac{V_\theta}{r} \tag{2.11}$$

where $V_r$ and $V_\theta$ are the radial and circumferential velocity distributions at the diffuser inlet.

## 2.3. Discretization and calculation

### 2.3.1. Spatial discretization

Among the widely used spatial discretization methods, spectral methods have played a prominent role in early instability analyses. At present they are particularly useful. In this study, the spectral method is accomplished with Chebyshev-Gauss-Lobatto points. The two-dimensional linear eigenvalue problems posed above can be solved by constructing an operator that discretizes a $n$-th order linear ODE in the form of

$$L_{ij} = a_n(r_i)D_{ij}^{(n)} + \ldots + a_1(r_i)D_{ij}^{(1)} + a_0(r_i) \tag{2.12}$$

where $D_{ij}^{(m)}$, $m = 1, 2, \ldots, n$, is the $m$-th derivative matrix corresponding to the collocation points $r_i$, and $a_0, a_1, \ldots, a_n$ are evaluated at $r_i$.

When using spectral collocation methods, the value of the functions at collocation points is expressed as follows

$$\phi(r) = \sum_{j=0}^{N} \varphi_j(r)\widetilde{\phi}(r_i) \tag{2.13}$$

where $\phi(r)$ is the value of the function at the point $r$ obtained by using interpolant polynomials constructed for the variables in terms of their values at the collocation points, and $\varphi(r)$ is known as the basis function.

The collocation points in the calculation domain $\Omega$ are chosen as

$$r_\Omega = \cos\frac{\pi j}{N} \qquad j = 0, 1, \ldots, N \tag{2.14}$$

The extrema of the $N$-th order Chebyshev polynomial $T_N$ are defined in the interval $-1 < r_\Omega < 1$. Then the interpolant $\varphi_j(r_\Omega)$ for the Chebyshev scheme is given as

$$\varphi_j(r_\Omega) = \frac{1 - r_{\Omega j}^2}{r - r_{\Omega i}} \frac{T_N'(r_\Omega)}{N^2 c_j}(-1)^{j+1}$$

$$c_0 = c_N = 2 \qquad c_j = 1 \qquad 0 < j < N \tag{2.15}$$

The collocation derivative matrix $\mathbf{D}$ for the Gauss-Lobatto grid is denoted by

$$D_{GL}^{(1)} = (d_{ij}) \qquad 0 \leqslant i \qquad j \leqslant N \tag{2.16}$$

where the elements $d$ are defined by Canuto $et\ al.$ (2010) as follows

$$d_{00} = -d_{NN} = \frac{2N^2 + 1}{6} \qquad d_{jj} = \begin{cases} \dfrac{r_{\Omega j}}{2(r_{\Omega j}^2 - 1)} & 1 \leqslant j \leqslant N - 1 \\ \dfrac{c_i}{c_j} \dfrac{(-1)^{i+j}}{r_{\Omega i} - r_{\Omega j}} & i \neq j \end{cases} \tag{2.17}$$

In our case, the physical domain of interest $r \in [1, Rf]$ is mapped onto the standard collocation domain, based on the following equation

$$r_\Omega = -1 + 2\frac{r - 1}{Rf - 1} \tag{2.18}$$

Thereby, linearized Euler's equation (2.8) can be illustrated in the collocation domain as follows

$$\mathbf{M}_\Omega \phi = \omega \mathbf{J}_\Omega \phi \tag{2.19}$$

For the 2D incompressible problem, when $N$ collocation points are adopted to discretize the domain of interest, $\mathbf{M}_\Omega$ is a matrix of size $3N \times 3N$ arising from the three equations for the problem.

### 2.3.2. Numerical calculation of the generalized eigenvalue problem

One widely used algorithm for solving generalized eigenvalue problems is the QZ algorithm of Moler and Stewart (1973). This is a generalization of the QR algorithm for standard eigenvalue problems. Compared with other algorithms such as the Anorldi method (Meerbergen and Roose, 1997), inverse iteration (Peters and Wilkinson, 1979) and the Jacobi-Davidson method (Sleijpen and Van der Vorst, 1994), an important feature of the QZ algorithm is that it functions perfectly well with the presence of an infinite eigenvalue due to singularity of the matrix $\mathbf{j}_\Omega$. In the current study, the calculation of the generalized eigenvalue problem proposed in equations (2.17) is carried out by the QZ algorithm. Matlab is a software with high capability on computational mathematics, and the function eig based on the QZ method in Matlab has been widely used for eigenvalue problems such as for the calculation in the present model. For a matrix with leading dimension of 200 in the present model, the calculation with the function eig can be quite time-saving.

What should be paid much attention to is that spurious eigenvalues derived from numerical calculation rather than real physical problem also exist while using the QZ algorithm. One way to distinguish the spurious eigenvalues from the real ones is to vary the number of collocation points. The eigenvalues which remain the same are the real ones.

### 3. Validation of the model

#### 3.1. Influence of the collocation point number on the calculations

Firstly, the number of collocation points and its independence of the calculation is verified through changing this number. The eigenvalue spectra with different numbers of collocation points $N$ at $Rf = 2$, $V_r = 0.1$, $m = 1$ are shown in Fig. 2.

It can be seen that although the largest eigenvalue with the same imaginary part can be obtained for all numbers of collocation points, the number larger than 50 is preferred to have a proper, whole sketch of the eigenvalue spectrum. In the subsequent study, 50 collocation points are adopted in the following calculations considering both numerical accuracy and computational efficiency. When the collocation number is more than 200 in the subsequent study, a $600 \times 600$ matrix is solved, and spurious eigenvalues which are at least two orders of magnitude higher than the real ones come into being.
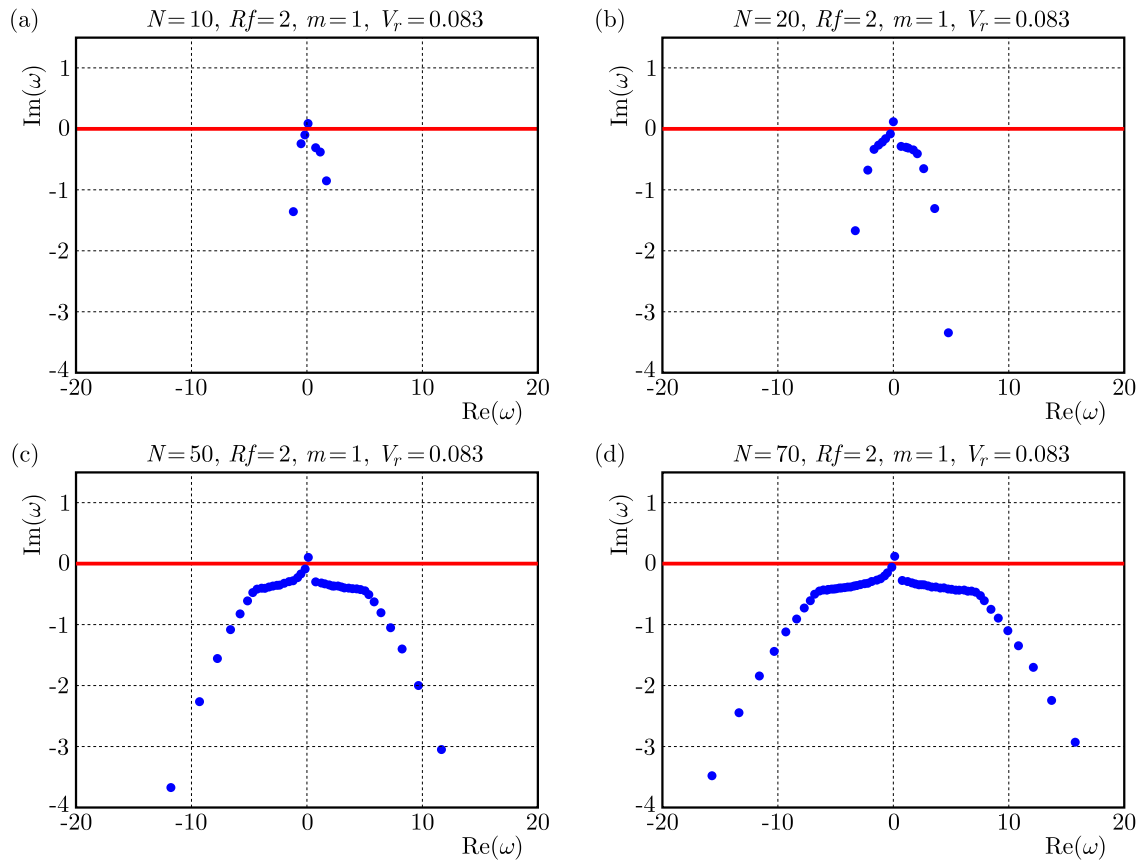


Fig. 2. Eigenvalue spectrum for different numbers of collocation points

#### 3.2. Influence of diffuser inlet velocity of the base flow on the calculations

Generally, the inlet radial velocity distribution of the diffuser is highly influenced by the impeller, and the axial uniform radial velocity can seldom be obtained in a practical diffuser flow. However, the uniform distributed radial velocity for an inviscid flow is associated with the average inflow angle. A brief connection between the average inflow angle and diffuser stability can be revealed rapidly with the help of the present 2D stability model. Figure 3 shows the influence of variability of the inlet velocity of the base flow $V_r$ on the stability of the vaneless diffuser with the same number $N$ of collocation points, radius ratio $Rf$ and wave number $m$. Different inflow angles are also listed corresponding to different inlet velocities.

It can be seen that with a decrease in the inlet radial velocity of the base flow, the flow in the vaneless diffuser turns from stability to instability. In other words, with a decrease in the inlet circumferential flow angle, the flow in the vaneless diffuser tends to instability, which well agrees with Senoo and Kinoshita (1978). Correspondingly, the inflow circumferential velocity angle when the rotating stall occurs is taken as the critical inflow angle $\alpha_c$.
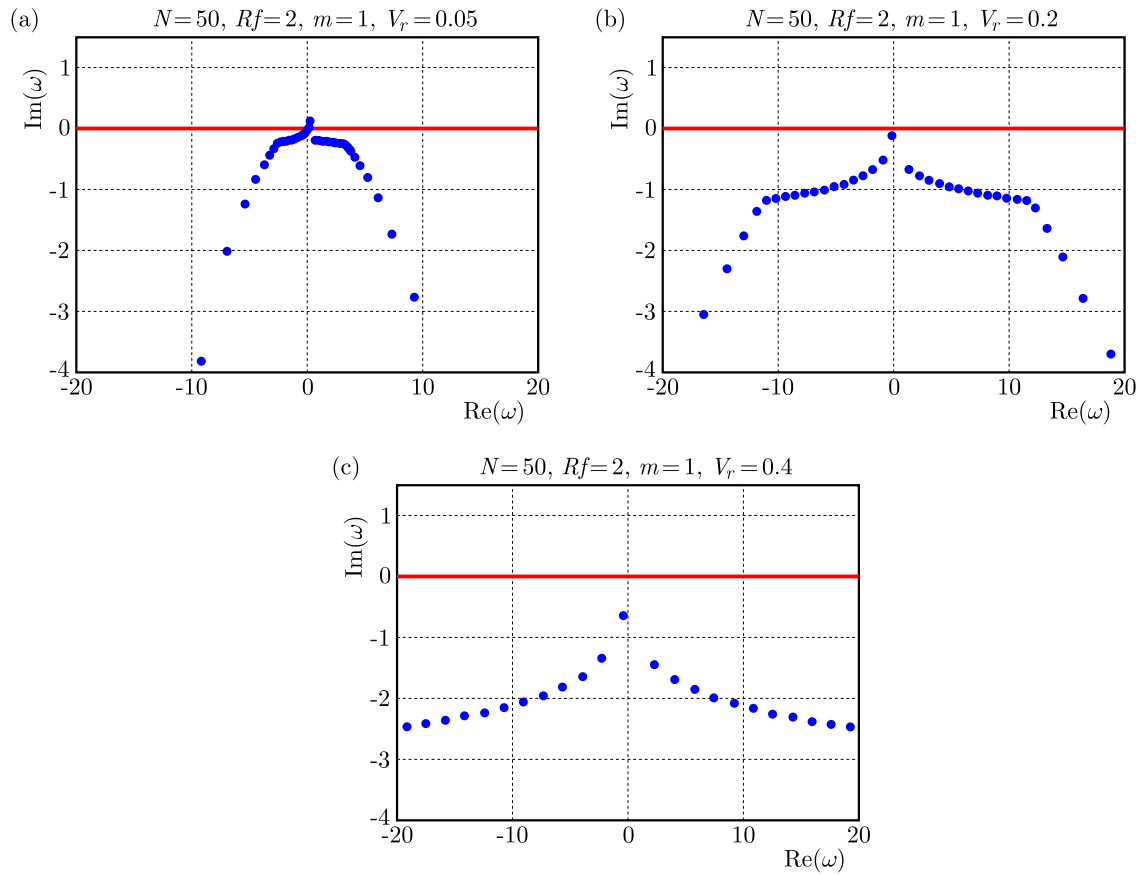


Fig. 3. Eigenvalue spectrum for different inlet radial velocities of the base flow

## 3.3. Influence of geometric parameters on the instability

### 3.3.1. Influence of the radius ratio $Rf$

As shown in Table 1, six leading eigenvalues in a descending order of the imaginary part of $\omega$ are presented. Compared with the cases for $Rf = 1.5$ and 1.67, the imaginary part of the leading eigenvalue for $Rf = 2$ and 2.2 become positive. The leading eigenmode of the cases with larger values of $Rf$ turns to instability. A larger value of the imaginary part of the leading eigenvalue indicates a higher time growth rate, which means stronger instability of the flow field. Therefore, the flow tends to instability with an increase in $Rf$.

### 3.3.2. Influence of the wave number $m$

A common feature of the centrifugal compression system is that it exhibits two kinds of rotating stall. One is known as the impeller stall, having a relatively high rotational speed of usually more than 50% of the impeller speed; and the other known as the diffuser stall, having a slower rotational speed at about 10% of the impeller speed. The present stability model is also applicable to confirmation of the stall number and rotational speed, therefore 3 cases with different radius ratios $Rf$ are calculated for 5 different wave numbers $m$.

**Table 1.** Six leading eigenvalues for different values of $Rf$ with $V_r = 0.131$, $N = 50$ and $m = 1$

| $Rf = 1.5$ | $Rf = 1.67$ | $Rf = 2$ | $Rf = 2.2$ |
|---|---|---|---|
| $-0.10977 - 0.25458i$ | $-0.024169 - 0.05096i$ | $0.03898 + 0.079355i$ | $0.05377 + 0.104624i$ |
| $-2.91568 - 0.64371i$ | $-2.22947 - 0.323566i$ | $-2.01654 - 0.236903i$ | $-0.29436 - 0.223245i$ |
| $0.70504 - 0.72005i$ | $0.332469 - 0.474960i$ | $-2.87547 - 0.395488i$ | $-1.7518 - 0.28062i$ |
| $-4.28143 - 0.86662i$ | $-3.180583 - 0.49452i$ | $0.327611 - 0.416233i$ | $-2.18808 - 0.32481i$ |
| $2.04559 - 0.91810i$ | $1.25444 - 0.59218i$ | $-3.73096 - 0.495389i$ | $-2.623871 - 0.33961i$ |
| $-5.62630 - 1.01110i$ | $-4.12054 - 0.602551i$ | $1.161860 - 0.514977i$ | $-0.08285 - 0.38274i$ |

When $m = 0$, the flow tends to be stable under any inlet flow condition. This is because that the time growth rate of circumferential disturbances are the main concern in our study, and zero wave number in the circumferential direction indicates that the circumferential disturbances are neglected, resulting in the absolutely stable condition in the calculation.

As shown in Fig. 4a, the influence of the wave number m on the critical stall angle is illustrated. It is clearly shown that the critical angle decreases with a decrease in $Rf$. According to Abidogum (2002), the most unstable mode (or stall) is often obtained for the wave number $m$ of 3. It can be seen that the largest critical angle is obtained when $m$ is around 3 with the radius ratio of 2.2. This is consistent with the result of Abidogum. The wave number corresponding to the most unstable mode differs for various radius ratios.

In Fig. 4b, the rotational speed of the disturbance corresponding to the onset of instability $f$ vs. the wave number $m$ is illustrated. It can be seen that the rotational speed of disturbance linearly increases with an increase in the wave number $m$ while the wave speed decreases quickly with the diffuser radius ratio, which is consistent with the results of Moore (1989) and Chen *et al.* (2011).
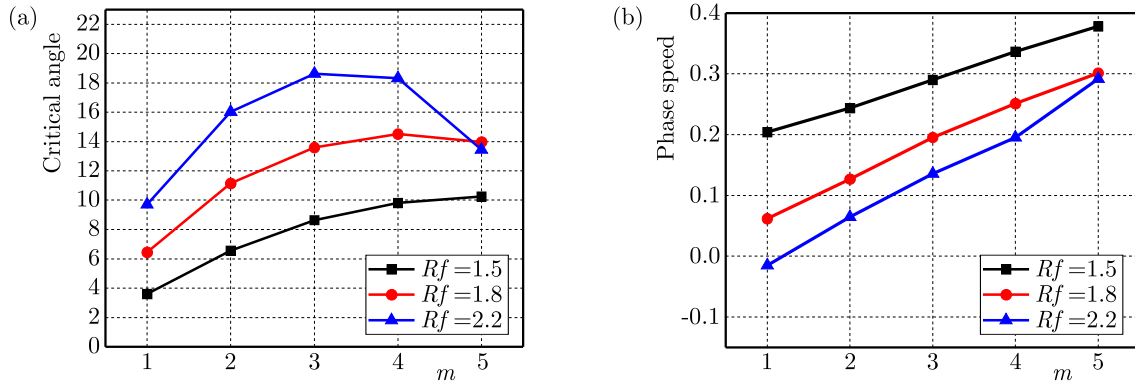


Fig. 4. Influence of the wave number $m$ on the critical angle and rotational speed: (a) critical angle vs. wave number, (b) rotational speed vs. wave number

### 3.4. Some eigenfunctions

In the theory of linear stability, the maximum response to varyiable initial conditions are what we concern the most. In the present analysis, the amplification of disturbances is characterized in terms of the least stable mode of the matrix $\mathbf{M}$. The eigenvalue spectrum when the radius ratio $Rf$ is 2, wave number $m$ is 1 and the inlet radial velocity is 0.04 are shown in Fig. 5. Among the eigenvalues obtained, the leading three least stable eigenvalue spectra are selected and labeled as $\omega_1, \omega_2, \omega_3$. The eigenfunctions for pressure and velocity perturbations corresponding to the three different eigenvalues are illustrated in Fig. 6, respectively. The eigenfunctions corresponding to the three eigenvalues are proved to be sort of non-orthogonal. The non-normality of the linearized Euler equations has influence on the growth rate of the perturbations in a short timescale.
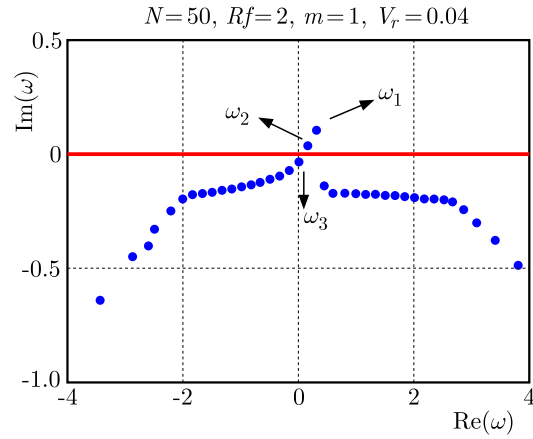
Fig. 5. Eigenvalue spectrum for $Rf = 2$, $m = 1$, $V_r = 0.04$

(a)



(b)



(c)
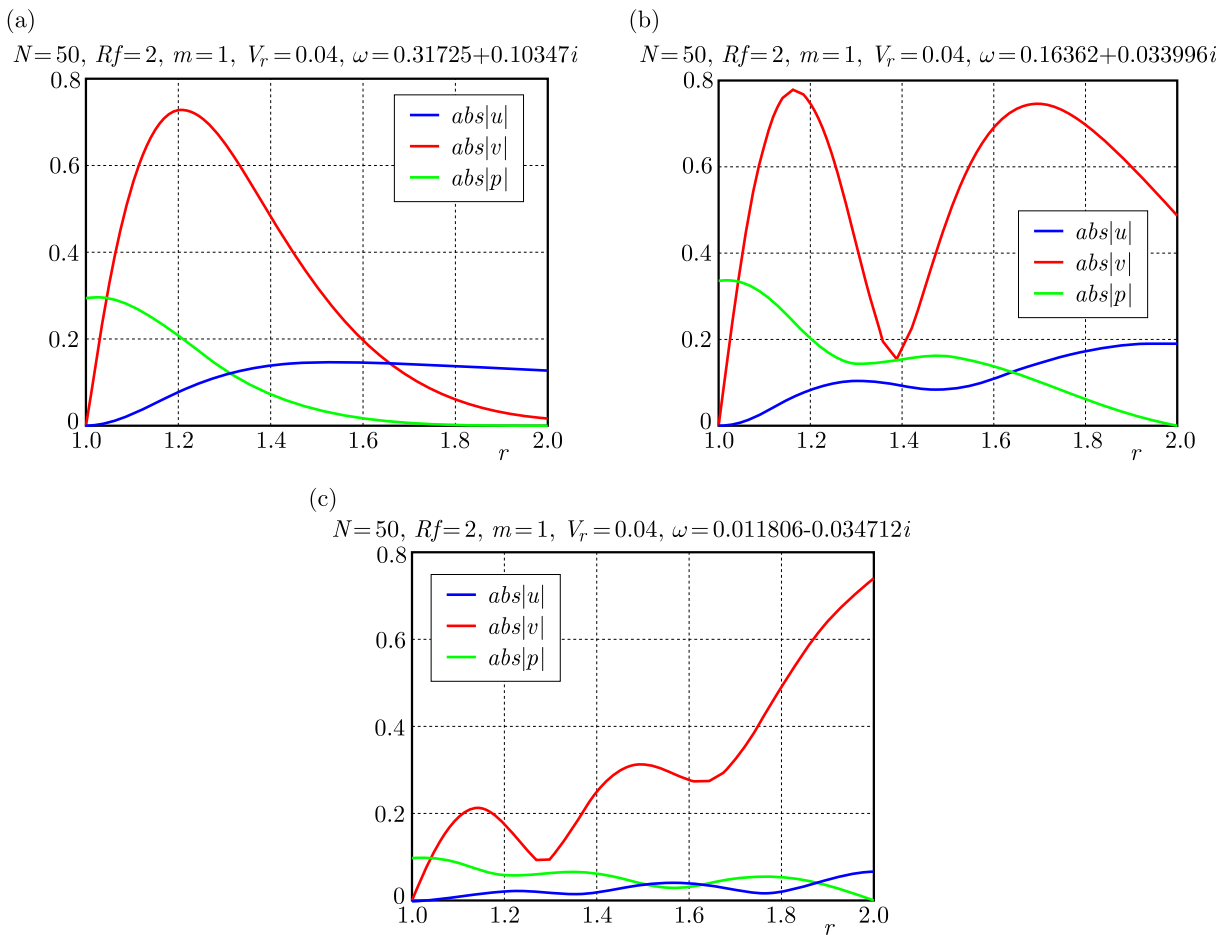


Fig. 6. Eigenfunctions corresponding to three eigenvalues for pressure and velocity perturbations: (a) – $\omega_1$, (b) – $\omega_2$, (c) – $\omega_3$

## 4.    Application of the present stability model

### 4.1.    Comparison with experimental results in (Kinoshita and Senoo, 1985)

In order to verify the results of the present analysis, the experiment results by Kinoshita and Senoo (1985) are compared with the predictions from the 2D stability model. In the experiment by Kinoshita and Senoo (1985), a back sweep angle of $\beta = 24.6°$ was set at the impeller exit,

and two different values of the radial ratio $Rf$ were tested. The experiment was undertaken at a low speed, and the inlet velocity distribution was not reported. The present 2D incompressible stability model has been applied to the experimental set up with a uniform inlet velocity distribution.

Since the rotating stall number observed in (Kinoshita and Senoo, 1985) is 3, the comparison of the critical flow angle in (Kinoshita and Senoo, 1985), Shen's in (Chen *et al.*, 2011) and the present method for the wave number $m = 3$ is given in Table 2. It can be shown that the result of the present stability analysis is much closer to the experiential data by Kinoshita and Senoo (1985) than those derived from Shen's 3D model.

**Table 2.** Comparison of the critical flow angle from experiment (Kinoshita and Senoo, 1985), Shen's result and current analysis

| $Rf$ | $\beta$ [°] | $m$ | $\alpha$ [°] | | |
|---|---|---|---|---|---|
| | | | experiment | Shen | present model |
| 1.4 | 24.6 | 3 | 5.2 | 7.925 | 6.657 |
| 1.67 | 24.6 | 3 | 5.5 | 12.82 | 11.631 |

At a smaller $Rf$, the agreement between the current method and the experiment is good. At the same time, this study suggests that the flow becomes significantly less stable for a larger radial ratio, whereas the experiment shows only a small deterioration of the stability.

### 4.2. Comparison with the experimental results in (Abidogun, 2002)

In (Abidogun, 2002) the experimental rig, as shown in Fig. 7, consists of an impeller with radial blades and a vaneless diffuser. Three different values of $Rf$ were tested. According to the results given in (Abidogun, 2002), the stall wave number were always between 2-4. What makes rig in (Abidogun, 2002) different from that in (Kinoshita and Senoo, 1985) is the larger axial width $b_z$ ($> 0.1$), which is more suitable for the models based on inviscid core flow theories such as Shen's and the present analysis.
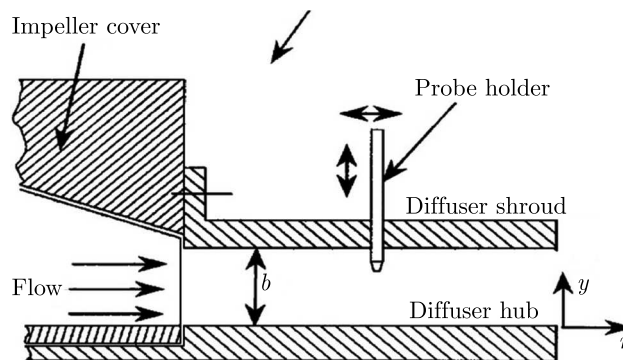


Fig. 7. The experimental rig for a vaneless diffuser in (Abidogun, 2002)

It is illustrated in Table 3 that the inlet critical flow velocity at the onset of stall derived by Abidogun (2002), Shen's model and the present stability analysis shows the same trend of increase with the diffuser radial ratio $Rf$. For a smaller radius ratio of the diffuser $Rf$, the prediction results of the present model and Shen's model show a higher accuracy than those for the radius ratio 2.0. Compared with the results in (Kinoshita and Senoo, 1985), the predicted critical inlet velocity for different radius ratios obtained in this test are all much closer to the experimental results. One main reason for this lies in that the present analysis and Shen's model are both based on the core flow assumption, which is more suitable for vaneless diffusers with large width.

**Table 3.** Comparison of the inlet critical flow in (Abidogun, 2002), Shen's and the present stability analysis

| $Rf$ | $m$ | $V_{rc}$ | | |
|---|---|---|---|---|
| | | Abidogun | Shen | present model |
| 1.5 | 3 | 0.16 | 0.1525 | 0.152 |
| 1.7 | 3 | 0.216 | 0.2150 | 0.215 |
| 2.0 | 3 | 0.255 | 0.2925 | 0.294 |

## 5.  Conclusions

In this research, a two dimensional stability model of a vaneless diffuser in a centrifugal compressor based on stability analysis is proposed. The independence of the number collocation points and the influence of geometric parameters on the stability of the vaneless diffuser are verified. The capability of the present model to predict the onset of stall with different radius ratios is validated against several experimental data. The present model is effective in stall prediction for a wide vaneless diffuser. Compared to Moore's and Shen's stability models, the advantage of the present model lies in direct calculation and providing both the complex eigenspectrum and rotational speed instead of multiple trials and iterations. Another remarking superiority is that the present model investigates the instability induced by the inviscid main flow, and provides the fundamental research for further study of the unsteady interaction of the inviscid main flow and the boundary layers.

In our investigation, the significant effects of the diffuser radius ratio on diffuser stability are confirmed. The stability deteriorates rapidly with an increase in the radius ratio. The largest critical inflow angle is obtained when the wave number $m$ is around 3-5 for the radius ratio between 1.5 to 2.2. Through model assessment, this model has the capability of predicting the onset of stall in vaneless diffusers and can be applied in the cases without considering the axial distribution of inlet velocity. However, in the cases where the axial distribution of inlet velocity plays significant role, the application of a 3D stability model is required.

## References

1. ABDELHAMID A.N., 1980, Analysis of rotating stall in vaneless diffusers of centrifugal compressors, *Canadian Aeronautics and Space Journal*, **26**, 118-128

2. ABDELHAMID A.N., 1983, Effects of vaneless diffuser geometry on flow instability in centrifugal compression systems, *Canadian Aeronautics and Space Journal*, **29**, 259-266

3. ABIDOGUN K.B., 2002, Effects of vaneless diffuser geometries on rotating stall, *Journal of Propulsion and Power*, **22**, 3, 542-549

4. BIANCHINI A., BILIOTTI D., BELARDINI E., GIACHI M., TAPINASSI L., VANNINI G., FERRARI L., FERRARA G., 2013, A systematic approach to estimate the impact of the aerodynamic force induced by rotating stall in a vaneless diffuser on the rotordynamic behavior of centrifugal compressor, *Journal of Engineering for Gas Turbines and Power*, **135**, 11

5. CANUTO B.C., HUSSAINI M.Y., QUARTERONI A., ZANG T.A., 2010, *Spectral Methods: Evolution to Complex Geometries and Applications to Fluid Dynamics*, Springer

6. CHEN H., SHEN F., ZHU X.C., DU Z.H., 2011, A 3D compressible flow model for weak rotating waves in vaneless diffusers. Part I: The model and Mach number effects, *Journal of Turbomachinery*, **134**, 4, 041010

7. DAY I.J., 2016, Stall, surge, and 75 years of research, *Journal of Turbomachinery*, **138**

8. EVERITT J.N., 2010, Investigation of stall inception in centrifugal compressors using isolated diffuser simulations, M.S. Thesis, MIT, Cambridge, MA

9. EVERITT J., SPAKOVSZKY Z., 2013, An investigation of stall inception in centrifugal compressor vaned diffuser, *Journal of Turbomachinery*, **135**

10. FRIGNE P., BRAEMBUSSCHE R.V.D., 1985, A theoretical model for rotating stall in the vaneless diffuser of a centrifugal compressor, *Journal of Engineer for Gas Turbines and Power*, **107**, 2. 507-513

11. JANSEN W., 1964, Rotating stall in a radial vaneless diffuser, *ASME Journal of Basic Engineering*, **86**, 4, 750-758

12. KINOSHITA Y., SENOO Y., 1985, Rotating stall induced in vaneless diffusers of very low specific speed centrifugal blowers, *Journal of Engineering for Gas Turbines and Power*, **107**, 514-521

13. MEERBERGEN K., ROOSE D., 1997, The restarted Arnoldi method applied to iterative linear system solvers for the computation of rightmost eigenvalues, *SIAM Journal on Matrix Analysis and Applications*, **18**, 1, 1-20

14. MOLER C.B., STEWART G.W., 1973, An algorithm for generalized matrix eigenvalue problems, *SIAM Journal on Numerical Analysis*, **10**, 2, 241-256

15. MOORE F.K., 1989, Weak Rotating flow disturbances in a centrifugal compressor with a vaneless diffuser, *Journal of Turbomachinery*, **111**, 442-449

16. PETERS G., WILKINSON J.H., 1979, Inverse iteration, Ill-conditioned equations and Newton's method, *SIAM Review*, **21**, 3, 339-360

17. SENOO Y., KINOSHITA Y., 1977, Influence of inlet flow condition and geometries of a centrifugal vaneless diffuser on critical flow angle for reverse flow, *Journal of Fluids Engineering*, **99**, 1, 98-103

18. SENOO Y., KINOSHITA Y., 1978, Limits of rotating stall and stall in vaneless diffuser of centrifugal compressors, *ASME Paper 78-GT-19*

19. SLEIJPEN G.L.G., VAN DER VORST H.A., 1994, A Jacobi-Davidson iteration method for linear eigenvalue problems, *SIAM Review*, **17**, 2, 267-293

20. SPAKOVSZKY Z., RODUNER C., 2009, Spike and modal stall inception in an advanced turbocharger centrifugal compressor, *Journal of Turbomachinery*, **131**

21. SUN X.F., LIU X.H., SUN D.K., SUN X., 2013, A theoretical model for flow instability inception in transonic fan/compressors, *ASME Turbo Expo 2013: Turbine Technical Conference and Exposition*

22. SUN X.F., MA Y.F., LIU X.H., SUN D.K., 2016, Flow stability model of centrifugal compressor based on eigenvalue approach, *AIAA Journal*

23. UBBEN S., NIEHUIS R., 2015, Experimental investigation of the diffuser vane clearance effect in a centrifugal compressor stage with adjustable diffuser geometry. Part I: Compressor performance analysis, *Journal of Turbomachinery*, **137**

# EXACT SOLUTION FOR LARGE AMPLITUDE FLEXURAL VIBRATION OF NANOBEAMS USING NONLOCAL EULER-BERNOULLI THEORY

Reza Nazemnezhad

*School of Engineering, Damghan University, Damghan, Islamic Republic of Iran*

*e-mail: rnazemnezhad@du.ac.ir*

Shahrokh Hosseini-Hashemi

*School of Mechanical Engineering, Iran University of Science and Technology, Narmak, Tehran, Iran and*

*Center of Excellence in Railway Transportation, Iran University of Science and Technology, Narmak, Tehran, Iran*

In this paper, nonlinear free vibration of nanobeams with various end conditions is studied using the nonlocal elasticity within the frame work of Euler-Bernoulli theory with von Kármán nonlinearity. The equation of motion is obtained and the exact solution is established using elliptic integrals. Two comparison studies are carried out to demonstrate accuracy and applicability of the elliptic integrals method for nonlocal nonlinear free vibration analysis of nanobeams. It is observed that the phase plane diagrams of nanobeams in the presence of the small scale effect are symmetric ellipses, and consideration the small scale effect decreases the area of the diagram.

*Keywords:* nonlinear free vibration, nonlocal elasticity, nanobeam, exact solution, elliptic integrals

## 1. Introduction

Due to superior properties, nanostructures have attracted much attention in the recent years. Multiple recent experimental results have shown that as the size of the structures reduces to micro/nanoscale, the influences of atomic forces and small scale play a significant role in mechanical properties of these nano-structures (Chong *et al.*, 2001; Fleck *et al.*, 1994; Ma and Clarke, 1995). Thus, neglecting these effects in some cases may results in completely incorrect solutions and hence wrong designs. The classical continuum theories do not include any internal length scale. Consequently, these theories are expected to fail when the size of the structure becomes comparable with the internal length scale. Eringen's nonlocal theory is one of the well-known continuum mechanics theories (Eringen, 2002) that includes small scale effects with good accuracy to micro/nanoscale devises modeling. The nonlocal elasticity theory assumes that the stress at a point is a function of the strain at all neighbor points of the body.

In the recent years, studies of nanostructures by using the nonlocal elasticity theory have been an area of active research. Based on this theory, Reddy (2007) derived the equation of motion of various kinds of beam theories available (Euler-Bernoulli, Timoshenko, Reddy and Levinson) and reached analytical and numerical solutions on static deflections, buckling loads, and natural frequencies. Hosseini-Hashemi *et al.* (2013) considered surface effects on free vibration of Euler-Bernoulli and Timoshenko nanobeams by using the nonlocal elasticity theory. Xie *et al.* (2006) considered the radial buckling pressure of a simply supported multi-walled carbon nanotube in the presence of the small scale effects. Kiani (2010) studied free longitudinal vibration of tapered nanowires. In (Heireche *et al.*, 2008; Narendar and Gopalakrishnan, 2009; Wang and Hu, 2005; Wang, 2005; Wang and Varadan, 2007), the effect of small scales on wave propagation of single- and multi-walled carbon nanotubes was considered. As an application of Eringen's

nonlocal theory to post-buckling analysis of single-walled carbon nanotubes, it can be referred to the work done by Setoodeh *et al.* (2011).

The nonlocal elasticity theory has also been used for nonlinear analyses of nanostructures, especially nanobeams. In this area, Reddy (2010) derived a nonlocal nonlinear formulation for bending of classical and shear deformation theories of beams and plates, but he did not present any numerical results. Yang and Lim (2009) examined the effect of the nonlocal parameter on nonlinear vibrations of Euler nanobeams. To evaluate the nonlinear natural frequencies, the method of multiple scales was applied to the governing equation. The method of multiple scales was also used in (Nazemnezhad and Hosseini-Hashemi, 2014; Hosseini-Hashemi *et al.*, 2014) for evaluating the nonlocal nonlinear natural frequencies of functionally graded Euler-Bernoulli nanobeams. Fang *et al.* (2013), Ghorbanpour Arani *et al.* (2012), Ansari and Ramezannezhad (2011), Yang *et al.* (2010) and Ke *et al.* (2009) investigated nonlinear free vibration of single and multi-walled carbon nanotubes with the aid of the nonlocal elasticity theory.

In the mentioned references, a numerical method, the DQ method, semi analytical methods, the harmonic balance method and the method of multiple scales have been employed to solve the nonlocal nonlinear governing equations. Hence, no exact closed-form solution is available in the literature for nonlocal nonlinear analyses of nanobeams. Motivated by the literature survey, this study aims to investigate the nonlocal nonlinear free vibration of Euler-Bernoulli nanobeams by an exact solution called the elliptic integrals. To this end, firstly, the governing equation of motion of the Euler-Bernoulli nanobeam has been obtained in the nonlocal form. Then, a closed-form expression for the nonlocal nonlinear natural frequencies has been presented by using the elliptic integrals. Finally, the accuracy of the present exact results are compared with those reported in literature, and the small scale effects on the phase plane diagram and higher frequency ratios are considered in the results and discussion śection.

## 2. Formulation

Consider a nanobeam with length $L$ ($0 \leqslant x \leqslant L$), thickness $2h$ ($-h \leqslant z \leqslant h$) and width $b$ ($-b/2 \leqslant y \leqslant b/2$) (Fig. 1). Upon the Euler-Bernoulli beam model, the displacement field at any point of the nanobeam can be written as

$$u_x(x,z,t) = U(x,t) - z\frac{\partial W(x,t)}{\partial x} \qquad u_z(x,z,t) = W(x,t) \tag{2.1}$$

where $U(x,t)$ and $W(x,t)$ are the displacement components of the mid-plane at time $t$. In accordance, the von Kármán type of the nonlinear strain-displacement relationship is

$$\varepsilon_{xx} = \frac{\partial u_x}{\partial x} + \frac{1}{2}\Big(\frac{\partial u_z}{\partial x}\Big)^2 = \frac{\partial U}{\partial x} - z\frac{\partial^2 W}{\partial x^2} + \frac{1}{2}\Big(\frac{\partial W}{\partial x}\Big)^2 \tag{2.2}$$
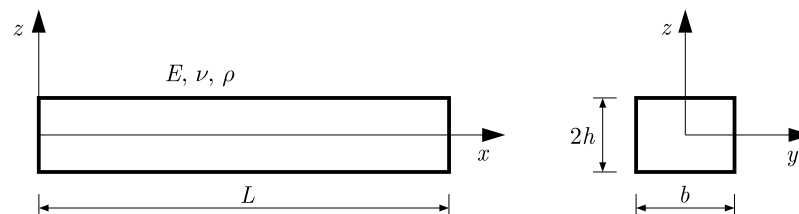


Fig. 1. Geometry of the problem

Now, by using Hamilton's principle, the nonlinear equations of motion of the nanobeam can be derived as

$$\frac{\partial N_{xx}}{\partial x} = \rho A\frac{\partial^2 U}{\partial t^2} \qquad \frac{\partial^2 M_{xx}}{\partial x^2} + \frac{\partial}{\partial x}\Big(N_{xx}\frac{\partial W}{\partial x}\Big) = \rho A\frac{\partial^2 W}{\partial t^2} \tag{2.3}$$

where $N_{xx}$ and $M_{xx}$ are the local force and bending moment resultants, respectively, given by

$$N_{xx} = \int_A \sigma_{xx}\, dA = EA\left[\frac{\partial U}{\partial x} + \frac{1}{2}\left(\frac{\partial W}{\partial x}\right)^2\right] \qquad M_{xx} = \int_A z\sigma_{xx}\, dA = -EI\frac{\partial^2 W}{\partial x^2} \qquad (2.4)$$

Equations of motions, Eqs. (2.3), can be used in the nonlocal form

$$\frac{\partial N_{xx}^{nl}}{\partial x} = \rho A\frac{\partial^2 U}{\partial t^2} \qquad \frac{\partial^2 M_{xx}^{nl}}{\partial x^2} + \frac{\partial}{\partial x}\left(N_{xx}^{nl}\frac{\partial W}{\partial x}\right) = \rho A\frac{\partial^2 W}{\partial t^2} \qquad (2.5)$$

where the superscript *nl* denotes nonlocal. If the axial inertia is neglected, Eq. $(2.5)_1$ gives

$$N_{xx}^{nl} = N_0 = \text{const} \qquad (2.6)$$

The nonlocal force and bending moment resultants can be obtained by multiplying the left-
-hand side of Eqs. (2.4) by $(1 - \mu\nabla^2)$, using Eqs. (2.5) and (2.6), and doing some mathematical manipulation. Then they are given by

$$N_{xx}^{nl} = EA\left[\frac{\partial U}{\partial x} + \frac{1}{2}\left(\frac{\partial W}{\partial x}\right)^2\right] \qquad M_{xx}^{nl} = -EI\frac{\partial^2 W}{\partial x^2} + \mu\left(-N_{xx}^{nl}\frac{\partial^2 W}{\partial x^2} + \rho A\frac{\partial^2 W}{\partial t^2}\right) \qquad (2.7)$$

For nanobeams with immovable ends (i.e. $U$ and $W = 0$, at $x = 0$ and $L$) and with Eq. (2.6) in mind, integrating Eq. $(2.7)_1$ with respect to $x$ leads to

$$N_{xx}^{nl} = N_0^{nl} = \frac{EA}{2L}\int_0^L \left(\frac{\partial W}{\partial x}\right)^2 dx \qquad (2.8)$$

Finally, by substituting Eqs. $(2.7)_2$ and (2.8) in Eq. $(2.5)_2$, the nonlocal nonlinear governing equation for the Euler-Bernoulli nanobeam can be obtained as

$$-EI\frac{\partial^4 W}{\partial x^4} + \mu\rho A\frac{\partial^4 W}{\partial x^2\partial t^2} + P\int_0^L \left(\frac{\partial W}{\partial x}\right)^2 dx\left(\frac{\partial^2 W}{\partial x^2} - \mu\frac{\partial^4 W}{\partial x^4}\right) - \rho A\frac{\partial^2 W}{\partial t^2} = 0 \qquad (2.9)$$

where $P = EA/(2L)$, $I = 2bh^3/3$, and the equation of motion of the conventional Euler–Bernoulli beam theory can be obtained from Eq. (2.9) by setting $\mu = 0$.

For nonlinear free vibration analysis, the averaging technique over the space variable (Galerkin's method) is used to convert Eq. (2.9) into an ordinary differential equation. Hence, the transverse displacement of the $n$-th mode can be assumed as (Azrar *et al.*, 1999, 2002)

$$W(x,t) = D\phi(x)q(t) \qquad (2.10)$$

where $D$ is an arbitrary constant which represents the amplitude of deflection, $q(t)$ is a time dependent function to be determined and $\phi(x)$ is the linear mode shape obtained as follows (Rao, 2007)

$$\begin{aligned} \text{SS}: \quad & \phi_n(x) = \sin\left(\frac{n\pi}{L}x\right) \\ \text{SC}: \quad & \phi_n(x) = \sin(\zeta_1 x) - \frac{\sin(\zeta_1 L)}{\sinh(\zeta_2 L)}\sinh(\zeta_2 x) \end{aligned} \qquad (2.11)$$

where

$$\zeta_{1,2} = \sqrt{\frac{1}{2}\left(\pm\frac{\mu\rho A\omega^2}{EI} + \sqrt{\left(\frac{\mu\rho A\omega^2}{EI}\right)^2 + \frac{4\rho A\omega^2}{EI}}\right)}$$

The parameters $\zeta_1$ and $\zeta_2$ can be determined from the eigenvalue equation

$$\zeta_2 \tan(\zeta_1 L) - \zeta_1 \tanh(\zeta 2L) = 0$$

Substituting Eq. (2.10) and its derivatives into Eq. (2.9), then multiplying by the linear mode shape and integrating along the length of nanobeam, results in

$$\ddot{q} - \gamma_1 q + \gamma_2 q^3 = 0 \tag{2.12}$$

where

$$\gamma_1 = \frac{EIa_4}{\mu\rho Aa_3 - \rho Aa_1} \qquad \gamma_2 = \frac{IPa_2(a_3 - \mu a_4)}{\mu\rho A^2 a_3 - \rho A^2 a_1}\left(\frac{D}{r}\right)^2$$

$$a_1 = \int_0^L \phi^2(x)\,dx \qquad a_2 = \int_0^L \left(\frac{d\phi(x)}{dx}\right)^2 dx$$

$$a_3 = \int_0^L \phi(x)\frac{d^2\phi(x)}{dx^2}\,dx \qquad a_4 = \int_0^L \phi(x)\frac{d^4\phi(x)}{dx^4}\,dx$$

and $r = \sqrt{I/A}$ is the radius of gyration.

Multiplying Eq. (2.12) by $\dot{q}$ and then integrating with respect to time, with the initial conditions $q(0) = 1$ and $\dot{q}(0) = 0$, leads to

$$\left(\frac{dq}{dt}\right)^2 = -\gamma_1(1 - q^2) + \frac{\gamma_2}{2}(1 - q^4) \tag{2.13}$$

Equation (2.13) can be rewritten as

$$\left(\frac{dq}{d(pt)}\right)^2 = (1 - q^2)(k^2 q^2 - k^2 + 1) \tag{2.14}$$

where $p^2 = -\gamma_1 + \gamma_2$ and $k^2 = \gamma_2/(2p^2)$. Supposing $q = \cos\theta$, and complement the modulus as $pt = \int_0^\theta (1 - k^2 \sin^2\theta)^{-1/2}\,d\theta$, the solution to Eq. (2.14) can be given by (Lestari and Hanagud, 2001)

$$q(t) = cn[pt, k] \tag{2.15}$$

where $cn$ is a Jacobi elliptic function. The Jacobi elliptic functions are real for real $p$ and real $k^2$ between 0 and 1 (Byrd $et\ al.$, 1971). $K$ is defined by using the complete elliptic integral as

$$K = \int_0^{\pi/2} \frac{d\theta'}{\sqrt{1 - k^2 \sin^2\theta'}} \tag{2.16}$$

Therefore, the nonlocal natural frequency for nonlinear free vibration of nanoscale beams for each mode can be expressed as

$$\omega_{nl}^{nl} = \frac{\pi\sqrt{-\gamma_1 + \gamma_2}}{2K} \tag{2.17}$$

where the subscript $nl$ denotes nonlinear.

### 3. Results and discussion

Before presenting numerical results, it is worth to note here that in order to convert the governing equation of motion, Eq. (2.9), into an ordinary differential equation, Eq. (2.12), single-mode Galerkin's method is used. This method can provide the nonlinear natural frequency of nanobeams with a good accuracy at low amplitude ratios (Ke *et al.*, 2010). At higher amplitude ratios, multi-mode Galerkin's method is proposed because the effect of coupling of modes increases (Chandra and Raju, 1975). Therefore, in order to have the highest possible accuracy in the following discussion all results are presented for low amplitude ratios, $D/r \leqslant 3$.

Table 1 gives the fundamental local nonlinear frequency to fundamental local linear frequency ratio $\omega_{nl}/\omega_l$ of a nanobeam with SS and SC end conditions for various values of the amplitude ratio $D/r$. The solutions obtained by using numerical and approximate methods like GFEM (Galerkin Finite Element Method) (Bhashyam and Prathap, 1980), RGFEM (Reduced Galerkin Finite Element Method) (Bhashyam and Prathap, 1980), ASM (Assumed Space Method) (Evensen, 1968), and DQM (Differential Quadrature Method) (Malekzadeh and Shojaee, 2013) are also provided for direct comparison. It is observed that the present results agree very well with those given by Malekzadeh and Shojaee (2013), Bhashyam and Prathap (1980) and Evensen (1968). It is also seen from Table 1 that the present results obtained by the exact method are smaller than those given by numerical and approximate methods. It can be attributed to this fact that natural frequencies obtained by numerical and approximate methods are the upper bound of the exact ones.

**Table 1.** Comparison of the fundamental local frequency ratio $\omega_{nl}/\omega_l$ for a nanobeam with SS and SC end conditions $\mu = 0$, $E = 70$ GPa, $\rho = 2700$ kg/m$^3$, $\nu = 0.3$, $L/h = 100$

| $D/r$ | SS | | | | SC | | | | |
|---|---|---|---|---|---|---|---|---|---|
| | Present (Exact) | GFEM [4] | RGFEM [4] | ASM [9] | Present (Exact) | GFEM [4] | RGFEM [4] | ASM [9] | DQM [21] |
| 0.5 | 1.0231 | 1.0308 | 1.0308 | 1.0308 | 1.0130 | 1.0165 | 1.0165 | 1.0676 | – |
| 1.0 | 1.0892 | 1.1180 | 1.1180 | 1.1180 | 1.0507 | 1.0641 | 1.0641 | 1.0763 | 1.0641 |
| 1.5 | 1.1902 | 1.2499 | 1.2499 | 1.2500 | 1.1105 | 1.1379 | 1.1379 | 1.0905 | – |
| 2.0 | 1.3178 | 1.4142 | 1.4142 | 1.4142 | 1.1886 | 1.2319 | 1.2319 | 1.1099 | 1.2319 |
| 2.5 | 1.4647 | 1.6008 | 1.6008 | 1.6008 | 1.2814 | 1.3407 | 1.3407 | 1.1342 | – |
| 3.0 | 1.6257 | 1.8028 | 1.8028 | 1.8028 | 1.3860 | 1.4601 | 1.4601 | 1.1631 | 1.4605 |
| 3.5 | 1.7970 | 2.0158 | 2.0158 | 2.0156 | 1.4998 | 1.5865 | 1.5865 | 1.1963 | – |
| 4.0 | 1.9760 | 2.2365 | 2.2365 | 2.2361 | 1.6209 | 1.7166 | 1.7166 | 1.2334 | – |
| 4.5 | 2.1608 | 2.4630 | 2.4630 | 2.4622 | 1.7477 | 1.8455 | 1.8455 | 1.2741 | – |
| 5.0 | 2.3501 | 2.6937 | 2.6937 | 2.6926 | 1.8792 | 1.9651 | 1.9651 | 1.3181 | – |

[4] – Bhashyam and Prathap (1980), [9] – Evensen (1968),
[21] – Malekzadeh and Shojaee (2013)

In Table 2, the fundamental nonlocal nonlinear frequency to fundamental local nonlinear frequency ratios $\omega_{nl}^{nl}/\omega_{nl}$ obtained by the present exact solution for a nanobeam with SS and SC boundary conditions is compared with those given by the semi-analytical approach called the multiple scales method (MSM) (Nazemnezhad and Hosseini-Hashemi, 2014). The results are listed for various values of the nanobeam length, amplitude ratio, and nonlocal parameter. Table 2 shows that the present exact results are identical to those reported by Nazemnezhad and Hosseini-Hashemi (2014) using the multiple scales method. However, the difference between the two approaches increases for higher amplitude ratios. This is due to the fact that the accuracy of the multiple scales method depends on the number of slow scale variables in the expansion series.

**Table 2.** Comparison of the fundamental nonlocal frequency ratio $\omega_{nl}^{nl}/\omega_{nl}$ for a nanobeam with SS and SC end conditions $E = 210\,\text{GPa}$, $\rho = 2370\,\text{kg/m}^3$, $\nu = 0.24$, $b = h = 0.1L$

| Boundary condition | Length [nm] | $\mu$ [nm$^2$] | $D/r = 1$ | | | $D/r = 2$ | | |
|---|---|---|---|---|---|---|---|---|
| | | | Present (Exact) | MSM [23] | $AD^* \cdot 100$ | Present (Exact) | MSM [23] | $AD \cdot 100$ |
| SS | 10 | 2 | 0.9278 | 0.9293 | 0.15 | 0.9509 | 0.9631 | 1.22 |
| | | 4 | 0.8724 | 0.8754 | 0.30 | 0.9141 | 0.9379 | 2.38 |
| | 20 | 2 | 0.9800 | 0.9803 | 0.03 | 0.9863 | 0.9893 | 0.30 |
| | | 4 | 0.9613 | 0.9621 | 0.08 | 0.9736 | 0.9797 | 0.61 |
| | 30 | 2 | 0.9909 | 0.9911 | 0.02 | 0.9938 | 0.9951 | 0.13 |
| | | 4 | 0.9821 | 0.9824 | 0.03 | 0.9877 | 0.9905 | 0.28 |
| SC | 10 | 2 | 0.9189 | 0.9202 | 0.13 | 0.9547 | 0.9676 | 1.29 |
| | | 4 | 0.8596 | 0.8625 | 0.29 | 0.9239 | 0.9519 | 2.80 |
| | 20 | 2 | 0.9771 | 0.9774 | 0.03 | 0.9869 | 0.9899 | 0.30 |
| | | 4 | 0.9561 | 0.9567 | 0.06 | 0.9751 | 0.9812 | 0.61 |
| | 30 | 2 | 0.9896 | 0.9897 | 0.01 | 0.9940 | 0.9953 | 0.13 |
| | | 4 | 0.9795 | 0.9798 | 0.03 | 0.9883 | 0.9909 | 0.26 |

$^*$ – Absolute of difference, [23] – Nazemnezhad and Hosseini-Hashemi (2014)

**Table 3.** Frequency ratios of the nanobeam for various mode numbers, amplitude ratios, nanobeam lengths, nonlocal parameters and boundary conditions

| $D/r$ | Length [nm] | $\mu$ [nm$^2$] | Boundary condition | Mode number $n$ | | |
|---|---|---|---|---|---|---|
| | | | | 1 | 2 | 3 |
| 1 | 10 | 2 | SS | 0.9278 | 0.7921 | 0.6778 |
| | | | SC | 0.9189 | 0.7864 | 0.6800 |
| | | 4 | SS | 0.8724 | 0.6948 | 0.5832 |
| | | | SC | 0.8595 | 0.6959 | 0.5982 |
| | 20 | 2 | SS | 0.9800 | 0.9278 | 0.8605 |
| | | | SC | 0.9771 | 0.9233 | 0.8561 |
| | | 4 | SS | 0.9613 | 0.8724 | 0.7764 |
| | | | SC | 0.9561 | 0.8661 | 0.7728 |
| 2 | 10 | 2 | SS | 0.9509 | 0.8621 | 0.7918 |
| | | | SC | 0.9547 | 0.8751 | 0.8141 |
| | | 4 | SS | 0.9141 | 0.8020 | 0.7377 |
| | | | SC | 0.9239 | 0.8316 | 0.7806 |
| | 20 | 2 | SS | 0.9863 | 0.9509 | 0.9062 |
| | | | SC | 0.9869 | 0.9528 | 0.9100 |
| | | 4 | SS | 0.9736 | 0.9141 | 0.8522 |
| | | | SC | 0.9751 | 0.9190 | 0.8620 |
| 3 | 10 | 2 | SS | 0.9677 | 0.9108 | 0.8674 |
| | | | SC | 0.9867 | 0.9423 | 0.9069 |
| | | 4 | SS | 0.9439 | 0.8736 | 0.8352 |
| | | | SC | 0.9790 | 0.9281 | 0.8990 |
| | 20 | 2 | SS | 0.9909 | 0.9677 | 0.9388 |
| | | | SC | 0.9960 | 0.9768 | 0.9513 |
| | | 4 | SS | 0.9826 | 0.9439 | 0.9046 |
| | | | SC | 0.9925 | 0.9610 | 0.9274 |

The above discussion verified the merit, high accuracy and applicability of the present exact solution, elliptic integrals, for nonlocal nonlinear free vibration analysis of nanobeams with various boundary conditions. In the following discussion, the small scale effects on the nonlinear free vibration of nanobeams are considered for higher mode numbers and phase plane diagrams ($\dot{q}(t)$ versus $q(t)$). A nanobeam made of aluminum (Al) with the bulk elastic properties $E = 70\,\text{GPa}$, $\nu = 0.35$, $\rho = 2700\,\text{kg/m}^3$ (Ogata *et al.*, 2002) and square cross section $b = 2h = 0.1L$ is considered as an illustrative example.
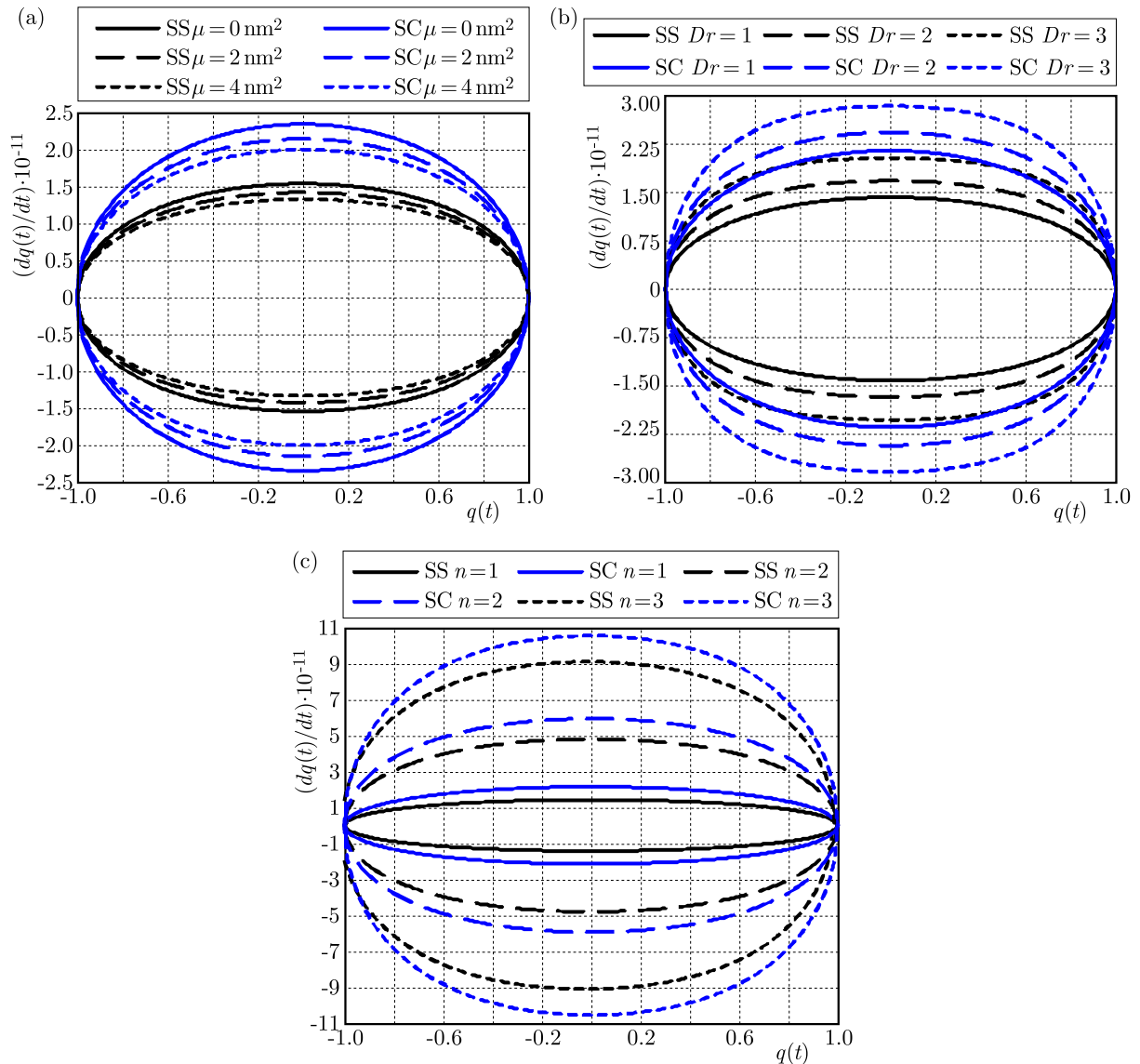


Fig. 2. Phase plane diagrams for the nanobeam: (a) $D/r = 1$, $n = 1$, $L = 10\,\text{nm}$; (b) $n = 1$, $L = 10\,\text{nm}$, $\mu = 2\,\text{nm}^2$, (c) $D/r = 1$, $L = 10$, $\mu = 2\,\text{nm}^2$

Table 3 examines the small scale effects on the first three nonlocal to local nonlinear frequency ratios $\omega_{nl}^{nl}/\omega_{nl}$ of the SS and SC nanobeams for various amplitude ratios and nanobeam lengths. It is seen from Table 3 that the decreasing effect of the nonlocal parameter on the frequency ratios is greater at higher mode numbers. In addition, regardless of the mode number, by increasing the nanobeam length and amplitude ratio, the decreasing effect of the nonlocal parameter on the frequency ratio decreases. Moreover, except for $D/r = 1$, the decreasing effect of the nonlocal parameter on the frequency ratio is more pronounced for nanobeams with softer boundary

conditions. When the amplitude ratio equals to 1, similar effects can only be seen at higher mode numbers and small lengths.

Figures 2a-2c display the phase plane diagrams ($\dot{q}(t)$ versus $q(t)$) for nanobeams with different conditions. It is observed from Figs. 2a-2c that the phase plane diagrams of nanobeams in the presence of the small scale effect are symmetric ellipses, and the diagrams of SC nanobeams are similar to those of SS nanobeams. Figure 2a exhibits that consideration of the small scale effect decreases the area of the diagram, and this reduction becomes greater by increasing the value of the nonlocal parameter. But it is seen from Figs. 2b and 2c that the area of the diagrams increases as the mode number and the amplitude ratio increase. In other words, an increase/decrease in the area of the diagrams due to the mentioned parameters is equivalent to an increase/decrease in the initial velocity condition.

## 4. Conclusion

This paper deals with exact solutions for large amplitude flexural vibration analysis of nonlocal Euler-Bernoulli nanobeams with SS and SC end conditions and von Kármán geometric nonlinearity. The equation of motion of nanobeam has been obtained in a nonlocal form and the exact analytical solution for natural frequency has been established using the exact elliptic integrals method. Two test examples are presented to demonstrate the accuracy of the formulation and applicability of the elliptic integrals method for nonlocal nonlinear free vibration analysis of nanobeams. It is observed that the small scale effect on the frequency ratios not only depends on the nanobeam dimensions and vibration amplitude, but also depends on the mode number and boundary conditions. In addition, it is seen that the small scale effect caused a reduction in the area of the phase plane diagrams of the nanobeams.

## References

1. ANSARI R., RAMEZANNEZHAD H., 2011, Nonlocal Timoshenko beam model for the large-amplitude vibrations of embedded multiwalled carbon nanotubes including thermal effects, *Physica E*, **43**, 1171-1178

2. AZRAR L., BENAMAR R., WHITE R., 1999, Semi-analytical approach to the non-linear dynamic response problem of S-S and C-C beams at large vibration amplitudes. Part I: General theory and application to the single mode approach to free and forced vibration analysis, *Journal of Sound and Vibration*, **224**, 183-207

3. AZRAR L., BENAMAR R., WHITE R., 2002, A semi-analytical approach to the non-linear dynamic response problem of beams at large vibration amplitudes. Part II: Multimode approach to the steady state forced periodic response, *Journal of Sound and Vibration*, **255**, 1-41

4. BHASHYAM G., PRATHAP G., 1980, Galerkin finite element method for non-linear beam vibrations, *Journal of Sound and Vibration*, **72**, 191-203

5. BYRD P.F., FRIEDMAN M.D., BYRD P., 1971, *Handbook of Elliptic Integrals for Engineers and Scientists*, Springer Berlin

6. CHANDRA R., RAJU B.B., 1975, Large deflection vibration of angle ply laminated plates, *Journal of Sound and Vibration*, **40**, 393-408

7. CHONG A., YANG F., LAM D., TONG P., 2001, Torsion and bending of micron-scaled structures, *Journal of Materials Research*, **16**, 1052-1058

8. ERINGEN A.C., 2002, *Nonlocal Continuum Field Theories*, Springer

9. EVENSEN D., 1968, Nonlinear vibrations of beams with various boundary conditions, *AIAA Journal*, **6**, 370-372

10. Fang B., Zhen Y.-X., Zhang C.-P., Tang Y., 2013, Nonlinear vibration analysis of double-walled carbon nanotubes based on nonlocal elasticity theory, *Applied Mathematical Modelling*, **37**, 1096-1107

11. Fleck N., Muller G., Ashby M., Hutchinson J., 1994, Strain gradient plasticity: theory and experiment, *Acta Metallurgica et Materialia*, **42**, 475-487

12. Ghorbanpour Arani A., Atabakhshian V., Loghman A., Shajari A., Amir S., 2012, Nonlinear vibration of embedded SWBNNTs based on nonlocal Timoshenko beam theory using DQ method, *Physica B*, **407**, 2549-2555

13. Heireche H., Tounsi A., Benzair A., Maachou M., Adda Bedia E., 2008, Sound wave propagation in single-walled carbon nanotubes using nonlocal elasticity, *Physica E*, **40**, 2791-2799

14. Hosseini-Hashemi S., Fakher M., Nazemnezhad R., 2013, Surface effects on free vibration analysis of nanobeams using nonlocal elasticity: A comparison between Euler-Bernoulli and Timoshenko, *Journal of Solid Mechanics*, **5**, 290-304

15. Hosseini-Hashemi S., Nazemnezhad R., Bedroud M., 2014, Surface effects on nonlinear free vibration of functionally graded nanobeams using nonlocal elasticity, *Applied Mathematical Modelling*, **38**, 3538-3553

16. Ke L.-L., Yang J., Kitipornchai S., 2010, An analytical study on the nonlinear vibration of functionally graded beams, *Meccanica*, **45**, 743-752

17. Ke L., Xiang Y., Yang J., Kitipornchai S., 2009, Nonlinear free vibration of embedded double-walled carbon nanotubes based on nonlocal Timoshenko beam theory, *Computational Materials Science*, **47**, 409-417

18. Kiani K., 2010, Free longitudinal vibration of tapered nanowires in the context of nonlocal continuum theory via a perturbation technique, *Physica E*, **43**, 387-397

19. Lestari W., Hanagud S., 2001, Nonlinear vibration of buckled beams: some exact solutions, *International Journal of Solids and Structures*, **38**, 4741-4757

20. Ma Q., Clarke D.R., 1995, Size dependent hardness of silver single crystals, *Journal of Materials Research*, **10**, 853-863

21. Malekzadeh P., Shojaee M., 2013, Surface and nonlocal effects on the nonlinear free vibration of non-uniform nanobeams, *Composites, Part B – Engineering*, **52**, 84-92

22. Narendar S., Gopalakrishnan S., 2009, Nonlocal scale effects on wave propagation in multi-walled carbon nanotubes, *Computational Materials Science*, **47**, 526-538

23. Nazemnezhad R., Hosseini-Hashemi S., 2014, Nonlocal nonlinear free vibration of functionally graded nanobeams, *Composites Structures*, **110**, 192-199

24. Ogata S., Li J., Yip S., 2002, Ideal pure shear strength of aluminum and copper, *Science*, **298**, 807-811

25. Rao S.S., 2007, *Vibration of Continuous Systems*, John Wiley & Sons

26. Reddy J., 2007, Nonlocal theories for bending, buckling and vibration of beams, *International Journal of Engineering Science*, **45**, 288-307

27. Reddy J., 2010, Nonlocal nonlinear formulations for bending of classical and shear deformation theories of beams and plates, *International Journal of Engineering Science*, **48**, 1507-1518

28. Setoodeh A., Khosrownejad M., Malekzadeh P., 2011, Exact nonlocal solution for post-buckling of single-walled carbon nanotubes, *Physica E*, **43**, 1730-1737

29. Wang L., Hu H., 2005, Flexural wave propagation in single-walled carbon nanotubes, *Physical Review B*, **71**, 195412

30. Wang Q., 2005, Wave propagation in carbon nanotubes via nonlocal continuum mechanics, *Journal of Applied Physics*, **98**, 124301

31. WANG Q., VARADAN V., 2007, Application of nonlocal elastic shell theory in wave propagation analysis of carbon nanotubes, *Smart Materials and Structures*, **16**, 178

32. XIE G., HAN X., LIU G., LONG S., 2006, Effect of small size-scale on the radial buckling pressure of a simply supported multi-walled carbon nanotube, *Smart Materials and Structures*, **15**, 1143

33. YANG J., KE L., KITIPORNCHAI S., 2010, Nonlinear free vibration of single-walled carbon nanotubes using nonlocal Timoshenko beam theory, *Physica E*, **42**, 1727-1735

34. YANG X., LIM C., 2009, Nonlinear vibrations of nano-beams accounting for nonlocal effect using a multiple scale method, *Science China Technological Sciences*, **52**, 617-621

# NUMERICALLY PREDICTED *J*-INTEGRAL AS A MEASURE OF CRACK DRIVING FORCE FOR STEELS 1.7147 AND 1.4762

GORAN VUKELIC

*University of Rijeka, Faculty of Maritime Studies Rijeka, Croatia*

*e-mail: gvukelic@pfri.hr*

JOSIP BRNIC

*University of Rijeka, Faculty of Engineering, Rijeka, Croatia*

Fracture behavior of two types of steel (1.4762 and 1.7147) is compared based on their numerically obtained *J*-integral values. The *J*-integral are chosen to quantify the crack driving force using the finite element (FE) stress analysis applied to single-edge notched bend (SENB) and compact tensile (CT) type fracture specimens. The resulting *J*-values are plotted for growing crack length ($\Delta a$ – crack length extension) at different $a/W$ ratios ($a/W$ – relative crack length; 0.25, 0.5, 0.75). Slightly higher resulting values of the *J*-integral for 1.4762 than 1.7147 can be noticed. Also, higher $a/W$ ratios correspond to lower *J*-integral values of the materials and vice versa. *J*-integral values obtained by using the FE model of the CT specimen give somewhat conservative results when compared with those obtained by the FE model of the SENB specimen.

*Keywords:* crack, steel 1.7147, steel 1.4762, FE analysis

## 1. Introduction

Material imperfections and failures due to the manufacturing process coupled with severe service conditions can lead to flaw appearance in engineering structures. Consequently, crack occurrence and its growth can seriously affect integrity of such structures leading to catastrophic failure. In order to avoid such a scenario, proper selection of materials is a step of great importance in the process of structural design. Selection of an improper material may affect product profitability, reduce its service lifetime and finally result in appearance of flaws and failure. Several requirements have to be met during the material selection process. These requirements include adequate strength of the material, acceptable rigidity level, resistance to elevated temperatures, etc., but also the material must be sufficiently resistant to crack propagation.

The resistance of the material to crack propagation in fracture mechanics is usually described through one or more parameters obtained by experimental research, like crack tip opening displacement (CTOD), *J*-integral or stress intensity factor $K$. Of all the above mentioned, the *J*-integral is suitable for trying to quantify the material resistance to crack elongation when observing ductile fracture in metallic materials (Kossakowski, 2012). When dealing with a growing crack, the obtained *J* values can be correlated to appropriate crack length extensions $\Delta a$ giving the resistance $R$ curve. Standardized experimental procedures are used to obtain the $R$ curve. Extensive experimental procedures can be, in some cases, accompanied or even substituted using some of the modern numerical methods, e.g. the finite element (FE) method. Recent research on the topic of numerical fracture mechanics includes accuracy check of *J*-integral values obtained by experiments, planar (2D) FE analysis, space (3D) FE analysis or the EPRI method (Qiao *et al.*, 2014). FE analysis of Mode I fracture in a compact tensile (CT) specimen has been conducted to reveal effects on micro, meso and macroscale (Saxena and Ramakrishnan, 2007),

while plastic geometry factors were determined numerically in order to calculate the $J$-integral from the load vs. crack mouth opening displacement or load-line displacement curve in the $J$-$R$ curve test (Huang *et al.*, 2014). Elastic and plastic constraint parameters for 3D problems were studied on single-edge notched bend (SENB) and CT specimens of non-standard configuration to characterize fracture resistance parameters (Shlyannikov *et al.*, 2014). Research on explaining procedures that guarantee the domain independent property when calculating the 3D $J$-integral for large deformation problems was carried out by Koshima and Okada (2015). A 3D domain integral method based on the extended FE method for extracting mixed-mode stress intensity factors was described by Wu *et al.* (2012).

The work presented in this paper is a comparison of numerically obtained $J$-integral values taken as a measure of the crack driving force for steels 1.7147 and 1.4762. Steel 1.7147 is usually used in production of spindles, pistons, bolts, levers, camshafts, gears, shafts, etc. The latter is a heat-resistant steel used in furnace industry, ceramics and cement industry, etc., i.e., in applications with high temperature and relatively low tensile requirements. Carbon, low alloy or high alloy ferritic steels can exhibit ductile fracture at elevated temperatures (Zhu and Joyce, 2015). Structures made of these or similar steels are more than susceptible to the flaw appearance and crack growth (Wagner *et al.*, 2010; Zangeneh *et al.*, 2014; Gojic *et al.*, 2011). Observing these examples, it is easy to understand the need for fracture characterization of such materials.

## 2.    Material properties

Two materials are compared: structural steel 1.7147 (AISI 5120, 20MnCr5) and high chromium stainless steel 1.4762 (AISI 446, X10CrAlSi25). Chemical compositions of the mentioned materials are given in Tables 1 and 2. Composition of steel 1.7147 can be compared to the standard EN 10084-2008. Here, the content of carbon equals the maximum standard value (0.22%) while the rest of the alloying elements are within the prescribed values. Comparing steel 1.4762 to the standard EN 10095-1999, all of the alloying elements are in the standard ranges.

**Table 1.** Chemical composition of steel 1.7147 (wt%) (Brnic *et al.*, 2014a)

| Material | C | Mn | Si | S | Nb | Cu | Cr | Ni | P | Ti | Rest |
|----------|------|------|------|-------|------|------|------|------|-------|------|--------|
| 1.7147 | 0.22 | 1.23 | 0.29 | 0.025 | 0.03 | 0.06 | 1.11 | 0.08 | 0.021 | 0.02 | 96.914 |

**Table 2.** Chemical composition of steel 1.4762 (wt%) (Brnic *et al.*, 2014b)

| Material | C | Mn | Si | S | Mo | Al | Cr | Ni | P | V | Rest |
|----------|-------|-------|-----|------|-------|------|-------|--------|--------|-------|---------|
| 1.4762 | 0.102 | 0.519 | 1.2 | 0.01 | 0.116 | 1.23 | 23.05 | 0.6855 | 0.0217 | 0.201 | 72.8648 |

Engineering stress-strain ($\sigma$-$\varepsilon$) diagrams for both steels are given in Fig. 1, while the yield strength $\sigma_{YS}$, tensile strength $\sigma_{TS}$ and Young's modulus $E$ are given in Table 3.

**Table 3.** Yield strength $\sigma_{YS}$, tensile strength $\sigma_{TS}$ and Young's modulus $E$ of the considered materials (Brnic *et al.*, 2014a,b)

| Material | $\sigma_{YS}$ [MPa] | $\sigma_{TS}$ [MPa] | $E$ [GPa] |
|----------|------|------|------|
| 1.7147 | 398 | 562 | 219 |
| 1.4762 | 487 | 584 | 192 |
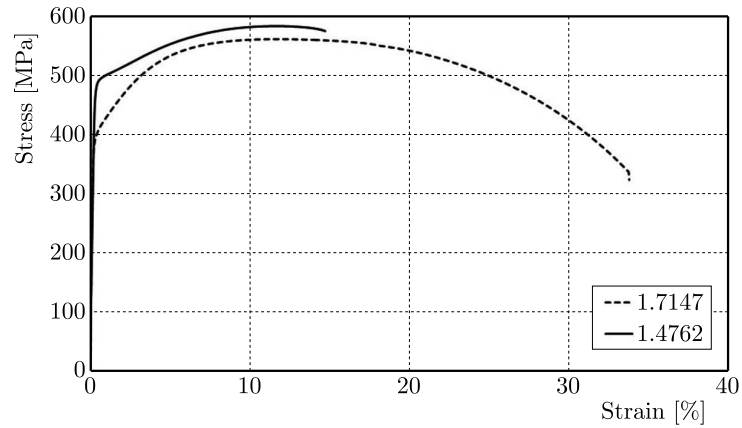
Fig. 1. Steel 1.7147 and steel 1.4762: uniaxial engineering stress-strain diagrams

## 3. Importance of $J$-integral

Rice (1968) introduced the $J$-integral as a path-independent integral that can be encircled around the tip of a crack and considered equally as an energy release rate parameter and a stress intensity parameter. In a 2D form and with reference to Fig. 2, it can be written as

$$J = \int_{\Gamma} \left( w \, dy - T_i \frac{\partial u_i}{\partial x} \, ds \right) \tag{3.1}$$
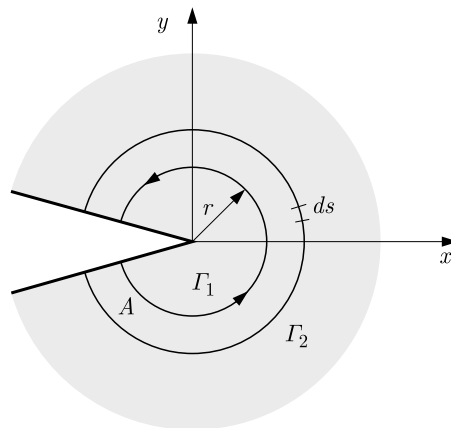


Fig. 2. $J$-integral arbitrary contour path enclosing the tip of a crack

Equation (3.1) comprises of $T_i = \sigma_{ij} n_j$ that are components of the traction vector, $u_i$ are the components of the displacement vector and ds is an incremental length along the integral contour $\Gamma$. The strain energy density $w$ can be written as

$$w = \int \sigma_{ij} \, d\varepsilon_{ij} \tag{3.2}$$

where $\varepsilon_{ij}$ is the sum of elastic and plastic strains at a specific point. The $J$-integral is path independent as long as the stress is a function of the strain alone and provided the crack tip is the only singularity within the contour. The $J$-integral equation shows that the energy of the integral contour increases for the crack growth per unit length. The $J_{Ic}$ parameter, that can be

derived, describes the fracture resistance of the material, i.e. required energy for crack growth per unit length when the contour $\Gamma$ must shrink to the crack tip

$$J = \lim_{r \to 0} \int_{\Gamma} \left( w \, dy - T_i \frac{\partial u_i}{\partial x} \, ds \right) \tag{3.3}$$

## 4. Numerical prediction of $J$-integral

The experimental single specimen test method following an elastic unloading compliance technique was numerically simulated in order to predict fracture behavior of steels 1.7147 and 1.4762. It is an experimental test method that estimates the size of the expanding crack based on measured values of the crack mouth opening displacement. The resulting $J$ values serve as a fracture toughness parameter and can be correlated to crack extension values. The numerical procedure begins with FE stress analysis. Two-dimensional FE models of two types of fracture specimens, single edge notched bend (SENB) and compact tensile (CT), are defined according to the ASTM standard (2005), see Fig. 3. Three initial relative crack length $a/W$ ($W = 50$ mm) ratios are taken, 0.25, 0.5 and 0.75. As for the material behavior, it is considered to be multilinear isotropic hardening. Specimens are discretized with 8-node isoparamateric quadrilateral elements. High deformation gradients occur in the yielding regions around the crack tip. That is why the FE mesh is refined there. Quasi-static load is imposed on the specimen in order to simulate the compliance procedure of the single specimen test method. Since the specimen is symmetrical, only half of it needs to be modelled. To simulate crack propagation, the node releasing technique has been used.
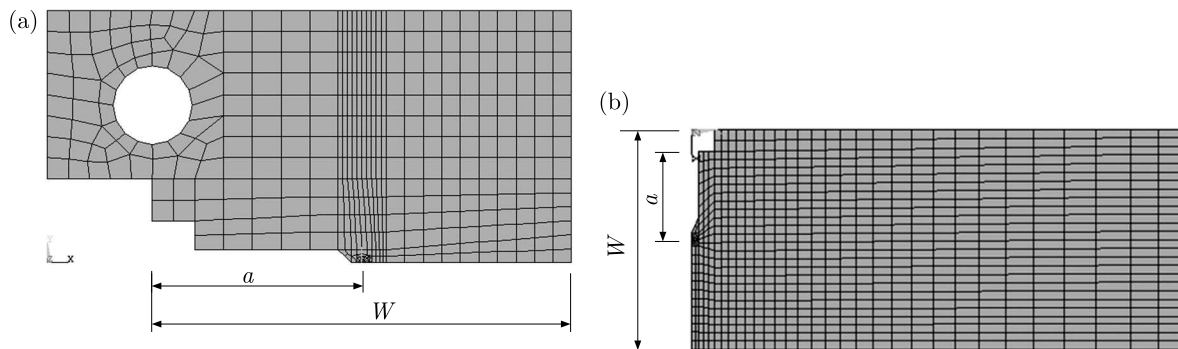


Fig. 3. Finite element model of: (a) CT specimen, (b) SENB specimen

The second step is to extract stress analysis results from the integration points of finite elements enclosing the crack tip. This results are used to evaluate $J$ values in the integration points by Eq. (4.1) (De Araujo *et al.*, 2008) and sum them along the path $\Gamma$ that encloses the crack tip giving the total value of $J$, see Fig. 4

$$J = \sum_{p=1}^{np} G_p I_p(\xi_p, \eta_p) \tag{4.1}$$

In Eq. (4.1), $G_p$ represents Gauss weighting factor, $np$ stands for the number of integration points and $I_p$ is the integrand evaluated at each Gauss point $p$

$$I_p = \left\{ \frac{1}{2} \left[ \sigma_{xx} \frac{\partial u_x}{\partial x} + \sigma_{xy} \left( \frac{\partial u_x}{\partial y} + \frac{\partial u_y}{\partial x} \right) \frac{\partial u_x}{\partial x} + \sigma_{yy} \frac{\partial u_y}{\partial y} \right] \frac{\partial y}{\partial \eta} \right.$$
$$\left. - \left[ (\sigma_{xx} n_1 + \sigma_{xy} n_2) \frac{\partial u_x}{\partial x} + (\sigma_{xy} n_1 + \sigma_{yy} n_2) \frac{\partial u_y}{\partial x} \right] \sqrt{\left( \frac{\partial x}{\partial \eta} \right)^2 + \left( \frac{\partial y}{\partial \eta} \right)^2} \right\}_g \tag{4.2}$$
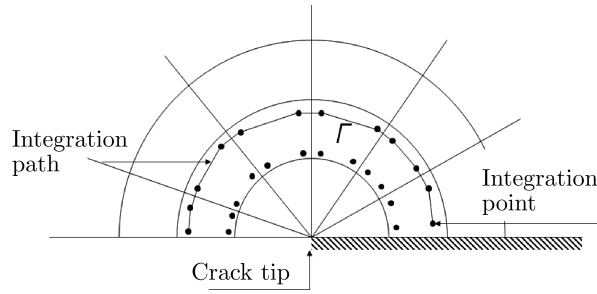
Fig. 4. *J*-integral path $\Gamma$ encircled around the crack tip through FE integration points

Although the crack tip plastic zone radius can be taken as variable using von Mises yield criterion (Bian, 2009), here it is taken as a constant value. Since a slight variation of $J$ values is possible in the numerical analysis, three different paths around the crack tip are defined in each example. The average value of these three paths is taken as the final value of the $J$-integral. In order to verify the procedure, the $J$-integral values are first compared to the available experimental results. Since there is no available experimental results for steels 1.7147 and 1.4762, the procedure has been first validated on steel 1.6310 (Narasaiah *et al.*, 2010), Fig. 5.
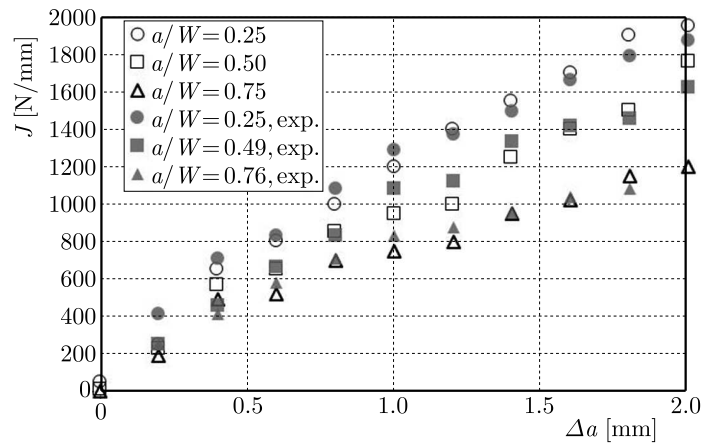


Fig. 5. Validation of numerically obtained *J*-integral values on steel 1.6310

Good compatibility of the experimental and numerical results encouraged further use of the numerical procedure for steels 1.7147 and 1.4762. Figures 6 and 7 show the final $J$ values for 1.7147 and 1.4762 taken as a measure of the crack driving force for different initial crack lengths $a/W$ according to the crack propagation $\Delta a$.
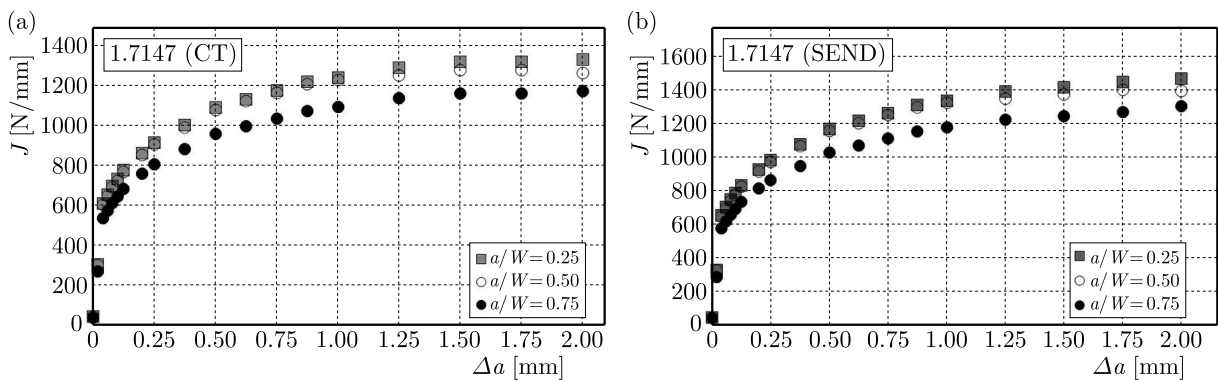


Fig. 6. *J*-integral values obtained numerically for steel 1.7147: (a) CT specimen, (b) SENB specimen
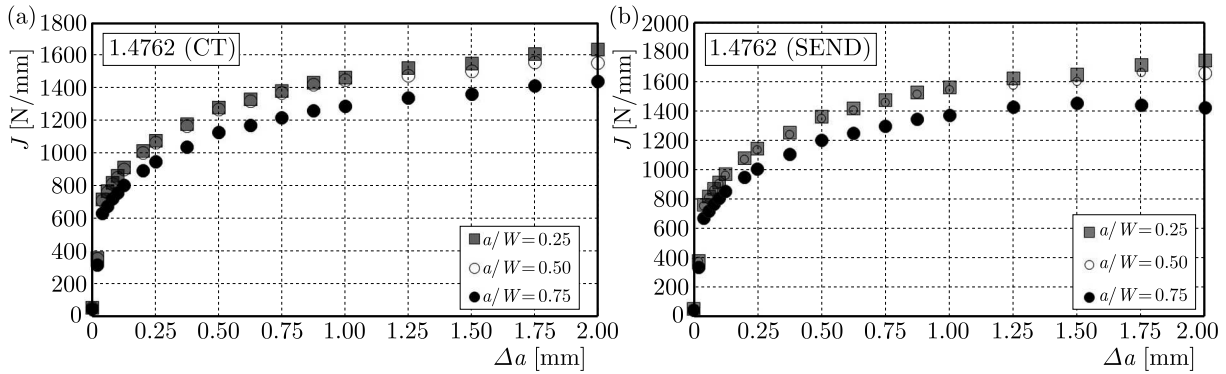
Fig. 7. $J$-integral values obtained numerically for steel 1.4762: (a) CT specimen, (b) SENB specimen

## 5. Discussion

Fracture behavior of steel 1.7147 and steel 1.4762 can be predicted based on the numerical investigation results presented in Figs. 6 and 7 using $J$-integral values as a measure of the crack driving force. Observing the obtained diagrams, it is clear that steel 1.4762 has slightly higher values of the $J$-integral than 1.7147. This makes steel 1.4762 a bit more adequate to structures that need less susceptibility to fracture.

The predicted discrepancy in the numerically obtained $J$ values and, therefore, the difference in resistance to crack extension comparing steels 1.7147 and 1.4762 can be contributed to different composition and properties (Tables 1-3) of the two steels. Steel 1.4762 has a somewhat higher value of the nickel content which can add to the noted behavior. Nickel, as the alloying element, is usually added to stainless steels to reach a certain level of increased strength and hardness without compromising ductility and toughness levels. Nickel also improves the oxidization and corrosion resistance when added in suitable quantities to stainless steels. Although steel 1.7147 has an elevated chromium content (1.11%) making it suitable for corrosive environment. Steel 1.4762 is a true stainless steel in which chromium exceeds 12% content (here 23.05%) significantly improving corrosion resistance. Benefits of chromium as an alloying element in steel are also improved strength, hardenability, wear resistance and response to heat treatment.

Also, observing Figs. 6 and 7, lower $a/W$ ratios corresponding to higher $J$ values exhibit a trend observed by other authors (Cravero and Ruggieri, 2003). Also, the $J$-integral differs greatly for $a/W = 0.75$ if matched with $a/W = 0.25$ and 0.5, then they tend to be close in values. In addition, $J$-integral values obtained by the FE model of the CT specimen give a bit conservative results when comparing them to those obtained from the SENB specimen. That can be ascribed to the specimen geometry and loading effect. As for the crack geometry, $a/W$ ratios are kept equal for both steels in relative specimens. That way, the influence of geometry on the difference in $J$ values for the two steels is negligible.

## 6. Conclusion

Numerical assessment of the $J$-integral for steels 1.7147 and 1.4762 can be useful as a prediction of the possible fracture behavior of materials. Although not validated by an experiment, the fine correspondence between numerical and experimental results for steel 1.6310 assures confidence in using $J$-integral values for steels 1.7147 and 1.4762. In the structural design procedure that includes any of the considered material, the obtained results can be useful in the initial assessment of the material susceptibility to crack growth.

The presented work intends to attract attention on the need for fracture behavior characterization of materials recommended for use in specific engineering components. Here, the novelty of the research lies in numerically predicted values of the *J*-integral taken as a measure of the crack driving force for steels 1.7147 and 1.4762 which are, according to the authors' knowledge, unavailable to construction designers in the presented form. Both materials offer improved corrosion resistance and can be considered for engineering applications intended to be used in corrosive environment and susceptible to crack growth and fracture like spiral bevel gears in truck differential systems prone to failure (Sekercioglu and Kovan, 2007) or stainless steel tubes found in recuperators and exposed to elevated temperatures that cause failures (Bhattacharyya *et al.*, 2008). The results of the investigation presented in this paper can be used to avoid such failure scenarios.

# References

1. American Society for Testing and Materials (ASTM), 2005, Standard test method for measurement of fracture toughness E1820, ASTM, Baltimore

2. Bhattacharyya S., Das M.B., Sarkar S., 2008, Failure analysis of stainless steel tubes in a recuperator due to elevated temperature sulphur corrosion, *Engineering Failure Analysis*, **15**, 6, 711-722

3. Bian L., 2009, Crack growth prediction and non-linear analysis for an elasto-plastic solid, *International Journal of Engineering Science*, **47**, 3, 325-41

4. Brnic J., Turkalj G., Lanc D., Canadija M., Brcic M., Vukelic G., 2014a, Comparison of material properties: Steel 20MnCr5 and similar steels, *Journal of Constructional Steel Research*, **95**, 81-89

5. Brnic J., Turkalj G., Krscanski S., Lanc D., Canadija M., Brcic M., 2014b, Information relevant for the design of structure: ferritic-heat resistant high chromium steel X10CrAlSi25, *Materials and Design*, **63**, 508-518

6. Cravero S., Ruggieri C., 2003, A two-parameter framework to describe effects of constraint loss on cleavage fracture and implications for failure assessments of cracked components, *Journal of the Brazilian Society of Mechanical Sciences and Engineering*, **25**, 4, 403-412

7. De Araujo T.D., Roehl D., Martha L.F., 2008, An adaptive strategy for elastic-plastic analysis of structures with cracks, *Journal of the Brazilian Society of Mechanical Sciences and Engineering*, **30**, 4, 341-350

8. Gojic M., Nagode A., Kosec B., Kozuh S., Savli S., Holjevac-Grguric T., Kosec L., 2011, Failure of steel pipes for hot air supply, *Engineering Failure Analysis*, **18**, 8, 2330-2335

9. Huang Y., Zhou W., Yan Z., 2014, Evaluation of plastic geometry factors for SE(B) specimens based on three-dimensional finite element analyses, *International Journal of Pressure Vessels and Piping*, **123-124**, 99-110

10. Koshima T., Okada H., 2015, Three-dimensional *J*-integral evaluation for finite strain elastic-plastic solid using the quadratic tetrahedral finite element and automatic meshing methodology, *Engineering Fracture Mechanics*, **135**, 34-63

11. Kossakowski P.G., 2012, Simulation of ductile fracture of S235JR steel using computational cells with microstructurally-based length scales, *Journal of Theoretical and Applied Mechanics*, **50**, 589-607

12. NARASAIAH N., TARAFDER S., SIVAPRASAD S., 2010, Effect of crack depth on fracture toughness of 20MnMoNi55 pressure vessel steel, *Material Science and Engineering A*, **527**, 2408-2411

13. QIAO D., CHANGYU Z., JIAN P., XIAOHUA H., 2014, Experiment, Finite Element Analysis and EPRI Solution for *J*-integral of Commercially Pure Titanium, *Rare Metal Materials Engineering*, **42**, 2, 257-263

14. RICE J.R., 1968, A path independent integral and the approximate analysis of strain concentration by notches and cracks, *Journal of Applied Mechanics*, **35**, 379-386

15. SAXENA S., RAMAKRISHNAN N., 2007, A comparison of micro, meso and macroscale FEM analysis of ductile fracture in a CT specimen (mode I), *Computational Materials Science*, **39**, 1, 1-7

16. SEKERCIOGLU T., KOVAN V., 2007, Pitting failure of truck spiral bevel gear, *Engineering Failure Analysis*, **14**, 4, 614-619

17. SHLYANNIKOV V.N., BOYCHENKO N.V., TUMANOV A.V., FERNÁNDEZ-CANTELI A., 2014, The elastic and plastic constraint parameters for three-dimensional problems, *Engineering Fracture Mechanics*, **127**, 83-96

18. WAGNER D., RANC N., BATHIAS C., PARIS P.C., 2010, Fatigue crack initiation detection by an infrared thermography method, *Fatigue and Fracture of Engineering Materials and Structures*, **33**, 1, 12-21

19. WU L., ZHANG L., GUO Y., 2012, Extended finite element method for computation of mixed-mode stress intensity factors in three dimensions, *Proceedia Engineering*, **31**, 373-380

20. ZANGENEH S., KETABCHI M., KALAKI A., 2014, Fracture failure analysis of AISI 304L stainless steel shaft, *Engineering Failure Analysis*, **36**, 155-165

21. ZHU X.K., JOYCE J.A., 2015, Review of fracture toughness (G, K, J, CTOD, CTOA) testing and standardization, *Engineering Fracture Mechanics*, **85**, 1-46

# ROLE OF WAVE REVERBERATIONS IN EXIT VIBRATIONS OF PROJECTILES AND SHELLS

Radosław Trębiński

*Military University of Technology, Faculty of Mechatronics and Aerospace, Warszawa, Poland*

*e-mail: rkt@wat.edu.pl*

Carlucci *et al.* (2013) proposed a theoretical model describing exit vibrations of a shell launched by a gun. The model treats the shell as a system of a spring, damper and a rigid mass. In this paper, similar models describing vibrations of shells and monolithic projectiles are compared with some 1D models taking into account wave reverberations. The comparison proves that the models taking into account the wave motion, forecast similar amplitudes and frequencies of vibrations as discrete models. However, details of acceleration time courses differ considerably. The problem of the influence of the friction force between the shell wall and the filling is also discussed. The results of modelling serve as well for assessing if some projectile velocity oscillations detected by making use of the Doppler radar can be solely attributed to the exit vibrations.

*Keywords:* intermediate ballistics, projectile vibrations, wave reverberation

## 1. Introduction

Projectiles and shells moving inside a gun tube undergo compression. After leaving the muzzle, they experience a sudden drop of pressure acting on their base. This decompression causes vibrations of the projectiles and shells, which can be detrimental for the integrity of their inner structure. Ammunition designers take this into account by assuming that there is a step drop of the pressure from the muzzle pressure to the ambient pressure. However, recently some data became available enabling designers to take into account the continuous character of the pressure changes. On the basis of accelerometer records, Carlucci and Vega (2007) proposed an approximation of pressure changes by the exponential decay curve

$$p(t) = p_m \exp(-\beta t) = p_m \exp\left(-\frac{t}{t_m}\right) \tag{1.1}$$

Values of the muzzle pressure $p_m$ and the coefficient $\beta$ were published for a 155 mm cannon in Carlucci and Vega (2007) and Carlucci *et al.* (2013).

Some theoretical models were considered by Trębiński and Czyżewska (2015a,b), enabling calculation of pressure courses acting on the projectile in the intermediate period. On the basis of the results of calculations for a broad range of launching systems, an approximate formula was proposed for calculating the value of the coefficient $\beta$ for a launching system of the caliber $d$

$$\beta = (0.74 + 0.24M_m)\frac{u_m}{d} \tag{1.2}$$

Values of the muzzle flow Mach number $M_m$ and the muzzle velocity $u_m$ can be determined on the basis of results of internal ballistics calculations.

In Carlucci *et al.* (2013), a model was proposed describing vibrations of a shell subjected to the action of a pressure pulse (1.1). The motion of the ogive of the shell was modeled in

the reference frame moving with the center of gravity of the shell. The ogive was treated as a rigid mass, whereas the wall of the shell was treated as a spring. Its inertia was taken into account by adding one third of its mass to the mass of the ogive. A damper was added in order to take into account damping of the vibrations. The model predicts a considerable magnitude of acceleration oscillations, which is in qualitative agreement with experimental observations. Considering accelerometers as vibrating systems showed very small influence of their inertia and rigidity on the courses of acceleration, except for the very beginning of the process.

The determined values of the period of vibrations of projectiles and shells as well as the characteristic time $t_m$ in expression (1.1) are close to the values of the reverberation time of elastic waves moving in projectiles and shells. In such a case, one can expect that the results of modeling with the use of discrete models and models incorporating wave motion may differ considerably. This paper is devoted to analysis of the role of wave reverberations. The main objective of this analysis is to determine to which extent the amplitudes and frequencies of the exit vibrations of projectiles and shells forecasted by discrete models and models taking into account wave reverberations differ. Several 1D models of the wave motion in a projectile or a shell, when subjected to action of the pressure pulse described by (1.1), are considered. Conclusions concerning the potential influence of wave processes on the indications of accelerometers embedded in the projectiles and shells are formulated.

Doppler radar measurements of the velocity changes of a projectile leaving the muzzle of a 30 mm launching system, presented in Leciejewski *et al.* (2013), showed oscillations of the velocity value (Fig. 1). The question arose whether these oscillations can be attributed solely to the vibrations of the projectile. Finding the answer to this question was the secondary objective of the analysis presented in this paper.
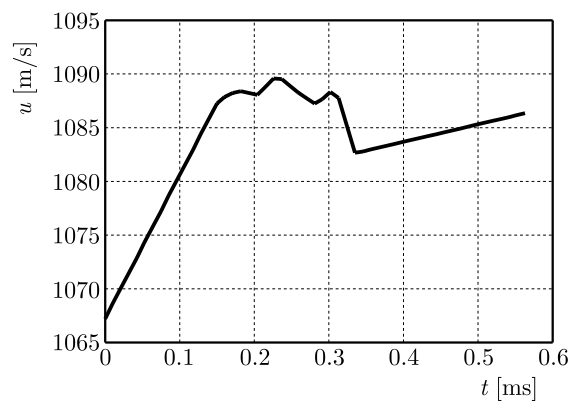


Fig. 1. Results of measurements of the projectile velocity changes outside the muzzle of a 30 mm launching system (Leciejewski *et al.*, 2013)

## 2.   Models

### 2.1.   Models of a monolithic projectile

The sense of physical models considered can be explained by referring to Fig. 2. In model 1, the projectile is considered as a system of two rigid masses $m_1$ and $m_2$ connected by a spring. The stiffness of the spring is determined as

$$k_s = \frac{AE}{l_0} \qquad A = \frac{\pi d^2}{4} \tag{2.1}$$
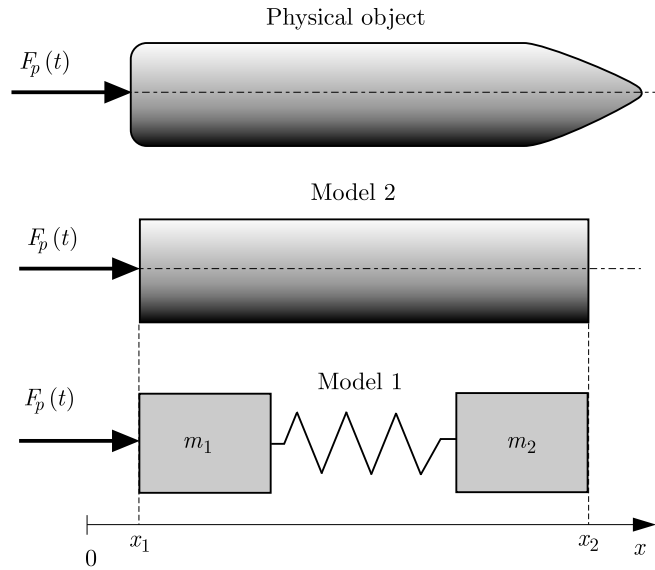
Fig. 2. Schemes of models 1 and 2

The mathematical model corresponding to physical model 1 is given by the following initial value problem

$$m_1\frac{d^2x_1}{dt^2} - k_s(x_2 - x_1 - l_0) = Ap_m\mathrm{e}^{-\frac{t}{t_m}} \qquad m_2\frac{d^2x_2}{dt^2} + k_s(x_2 - x_1 - l_0) = 0$$
$$x_1(0) = 0 \qquad x_2(0) = l_0 - \frac{m_2Ap_m}{(m_1 + m_2)k_s} \qquad \frac{dx_1}{dt}\bigg|_{t=0} = \frac{dx_2}{dt}\bigg|_{t=0} = u_m \tag{2.2}$$

Dividing the first equation by $m_1$ and the second one by $m_2$ and summing up the equations, we obtain

$$\frac{d^2(x_2 - x_1)}{dt^2} + \Big(\frac{k_s}{m_1} + \frac{k_s}{m_2}\Big)(x_2 - x_1 - l_0) = -\frac{F_p(t)}{m_1} \tag{2.3}$$

Defining a new variable

$$w = x_2 - x_1 - l_0 \tag{2.4}$$

we obtain the following initial value problem

$$\frac{d^2w}{dt^2} + \omega^2 w = -\frac{Ap_m}{m_1}\mathrm{e}^{-\frac{t}{t_m}} \qquad \omega^2 = k_s\Big(\frac{1}{m_1} + \frac{1}{m_2}\Big)$$
$$w(0) = -\frac{m_2Ap_m}{(m_1 + m_2)k_s} \qquad \frac{dw}{dt}\bigg|_{t=0} = 0 \tag{2.5}$$

The solution to the problem is given by

$$w(t) = -\frac{Ap_m}{m_1\omega^2(1 + \omega^2 t_m^2)}\Big[\omega t_m \sin(\omega t) + \cos(\omega t) + \omega^2 t_m^2 \mathrm{e}^{-\frac{t}{t_m}}\Big] \tag{2.6}$$

Making use of this, we obtain from the second equation of (2.2) an expression for acceleration of the forward part of the projectile

$$a(t) = \frac{Ap_m}{m(1 + \omega^2 t_m^2)}\Big[\omega t_m \sin(\omega t) + \cos(\omega t) + \omega^2 t_m^2 \mathrm{e}^{-\frac{t}{t_w}}\Big] \qquad m = m_1 + m_2 \tag{2.7}$$

Integrating (2.7) from 0 to $t$, we obtain the following formula for the velocity increase of the forward part of the projectile

$$\Delta u(t) = \frac{A p_m t_m}{m(1 + \omega^2 t_m^2)}\Big[1 - \cos(\omega t) + \frac{1}{\omega t_m}\sin(\omega t) + \omega^2 t_m^2\Big(1 - e^{-\frac{t}{t_m}}\Big)\Big] \tag{2.8}$$

In model 2, the projectile is treated as an elastic cylindrical rod with the same caliber $d$ and mass $m$ as the real projectile and length $l_0 = 4m/(\pi d^2)$. The material properties of the rod are determined by its density $\rho$ and Young's modulus $E$. It is assumed that the force $F_p(t)$ is produced by the pressure uniformly distributed at the left end of the rod. The pressure changes in time are described by (1.1). The loading produces a uniaxial stress state in the rod. It is assumed that there is no force at the right end of the rod. This assumption is justified by the observation that the pressure acting on the forward part of the projectile is much less than the pressure acting on its base in the whole phase when the projectile is accelerated. We assume that at the beginning of the process all parts of the rod have the same velocity and acceleration.

The mathematical model corresponding to physical model 2 is given by the following initial-boundary value problem in the Lagrangian coordinates

$$\rho u,_t = \sigma,_x \qquad \sigma,_t = E u,_x$$
$$u(x, 0) = u_m \qquad \sigma(x, 0) = p_m\Big(\frac{x}{l_0} - 1\Big) \tag{2.9}$$
$$\sigma(0, t) = -p_m e^{-\frac{t}{t_m}} \qquad \sigma(l_0, t) = 0$$

Initial condition $(2.9)_{3,4}$ for the stress $\sigma$ follows from the assumption that the whole rod has initially the same acceleration.

Solving the problem, we obtain the following expressions for the velocity increase and acceleration of the forward part of the projectile

$$\Delta u(t) = \Delta u_m\Big[\frac{t}{T_w} - 2N + 2\sum_{j=1}^{N}\exp\Big(-\frac{t - (2j-1)T_w}{t_m}\Big)\Big] \qquad \Delta u_m = \frac{p_m}{\rho c}$$
$$N = E\Big(\frac{n+1}{2}\Big) \qquad n = 0, 1, 2, \ldots \qquad T_w = \frac{l_0}{c} \qquad c = \sqrt{\frac{E}{\rho}} \tag{2.10}$$
$$a(t) = \Delta u_m\Big[\frac{1}{T_w} - \frac{2}{t_m}\sum_{j=1}^{N}\exp\Big(-\frac{t - (2j-1)T_w}{t_m}\Big)\Big]$$

## 2.2. Models of the shell

The physical object considered and its physical models are illustrated in Fig. 3. In model 3, the ogive and the base of the shell are treated as rigid masses. The wall of the shell of length $l_0$ is treated as an elastic hollow cylinder, whereas the filling (explosive) is treated as an elastic cylindrical rod with density $\rho_f$ and velocity of sound $c_f$. It is assumed that there is no friction between the wall and the filling. Because the filling is more compressible than the wall, it can also be assumed that there is no contact between the filling and the ogive. A uniaxial stress state is assumed inside the wall and the filling.

The mathematical description of model 3 is given by the following initial-boundary value problem (the subscript $f$ refers to the filling)

$$\rho u,_t = \sigma,_x \qquad \sigma,_t = \rho c^2 u,_x \qquad \rho_f u_f,_t = \sigma_f,_x \qquad \sigma_f,_t = \rho_f c_f^2 u_f,_x$$
$$u(x, 0) = u_m \qquad u_f(x, 0) = u_m \tag{2.11}$$
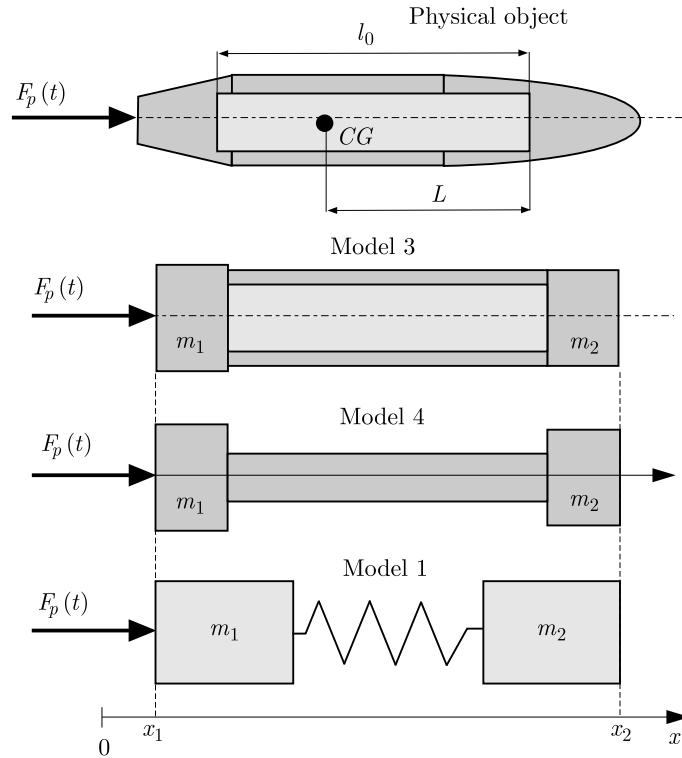
Fig. 3. Schemes of the physical object (a shell) and of models 1, 3 and 4 used for the analysis

and

$$
\sigma(x,0) = \rho a_0(x - l_0) - \frac{m_2 a_0}{A_c} \qquad a_0 = \frac{p_m A}{m_1 + m_2 + \rho l_0 A_c + \rho_f l_0 A_f}
$$

$$
\sigma_f(x,0) = \frac{(m_1 + m_2 + A_c \rho l_0)a_0 - A p_m}{A_f} + \rho_f a_0 x \tag{2.12}
$$

and

$$
m_1 u_{,t}(0,t) = A p_m \mathrm{e}^{-\frac{t}{t_m}} + A_c \sigma(0,t) + A_f \sigma_f(0,t)
$$

$$
m_2 u_{,t}(l_0,t) = -A_c \sigma(l_0,t) \qquad \sigma_f(l_0,t) = 0 \tag{2.13}
$$

where $A_f$, $A_c$ mean the cross-sectional area of the filling and the wall.

The initial condition for stress (2.12) has been derived on the assumption that at the beginning of the process the whole shell has the same acceleration $a_0$ and on the assumption that there is no contact between the filling and the ogive. The second assumption has also been applied in the formulation of the boundary condition at $x = l_0$.

Problem (2.11)-(2.13) has been solved by the method of characteristics. The characteristic grid is shown in Fig. 4. It shows wave trajectories in the wall of the shell. The values of velocity and stress in the grid nodes are calculated using the characteristic relations

$$
\Delta\sigma = \pm\rho c \Delta u \qquad \Delta x = \pm c \Delta t \qquad \Delta\sigma_f = \pm\rho_f c_f \Delta u_f \qquad \Delta x = \pm c_f \Delta t \tag{2.14}
$$

In the node $i$, we have

$$
\sigma_i = \frac{\sigma_{i+1} + \sigma_{i-1} + \rho c(u_{i+1} - u_{i-1})}{2} \qquad u_i = u_{i-1} + \frac{\sigma_i - \sigma_{i-1}}{\rho c}
$$

$$
\sigma_{fi} = \frac{\sigma_{fL} + \sigma_{fR} + \rho_f c_f(u_{fR} - u_{fL})}{2} \qquad u_{fi} = u_{fL} + \frac{\sigma_{fi} - \sigma_{fL}}{\rho_f c_f} \tag{2.15}
$$
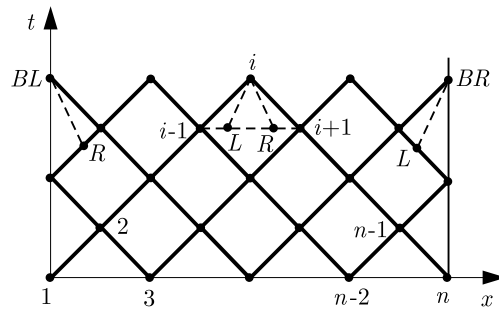
Fig. 4. Characteristic grid used for calculations for models 3, 4 and 5

The values of velocity and stress inside the filling in the auxiliary nodes $L$ and $R$ (characteristics $L - i$ and $R - i$ correspond to the wave velocity $c_f$) are calculated by a linear interpolation between the nodes $i - 1$ and $i + 1$

$$
q_L = q_{i-1} + (q_{i+1} - q_{i-1})\frac{c - c_f}{2c}
$$
$$
q_R = q_{i-1} + (q_{i+1} - q_{i-1})\frac{c + c_f}{2c} \qquad q = \{u_f, \sigma_f\}
$$
(2.16)

The values of velocity and stress in nodes 1 and $n$ are calculated by making use of an approximate form of boundary conditions (2.13) and relations at characteristics $1 - BL$ and $n - BR$

$$
u_{BL} = u_1 + a_1 e^{-\frac{t}{t_m}}\left(1 - e^{-\frac{2\Delta t}{t_m}}\right) + a_2(\sigma_1 + \sigma_{BL}) + a_3(\sigma_{f1} + \sigma_{fBL})
$$
$$
u_{fBL} = u_{BL} \qquad a_1 = \frac{A p_m t_m}{m_1} \qquad a_2 = \frac{A_c \Delta t}{m_1} \qquad a_3 = \frac{A_f \Delta t}{m_1}
$$
$$
\sigma_{BL} = \sigma_2 - \rho c(u_B - u_2) \qquad \sigma_{fBL} = \sigma_{fR} - \rho_f c_f(u_{BL} - u_{fR})
$$
$$
u_{BR} = u_n - a_4(\sigma_n + \sigma_{BR}) \qquad a_4 = \frac{A_c \Delta t}{m_2} \qquad u_{fBR} = u_{fL} - \frac{\sigma_{fL}}{\rho_f c_f}
$$
$$
\sigma_{BR} = \sigma_{n-1} + \rho c(u_{BR} - u_{n-1}) \qquad \sigma_{fBR} = 0
$$
(2.17)

The values of velocity and stress inside the filling in the auxiliary nodes $L$ and $R$ are calculated by a linear interpolation between nodes 1-2 and $(n-1)$-$n$

$$
q_L = q_n + (q_{n-1} - q_n)\frac{2c_f}{c + c_f} \qquad q_R = q_1 + (q_2 - q_1)\frac{2c_f}{c + c_f} \qquad q = \{u_f, \sigma_f\} \quad (2.18)
$$

Calculations are performed in two iterations. In the first iteration, the values of stress are set as

$$
\sigma_{BL} = \sigma_1 \qquad \sigma_{fBL} = \sigma_{f1} \qquad \sigma_{BR} = \sigma_n
$$
(2.19)

In the second iteration, the values of stress calculated in the first iteration are used.

Neglecting friction between the wall and the filling is questionable because the filling is compressed and it exerts pressure on the wall. Instead of introducing the friction force into the model, two limiting cases are considered. The model without friction is the first limiting case. The second limiting case is a model for which it is assumed that the friction force is strong enough to exclude any displacement between the filling and the wall. If both models give similar results, it will be no necessity to take into account the friction force. In the second limiting case, the compressibility of the filling has no influence on the process. Its inertia can be taken

into account as an additional mass added to mass of the wall. This can be done by artificially increasing density of the wall material

$$\rho_a = \rho + \rho_f \frac{A_f}{A_c} \tag{2.20}$$

The central part of the shell can be treated as a cylindrical rod with cross-section area $A_c$ and density $\rho_a$. This is the sense of model 4. Its mathematical form is not presented because it can be easily derived from problem (2.11)-(2.13) by neglecting all the expressions corresponding to the filling. Also the method of solving the problem is similar to that described for model 3.

In the modeling of the vibrations of the shell, model 1 can be used. The mass $m_1$ is calculated as the sum of mass of the base of the shell and mass of the wall and the filling lying between the base and the center of gravity. The mass $m_2$ is calculated as the sum of mass of the ogive and mass of the wall and the filling lying between the ogive and the center of gravity. The stiffness of the spring is calculated by using formula (2.1) with $A$ replaced by $A_c$.
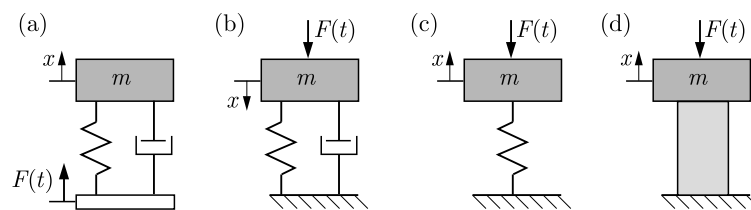


Fig. 5. Schemes of the model by Carlucci *et al.* (2013) (a), (b) and models 5 and 6 (c), (d)

In order to make comparison with the results of the model described by Carlucci *et al.* (2013), two more models are considered, as shown in Fig. 5. The vibrations are modeled in the reference frame moving with the center of gravity. Figure 5a shows the scheme of the model presented in Fig. 4 in the cited paper. It is erroneous because the force $F(t)$ should be applied to the mass $m$, not to the spring and the damper. It is the inertial force, so its value should be expressed as

$$F(t) = \frac{m}{m_s} F_p(t) \tag{2.21}$$

where $m_s$ is the total mass of the shell. In Carlucci *et al.* (2013), the equality of both the forces was assumed. The proper form of the scheme is shown in Fig. 5b. The equations given in the cited paper correspond to this scheme. Figure 5c presents a scheme of model 5 considered in this work. It differs from the scheme in Fig. 5b by the absence of the damper and by the sign of the coordinate $x$. The mass $m$ in model 5 is taken as the sum of mass of the ogive and $1/3$ of mass of the shell wall. Figure 5d corresponds to model 6. The spring is replaced by an elastic rod with cross-section area $A_c$.

The mathematical model corresponding to model 5 is given by the following initial value problem

$$m\frac{d^2w}{dt^2} + k_s w = -\frac{m}{m_s} A p_m e^{-\frac{t}{t_m}} \qquad w = x - l_0$$

$$w(0) = -\frac{m}{m_s}\frac{A p_m}{k_s} \qquad \frac{dw}{dt}\bigg|_{t=0} = 0 \tag{2.22}$$

Solving this problem, the following expressions for the velocity increase and acceleration can be obtained

$$\Delta u(t) = \frac{A m^2 p_m}{m_s(m + k_s t_m^2)}\left[t_m e^{-\frac{t}{t_m}} + t_m \sin(\omega t) - \frac{\omega}{k_s}\cos(\omega t)\right]$$

$$a(t) = \frac{A m^2 p_m}{m_s(m + k_s t_m^2)}\left[\omega t_m \cos(\omega t) + \frac{\omega^2}{k_s}\cos(\omega t) - e^{-\frac{t}{t_m}}\right] \tag{2.23}$$

The mathematical model corresponding to model 6 is given by the following initial-boundary value problem

$$\rho u_{,t} = \sigma_{,x} \qquad \sigma_{,t} = \rho c^2 u_{,x} \qquad u(x,0) = u_m \qquad \sigma(x,0) = -\frac{mAp_m}{m_s A_c}$$

$$u(0,t) = 0 \qquad m_2 u_{,t}(l_0,t) = -\frac{m}{m_s} Ap_m e^{-\frac{t}{t_m}} - A_c \sigma(l_0,t)$$

(2.24)

The problem is solved by the method of characteristics in the way described for model 3.

## 3. Results of the modeling

Calculations have been performed by making use of models 1 and 2 for a 30 mm gun used in the investigations presented by Leciejewski *et al.* (2012). The following values of parameters have been applied: $A = 7.07\,\text{cm}^2$, $l_0 = 66\,\text{mm}$, $m_1 = m_2 = 183\,\text{g}$, $\rho = 7850\,\text{kg/m}^3$, $E = 200\,\text{GPa}$, $p_m = 51.5\,\text{MPa}$, $t_m = 0.0211\,\text{ms}$. The value of parameters $p_m$ and $t_m$ have been determined by the regression of the pressure course calculated by the model described in Trębiński and Czyżewska (2015). They are shown in Fig. 6. The dotted line corresponds to the approximation given by (1.2).
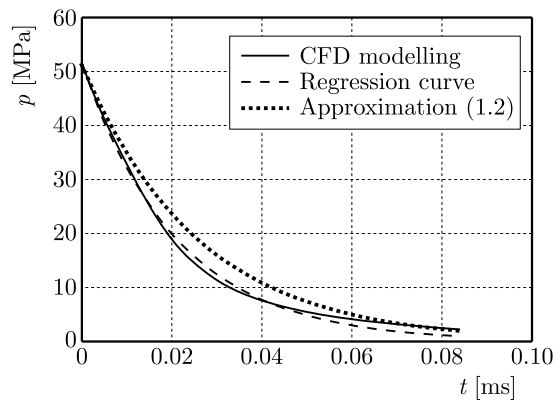


Fig. 6. Pressure course for a 30 mm gun calculated by the model proposed in Trębiński and Czyżewska (2015b), regression curve and approximation of the course using formulae (1.1) and (1.2)

Figures 7a and 7b present a comparison of the results obtained by models 1 and 2. Although the character of the velocity changes is different for the two models, the amplitude of oscillations is similar. It is much less than the amplitude of the velocity oscillations presented in Fig. 1. This suggests that these oscillations cannot be attributed to axial vibrations or wave reverberations in the projectile. We can suppose that these oscillations are caused by yawing of the projectile or by the effect of ionization of gases in strong shock waves arising in the vicinity of the muzzle (description of wave processes accompanying the exit of projectiles are given in Klingenberg and Heimerl (1988)).

As far as acceleration is concerned, the differences between the two models are much more pronounced. This means that it is recommended to take into account the wave motion in predicting the acceleration of a projectile leaving the muzzle.

Figures 8a and 8b present a comparison of the results obtained by models 5 and 6. The values of parameters used in calculations have been the same as in Carlucci *et al.* (2013): $A = 188\,\text{cm}^2$, $A_c = 35\,\text{cm}^2$, $l_0 = 508\,\text{mm}$, $m = 3.75\,\text{kg}$, $\rho = 7850\,\text{kg/m}^3$, $E = 199\,\text{GPa}$, $p_m = 68.9\,\text{MPa}$, $t_m = 0.1731\,\text{ms}$. For the purpose of comparison, it has been assumed that $m = m_s$. The two models give very close results. This means that in this case taking into account the wave reverberations is not necessary.

(a)



(b)
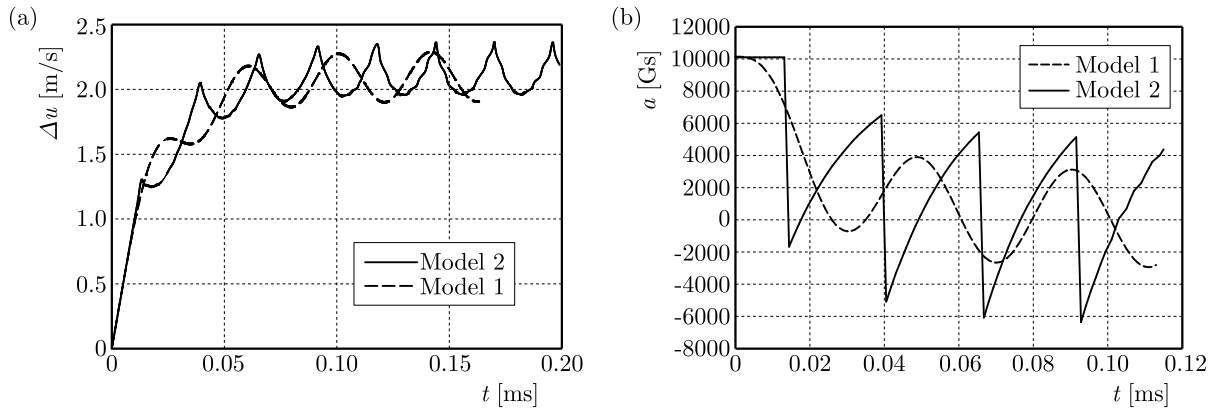
Fig. 7. Comparison of the (a) velocity increase and (b) acceleration courses calculated by the use of models 1 and 2

(a)



(b)
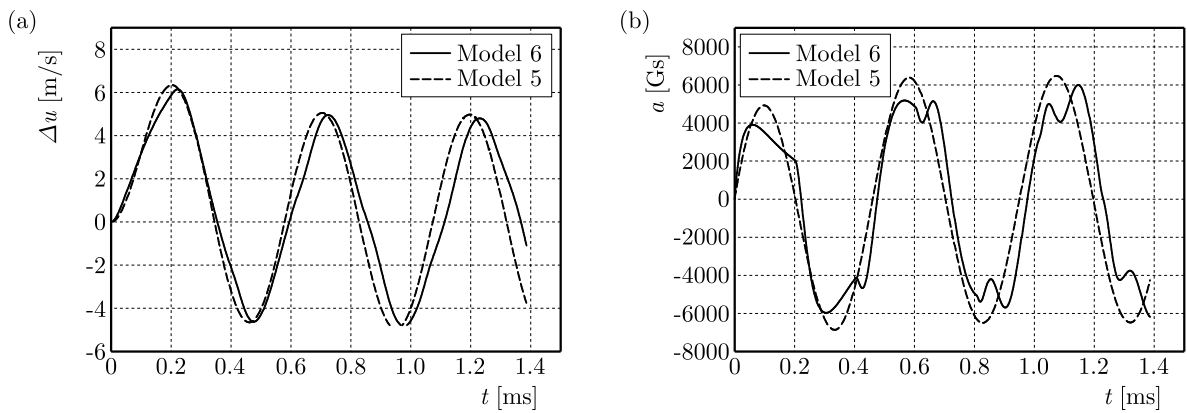
Fig. 8. Comparison of the (a) velocity increase and (b) acceleration courses of the shell ogive calculated by the use of models 5 and 6

The picture is somewhat different if we consider the wave motion in the whole shell. Figures 9a and 9b show a comparison of the calculated acceleration courses of the shell base and the shell ogive calculated by the use of models 3 and 4. The values of parameters applied in calculations have been as follows: $A = 188\,\mathrm{cm}^2$, $A_c = 93\,\mathrm{cm}^2$, $A_f = 95\,\mathrm{cm}^2$, $l_0 = 590\,\mathrm{mm}$, $m_1 = 6\,\mathrm{kg}$, $m_2 = 5\,\mathrm{kg}$, $\rho = 7850\,\mathrm{kg/m}^3$, $c = 5035\,\mathrm{m/s}$, $\rho_f = 1715\,\mathrm{kg/m}^3$, $c_f = 2470\,\mathrm{m/s}$, $p_m = 68.9\,\mathrm{MPa}$, $t_m = 0.1731\,\mathrm{ms}$.

(a)



(b)
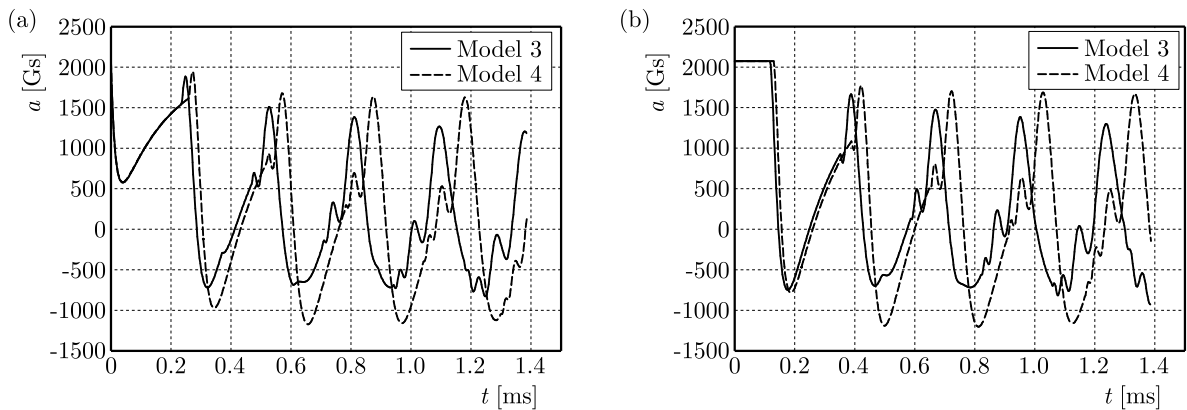
Fig. 9. Comparison of the (a) velocity increase and (b) acceleration courses of the shell ogive calculated by the use of models 3 and 4

Although models 3 and 4 represent the opposite limiting cases, as far as friction between the wall and the filling is concerned, they give close results. Therefore, simpler model 4 is recommended. The results obtained by making use of it are compared with the results from model 1 in Figs. 10a and 10b. Although the frequency of oscillations of the velocity and the acceleration values are very close, model 4 forecasts considerably larger amplitudes of oscillations.
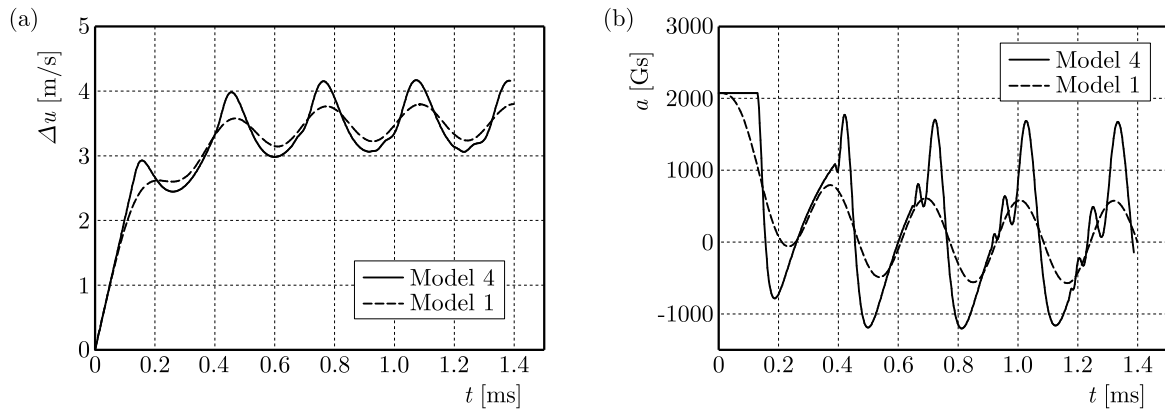


Fig. 10. Comparison of the (a) velocity increase and (b) acceleration courses of the shell ogive calculated by the use of models 4 and 1

Figure 11 presents the acceleration courses of the static center of gravity of the shell calculated by model 4. These are compared with the acceleration calculated for the shell treated as a rigid body. It can be seen that an accelerometer positioned in the static center of gravity will record acceleration courses that considerably differ from the mean acceleration of the shell.
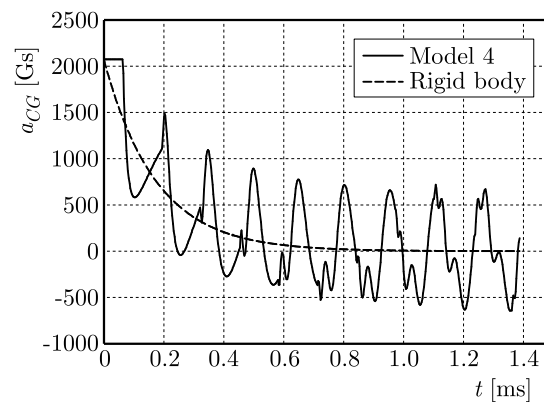


Fig. 11. Comparison of the acceleration courses of the shell static center of gravity calculated by the use of model 4 and for the shell treated as a rigid body

## 4.    Conclusions

- Models taking into account wave reverberations generally predict similar frequencies and amplitudes of vibrations to the simple vibrational models. However, the character of time changes of acceleration differs considerably. Therefore, modeling of the wave motion is recommended for interpretation of the signals from accelerometers embedded in the shells.

- Close results obtained for models 3 and 4 prove it to be acceptable to assume that there is no displacement between the wall of the shell and the filling.

- The predicted amplitudes of velocity oscillations of the projectile leaving the muzzle are much smaller than those which can be deduced from the results of Doppler radar me-

asurements. Therefore, the observed oscillations of velocity cannot be solely attributed to vibrations of the projectile.

## References

1. CARLUCCI D., VEGA J., 2007, Empirical relationship for muzzle exit pressure in a 155 mm gun tube, [In:] *Computational Ballistics III*, C. A. Brebbia, edit., WIT Press, Ashurst, UK

2. CARLUCCI D.E., FRYDMAN A.M, CORDES J.A., 2013, Mathematical description of projectile exit dynamics (set-forward), *ASME Journal of Applied Mechanics*, **80**, 031501-1

3. KLINGENBERG G., HEIMERL J.M., 1988, *Gun Muzzle Blast and Flash*, **139**, AIAA Progress in Astronautics and Aeronautics edition

4. LECIEJEWSKI Z., SURMA Z., TORECKI S., TRĘBIŃSKI R., CZYŻEWSKA M., 2013, Theoretical and experimental investigations of projectile motion specifity in the intermediate period, *Proceedings of the 27th International Symposium on Ballistics*, Freiburg, Germany, 333-343

5. TRĘBINSKI R., CZYŻEWSKA M., 2015a, Approximate model of the intermediate ballistics, *Central European Journal of Energetic Materials*, **12**, 1, 77-88

6. TRĘBIŃSKI R., CZYŻEWSKA M., 2015b, Estimation of projectile velocity increase in the intermediate ballistics period, *Central European Journal of Energetic Materials*, **12**, 1, 63-76

# EFFECT OF GEOMETRY AND IMPEDANCE VARIATION ON THE ACOUSTIC PERFORMANCE OF A POROUS MATERIAL LINED DUCT

Abdelmonem Masmoudi, Amine Makni, Mohamed Taktak, Mohamed Haddar

*Mechanics, Modelling and Production Laboratory (LA2MP), Mechanical Department, National School of Engineers of Sfax,*
*University of Sfax, Sfax, Tunisia; e-mail: mohamed.taktak@fss.rnu.tn*

In this paper, the effect of geometry and impedance on the acoustic behavior of wall and lined cylindrical ducts is investigated using a numerical model which enables one to compute the reflection and the transmission coefficients of such ducts using the multimodal scattering matrix. From this matrix, the acoustic power attenuation is deduced. By using these tools, the effect of duct diameter increase and duct diameter decrease of the wall or lined duct section is studied. The numerical results are obtained for two configurations of wall and lined ducts. Numerical coefficients of transmission and reflection as well as the acoustic power attenuation show the relative influence of each type of variation.

*Keywords:* cylindrical duct, discontinuity effect, transmission, reflection, acoustic attenuation

## 1. Introduction

The acoustic performance of duct systems is evaluated with different matrices such as the transfer matrix, the mobility matrix and the scattering matrix. This later showed its efficiency not only because it describes the reflection and the transmission phenomena of the studied duct as presented in Abom (1991), Leroux *et al.* (2003), Bi *et al.* (2006), Sitel *et al.* (2006) and Taktak *et al.* (2010), but also because it describes the energetic state of the duct element as presented in Sitel *et al.* (2006), Taktak *et al.* (2010), Aurégan and Starobinski (1998).

In a previous work, Taktak *et al.* (2010) developed a numerical method based on the finite element method to compute the multimodal scattering matrix of a lined axisymetric duct element to investigate the effect of a locally reacting liner. Then, that numerical method was developed to incorporate the flow effect in Taktak *et al.* (2012, 2013). Finally, Ben Jdidia *et al.* (2014) used the multimodal scattering matrix to evaluate the effect of temperature on acoustic behavior of the duct element lined with porous materials.

In this work, the effect of discontinuities in duct systems is investigated based on the use of the multimodal scattering matrix. This objective is achieved by studying two types of cylindrical ducts having sudden changes of the section. In the present work, it is supposed that these section changes are lined. Then, the effect of geometrical dimensions and the liner on the acoustic performances of the studied ducts is investigated by computing the reflection, transmission coefficients and the acoustic power attenuation of these ducts.

The outline of the paper is as follows. The studied problem and numerical computation of the multimodal scattering matrix are presented in Section 2. Then, the used acoustic impedance to model the liner is presented in Section 3. Section 4 presents the computation of acoustic power attenuation from the multimodal scattering matrix. Finally, numerical results are presented and discussed in Section 5 to evaluate the influence of duct diameter increase or duct diameter decrease effects on the reflection and transmission coefficients and the acoustic power attenuation of the studied ducts.

## 2.    Numerical computation of the multimodal scattering matrix

In this study, a 1 m length cylindrical duct element is studied. Two cases of this duct are investigated:

- The first case, as presented in Fig. 1, is a cylindrical duct with radius $R$ located between the two axial coordinates $z_L$ and $z_R$ and presenting an abrupt stricture of the section between $z_1$ and $z_2$ with radius $\rho$. The length of the duct is divided into three parts: two identical parts with length $b$ and radius $R$ and the third part in the middle with length $c$ and radius $\rho$.
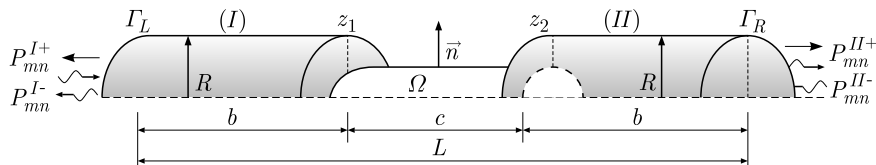


Fig. 1. Section having a duct diameter decrease and then a sudden duct diameter increase section

- The second case, as presented in Fig. 2, is a cylindrical duct with radius $\rho$ located between the two axial coordinates $z_L$ and $z_R$ and presenting an abrupt expansion of the section between $z_1$ and $z_2$ with radius $R$. The length of the duct is divided into three parts: two identical parts with length $b$ and radius $\rho$ and the third part in the middle with length $c$ and radius $R$.
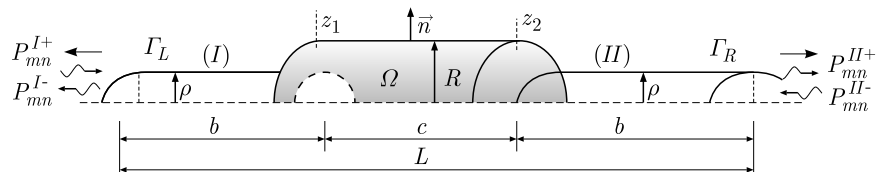


Fig. 2. Section with a duct diameter increase and then a sudden duct diameter decrease section

In the present study, we suppose that the abrupt change of the section is lined by a liner composed of a perforated plate and an absorbing porous material backed by a rigid plate. This liner is modeled later by its normalized acoustic impedance $Z$.

The multimodal scattering matrix is relating the out-coming modal pressures array

$$\mathbf{P}_{2N}^{out} = [P_{00}^{I-}, \ldots, P_{mn}^{I-}, \ldots, P_{PQ}^{I-}, P_{00}^{II+}, \ldots, P_{mn}^{II+} \ldots, P_{PQ}^{II+}]_N^{\mathrm{T}}$$

to the incoming modal pressures array

$$\mathbf{P}_{2N}^{in} = [P_{00}^{I+}, \ldots, P_{mn}^{I+}, \ldots, P_{PQ}^{I+}, P_{00}^{II-}, \ldots, P_{mn}^{II-}, \ldots, P_{PQ}^{II-}]_N^{\mathrm{T}}$$

as follows (Abom $et$ $al.$, 1991; Taktak $et$ $al.$, 2010)

$$\mathbf{P}_{2N}^{out} = \mathbf{S}_{2N \times 2N} \mathbf{P}_{2N}^{in} = \begin{bmatrix} \mathbf{R}_{N \times N}^{I} & \mathbf{T}_{I \to II\,N \times N} \\ \mathbf{T}_{II \to I\,N \times N} & \mathbf{R}_{N \times N}^{II} \end{bmatrix}_{2N \times 2N} \mathbf{P}_{2N}^{in} \tag{2.1}$$

where $m$ and $n$ are respectively the circumferential and radial wave numbers, $N$ is the number of propagating modes in both cross sections.

$R_{mn,pq}^{I}$ is the reflection coefficient of the wave incident to the element from side I, $T_{II \to I\,mn,pq}$ is the transmission coefficient of the wave from side II to side I, $R_{mn,pq}^{II}$ is the reflection coefficient of the wave incident to the element from side II and $T_{I \to II\,mn,pq}$ is the transmission coefficient of the wave from side I to side II.

The acoustical pressure $p$ in the duct is obtained by solving the Helmholtz equation with the boundary conditions

$$k^2 p + \Delta p = 0 \qquad \text{for} \quad \Omega$$

$$\frac{\partial p}{\partial n_W} = 0 \qquad \text{for} \quad \Gamma_{WD} \tag{2.2}$$

$$Z \frac{\partial p}{\partial n_L} = \mathrm{i}\omega\rho p \qquad \text{for} \quad \Gamma_{LD}$$

$k$ is the wave number, $\Omega$ is the acoustic domain inside the duct, $\Gamma_{WD}$ and $\Gamma_{LD}$ correspond to the rigid and lined walls, respectively, $\mathbf{n}_W$ and $\mathbf{n}_L$ are the normal vectors of these walls.

The corresponding weak variational formulation of the studied problem is

$$\Pi = -\int_\Omega (\nabla q \cdot \nabla p) \, d\Omega + k^2 \int_\Omega qp \, d\Omega + \int_{\bigcup \Gamma_i} q \frac{\partial p}{\partial n_i} \, d\Gamma_i = 0 \tag{2.3}$$

$q$ is the test function, $d\Omega$ and $d\Gamma_i$ are the integration elements through the duct domain and boundaries, respectively, and $\bigcup \Gamma_i$ presents the whole boundary. The use of modal decomposition at left and right boundaries ($\Gamma_L$ and $\Gamma_R$) introduces the modal pressures as additional degrees of freedom of the model as presented in the following expression

$$\int_{\Gamma_L} p J_m \left( \frac{\chi_{mn}}{a} r \right) d\Gamma_L = (P_{mn}^{I+} + P_{mn}^{I-}) \int_{\Gamma_L} J_m \left( \frac{\chi_{mn}}{a} r \right)^2 r \, d\Gamma_L$$

$$\int_{\Gamma_R} p J_m \left( \frac{\chi_{mn}}{a} r \right) d\Gamma_R = (P_{mn}^{II+} + P_{mn}^{II-}) \int_{\Gamma_R} J_m \left( \frac{\chi_{mn}}{a} r \right)^2 r \, d\Gamma_R \tag{2.4}$$

with $a$ being the duct radius ($a = R$ or $\rho$) and $r$ the radial coordinate.

The last integral of formulation (2.3) is given by the following expression by adding the modal incoming and outcoming pressures as additional degrees of freedom to the model

$$\int_{\bigcup \Gamma_i} q \frac{\partial p}{\partial n} \, d\Gamma = \int_{\Gamma_t} q \left( \frac{\mathrm{i}\omega\rho p}{Z} \right) d\Gamma_{LD} + \sum_n^{N_r} \mathrm{i} k_{mn} \left[ \left( n_L (P_{mn}^{I+} - P_{mn}^{I-}) \int_{\Gamma_L} q J_m(\chi_{mn} r) \, d\Gamma_L \right) \right.$$

$$\left. + \left( n_R (P_{mn}^{II+} - P_{mn}^{II-}) \int_{\Gamma_R} q J_m(\chi_{mn} r) \, d\Gamma_R \right) \right] \tag{2.5}$$

$J_m$ is the Bessel function of the first kind of the order $m$, $\chi_{mn}$ is the nth root satisfying the radial hard-wall boundary condition on the wall of the main duct, $r$ is the radial coordinate, $\mathbf{n}_L$ and $\mathbf{n}_R$ are the normal vectors.

For a fixed $m$, system (2.3) results in the following matrix system by taking into account the boundary conditions (Taktak *et al.*, 2010)

$$\left[ [q_1, \ldots, q_M], [1, \ldots, 1] \right] \begin{bmatrix} \mathbf{K} & \mathbf{E}_1 & \mathbf{E}_2 & \mathbf{F}_1 & \mathbf{F}_2 \\ \mathbf{G}_1 & \mathbf{G}_2 & \mathbf{G}_3 & \mathbf{0} & \mathbf{0} \\ \mathbf{0} & \mathbf{0} & \mathbf{0} & \mathbf{0} & \mathbf{0} \\ \mathbf{0} & \mathbf{0} & \mathbf{0} & \mathbf{0} & \mathbf{0} \\ \mathbf{H}_1 & \mathbf{0} & \mathbf{0} & \mathbf{H}_2 & \mathbf{H}_3 \end{bmatrix} \left\{ \begin{array}{c} \left\{ \begin{array}{c} p_1 \\ \vdots \\ p_M \end{array} \right\} \\ \mathbf{P}_{mn}^{I-} \\ \mathbf{P}_{mn}^{I+} \\ \mathbf{P}_{mn}^{II-} \\ \mathbf{P}_{mn}^{II+} \end{array} \right\} = \left\{ \begin{array}{c} \mathbf{0} \\ \vdots \\ \mathbf{0} \end{array} \right\} \tag{2.6}$$

$M$ is the node number in the domain $\Omega$, $\mathbf{K}$ is a matrix relating the test function to the nodal pressures in the domain, $\mathbf{E}_1$, $\mathbf{E}_2$, $\mathbf{F}_1$ and $\mathbf{F}_2$ are matrices relating the test function to the modal pressures on $\Gamma_L$ and $\Gamma_R$, $\mathbf{G}_1$, $\mathbf{G}_2$ and $\mathbf{G}_3$ are matrices relating the nodal acoustic pressures in $\Omega$ to different modal pressures on the boundary $\Gamma_L$, $\mathbf{H}_1$, $\mathbf{H}_2$ and $\mathbf{H}_3$ are matrices relating the nodal acoustic pressures to different modal pressures on the boundary $\Gamma_R$.

The azimutal scattering matrix is written as

$$\boldsymbol{\Delta} = (\mathbf{V} - \mathbf{C}\mathbf{K}^{-1}\mathbf{B}^{-1})(\mathbf{U} - \mathbf{C}\mathbf{K}^{-1}\mathbf{A}^{-1}) \tag{2.7}$$

where $\mathbf{A}$, $\mathbf{B}$, $\mathbf{C}$, $\mathbf{U}$ and $\mathbf{V}$ are defined as

$$\begin{aligned} \mathbf{A} = \begin{bmatrix} \mathbf{E}_1 & \mathbf{F}_2 \end{bmatrix} && \mathbf{B} = \begin{bmatrix} \mathbf{E}_2 & \mathbf{F}_1 \end{bmatrix} && \mathbf{C} = \mathbf{G}_1 + \mathbf{H}_1 \\ \mathbf{U} = \begin{bmatrix} \mathbf{G}_2 & \mathbf{H}_3 \end{bmatrix} && \mathbf{V} = \begin{bmatrix} \mathbf{G}_3 & \mathbf{H}_2 \end{bmatrix} \end{aligned} \tag{2.8}$$

The total scattering matrix $\mathbf{S}_{2N\times 2N}$ is achieved by repeating this operation for each m and by gathering the azimutal matrices $\boldsymbol{\Delta}_{2N_r\times 2N_r}$.

## 3. Normalized acoustic impedance of the liner

In this study, a liner composed of a perforated plate and an absorbing porous material backed by a rigid plate is used. The normalized acoustic impedance of the liner is obtained as follows

$$Z = Z_{porous\ material} + Z_{perforated\ plate} \tag{3.1}$$

with

$$Z_{porous\ material} = Z_c \coth(jk_c d_m) \tag{3.2}$$

$Z_c$ and $k_c$ are the surface characteristic impedance and propagation constant of the porous material, respectively, and $d_m$ is the material depth. The values of $Z_c$ and $k_c$ are estimated by the Delany-Bazley model (Delany and Bazley, 1970) expressed as follows

$$\begin{aligned} Z_c &= Z_0\left[1 + 9.08\left(\frac{f}{\sigma}\right)^{-0.754} - 11.9j\left(\frac{f}{\sigma}\right)^{-0.732}\right] \\ k_c &= \frac{\omega}{c_0}\left[1 + 10.8\left(\frac{f}{\sigma}\right)^{-0.700} - 10.3j\left(\frac{f}{\sigma}\right)^{-0.595}\right] \end{aligned} \tag{3.3}$$

where $f$ is the frequency, $\sigma$ is the flow resistivity, $Z_0 = \rho_0 c_0$ is the characteristic impedance of the air, $\rho_0$ is the air density, $c_0$ is the sound celerity in the air and $\omega$ is the pulsation ($\omega = 2\pi f$).

For the perforated plate, the acoustic impedance model of Elnady and Boden (2003) is used

$$Z_E = \mathrm{Re}\left\{\frac{ik}{\sigma_p C_D}\left[\frac{t}{F(k_s'd_p/2)} + \frac{\delta_{re}}{F(k_s d_p/2)}\right]\right\} + \mathrm{iIm}\left\{\frac{ik}{\sigma_p C_D}\left[\frac{t}{F(k_s'd_p/2)} + \frac{\delta_{im}}{F(k_s d_p/2)}\right]\right\} \tag{3.4}$$

with $C_D$ being the discharge coefficient, $d_p$ – pore diameter, $t$ – plate thickness, $\sigma_p$ – plate porosity, $\delta_{re}$ and $\delta_{im}$ – correction coefficients

$$\begin{aligned} &\delta_{re} = 0.2d_p + 200d_p^2 + 16000d_p^3 && \delta_{im} = 0.2856d_p \\ &F(k_s d_p/2) = 1 - \frac{J_1(k_s d_p/2)}{k_s\frac{d}{2}J_0(k_s d_p/2)} && F(k_s'd_p/2) = 1 - \frac{J_1(k_s'd_p/2)}{k_s'\frac{d}{2}J_0(k_s'd_p/2)} \\ &k_s' = \sqrt{\frac{-\mathrm{i}\omega}{\nu'}} && k_s = \sqrt{-\frac{\mathrm{i}\omega}{\nu}} \end{aligned} \tag{3.5}$$

with $\nu$ as the kinematic viscosity and

$$\nu' = 2.179\frac{\mu}{\rho_m} \tag{3.6}$$

where $\mu$ is the dynamic viscosity and $\rho_m$ is the material density.

## 4. Computation of the acoustic power attenuation

The acoustic power attenuation $W_{att}$ which is defined by the ratio between the incoming acoustic power $W^{in}$ and the outcoming acoustic power $W^{out}$ of the duct can be written as follows (Taktak *et al.*, 2010)

$$W_{att}(dB) = 10\log\frac{W^{in}}{W^{out}} = 10\log\frac{\sum\limits_{i=1}^{2N}|d_i|^2}{\sum\limits_{i=1}^{2N}\lambda_i|d_i|^2} \tag{4.1}$$

where $\lambda_i$ and $d_i$ are respectively the eigenvalues and the components of eigenvectors of the matrix $\mathbf{H}$ defined as follows

$$\mathbf{H}_{2N\times 2N} = \mathbf{S'}^{\mathrm{T}*}_{2N\times 2N}\mathbf{S'}_{2N\times 2N} \qquad \mathbf{S'}_{2N\times 2N} = \mathbf{X}_{2N\times 2N}\mathbf{S}_{2N\times 2N}\mathbf{X}^{-1}_{2N\times 2N}$$

$$\mathbf{X}_{2N\times 2N} = \begin{bmatrix} \left[\mathrm{diag}\left(\sqrt{N_{mn}k_{mn}/(2\rho_0 c_0 k)}\right)\right]_{N\times N} & \mathbf{0}_{N\times N} \\ \mathbf{0}_{N\times N} & \left[\mathrm{diag}\left(\sqrt{N_{mn}k_{mn}/(2\rho_0 c_0 k)}\right)\right]_{N\times N} \end{bmatrix} \tag{4.2}$$

with

$$N_{00} = 1 \qquad N_{mn} = SJ_m^2(\chi_{mn})\left(1 - \frac{m^2}{\chi_{mn}^2}\right) \tag{4.3}$$

where $S = \pi a^2$ is the cross section area, and

$$k_{mn} = \sqrt{k^2 - \left(\frac{\chi mn}{a}\right)^2} \tag{4.4}$$

where $k_{mn}$ is the axial wave number associated to the mode $(m, n)$ in the main duct.

## 5. Numerical results

The characteristics of the used liner are:

- The perforated plate: thickness $e = 1\,\mathrm{mm}$, hole diameter $d_p = 1\,\mathrm{mm}$ with a perforation ratio $\sigma_p = 2.5\%$.
- The porous material: thickness $d_m = 20\,\mathrm{mm}$ and the flow resistivity $\sigma = 26000\,\mathrm{Nsm}^{-1}$.
- The rigid wall plate.

The acoustic impedance computed using these characteristics according to the Delany and Bazley (1970) model is then used as an input for computation of the numerical multimodal scattering matrix and the acoustic power attenuation of the studied ducts. The effect of two geometrical parameters is studied: the length and the radius of the section change.

## 5.1.  Duct having a diameter decrease

In this part, the case presented in Fig. 1 is treated: the duct presents a diameter decrease characterized with length equal to $c$ and radius equal to $\rho$. This part of the duct is lined with the studied liner. In the following, the ffect of change of these parameters is investigated.

### 5.1.1.  Effect of change in length

The scattering matrix coefficients and the acoustic power attenuation are calculated in the cases of wall and lined ducts having a duct diameter decrease in order to determine the influence of duct diameter decrease part length on its acoustic behavior. The duct has $0.05\,\mathrm{m}$ radius and length of $1\,\mathrm{m}$. The duct diameter decrease is $0.025\,\mathrm{m}$. Fourth configurations of the ducts are studied:

- First configuration: the length of the duct is divided into three portions: $b = 0.4\,\mathrm{m}$ and $c = 0.2\,\mathrm{m}$, which makes the percentage of the duct diameter decrease portion equal to 20%.
- Second configuration: the length of the duct is divided into three portions: $b = 0.3\,\mathrm{m}$ and $c = 0.4\,\mathrm{m}$, which makes the percentage of the duct diameter decrease portion equal to 40%.
- Third configuration: the length of the duct is divided into three portions: $b = 0.2\,\mathrm{m}$, $c = 0.6\,\mathrm{m}$, which makes the percentage of the duct diameter decrease portion equal to 60%.
- Fourth configuration: the length of the duct is divided into three portions: $b = 0.1\,\mathrm{m}$, $c = 0.8\,\mathrm{m}$, which makes the percentage of the duct diameter decrease portion equal to 80%.

The reflection coefficients $R_{00,00}$ with and without the liner have the same shape (Fig. 3), except that in the treated length these coefficients are significantly attenuated. Note that all $R_{10,10}$ (Fig. 4) are equal to zero except for the forth configuration for values of $k_a$ ranging 2.5 to 3.8 when not treated. On the other hand, $R_{20,20}$ reflection coefficients do not show a difference for the treated or not treated length.
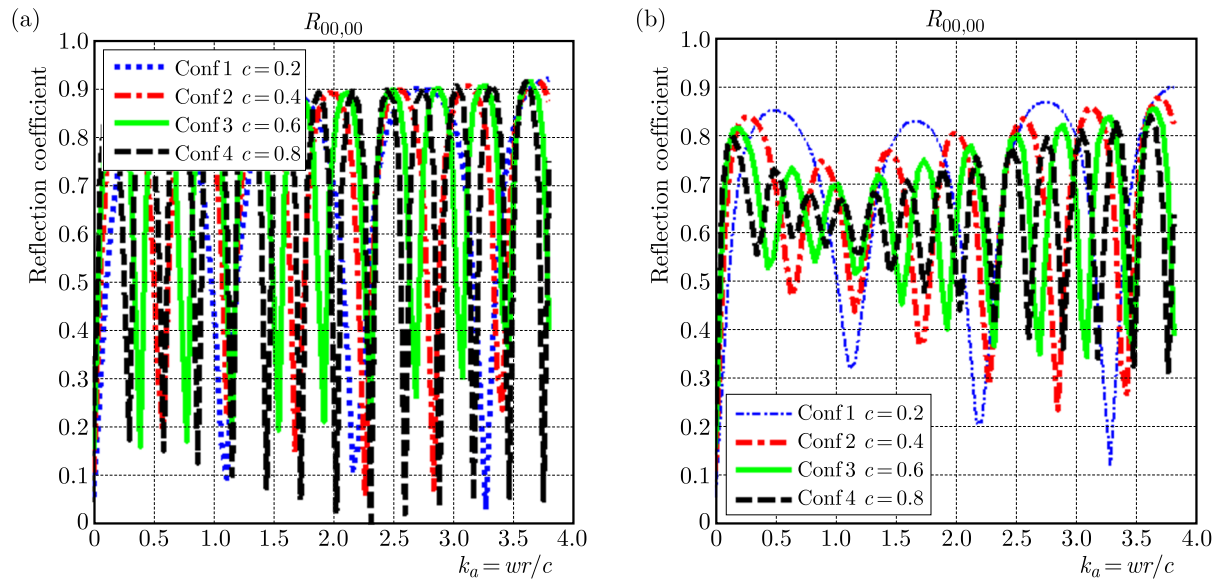


Fig. 3. Reflection coefficient $R_{00,00}$ versus $k_a$ for several configurations. Duct diameter decrease case (a) without liner, (b) with liner

The more the length of the duct diameter decrease increases, the more the transmission decreases and the transmission decreases as the attenuation increases. Note that all transmissions $T_{10,10}$ and $T_{20,20}$ in the free driving material are equal to zero throughout the frequency range studied (no transmission according to both directions of wave propagation) except for $T_{00,00}$
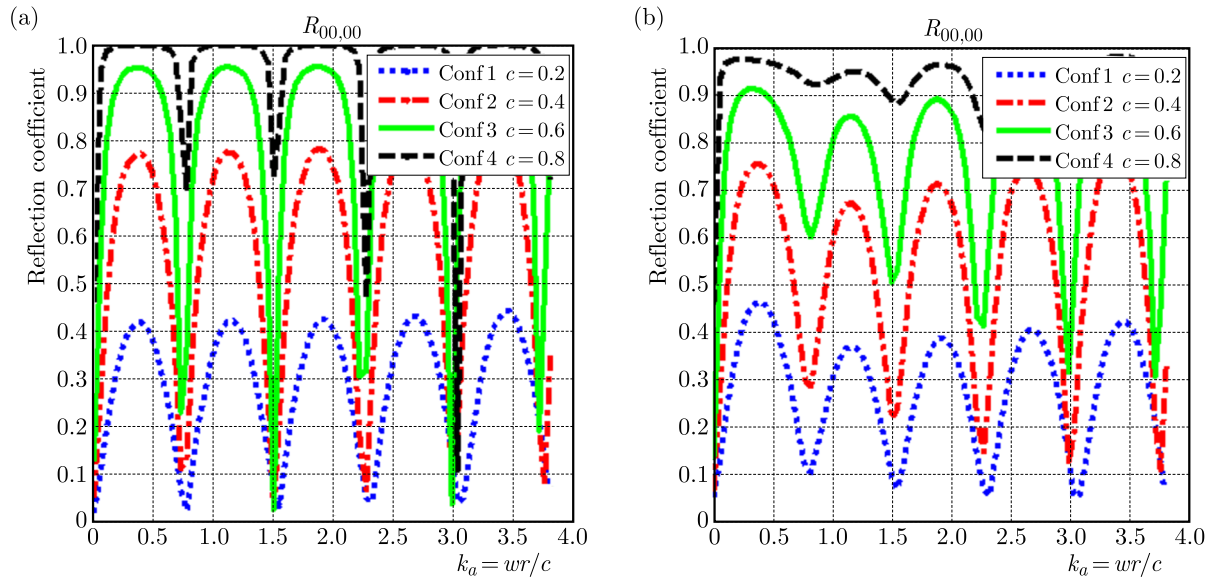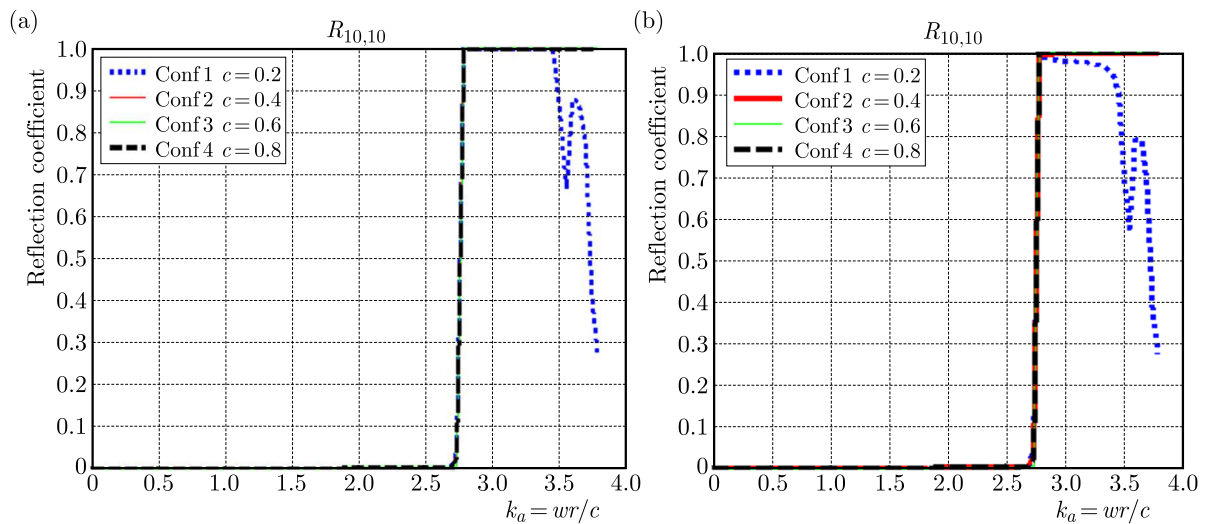
(a)



(b)
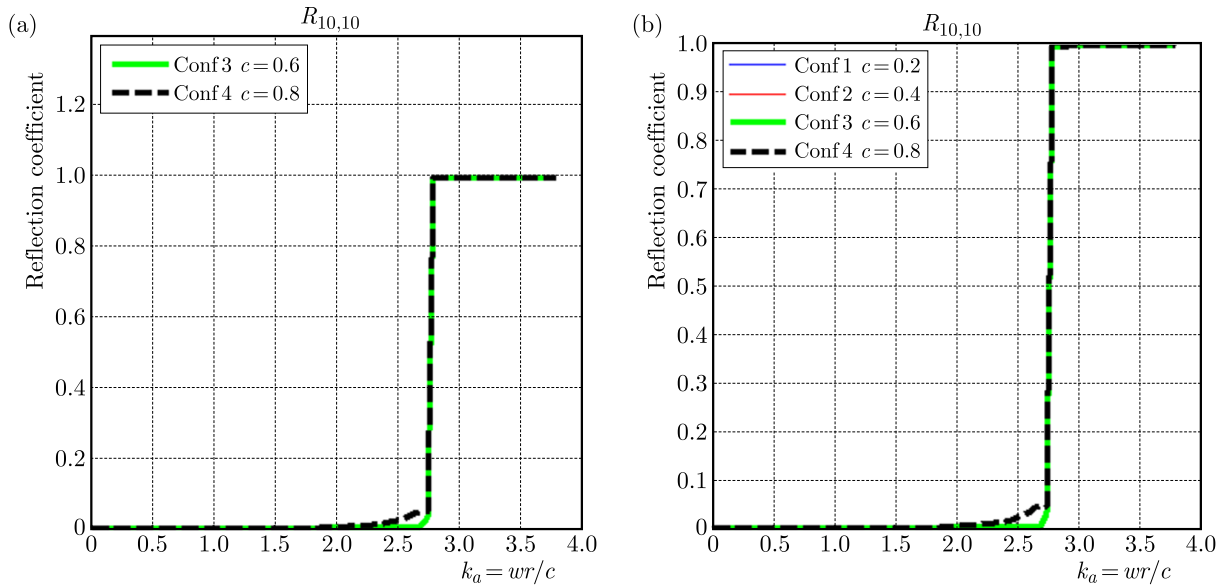
Fig. 4. Modulus of the reflection coefficient $R_{10,10}$ versus $k_a$ for several configurations. Duct diameter decrease case (a) without liner, (b) with liner
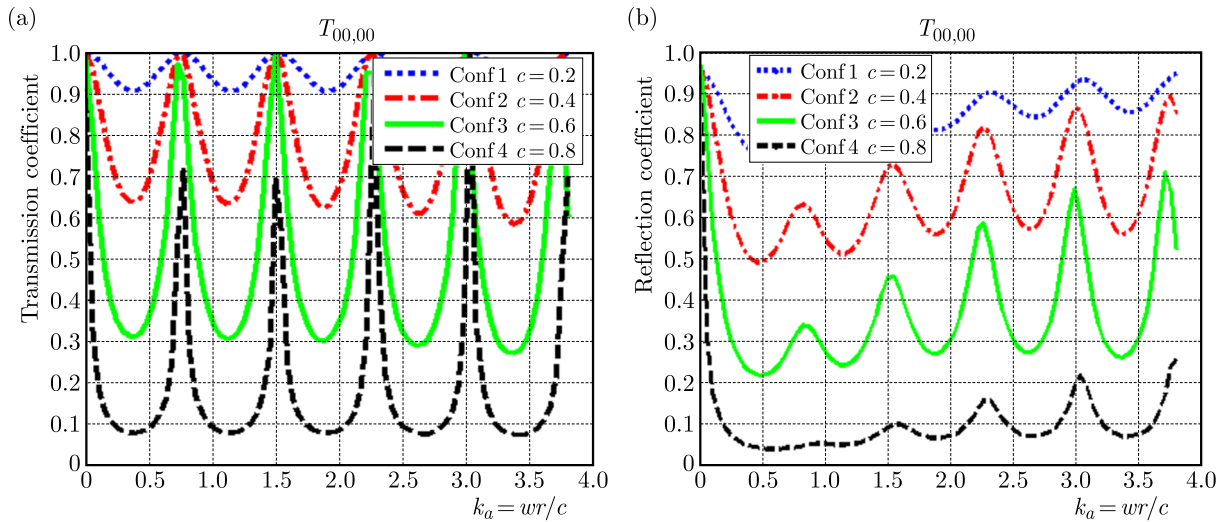
(a)



(b)
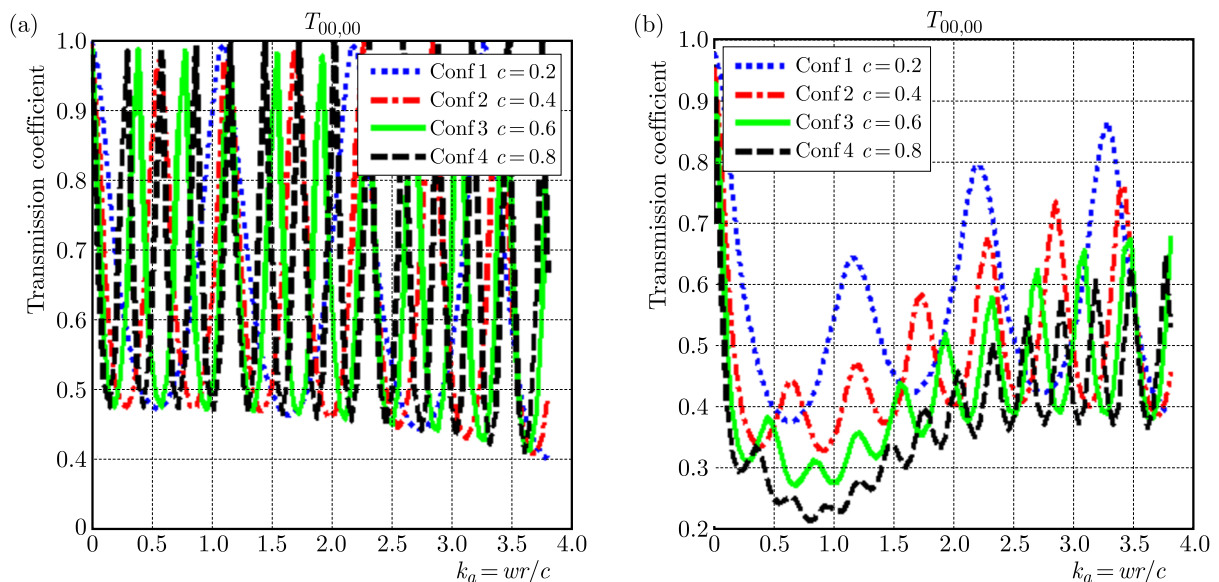
Fig. 5. Modulus of the transmission coefficient $T_{00,00}$ versus $k_a$ for several configurations. Duct diameter decrease case (a) without liner, (b) with liner

transmission submitting a response for values of $k_a$ ranging $[0, 4]$. For $T_{00,00}$ (Fig. 5), all configurations exhibit harmony behavior for $k_a$ ranging from 0 to 4. Figure 6 presents the acoustic power attenuation of the studied cylindrical duct versus $k_a$ for different studied configurations. The results show that attenuation reaches a maximum near $k_a$ equal 2.5. The amplitude of this maximum is about $4.8\,\mathrm{dB}$, $4.3\,\mathrm{dB}$, $4\,\mathrm{dB}$ and $3\,\mathrm{dB}$ for the fourth, third, second and first configuration, respectively. These figures show more clearly that the length of the duct diameter decrease increases more than the attenuation increases. In terms of materials without reflection, the more the length of the duct diameter decrease increases, the more the reflections decrease. The unreflective wave will be absorbed. For the treated length, the unreflective wave will be partly absorbed and the rest part refracted. The more the length of the duct diameter decrease increases (from the fourth to first configuration), the more the large part of the wave will be
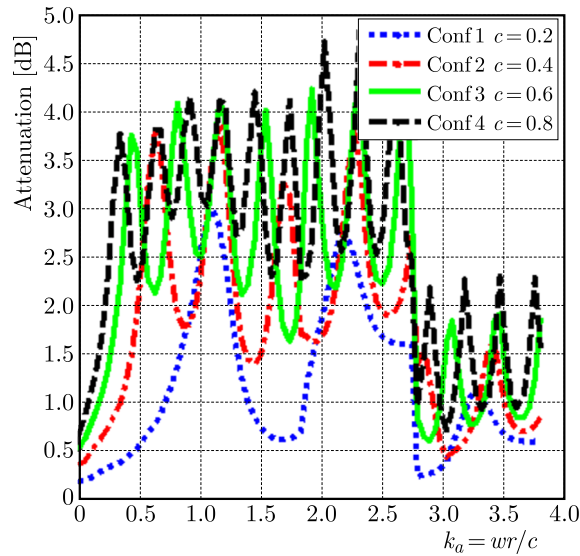
Fig. 6. Acoustic attenuation versus $k_a$ for several configurations. Duct diameter decrease with liner

absorbed. This seems logical as the more the length of the duct diameter decrease increases, the more the surface of the material increases, and the absorption is greater.

### 5.1.2. Effect of the variation of the radius

The scattering matrix coefficients and the acoustic power attenuation are calculated in the cases of wall and lined ducts having a duct diameter decrease in order to determine the influence of the duct diameter decrease part radius on its acoustic behavior. The duct has 0.05 m in radius and length of 1 m. The length of the duct is divided into three portions: the rigid length is equal to 0.35 m, the length treated is 0.3 m, the rigid length is equal to 0.35 m. Fourth configurations of ducts are studied:

- First configuration: the radius of duct diameter decrease is 0.04 m, which makes a radius reduction of 20%.

- Second configuration: the radius of duct diameter decrease is 0.03 m, which makes a radius reduction of 40%.

- Third configuration: the radius of duct diameter decrease is 0.02 m, which makes a radius reduction of 60%.

- Fourth configuration: the radius of duct diameter decrease is 0.01 m, which makes a radius reduction of 80%.

The radius variation affects the amplitude of the reflection coefficients. The reflection modules have a good harmony for all configurations for $k_a$ values $[0, 4]$. It is noted that configurations 3 and 4 (Fig. 7) show good attenuation in the case of treated conduct. The reflection module $R_{10,10}$ shows no change for the first configuration (with and without material), for configuration 3 against improved significantly in the case of the treated conduct going from $k_a = 0$ to 2.6 (Fig. 8). For a more increase of the duct diameter decrease, the transmission decreases (0.9 dB to 0.1 dB). For the fourth configuration, the attenuation of the transmission is 65% near $k_a$ equal 0.75 (Fig. 9). The four configurations have a good harmony for $k_a$ ranging from 0 to 4. The modulus of transmission $T_{10,10}$ and $T_{20,20}$ is zero for the second and third configuration, leading to say that the length treated has no effect contrary to configurations 1 and 2 (Fig. 10) in with the liner of conduct has a considerable effect.
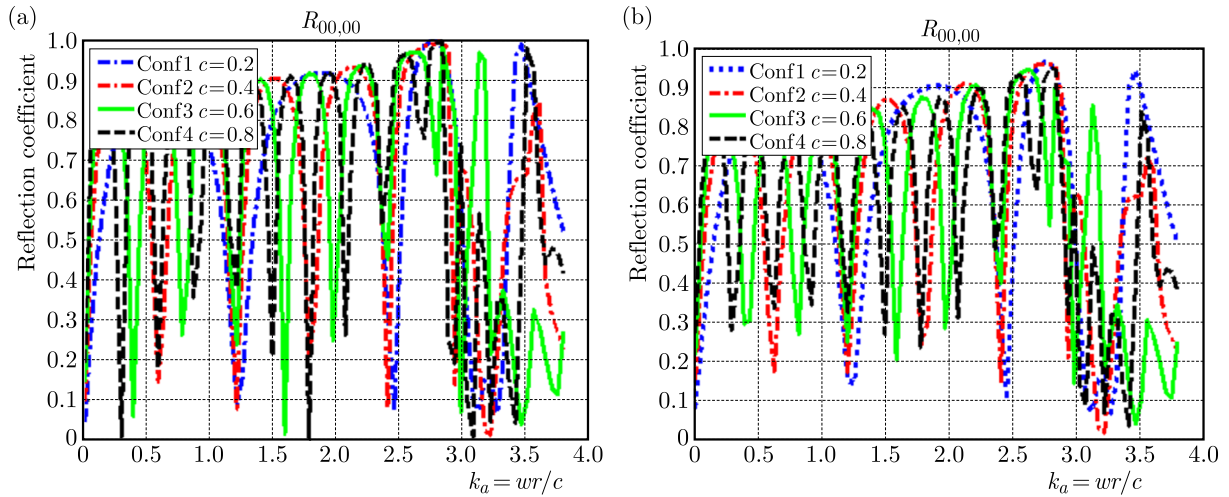
(a)



(b)

Fig. 7. Modulus of the reflection coefficient $R_{00,00}$ versus $k_a$ for several configurations. Duct diameter decrease case (a) without liner, (b) with liner
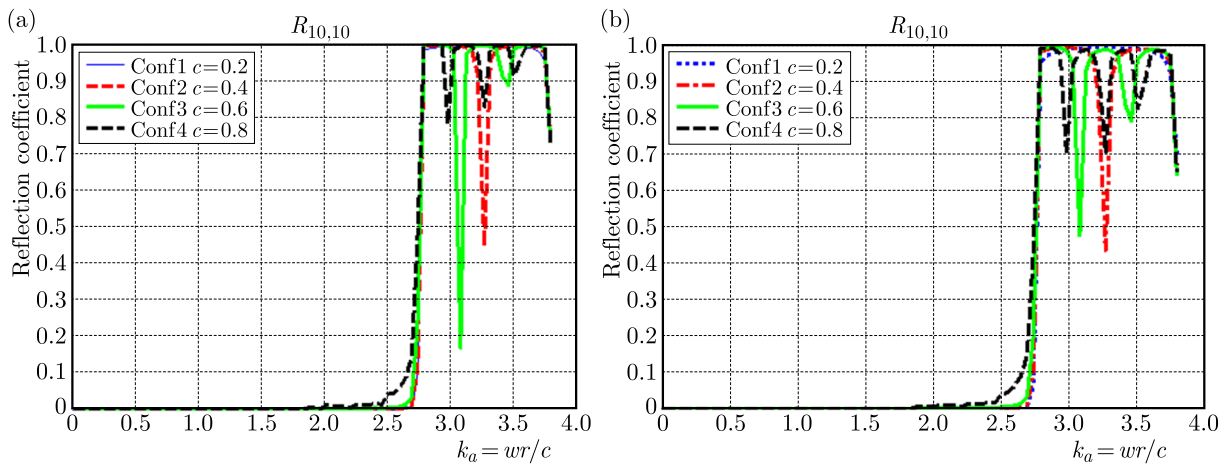
(a)



(b)

Fig. 8. Modulus of the reflection coefficient $R_{10,10}$ versus $k_a$ for several configurations. Duct diameter decrease case (a) without liner, (b) with liner
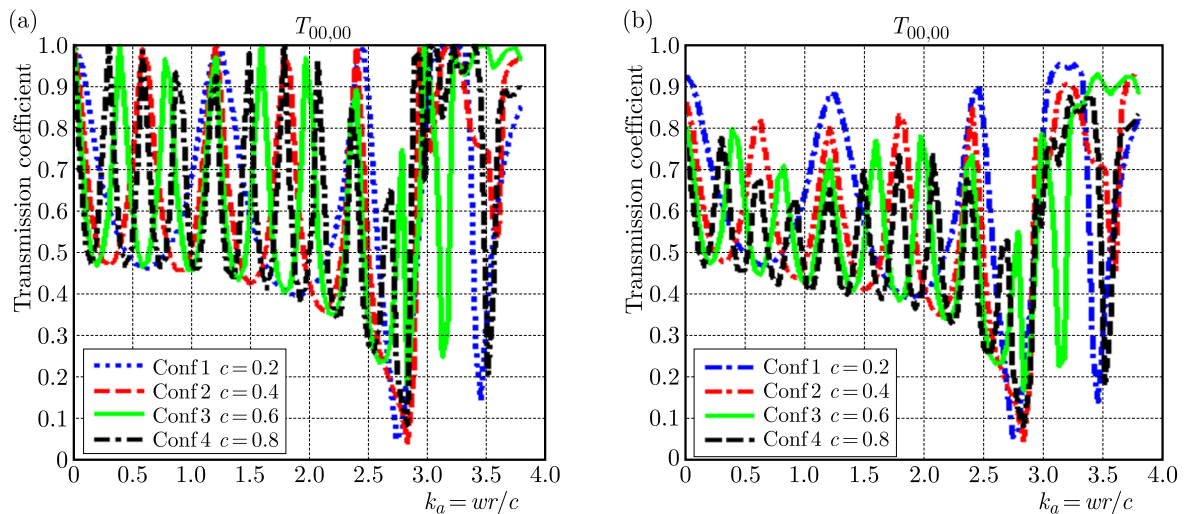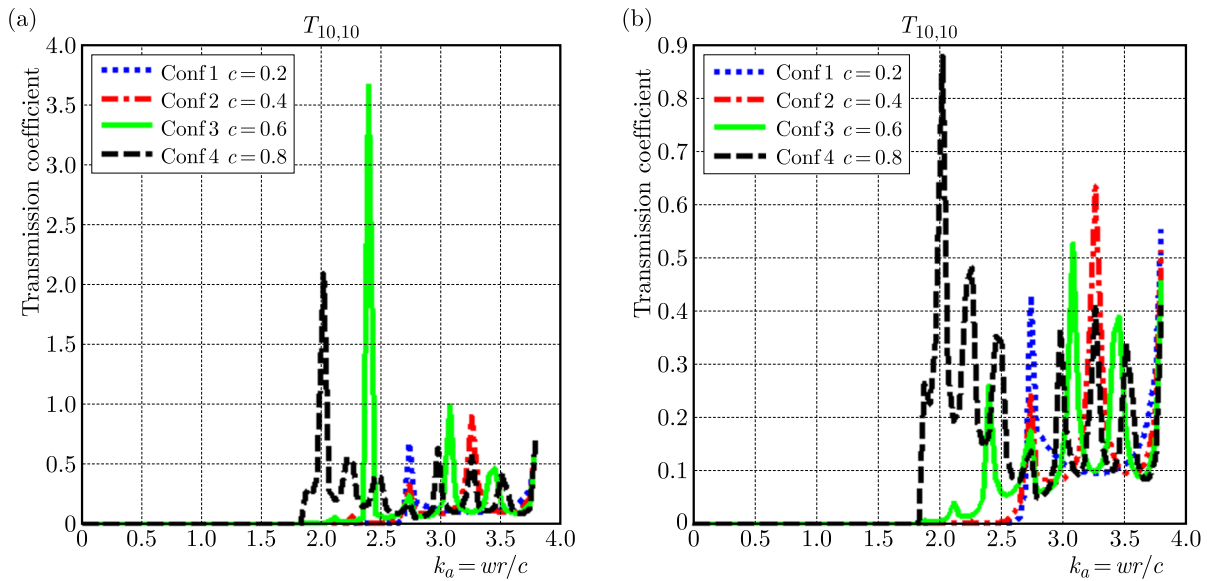
## 5.2. Duct with a diameter increase

In this part, the case presented in Fig. 2 is treated: the duct presents a diameter increase characterized with length equal to $c$ and radius equal to $\rho$. This part of the duct is lined with the studied liner. In the following, the effect of changing these parameters is investigated.

### 5.2.1. Effect of change in length

The scattering matrix coefficients and the acoustic power attenuation are calculated in the cases of rigid and lined ducts having a diameter increase in order to determine the influence of duct diameter increase part length on its acoustic behavior. The duct is 0.05 m in radius and length of 1 m. The duct diameter increase amounts to 0.1 m. Fourth configurations of ducts are studied:

(a)



(b)

Fig. 9. Modulus of the transmission coefficient $T_{00,00}$ versus $k_a$ for several configurations. Duct diameter decrease case (a) without liner, (b) with liner
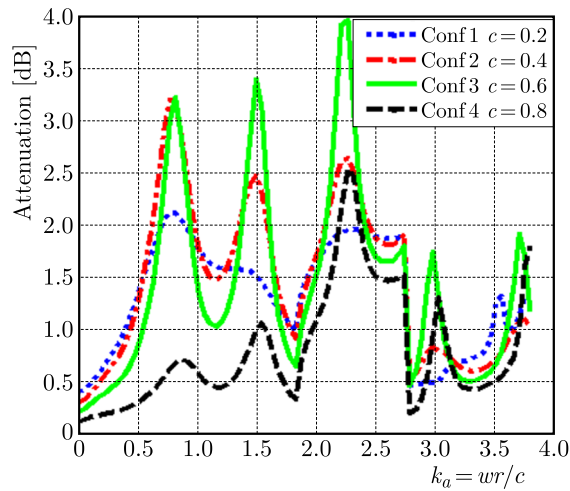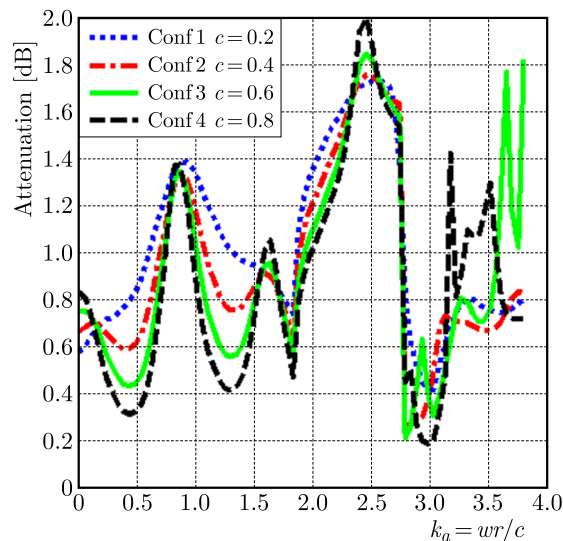


Fig. 10. Acoustic attenuation versus $k_a$ for several configurations

- First configuration: the length of the duct is divided into three portions: $b = 0.4\,\text{m}$ and $c = 0.2\,\text{m}$, which makes the percentage of the duct diameter decrease portion equal to 20%.

- Second configuration: the length of the duct is divided into three portions: $b = 0.3\,\text{m}$ and $c = 0.4\,\text{m}$, which makes the percentage of the duct diameter decrease portion equal to 40%.

- Third configuration: the length of the duct is divided into three portions: $b = 0.2\,\text{m}$, $c = 0.6\,\text{m}$, which makes the percentage of the duct diameter decrease portion equal to 60%.

- Fourth configuration: the length of the duct is divided into three portions: $b = 0.1\,\text{m}$, $c = 0.8\,\text{m}$, which makes the percentage of the duct diameter decrease portion equal to 80%.

Figures 11 and 12 present the variation of the modulus of reflection coefficients $R_{00,00}$ and $R_{10,10}$ versus $k_a$, whereas Figs. 13 and 14 present the variation of the modulus of transmission coefficients $T_{00,00}$ and $T_{10,10}$ versus $k_a$ for several studied configurations. One can observe that the more the length of duct diameter decrease increases, the more transmission decreases and the transmission decreases as the attenuation increases. This is presented in Fig. 15 which shows that the attenuation has a maximum when the transmission is low. Indeed, the fourth configuration has an attenuation of 2 dB for $k_a = 2.5$. In the case without materials, there is no attenuation.
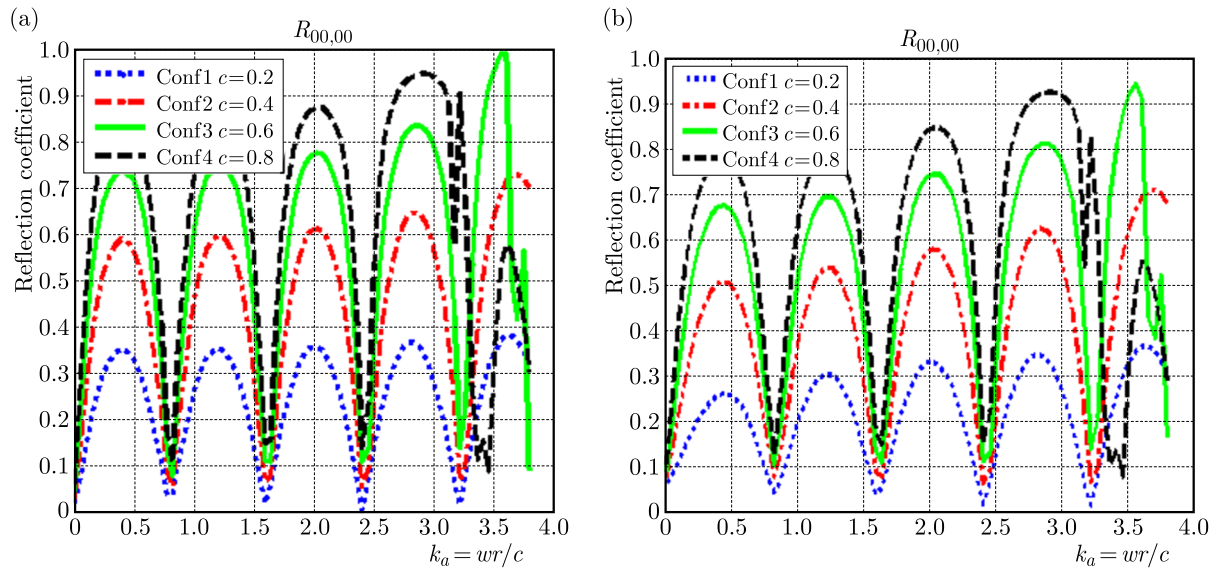
Fig. 11. Modulus of the reflection coefficient $R_{00,00}$ versus $k_a$ for several configurations. Duct diameter increase case (a) without liner, (b) with liner
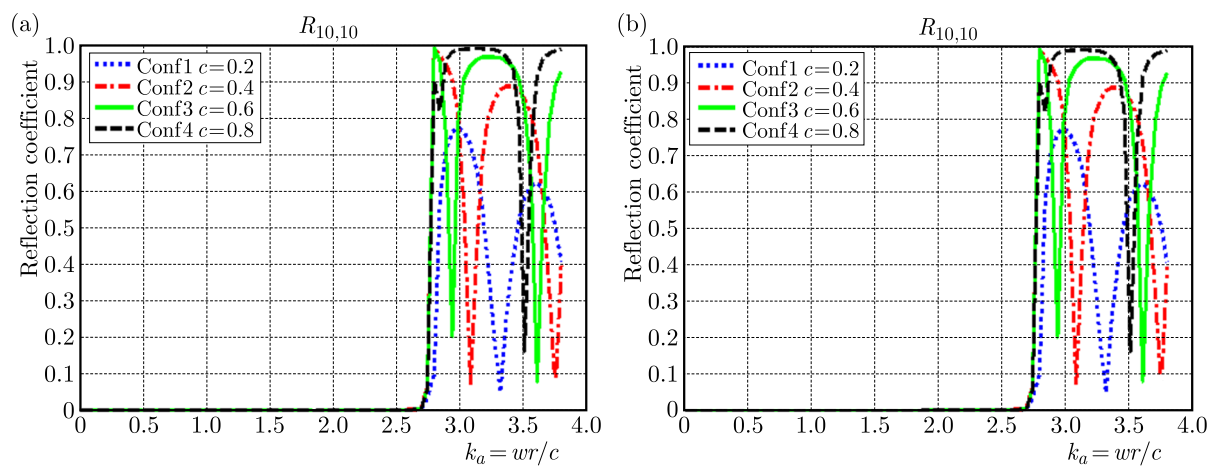


Fig. 12. Modulus of the reflection coefficient $R_{10,10}$ versus $k_a$ for several configurations. Duct diameter increase case (a) without liner, (b) with liner
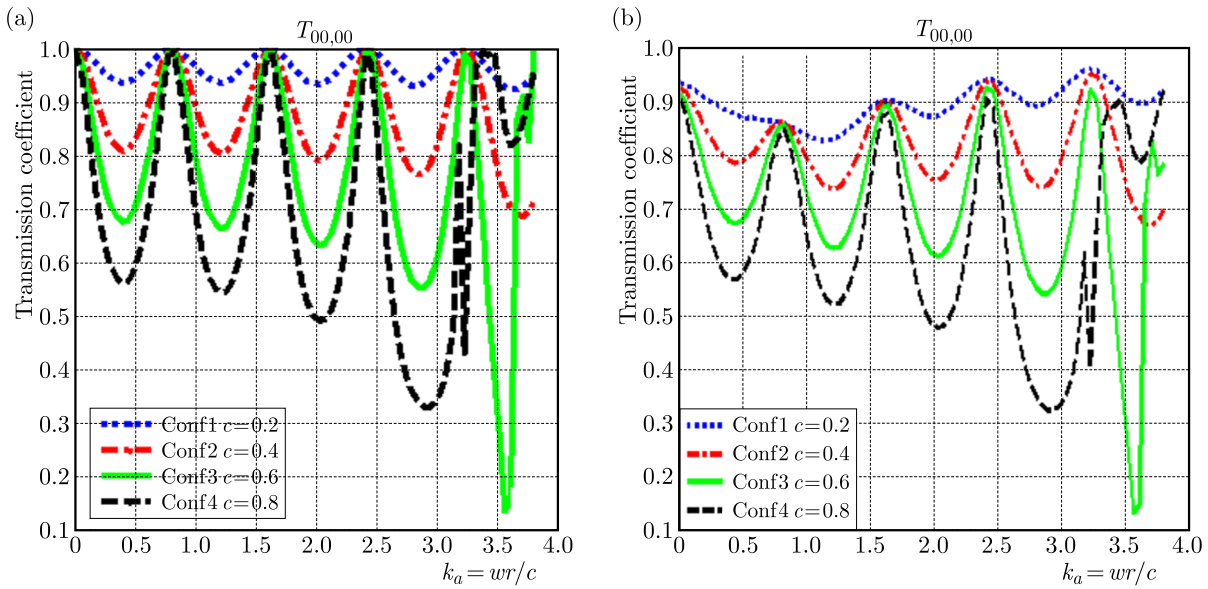


Fig. 13. Modulus of the transmission coefficient $T_{00,00}$ versus $k_a$ for several configurations. Duct diameter increase case (a) without liner, (b) with liner
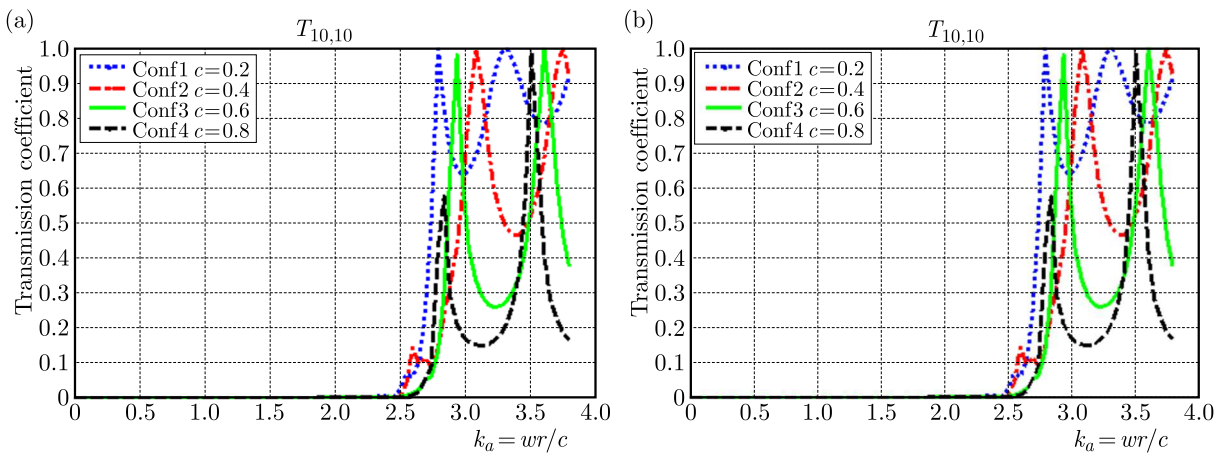
Fig. 14. Modulus of the transmission coefficient $T_{10,10}$ versus $k_a$ for several configurations. Duct diameter increase case (a) without liner, (b) with liner
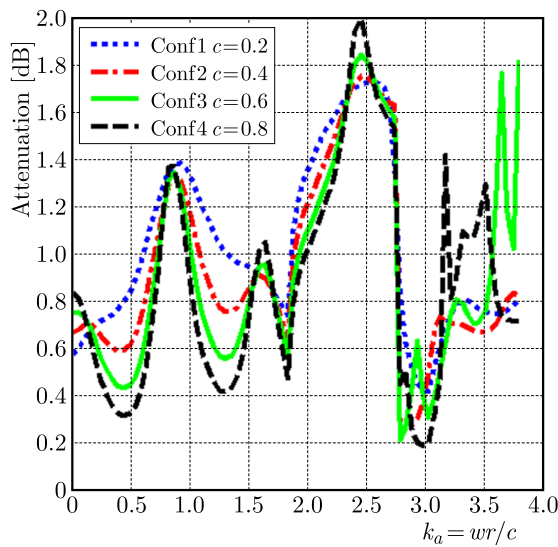


Fig. 15. Acoustic attenuation versus $k_a$ for several configurations (duct diameter increase with liner)

### 5.2.2. Effect of variation of radius

The scattering matrix coefficients and the acoustic power attenuation are calculated in the cases of rigid and lined ducts having a diameter increase in order to determine the influence of the duct diameter increase on its acoustic behavior. The duct has radius of 0.05 m and length of 1 m. The length of the duct is divided into three portions. The rigid length is equal to 0.35 m, the length treated is 0.3 m and the rest rigid length is equal to 0.35 m. Fourth configurations of ducts are studied:

- First configuration: the duct diameter increase is 0.06 m which makes an increase in radius equal to 20%.

- Second configuration: the duct diameter increase is 0.07 m which makes an increase in radius equal to 40%.

- Third configuration: the duct diameter increase is 0.08 m which makes an increasee in radius equal to 60%.

- Fourth configuration: the duct diameter increase is $0.09\,\mathrm{m}$ which makes an increase in radius equal to 80%.

Figures 16, 17 present the variation of the modulus of reflection coefficients $R_{00,00}$ and $R_{10,10}$ versus $k_a$, whereas Figs. 18 and 19 present the variation of the modulus of transmission coefficients $T_{00,00}$ and $T_{10,10}$ versus $k_a$ for several studied configurations. From these figures it can be concluded that the more the duct diameter increases, the more transmission decreases and the reflection increases. There is not much difference in the transmission in the case of conduct treated materials (it falls slightly from 1 to 0.9). Figure 20 presents the acoustic attenuation of the four studied cases. The fourth configuration is the more absorbent with a maximum of $2\,\mathrm{dB}$ at $k_a = 2.5$. This leads to say that the duct diameter decrease configuration is more absorbent, therefore, more efficient than the configuration with the duct diameter increase. Indeed, the configuration with the duct diameter increase section shows no great reflection (low values for $R_{00,00}$ and $R_{10,10}$).



Fig. 16. Modulus of the reflection coefficient $R_{00,00}$ versus $k_a$ for several configurations. Duct diameter increase case (a) without liner, (b) with liner



Fig. 17. Modulus of the reflection coefficient $R_{10,10}$ versus $k_a$ for several configurations. Duct diameter increase case (a) without liner, (b) with liner

Fig. 18. Modulus of the transmission coefficient $T_{00,00}$ versus $k_a$ for several configurations. Duct diameter increase case (a) without liner, (b) with liner



Fig. 19. Modulus of the transmission coefficient $T_{10,10}$ versus $k_a$ for several configurations. Duct diameter increase case (a) without liner, (b) with liner



Fig. 20. Acoustic attenuation versus $k_a$ for several configurations (duct diameter increase with liner)

## 6. Conclusions

In this paper, effect of geometry and impedance variation on the Acoustic Performance of Porous Material Lined Duct is studied. The main conclusions drawn from the study are as follows:

For the case of duct diameter decrease:

- The more the length of the duct diameter decrease increases, the more attenuation increases.

- In terms of materials, the more the length of duct diameter decrease increases, the more reflections decreases and the unreflective wave is absorbed.

- For the treated length, the unreflective wave will be partly absorbed and the rest part refracted. The more the length of duct diameter decrease increases, the more the wave is absorbed.

- The more the length of the duct diameter decrease increases, the more the surface of the material increases, and the absorption is greater.

- The radius variation affects the amplitude of the reflection coefficients. The more the duct diameter decrease increases, the more the transmission decreases.

For the case of duct diameter increase:

- The more the length of the duct diameter increase increases, the more the transmission decreases and the transmission decreases, the more the attenuation increases.

- With the treated length, the more the radius of the duct diameter increase increases, the more reflection increases and the reflection increases, the more the transmission decreases. There is not much difference transmission.

It is concluded from the results presented above that the duct diameter decrease configuration is more absorbent, therefore, more efficient than the configuration with the duct diameter increase.

## References

1. ABOM M., 1991, Measurement of the scattering matrix of acoustical two-ports, *Mechanical Systems Signal Processing*, **5**, 2, 89-104

2. AURÉGAN Y., STAROBINSKI R., 1998, Determination of acoustical energy dissipation/production potentiality from the acoustic transfer functions of a multiport, *Acta Acustica United with Acustica*, **85**, 788-792

3. BEN JDIDIA M., AKROUT A., TAKTAK M., HAMMAMI L., HADDAR M., 2014, Thermal effect on the acoustic behavior of an axisymmetric lined duct, *Applied Acoustics*, **86**, 138-145

4. BI W.P., PAGNEUX V., LAFARGE D., AURÉGAN Y., 2006, Modelling of sound propagation in non-uniform lined duct using a multi-modal propagation method, *Journal of Sound and Vibration*, **289**, 1091-1111

5. DELANY M.E., BAZLEY E.N., 1970, Acoustical properties of fibrous absorbent materials, *Applied Acoustics*, **3**, 105-116

6. ELNADY T., BODEN H., 2003, On semi-empirical liner impedance modeling with grazing flow, *Proceedings of 9th AIAA/CEAS Aeroacoustics Conference*, U.S.A.

7. LEROUX M., JOB S., AURÉGAN Y., PAGNEUX V., 2003, Acoustical propagation in lined duct with flow. Numerical simulations and measurements, *10th International Congress of Sound and Vibration*, Stockholm, Sweden, 3255-3262

8. SITEL A., VILLE J.M., FOUCART F., 2006, Multimodal procedure to measure the acoustic scattering matrix of a duct discontinuity for higher order mode propagation conditions, *Journal of the Acoustical Society of America*, **120**, 5, 2478-2490

9. TAKTAK M., MAJDOUB M.A., BENTAHAR M., HADDAR M., 2012, Numerical modelling of the sound propagation in axisymmetric lined flow duct, *Archives of Acoustics*, **37**, 2, 151-160

10. TAKTAK M., MAJDOUB M.A., BENTAHAR M., HADDAR M., 2013, Numerical characterization of an axisymmetric lined duct with flow using multimodal scattering matrix, *Journal of Theoretical and Applied Mechanics*, **51**, 2, 313-325

11. TAKTAK M., VILLE J.M., HADDAR M., GABARD G., FOUCART F., 2010, An indirect method for the characterization of locally reacting liners, *Journal of the Acoustical Society of America*, **127**, 6, 3548-3559

# A FINITE ELEMENT APPROACH TO DEVELOP TRACK GEOMETRICAL IRREGULARITY THRESHOLDS FROM THE SAFETY ASPECT

Amin Miri

*School of Civil Engineering, Sharif University of Technology, Tehran, Iran*

*e-mail: amin.miri.iust@gmail.com*

Saeed Mohammadzadeh, Hoda Salek

*School of Railway Engineering, Iran University of Science and Technology, Tehran*

Riding quality and safety of rail tracks are directly influenced by track geometry; hence, their degradation along time could reduce safety and cause serious accidents. Standards propose thresholds for track geometrical parameters to keep track safety and riding comfort at an acceptable level. In this study, a method is proposed to select or define a set of proper thresholds for geometrical parameter irregularities according to desirable to safety level. The impact of track geometry irregularities on the derailment index has been investigated through the finite element model. The results suggest that twist and gauge shortage have a greater effect on the derailment index compared to the vertical profile of the track. Having the critical values of geometrical irregularities that result in derailment, safety factors of Iranian and Euro code standards in determining their thresholds are calculated and compared. It is shown that each standard has a unique set of safety factors that depend on speed and geometrical parameters.

*Keywords:* maintenance and inspection, track geometry parameters, finite element, Adams/rail software

## Notations

| | | |
|---|---|---|
| $Q, Y$ | – | vertical and lateral forces between rail and wheel flange, respectively |
| $\beta$ | – | contact angle of rail and wheel flange |
| $\mu$ | – | coefficient of friction between rail and wheel flange |
| $Z$ | – | alignment of modeled track |
| $X$ | – | longitudinal coordinate of modeled tracks |
| $I$ | – | alignment irregularity value |
| $m_o, m_b, m_w$ | – | mass of car body, bolster and wheel set, respectively |
| $I_{ox}, I_{oy}, I_{oz}$ | – | inertia of car body around $x$, $y$ and $z$ axis, respectively |
| $I_{wx}, I_{wy}, I_{wz}$ | – | inertia of wheel set around $x$, $y$ and $z$ axis, respectively |
| $K_{PV}, K_{SV}$ | – | primary and secondary vertical dampers stiffness, respectively |
| $K_{LS}$ | – | lateral dampers stiffness |

## 1. Introduction

Safety and ride comfort are two important characteristics of any railway network. These characteristics are closely related to the geometrical condition of track superstructure, meaning whenever the track superstructure is at standard condition, so are the safety and ride comfort of passing trains. To monitor geometrical conditions of railway tracks, track quality indexes are proposed that are based on track geometrical irregularities.

Whether a geometrical parameter is considered irregular or normal, it is assessed through comparing the measured geometrical parameter with the pre-determined set of thresholds proposed in standard guidelines and standards. Table 1 presents the geometrical parameter threshold as stated in Iranian guideline and Euro code standard (Alert limit state) (Iran Ministry of Roads and Transportation, 2005; EN-13848-5, 2008). It is clear from Table 1 that for a certain geometrical parameter at a certain speed, each guideline proposes different threshold values due to different operational regime and characteristics of the networks in which they are applied.

**Table 1.** Iran and Euro-code thresholds (all values in mm)

| $V > 230$ | $200 < V < 230$ | $160 < V < 200$ | $120 < V < 160$ | $80 < V < 120$ | $V < 80$ | Speed [km/h] | Track parameter |
|---|---|---|---|---|---|---|---|
| – | – | 12 | 16 | 16 | 18 | Iran | Vertical profile |
| 16 | 20 | 20 | 23 | 26 | 28 | Euro code | |
| – | – | 6 | 8 | 10 | 12 | Iran | Gauge + |
| 28 | 28 | 28 | 35 | 35 | 35 | Euro code | |
| – | – | 2 | 2 | 2 | 2 | Iran | Gauge - |
| 5 | 7 | 7 | 10 | 11 | 11 | Euro code | |
| – | – | 5 | 5 | 5 | 5 | Iran | Alignment |
| 10 | 12 | 12 | 14 | 17 | 22 | Euro code | |
| – | – | 1.5 | 1.5 | 1.5 | 1.5 | Iran | Twist |
| 5 | 7 | 7 | 7 | 7 | 7 | Euro code | |

The point to keep in mind regarding the thresholds is that maintenance operations are dependent upon them. So proposing restricted values for thresholds would result in frequent maintenance operations and higher maintenance expenditures, while loose thresholds may increase the possibility of accidents due to excessive irregularities. In this regard, developing an optimized set of thresholds would not only reduce expenses, but also guarantee safety of the operation.

Although defining thresholds of track geometrical irregularities seems to be of great importance, the focus of studies is rather on track geometrical parameters. Some papers have proposed novel track quality indexes based on track geometrical parameters (Madejski and Grabczyk, 2002; ORE, 1981; Miri and Mohammadzadeh, 2014). Others studied the effect of track geometrical irregularities on the performance and conditional assessment of the track, such as initiation and evolution of rail corrugation (Jin *et al.*, 2005), effects of maintenance operations on track quality (Ataei *et al.*, 2014), proposing an inspection interval for track geometrical parameters (Arasteh Khouy *et al.*, 2013), and evaluating the probability of derailment (Mohammadzadeh *et al.*, 2011). Also, there are emerging technologies such as the performance-based track geometry inspection system that relate geometrical parameters of track to vehicle performance in real time (Li *et al.*, 2006). In a recent study by Arasteh Khouy *et al.* (2014) a cost model is proposed to specify the cost-effective maintenance limits for track geometry maintenance. The model considers degradation rates of different track sections and takes into account the costs associated with inspection, tamping, delay time penalties and risk of accidents due to poor track quality to come up with the cost-effective intervention limit of the longitudinal level for tamping.

The aim of this paper is to propose a method that could be used to develop a set of track geometrical irregularity thresholds from the safety point of view. Track geometrical parameters considered in this paper include vertical profile, alignment, track gauge, cross level (also known as "cant") and twist, which are schematically presented in Fig. 1. To measure safety of proposed thresholds for each track geometrical parameter, the derailment index is considered as the safety indicator.
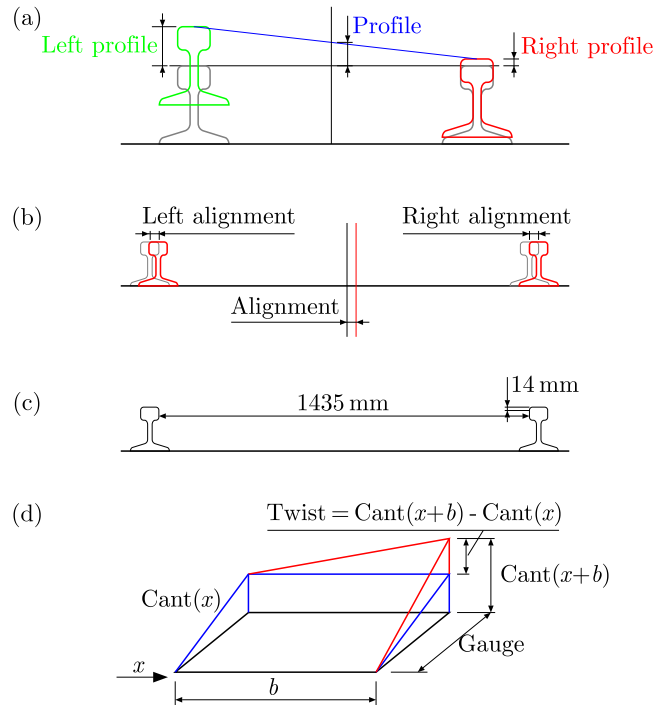
Fig. 1. (a) Vertical profile, (b) alignment, (c) gauge, (d) cant and twist irregularities

Derailment occurs when car wheels run off the rail that supplies support and guidance of the vehicle. Many papers have been published concerning this subject since it is crucial to railway safety (Yadav, 2007; Wu and Wilson, 2006; Elkins and Wu, 2000; Nadal, 1908; Weinstock, 1984; Karmel and Sweet, 1981). Derailment is divided into two main categories: sudden derailment and flange climbing derailment, of which the second category is taken into account in this study.

Flange climb derailment is the case in which wheels climb to the top of the rail individually and then run over it. In this condition, forces causing derailment are higher than resisting forces, but not powerful enough to cause the first case (Yadav, 2007). Such derailment occurs as vertical forces tend to decrease or as a result of increasing lateral forces which are combined with the forwarding movement of the vehicle. In the case of the vertical profile, the vertical forces $Q$ would decrease and as a result, $Y/Q$ increases and may reach the critical limit. This case is also known as "unloading".

There are different theories in the field of the derailment phenomenon such as Nadal theory (Nadal, 1908), Weinstocks (Weinstock, 1984) and Kereszty (Yadav, 2007). According to Nadal (1908), if the resisting forces are higher than the derailing forces, no derailment will occur. Therefore, by analyzing forces applied to the flange – according to the condition stated above – it could be concluded that

$$\mu(Y \sin \beta + Q \cos \beta) + Y \cos \beta \leqslant Q \sin \beta \tag{1.1}$$

which could be restated as

$$\frac{Y}{Q} \leqslant \frac{\tan \beta - \mu}{1 + \mu \tan \beta} \tag{1.2}$$

in which $Y$ and $Q$ are the lateral and vertical forces between the rail and wheel flange, respectively. $\beta$ is the contact angle of the rail and wheel flange and $\mu$ is the coefficient of friction between the flange and rail. For most wheel types, $\beta$ is equal to $68°$ (Yadav, 2007). Also depending on

the geometry and roughness of contact surface, $\mu$ varies between 0.25 and 0.27 (Yadav, 2007). Using these values, equation (1.2) simplifies as

$$\frac{Y}{Q} \leqslant 1.4 \tag{1.3}$$
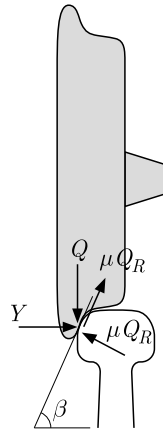


Fig. 2. Free-body diagram of wheel-rail contact forces

Considering the simplicity and comprehensiveness of Nadal theory, it is used as derailment theory in this study. Different values have been stated as the critical limit of the $Y/Q$ ratio. According to UIC 518 and EN14363, in tracks with curve radii of more than 250 meters, the $Y/Q$ ratio shall not be greater than 0.8 according to the sliding mean over 2 m of the track. Also, 0.8 has been stated as the critical value for $Y/Q$ ratio in various works (Elkins and Wu, 2000; Karmel and Sweet, 1981; Kik *et al.*, 2002). In this regard, the critical value of the $Y/Q$ ratio is considered to be 0.8 throughout the paper.

Another important factor in developing thresholds of geometrical irregularities is the chord length. Most guidelines and standards consider chord lengths of 10, 19, and 37 meters. Throughout this paper, a 10 meter chord is selected to control short wavelength defects that can result in high wheel forces over a short portion of the track. These forces may not produce excessive car body motion yet their action on the wheels and track may cause derailment, which is in line with the purpose of this paper.

## 2.  Methodology of research

The aim of this paper is to find the amplitude of track geometrical irregularities that result in derailment. To do so, tracks with a length of 100 meters are modeled in Adams/Rail. Solid elements are used to model the track, and the space between each sleeper is divided into two distinct elements. Geometrical defects are simulated based on the definition of track geometrical parameters using mathematical functions which are characterized by wavelength and amplitude and applied to a 10 meter chord of the modeled tracks.

Next, a freight wagon (characteristics of the wagon are presented in Table 2) passes over the modeled track with a geometrical defect, and dynamic analyses are carried out to determine lateral and vertical forces. Hence, the derailment index is determined for a certain amplitude of geometrical irregularity. Next, the amplitude of geometrical irregularity is increased and the whole process repeats until the derailment index reaches the critical threshold of 0.8; so the corresponding amplitude of geometrical irregularity that results in derailment is determined. Since the speed is an effective parameter in the derailment phenomenon, the whole process is carried out for speeds of 40, 80, and 120 km/h.

**Table 2.** Characteristics of freight wagon used in simulations

| Symbols | Values | Unit | Name |
|---------|--------|------|------|
| $m_o$ | 32 000 | kg | mass of car body |
| $m_b$ | 1503 | kg | mass of a bolster |
| $m_w$ | 1503 | kg | mass of wheel set |
| $I_{ox}$ | $5.68 \cdot 10^4$ | $\mathrm{kg\,m^2}$ | inertia of car body around $x$ axis |
| $I_{oy}$ | $1.97 \cdot 10^6$ | $\mathrm{kg\,m^2}$ | inertia of car body around $y$ axis |
| $I_{oz}$ | $1.97 \cdot 10^6$ | $\mathrm{kg\,m^2}$ | inertia of car body around $z$ axis |
| $I_{wx}$ | 810 | $\mathrm{kg\,m^2}$ | inertia of wheel set around $x$ axis |
| $I_{wy}$ | 810 | $\mathrm{kg\,m^2}$ | inertia of wheel set around $y$ axis |
| $I_{wz}$ | 112 | $\mathrm{kg\,m^2}$ | inertia of wheel set around $z$ axis |
| $K_{PV}$ | 6 | MN/m | primary vertical dampers stiffness |
| $K_{SV}$ | 6 | MN/m | secondary vertical dampers stiffness |
| $K_{LS}$ | 6 | MN/m | lateral dampers stiffness |

## 3. Investigating the effects of alignment

The alignment of the track increases lateral forces on the rail which, according to Nadal theory, could result in derailment if the irregularity is high enough. A polynomial function of the 4th order is chosen to model the alignment, which is as follows

$$z = x^4 - 2lx^3 + l^2x^2 \tag{3.1}$$

in which $z$ is the alignment of the modeled track, $x$ is the longitudinal coordinate of the modeled track, and $l$ is the alignment irregularity value. Figure 3 shows a 12 mm left rail alignment in a 100 meters track that starts from the point at 50 meters and continues up to the point at 60 meters. Dynamic analysis for this track is carried out and Fig. 4 demonstrates the results of the front axle of front and rear bogies, at a speed of 80 km/h.
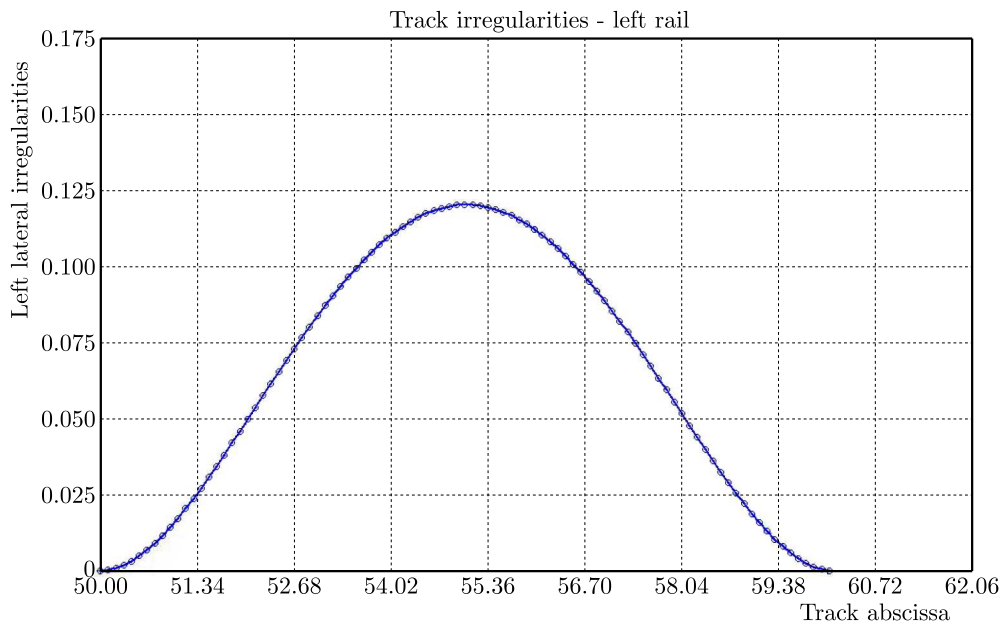


Fig. 3. Model of the alignment defect
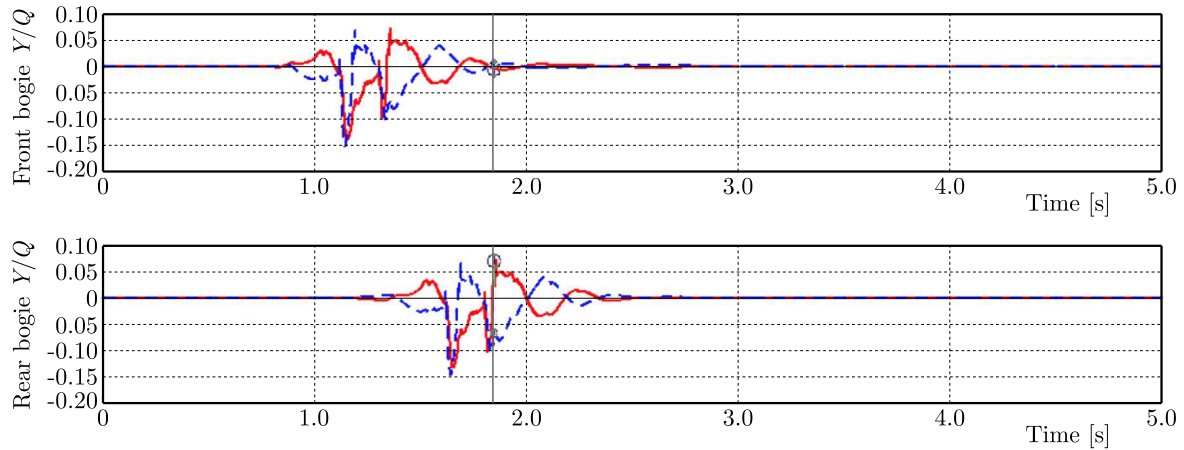
Fig. 4. Result of dynamical analysis of the modeled track with the alignment defect in Adams rail
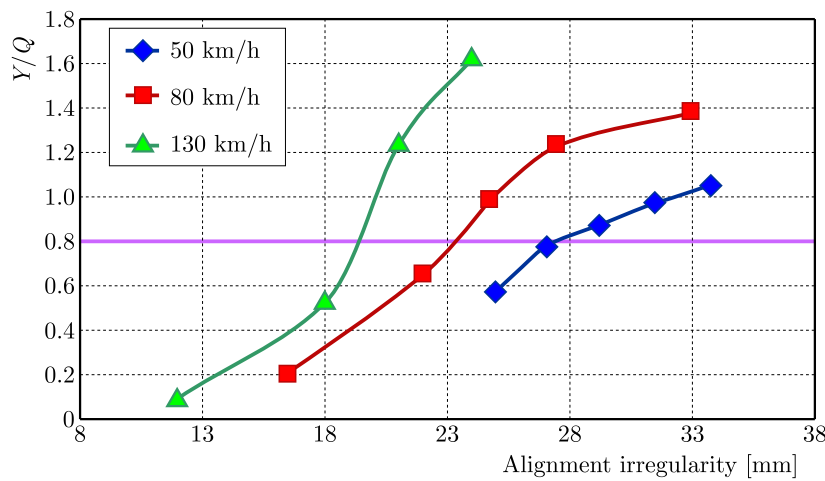


Fig. 5. Derailment index $(Y/Q)$ versus alignment irregularity for speeds of 50, 80, and 140 km/h

Figure 5 presents the results of dynamic analyses of tracks with the alignment defect for speeds of 50, 80, and 140 km/h. It is evident that as train speed increases, derailment occurs at lower wavelengths of the alignment defect. For speeds of 50, 80, and 140 km/h, derailment occurs at alignment irregularities of 27, 21, and 18, respectively. These values are close to the thresholds stated in Euro code standard, but considerably higher than those stated in Iranian standard.

## 4. Investigating the effects of the vertical profile

Vertical forces of the wheel on the rail could decrease in the presence of the vertical profile irregularity which increases the $Y/Q$ value and could result in derailment. The vertical profile is modeled using the same geometrical function used to model the alignment defect. The results of dynamic analysis are presented in Fig. 6. In a lower speed of 50 km/h, the derailment ratio remains below the critical value of 0.8 for vertical profiles of up to 350 mm. But at 140 km/h, derailment occurs at a vertical profile irregularity of 40 mm. Generally, it could be seen that the derailment ratio is less sensitive to the vertical profile than to the alignment, since $Y/Q$ remains fairly below the critical value for higher vertical profile irregularities.
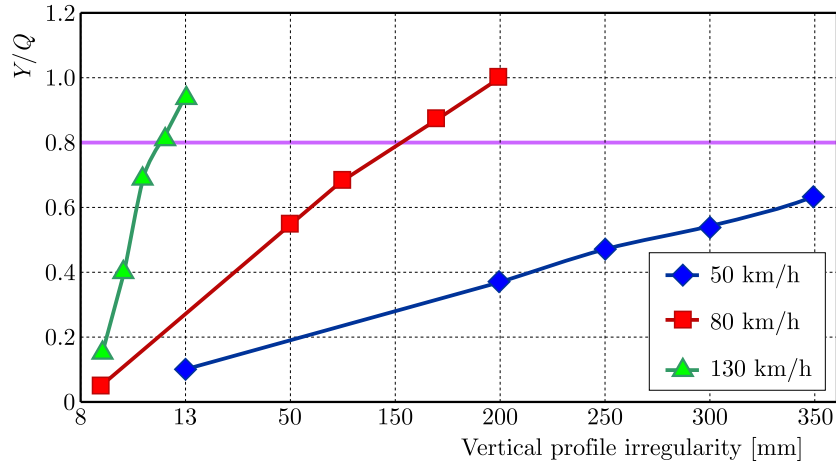
Fig. 6. Derailment index versus vertical profile irregularity for speeds of 50, 80, and 140 km/h

## 5.   Investigating the effects of the track gauge

Track gauge variations can lead to large lateral wheel forces resulting in derailment. Both extra and shortage of the gauge are undesirable, since an extra gauge may end up in wheels falling off the rail, while shortage of gauge could result in wheels climbing on the top of the rail. A trapezoidal function is used to model extra and shortage of the track gauge, as shown in Fig. 7. Figures 8a and 8b present the results of dynamical analysis for the modeled tracks with extra and shortage of the gauge, respectively.
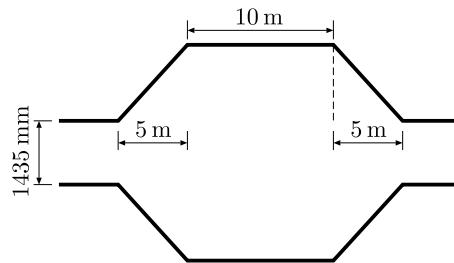


Fig. 7. Geometrical function used to model track gauge irregularities
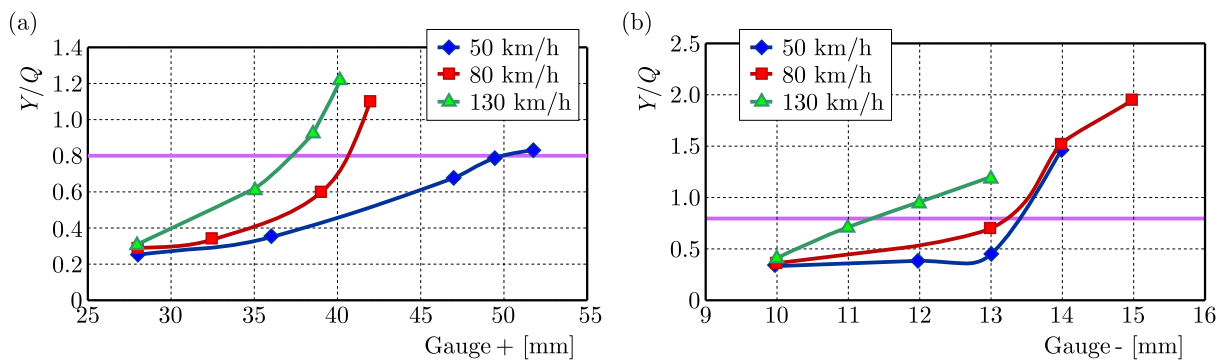


Fig. 8. Derailment index versus (a) extra gauge irregularity and (b) gauge shortage irregularity for speeds of 50, 80, and 140 km/h

## 6. Investigating the effects of twist

To model the twist irregularity, sinusoidal waves with amplitudes of 1, 2 and 3 mm and wavelengths of 2-6 mm are used. The results of dynamical analysis of the modeled tracks with twist defects are presented in Figs. 9a to 9c. As these figures suggest, derailment is sensitive to both wavelength and amplitude of the twist. Keeping the amplitude constant, derailment occurs at shorter wavelengths. On the other hand, an increasing amplitude results in higher $Y/Q$ ratios. The twist with an amplitude of 3 mm results in derailment in speeds of 80 and 140 km/h regardless of the wavelength, as shown in Fig. 9c. These results suggest that the twist is an influential parameter affecting derailment.
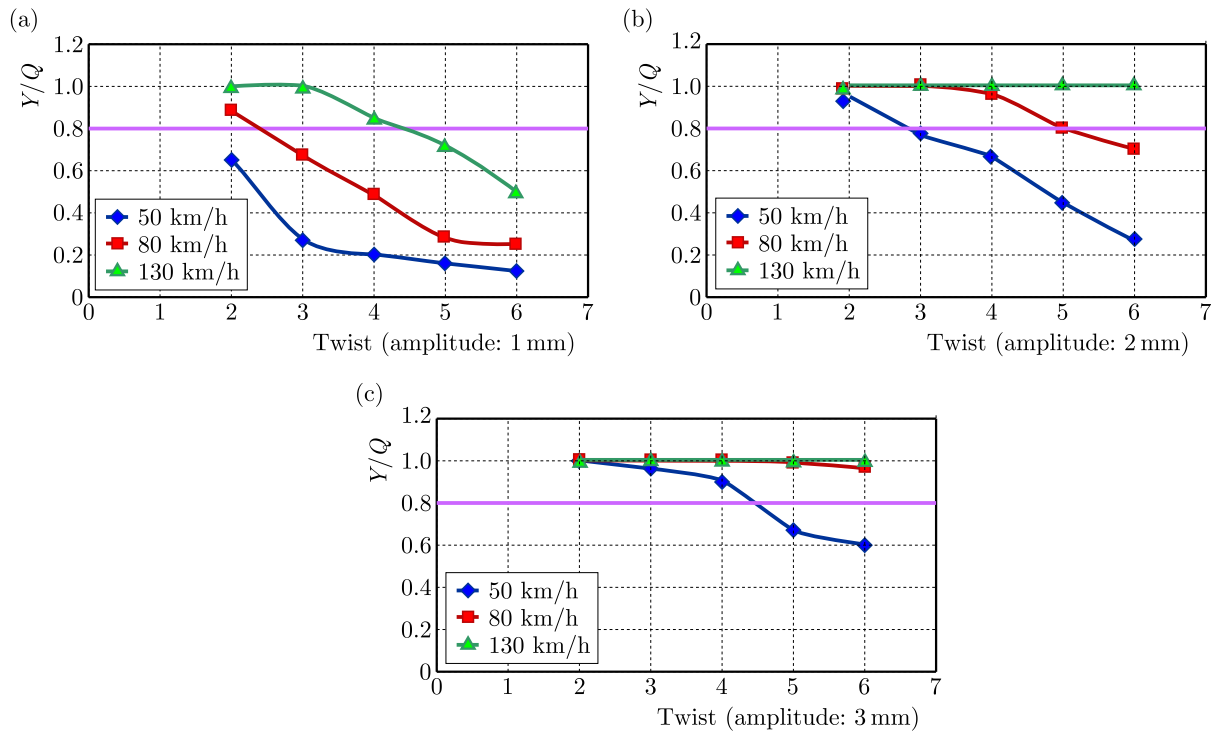


Fig. 9. Derailment index versus twist with an amplitude of (a) 1 mm, (b) 2 mm and (c) 3 mm for speeds of 50, 80, and 140 km/h

## 7. Comments on the results

Critical amplitudes of track geometrical irregularities are concluded in Table 3 for speeds of 50, 80, and 140 km/h. Having the amplitude of track geometrical irregularities that result in derailment, thresholds could be developed by applying the safety factor to the values in Table 3. Moreover, by dividing the critical values in Table 3 to the thresholds stated in the guidelines, it is possible to estimate the safety factors considered in the guidelines from the safety point of view. Figure 10 presents the safety factors determined for Iranian and Euro code standards. Alert limit state of Euro code is considered, since it is recommended based on safety issues related to derailment (EN-13848-5, 2008).

According to Fig. 10, Iranian standard is very conservative in defining thresholds since all safety factors are below 0.5, while Euro code considers logical safety factors. For example, Iranian standard considers a safety factor of 0.1 for the gauge shortage for a speed of 50 km/h, while this value is 0.8 in Euro Code standard. This shows that each standard considers a unique set of safety factors that depend on many parameters, such as the network in which it is applied, maintenance operations frequency and quality, rolling stock characteristics and operational regimes. Also, the

**Table 3.** Critical values of geometrical irregularities that result in derailment

| Parameter | Speed [km/h] | | |
|---|---|---|---|
| | 50 | 80 | 140 |
| Alignment | 27 | 21 | 18 |
| Profile | – | 150 | 40 |
| Gauge + | 49.5 | 41 | 37 |
| Gauge - | −13.5 | −13 | −11.5 |
| Twist (1 mm) | – | 2.5 | 4.5 |
| Twist (2 mm) | 3 | 5 | – |
| Twist (3 mm) | 4.5 | – | – |
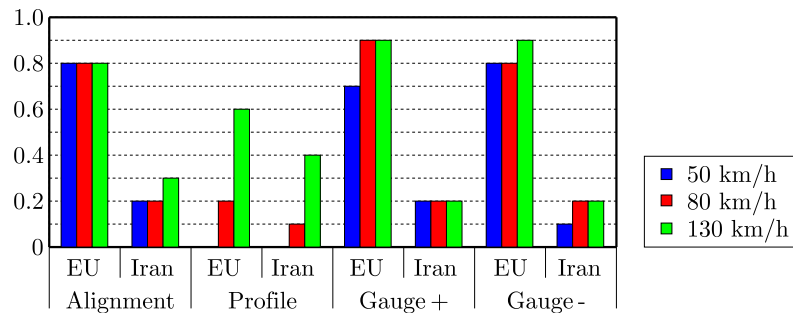


Fig. 10. Safety factors of Iranian and Euro code standard thresholds from the safety point of view

safety aspect is not the sole determinant of the thresholds, and restricted thresholds could be result from considering a plethora of factors for determining the thresholds.

According to Fig. 10, a single value is not considered as the safety factor for all geometrical parameters. For a speed of 140 km/h, safety factors for the alignment, vertical profile, extra gauge and shortage of gauge are 0.8, 0.6 and 0.9, respectively, according to Euro code. As expected, the safety factor of a geometrical parameter varies with speed as well. For example, Euro code takes safety factors of 0.8, 0.6, and 0.9 for the shortage of gauge irregularity at speeds of 50, 80, and 140, respectively.

## 8. Conclusion

Track performance is highly dependent on the condition of geometrical parameters. Using a predefined set of thresholds, it is possible to monitor geometrical irregularities of the track and determine the quality index for a portion of the track. In this study, a method is proposed which could be used to select or define a new set of thresholds from the point of view of safety. To do so, geometrical irregularities are modeled in Adams/Rail finite element software and dynamical analyses are carried out to determine the derailment index. Varying the amplitude of geometrical irregularities, it is possible to determine the critical geometrical irregularity that results in derailment of the train.

The results suggest that derailment is highly correlated to twist and gauge shortage. According to the results, the twist with an amplitude of 3 mm results in derailment at speeds of 80 and 140 km/h regardless of the wavelength. On the other hand, derailment is less sensitive to variations in the vertical profile irregularity, since no derailment occurs the vertical profile irregularity of 350 mm at a speed of 50 km/h.

Multiplying the critical values of track geometrical irregularities by safety factors, it is possible to develop a new set of thresholds from the safety aspect. The reverse could be done to

determine safety factors of guidelines for developing thresholds, which is calculated in this paper for Euro code and Iranian standards. It is observed that each standard considers a unique set of safety factors to determine thresholds of geometrical irregularities. Iranian standard considers very restrictive safety factors, while Euro code choses a logical approach. This is mainly due to the fact that characteristics of the railway networks in which they are applied are different.

Considering high costs of maintenance operations and the importance of geometrical parameters to the safety of tracks, the selection of an optimized set of thresholds for a railway track is crucial. Using the proposed method of this paper could lead to an optimum set of thresholds that satisfies both financial and safety aspects at the same time. The same finite element model could also be used to determine the thresholds from any other aspect, such as ride comfort.

# References

1. AMANI J., AMINI R., 2012, Prediction of shear strength of reinforced concrete beams using adaptive neuro-fuzzy inference system and artificial neural network, *Scientica Iranica*, DOI: 10.1016/j.scient.2012.02.009

2. ARASTEH KHOUY I., LARSSON-KRÅIK P.O., NISSEN A., JUNTTI U., SCHUNNESSON H., 2013, Optimization of track geometry inspection interval, *Journal of Rail and Rapid Transit*, DOI: 10.1177/0954409713484711

3. ARASTEH KHOUY I., LARSSON-KRÅIK P.O., NISSEN A., KUMAR U., 2014, Cost-effective track geometry maintenance limits, *Journal of Rail and Rapid Transit*, **228**, 5, 546-556

4. ATAEI S., MOHAMMADZADEH S., JADIDI A., MIRI A., 2014, Effects of maintenance operations on railway track's mechanical behavior by field load testing, *International Journal of Pavement Engineering*, **15**, 3, 215-227

5. BERGGREN E.G., LI X.D.M., SPÄNNAR J., 2008, A new approach to the analysis and presentation of vertical track geometry quality and rail roughness, *Wear*, **265**, 1488-1496, DOI: 10.1016/j.wear.2008.01.029

6. CORRIEREA F., DI VINCENZO D., 2012, The rail quality index as an indicator of the „global comfort" in optimizing safety, quality and efficiency in railway rails, *Procedia – Social and Behavioral Sciences*, **53**, 1090-1099, DOI: 10.1016/j.sbspro.2012.09.958

7. ELHAG T.M.S., BOUSSABAINE A.H., 2002, Tender price estimation using artificial neural network, II – Modeling, *Journal of Financial Management of Property and Construction*, **7**, 1, 49-64

8. ELKINS J., WU H., 2000, New criteria for flange climb derailment, *Proceedings of 2000 IEEE ASME Joint Rail-road Conference*, Newark, NJ, April 4-6, DOI: 10.1109/RRCON.2000.869983

9. EN 14363, 2005, Railway Applications, Testing for the Acceptance of Running Characteristics of Railway Vehicles, Testing of Running Behaviour and Stationary Tests, CEN, Brussels

10. EN-13848-5, 2008, Track Geometry Quality, Geometric Quality Levels

11. HONG-GUANG NI., AND J.Z. WANG, 2000, Prediction of compressive strength of concrete by neural networks, *Cement and Concrete Research*, **30**, 8, 1245-1250, DOI: 10.1016/S0008-8846(00)00345-8

12. Iran Ministry of Roads and Transportation, 2005, Railway Track Superstructure General Technical Specifications, Standard No. 301, Ministry Publication Service, pp. 9-12

13. JIN X.S., WEN Z.F., WANG K.Y., 2005, Effect of track irregularities on initiation and evolution of rail corrugation, *Journal of Sound and Vibration*, **285**, 21-148, DOI: 10.1016/j.jsv.2004.08.042

14. KARMEL A., SWEET L.M., 1981, Evaluation of time-duration dependent wheel load criteria for wheel climb derailment, *ASME Journal of Dynamic Systems Measurement and Control*, **103**, 219-227, DOI: 10.1115/1.3140632

15. Kik W., Menssen R., Moelle D., Bergerder B., 2002, Comparison of results of calculations and measurements of DYSAF-tests, A research project to investigate safety limits of derailment at high speeds, *Vehicle System Dynamics*, **37**, Suppl., 543-553

16. Li D., Meddah A., Hass K., Kalay S., 2006, Relating track geometry to vehicle performance using neural network approach, *Journal of Rail and Rapid Transit*, **220**

17. Madejski J., Grabczyk J., 2002, Continuous geometry measurement for diagnostics of track and switches, *Proceedings of the International Conference on Switches*, Delft University of Technology, Delft, The Netherlands

18. Miri A., Mohammadzadeh S., 2014, Acceleration-based quality assessment of railway tracks using a 2D simulation model and recorded track data, *Advances in Railway Engineering*, **2**, 1, 13-20

19. Mohammadzadeh S., Ghahremani S., 2010, Estimation of train derailment probability using rail vertical profile alterations, *Structure and Infrastructure Engineering*, 1-20, iFirst article alterations, DOI: 10.1080/15732479.2010.500670

20. Mohammadzadeh S., Sangtarashha M., Molatefi H., 2011, A novel method to estimate derailment probability due to track geometric irregularities using reliability techniques and advanced simulation methods, *Archive of Applied Mechanics*, **81**, 1621-1637, DOI: 10.1007/s00419-011-0506-3

21. Nadal M.J., 1908, *Locomotives à Vapeur*, Collection Encyclopédie Scientifique, Bibliotèque de Mécanique Appliquée et Génie, vol. 186, Paris

22. ORE – International Union of Railways, (1981), Quantitative Evaluation of Geometric Track Parameters Determining Vehicle Behavior, Office of research and experiments, C152, RP1

23. Sibaie M.El., Jamieson D., Tyrell D., Dorcey J., Mee B., Whutten B., Kesler K., 1997, Engineering studies in support of the development of high speed track geometry specifications, *IEEE/ASME Joint Railroad Conference*, Boston, Massachusetts

24. Song H., Kwon S., 2009, Evaluation of chloride penetration in high performance concrete using neural network algorithm and micropore structure, *Cement and Concrete Research*, **39**, 9, 814-824, DOI: 10.1016/j.cemconres., 05.013

25. Union Internationale des CheminsdeFer, 2003, UIC CODE518, Sec.10-1-1-1, Second edition

26. Weinstock H., 1984, Wheel-climb derailment criteria for evaluation of rail vehicle safety, *ASME Winter Annual Meeting*, Paper No. 84-WA/RT-1

27. White H., 1989, Some asymptotic results for learning in single hidden layer feed forward network models, *Journal of the American Statistical Association*, **84**, 408, 1003-1012, DOI: 10.1080/01621459, 1989.10478

28. Wu H., Wilson N., 2006, Railway vehicle derailment and prevention, [In:] *Handbook of Railway Vehicle Dynamics*, S. Inwicki (Edit.), 209-238. Taylor & Francis, UK

29. Xia F., True H., 2004, The dynamics of the three-piece-freight truck, *Vehicle System Dynamics*, **41**, 212-221, DOI: 10.1109/RRCON.2003.1204661

30. Yadav R.K., 2007, *The Investigation of Derailments*, 3rd ed., Indian Railways Institute of Civil Engineering

# EXPERIMENTAL AND NUMERICAL INVESTIGATION OF THE DEEP DRAWING PROCESS FOR AN AUTOMOBILE PANEL AND PREDICTION OF APPROPRIATE AMOUNT OF PARAMETERS BY MULTI-LAYER NEURAL NETWORK

SAEED SIROUS NAJAFABADI

*Young Researchers and Elite Club, Najafabad Branch, Islamic Azad University, Najafabad, Iran*
*e-mail: saeed.sirous89@gmail.com*

ALI TALEBI ANARAKI

*Department of Mechanical Engineering, Najafabad Branch, Islamic Azad University, Najafabad, Iran*

MEHRAN MORADI

*Department of Mechanical Engineering, Isfahan University of Technology, Isfahan, Iran.*

In this paper, the deep drawing process of an automobile panel in order to select the appropriate amount of parameters has been investigated. The parameters include friction between the blank and die, blank width and length, blank thickness and gap between the blank and blank-holder. A multi-layer artificial neural network (ANN) trained by finite element analyses (FEA) is applied in order to improve forming parameters and achieve a better quality. As the FEA results are used to train the ANN, the FEA results have been verified by three experiments. Finally, an appropriate amount of each parameter is predicted by the trained ANN and a FEA has been done based on the ANN prediction to evaluate the accuracy of the trained ANN. Moreover, it is shown that the ANN could predict results within a 10 percent error. In addition, the proposed method for prediction of the appropriate parameters (ANN) is confirmed by comparing with the Taguchi design of experiment prediction. It is also shown that the model obtained by the former method has lower errors than the latter one. In this study, the Taguchi model is used to evaluate the effect of parameters on tearing and wrinkling. Based on the Taguchi design of experiment, while the blank length is the most effective parameter on tearing, the maximum height of wrinkles on flanged parts mainly depends on the blank thickness.

*Keywords:* deep drawing, finite element analysis (FEA), multi-layer artificial neural network (ANN), Taguchi design

## 1. Introduction

Sheet metal forming is one of the most widely used industrial processes, which is fast and cost-effective. Deep drawing, which is widespread among other sheet metal forming processes, is used for a wide variety of industrial purposes. In the deep drawing process (Fig. 1), the blank is positioned on a die. Then, the blank-holder places the blank at a certain position and the punch forms the blank with a downward movement. There are lots of parameters that affect the deep drawing process and quality of the final product such as geometry of the forming tool, punch and blank-holder force, friction, blank dimensions, and material properties (Singh and Agnihotri, 2015; Fereshteh-Saniee and Montazeran, 2003). These parameters affect the appearance of the final product. Adjustment of each mentioned parameter might prevent forming defects such as tearing, wrinkling, thinning, earing, and springback. Therefore, selection and optimization of the process parameters is an effective way to form the blank with better appearance, in a cost effective way and without any defects.
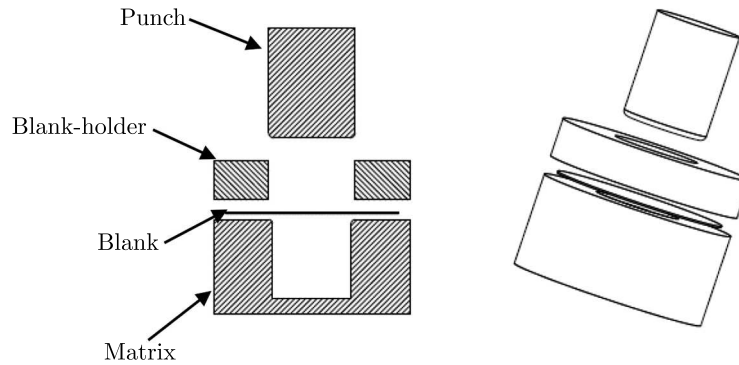
Fig. 1. Schematic of the deep drawing process

Colgan and Monaghan (2003) tried to find effective parameters based on a statistical method using orthogonal arrays. They conducted an experiment on four hundred steel parts with 1 mm thickness. The results showed that the punch radius and matrix radius were the main effective parameters in final thickness. They reported that smaller punch edge radius needed more force and it was shown that the lubricant type affected the punch force significantly. In addition, in a recent research by Laurent *et al.* (2015) warm deep drawing of AA5754-O alloy was investigated. They manufactured a warm die for their experiment and studied the influence of temperature on springback. They conducted their experiments between room temperature and 200°C. In their research, Abaqus/Explicit was used to simulate the procedure in which an anisotropic temperature-dependent model was utilized. Furthermore, they verified the simulation results using an experiment.

Sezek *et al.* (2010) studied the effect of deep drawing factors such as die radius, friction and blank thickness both numerically and experimentally. The results showed that the friction coefficient and the blank-holder angle were main factors. They also concluded that the drawing ratio was reduced by increasing the die angle and the results of experiment were close to the simulation. Demirci *et al.* (2008) investigated deep drawing parameters for Al1050 alloy by both FEA and experiment. They focused on the blank-holder force and thickness distribution in the drawn part.

Chamekh *et al.* (2009) used trained ANN to investigate the anisotropy behavior based on FEA results. A back propagation ANN was implemented in their study and the results of FE were in good agreement with the results of ANN. They declared that the combination of ANN and FE could be used to optimize the deep drawing process. Moreover, Forouzan and Akbarzadeh (2007) utilized a back propagation ANN to predict some material properties such as yield stress, elongation, ultimate stress and average of anisotropy for rolled AA3004 aluminum alloy. The maximum percentage of error was estimated about 6.35 by trained ANN. Finally, they inferred that mechanical properties and anisotropy of the material were predictable by using their method.

El Sherbiny *et al.* (2014) investigated changes in thickness and residual stress in the deep drawing process. Their paper analyzed the process by using FEA. The results of simulation were verified by experimental results. In their article, geometrical parameters were radius of the matrix edge, radius of the punch edge and the friction coefficient. They investigated the effect of the mentioned parameters on the drawn blank in 8 sections. The maximum amount of residual stress was also measured. Furthermore, Padmanabhan *et al.* (2007) investigated the effect of three parameters including matrix radius, blank-holder force and friction coefficient in deep drawing of symmetric parts. They combined the FE method with the Taguchi method. The results showed that the most effective parameter in thickness distribution was the matrix edge radius which was followed by the blank-holder force and the friction coefficient.

Yagami *et al.* (2007) investigated the effect of blank-holder motion on formability factors such as wrinkling and drawing of a copper blank during the deep drawing process. They designed an algorithm that controlled the process and compared the results with finite element simulation. The results illustrated that the wrinkles which were lower than $200\,\mu$m could be omitted. Furthermore, the FE results reported improvement of the formability and reduction of the ductile damage behavior. Additionally, Zein *et al.* (2014) analyzed a typical deep drawing die and focused on improving finial dimensions using plastic return. First, they verified the FEA with experiments. Then, they changed a single parameter while other parameters were kept constant, and repeated the finite element simulation trying to optimize the main parameters such as matrix edge radius, punch radius, blank thickness and clearance. Finally, optimum amounts were suggested for main parameters.

Candra *et al.* (2015) investigated the variable blank-holder force during punch motion in order to prevent tearing. In their research, they used FEA with a slab method. Although their results contained slight errors, they inferred that the presented method assisted to prevent the sheet from tearing during the deep drawing process. Fereshteh-Saniee and Montazeran (2003) studied the drawing force using analytical, numerical, and experimental methods. They investigated the effect of element type on the drawing force and strain alteration and studied the effect of friction coefficient on the force-displacement diagram using the Finite Element Method. It was also inferred that the Sieble equation could estimate the results more accurate than other analytical methods and proved that the Sieble equation was more sensitive to the friction coefficient than FEA. Finally, by comparing FE results with experimental results, it was determined that shell elements estimated more accurate results than four-node elements.

Singh *et al.* (2011) conducted a research on optimum amounts for the matrix and punch radius, friction coefficient and drawing ratio for St14 blank with 1mm thickness. They obtained optimum amounts using 28 experiments, neural network and genetic algorithm coupling. In an comprehensive study, Wifi and Abdelmaguid (2012) worked on a review article introducing optimization methods for both single and progressive dies.

In this paper, by using artificial neural network trained by FEA results, an appropriate amount of each parameter is selected in three steps. First, FEA is done and verified by three experiments. Second, the ANN is trained based on the design of experiment data. Third, the appropriate amount of each parameter is found using the trained ANN. These three steps are shown in Fig. 2. The main parameters which are selected to be investigated are the friction between matrix, blank-holder and blank, friction between punch and blank, blank width and length, blank thickness and the gap between blank and blank-holder. In addition, outputs which are defined as impact indicators are tearing and wrinkling.

## 2. Simulation of the deep drawing process

### 2.1. Finite Element modeling

As it can be seen in Fig. 3, four parts are modeled in the Finite Element software. These parts include the blank, punch, matrix, and blank-holder. Due to symmetry of the matrix, half of it has been modeled in Abaqus/Explicit. The punch, matrix, and blank-holder are assumed to be discrete rigid parts and their displacements are controlled by reference points. The mesh used in this simulation is R3D3 which means 3 points and 3 dimensional solid elements.

The blank is the only deformable part which is meshed by S4R shell elements. S4R means four points with reduced integration. These meshes are suitable for simulation of sheet behavior with respect to thickness variation (Abaqus v. 6.11).
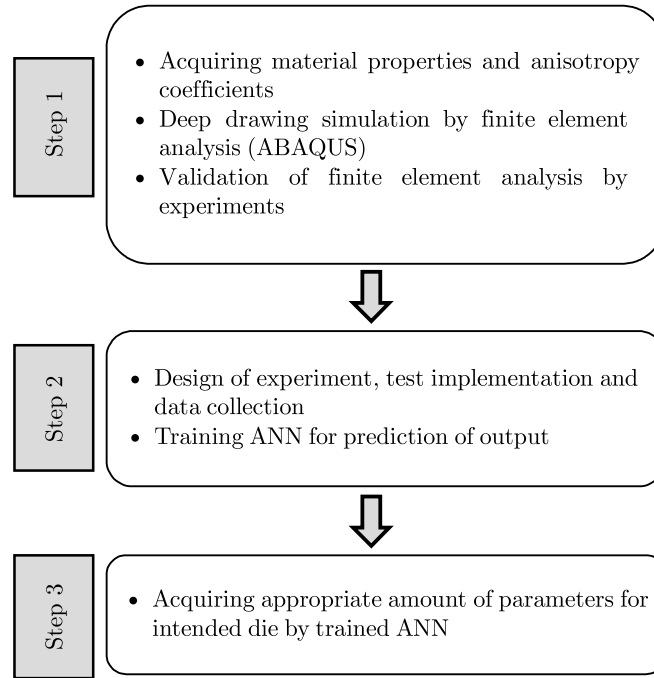
Fig. 2. Proposed steps in the investigation



Fig. 3. Defined parts used in FE simulation

## 2.2.  Material properties

A deformable St14 blank is analysed in this article. The chemical composition of this material is shown in Table 1. Its stress-strain curve is evaluated with INSTRON 4486 simple tensile test machine under ASTM E8 standard and 0.8 mm sheet thickness (Fig. 4a). Mechanical properties are demonstrated in Table 2. It should also be noted that values of anisotropy have been calculated with the Hill criterion which is shown in formula as

$$R_{22} = \sqrt{\frac{r_{90}(r_0 + 1)}{r_0(r_{90} + 1)}} \qquad R_{33} = \sqrt{\frac{r_{90}(r_0 + 1)}{r_{90} + r_0}} \qquad R_{12} = \sqrt{\frac{3r_{90}(r_0 + 1)}{(2r_{45} + 1)(r_0 + r_{90})}} \quad (2.1)$$

The values of $R_{11}$, $R_{13}$ and $R_{23}$ are equal to 1.

**Table 1.** Chemical composition of St14 [wt%]

| C | Mn | S | P | Al |
|---|---|---|---|---|
| 0.037 | 0.222 | 0.03 | 0.05 | 0.061 |

Furthermore, to evaluate tearing, the FLD criterion is used. The FLD diagrams are found from the library of Autoform software (Fig. 4b). It has been assumed that thickness differentials have not affected the FLD (Hashemi *et al.*, 2012).

**Table 2.** Mechanical properties of St14

| Parameters | Value |
|---|---|
| Density, $\rho$ | $7800\,\text{kg/m}^3$ |
| Young's modulus, $E$ | $210\,\text{GPa}$ |
| Poisson's coefficient, $\nu$ | 0.3 |
| Yield Stress, $\sigma$ | $169.54\,\text{MPa}$ |
| Ultimate Stress, UTS | $520\,\text{MPa}$ |
| $r_0$ | 1.87 |
| $r_{45}$ | 1.3 |
| $r_{90}$ | 2.14 |
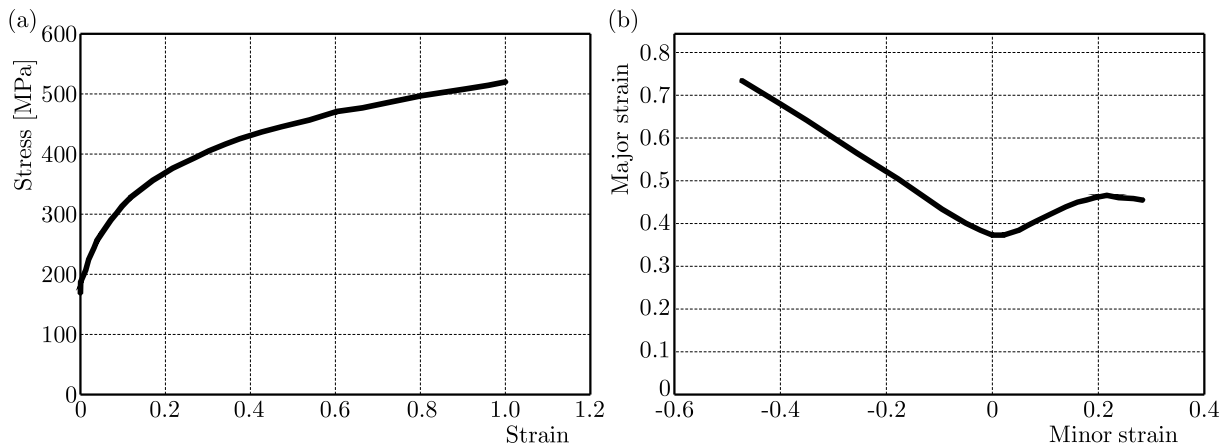


Fig. 4. (a) Stress-strain graph for St14, (b) FLD graph for St14

### 2.3. Validation of FEA results

Validation of FEA results is done in three steps. These steps are mesh independence and include investigation of energy graphs and comparison between FEA and experiments. Regarding the mesh independence, as can be seen in Table 3, several analyses with different mesh sizes are done. Meshes are sized from 3 mm to 14 mm and the results showed that 8, 10 and 12 mm meshes lead to similar results. Therefore, for precise estimation and optimization of the analysis time, a 10 mm mesh has been used. In the second part of the validation, in which energy graphs were scrutinized, kinetic energy and artificial energy graphs were compared with internal energy. Finally, in the third part of the validation, FEA results were compared with three specimens drawn in different circumstances.

**Table 3.** Independence of the mesh size

| Mesh size [mm] | Number of element | Number of node | Time resolution [s] | STH [mm] | FLD |
|---|---|---|---|---|---|
| 3 | 97200 | 97844 | 26640 | 0.416 | 1.250 |
| 4.5 | 43254 | 43684 | 11435 | 0.652 | 0.919 |
| 5.5 | 28994 | 29346 | 6756 | 0.606 | 0.906 |
| 6 | 24400 | 24723 | 4192 | 0.679 | 0.815 |
| 8 | 13650 | 13892 | 2216 | 0.687 | 0.805 |
| 10 | 8760 | 8954 | 1354 | 0.701 | 0.793 |
| 12 | 6100 | 6262 | 856 | 0.727 | 0.707 |

Regarding the third part of validation, Fig. 5 shows the drawing result for the first specimen in which wrinkles occurs on the flanging part and wall of the specimen both in the experiment and FEA. The input parameters for this experiment are 0.3 mm gap between the blank-holder and blank, 0.8 mm blank thickness, 1200 × 1460 mm blank size. Lubricant films between the punch and blank and a piece of plastic between the matrix, blank-holder and blank are taken into account used. It should be noted that the friction coefficient is selected based on the previous studies (Colgan and Monaghan, 2003; Watiti and Labeas, 2010; Gao *et al.*, 2010). In the second experiment, shown in Fig. 6, all parameters except the gap between blank-holder and blank remained constant. As the gap was closed for drawing the second specimen, tearing occurred in FEA and the experiment. In FEA, the elements with the FLD criterion higher than 1 were eliminated to show tearing. Finally, in the third experiment, increasing the gap up to 0.05 mm resulted in thorough drawing without tearing and severe wrinkling. As shown in Fig. 7 and Table 4, thickness and wrinkling in the third drawing specimen are evaluated by FEA and experimentally.
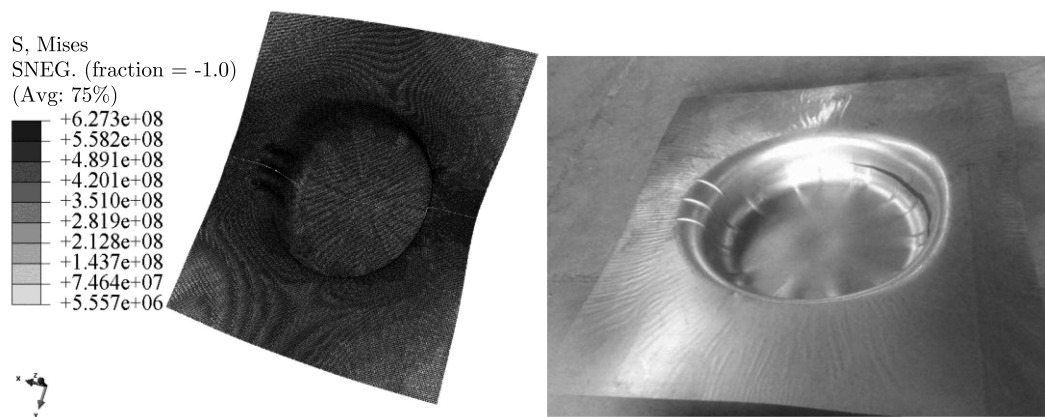


Fig. 5. Comparison between finite element analysis and experiment for the first sample
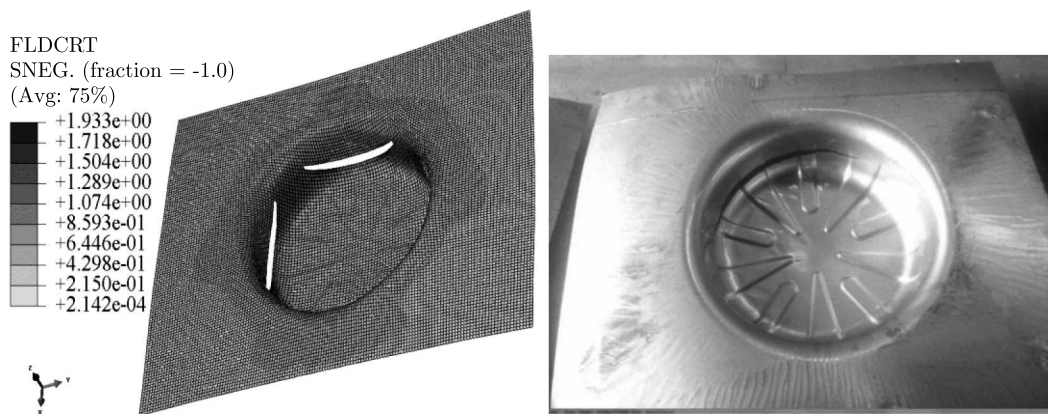


Fig. 6. Comparison between finite element analysis and experiment for the second sample

**Table 4.** Comparison of wrinkling length between experiment and FEA for the third sample

| Wrinkling location based on Fig. 3 | Experiment [mm] | FEA [mm] | Error [%] |
|---|---|---|---|
| Wrinkling length (left) | 1.75 | 1.90 | 8.21 |
| Wrinkling length (right) | 1.55 | 1.67 | 7.45 |
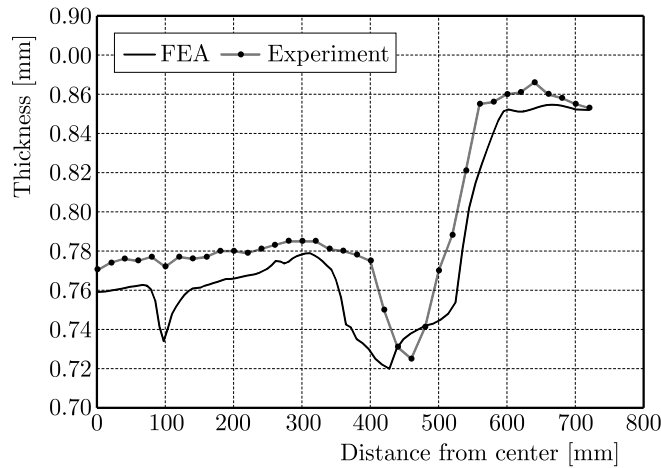
Fig. 7. Comparison of thickness between finite element analysis and experiment for the third sample

Given the validation procedure, it can be concluded that FEA results are precise. Therefore, these results could be used to train an ANN.

## 3. Modeling

### 3.1. Design of the experiment

After determination of six influential parameters in the final step of panel production, each parameter is defined in three levels based on a multiple experiment and FEA. As it can be seen in Table 5, these parameters include friction between the blank and die surface, blank width, blank length, blank thickness and blank-holder gap.

Provided that the design of experiment was based on the full factorial design, 729 experiments should be done which was time consuming. Therefore, the method of training an ANN has been used to determine an appropriate amount of each parameter. The Taguchi method was utilized to evaluate the effect of each parameter on tearing and wrinkling. Based on the number of parameters and their levels in the Minitab software, it was determined that the L27 model should be used for the Taguchi design of the experiment.

**Table 5.** Input parameters and selected levels

| Parameters | Factor number | Level 1 | Level 2 | Level 3 |
|---|---|---|---|---|
| Friction matrix/blank-holder and blank | Factor 1 | 0.04 | 0.07 | 0.1 |
| Friction punch and blank | Factor 2 | 0.04 | 0.07 | 0.15 |
| Blank width | Factor 3 | 1150 | 1200 | 1250 |
| Blank length | Factor 4 | 1360 | 1460 | 1560 |
| Blank thickness | Factor 5 | 0.7 | 0.8 | 0.9 |
| Blank-holder gap | Factor 6 | 0.02 | 0.05 | 0.07 |

### 3.2. Training an artificial neural network

ANN is an effective method for solving problems in which relationships between parameters are complex or defining them in one formula is difficult. In the deep drawing process, numerous parameters exist and an analytical formula could not explain them. In the present research, a network with 2 hidden layers is utilized. The first hidden layer has 10 neurons with the

sigmoid transfer function, and in the second hidden layer a linear transfer function is used. The neural network is a feed-forward network which uses the back propagation error algorithm and the Levenberg-Marquardt training algorithm and in order to train it 109 data are used. The network is selected based on testing a wide variety of networks with different numbers of layers and available training algorithms.

As it is obvious in Fig. 8, there are six input parameters in the first layer and two outputs including the value of the FLD criterion and maximum wrinkling height. Figure 9 illustrates the training process with the best performance in the first epoch and the training process terminated after six epochs. It can be seen that the precision of the network with respect to validation data has been decreased after the first epoch. Figure 10 shows the regression graph of the trained network. In this graph, values of $R$ near 1 reveal network precision and, more importantly, the similar $R$ values for training data, test data and validation data indicate that this network does not memorize the training data.
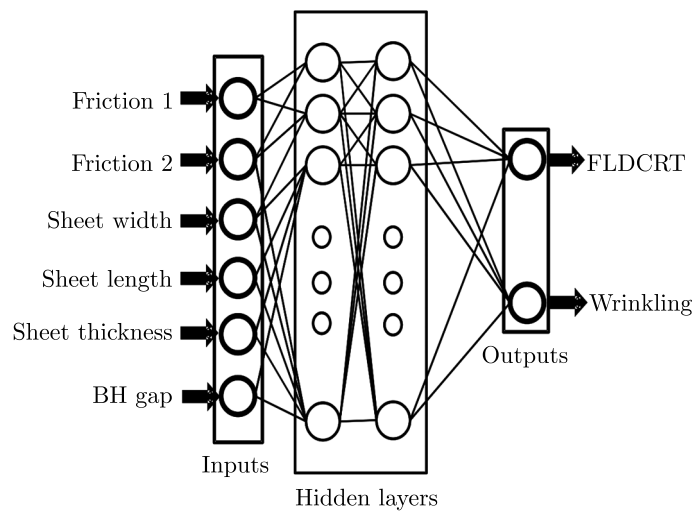


Fig. 8. Schematic of the applied artificial neural network
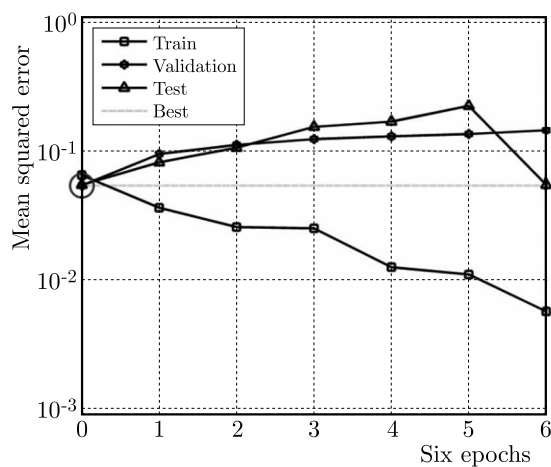


Fig. 9. Training process of artificial neural network
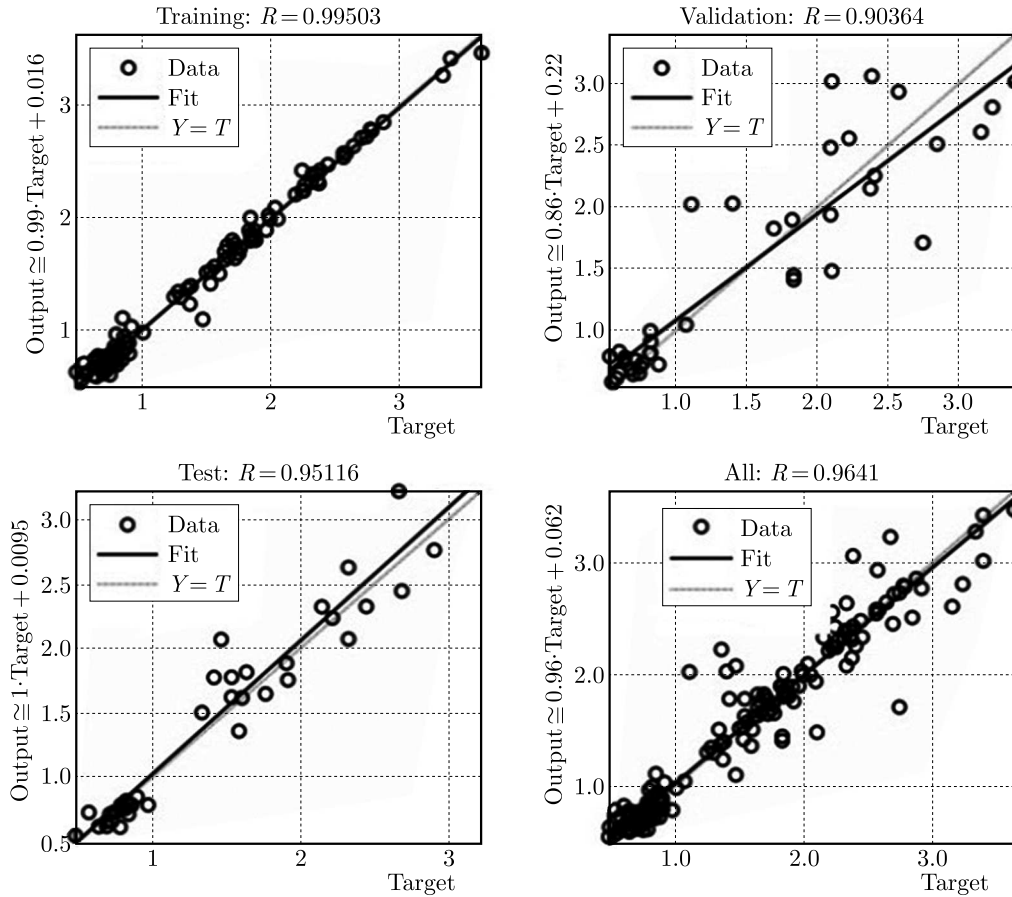
Fig. 10. Regression graph of trained artificial neural network

## 4. Selection of appropriate amounts for input parameters

In this article, two methods are used for the selection of appropriate amount of the input parameters in order to reach the best output amounts. The first method is to predict using a trained ANN and the second one is the Taguchi DOE. It is attempted to reduce the maximum height of wrinkling and keep the FLD criterion below 1 to prevent tearing.

## 5. Results and discussion

As for the Taguchi DOE, graphs which are called signal to noise ratio are obtained. Each of these graphs demonstrates the influence of input parameters on the outputs. In fact, the more differentials in a line, the greater effect of that parameter. In Figs. 11a and 11b, the influence of inputs on the FLD criterion and the maximum wrinkling height are shown, respectively. In Fig. 11a, it can be seen that the blank length is the most effective parameter and friction between the matrix, blank-holder and blank is the least influential parameter among the FLD criterion parameters. Moreover, in Fig. 11b, it is obvious that the blank thickness is the most important, and the blank length is the least important parameter affecting the maximum wrinkling height created on the flanging part of the product.

Regarding prediction of appropriate input parameters by the Taguchi DOE as shown in Table 6, a test with 121331 code is suggested. This code shows the level of each parameter. For example, the aforementioned code shows that friction between the matrix, blank-holder and blank is in the first level which is 0.04 mm, friction between the punch and blank is in the
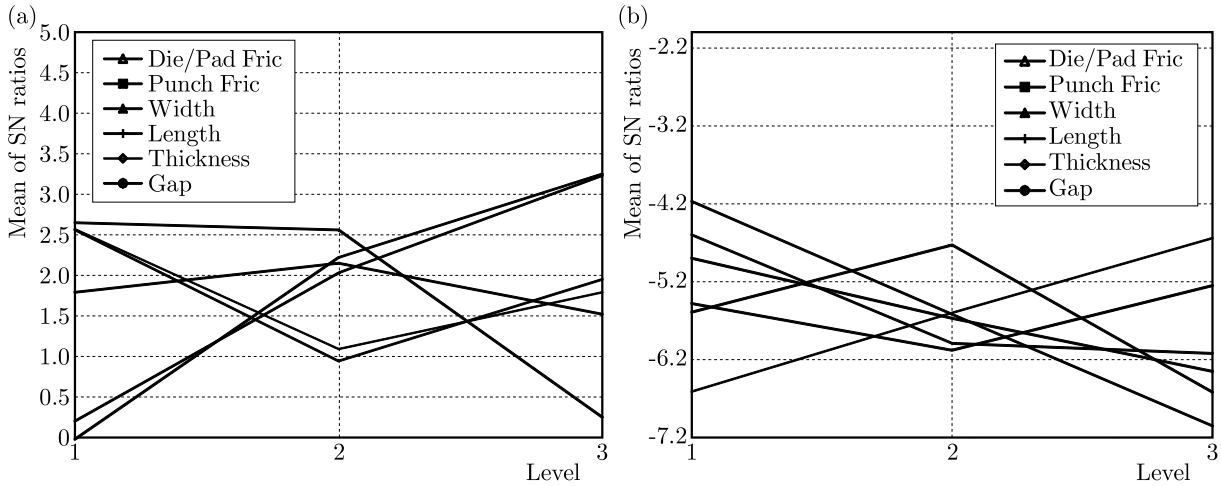
Fig. 11. Influence of input parameters on (a) FLDCRT and (b) maximum wrinkling length

second level which is 0.07 mm, the blank width is in the first level which is 1150 mm. Similarly, the blank height is 1560 mm, blank thickness is 0.09 mm and the gap between the blank and blank-holder is 0.02 mm. The results which are shown in Table 6, show that there is a great discrepancy between the Taguchi prediction and FEA, especially for the maximum wrinkling height. Therefore, it could be concluded that the Taguchi DOE would not be a successful method for prediction of input parameters.

**Table 6.** Comparison between the Taguchi prediction and the finite element for test number 121331

| Outputs | Taguchi | Finite element | Percentage of error |
|---|---|---|---|
| FLD Criterion | 0.597 | 0.657 | 9.13 |
| Wrinkling height | 7.12 | 2.24 | 217.85 |

On the other hand, the trained ANN predicts the experiment with 231333 code as an appropriate combination of inputs (Table 7). This code shows that friction between the matrix/blank-holder and blank is 0.07 mm, friction between the punch and blank is 0.15, blank width is 1150 mm, blank height is 1560, blank thickness is 0.9 and the gap between the blank and blank-holder is 0.07 mm. By comparing these results with the prediction of Taguchi, the trained ANN has predicted the outputs with a less error. This error for the FLD criterion or the maximum wrinkling height is less than 10%.

**Table 7.** Comparison between the artificial neural network prediction and finite element for test number 231333

| Outputs | ANN | Finite element | Percentage of error |
|---|---|---|---|
| FLD Criterion | 0.536 | 0.572 | 6.29 |
| Wrinkling height | 1.198 | 1.32 | 9.84 |

## 6. Conclusion

In this paper, a combination of an experiment, finite element analysis and artificial neural network is used. In fact, based on a finite number of FEA results, which are validated by experiment, an ANN with 2 hidden layers is trained and utilized to predict specified outputs (maximum wrinkling height and tearing) quickly and accurately. First of all, it could be concluded that a

trained neural network is able to predict outputs with an error of 0.1 (Mean Square Error). The prediction by the trained ANN could be done by less than 10% and some acceptable error. For this panel, the maximum wrinkling height predicted by the Taguchi DOE shows a great numerical difference with FEA results. Moreover, the results show that by increasing the training data up to 15% of full factorial DOE, the accuracy of the trained ANN prediction could improve. Also, using the parameters predicted by the trained ANN leads to smaller wrinkling which could be a sign of better quality. Finally, it is inferred that the blank length is the most effective parameter and friction between the matrix, blank-holder and blank is the least important parameter affecting tearing. That the blank thickness is the most effective parameter in the maximum wrinkling height and the blank length is the least effective one.

# References

1. ABAQUS version 6.11 User Manual

2. CANDRA S., BATAN I.M.L., BERATA W., PRAMONO A.S., 2015, Analytical study and FEM simulation of the maximum varying blank holder force to prevent cracking on cylindrical cup deep drawing, *Procedia CIRP*, **26**, 548-553

3. CHAMEKH A., SALAH H.B.H., HAMBLI R., 2009, Inverse technique identification of material parameters using finite element and neural network computation, *International Journal of Advanced Manufacturing Technology*, **44**, 1/2, 173-179

4. COLGAN M., MONAGHAN J., 2003, Deep drawing process: analysis and experiment, *Journal of Materials Processing Technology*, **132**, 1, 35-41

5. DEMIRCI I.H., YAŞAR M., DEMIRAY K., KARALI M., 2008, The theoretical and experimental investigation of blank holder forces plate effect in deep drawing process of AL 1050 material, *Materials and Design*, **29**, 2, 526-532, doi:http://dx.doi.org/10.1016/j.matdes.2007.01.008

6. EL SHERBINY M., ZEIN H., ABD-RABOU M., EL SHAZLY M., 2014, Thinning and residual stresses of sheet metal in the deep drawing process, *Materials and Design*, **55**, 0, 869-879, doi:http://dx.doi.org/10.1016/j.matdes.2013.10.055

7. FERESHTEH-SANIEE F., MONTAZERAN M.H., 2003, A comparative estimation of the forming load in the deep drawing process, *Journal of Materials Processing Technology*, **140**, 1/3, 555-561, doi: http://dx.doi.org/10.1016/S0924-0136(03)00793-3

8. FOROUZAN S., AKBARZADEH A., 2007, Prediction of effect of thermo-mechanical parameters on mechanical properties and anisotropy of aluminum alloy AA3004 using artificial neural network, *Materials and Design*, **28**, 5, 1678-1684

9. GAO E., LI H., KOU H., CHANG H., LI J., ZHOU L., 2010, Finite element simulation on the deep drawing of titanium thin-walled surface part, *Rare Metals*, **29**, 1, 108-113

10. HASHEMI R., GHAZANFARI A., ABRINIA K., ASSEMPOUR A., 2012, Forming limit diagrams of ground St14 steel sheets with different thicknesses, *SAE International Journal of Materials and Manufacturing*, **5**, 2012-01-0018, 60-64

11. LAURENT H., COËR J., MANACH P., OLIVEIRA M., MENEZES L., 2015, Experimental and numerical studies on the warm deep drawing of an Al-Mg alloy, *International Journal of Mechanical Sciences*, **93**, 59-72

12. PADMANABHAN R., OLIVEIRA M., ALVES J., MENEZES L., 2007, Influence of process parameters on the deep drawing of stainless steel, *Finite Elements in Analysis and Design*, **43**, 14, 1062-1067

13. SEZEK S., SAVAS V., AKSAKAL B., 2010, Effect of die radius on blank holder force and drawing ratio: a model and experimental investigation, *Materials and Manufacturing Processes*, **25**, 7, 557-564

14. Singh C.P., Agnihotri G., 2015 Study of deep drawing process parameters: a review, *International Journal of Scientific and Research Publication*, **5**, 2, 1-15

15. Singh D., Yousefi R., Boroushaki M., 2011, Identification of optimum parameters of deep drawing of a cylindrical workpiece using neural network and genetic algorithm, *World Academy of Science, Engineering and Technology*, **78**, 211-217

16. Watiti V.B., Labeas G.N., 2010, Finite element optimization of deep drawing process forming parameters for magnesium alloys, *International Journal of Material Forming*, **3**, 1, 97-100

17. Wifi A., Abdelmaguid T., 2012, Towards an optimized process planning of multistage deep drawing: an overview, *Journal of Achievements in Materials and Manufacturing Engineering*, **55**, 1, 7-17

18. Yagami T., Manabe K., Yamauchi Y., 2007, Effect of alternating blank holder motion of drawing and wrinkle elimination on deep-drawability, *Journal of Materials Processing Technology*, **187**, 187-191

19. Zein H., El Sherbiny M., Abd-Rabou M., 2014, Thinning and spring back prediction of sheet metal in the deep drawing process, *Materials and Design*, **53**, 797-808

# EXPERIMENTAL STUDY ON MECHANICAL PROPERTIES OF PE/CNT COMPOSITES

A.M. Fattahi, A. Najipour

*Department of Mechanical Engineering, Tabriz Branch, Islamic Azad University, Tabriz, Iran*

*e-mail: a.fattahi@iaut.ac.ir*

High density polyethylene/carbon nanotube composites have been produced for investigations. Four CNT volume fractions and two injection pressures were considered. According to the Taguchi approach, eight experiments were designed. The effect of the carbon nanotubes weight fraction and injection pressure on hardness and impact strength of nanocomposite samples were investigated. The results showed that the effect of the carbon nanotube weight fraction on hardness and impact strength of nanocomposite samples was much higher than the effect of injection pressure. By adding 1%wt (weight) carbon nanotube into the polymer, the impact strength and hardness of the samples improved by 74% and 47%, respectively.

*Keywords:* nanocomposite, carbon nanotube, polyethylene, injection molding, mechanical properties

## 1. Introduction

Carbon nanotube composites hold a great potential as the materials to be used in the future. Extraordinary properties of these fantastic materials lead to an exhaustive research. One of the first investigations about polymer/carbon nanotube composites was carried out by Ajayan *et al.* (1994). In their study, they dispersed randomly multi-walled carbon nanotubes in a liquid epoxy resin by mechanical mixing. After that, a large number of theoretical and experimental researches using carbon nanotubes as reinforcing fibers have been performed to address the exceptional mechanical and electrical properties of nanotube-based composites (Schadler *et al.*, 1998; Jin *et al.*, 1998; Haggenmueller *et al.*, 2000; Azizi *et al.*, 2015a,b; Najipour and Fattahi, 2016; Safaei and Fattahi, 2016; Sahmani and Fattahi, 2016, 2017; Fattahi and Safaei, 2017). In the last few years, nanocomposites have significantly advanced compared to composite materials in convention dimensions due to changes in the composition and structure of the materials in nanoscale and presenting unique and special properties. Improvement of mechanical and other properties of such composites strongly depends on the particle content, particle shape and size, surface characteristics and dispersion degree (Komarneni, 1992; Jordan *et al.*, 2005). Consequently, toughening of these composites could be caused by a number of mechanisms such as crack-tip pinning, crack-surface bridging, debonding/microcracking and crack deflection. According to previous reports, mechanical and thermomechanical properties of composites filled with micron-sized filler particles are inferior to those filled with nanoparticles of the same filler. Carbon nanotubes exhibit exceptional mechanical (modulus= 1 TPa, strength= 10 times that of steel), thermal and electrical properties. Accordingly, it can be suggested that development of these nano-level particles can offer tailorability of desired properties in a material. Increasing economic need for fuel in different areas has increased the demand for using lighter new materials such as polymers. On the other hand, because of lower strength of polymers compared to metals, their reinforcement seems inevitable. Nylon 6 was the first polymer which was used to produce nanocomposite by Toyota Company in 1990; but today thermosetting polymers

such as epoxy and polyimide, polypropylene, polyethylene, and polystyrene are being used as matrix materials in composites. Among the nanocomposites, most attention has been paid to polymer based nanocomposites. One reason for the progress of polymer nanocomposites is their unique mechanical, chemical and physical properties. Polymer nanocomposites generally have high strength, low weight, high thermal stability, high electrical conductivity and high chemical resistance. The second reason for the progress of polymer based nanocomposites and increased research in this area is the discovery of carbon nanotubes in 1991. The strength and electrical properties of carbon nanotubes are significantly different from those of graphite nanolayers and other filling materials. Supreme mechanical and physical properties of carbon nanotubes along with their low density have made carbon a perfect candidate for strengthening the composites. The diameter of these nanotubes can range from 1 to 100 nm and their aspect ratio is bigger than 100 or even 1000. Numerous works have been done on polymer based nanocomposites. Among them the most significant works by Navidfar (2014) can be mentioned. He produced polymethyl methacrylate/carbon nanotube composites using the injection method. Effects of CNT weight fraction, injection temperature, and maintenance pressure on the mechanical properties of the samples were investigated. According to his results, the increasing of the concentration of carbon nanotubes in the nanocomposites slightly increased their hardness and the impact strength. Among other works done in this area Shishavan *et al.* (2014) can be mentioned. They mixed acrylonitrile butadiene styrene polymer with 0, 2, and 4%wt nanoclay, and the effects of nanoclay and process conditions on the mechanical properties of nanocomposite were investigated. They found that by adding 4%wt nanoclay, the hardness of the samples was slightly increased.

In the present study, the effect of the addition of multi walled carbon nanotubes and the process conditions on the hardness and impact strength of high density polyethylene-carbon nanotube nanocomposite samples with different carbon nanotube weight fractions is investigated.

## 2.    Experimental research

### 2.1.    Materials and equipment

In this study, high density polyethylene (HDPE) polymer produced in Ilam Petrochemical Company was used as the matrix phase. Also multi-walled carbon nanotubes with 5-10 nm inner diameter, 10-30 nm outer diameter and 90% purity, obtained from US Research Nanomaterials, USA, were used as the reinforcement phase. Following primary manual mixing with certain weight fractions, mixing was completed by fusion in a twin screw extruder (ZSK-25, Coperion Werner & Pfleiderer, Germany) device at Iranian Petrochemical and Polymer Research Center, and the nanocomposites were obtained as granules. Then the samples were prepared using a plastic injection device NBM HXF-128 obtained from Neckou Behine Mashin Company and were subject to mechanical hardness and impact tests. In order to conduct Rockwell hardness tests on the samples, Zwick/Roell device (UK) which is shown in Fig. 1a, was used. To obtain the impact strength of the samples, a Charpy impact tester device with pendulum weight of 2.036 kg and arm length of 39.48 cm, which is shown in Fig. 1b, was employed.

In this study, Taguchi approach (Montgomery, 2013) has been used to evaluate the tests and draw final conclusions. Taguchi's method is one of the most popular methods of statistical analysis. The weight of carbon nanotubes in four levels and the pressure injection in two levels were considered, and according to Taguchi's approach, eight experiments were designed. The parameters and levels are shown in Table 1. Also, Table 2 shows the tests designed in accordance with the Taguchi method. In the experiments designed according to Taguchi's method, there is
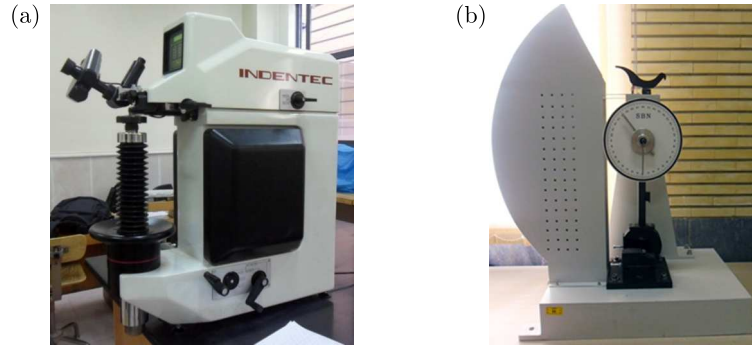
Fig. 1. (a) Hardness test device, (b) impact test device

a loss function which is ultimately introduced as the signal to noise ratio $S/N$ (Montgomery, 2013)

$$S/N = -10 \log \left( \frac{1}{n} \sum_{i=1}^{n} \frac{1}{y_i^2} \right) \tag{2.1}$$

where $S/N$ is the signal to noise ratio, $n$ is the number of observations on the particular product and $y$ is the respective characteristic. According the Taguchi method, the parameter with the biggest $S/N$ has the biggest effect on the experiment.

**Table 1.** Experimental parameters and their levels

| Level | 1 | 2 | 3 | 4 |
|---|---|---|---|---|
| Carbon nanotube weight fraction [wt%] | 0 | 0.5 | 1.0 | 1.5 |
| Injection pressure [MPa] | 60 | 80 | – | – |

**Table 2.** Experiments designed according to Taguchi method

| Sample number | CNT weight fraction [wt%] | Injection pressure [MPa] |
|---|---|---|
| 1 | 0 | 60 |
| 2 | 0 | 80 |
| 3 | 0.5 | 60 |
| 4 | 0.5 | 80 |
| 5 | 1.0 | 60 |
| 6 | 1.0 | 80 |
| 7 | 1.5 | 60 |
| 8 | 1.5 | 80 |

In order to produce nanocomposite samples, first polyethylene and carbon nanotube with different weight fractions, which are presented in Table 2, were mixed in a two screw extruder device using the fusion mixing method at 170°C, and the nanocomposites were produced as granules. Then the granules were dehydrated in the feeding funnel of the injection device at 60°C for 20 h and the samples were produced based on the designed experiments according to ASTM D638 standard. Once the nanocomposite samples were prepared, hardness and impact mechanical tests were conducted on the samples. Three samples were made, then hardness and impact tests according to Rockwell and Charpy methods were done (see Fig. 2). The hardness test according to the Rockwell M method with three replications in each experiment and the Charpy impact test with three replications in each experiment were conducted for every sample.
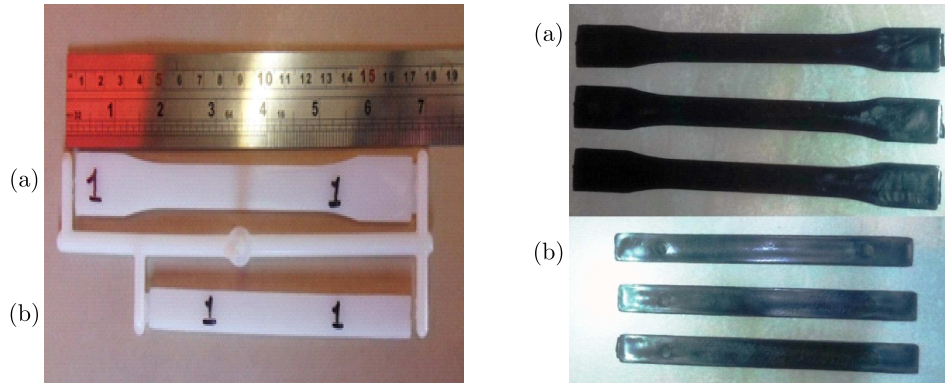
Fig. 2. Left – pure polyethylene samples and right – the produced samples (1%wt CNT): (a) hardness test sample, (b) impact test sample

## 3. Results

Once the mechanical tests were done, the results obtained for the hardness and impact tests of the samples were obtained and then were analyzed using Minitab software. Taguchi's method was used to evaluate the tests.

### 3.1. Impact test

In order to prepare the samples for the impact test, a crotch with 45° angle and 2 mm depth was created on the sample and then the sample was subject to the Charpy impact test. Some of the tested samples are shown in Fig. 3. Once the impact test was done, impact strength results were obtained according to Table 3.
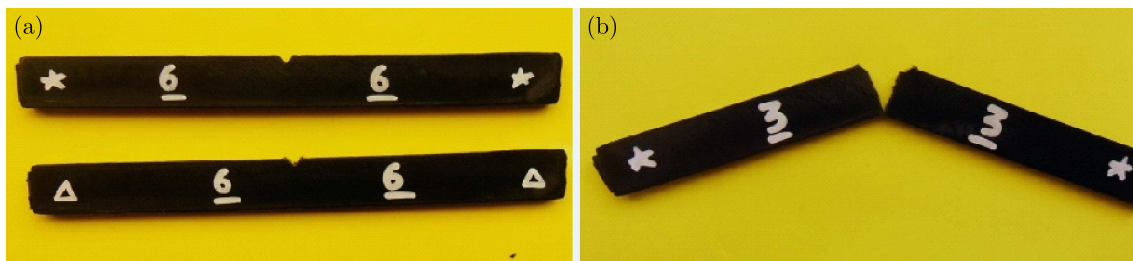


Fig. 3. (a) Selected samples prepared for impact tests, (b) nanocomposite sample after the impact test

**Table 3.** Impact strength test results

| Sample number | Impact strength [kJ/m$^2$] | | | Average impact strength [kJ/m$^2$] |
|---|---|---|---|---|
| | Test 1 | Test 2 | Test 3 | |
| 1 | 105.455 | 111.766 | 133.128 | 116.783 |
| 2 | 199.720 | 172.644 | 154.208 | 175.524 |
| 3 | 232.168 | 178.364 | 200.776 | 203.776 |
| 4 | 175.385 | 170.112 | 181.075 | 175.524 |
| 5 | 232.168 | 302.462 | 228.168 | 254.266 |
| 6 | 276.364 | 221.486 | 264.950 | 254.267 |
| 7 | 201.385 | 238.350 | 198.866 | 212.867 |
| 8 | 199.720 | 252.665 | 2228.720 | 225.035 |

**Table 4.** Signal to noise ratio $S/N$ for impact strength data

| | Effect of CNT [wt%] | | | Effect of pressure | |
|---|---|---|---|---|---|
| Level | Impact strength [kJ/m$^2$] | $S/N = -10\log\left(\frac{1}{2}\sum\limits_{i=1}^{2}\frac{1}{y_i^2}\right)$ | Level | Impact strength [kJ/m$^2$] | $S/N = -10\log\left(\frac{1}{4}\sum\limits_{i=1}^{4}\frac{1}{y_i^2}\right)$ |
| 1 | $y_1 = 116.783$ $y_2 = 175.524$ | 43.12 | 1 | $y_1 = 116.783$ $y_2 = 203.776$ $y_3 = 254.266$ $y_4 = 212.867$ | 45.55 |
| 2 | $y_1 = 203.776$ $y_2 = 175.385$ | 45.53 | | | |
| 3 | $y_1 = 254.266$ $y_2 = 254.222$ | 48.11 | 2 | $y_1 = 175.524$ $y_2 = 175.385$ $y_3 = 254.266$ $y_4 = 225.035$ | 46.23 |
| 4 | $y_1 = 212.867$ $y_2 = 225.035$ | 46.80 | | | |
| $\Delta$ | $48.11 - 43.12 = 4.99$ | | | $46.23 - 45.55 = 0.68$ | |
| Rank | 1 | | | 2 | |
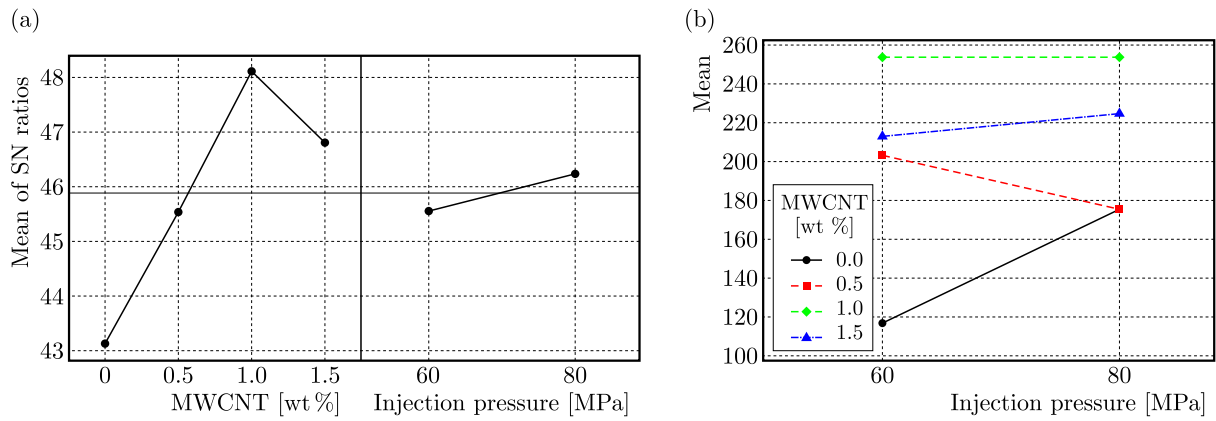


Fig. 4. (a) Signal to noise diagram for the impact strength data, (b) diagram of the counter effects of the parameters on the impact strength

By using these data as the input for Minitab software and analyzing them, the signal to noise ratio data were obtained according to Table 4 and Fig. 4a, where $\Delta$ is the difference between the largest and smallest data and Rank shows the impact of the parameter with respect to size of $\Delta$. According to signal to noise results, carbon nanotube weight fraction had much more effect of the impact strength of the nanocomposite samples compared to the injection pressure. By increasing carbon nanotube weight fractions up to level 3 (1%wt carbon nanotubes), the impact strength of the samples were increased almost by 74% (Appendix A), and then it was decreased. This means that the optimum level for carbon nanotube weight fraction was level 3 with 1%wt carbon nanotube in which the highest value for the signal to noise ratio and impact strength was obtained. Increasing the carbon nanotube weight fraction to 1.5%, the signal to noise ratio and impact strength values were decreased, which could be attributed to the agglomeration of carbon nanotubes by increasing their weight fraction. Strong Van der Waals attractions along with their high contact surface (length to diameter ratio of 1000) generally results in special aggregation of carbon nanotubes and, therefore, prevents the transfer of their extraordinary properties to the matrix. The most optimum state for the impact strength among the experiments was when the carbon nanotube weight fraction was at level 3 and injection pressure was at level 2, which corresponded to test sample 6. Also Fig. 4b shows the counter effects of the parameters on the impact test. According to this diagram, when the injection pressure was at its lower level

(60 MPa), the highest impact strength was achieved when 1%wt carbon nanotube was chosen. Also when the injection pressure was at its higher level (80 MPa), the impact strengths of pure samples and samples with 0.5%wt carbon nanotube were similar. Another conclusion which was obtained from the diagram was that when the carbon nanotube weight fraction was at its third level being 1%wt, the impact strengths of the samples produced at 60 and 80 MPa were almost similar. Also according to the results of the signal to noise analyses, the injection pressure had less effect on the impact strength, which, through increasing the injection pressure from 60 to 80 MPa, ingreased the impact strength of samples by only 5%.

### 3.2. Hardness test

Hardness tests of the samples were conducted according to the Rockwell M method, and the obtained results are shown in Table 5.

**Table 5.** Hardness test results

| Sample number | Hardness (Rockwell) | | | Average hardness (Rockwell) |
|---|---|---|---|---|
| | Test 1 | Test 2 | Test 3 | |
| 1 | 43.0 | 44.3 | 42.3 | 43.20 |
| 2 | 37.2 | 35.6 | 42.5 | 38.43 |
| 3 | 63.3 | 61.0 | 61.4 | 61.90 |
| 4 | 56.0 | 53.4 | 54.8 | 54.73 |
| 5 | 63.7 | 62.9 | 62.9 | 63.17 |
| 6 | 54.2 | 55.7 | 59.9 | 56.60 |
| 7 | 61.3 | 61.7 | 63.7 | 62.23 |
| 8 | 52.5 | 52.4 | 49.8 | 51.57 |

By analyzing the results obtained from the hardness test using Minitab software, the signal to noise analysis results were obtained and are presented in Table 6 and Fig. 5a.

**Table 6.** Signal to noise ratio for hardness data

| Effect of MWCNT [wt%] | | | Effect of pressure | | |
|---|---|---|---|---|---|
| Level | Hardness (Rockwell) | $S/N = -10\log\left(\frac{1}{2}\sum_{i=1}^{2}\frac{1}{y_i^2}\right)$ | Level | Hardness (Rockwell) | $S/N = -10\log\left(\frac{1}{4}\sum_{i=1}^{4}\frac{1}{y_i^2}\right)$ |
| 1 | $y_1 = 43.2$ $y_2 = 38.4$ | 32.2 | 1 | $y_1 = 43.2$ $y_2 = 61.9$ $y_3 = 63.2$ $y_4 = 62.2$ | 34.8 |
| 2 | $y_1 = 61.9$ $y_2 = 54.7$ | 35.3 | | | |
| 3 | $y_1 = 63.2$ $y_2 = 56.6$ | 35.53 | 2 | $y_1 = 38.4$ $y_2 = 54.7$ $y_3 = 56.6$ $y_4 = 51.6$ | 33.9 |
| 4 | $y_1 = 56.6$ $y_2 = 62.2$ | 35.06 | | | |
| $\Delta$ | $33.53 - 32.2 = 3.33$ | | | $34.8 - 33.9 = 0.9$ | |
| Rank | 1 | | | 2 | |

According to the results obtained from the signal to noise analysis for the hardness test, the carbon nanotube weight fraction had a more significant effect on the hardness of the samples compared to the injection pressure. The addition of up to 1%wt carbon nanotubes to polyethylene resulted in a significant increase in the hardness of the samples almost by 47% (Appendix A), and the highest values of the hardness and signal to noise ratio was obtained at level 3 (1%wt

(a)



(b)
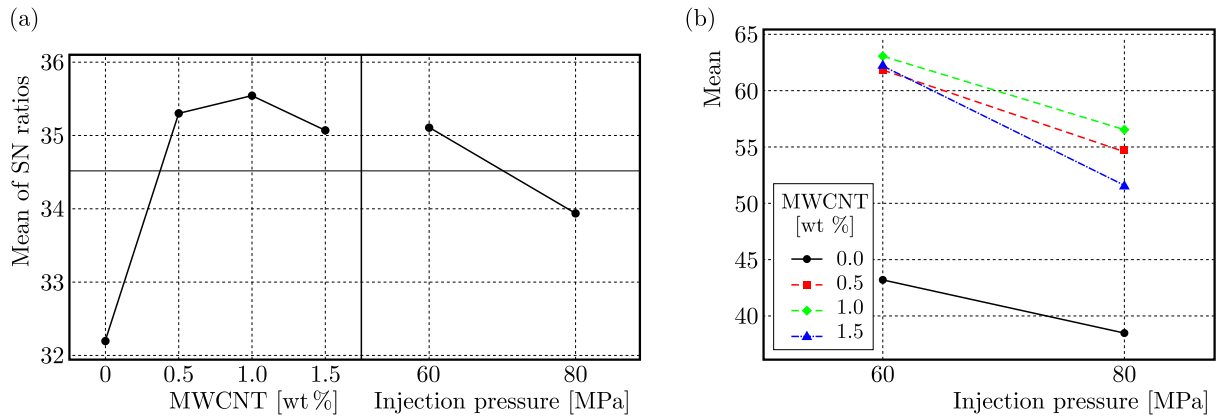
Fig. 5. (a) Signal to noise analysis diagram for hardness data, (b) diagram counter effects of the parameters on the hardness test

carbon nanotubes). A further increase in the carbon nanotube weight fraction up to 1.5% slightly decreased the hardness of the samples which was attributed to agglomeration of the carbon nanotubes as it was mentioned before. On the other hand, wt% by increasing the injection pressure from level 1 to level 2, the hardness and signal to noise ratio of the samples were decreased. The most optimum state regarding the hardness was achieved when the nanotube weight fraction and injection pressure were at levels 3 and 2, respectively, which corresponded to sample 5. Also Fig. 5b shows the counter effects of the parameters on the hardness test. According to this diagram, the hardness of the nanocomposites were significantly higher (almost 47%) than the pure samples and at either 60 or 80 MPa injection pressure. The hardness of the samples containing 1.5%wt showed the highest values. Also another conclusion from this diagram was that at 60 MPa injection pressure the hardness of the samples with 1.5%wt was higher than for the samples containing 0.5%wt while at 80 MPa injection pressure the order was opposite.

## 4. Conclusion

In this work, high density polyethylene-carbon nanotube nanocomposites were produced according to the injection molding method. The effect of addition of carbon nanotubes at four different levels of 0, 0.5, 1, and 1.5 and of two injection pressure levels of 60 and 80 MPa on hardness and impact strength of the nanocomposite samples was investigated. The results showed that the effect of the carbon nanotube weight fraction on the hardness and impact strength of nanocomposite samples was much higher than the effect of the injection pressure. Addition of 1%wt carbon nanotube into the polymer significantly increased hardness and impact strength of the samples; however addition of 1.5%wt carbon nanotube reduced the values, which was due to agglomeration of carbon nanotubes in the polyethylene matrix.

## A. Appendix

From Table 4, the average amount of impact strength at 0% and 1%wt CNT are 146.2 and 254.266 kJ/m$^2$, then the impact strength increment is

$$\frac{254.266 - 146.2}{146.2} \cdot 100 \approx 74 \tag{A.1}$$

From Table 6, the average amount of hardness at 0% and 1%wt CNT are 40.8 and 59.9 Rockwell, then the hardness increment is

$$\frac{59.9 - 40.8}{40.8} \cdot 100 \approx 47 \qquad (A.2)$$

## References

1. AJAYAN P.M., STEPHAN O., COLLIEX C., TRAUTH D., 1994, Aligned carbon nanotube arrays formed by cutting a polymer resin-nanotube composite, *Science*, **265**, 1212-1214

2. AZIZI S., FATTAHI A.M., KAHNAMOUEI J.T., 2015a, Evaluating mechanical properties of nano-platelet reinforced composites under mechanical and thermal loads, *Journal of Computational and Theoretical Nanoscience*, **12**, 1, 4179-4185

3. AZIZI S., SAFAEI B., FATTAHI A.M., TEKERE M., 2015b, Nonlinear vibrational analysis of nano-beams embedded in an elastic medium including surface stress effects, *Advances in Materials Science and Engineering*, **12**, 1, 1-7

4. DOUGLAS C., 2013, *Statistical Quality Control*, Wiley, 7th Edition

5. FATTAHI A.M., SAFAEI B., 2017, Buckling analysis of CNT-reinforced beams with arbitrary boundary conditions, *Microsystem Technologies*, **2017**, 3, 1-13

6. HAGGENMUELLER R., GOMMANS H.H., RINZLER A.G., FISCHER J.E., WINEY K.I., 2000, Aligned single wall carbon nanotubes in composites by melt processing methods, *Chemical Physics Letters*, **330**, 219-225

7. JIN L., BOWER C., ZHOU O., 1998, Alignment of carbon nanotubes in a polymer matrix by mechanical stretching, *Applied Physics Letters*, **73**, 1197-1199

8. JORDAN J., JACOB K.I., TANNENBAUM R., SHARAF M.A., JASIUK I., 2005, Experimental trends in polymer nanocomposites-a review, *Materials Science and Engineering A*, **393**, 1-11

9. KOMARNENI S., 1992, Nanocomposites, *Journal of Materials Chemistry*, **2**, 1219-1230

10. NAVIDFAR A., 2014, Experimental study of mechanical properties of nano-composites containing carbon nanotubes produced by injection molding, M.D. Thesis, Ourmieh University, Ourmieh

11. NAJIPOUR A., FATTAHI A.M., 2016, Experimental study on polyethylene/carbon nanotube injected composites, *Croizatia*, **93**, 2, 145-152

12. SAFAEI B., FATTAHI A.M., 2016, Vibrational response analysis of polymer/CNT plates using molecular dynamics simulation, *Croizatia*, **93**, 2, 65-79

13. SAHMANI S., FATTAHI A.M., 2016, Size-dependent nonlinear instability of shear deformable cylindrical nanopanels subjected to axial compression in thermal environments, *Microsystem Technologies*, **2016**, 12, 1-15

14. SAHMANI S., FATTAHI A.M., 2017. Thermo-electro-mechanical size-dependent postbuckling response of axially loaded piezoelectric shear deformable nanoshells via nonlocal elasticity theory, *Microsystem Technologies*, **2017**, 2, 1-15

15. SCHADLER L.S., GIANNARIS S.C., AJAYAN P.M., 1998, Load transfer in carbon nanotube epoxy composites, *Applied Physics Letters*, **73**, 3842-3844

16. SHISHAVAN, MAMAGHANI S., AZDAST T., AHMADI S.R., 2014, Investigation of the effect of nanoclay and processing parameters on the tensile strength and hardness of injection molded Acrylonitrile Butadiene Styrene-organoclay nanocomposites, *Materials and Design*, **58**, 527-534

# TIRE RUBBER TESTING PROCEDURE OVER A WIDE RANGE OF STRAIN RATES

PAWEŁ BARANOWSKI

*Military University of Technology, Faculty of Mechanical Engineering, Warsaw, Poland*

*e-mail: pawel.baranowski@wat.edu.pl*

JACEK JANISZEWSKI

*Military University of Technology, Faculty of Mechatronics and Aviation, Warsaw, Poland*

*e-mail: jacek.janiszewski@wat.edu.pl*

JERZY MAŁACHOWSKI

*Military University of Technology, Faculty of Mechanical Engineering, Warsaw, Poland*

*e-mail: jerzy.malachowski@wat.edu.pl*

The main aim of the paper is to present the procedure allowing one to determine correct mechanical characteristics of a rubber material compressed within a wide range of strain rates. In order to obtain a satisfactory wide spectrum of material data, a number of tests were conducted both under low and high strain rates with the use of a universal strength machine and split Hopkinson pressure bar set-up equipped with polymethyl methacrylate and 7075-T6 alloy bars. During the investigations, the necessity of performing pre-compression tests and the problem of specimen geometry were pointed out as key methodical requirements to guarantee achieving valid experimental data both from quasi-static and high strain rate tests.

*Keywords:* tire rubber, uniaxial compression test, SHPB test, strain rates, spectral analysis

## 1. Introduction

Nowadays, rubber is considered as one of the most important materials for many applications. Its mechanical characteristics, including ability to reversible deformation under loading of mechanical forces, result in the fact that various forms of rubber are very popular in many industries. Elastomeric structures, due to their low stiffness modulus and high damping characteristics, are used to absorb energy in dynamic (impulse or impact) loadings as isolation bearings, shock absorbers, etc. For example, the automotive industry, often uses materials and rubber-based composites to produce tires with high strength and durability. Nevertheless, development of the pneumatic tire structure with a high operating standard is associated with carrying out a series of experimental studies for determining stability and reliability of its implementation. Numerical modelling using the Finite Element Method (FEM), which is found to be a very useful and effective tool for deformation and stress state analysis in the tire structure (Helnwein *et al.*, 1993; Reid *et al.*, 2007), is an alternative to experimental testing. Thus, for effective and correct analyses, its numerical model should be developed with particular attention and care. Therefore, an accurate assessment of mechanical properties of the tire rubber in various operational conditions is essential in the tire numerical modelling (Malachowski *et al.*, 2007).

It can be observed that mechanical properties of rubber and rubber-like materials have been effectively determined and understood over the past decades. Such materials were examined using static experimental tests (Gent, 1994; Szurgott *et al.*, 2012; Sridharan and Sivaramakrishnan, 2013), as well as fatigue testing was performed by many authors (Kim and Jeong, 2005; Saintier

*et al.*, 2006; Zine *et al.*, 2006). Static experimental tests for both tension and compression are usually carried out on universal strength machines. During testing, the rubber material exhibits nonlinear stress distribution and its behaviour considerably changes. When a rubber specimen is compressed, its contact area increases drastically and a friction effect can be clearly observed, manifested as a barrelling effect. Therefore, it is intended to reduce friction as much as possible using lubricants or water (Nakajima and Takahashi, 2002).

Recently, behaviour of rubber under high-strain rates loading has been more thoroughly investigated with compression, tension or shear characteristics taking into consideration (Giovanola, 1988; Lindholm and Yeakley, 1968; Nicholas, 1981; Roland, 2006; Song and Chen, 2003). It resulted from the fact that many types of elastomers (e.g. rubber, polyuera) were applied as blast/ballistic protection materials in combat vehicles (Auckland *et al.*, 2013; Roland *et al.*, 2010). The specific properties of elastomers, such as: high toughness-to-density ratio, capability to accommodate large deformations and their high damping characteristics, make them suitable for employment in the dissipation of kinetic energy coming from impacts and shocks.

A device most commonly used for investigating the dynamic behaviour of solid materials at high strain rates within the range of $10^2$ to $10^4\,\mathrm{s}^{-1}$ is the Kolsky bar, more commonly known as split Hopkinson pressure bar (SHPB) named after Bertram Hopkinson (Chen *et al.*, 2000, 2011; Song and Chen, 2005; Ellwood *et al.*, 1982; Gray, 1994; Hopkinson, 1904; Hopkinson, 1872; Janiszewski, 2012; Meyers, 1994). It is used to obtain stress-strain curves of investigated materials for certain strain rates. The basic test using SHPB is a compression test, where a cylindrical specimen is deformed between two flat surfaces of the bars (input and output, or incident and transmitted). If the tested material is a soft material, such as an elastomer, the applicability of the conventional SHPB technique needs to be carefully examined to meet methodical requirements (stress equilibrium in the specimen, constant strain rate conditions during the test) and to solve many technical and methodological problems. These problems arise mainly because the transmitted signal may be too weak to be measured, which results from large mismatch of impedance between the specimen and the metallic bars. The specimen thickness also influences the attenuation of the transmitted signal since a stress wave propagates in soft materials with a relatively low velocity. Due to these limitations, many modifications of the conventional SHBP technique were developed.

The simplest approach is to increase sensitivity of the gauges recording the transmitted pulse. Chen *et al.* (1999) used piezoelectric quartz gauges embedded on the aluminium bars. An other method includes reduction of mechanical impedance differences between the bars and the specimen using mainly three options: (1) modifying cross section of the specimen, (2) altering cross section of the pressure bar, e.g. using a hollow transmission bar (Zhao *et al.*, 1997) and (3) changing the material of the pressure bars, e.g. by replacing metals bars with polymeric bars (Casem *et al.*, 2003). The latter is frequently chosen by many investigators.

The substitution of polymeric bars with metallic ones, however, causes many problems due to the viscoelastic nature of the polymer material (Wang *et al.*, 1994; Zhao *et al.*, 1997). For metal bars, it can be assumed that elastic wave signals, which are determined from the strain measured by strain gauges, are not only known at the measuring points but everywhere along the bar. Therefore, the transmitted wave can be shifted to the transmitted bar-specimen interface to calculate the transmitted force and velocity, whereas the incident force and velocity can be obtained from incident and reflected signals shifted to the incident bar-specimen interface. Unfortunately, this procedure is not valid for polymeric bars because of the attenuation and dispersion of the wave pulse during its propagation along the bar. Therefore, the correction of the wave signals is necessary in the case of a viscoelastic SHPB.

There are two approaches to correction of the wave signals. The first method is based on a theoretical viscoelastic constitutive equation and a characteristics theory of wave propagation (Bacon, 1998). An alternative approach is to use spectral analysis to correct wave pulses (Cheng

*et al.*, 1998; Zhao *et al.*, 1997; Duyle, 1989). In this paper, spectral analysis and a wave shifting procedure are applied to a PMMA split Hopkinson pressure bar setup.

All the facts described above were included and taken into consideration in the authors' experimental tests. The present paper describes – in a comprehensive way – the procedure of determining correct mechanical characteristics of a selected rubber material deformed within a wide range of strain rates. The paper is organized as follows: Section 2 is devoted to the description of quasi-static compression testing of tire rubber. In this Section, the procedure of performed tests under low strain rates and the stress-strain curves obtained are presented. In Section 3, the study of rubber properties under high strain deformation rates is described. Particular emphasis is placed on presenting the specificity of performing mechanical tests under dynamic loading with the use of aluminium alloy and polymethyl methacrylate (PMMA) bars system.

The genesis of the paper is related to the recent events including many world military operations, where the Improvised Explosive Devices (IED) are commonly used on the battlefield. IED explosions can destroy wheels or even the suspension system which makes the vehicle unable to drive (Borkowski and Motrycz, 2012). Its destructive effect results in tire tearing followed by large deformation of other elements of the suspension system. Such problems are also simulated using numerical methods (Baranowski *et al.*, 2011; Baranowski and Malachowski, 2015). However, the authors found lack of material data of tire rubber in terms of tire numerical simulations under dynamic loading conditions, especially blast waves. Possessing a wide range of the stress-strain curves within a number of strain rates and a proper constitutive model, the modelling and simulation of different problems will ensure that the obtained results are correct and close to the real findings

## 2. Quasi-static tests

Quasi-static compression tests were carried out using MTS Criterion C45.105 electromechanical universal test machine. The specimens were compressed with three different strain rates: $0.001\,\mathrm{s^{-1}}$, $0.01\,\mathrm{s^{-1}}$ and $1.00\,\mathrm{s^{-1}}$. Cylindrical specimens were prepared with a diameter-to-height ratio according to ASTM D575-91 standard (D575-91 ASTM 2001). The specimens with 8.10 mm height and 17.60 mm diameter were cut out from the tire using the water jet cutting technique.
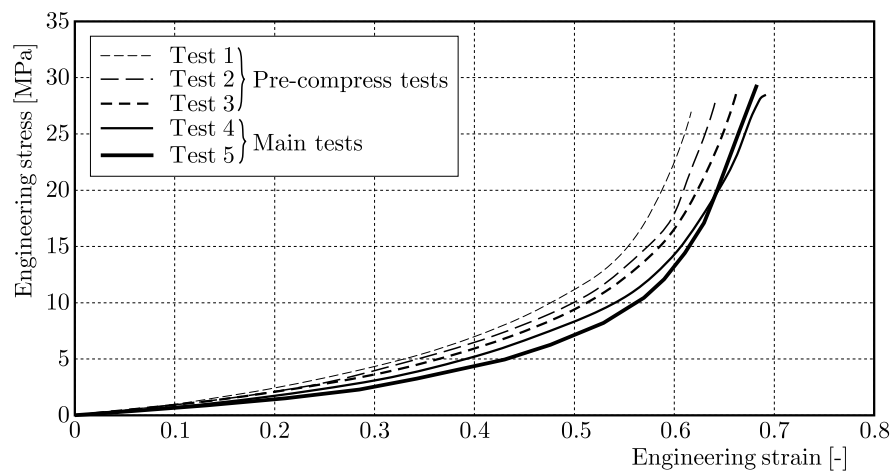


Fig. 1. Stress-strain curves for one specimen with pre-compression tests (strain rate of $1.0\,\mathrm{s^{-1}}$)

Friction between the specimens and compressing grip surfaces was reduced using a lubricant, however, a barrelling effect was not completely omitted, which was negligible. In Fig. 1,

exemplary stress-strain curves from five compression tests of the same specimen are presented for a chosen strain rate $1.0\,\mathrm{s}^{-1}$. In this case, an interesting phenomenon, which was also noticed during the dynamic SHPB testing, was observed.

It can be observed that the curves from tests 1-4 differ from each other, whereas the curves from tests 4 and 5 are similar. It is noticed that the specimen after "pre-compression" behaves repetitively and gives nearly coincident stress-strain curves for the same conditions of the tests, even for large deformation. Such a phenomenon can be caused by changes initiated in the material structure. In all probability, during the first pre-compression tests, crosslinks and polymer chains which transfer most of the force break up. In the next tests (#4 and #5), when the load is applied and the crosslinks as well as chains are broken, only particles (molecules, globules) accommodate the compression force (Fig. 2). Similar rubber structure phenomena were also discussed in (Pouriayevali and Shim, 2012). The pre-compressed behaviour was confirmed in five tests for a strain rate of $1.00\,\mathrm{s}^{-1}$, therefore, in two other cases, each specimen was loaded only four times (the fourth curve was considered as the proper one). From the uniaxial compression test at three quasi-static rates of strain, the engineering stress vs. engineering strain curves were obtained, as presented in Fig. 3.
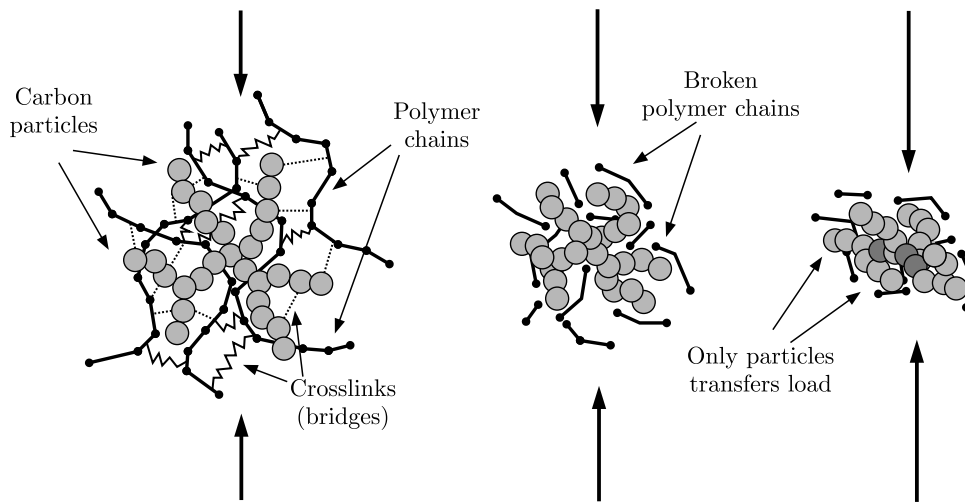


Fig. 2. Likely change of a rubber structure during compression (Pouriayevali and Shim, 2012)
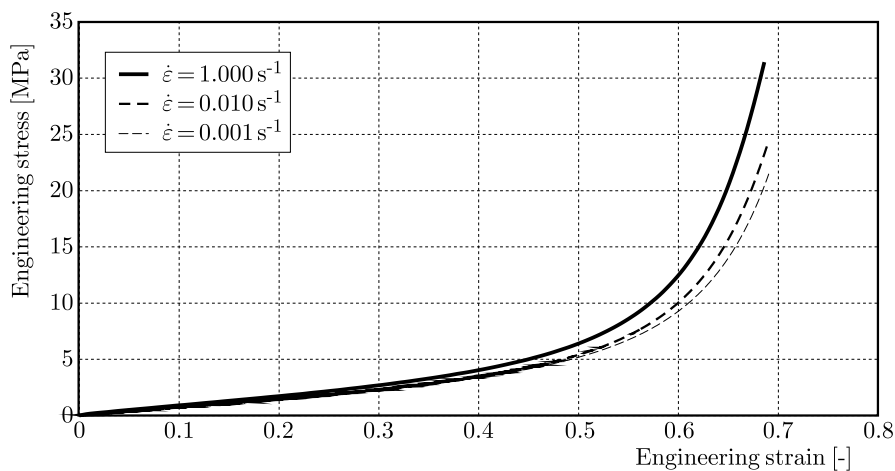


Fig. 3. Average stress-strain curves calculated from the obtained results

The carried out tests revealed a strain rate dependency on the tested rubber material samples, which is clearly visible in Fig. 1. Comparison of the results from papers by Gent (1994),

Pouriayevali and Shim (2012), Sridharan and Sivaramakrishnan (2013), Szurgott *et al.* (2012) confirms the authors' belief that the material mechanical data are correct and provide the basis for a theorem that the investigated material behaviour is different under dynamic loading conditions with various strain rates. In fact, the next Section confirms it.

## 3. Dynamic SHPB tests

### 3.1. Experimental set-up

The rubber testing at higher strain rates was carried out with the use of a classical compression SHPB arrangement (Fig. 4), which consists mainly of a loading device (an air pressure gun), bar components (a striker, input and output bars), a striker velocity measurement system (Micro-Epsilon optoCONTROL1200 with dynamic resolution $50\,\mu$m) and a data acquisition system.
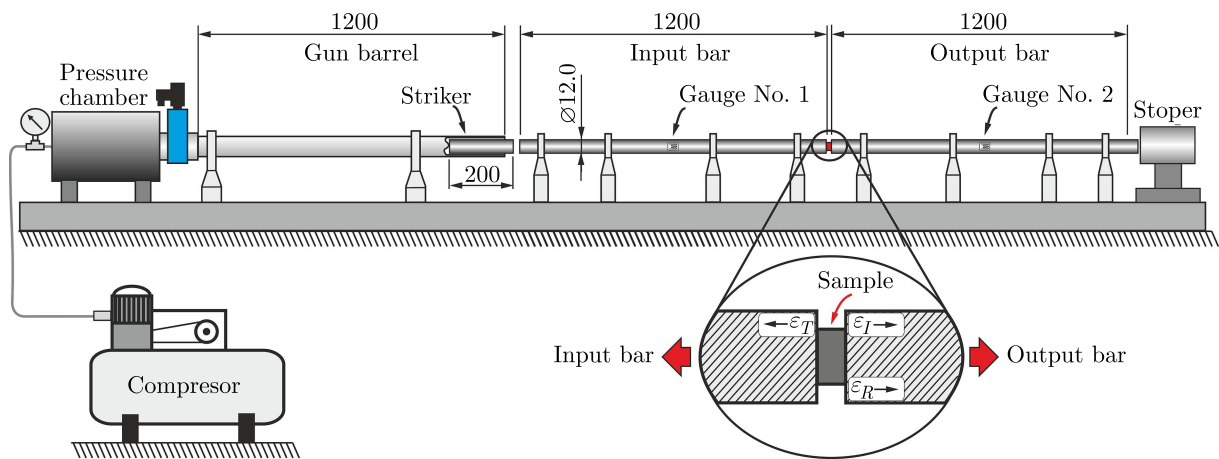


Fig. 4. Scheme of SHPB apparatus used in investigations

The bars were $1200 \pm 0.5$ mm long each, while the striker length was $200 \pm 0.1$ mm. All three bars had the diameter of $12.0$ mm. The input and output bars were supported by four linear bearing stands which were mounted on an optical bench allowing precise alignment of the bars system. For tire rubber testing, low impedance bar materials, i.e. PMMA and Al 7075-T6 were used to avoid large mismatch between the material impedance and the impedance of the soft material tested (Chen *et al.*, 1999, 2000). However, the purpose of using pressure bars made of different materials was to compare the two set-ups and to make recommendations for future SHPB testing of soft materials.

For both bar materials, the wave signals in the incident and transmitted bars were captured using a pair of strain gauges attached symmetrically to the opposite surfaces of the bars and in their middle length. The strain gauges were connected to the opposite legs of the Wheatstone bridge, which was a half bridge configuration. In the other legs of the bridge, the dummy resistors were mounted, the resistance of which matched the strain gauges resistance. Typical electrical strain gauges of 1.6 mm gauge length were used (CEA-13-062UW-350, Vishay Micro Measurements). The amplified signals of the strain gauges were recorded using a signal conditioning unit with frequency band of 1 MHz (SGA-0B V5 Wheatstone bridge with signal conditioning amplifiers, ESA Messtechnik) and a data acquisition system (LeCroy WJ354A high-speed digital oscilloscope).

The raw signals from the strain gauges conditioned with the applied measuring equipment are shown in Fig. 5a for aluminium alloy bars configuration, and in Fig. 5b for PMMA bars

set-up. As it can be observed in these figures, the wave signal profiles recorded in the aluminium alloy bars differ significantly in comparison to profiles in the PMMA bars. In the case of aluminium alloy set-up, the pulse generated by the impact of the striker on the incident bar has a nearly rectangular profile with visible oscillations, called Pochhammer-Chree oscillations, which are a result of geometry dispersion. It is an undesirable effect, which leads to waveform distortion as the wave propagates over a distance. Nonetheless, dispersion effects for the considered aluminum alloy bars configuration is not significant due to the large ratio of the wavelength to bar diameter, and it may be neglected (waveforms of incident and transmitted pulses are consistent). Unfortunately, it cannot be stated for the PMMA bars. In this case, the viscoelastic nature of wave propagation in the PMMA rods is clearly evident by a longer time (due to PMMA damping properties), attenuation (amplitude decreasing) and signals dispersion (waveform changing). Therefore, numerical correction of the wave signals is necessary. In the present paper, the correction procedure of viscoelastic wave signals for PMMA bars was adopted from papers by Bacon (1998), Butt and Zue (2013), Cheng *et al.* (1998), Franz *et al.* (1984), Zhao and Gary (1995) and was discussed in an other paper by Janiszewski *et al.* (2016). Briefly, this procedure was as follows:

- use a proper time window to digitize the wave signal from each strain gauge position,

- apply the FFT to obtain a frequency spectrum for the digitalized wave signals,

- identify the attenuation factor ?n and wave number kn for each frequency component of the wave,

- for a selected position of xc (e.g. front surface of specimen), construct a frequency spectrum for the wave to be corrected or predicted from the measured wave signal,

- use the IFFT algorithm to obtain the corrected or predicted wave signal for the given position.
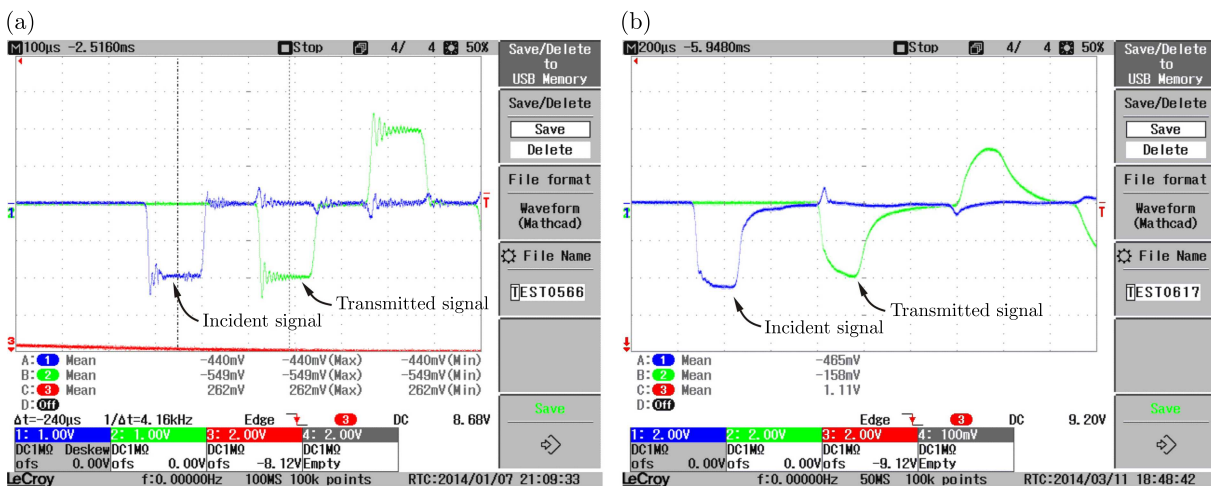


Fig. 5. Raw wave signals measured by strain gauges: (a) incident and reflected signals for aluminium alloy bars; (b) incident and transmitted signals for PMMA bars

To minimalize wave disturbances (oscillations) caused by dispersion and also to control loading conditions to facilitate stress equilibrium in the specimen, pulse shapers were used, i.e. small disks with 4.00 mm in diameter and 0.30 mm in thickness made of polyethylene sheet and 5.56 mm in diameter with 0.30 mm in thickness made of Cu-ETP copper sheet for PMMA and Al 7075-T6 bars configuration, respectively. The wave shapers were placed on the impact end of the input bar with the use of lubricant (molybdenum disulphide – $MoS_2$), which was also added between the specimens and the input and output bars. Application of the wave shapers was revealed especially by an increase in the rise time of incident pulses and smoothing waveform

(Fig. 6). Moreover, the copper pulse shapers applied in the aluminium alloy bar system facilitated constant strain rate deformation in the specimen. One can also noticed that the rise time of the transmitted signal in both cases (PMMA and Al 7075-T6 setups) was longer than the loading time of the incident signals. This was due to the fact that its profile and shape depended on high-strain rate behaviour of the specimen material, whereas properties of incident signal were affected by the shaper (geometry, material) and material of the bars.
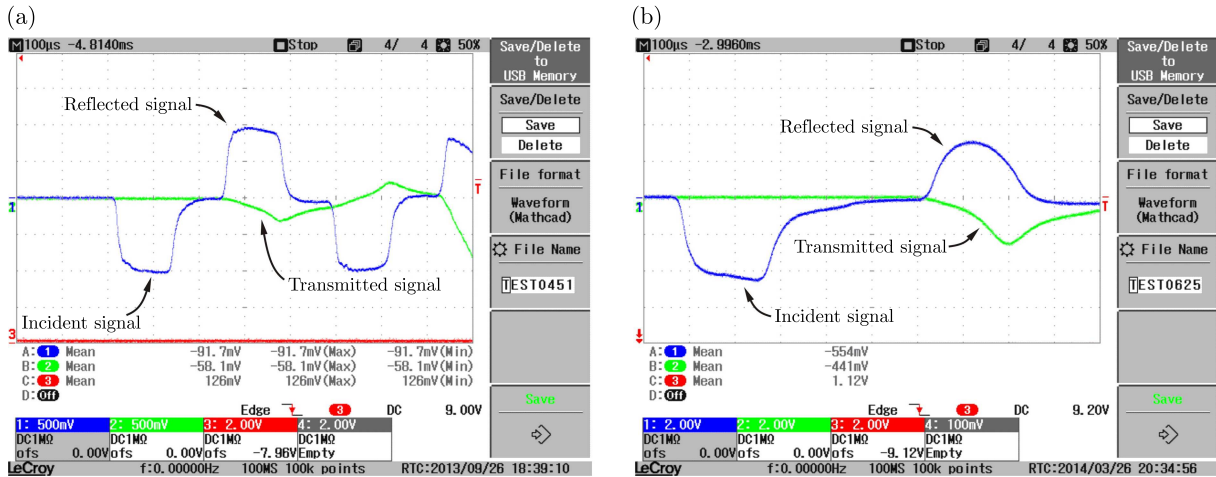


Fig. 6. Raw wave signals measured by strain gauges attached on: (a) aluminium alloy bars, (b) PMMA bars

Geometry of the rubber specimen was chosen experimentally. At the first stage of those works, the initial specimen length was selected to meet the main methodological requirement of SHPB technique, i.e. the requirement of stress uniformity. The low wave velocity in the rubber specimens make stress equilibrium much more difficult to obtain than in a metal sample. Moreover, the problem is complicated by low strength of rubber, which for improperly long specimen makes the amplitude of the transmitted pulse too weak to be precisely measured. For the aluminium alloy bar set-up, special attention was paid to find a proper specimen length, sufficient loading conditions (striker velocity) and suitable signal gain to obtain a required quality of the transmitted signals for which the signal-to-noise ratio was higher than 25 dB. It was observed that for specimens with a thickness greater than 3 mm and for striker velocities less than 5 m/s, the transmitted signal was too weak and had poor quality, although the applied signal gain was relatively high and equal to 500 V/V. It should be mentioned though that the signals recorded by strain gages glued on the PMMA bars were amplified only with gain 200 V/V, giving the voltage amplitude in the order of several volts, whereas for the same signal gain the voltage amplitude recorded from the strain gage attached on the aluminium alloy bars was only in the order of several dozen millivolts, depending on striker velocity.

The initial diameter of the specimen was also chosen for the assumed maximal testing conditions: striker impact velocity of $\sim 15$ m/s, strain level of $\varepsilon \approx 1$. The need to determine the diameter of the sample results from the fact that during dynamic testing, elastomer materials deform very easy with the extremely large strain, causing an "escape" of a certain part of the sample material beyond the bar diameter (see Fig. 7). Therefore, by using a high-speed camera, the deformation process of specimens with various diameters were monitored to assess the correctness of the carried out tests.

Finally, it was assumed that for the comparison purpose, the dimensions of the specimens were the same for both bar systems and were as follows: diameter 6 mm; thickness $\sim 1$ mm (Al 7056-T6) and $\sim 2$ mm (PMMA). Similarly to quasi-static testing, each rubber specimen was pre-compressed dynamically four times, before the final test.
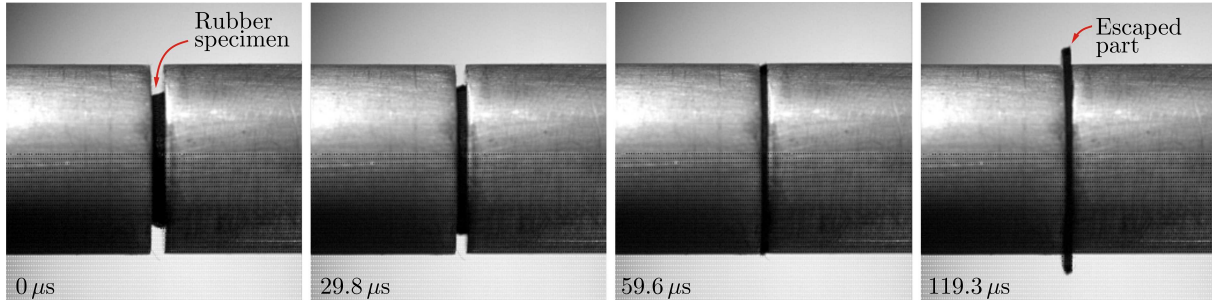
Fig. 7. A sequence of images showing the deformation process of a rubber specimen with diameter 8 mm and length 1.2 mm

## 3.2. Dynamic SHPB tests results

Verification of the rubber testing procedure at high strain rate loading was based on the assessment of the stress equilibrium state in the specimen for both bars configurations. The stress curves in Fig. 8 represent stress conditions on the front $\sigma_1$ and rear $\sigma_2$ (dotted line) ends of the specimens for PMMA and aluminium alloy bars. In each case, the impact velocity of the striker bars and specimen length were comparable, and they were about 6 m/s and 1 mm, respectively. However, the stress equilibrium state was different for each experiment. The specimen tested with the aluminium alloy SHPB deformed initially non-uniformly, and only after 60 μs the stress equilibrium was achieved. In the case of the experiment with the PMMA bars, non-equilibrium of stresses was also observed on the specimen interfaces during the initial stage of deformation; however, the non-equilibrium degree was significantly lower. It is, first of all, a result of differences at the rates of strain. Despite a similar impact velocity and specimen length, the strain rate during the experiment with the aluminium alloy bars was higher ($\dot\varepsilon = 5700\,\mathrm{s}^{-1}$) since the sound speed in aluminium alloy bars was considerably higher ($C_o = 5117\,\mathrm{m/s}$) than in the PMMA bars ($C_o \approx 1900\,\mathrm{m/s}$). Moreover, the rise times of the incident wave for both experiments were very different: 12 μs for the aluminium alloy and 76 μs for the PMMA bars (Fig. 9). As it was mentioned before, a long rise time for PMMA was, on one hand, a result of its damping properties, however, on the other hand, it resulted from application of the wave shaper. It should also be noted that loading duration of the specimen during the PMMA bar experiment was considerably longer ($\approx 290\,\mu\mathrm{s}$), whereas in the other case, it was only 126 μs. It was due to the significant difference between propagation velocity of a viscoelastic wave in the PMMA bar in comparison to the wave velocity in the aluminium alloy bar. Moreover, a constant strain rate was achieved for a relatively long time, as presented in Fig. 10. It should be stated that in the authors' opinion all aforementioned observations are in accordance to the findings by Chen *et al.* (2000), Zhao *et al.* (1997), Roland (2006), Song and Chen (2003) and they also prove the validity of the method used to correct the wave attenuation and dispersion effects.
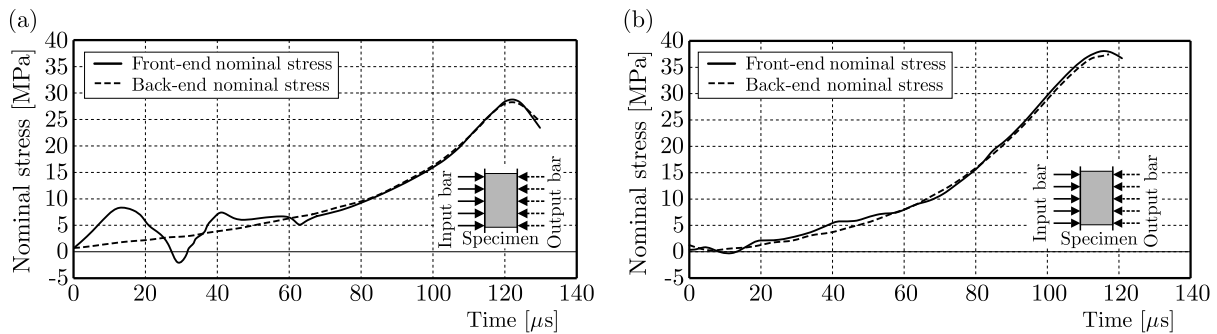


Fig. 8. Comparison of stresses at the front $\sigma_1$ and rear $\sigma_2$ ends of rubber specimens tested with the use of (a) PMMA bars and (b) Al 7075-T6 bars
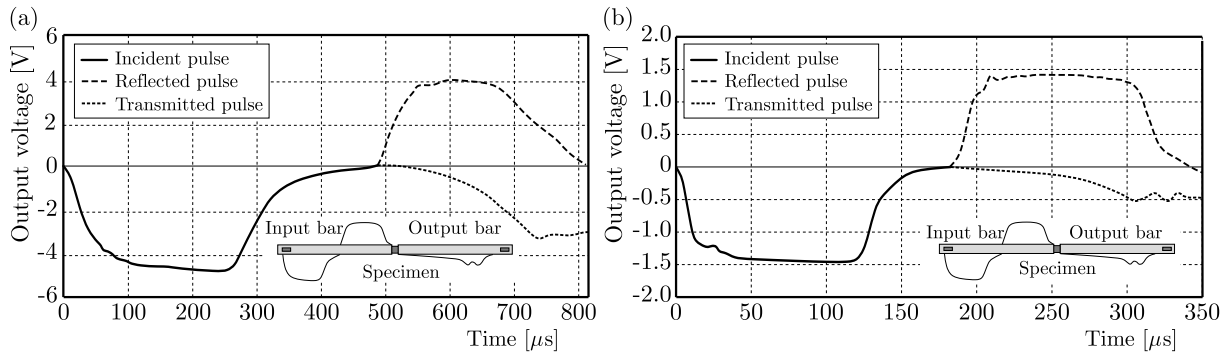
Fig. 9. Incident, transmitted and reflected pulses obtained for (a) PMMA bars and (b) Al 7075-T6 bars
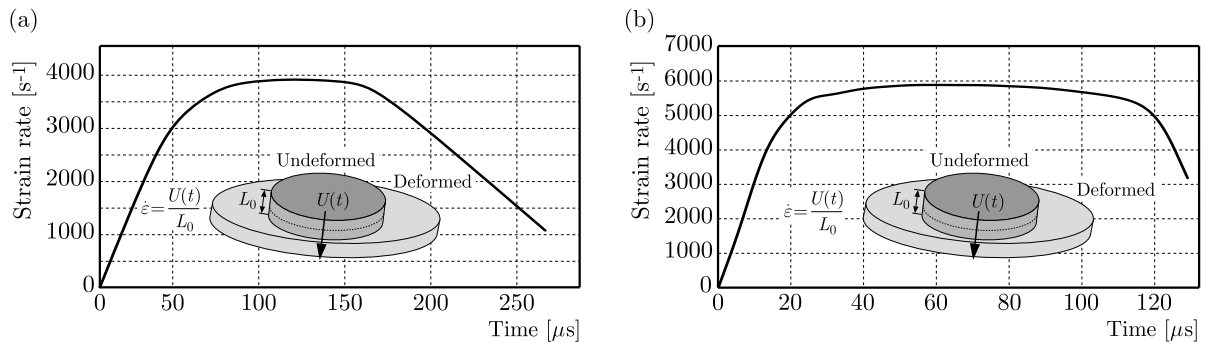


Fig. 10. Strain-rate history in the rubber specimen during SHPB with (a) PMMA bars and
(b) Al 7075-T6 bars

During the quasi-static tests, each specimen was compressed several times. The first four were pre-compression tests, whereas the fifth was the main one whose results were taken into consideration. The same approach was followed in SHPB testing and the analogous results were also obtained. One of the specimens was pre-compressed five times for confirming the phenomenon, while the others were pre-compressed three times and tested only once. In Fig. 11, five engineering stress vs. engineering strain curves for the same specimen are presented for the PMMA (a) and aluminium alloy bars system, while in Fig. 12 chosen curves are collected for the comparison purpose. In turn, the summary characteristics for 5 different strain rates are presented in Fig. 13 for quasi-static and dynamic loading conditions.
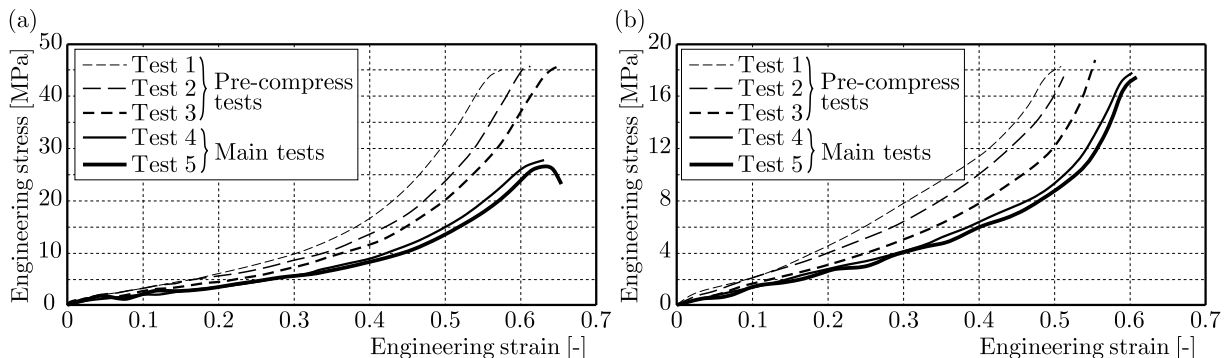


Fig. 11. Stress-strain curves for one specimen with pre-compression in SHPB test with (a) PMMA bars
and (b) Al 7075-T6 bars

Observing the curves shown in Fig. 11, it can be concluded that the mechanical behaviour of the rubber specimen varies significant during pre-compression tests No. 1, 2 and 3. Tests No. 4 and 5 resulted in stress-strain curves with profiles similar to each other, as it was in the case of quasi-static tests. The necessity of performing pre-compression tests is therefore an
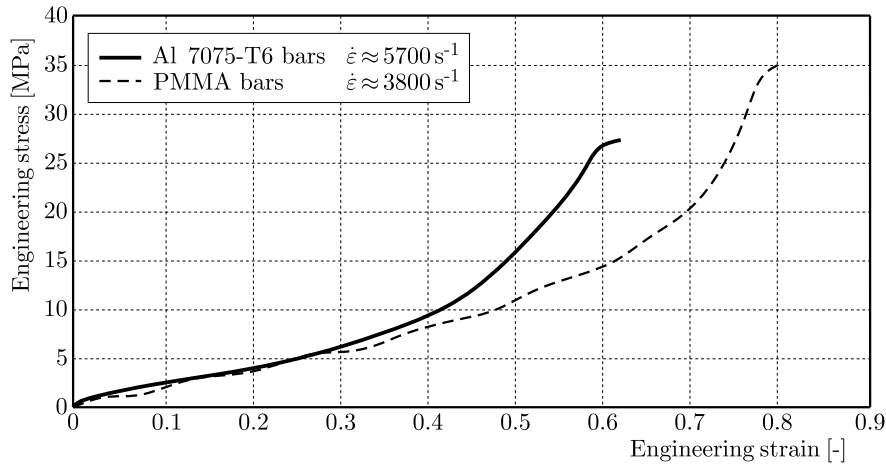
Fig. 12. Engineering stress-strain curves for tested tire rubber samples using SHPB with PMMA and Al 7075-T6 bars
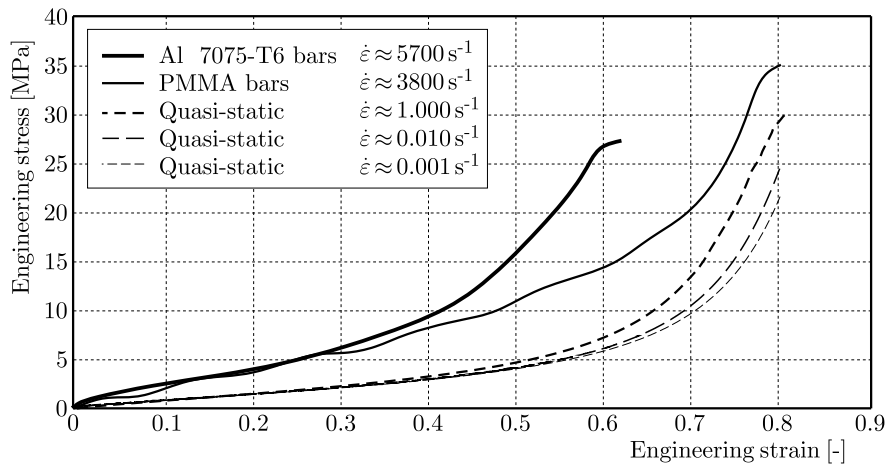


Fig. 13. Summary engineering stress-strain curves for tested rubber material samples

important methodological requirement to achieve valid experimental data from both quasi-static and dynamic tests.

The curves shown in Fig. 12 obtained from the high strain rate experiments suggests that the tested tire rubber is weakly sensitive to the rate of strain. For strains up to 0.3, the stress level is almost the same, despite the fact that experiments were carried out with different strain rates of $3800\,\mathrm{s}^{-1}$ and $5700\,\mathrm{s}^{-1}$, respectively. A difference between the curves appears only after strains larger than 0.3, suggesting high strain rate sensitivity of the tested rubber. It may also be caused by inertia and friction effects which increase the value of flow stress in principle. However, it is commonly known that rubber and other elastomers are sensitive to the rate of strain (Roland, 2006; Song and Chen, 200, 2005; Chen and Song, 2010). A clear evidence of the strain rate sensitivity of the tested rubber is shown in Fig. 13 presenting a combination of quasi-static and dynamic curves obtained during the testing.

## 4. Summary

The procedure of determining correct mechanical characteristics for the tire material with rubber-like parameters has been presented in a comprehensive way. A uniaxial compression test was carried out under quasi static and high strain rate loading conditions. The obtained results provided evidence on the correctness of the applied testing procedures.

During testing, a necessity of performing pre-compression tests to achieve valid experimental data both from quasi-static and dynamic tests was highlighted. Moreover, it was proved that high strain rate testing of soft materials with the use of polymeric bars provided several benefits, such as an increased sensitivity of the experimental setup and reduction of mechanical impedance mismatch. However, the use of polymeric SHPB technique required an additional analysis for data reduction, temperature complications and additional restrictions compared to traditional metallic pressure bars. In addition, some methodical requirements guaranteeing the validity of high strain rate rubber testing were pointed out. Among them:

- use of low impedance Al 7075-T6 and PMMA material for bars to measure a weak signal, omit the problem with impedance mismatch between the specimen and the bars,
- applying proper shaping of the incident pulse guaranting a uniform stress and constant strain rate within a certain duration of loading,
- appropriate selection of specimen dimensions and experimental conditions to meet the stress equilibrium requirement and to minimalize inertial and friction effects.

Soft material testing, especially with the use of SHPB technique, requires knowledge, time and patience in preparing specimens, apparatus or data processing. Nevertheless, obtaining proper results has great importance in the case of simulation of strongly dynamic problems. Some data obtained during the experiments presented in the paper were used in parallel investigations concerning tire modelling (Baranowski *et al.*, 2016a,b).

# References

1. ACKLAND K., ANDERSON C.H., NGO T.D., 2013, Deformation of polyurea-coated steel plates under localised blast loading, *International Journal of Impact Engineering*, **51**, 13-22

2. BACON C., 1998, An experimental method for considering dispersion and attenuation in a viscoelastic Hopkinson bar, *Experimental Mechanics*, **38**, 242-249

3. BARANOWSKI P., MAŁACHOWSKI J., JANISZEWSKI J., WEKEZER J., 2016a, Detailed tyre FE modelling with multistage validation for dynamic analysis, *Materials and Design*, **96**, 68-79

4. BARANOWSKI P., MAŁACHOWSKI J., MAZURKIEWICZ Ł., 2016b, Numerical and experimental testing of vehicle tyre under impulse loading conditions, *International Journal of Mechanical Sciences*, **106**, 346-356

5. BUTT H.S.U, XUE P., 2013, Determination of the wave propagation coefficient of viscoelastic SHPB: Significance for characterization of cellular materials, *International Journal of Impact Engineering*, **74**, 83-91

6. BARANOWSKI P., MALACHOWSKI J., 2015, Numerical study of selected military vehicle chassis subjected to blast loading in terms of tire strength improving, *Bulletin of the Polish Academy of Sciences Technical Sciences*, **3**, 4, 1-12

7. BARANOWSKI P., MAŁACHOWSKI J., NIEZGODA T., 2011, Numerical analysis of vehicle suspension system response subjected to blast wave, *Applied Mechanics Materials*, **82**, 728-733

8. BORKOWSKI W., MOTRYCZ G., 2012, Analysis of IED explosion on carrier road safety, *Journal of KONES and Powertrain Transport*, **19**, 4, 75-82

9. CASEM D.T., FOURNEY W.L., CHANG P., 2003, A polymeric split Hopkinson pressure bar instrumented with velocity gages, *Experimental Mechanics*, **43**, 4, 420-427

10. CHEN W., LU F., ZHOU B., 2000, A quartz-crystal-embedded split Hopkinson pressure bar for soft materials, *Experimental Mechanics*, **40**, 1, 1-6

11. CHEN W., SONG B., 2010, Dynamic characterization of soft materials, *Dynamic Failure of Materials and Structures*, 1-28

12. CHEN W., SONG B., 2011, *Split Hopkinson (Kolsky) Bar, Design, Testing and Applications*, Springer

13. CHEN W., ZHANG B., FORRESTAL M.J., 1999, A split Hopkinson bar technique for low-impedance materials, *Experimental Mechanics*, **39**, 81-85

14. CHENG Z.Q., CRANDALL J.R., PILKEY W.D., 1998, Wave dispersion and attenuation in viscoelastic split Hopkinson pressure bar, *Shock and Vibration*, **5**, 307-315

15. D575-91 AS, 2001, Standard Test Methods for Rubber Properties in Compression, USA

16. DUYLE J.F., 1989, *Wave Propagation in Structures – An FFT-Based Spectral Analysis Methodology*, Springer-Verlag, New York

17. ELLWOOD S., GRIFFITHS L.-J., PARRY D.J., 1982, Materials testing at high constant strain rates, *Journal of Physics Engineering: Scientific Instruments*, **15**, 280-282

18. FRANZ C.E., FOLLANSBEE P.S., BERMAN I., SCHROEDER J.W., 1984, *High Energy Rate Fabrication*, American Society of Mechanical Engineers, New York

19. GENT A.N., 1994, Compression of rubber blocks, *Rubber Chemistry and Technology*, **67**, 549-558

20. GIOVANOLA J.H., 1988, Adiabatic shear banding under pure shear loading: part I, *Mechanics of Materials*, **7**, 59-71

21. GRAY III GT., 2000, ASM Handbook: Mechanical testing and evaluation, [In:] *Materials Park*, Kuhn H., Medlin D. (Edit.), OH: ASM International, 8, 939-1270

22. HELNWEIN P., LIU C.H., MESCHKE G., MANG H.A., 1993, A new 3D finite element model for cord-reinforced rubber composites application to analysis of autobomile tires, *Finite Elements in Analysis and Design*, **4**, 1-16

23. HOPKINSON B., 1904, The effect of momentary stress in metals, *Proceedings of the Royal Society of London*, **74**, 498-507

24. HOPKINSON J., 1872, On the rapture of iron wire by a blow, *Proceedings of the Manchester Literary and Philosophical Society*, **1**, 4-45

25. JANISZEWSKI J., 2012, *Testing of Engineering Materials Under Dynamic Loading Conditions* (in Polish), Military University of Technology, Warsaw

26. JANISZEWSKI J., BUŻANTOWICZ W., BARANOWSKI P., 2016, Correction procedure of wave signals for a viscoelastic split Hopkinson pressure bar, *Problems of Mechatronics: Armament, Aviation, Sefety Engineering*, **7**, 1, 17-30

27. KIM J.H., JEONG H.Y., 2005. A study on the material properties and fatigue life of natural rubber with different carbon blacks, *International Journal of Fatigue*, **27**, 263-272

28. KOLSKY H., 1953, *Stress Waves in Solids*, Oxford University Press, London

29. LINDHOLM U.S., YEAKLEY L.M., 1968, High strain-rate testing: tension and compression, *Experimental Mechanics*, **8**, 1, 1-9

30. MALACHOWSKI J., WESOLOWSKI M., KRASON W., 2007, Computational study of transport aircraft landing gear during touchdown, *Journal of KONES and Powertrain Transport*, **13**, 4, 187-195

31. MEYERS M.A., 1994, *Dynamic Behaviour of Materials*, Johs Wiley and Sons, INC, New York-Chichester-Brisbane-Toronto-Singapoure

32. NAKAJIMA Y., TAKAHASHI F., 2002, Increase of frictional force of rubber block by uniform contact pressure distribution and its application to tire, *Rubber Chemistry and Technology*, **75**, 589-604

33. NICHOLAS T., 1981, Tensile testing of Materials at high rates of strain, *Experimental Mechanics*, **21**, 5, 177-185

34. POURIAYEVALI H., SHIM V.P.W., 2012, A constitutive description of elastomer behaviour at high strain rates – A strain dependent relaxation time approach, *International Journal of Impact Engineering*, **47**, 71-78

35. REID J.D., BOESCH D.A., BIELENBERG R.W., 2007, Detailed tire modeling for crash applications, *International Journal of Crashworthines*, **12**, 5, 521-529

36. ROLAND C.M., 2006, Mechanical behaviour of rubber at high strain rates, *Rubber Chemistry and Technology*, **79**, 429-459

37. ROLAND C.M., FRAGIADAKIS D., GAMACHE R.M., 2010, Elastomer-steel laminate armor, *Composite Structures*, **92**, 1059-1064

38. SAINTIER N., CAILLETAUD G., PIQUES R., 2006, Multiaxial fatigue life prediction for a natural rubber, *International Journal of Fatigue*, **28**, 530-539

39. SONG B., CHEN, W., 2003, One-dimensional dynamic compressive behaviour of EPDM rubber, *Journal of Engineering Materials and Technology*, **125**, 294-301

40. SONG B., CHEN W., 2005, Split Hopkinson pressure bar techniques for characterizing soft materials, *Latin American Journal of Solids and Structures*, **2**, 113-152

41. SRIDHARAN K., SIVARAMAKRISHNAN R., 2013, Compressive and shear analysis of rubber block under large strain, *American Journal of Applied Sciences*, **10**, 7, 681-687

42. SZURGOTT P., GOTOWICKI P., NIEZGODA T., 2012, Numerical analysis of a shaped rail pad under selected static load, *Journal of KONES and Powertrain Transport*, **19**, 1, 407-414

43. WANG L., LABIBES Z., AZARI Z., PLUVINAGE G., 1994, Generalization of split Hopkinson bar technique to use viscoelastic bars, *International Journal of Impact Engineering*, **15**, 669-686

44. ZHAO H., GARY G., 1995, A three dimensional analytical solution of the longitudinal wave propagation in an infinite linear viscoelastic cylindrical bar. Application to experimental techniques, *Journal of the Mechanics and Physics of Solids*, **43**, 8, 1335-1348

45. ZHAO H., GARY G., KLEPACZKO J.R., 1997, On the use of a viscoelastic split Hopkinson pressure bar, *International Journal of Impact Engineering*, **19**, 4, 319-330

46. ZINE A., BENSEDDIQ N., NAIT ABDELAZIZ M., 2006, Rubber fatigue life under multiaxial loading: numerical and experimental investigations, *International Journal of Fatigue*, **33**, 1360-1368

# ANISOTROPIC FRACTURE CRITERION OF TI6AL4V TITANIUM ALLOY UNDER WIDE RANGE OF STRAIN RATES

Wojciech Moćko, Cezary Kostrzewski

*Motor Transport Institute, Warsaw, Poland*

*e-mail: wojciech.mocko@its.waw.pl*

The new fracture criterion taking into account stress triaxiality, strain rate and anisotropy is introduced in this paper. The model is capable to predict the influence of the loading direction on the fracture strain. The equation is applied to estimate the fracture locus of Ti6Al4V titanium alloy under quasi-static and dynamic loading regimes.

*Keywords:* titanium alloys, failure, fracture, anisotropy, Hopkinson bar

## 1. Introduction

In complex structures the fracture behavior depends on the multiaxial stress state which may be defined with the use of the stress triaxiality coefficient. Stress triaxiality is defined as $\eta = -p/q$, where $p$ is the pressure stress and $q$ is the Mises equivalent stress. In the basic approach, the fracture criterion $\overline{\varepsilon}_f$ is independent of the stress triaxiality. However, Johnson and Cook (JC) (1985) introduced a new definition of the fracture criterion as a monotonic function of the stress triaxiality in the following form

$$\overline{\varepsilon}_f = [C_1 + C_2 \exp(C_3 \eta)]\left(1 + C_4 \ln \frac{\dot{\overline{\varepsilon}}^{pl}}{\dot{\varepsilon}_0}\right)(1 + C_5 \widehat{T}) \tag{1.1}$$

where $C_1$, $C_2$ and $C_3$ are material parameters, $C_4$ – strain rate sensitivity, $C_5$ – temperature sensitivity, $\dot{\varepsilon}_0$ – reference strain rate, $\widehat{T}$ – temperature function described in other papers (Johnson and Cook, 1985).

The JC model given by Eq. (1.1) was applied for the analysis of fracture characteristics of OFHC copper, Armco iron, 7075 T-651 aluminium alloy and 4340 steel (Johnson and Cook, 1985). Further studies of Bao and Wierzbicki (BW) (2005) showed that in the case of some materials, like 2024-T351 aluminium alloy, fracture behavior is govern by two mechanisms, i.e. shear bands and voids formation. The BW fracture criterion taking into account both void formation due to tensile loadings and shear failure may be expressed in the following form (Bao and Wierzbicki, 2005)

$$\overline{\varepsilon}_f = \begin{cases} \dfrac{1}{1+3\eta}D_1 + D_2 & \text{for} \quad -1/3 < \eta < 0 \\[2mm] D_3\eta^2 + D_4\eta + D_5 & \text{for} \quad 0 < \eta < 0.4 \\[2mm] D_6 \exp(D_7\eta) & \text{for} \quad 0.4 < \eta < 0.95 \end{cases} \tag{1.2}$$

Comparison between the three mentioned fracture criteria is shown in Fig. 1. The curves present JC model calibrated using data obtained for 2024-T351 alloy (Bao and Wierzbicki, 2005) and BW fracture locus estimated for Ti6Al4V alloy (Giglio *et al.*, 2012). It can be observed that the BW criterion reveals two local minimums, the first corresponding to shear loadings (stress

triaxiality equal to 0) and the second corresponding to pure tensile loadings (stress triaxiality higher than 1). Comparing the JC and BW criteria, it can be stated that for tensile loadings (stress triaxiality higher than 0.4) the fracture strain estimated using both equations gives a comparable predictions, whereas for shear loading conditions the results may be substantially overestimated by the JC fracture model. Depending on the specimen geometry and pre-notch radius, various range of stress traixialities may be obtained (Bao and Wierzbicki, 2004, 2005; Driemeier *et al.*, 2010; Gruben *et al.*, 2011).
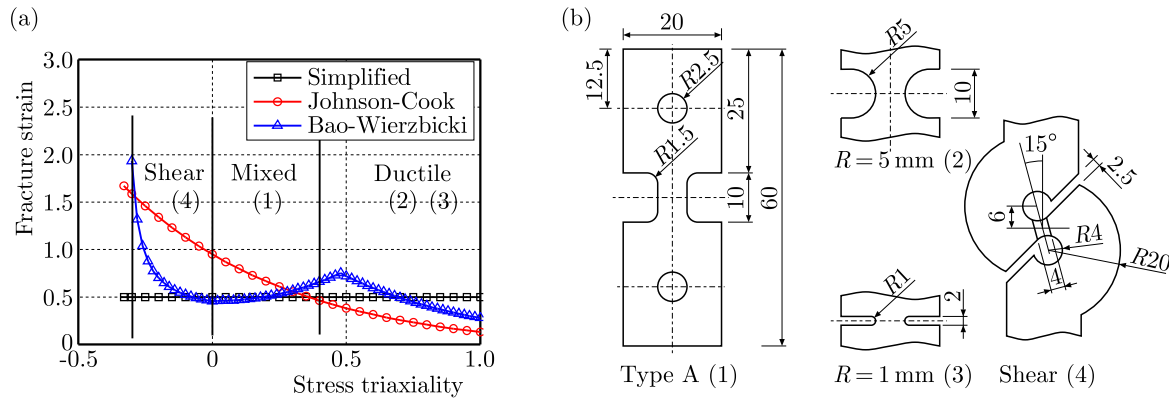


Fig. 1. (a) Comparison of the fracture criterion estimated on the basis of simplified, Johnson and Cook (1985) and Bao-Wierzbicki (2005) theory; (b) specimen geometry and dimensions applied to obtain various stress triaxiality; the number of geometry in figure (b) corresponds to triaxiality marked in figure (a)

Analysis of the ductile fracture locus of Ti6Al4V introduced by Giglio *et al.* (2012) proved that in the case of this grade of the material, the BW fracture criterion, taking into account both tensile and shear failure, must be considered. The results showed some discrepancies between force-elongation curves obtained experimentally and numerically. One of the probable reasons for these differences may be related to material anisotropy, usually observed for the Ti6Al4V titanium alloy, which was not considered in the cited work (Giglio *et al.*, 2012).

Summarizing, the fracture criterion for majority of ductile materials may be expressed in form proposed by Johnson and Cook or Bao and Wierzbicki. However, in the case of materials with texture introduced by the fabrication process, further studies are required to obtain more accurate fracture models. A new approach should take into account especially the influence of the loading direction on the elasto-plastic and fracture behavior. This works extends earlier analysis (Giglio *et al.*, 2012) of Ti6Al4V fracture criterion by introducing investigation of the titanium alloy anisotropy and deformation strain rate on the fracture locus.

## 2.    Experimental methodology

The material was delivered in form of a hot rolled Ti6Al4V titanium alloy sheet of 3 mm thickness. The specimens were cut along three orientations with respect to the rolling direction, that is, RD – along, 45D – 45 degree and TD – transverse to the rolling direction. Notched specimens with gauge length equal to 2 mm, 5 mm and 10 mm were given various stress triaxiality coefficients during tensile test (Fig. 1b). Additionally, shear specimens were designed and fabricated to obtain shear loading conditions (Fig. 1b). The same geometry was applied for both quasi-static and dynamic testing. The specimens were cut using electro-discharge machining (EDM). Tensile tests were carried out at quasi-static and dynamic loading regime using, respectively, with a servo-hydraulic testing machine and split Hopkinson tensile bar (Moćko *et al.*, 2015, 2016). Simultaneously, plastic deformation was recorded and analysed using a digital image correlation

software to determine strain distribution. Stress triaxiality during tensile tests was calculated using FEM simulation. Analysis was carried out using ABAQUS Standard software under quasi-static loading conditions. Digital models of specimens consists of 24554, 13070, 30555 and 10866 mesh elements, respectively, for type A, R1, R5 and shear samples. For geometry of type A, R1 and R5 C3D8R elements were applied, whereas for shear geometry C3D10M elements were used. Values presented in Fig. 2 are an average value calculated from the mesh elements located near the fracture surface.
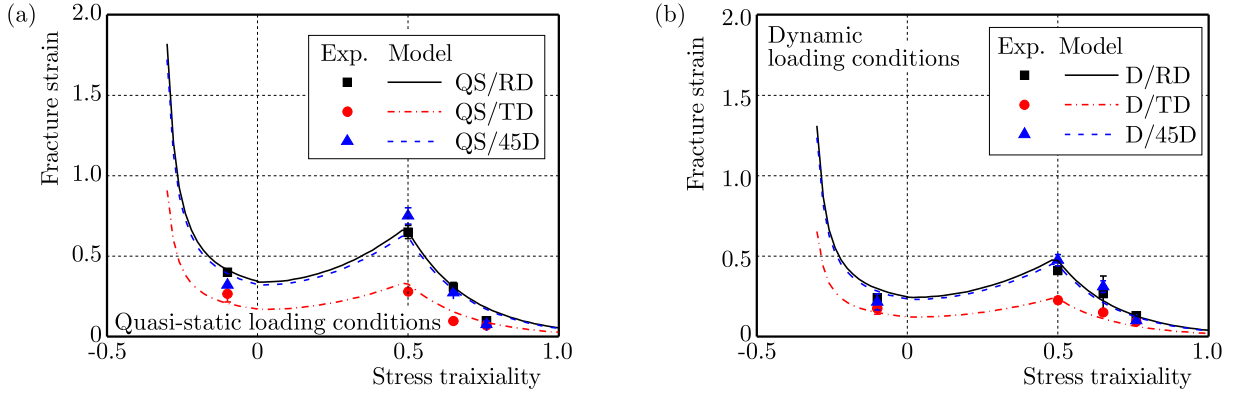


Fig. 2. Comparison of experimental data with predictions of the proposed model at (a) quasi-static and (b) dynamic loading conditions

## 3. Results and discussion

Fracture strain estimated using the digital image correlation method at various stress triaxialities and strain rates is shown in Fig. 2. It can be observed that similarly to the BW model Ti6Al4V titanium alloy loaded at the direction RD and 45D is clear to the observed maximum at the stress triaxiality equal to 0.5. At stress triaxialities higher than 0.5, the void formation mechanism is responsible for the fracture, whereas at stress triaxialities lower than 0.5, the failure of the material is governed by shear band formation or a mixed mechanism. In the case of the loading force transverse (TD) to the rolling direction, the local maximum observed at 0.5 for other orientations is significantly diminished. An other observed phenomenon is the decreasing of the fracture strain with an increase in the strain rate. It may be found that RD and 45D orientations are more sensitive to the strain rate effect than TD orientation.

On the basis of experimental results, a new analytical model, including the strain rate and anisotropic effect, has been developed. It is based on the original model proposed by Bao and Wierzbicki (2005) taking into account only the stress state. In the original BW criterion, the fracture strain is expressed as a function of stress triaxiality

$$\overline{\varepsilon}_f = f(\eta) \tag{3.1}$$

The experimental results show that in the case of a hot rolled titanium alloy sheet, the fracture model should additionally take into account the effect of strain rate $g(\dot{\overline{\varepsilon}}^{pl})$ anisotropy $h(\Theta)$ and temperature $\widehat{T}(T)$ as follows

$$\overline{\varepsilon}_f = f(\eta)g(\dot{\overline{\varepsilon}}^{pl})h(\Theta)\widehat{T}(T) \tag{3.2}$$

The effect of strain rate may be expressed in form introduced by Johnson and Cook (1985)

$$g(\dot{\overline{\varepsilon}}^{pl}) = 1 + A_1 \ln \frac{\dot{\overline{\varepsilon}}^{pl}}{\dot{\varepsilon}_0} \tag{3.3}$$

Anisotropic characteristics of Ti6Al4V titanium alloy are governed by two aspects: firstly, asymmetric geometry of the HCP crystallographic structure and its slipping plane and, secondly, texturing due to cold rolling processing. Results of material anisotropy on the fracture strain may be determined using the following equation

$$h(\Theta) = 1 + B_1 \exp\left(1 - \frac{B_2}{\Theta}\right) \qquad \text{for} \quad \Theta > 0 \tag{3.4}$$

where the loading angle $\Theta$ is estimated as an angle between the rolling direction and the loading force direction.

Finally, the new fracture criterion taking into account stress triaxiality, strain rate and loading direction with respect to rolling directions takes the form

$$\overline{\varepsilon}_f = \begin{cases} \left(\dfrac{1}{1+3\eta}D_1 + D_2\right)\mathcal{A} & \text{for} \quad -\dfrac{1}{3} < \eta < 0 \\[2mm] (D_3\eta^2 + D_4\eta + D_5)\mathcal{A} & \text{for} \quad 0 < \eta < 0.4 \\[2mm] D_6\exp(D_7\eta)\mathcal{A} & \text{for} \quad 0.4 < \eta < 0.95 \end{cases} \tag{3.5}$$

where

$$\mathcal{A} = \left(1 + C_1 \ln\frac{\dot{\overline{\varepsilon}}^{pl}}{\dot{\varepsilon}_0}\right)\left[1 + B_1 \exp\left(1 - \frac{B_2}{\Theta}\right)\right](1 + C_2\widehat{T})$$

In order to calibrate Eq. (3.5), initially coefficients of the BW fracture criterion $D_1$-$D_7$ are estimated using the last square method. Subsequently, the strain rate sensitivity factor C for the alloy loaded in the rolling direction has been determined. In the final stage of calibration the parameters $B_1$ and $B_2$ describing anisotropic properties at quasi-static loading conditions have been calculated. Values of the particular coefficients obtained using the mentioned procedure are shown in Table 1. Comparison between the experimental data and predictions of the new model are presented in Fig. 2. The influence of the anisotropy coefficients $B_1$ and $B_2$ on the fracture strain is shown in Fig. 3. It can be observed that a good agreement between them has been obtained.

**Table 1.** Coefficients of the new fracture criterion

| $B_1$ | $B_2$ | $C$ | $\dot{\varepsilon}_0$ [1/s] | $D_1$ | $D_2$ | $D_3$ | $D_4$ | $D_5$ | $D_6$ | $D_7$ |
|-------|-------|-------|------------------------------|-------|-------|-------|--------|-------|-------|-------|
| 200 | 1.7 | −0.18 | $10^{-4}$ | 0.164 | 0.18 | 1.5 | −0.052 | 0.34 | 8 | −5 |
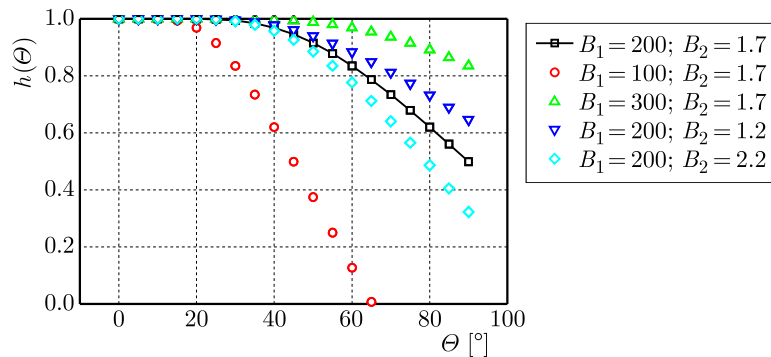


Fig. 3. Influence of the anisotropy coefficients $B_1$ and $B_2$ on the fracture strain

# References

1. BAO Y., WIERZBICKI T., 2004, On fracture locus in the equivalent strain and stress triaxiality space, *International Journal of Mechanical Sciences*, **46**, 81-98

2. BAO Y., WIERZBICKI T., 2005, On the cut-off value of negative triaxiality for fracture, *Engineering Fracture Mechanics*, **72**, 1049–1069

3. DRIEMEIER L., BRÜNIG M., MICHELI G., ALVES M., 2010, Experiments on stress-triaxiality dependence of material behavior of aluminum alloys, *Mechanics of Materials*, **42**, 207-217

4. GIGLIO M., MANES A., VIGAN F., 2012, Ductile fracture locus of Ti-6Al-4V titanium alloy, *International Journal of Mechanical Sciences*, **54**, 121-135

5. GRUBEN G., FAGERHOLT E., HOPPERSTAD O.S., BØRVIK T., 2011, Fracture characteristics of a cold-rolled dual-phase steel, *European Journal of Mechanics A/Solids*, **30**, 204-218

6. JOHNSON G.R., COOK W.H., 1985, Fracture characteristics of three metals subjected to various strains, strain rates, temperatures and pressures, *Engineering Fracture Mechanics*, **21**, 31-48

7. MOĆKO W., BRODECKI A., KRUSZKA L., 2016, Mechanical response of dual phase steel at quasi-static and dynamic tensile loadings after initial fatigue loading, *Mechanics of Materials*, **92**, 18-27

8. MOĆKO W., BRODECKI A., RADZIEJEWSKA J., 2015, Effects of pre-fatigue on the strain localization during tensile tests of DP 500 steel at low and high strain rates, *Journal of Strain Analysis for Engineering Design*, **50**, 571-583

# INFORMATION FOR AUTHORS

***Journal of Theoretical and Applied Mechanics*** (***JTAM***) is devoted to all aspects of solid mechanics, fluid mechanics, thermodynamics and applied problems of structural mechanics, mechatronics, biomechanics and robotics. Both theoretical and experimental papers as well as survey papers can be proposed.

We accept articles in English only. The text of a *JTAM* paper should not exceed **12 pages of standard format A4** (11-point type size, including abstract, figures, tables and references), short communications – **4 pages**.

The material for publication should be sent to the Editorial Office via electronic journal system: http://www.ptmts.org.pl/jtam/index.php/jtam

Papers are accepted for publication after the review process. Blind review model is applied, which means that the reviewers' names are kept confidential to the authors. The final decision on paper acceptance belongs to the Editorial Board.

After qualifying your paper for publication we will require LATEX or TEX or Word document file and figures.

The best preferred form of figures are files obtained by making use of editorial environments employing vector graphics:

- genertaed in CorelDraw (*.cdr), AutoCad and ArchiCad (*.dwg) and Adobe Illustrator (*.ai). We require original fioles saved in the standard format of the given program.

- genertaed by calculation software (e.g. Mathematica) – we need files saved in *.eps or *.pdf formats.

- made in other programs based on vector graphics – we ask for *.eps, *.wmf, *.svg, *.psfiles.

Any figures created without application of vector graphics (scans, photos, bitmaps) are strongly encouraged to be supplied in *.jpg, *.tif, *.png formats with resolution of at least 300 dpi.

## Requirements for paper preparation

Contents of the manuscripts should appear in the following order:

- Title of the paper
- Authors' full name, affiliation and e-mail
- Short abstract (**maximum 100 words**) and 3-5 key words (**1 line**)
- Article text (equations should be numbered separately in each section; each reference should be cited in the text by the last name(s) of the author(s) and the publication year)
- References in alphabetical order. See the following:

  1. Achen S.C., 1989, A new boundary integral equation formulation, *Journal of Applied Mechanics*, **56**, 2, 297-303
  2. Boley B.A., Weiner J.H., 1960, *Theory of Thermal Stresses*, Wiley, New York
  3. Canon W., 1955, Vibrations of heated beams, Ph.D. Thesis, Columbia University, New York
  4. Deresiewicz H., 1958, Solution of the equations of thermoelasticity, *Proceedings of Third U.S. National Congress of Applied Mechanics*, 287-305

- Titles of references originally published not in English, should be translated into English and formulated as follows:

  5. Huber M.T., 1904, Specific work of strain as a measure of material effort (in Polish), *Czasopismo Techniczne*, **XXII**, 3, 80-81

All the data should be reported in **SI units**.

# Contents